OPTICAL TECHNOLOGY
APOLLO EXTENSION SYSTEM
PART I

FINAL TECHNICAL REPORT

VOLUME I
(2 of 2)

Section 1 - Introduction

Section 2 - Experiment Development

GPO PRICE $ _____

CFSTI PRICE(S) $ _____

Hard copy (HC) 4.90

Microfiche (MF) 2.00

ff 653 July 65

CONTRACT NAS 8-20256

FACILITY FORM 602

N67 12055 (ACCESSION NUMBER) — (THRU)

141 (PAGES) — (CODE)

CR-79499 (NASA CR OR TMX OR AD NUMBER) — 14 (CATEGORY)

SPACE DIVISION CHRYSLER CORPORATION

OPTICAL TECHNOLOGY
APOLLO EXTENSION SYSTEM
PART I

FINAL TECHNICAL REPORT

VOLUME I
(2 OF 2)

Section 1 - INTRODUCTION

Section 2 - EXPERIMENT DEVELOPMENT

CONTRACT NAS 8-20256
October 21, 1966

Approved by: William W Kloepfer
William W. Kloepfer
Program Manager

CHRYSLER CORPORATION SPACE DIVISION, MICHOUD ASSEMBLY FACILITY
P. O. BOX 29200, NEW ORLEANS, LA. 70129

2857A-10-21-66

PREFACE

The final report of the Optical Technology Apollo Extension System prepared for NASA/Marshall Space Flight Center under Contract Number NAS8-20256 is presented in three volumes. The study was a team effort by Chrysler Corporation Space Division (prime contractor), Kollsman Instrument Corporation, and Sylvania Electronics Systems.

Volume I contains the introduction, the proposed optical technology experiments, and the discarded experiments. CCSD was responsible for the following experiments:

- 4.13 Comparison of Isolation Techniques.
- 4.14 Interferometer System.
- 4.15 Segmented Optics.

CCSD discarded experiments:

- 5.1 Spectrograph Development.
- 5.2 Baffle Systems Comparison.
- 5.7 Cyrogenic Cooling.
- 5.8 Photo-Electro-Optical Experiment.
- 5.9 Mirror Coating.

SES was responsible for the following experiments:

- 4.1 Optical Heterodyne Detection on Earth.
- 4.2 Optical Heterodyne Detection on the Spacecraft.
- 4.3 Direct Detection Space to Ground.
- 4.4 Communication with 10 Megahertz Bandwidth.
- 4.8 Phase Correlation Measurements.
- 4.9 Pulse Distortions Measurements.

SES discarded experiments:

- 5.3 Atmospheric Absorption Spectroscopy.
- 5.4 Photon-Photon Scattering.

KIC was responsible for the following experiments:

- 4.5 Precision Tracking of a Ground Beacon.
- 4.6 Point Ahead and Space-to-Ground-to-Space Loop Closure.
- 4.7 Transfer Tracking from One Ground Station to Another.
- 4.10 Primary Mirror Figure Test and Correction.
- 4.11 Thin Mirror Nesting Principle and Erection and Alignment of Large Optics in Space.
- 4.12 Fine Guidance.

KIC discarded experiments:

5.5 Remote Manual Optical Alignment.
5.6 Visual Tracking Rating.

Volume II contains systems integration. CCSD prepared the sections on Experiment Grouping (7.0), OTAES Mission Development (10.0) except for Ground Stations Concepts (10.4) which was an SES effort, Supporting Spacecraft Subsystems (11.0), Experiment/Mission Time Phasing (12.0), and Typical OTAES Subsystem Component Summary (13.0). The section on the Stellar Oriented Experiment Group was prepared by CCSD and KIC. The section on the Optical Communication Experiment Group was prepared by SES (8.0 and 8.1) and KIC (8.2, 8.3 and 8.4). Volume III containing the Technology Development Plan was the responsibility of CCSD. Study recommendations appear in the separate summary volume.

The OTAES team gratefully acknowledges the help given by the NASA Ad Hoc working group during the course of this study.

MASTER

TABLE OF CONTENTS

Volume	Title
I	Section I - Introduction Section II - Experiment Development
II	Section III - Systems Integration
III	Section IV - Technology Development Plan

VOLUME I (2 OF 2)*

TABLE OF CONTENTS

Section		Title	Page
II	EXPERIMENTS (Continued)		
	4.8	Phase Correlation Measurements	1-287
	4.9	Pulse Distortion Measurements	1-304
	4.10	Primary Mirror Figure Test and Correction	1-320
	4.11	Thin Mirror Nesting Principle	1-388
	4.12	Fine Guidance	1-427
	4.13	Comparison of Isolation Techniques	1-478
	4.14	Interferometer System	1-611
	4.15	Segmented Optics	1-631
	5.0	Discarded OTAES Experiments	1-650
	5.1	Spectrograph Development	1-650
	5.2	Baffles Comparison	1-653
	5.3	Atmospheric Absorption Apwxreoaxopy	1-661
	5.4	Photon-Photon Scattering	1-667
	5.5	Remote Manual Optical Alignment	1-669
	5.6	Visual Tracking Rating	1-672
	5.7	Cryogenic Cooling	1-675
	5.8	Photo-Electro-Optical Experiment	1-697
	5.9	Mirror Coating	1-709
	6.0	Potential OTAES Experiments	1-719

*See Volume I (1 of 2) for paragraphs 1.0 through 4.7.

PRECEDING PAGE BLANK NOT FILMED.

4.8 PHASE CORRELATION

4.8.1 Summary

Although atmospheric effects on the propagation of electromagnetic waves have been the subject of scientific and engineering interest for hundreds of years, increases in the spectral capabilities, resolution, and sensitivity of available instruments and sensors have revealed gaps in the knowledge of the atmosphere as well as renewed interest in measurements previously attained with great difficulty.

The effects on the transmission of optical frequencies can be determined by a detailed examination of the attenuation and refraction characteristics of the atmosphere. The absorption properties of the atmosphere have yielded much of the information now available. There is still much information to be gained, however, through measurement of refraction effects.

Temporally and spatially random variations in the index of refraction of the atmosphere have limited the performance of optical instruments. Now that optical wavelengths can be applied to communication, tracking, and mensuration, the need for detailed knowledge of these variations has become even more evident. Theoretical knowledge of the effect of these variations on optical wavefronts has progressed to the point where measurements must be made of the physical quantities and their functional relationships. To date, theoretical derivations have been based on correlation or structure functions either assumed a priori or extrapolated from the microwave frequencies in which the presence of water vapor is considerably more significant than at optical frequencies. The few available measurements at optical frequencies have been made with stellar or thermal sources that have such poor temporal coherence that extrapolation to the more coherent laser light applications is of questionable validity.

In this experiment, a technique for measuring the phase variations as functions of time and space, with a highly monochromatic laser source, is proposed (figure 4.8-1). With certain modifications, largely in the ground-based instrumentation, amplitude correlations could also be measured. From these measurements, the limitations on coherent apertures could be determined for ready application in the design of superheterodyne systems and an assessment made of the accuracy of scientific measurements that depend on signal frequency.

To correlate experiment and theory, which usually assumes a plane wave incident on a random medium, it is necessary that the turbulent medium be in the far field of the transmitting antenna. This cannot be done with a transmitting aperture located within the atmosphere. To make such measurements would require a monochromatic light source in orbit and a receiver that samples and correlates two points on a wavefront. To avoid spatial integrating effects, the measurements should be made with a small aperture.

The rather highly developed He-Ne laser is nearly monochromatic at the wavelength of 0.6328 microns. Since its output power is limited, a 1.0-meter transmitting aperture that calls for pointing and stabilization to about 0.023 arc second is required. In addition to this highly stable transmitting platform, there must be developed a ground-based interferometer that will permit these measurements to be made with aperture separations from a minimum of 2 centimeters to a maximum of several meters. Several forms of such an interferometer could be built; but the principal problems (namely stabilization and pointing of the ground-based instrument) will be common to any instrument designed to make these measurements. The choice of instrument will depend on the technical and economical solutions to these basic problems.

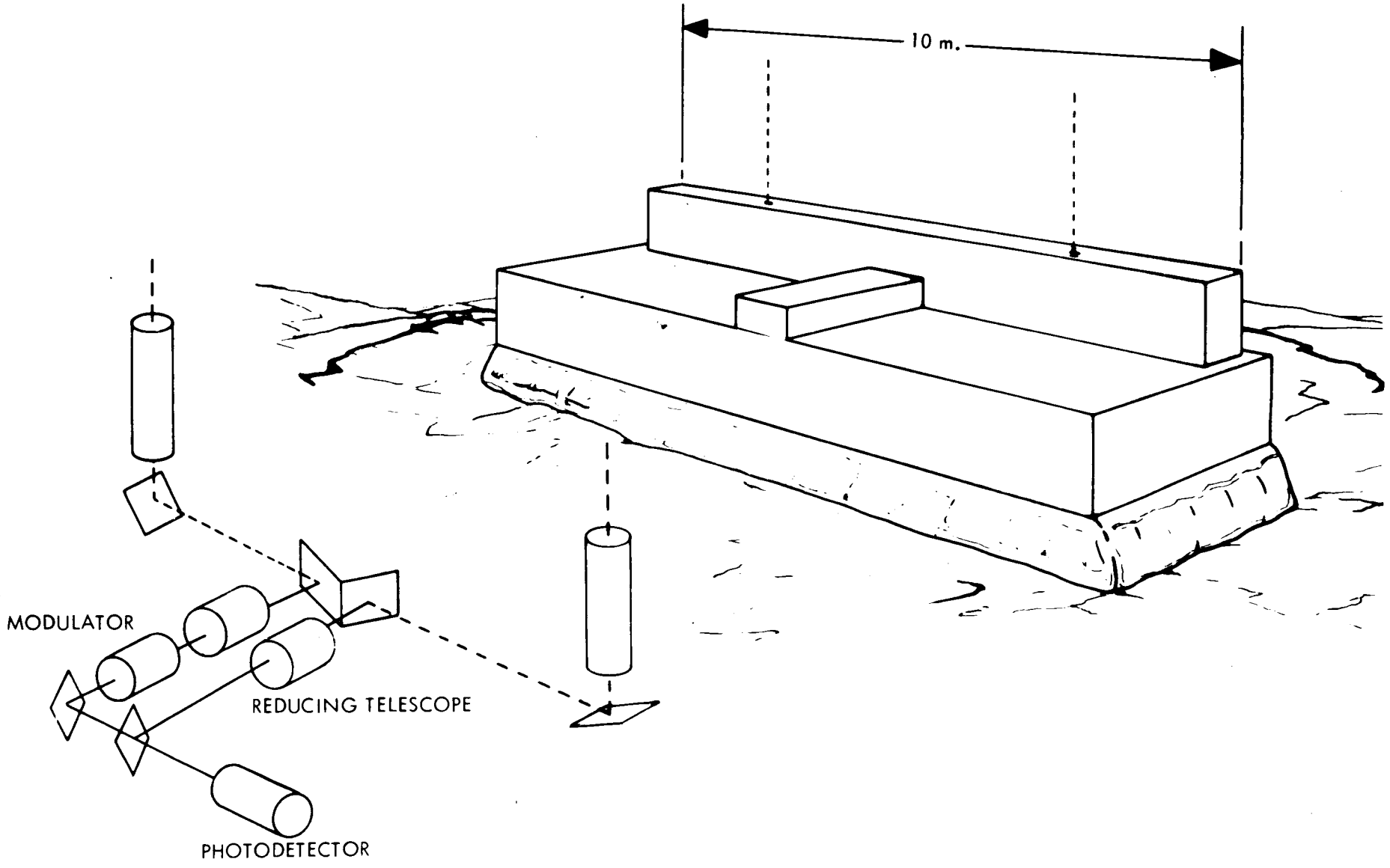


Figure 4.8-1. Phase Correlation Instrumentation

4.8.2 Experiment Objective

The object of this experiment is to measure the phase and amplitude perturbations imposed by the time varying atmosphere on a signal transmitted at optical frequencies, and to determine the correlation in the phase front of two points as a function of their separation. Amplitude correlations should also be measured.

4.8.3 Experiment Justification

4.8.3.1 Contribution And Need

It is anticipated that certain types of communications and scientific measurements will be conducted at optical frequencies from space to ground. In order to design optimum signal waveforms for communications, or in order to assess the accuracy of any scientific measurements that depend on precise signal frequency or amplitude it will be necessary to have an accurate measurement of the perturbations of the phase path and amplitude variations imposed by transmission through the Earth's atmosphere. Because the frequency deviations due to the atmosphere are of the same order of magnitude as those due to instability in the laser oscillator itself, it is important to measure these deviations as independent of the laser instabilities as is possible. Such measurements must be made in quantity to provide experimental data required for testing present theoretical treatments of the transmission of optical frequencies through the atmosphere.

In spite of the foreseeable difficulties in instrumentation it is felt that the important contribution that these measurements could make to the theory of atmospheric perturbations as well as to the practical design of optical instrumentation make such an experiment an important part of an OTAES.

4.8.3.2 Need For Space Testing

The information to be obtained by these measurements is required to interpret optical frequency signals measured after transmission through the entire atmosphere. Because the atmosphere is neither homogeneous nor isotropic, and because the applicable theory depends on the statistical properties of physical parameters, it is necessary that the measurements be made along actual transmission paths through the entire atmosphere. The few measurements made to date have been over relatively short, nearly horizontal paths that can not be considered representative of an actual space-to-ground transmission path. Present knowledge of the atmosphere does not permit accurate estimates to be extrapolated from measurements made along these horizontal paths. Many of the available measurements are of questionable validity because the effects of laser instabilities have not been removed.

Perhaps the most important consideration is that theoretical treatments of the passage of an electromagnetic wave through a random medium are often based on the assumption of a plane wave incident upon the medium. The assumption of a plane wave is valid only in the Fraunhofer or far-field region, defined[1] as

$$R_f \geq \frac{2D^2}{\lambda}$$

---

(1) Merrill I. Skolnik, "Introduction to Radar Systems," McGraw-Hill, (New York, 1962), p. 264.

R_f = minimum far-field distance
D = Diameter of transmitter aperture
λ = wavelength

It is apparent that at optical frequencies the transmitter must be placed at large distances (compared to those that apply at microwave frequencies) to be operating in the Fraunhofer region. In figure 4.8-2 the required altitude of a transmitter for the horizontal path shown is plotted as a function of aperture diameter, neglecting refraction. For apertures greater than 0.6 meters, spaceborne platforms are indicated. Specifically, a 1-meter aperture requires a range in the order of 900 Km.

Some research is being conducted into the application of near field measurements of relatively simple antennas to far field effects at microwave frequencies. Little has been done however at optical frequencies where the computations will probably be more complex because of a small optical aperture being a large number of wavelengths.

In principle, the measurements proposed could be made on stellar sources. However, the actual measuring must be made with a reasonable signal-to-noise ratio. The accuracy of measurement is further improved by the use of highly monochromatic light. Measurements on starlight as well as ground-based measurements of laser light have shown a dependency on the distance to the receiver as well as to the transmitter of the disturbing elements of the atmosphere. It seems, therefore, that the use of a satellite-borne retroreflector would introduce up-link effects that would be difficult, if not impossible, to separate from the down-link effects. Measurements made under these conditions would not be applicable to either up- or down-link optical systems design. As is shown in the feasibility considerations, a spaceborne laser seems to be the only practical device within the present state of technology.

4.8.3.3 Feasibility

Short term relative stabilities of a laser oscillator in the order of 3×10^{-9} have been reported(2). Theoretical studies(3) have also shown that the line broadening due to molecular scattering effects in the atmosphere is also in the order of 10^{-9}. In addition to the above effects, refractive index inhomogeneities moving relative to the receiving aperture will cause amplitude and angle modulation as well as undesirable image motion effects. Angular deviations of the phase front of the order of 1 to 3 seconds of arc have been observed in small apertures. If these deviations occur in 0.1 to 0.3 seconds with a 2-cm aperture, a phase shift, changing linearly across the aperture at about 1 to 2 cycles per second, is indicated.

The greatest instrumentation difficulties lie in the mechanical design of the rigid optics required. Random differences in the optical path following the initial sampling aperture are undesirable. The longer these paths are made the greater the chance for error. Processing of the data is simplified if two apertures can be separated enough to assure complete decorrelation between the two paths. At low altitudes this may be of the order of meters, but at higher altitudes separation of several meters may be required. It would probably be necessary to have evacuated optical paths to assure high accuracy. The

(2) R. Targ and W. D. Bush, "Automatic Frequency Control of a Laser Local Oscillator for Heterodyne Detection of Microwave-Modulated Light," Applied Optics, Vol. 4, No. 12, Dec. 1965.

(3) A. Consortini, L. Ronchi, A. M. Scheggi, and O. Toraldo di Francia, "Deterioration of the Coherence Properties of a Laser Beam by Atmospheric Turbulence and Molecular Scattering," Radio Science, Vol. 1, No. 4, April 1966.

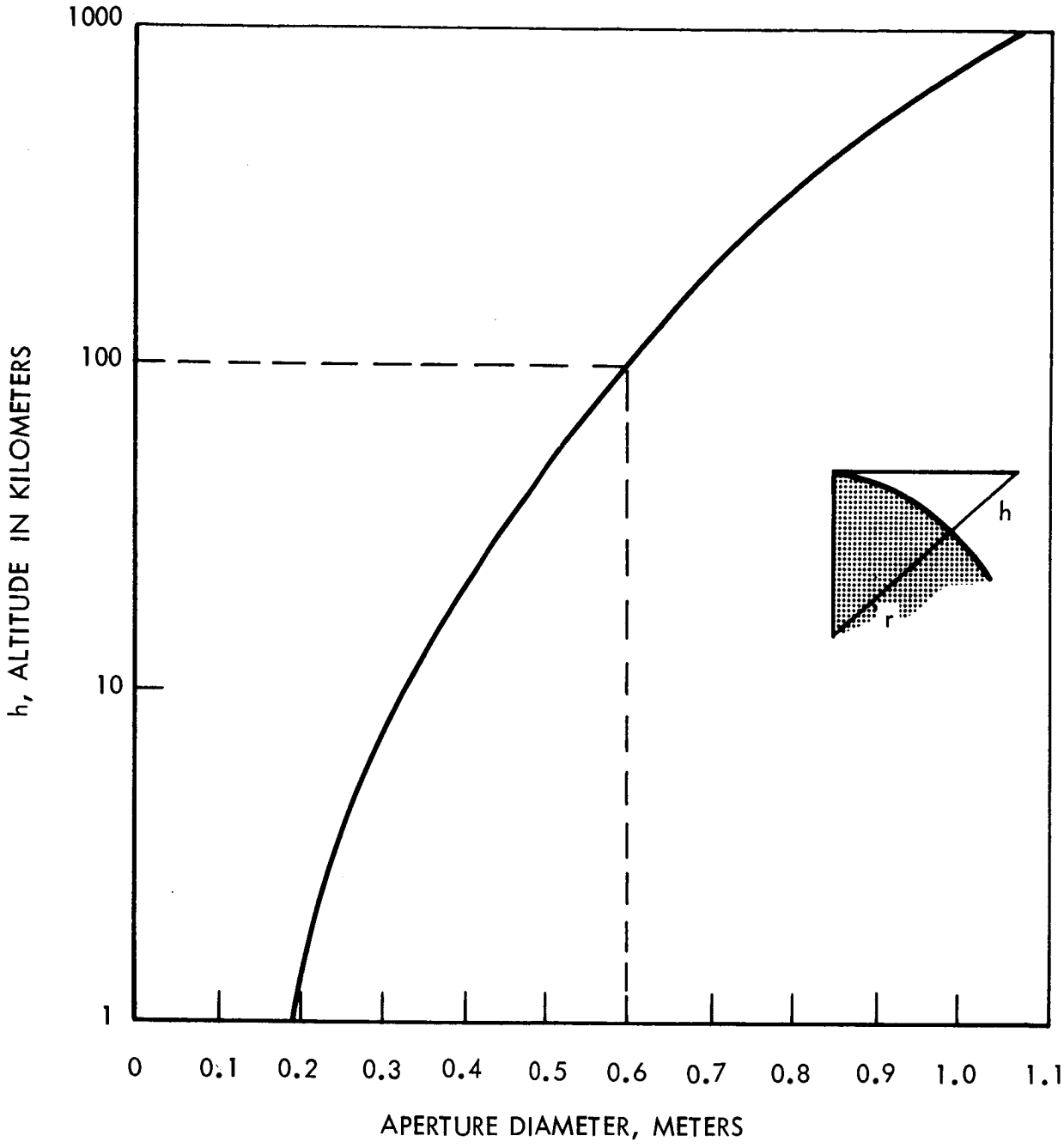


Figure 4.8-2. Transmitter Altitude Required for Far-Field Measurements at 0.6328 μ, Horizontal Path.

other important calibration point is at minimum separation. As the optical train is made more rigid, the difficulties of obtaining a minimum separation will probably increase. It is well to note that the implementation difficulties are entirely ground-based.

Although preliminary calculations have been made for a wavelength of 0.6328 micron, it would be desirable to make the same measurements at other frequencies. However, the use at other frequencies will require the design of refractive optics that cannot be considered state-of-the-art, e.g., modulators at 10.6 microns.

4.8.4 Implementation

4.8.4.1 Experiment Design

Obviously, knowledge of these perturbations due to the atmosphere is important in the design of future systems operating at the optical frequencies. They are, however, of the same order of magnitude or perhaps smaller than the perturbations due to frequency instability in the laser itself, and hence must be measured in such a manner that the laser instabilities are removed, or reduced in effect.

A possible method of measuring atmospheric perturbations that minimize the effect of laser instabilities is shown in figure 4.8-3.

Two small apertures of diameter D are capable of being separated a distance ρ, which can vary from D to a distance large enough to assure that the phase perturbations at aperture 1 are uncorrelated with those at aperture 2. The operation of the instrument is as follows. Nearly monochromatic light from a spaceborn laser is collected by the two apertures 1,2. The signals at time t, denoted by the subscript at the two apertures, can be denoted by

$$A_1 \cos\omega (t - \tau_1) + \delta_{t - \tau_1}$$

$$A_2 \cos\omega (t - \tau_2) + \delta_{t - \tau_2} \quad ,$$

where A_1 is the amplitude, ω the radian frequency, τ_i is the transit time from the source to the indicated aperture and δ is a phase angle that is due to instability in the laser. Assume for the rest of this discussion that the phase delays in both arms of the instrument are equal so that time t can be the time when the delays are compared at any time in the system. The signal in arm 1 will be attenuated, and fall on the surface of the photomultiplier with a different amplitude, say

$$a_1 \cos\left[\omega(t - \tau_1) + \delta_{t - \tau_1}\right] \quad .$$

The signal in arm 2 will be given an additional modulation $\omega_m (\omega_m << \omega)$ to aid in further processing of the signal, so that the signal in this arm becomes

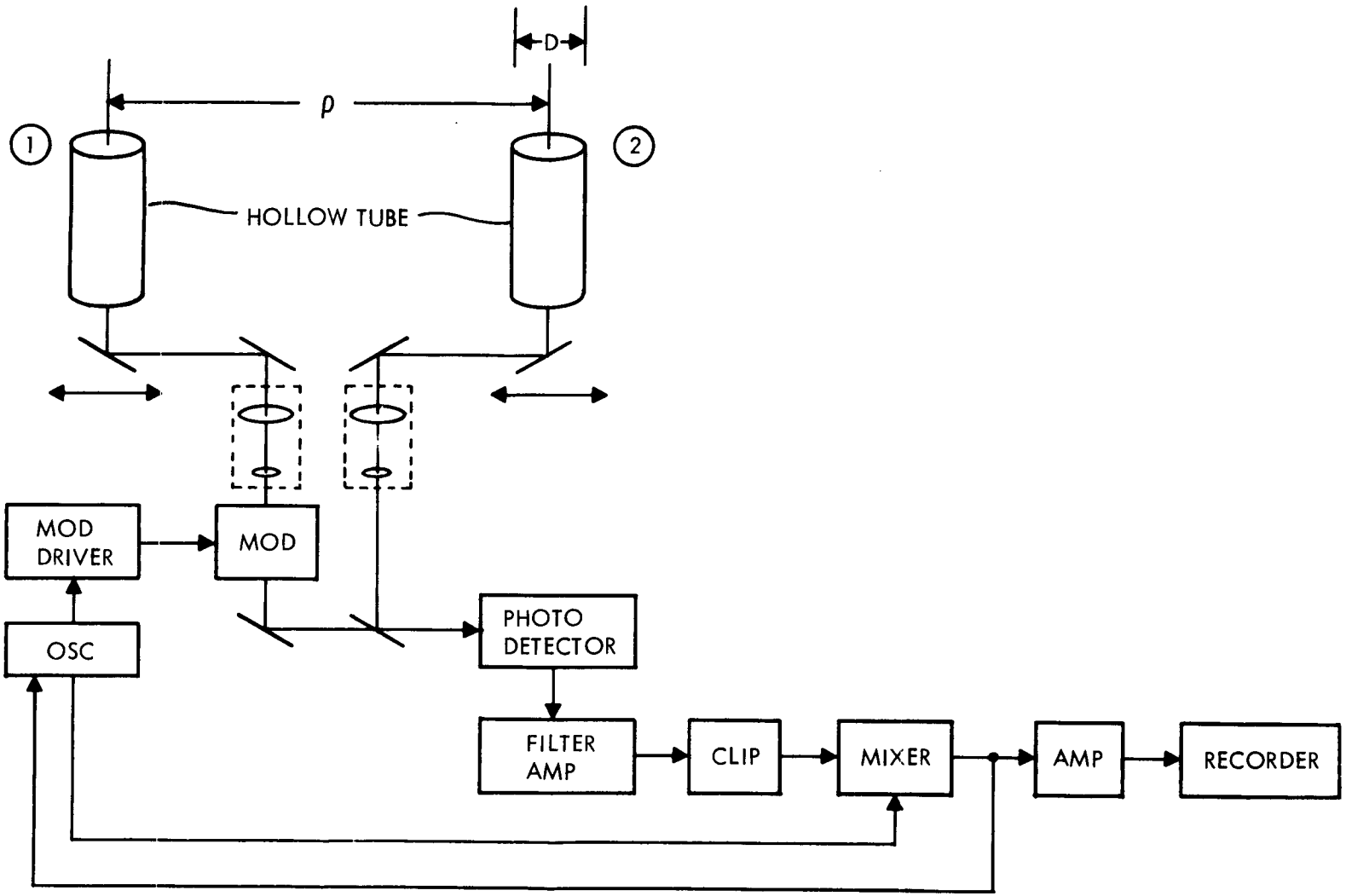


Figure 4.8-3. Atmospheric Measurement, Phase Correlation

$$a_2 \cos \left[\omega(t - \tau_1) + \omega_m t + \delta_{t - \tau_1} \right] .$$

The square law action of the photomultiplier will mix the two signals, resulting in a dc term, higher frequency terms (which are assumed attenuated by the circuits following), and the difference frequency term, which is of interest. This term is

$$K \cos \left[\omega_m t + \omega(\tau_1 - \tau_2) + \delta_{t - \tau_1} - \delta_{t - \tau_2} \right] . \qquad (1)$$

Now if $\tau_1 - \tau_2$ is constant, the output of the filter following the photomultiply will be at a constant frequency ω_m. If $\tau_1 - \tau_2$ is time varying, however, an angle modulation will result.

First, consider the relative value of the laser instability. Since τ_1 and τ_2 are travel times over very nearly the same path, they will not differ appreciably so that to a very good approximation:

$$\delta_{t - \tau_1} = \delta_{t - \tau_2} + \dot{\delta}_{t - \tau_2} (\tau_1 - \tau_2) ,$$

where the dot indicates the derivative with respect to time. Eq. (1) then becomes

$$K \cos \left[\omega_m t + (\omega + \dot{\delta}_{t - \tau_2}) (\tau_1 - \tau_2) \right] , \qquad (2)$$

where ω is the optical frequency and $\dot{\delta}$ is the instantaneous drift frequency.

A spaceborn laser may have $\dot{\delta}$ as great as 3×10^8 Hz. However, compared to the optical frequency of 5×10^{14}, $\delta << \omega$, and can be safely ignored, so that the signal of interest is

$$K \cos \left[\omega_m t + \omega(\tau_1 - \tau_2) \right] .$$

If this signal is passed through a phase shift discriminator centered at ω_m, the input to the recorder will be a signal proportional to the

$$\omega\tau_1 - \omega\tau_1 = \psi_1 - \psi_2,$$

where $\psi_1 - \psi_2$ is the difference in phase (averaged over the small aperture) at two points separated by a distance ρ. With proper design, phase shifts occurring at frequencies as high as 100 Hz. should be recorded. From this record of transit time delay, further pro-

cessing will provide the following information. First, squaring and averaging

$$\overline{(\tau_1 - \tau_2)^2} = \overline{\tau_1^2} + \overline{\tau_2^2} - \overline{2\tau_1\tau_2} \quad .$$

In that part of the record taken where ρ is large, $\tau_1\tau_2 = 0$, and assuming that

$$\overline{\tau_1^2} = \overline{\tau_2^2} \quad , \quad \text{then} \quad \overline{(\tau_1 - \tau_2)^2} = \overline{2\tau_i^2} \quad ,$$

so that the variance in transit time can be determined directly. Having found $\overline{\tau_i^2}$, at other portions of the record where ρ is shorter, the correlation in transit times as a function of ρ can be found from

$$\overline{\tau_1\tau_2} = \overline{\tau_i^2} - \frac{\overline{(\tau_1 - \tau_2)^2}}{2} \quad .$$

It has been shown that it is possible in principle to measure the phase difference along a wave front between two points separated by a distance ρ. If the two sampling apertures are exactly perpendicular to the line between the source and the center of the interferometer arm, the phase difference is caused by the path differences encountered by the light as it travels from the source to the receiving apertures. In the practical case, the arms of the interferometer cannot be aligned exactly. It is important to consider the effects of misalignment of the phase front as well as of the motion of the satellite relative to the apertures of the interferometer.

Although theoretical treatments are available in the literature, a quick appreciation of the magnitudes of phase front distortions involved can be obtained from the following considerations. As shown in figure 4.8-4, a distorted wavefront will have random displacements that will appear as a phase perturbation to any aperture parallel to the "average" phase front. For a sufficiently small aperture, the entire wave front will arrive at an angle θ, which will cause motion of the entire image in focal plane of the lens L. From measurements made by astronomers, θ has been found to be up to 3 arc seconds ($\approx 15 \times 10^{-6}$ radians) with the wave front correlated up to a distance of 6 inches (15 cm) or more, under conditions of great image motion.

With these numbers assumed, a short calculation shows that the phase pertubation at any point:

$$\frac{2\pi\rho\theta}{\lambda} = \frac{2\pi(0.15)\,15 \times 10^{-6}}{0.6328 \times 10^{-6}} \quad 2\pi(3.5) \text{ radians},$$

which is greater than an optical wavelength. The phase difference measuring instrumentation must be capable of measuring and recording phase differences of greater than a wave-

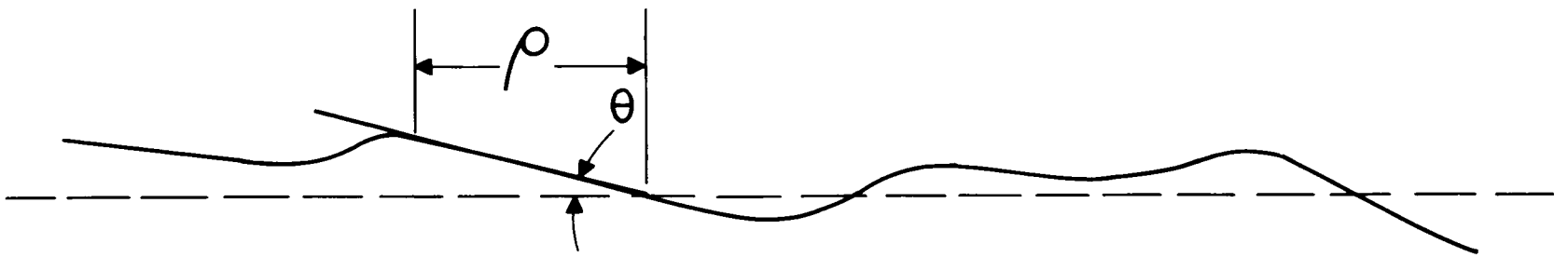


Figure 4.8-4. Distortion of Wave Front

length. Because these phase jumps can occur in $\frac{1}{10}$ second intervals or less, frequency shifts of greater than 30 cycles per second can be expected under rather ordinary conditions.

Because it is desirable to have the two apertures parallel to the average wavefront, the technique of tracking the source in angle was examined. Assuming that it was desirable to keep the tracking noise down to say $\frac{1}{10}$ of the expected phase deviation to be measured, this would require, for a 1-meter interferometer, a tracking accuracy of better than 0.25 micro-radians ($\approx \frac{1}{20}$ sec), which is nearly the goal for the OTAES, and does not seem to be a reasonable objective for ground based instrumentation unless absolutely required.

Another possible source of noise is that due to seismic activity. Observations have been made of the amplitude of seismic waves[4] of $\frac{1}{2}$ to 1 micron with periods of 0.01 to 0.05 second during which intervals of high activity (winter months) with larger amplitudes for longer period waves. During microseismic storms the amplitudes can be much greater. It is estimated that the effects of these disturbances can be minimized in the design of the instruments.

Noise due to wind buffeting could also be a problem. Isolation from seismic noise will introduce a degree of flexibility that must be protected from the wind. Structures designed to reduce wind effects will serve as thermal sources, as well as wind deflectors, the effects of which must be considered in interpretation of the recorded data. Careful design is required to minimize turbulence due to the protective structure.

In addition to the random noise sources that will cause random errors in the measurement of the phase difference between the two apertures, there will be a bias component due to the motion of the source relative to the interferometer. A synchronous satellite in a 24-hour circular orbit inclined 20° to the equator could have an angular rotation relative to an interferometer; this represents a frequency difference of $\approx$16 cps, which would be changing relatively slowly. Measurements made at this point in the orbit with a 3° field of view could cover an interval on the order of an hour or so. Subsequent processing of data containing this nearly steady frequency component should permit separation of the random phase errors from the steady components.

As previously discussed, expected phase variations can be several wavelengths. For a 1-meter baseline, an alignment to within microradians (at visible wavelength) would be required if the instrument were to be held parallel to the average wavefront. Wavefronts arriving at an angle will be delayed at the more distant aperture. However, assuming that the instrument is within $3^{\circ}(\approx \frac{1}{20}$ radian), the time delay (seconds per meter baseline length) is $\frac{1}{20\,C}$, where C is the velocity of light. For a 6-meter baseline, the delay is 10^{-9} seconds, which is two to three orders of magnitude smaller than the period of the highest frequencies expected. Although this represents a phase delay of many optical wavelengths, the phase disturbances will occur over intervals usually greater than 10^{-3} seconds, and hence should be measureable. Misalignment to the wavefront of large angles could introduce time delays greater than desired as well as reduce the base line separation by the cosine of the angular deviation.

As a result of the above considerations, it is concluded that the phase correlation measurements should be made without the aid of optical tracking because the tracking noise

(4) Handbook of Geophysics, p. 12, 49-50.

introduced is of the same order of magnitude as the effects being measured. A fixed interferometer of the type described, oriented within a few degrees of the average wavefront and properly protected from the wind and seismic disturbances, seems within the current capability of optical technology.

The associated phase difference measuring circuitry is considered within current technology although additional study is required to determine optimum circuit parameters. Little information is presently available on the power spectrum of phase variations, but variations at 100 cps or perhaps even 1000 cps rates should be measured.

Calculations of the possible signal-to-noise ratios obtainable must depend on more detailed design. However, if it is assumed that a diffraction-limited aperture 1 meter in diameter is available on the spacecraft, a transmitted power of 1 milliwatt at 0.6328 micron will provide approximately 10^9 photons/sec/cm^2, which is equivalent to the visible light from a -7.5 magnitude star (10^6 photons/sec/cms^2 being the equivalent of a 0 magnitude star). This is roughly 3 magnitudes above that of the planet Venus, which can often be seen in daylight. Narrow band optical filters will further reduce the background noise.

Amplitude correlations can also be measured with essentially the same equipment by transmitting pulses with the mode-locked laser. The FM modulator would be removed from one arm of the interferometer and be replaced by a delay line (an additional 0.3 to 0.5 meter optical path). Pulses received simultaneously at the instrument aperture would arrive at the photo detector in sequence. After amplification, the pulses could be recorded or displayed. Because of the very high pulse repetition rates a large number of pulses could be integrated before appreciable amplitude changes occurred.

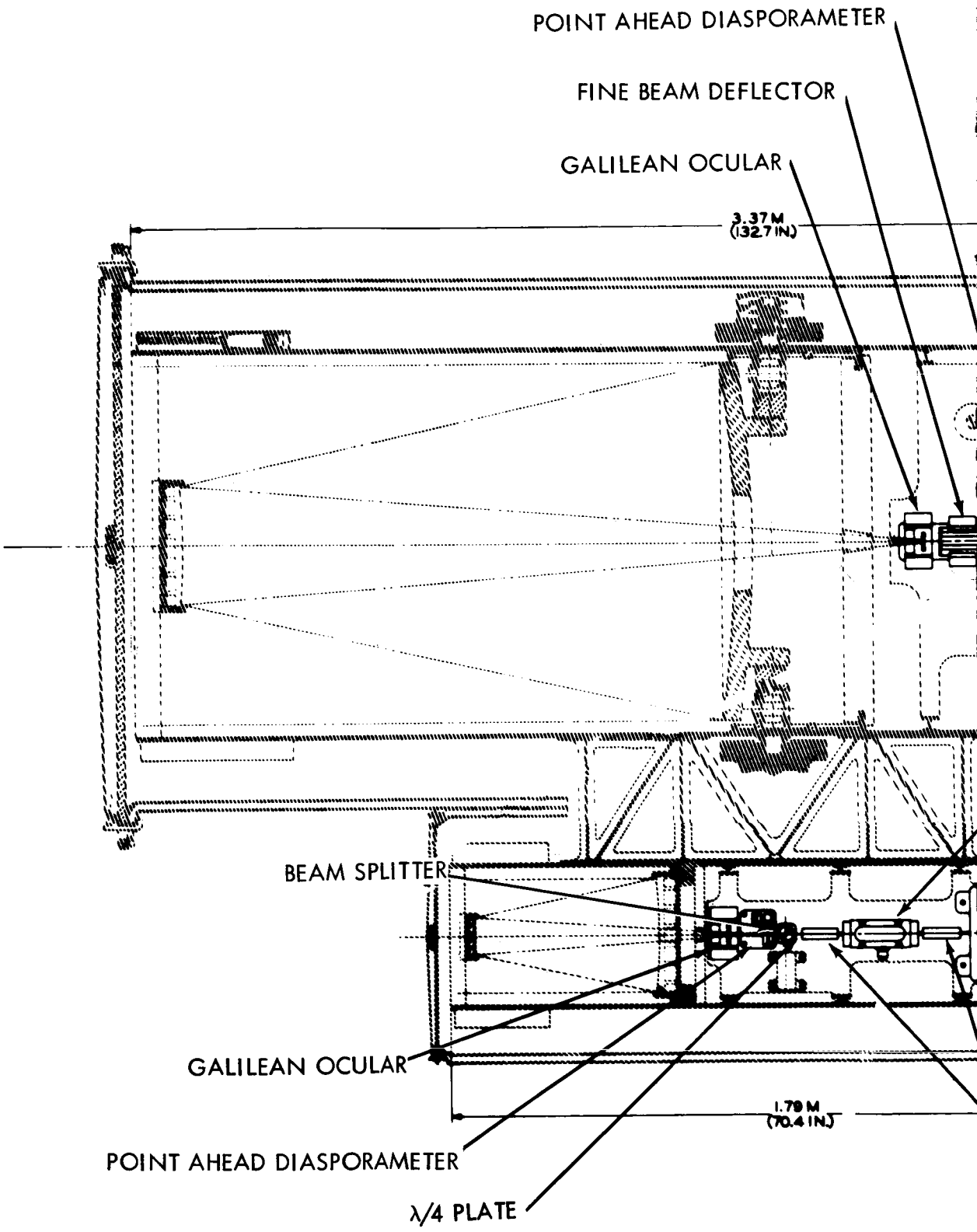
Optical modulators that will transmit roughtly 60 to 70 percent of the light input have been built. Photomultipliers of high sensitivity that will have a pass band up to 300 MHz or so are available. The bandwidth of the phase perturbations should be less than 1000 Hz, and a local oscillator of the desired frequency could be readily available.

Spaceborne Equipment

The spaceborne equipment (figure 4.8-5) required for this experiment is common to the space-ground heterodyne link. The major equipment necessary for the measurements described here are repeated here for completeness

a. 1 single-frequency laser transmitter operating at 0.6328 microns with power outputs of 1 to 10 milliwatts.
b. 1 high-voltage dc power supply.
c. 1 cavity tuning control and stabilization circuits for modelock or single-frequency operation.
d. 1 in-cavity modulator for FM operation at 0.6328 microns.
e. 1 external modulator for supermode (single-frequency) operation.
f. 2 modulator driver amplifiers for super-mode operation.
g. 1 output power monitor detector.
h. A transmitting telescope.

To reduce angular motion to a minimum the experiment should be conducted at synchronous altitudes. A diffraction limited aperture 1 meter in diameter, capable of tracking the receiving station on earth to an accuracy of better than 0.1 arc second is required to provide adequate signal to the narrow aperture required.


POINT AHEAD DIASPORAMETER
FINE BEAM DEFLECTOR
GALILEAN OCULAR
3.37 M
(132.7 IN.)
BEAM SPLITTER
GALILEAN OCULAR
1.79 M
(70.4 IN.)
POINT AHEAD DIASPORAMETER
λ/4 PLATE

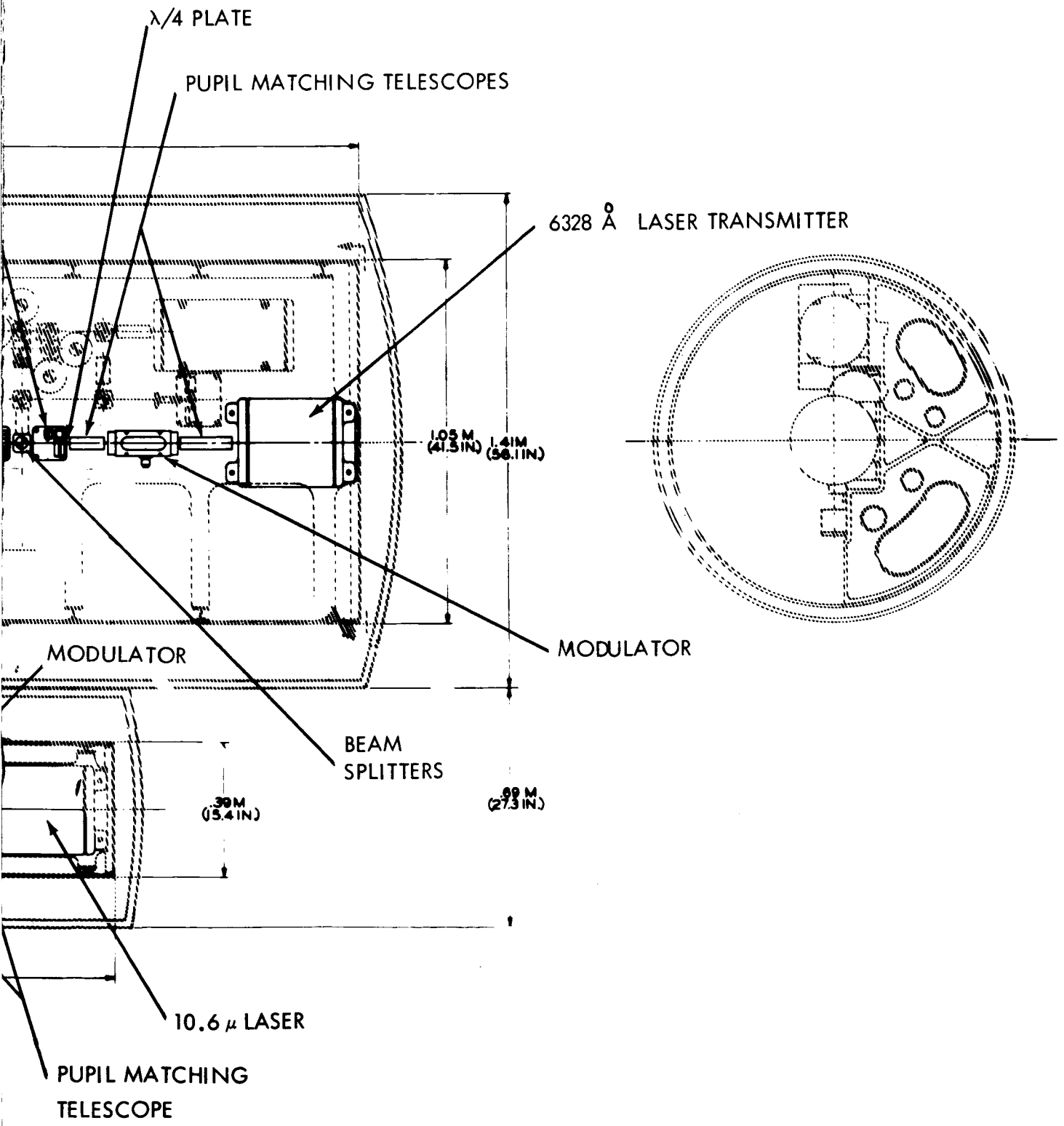


Figure 4.8-5. Telescope Numbers 1 and 2

Ground-Based Equipment

As described in the section on feasibility and implementation, the following major items will be required at the ground station.

Two folded optical telescopes evacuated with an aperture of 2 cm in diameter, capable of focusing their outputs on a common photomultiplier. Provision must be made to insert filters and attenuators or modulators in the optical path of either telescope. Separations up to 2 to 3 meters could probably be obtained with transportable equipment. Larger separations would require fixed installations, possibly having phase compensated paths at large separations. This could be accomplished with an auxiliary laser, ground-based.

Photomultiplier tube or other high speed photo detector capable of operation at 0.6328 micron with signals having a bandwidth of 2 kHz centered in the 10-80 MHz band. Quantum efficiency better than 10% is required if the receiving aperture is to be kept at 2 cm or lower.

Optical modulator that can frequency modulate an incoming laser signal with a 10 to 80 MHz offset frequency to enable filtering out the dc component of the received signal.

Stable RF oscillator to provide modulation signal indicated above.

Filters, amplifiers, phase tracking circuits, and recorders required for subsequent signal processing.

4.8.4.2 Operational Procedure

As indicated in the time line diagram (figure 4.8-6), the period from 10 to 13 hours, with the 0.6328 micron laser operating in the single frequency mode is allotted for the measurements described in this experiment. The 1-meter telescope with its beam stabilized on the ground site is required to make these measurements. If the phenomenon of beam breakup is evident, oscillations of the spacecraft beam must be kept to a minimum in order to separate beam swinging effects from atmospheric effects.

At the start of the measurement, the two apertures are placed as close together as possible. The output of the phase tracking circuits can be made proportional to the phase difference between the two apertures, and with appropriate circuitry steady frequency components such as are caused by a rotating line of sight can be removed. The phase difference is recorded as a function of time.

After a suitable data recording period, of the order of a few minutes, the apertures are separated to a new value of ρ, and data again recorded. The process is repeated until the output of the phase difference recorder approaches a maximum value.

The mathematical operations of squaring and averaging can be performed on the record of the phase difference as a function of ρ. If the record is not required, the data processing can be accomplished electronically with only the values of $\overline{(\theta_1 - \theta_2)^2}$ recorded as a function of ρ.

4.8.5 Required Technology Development

Except for extension of these measurements to other frequency bands no great advances in technology are required for this experiment other than those specified in the associated experiments concerning beam pointing, diffraction limited telescope operation in space,

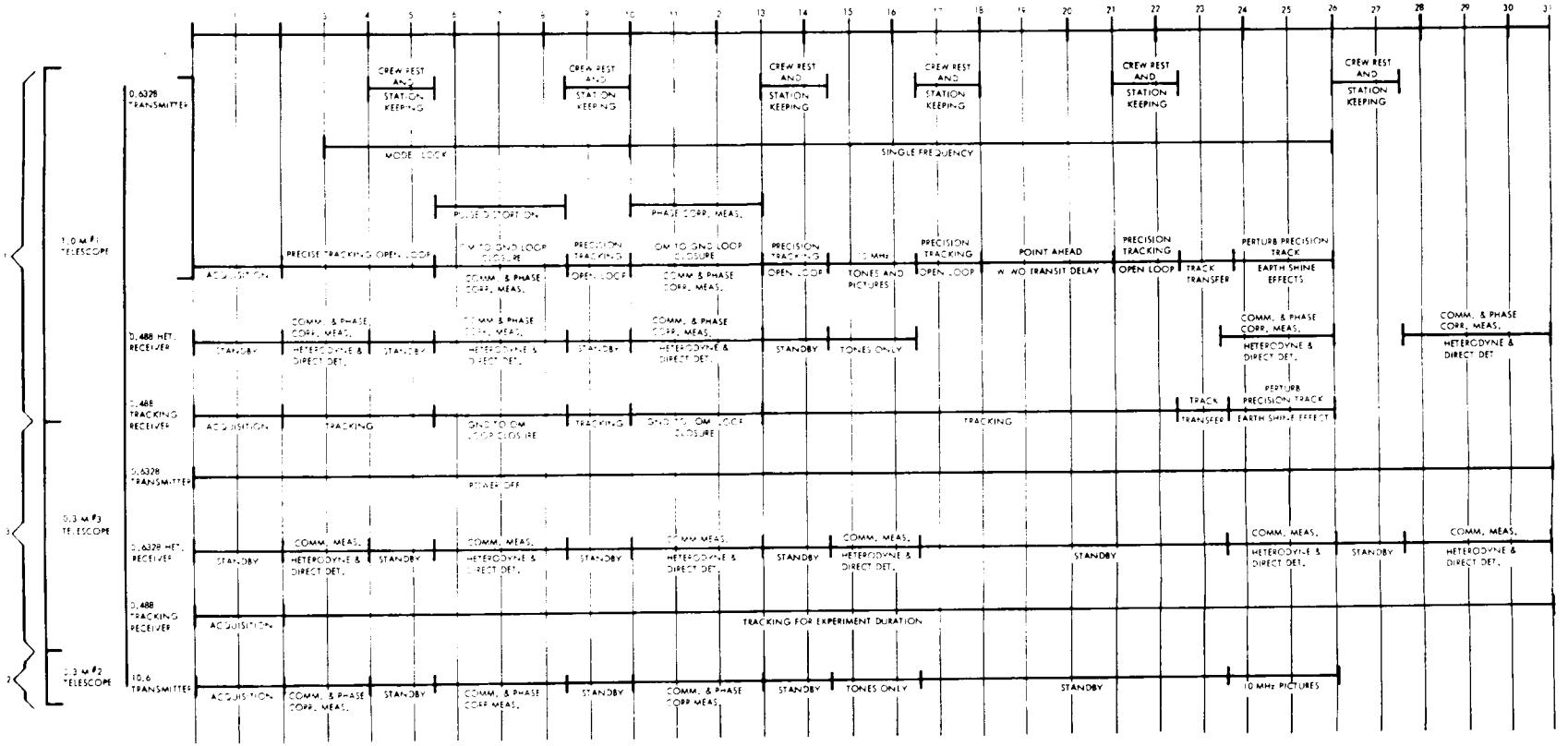


Figure 4.8-6. Time Lines for Optical Communication Telescopes

and laser communications. Obviously, improvements in the sensitivity of detectors, and the transmissivity of optical components at this frequency will increase the chances of obtaining more accurate measurements under poor conditions of atmospheric transmissivity.

FY 1966 Begin optical communication support facility study.

FY 1967 Begin one year phase correlation receiver development.
Begin optical communication support facility site measurements.

FY 1968 Begin 4-month fabrication of prototype phase correlation receiver.
Site preparation.

FY 1969 Conduct 6-month phase correlation test program using an airborne signal source.

FY 1970 Conduct phase correlation tests using an earth orbiting signal source.

4.9 PULSE DISTORTION MEASUREMENTS

4.9.1 Summary

The World Meteorological Organization[1] has reaffirmed the general conclusions of the nature and scope of satellite data, and the impact of such data on the atmospheric sciences. Although it was felt that vertical soundings would not be replaced by satellite observations, there is a good prospect of using suitably calibrated satellite measurements at optical frequencies to supplement local measurements. The particular targets of interest are the natural scatterers such as aerosols, micrometeorites, and high level clouds. Because of the very small scattering cross section of these targets, high power is required if back-scatter measurements are to be made. The presence of these scatters creates the possibility of multipath effects which may affect the performance of optical links. Computations of the scattering loss at the frequency considered for this experiment show that such effects would normally be so small as to be undetectable at the power densities required for the other laser experiments. It is possible, however, that a particularly favorable geometry combined with an unusual concentration of scatterers that are large compared to the wavelength would result in a measureable effect which would reduce the potential bandwidth of optical links.

The advent of optical techniques for communication and tracking has been induced by the need for wide-band information channels. There are currently identifiable needs for megahertz bandwidth transmissions over planetary distances. Furthermore, estimates of future terrestrial communication requirements lead rapidly to the conclusion that the frequency bands below the optical will one day be exhausted. Optical frequencies will be required, as a matter of course, to provide the needed bandwidth. Optical links passing through the Earth's atmosphere may be limited in bandwidth by the effects of Earth's atmosphere. In order to provide the data required in the design of such links, the characteristics of the transmission channel must be determined as independently of equipment characteristics as is possible.

One method of determining the phase and amplitude characteristics of a channel is to transmit a known wide-band waveform through the channel and compare the received waveform phase and amplitude characteristics with those of the transmitted characteristics. By accounting for changes due to the equipment used, the characteristics of the channel can be determined. The transmission, reception, and display of very narrow pulses are within the capability of present technology (figure 4.9-1). In fact, a pulse shorter than 10^{-9} seconds has been demonstrated in the laboratory using a helium-neon laser. This technique will permit the determination of channel characteristics up to bandwidths in the order of 10^{-9} Hz, well beyond presently definable needs.

The difficulty in instrumenting such a technique lies in the signal strength, hence, in received signal processing. This difficulty can be circumvented by adopting sampling oscillograph techniques. Present sampling rates are too low to be acceptable for the high repetition rates produced by the mode locked laser, but the required sampling rates can be generated if development effort is expended. The effects on a wideband channel are expected to be negligible so that the trace sampled at currently attainable rates would be truly representative of all pulses transmitted. Rapidly varying effects would be revealed by a noisy presentation which would be difficult to analyse without a real time display. Because effects are expected to be negligible or slowly changing (at less than kilocycle

(1) Second Report on the Advancement of Atmospheric Sciences and their Application in the Light of Developments in Outer Space, June 1963 Secretariat of the World Meteorological Organization, Geneva, Switzerland.

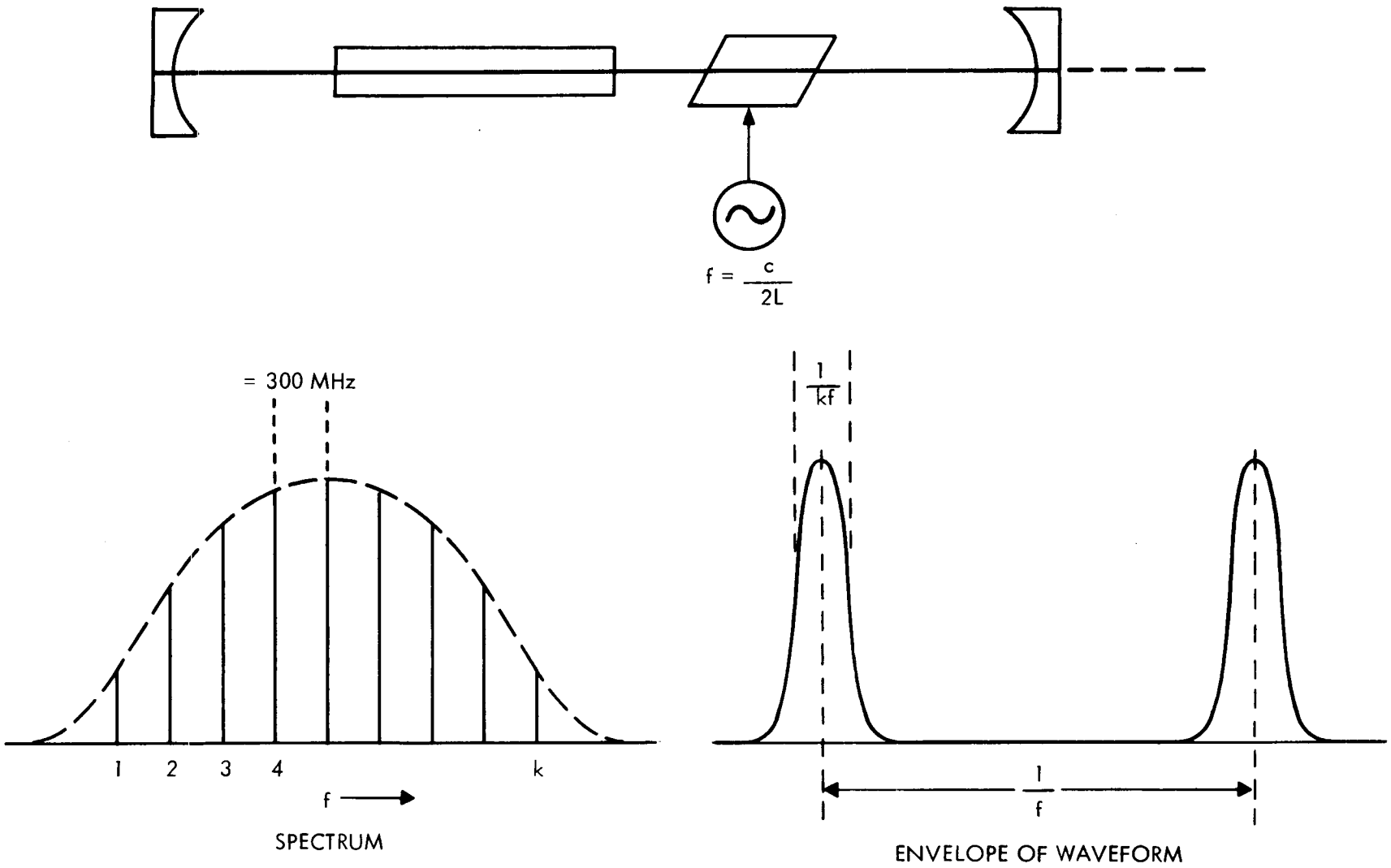


Figure 4.9-1. Mode-Locked Transmitter

rates) the pulse distortion experiment proposed for OTAES will explore a bandwidth more than adequate for presently definable needs and may reveal unanticipated limits imposed by atmospheric effects.

Since these pulse distortion measurements pertain to communication theory, the receiver must be located in the far field of the transmitting antenna. The difficulties of reliably extrapolating measurements made on a horizontal, near-field path to a high elevation, far-field path are formidable enough to make such extrapolations of doubtful validity in the design of optical links (see section 4.8.3.2). It follows that such measurements cannot be made within the atmosphere; hence, a spaceborne transmitter is indicated. Given a space-to-ground propagation path, the test results become directly applicable to space-to-Earth communication. The experiment is then capable of generating data of specific interest to future operational system designers if long term statistical data collection procedures are followed. It can thus be said that the experiment will be of most value if performed in synchronous orbit.

4.9.2 Objectives

The objective of this experiment is to determine the "impulse response" of the atmosphere in order to describe the characteristics of the communication channel provided by the atmosphere under a variety of transmission conditions.

4.9.3 Justification

4.9.3.1 Contribution and Need

One of the principal reasons for the interest in coherent light as a communication carrier is the potentially wideband communication channels available. As discussed in section 4.9.5.1, there seems to be no apparent physical reason why extremely wide bandwidths should not be obtained even on optical links transmitted through the atmosphere. Before such communication channels could be designed, efficient wideband modulators and demodulators would have to be developed to make full use of the available bandwidth. The development of such devices, particularly for spaceborne applications, will be expensive and time consuming. Before such a development program is undertaken, it would be prudent to explore the channel capabilities to ensure that the channel actually does exist. This is particularly pertinent in view of measurements[2] showing that, under certain conditions, bandwidths of only 200 MHz were available on horizontal paths.

One way to examine channel characteristics would be to observe the behavior, at several suitably spaced radio frequencies covering the bandwidth of interest, of a modulated optical carrier after transmission over a space-to-ground path. This technique would require a number of stable RF generators with a fixed phase relationship in the spacecraft, so that there would be no large gaps in the spectrum.

An alternative way of examining the channel would be to transmit a very short pulse, of the order of a nanosecond, and observe changes, if any, in the pulse shape received after transmission through the atmosphere. Such a pulse contains harmonics which cover a frequency span of the order of the reciprocal of the bandwidth, in this case, ≈ one gigahertz. Nonlinearities in the phase characteristics of the channel will be revealed as pulse distortions which can be analyzed to determine the phase shift characteristics of the channel.

---

(2) E. J. Chatterton, "Optical Communication Employing Semi-Conductor Lasers," MIT, Lincoln Laboratory, Technical Report 392, 9 June 1965.

In addition to providing useful information on the phase characteristics of the channel, a short pulse will reveal the presence of scatterers which could contribute to multipath effects over the optical channel. Aerosols of various sizes are known to be present at altitudes of around 70 to 100 km. Scattering from these aerosols form the "aureole" around the sun's image[3]. Aerosols have also been detected from back scattered measurements with a high powered laser radar. Because some of these aerosols are larger than the optical wavelengths at visual frequencies, there may be more scattering in the forward direction, perhaps by orders of magnitude, than in the backward (toward the transmitter) direction. If the forward scattering is sufficient to cause delayed pulses (computations of the path geometry required for this to occur are in section 4.9.5.1) to appear on the display, the effects on communication rates can be calculated. Additional ground based instrumentation will permit a measurement of the height of the scattering layers if sufficient scattered power is received.

4.9.3.2 Need for Space Testing

The information to be obtained by these measurements will describe the amplitude and phase characteristics as well as the time delay characteristics of the transmission channel over a communications bandwidth considerably wider than currently required. Knowledge of the atmosphere is insufficient to permit extrapolation of measurements over short horizontal paths to elevated paths through the atmosphere, particularly where knowledge of the paths is required accurately enough to determine whether the expensive development of wideband optical components for space use should or should not be undertaken. To avoid the phase front perturbations of the near-field, the measurements should be made in the Fraunhofer region. As discussed in the phase correlation experiment (section 4.8.3.2), spaceborne platforms are required for transmitting apertures greater than 0.6 meter. A one meter aperture is contemplated here.

In addition, the multipath characteristics will be determined by the presence, location and size distribution of the larger aerosol particles; measurements which will contribute to the knowledge of these particles will be of use in the study of the physics of the atmosphere.

4.9.3.3 Feasibility

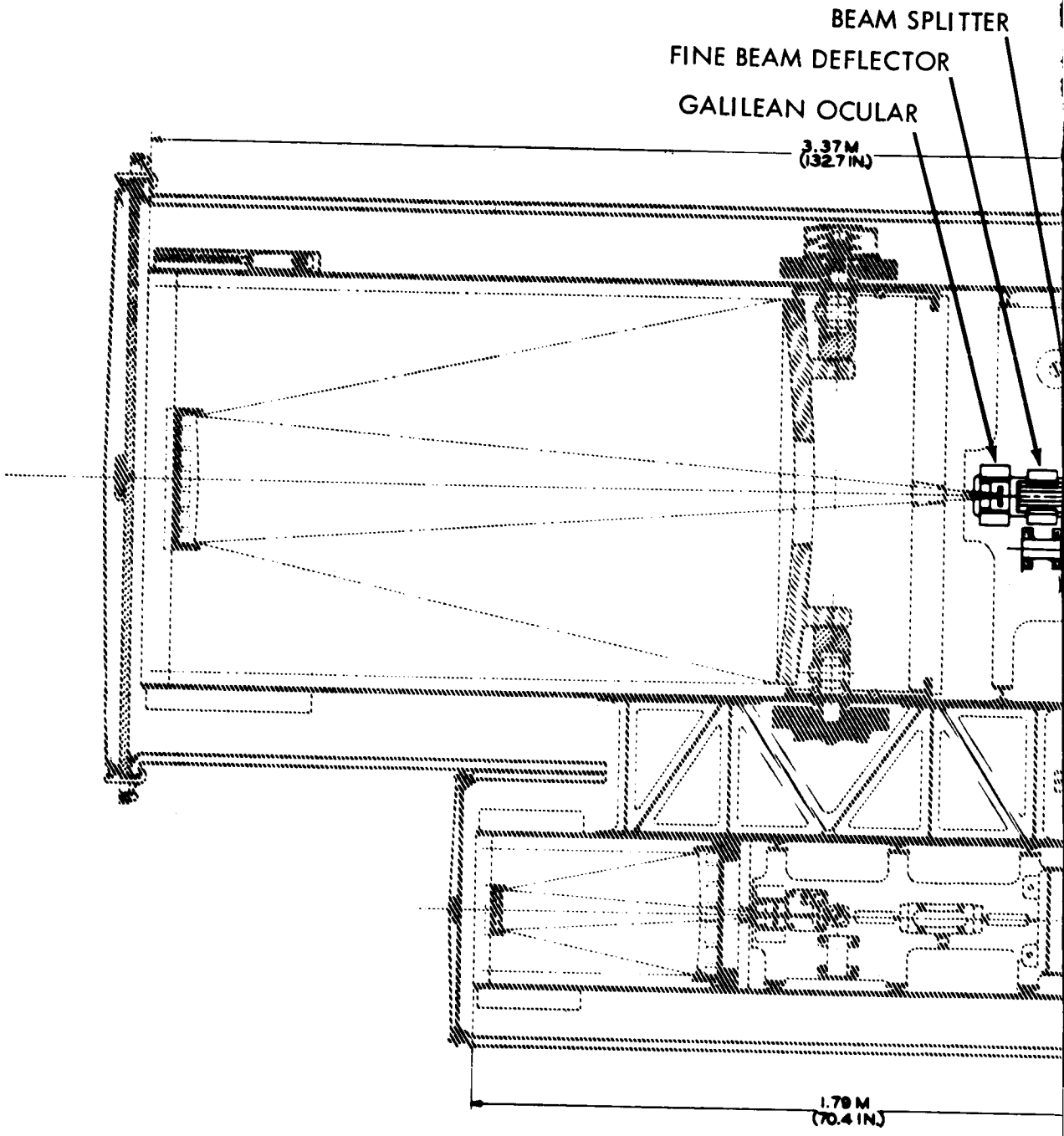
The critical components for the experiment are the spaceborne mode locked laser transmitter and the ground based receiver-display system. Mode locked lasers have been tested in the laboratory at this frequency and considerable success has been achieved in the display of nanosecond pulses in certain nuclear applications.

4.9.4 Implementation

4.9.4.1 Experiment Design

A space to ground link will be established. The ground based receivers will use both optical heterodyne detection and direct detection of the signal transmitted from the spacecraft. A spaceborne laser operating at 0.6328 microns (figure 4.9-2) is aimed at a ground-based receiving telescope as the satellite makes its pass over the ground site. The laser is operated in the "mode-locked" condition where all of the oscillating laser modes are coupled together and the output of the laser becomes a series of very short ($< 10^{-9}$ secs duration) pulses.

(3) F. Moller, Optics of the Lower Atmosphere, Applied Optics, vol. 3, no. 2, February 1964.



1-309

PRECEDING PAGE BLANK NOT FILMED.

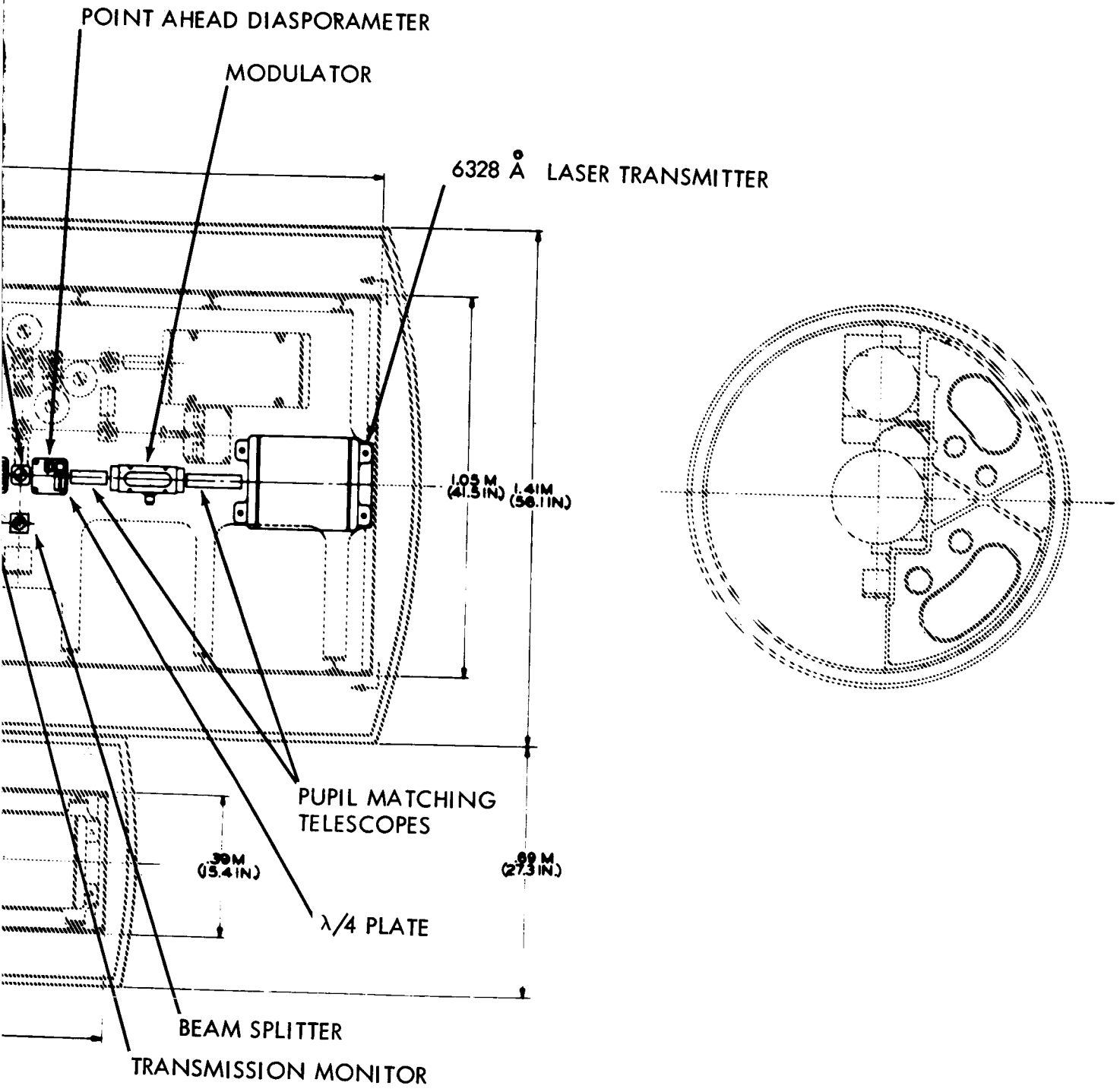


Figure 4.9-2. Telescope Numbers 1 and 2

The ground receiver detects the pulses, samples them and displays their waveform after transmission through the atmosphere. Any degradation of the initial waveform can be observed and the effects of the propagation path on other modulation waveforms can then be calculated.

4.9.4.1.1 Pulse Generation With the Mode-Locked Laser Transmitter

A He-Ne laser longer than about 10 cm has enough gain to oscillate at several frequencies simultaneously. The actual frequencies are determined by the laser resonator cavity, i.e., the separation between the laser cavity mirrors. The frequency spacing between oscillating modes is given by C/2L, where C is the velocity of light, and L is the length of the cavity. A laser 1.5 meters long will have mode spacing frequency of 100 MHz.

A laser of this length will have a number of independent modes oscillating, spaced by 100 MHz, over the whole region in the optical band where the laser gain is sufficient to support oscillation. The He-Ne transition at 0.6328 microns has a doppler broadened gain curve that is about 1000 to 1500 MHz wide, so that a family of about 10 separate oscillations can be sustained by a 1.5 meter laser.

It should be noted that these are independent oscillations. Their frequencies and phases are only weakly coupled to other oscillations, through such competition effects as "hole burnings", etc. If the light output is detected by a phototube, the beats between neighboring oscillations can be observed as 100 MHz modulation on the beam. Next-to-nearest neighbors generate a 200 MHz beat, and so forth. The phases of the modes are essentially random, however, so that the power of the 100 MHz beat signal does not increase linearly with the number and power of the contributing modes, but increases in a random-walk manner instead. The total output power fluctuates slightly because of mode competition effects, making the multimode laser a noisy transmitter.

This situation can be dramatically cleaned up by the use of an electro-optic phase modulator, placed within the laser cavity as shown in figure 4.9-1. When the modulator is driven by an external oscillator at exactly the mode spacing frequency, C/2L, each of the modes generates sidebands on top of all the others. In a very short time the original set of modes is quenched and is replaced by a new set of oscillations.

The new set of modes are strongly coupled to each other, as the phase is continually transferring energy between them. They are: (1) separated by exactly the frequency of the driving oscillator, and mode-pulling effects in the free-running laser are eliminated; and (2) their phases are not random but locked in step, so that the laser output becomes a series of very rapid pulses. The pulse width is roughly one nanosecond, and the PRF is 100 MHz, for the He-Ne laser described earlier, giving a duty cycle of 10 percent.

The average power output of the laser is not changed during mode-locked operation. Thus the peak pulse power will be many times the average power -- higher by the reciprocal of the duty cycle -- a factor of 10 in this case. The RF power required to drive the modulator is not large -- less than one watt.

The mode-locked laser is a unique transmitter source. It generates sub-nanosecond pulses at extremely high PRFs, and it can be easily implemented. The only requirements beyond those of a free-running laser are a low-loss modulator, its driver, and oscillator.

4.9.4.1.2 Received Signal Analysis

The pulses detected by the wideband photodetector must be analyzed by high speed sampling techniques. Sampling gates of 100 picosecond length are available, and sampling rates of 1 to 10 MHz are quite feasible. These sampling rates are lower than the transmitter PRF, so that sampling efficiency is low -- 1 percent to 10 percent. This is more than made up

for by the fact that changes in the atmosphere will occur at kilocycle rates, at most, so that the bandwidth of the display can be about 1 kHz. The S/N at the display will be greater than that at the front end by the ratio of the number of samples obtained and the number of resolution cells needed. This is a factor of 10 for a 10 MHz sampling rate, a 1 kHz display rate, and 100 time resolutions cells.

The laser transmitter power required under all these assumed conditions is 10 milliwatts of average power. Favorable trade-offs can be made in several directions: S/N versus sampling density versus collecting aperture size versus transmitter beamwidth.

As indicated in paragraph 4.9.5, no appreciable pulse distortion or multipath delay is expected with the beamwidths contemplated for this experiment. If such is indeed the case, a channel bandwidth of at least one gigahertz will be demonstrated. If pulse distortion or multipath effects are observed, analysis of the received waveform will determine the channel characteristics. An additional receiver located away from the direct path can be used to measure off-angle forward scatter to determine the height of possible scattering layers.

The pulse propagation experiment is fairly easy to implement, and should be performed over ground-to-ground and space-to-ground paths.

4.9.4.1.3 Spaceborne Equipment

The spaceborne equipment required for this experiment is common to the space-ground heterodyne link. The major equipment components necessary for the measurements described here are repeated for completeness.

A mode-locked laser operating at 0.6328 microns with a power output of 10 milliwatts.

A beam forming transmitting telescope with a one meter aperture to provide the required power density at synchronous altitudes.

Stabilizing and tracking capability to provide 0.1 arc second tracking to keep the beam pointed at the receiver.

4.9.4.1.4 Ground-Based Equipment

The ground-based receiving telescope with a one meter aperture (used in the superheterodyne experiment) equipped with a wideband photodetector such as a cross-field photomultiplier which is capable of faithfully reproducing the light pulses.

An electronic signal analysis system similar to that used in a sampling oscilloscope which can display the pulse shape and arrival time for further analysis.

4.9.4.2 Operational Procedure

This experiment will be performed during the period of mode-locked laser operation at 0.6328 microns, hours 3 to 10 of the time line diagram, figure 4.9-3. Transmission through the one meter telescope is required to provide the best signal-to-noise ratio in examining the pulse for possible frequency dispersion. Where multipath effects are sought, the beam will be spread in steps until the signal display is noise limited.

At hour 3, the 0.6328 micron laser will be temperature stabilized in a mode-locked condition providing a train of pulses at 300 pulses per second -- these pulses are of sub-nanosecond duration depending on the number of modes excited in the laser. Assume that the transmitted pulses are 1/2 nanosecond long.

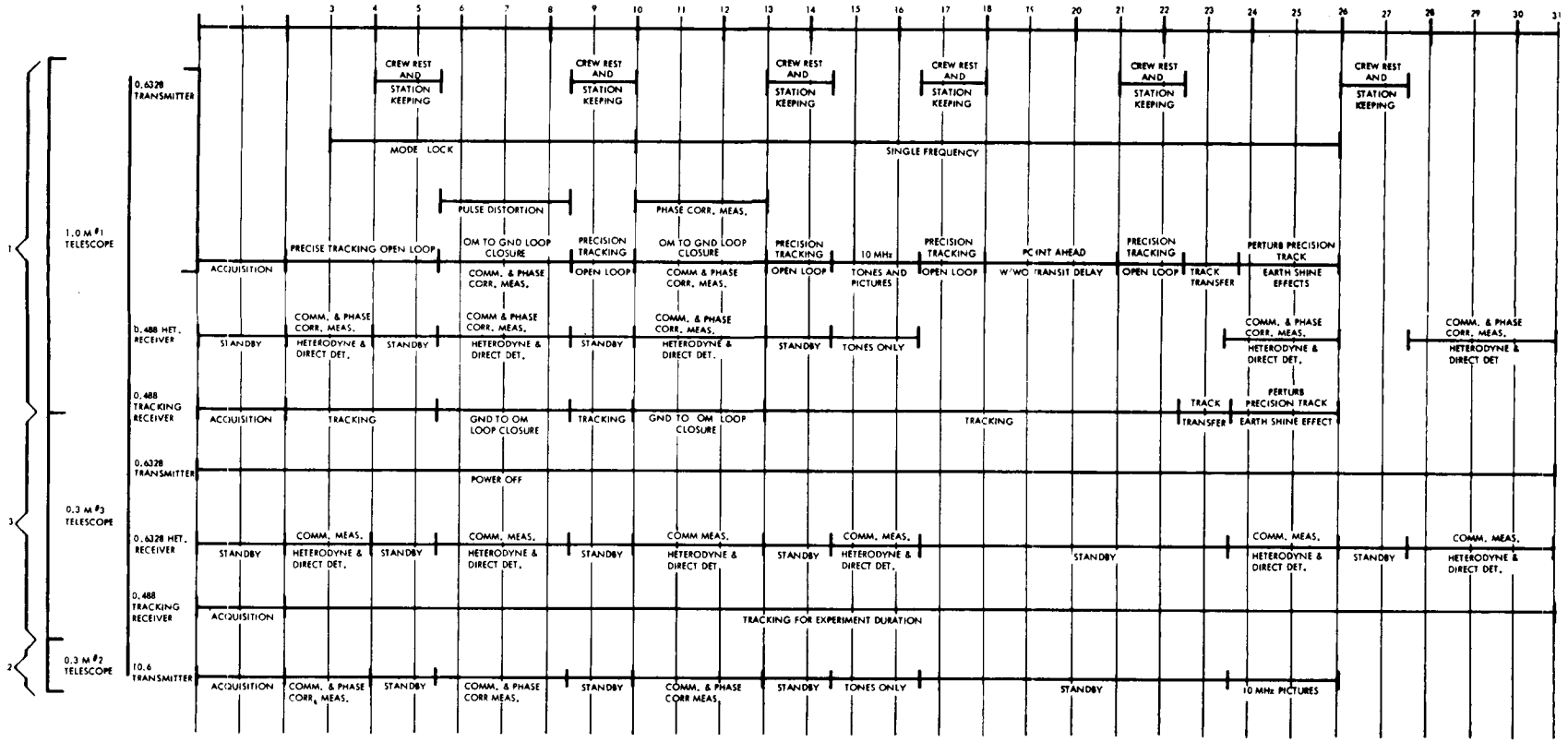


Figure 4.9-3. Time Lines for Optical Communications Telescopes

Using the one meter telescope on the ground, the pulse energy will be received through a wideband system and displayed with the aid of refined sampling oscilloscope techniques. Because little change in the pulse shape is expected, the received pulse can be compared to a standard one during the course of the experiment. Departures from the standard can be recorded photographically for further study and analysis.

4.9.5 Supporting Analyses

4.9.5.1 Computation of Possible Multipath Delay

If it is assumed that the center of the transmitter beamwidth (ϕ) is accurately aligned with the center of the angle of view (θ) cone angle, the geometry shown can be used to compute possible multipath delays. Misalignment of the beam and viewing cone angle could lead to larger delays than computed here. Although scatterers could be located anywhere within the beamwidth and view angle, the greatest delay will occur when the scatterer is at S, the intersection of the view angle cone and the transmitting beamwidth cone. As indicated in figure 4.9-4 the maximum path difference $\Delta\rho$ (Path TSR - r) is given by

$$\sqrt{(r - h)^2 + h^2 \tan^2 \frac{\theta}{2}} + \sqrt{h^2 - h^2 \tan^2 \frac{\theta}{2}} - r = \Delta\rho$$

Assume, for space to ground transmission, that $r \geq 2h$. If $\frac{\theta}{2}$ is less than 10 milliradians, so that $\tan \frac{\theta}{2} = \frac{\theta}{2}$, and using the approximation $\sqrt{1 + X^2} \simeq 1 + \frac{X^2}{2}$ for $X < 1$, the above equation reduces to

$$(r - h)\left[1 + \frac{h^2 \theta^2}{8(r-h)^2}\right] + h\left[1 + \frac{\theta^2}{8}\right] - r = \Delta\rho$$

$$\frac{h^2 \theta^2}{8(r-h)} + \frac{h\theta^2}{8} = \Delta\rho$$

$$\frac{\theta^2}{8}\frac{r h}{(r-h)} = \frac{\theta^2}{8}\frac{h}{\left(1 - \frac{h}{r}\right)} = \Delta\rho \qquad (1)$$

since $\frac{1}{2} \leq \left(1 - \frac{h}{r}\right) \leq 1$ the worst case for an r, is when r = 2h so Eq. (1) becomes

$$\frac{\theta^2}{4} h = \Delta\rho \qquad (2)$$

and $\Delta\tau$, the path delay is given by $\frac{\Delta\rho}{C}$ where C is the velocity of light.

$$\Delta\tau = \frac{\theta^2}{4}\frac{h}{C} \qquad (3)$$

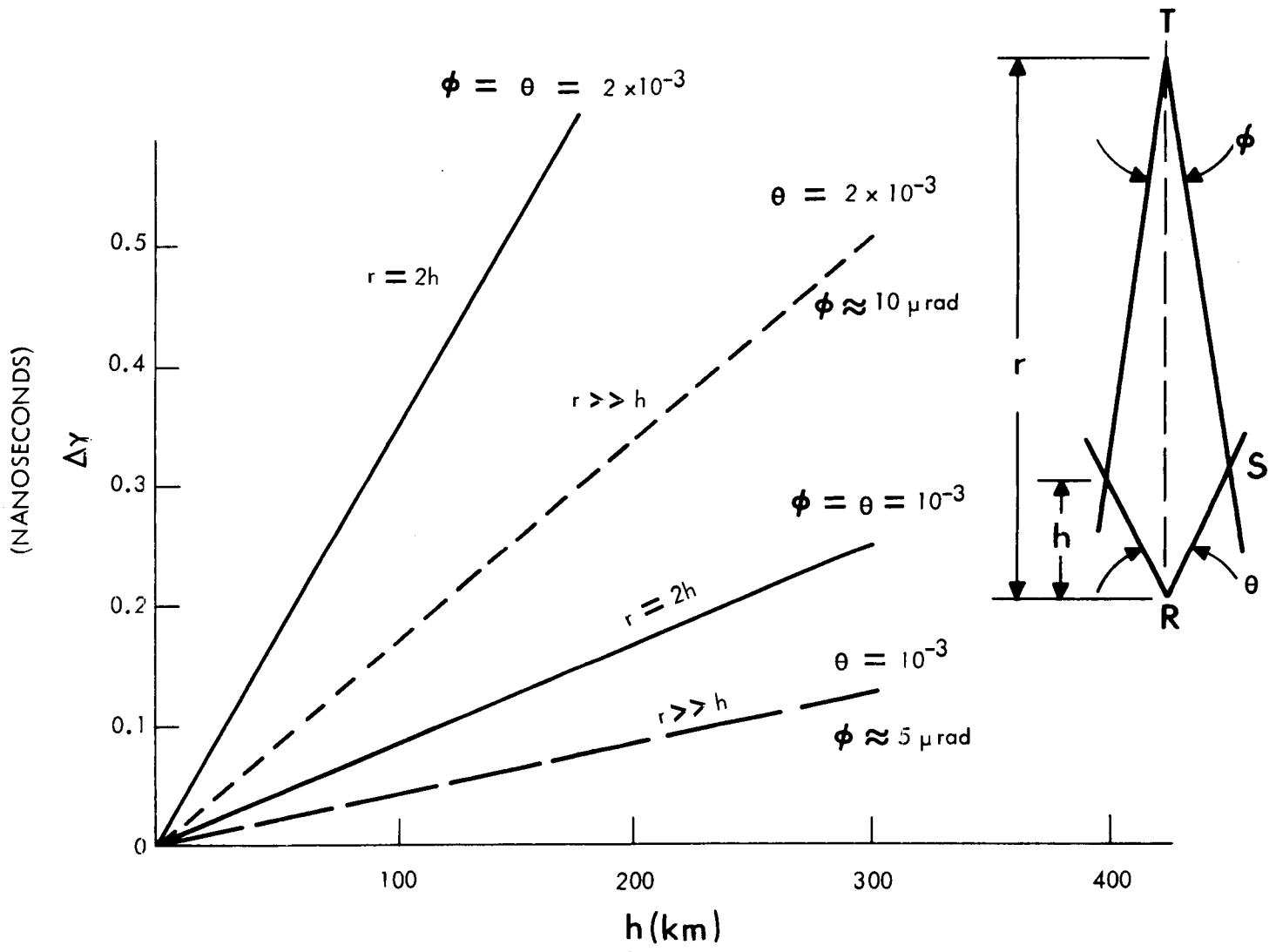


Figure 4.9-4. Multipath Delay

If h is 100 km, $\theta = 10^{-3}$ radians

$$\Delta\tau = \frac{10^{-6}}{4} \cdot \frac{100}{3 \times 10^{5}} \cdot 109 = \frac{1}{12} \text{ nanoseconds}$$

and probably could not be detected. However, at certain slant paths, h could be 500 km, and if θ is say 3×10^{-3} radians, $\Delta\tau$ increases by a factor of 45 to become ≈ 4 nanoseconds which could possibly be measured if the scattering cross sections are sufficient.

In the foregoing computations it is assumed that the scatterers are located at the intersection of the beam angles. Normally this will not be true, so that the actual multipath will probably be less than indicated in figure 4.9-4. If the scatterers are in a layer, at some distance other than that defined by the cone intersections, one beam or the other will limit the maximum multipath delay. As shown in the figure, the transmitting beam width ϕ is given approximately by

$$\phi = \frac{h\theta}{r-h} \qquad \theta, \phi < .01 \text{ radians} \tag{4}$$

For earth-space applications θ will be kept as small as is consistent with system considerations. For a given θ, reducing ϕ to as small a value as possible forces a reduction in h, the range to possible scatterers, which reduces the duration of possible multipath delay. Values of multipath delay for various distances to the scatterers are plotted in figure 4.9-4. Values of ϕ on the $r >> h$ curves are computed for synchronous altitudes. As shown by the curves of figure 4.9-4, possible multipath delays are expected to be very small. A very short pulse is required for their measurement. If scatterers are found in sufficient number, of the proper size, and in a favorable geometry, some multipath might be observed. Computations of the scattering cross sections required show that the probability of this event will be low.

If Eq. (1) and Eq. (4) are used, and dividing by the velocity of light, the maximum multipath delay (scatterers located at the intersection of the cone angles, τ becomes, for small angles,

$$\tau = \frac{\theta \phi r}{8 C} \tag{5}$$

This form of the equation is not particularly adaptable to earth space applications, however, if it is assumed that the maximum height of scatterers is of the order of 100 km, a maximum range to the scatterers on a slant path is 500 km. In Eq. (5) the distance to the scatter is not explicit.

4.9.5.2 Considerations on Pulse Stretching due to Frequency Dispersion in the Atmosphere

A pulse 10^{-9} seconds long will have a bandwidth of the order of 10^{9} cycles. If the index of refraction in the atmosphere is such that the frequency component at one end of the band is delayed by 10^{-9} seconds compared to the other end of the band, the pulse would be smeared out to roughly twice its length. It is of interest to compute the rate of change with frequency required for this dispersion to take place.

The travel time for a particular frequency component to travel a path distance L is

$$\tau = \frac{1}{c} \int_0^L n(\lambda)\, dx \text{ where } \tau \text{ is travel time,}$$

n is the index of refraction which is a function of λ, as well as position, and temperature, pressure, and water vapor content and c is the velocity of light. The dispersion in time between the two extreme frequencies traveling the same path would be

$$\Delta\tau = \tau_1 - \tau_2 = \frac{1}{c} \int_0^L (n_1 - n_2)\, dx$$

Data on index of refraction is usually given as the "Refractive Modulus"(4)

$$N = (n-1)\ 10^6$$

so that

$$\Delta\tau = \frac{1}{c} \int_0^L (N_n - N_2)\ 10^{-6}\, dx$$

If it is assumed that $N_1 + N_2$ are constant over the path for this short (at optical frequencies) range of frequencies

$$\Delta\tau = \frac{(N_1 - N_2)\ L\ 10^{-6}}{c} = \frac{\Delta N L\ 10^{-6}}{c} \qquad (6)$$

$$\Delta N = \frac{\Delta\tau c\ 10^{+6}}{L} \qquad (7)$$

and since the frequency spread ΔF (of 10^{+9}) cps sec is given by

(4) Handbook of Geophysics, Revised edition, U.S. Air Force, Air Research and Development Command, Macmillan, New York 1961, p. 13-1.

$$\Delta F = c\left(\frac{1}{\lambda_1} - \frac{1}{\lambda_2}\right) \approx \frac{c\ \Delta\tau}{\lambda_2} \tag{8}$$

the required gradient is

$$\frac{\Delta N}{\Delta \lambda} = \frac{\Delta\tau c^2\ 10^{+6}}{L\ \Delta F\ \lambda^2} \tag{9}$$

To approximately double the pulse length, $\Delta\tau \approx \frac{1}{\Delta F}$ and with $\frac{c}{\lambda} \approx F$, the above becomes

$$\frac{\Delta N}{\Delta \lambda} = \frac{10^6\ F^2}{L\ (\Delta F)^2} \tag{10}$$

If L is given in microns, Eq. (10) shows the change in N no. per unit change in wavelength (in microns) required to double the pulse length. For the nanosecond pulses at 0.6328 μ over a 100 km path Eq. (10) results in

$$\frac{\Delta N}{\Delta \lambda} \approx 25 \times 10^5\ \frac{\text{N nos.}}{\mu \text{ of wavelength}} \tag{11}$$

To compare the above with what is expected, use the approximate formula[5] for N

$$N = N_\infty \left[1 + \frac{7.52 \times 10^{-3}}{\lambda^2}\right]$$

where N_∞ is the refractive modulus for wavelengths $>> 20\ \mu$ and λ is given in microns. Assuming $N_\infty \approx 300$, differentiating with respect to λ, results in

$$\frac{dN}{d\lambda} = -\frac{3 \times 300 \times 7.52 \times 10^{-3}}{(.6328^3)} - \frac{27\ \text{N nos}}{\mu \text{ of wavelength}}$$

The required gradient is 5 orders of magnitude greater than would be expected in a uniform atmosphere. The approximations made in these computations tend to err on the conservative side so that the conclusion is that there will be no distortion of the pulse due to frequency dispersion in the atmosphere.

(5) Op Cit, P. 13-2

If the transmitted frequency were on the edge of a molecular absorption band it would be possible for some pulse distortion to occur because of the unequal absorption of the component frequencies. As shown in published high resolution (.2A) atmospheric absorption spectra[6], a number of sharply absorbing bands exist in the visible range. The wavelength of 0.6328 μ is not near any known absorption band however so that no pulse distortion from this effect is expected.

4.9.6 Required Technology Development

FY-67. Continue development of laser mode control and stabilization techniques.

FY-68. Make ground-to-ground measurements of pulse distortion at 0.6328 to test broadband detectors and display techniques.

FY-68. Begin a development of traveling wave oscilloscope technology so that sub-nanosecond pulses could be displayed in real time.

(6) J. A. Curcio, L. F. Drummeter and G. L. Knestrick, "An Atlas of the Absorption Spectrum of the Lower Atmosphere from 5400 Å to 8520 Å," Applied Optics, vol. 3, no. 12, December 1964.

4.10 PRIMARY MIRROR FIGURE TEST AND CORRECTION

4.10.1 Summary

Recent developments in booster technology permit a more serious consideration of placing large manned telescopes in orbit. The outstanding goal in space astronomy, announced by the Space Science Board is the 3 meter (120 inch) telescope. The light gathering power of an orbital 2.5 to 5 meter (100 to 200 inch) telescope is such, that if complemented with a very high resolution capability; i.e., to its diffraction limit, it will permit astronomical observation not heretofore possible with the largest earth observatories or the present series of OAO's. For example, the detection and observation of faint objects down to +29 magnitude will be facilitated as well as the separation and detection of faint companions of nearby stars.

The telescope aperture, by virtue of its size, establishes its light gathering capability. However, telescope resolution, exclusive of the particular optical configuration, is affected by mirror and/or lens surface shape deviation and smoothness, optical system alignment, optical materials and coatings, and lens material homogeneity. The most formidable problem is that of maintaining primary mirror diffraction limited quality. To do this requires sensible and precise techniques for determining the deviation of the mirror figure from its required shape; and, if a deviation exists, to use suitable methods for correcting the mirror figure so that the undesired deviations are removed.

It has been established that in order to maintain performance specifications in precision systems, an exact determination of proportional limit must be made. Minute permanent deformations occurring in materials below the conventional proportional limit now require a new limit. This limit has been termed as P.E.L. (Precision Elastic Limit) and is defined as "the stress which produces a residual strain or deformation of one micro inch per inch". This strain (one micro inch) is a permanent set in the material and is sufficient in magnitude to change the power of an optical element. These minute permanent deformations in a large mirror will impart an exceedingly small additional deflection when compared to the effect of gravity (ratio greater than 1000:1) and is therefore not reliably measured on earth.

Further, a mirror may return to its figure over most of its surface but fail to completely return on the balance. An evaluation of this condition in space would be the only way to ascertain that the ground test conditions were not the cause of the discrepancy from prediction. In addition, a study was made of various methods for simulation of a zero "g" environment on earth. Each approach reviewed had serious drawbacks resulting in a need for space testing.

The object of this experiment is to investigate if, after being launched into space, the figure of a light weight mirror can be actively controlled in order to achieve and maintain diffraction-limited optical performance.

In this experiment, a thin spherical 1.3 meter beryllium mirror is attached to a specially constructed base structure. The surface and figure of this mirror will be controlled by thermally controlling the expansion of rods between the mirror and its base structure. The temperature differences between the rods and surrounding will be used as an analog of the surface deflections. The evaluation of the mirror figure will be accomplished by obtaining interferograms of the mirror surface. Mirror figure patterns will be obtained during final figuring on Earth and during orbit. These patterns will be used to determine the precision of the correction capability and ultimately as a guide for the design of large, figure correctable, reflectors. The change in the interferogram from the ground-based case will be interpreted electronically on the spacecraft and transmitted to a ground based computer. Calculations will then be performed and the results transmitted back to the spacecraft in the form of commands for thermally expanding the rods behind the mirror, thereby correcting the figure. Only in the zero-g environment of space, where the gravity effects of the rods and other attachments to the mirror are nullified, can the proposed technique be investigated and design data for a larger mirror be obtained.

4.10.2 Experiment Objective

The purpose of this experiment is to gather technological data and thereby establish the requirements for a 3 meter or larger primary mirror that can be figure corrected and maintained in space. The objective is obtained by ground and space testing a model with selected design parameters so that the output data can be extrapolated to provide design specifications of all large mirrors utilizing the correctable diffraction limited concept.

4.10.3 Experiment Justification

4.10.3.1 Contribution and Need

The need for large diffraction limited mirrors in space has been discussed in Optical Technology Needs (Paragraph 3.0 of this report). The astronomical and scientific community (Woods Hole Report, 1965) have stressed the importance of penetrating deeper into the universe. The spaceborne telescope will not be resolution limited by the atmosphere and a significant reduction in terestrial telescope film exposure time for dim objects will be achieved.

The results of this experiment will provide the needed technological data for the ultimate design of the system. Major areas of data needed or to be gathered are:

a. The effect of the weightless condition of space on the mirror and correction system.

b. The effect of the various thermal conditions of space on the mirror correction system. Of concern will be the radiation coupling with space in addition to the thermal (radiation and conduction) within the telescope system.

c. The sensitivity and precision to which a mirror surface can be forceably corrected and maintained at Diffraction Limited quality.

Some of the advantages of this correctable system are as follows:

a. Fabrication of system, once it has been developed, will be low cost with a short manufacturing time span compared with comparable size earth telescopes.

b. Conservation of booster thrust requirements. Since the mirror system has a lower mass, the supporting structure will be lighter in weight resulting in a smaller pay load or allowing weight for additional instrumentation.

c. Figure correction capability. Loss of figure can be corrected to $\lambda/30$ from an error of the order of one wave.

4.10.3.2 Need for Space Testing

According to basic physical concepts, a thin membrane (shell mirror) can be figured to optical tolerances in a strain free supporting nest while in the gravitational field of one "g". Once removed from the nest for assembly in a telescope, gravitational effects will distort the mirror figure. However, when placed in orbit (zero "g"), the mirror will revert to the strain free condition thereby returning to the perfect optical figure that was attained on earth.

There is however one attendant problem. It is well known that a material experiences a permanent set or deformation when its elastic limit is exceeded. Accordingly, "hardware" has been designed to operate at stress levels below the elastic limit of the component materials. However, in precision instrumentation, it has been found that even when designs have been engineered to a substantial percentage of the elastic limit, unexplained errors have occurred.

It has been established that in order to maintain performance specifications in precision systems, an exact determination of proportional limit must be made. Minute permanent deformations occurring in materials below the conventional proportional limit now require a new limit. This limit has been termed P.E.L (Precision Elastic Limit) and is defined as "the stress which produces a residual strain or deformation of one micro inch per inch". This strain (one micro inch) is a permanent set in the material and is sufficient in magnitude to change the power of an optical element. These minute permanent deformations in a large mirror will impart an exceedingly small additional deflection when compared to the effect of gravity (ratio greater than 1000:1) and is therefore not reliably measured on earth.

Further, a mirror may return to its figure over most of its surface but fail to completely return on the balance. An evaluation of this condition in space would be the only way to ascertain that the ground test conditions were not the cause of the discrepancy from predication. In addition, a study was made of various methods for simulation of a zero "g" environment on earth. Each approach reviewed had serious drawbacks resulting in a need for space testing.

An earthbound simulated space lab to test optical mirrors for ultimate use in space should have a zero gravity or a uniform support pressure capability. Changes in pressure and gravity are changes in applied loads on the mirror and alter its characteristics. These parameters must be nullified on earth to duplicate a space environment. Some approaches to compensate for these loads and their merits are reviewed:

It is assumed that the mirror to be tested has a uniform section; e.g. 10 millimeters (3/8 inch) thick, mirror material is Beryllium, 1.3 meters (50 inches) diameter. For a mirror with a spherical shape and a radius of 3.2 meters (125 inches), the sagittal dip is approximately 6.35 centimeters (2-1/2 inches). The weight of this dish at 1 g is 22.6 kilograms (50 pounds). The surface area is 12600 cm^2 (1960 in^2). The temperature and relative humidity of air are maintained constant.

a. Water Flotation Method

The mirror may be floated on water with its reflecting surface up. The test instruments are rigidly supported above and independent of the mirror. The surface figure is tested as the mirror free-floats below.

The mirror and test instruments alignment will be difficult to maintain to obtain a paraxial focus condition:

(1) The free-floating mirror will shift due to seismic tremors.

(2) The mirror is subject to bending at the unsupported ends for the section above the water-level.

b. Mercury Flotation Method

The mirror is floated on a mercury pool as in "a" above. In this test, the mirror floats since Mercury has a specific gravity = 13.6 and Beryllium has a specific gravity = 1.85. Stability between test instruments and mirror surface cannot be obtained because:

(1) Seismic tremors will shift mirror axis with respect to test instruments and a stable interferogram cannot be obtained for $1/20\,\lambda$ or better.

(2) Mercury will support the mirror over a smaller area than water and permit a larger mirror overhang. This increases the bending moment at the unsupported ends.

NOTE: Attaching the test apparatus to the mirror to offset item (1) aggravates item (2).

c. Submersion Method

Ideally, the mirror should be totally submerged in a fluid whose specific gravity is equal to that of the mirror (1.85). A review

of known fluids does not indicate any fluid near the specific gravity of Beryllium which would also be clear enough for satisfactory light transmission.

d. "Zero-g" Aircraft Tests

Zero-g aircraft tests can be achieved for periods up to about 1 minute. The time required to obtain a good interferogram study is about 1 hour. The one minute test time available in airborne tests is inadequate to obtain satisfactory results.

e. Pneumatic Floatation Systems

The mirror is floated on a cushion of air similar to the method outlined in Figure 4.10-1a. Except for the loads of the 10 gram limit stops, the mirror is essentially free from the effects of gravity. This method is unsatisfactory because:

(1) The degree of uncertainty of obtaining 90% zero-g for the test period is about 50% since the control of the pressure support must be on the order of 81.0 $\pm$.51 m.m. of water.

(2) The temperature of the supporting gas must be uniform.

4.10.3.3 Feasibility

There are many major and varied problems which must be solved in order to successfully accomplish this experiment. These will be discussed in the text following. However, it should be understood that most of these problems are of complexities normally encountered in any development program and will be solved by techniques within the present "state-of-the-art".

The technological areas which must be advanced are:

a. Determination of Activator Parameters

b. Thin Mirror and Eggcrate Design

c. Thin Mirror and Eggcrate Fabrication

d. Space Testing Techniques for Mirror Figure

Preliminary studies of each area have been made and are described in the following text. The results of these studies indicate, with a high degree of confidence, that this experiment can be successfully engineered, implemented and executed.

This experiment also evaluates the advantages and problems encountered in the erection, alignment and testing of a large optical system in space. The design of such a system is shown schematically in Figure 4.10-1b. The life of this system is expected to be far greater than the experiment requirements.

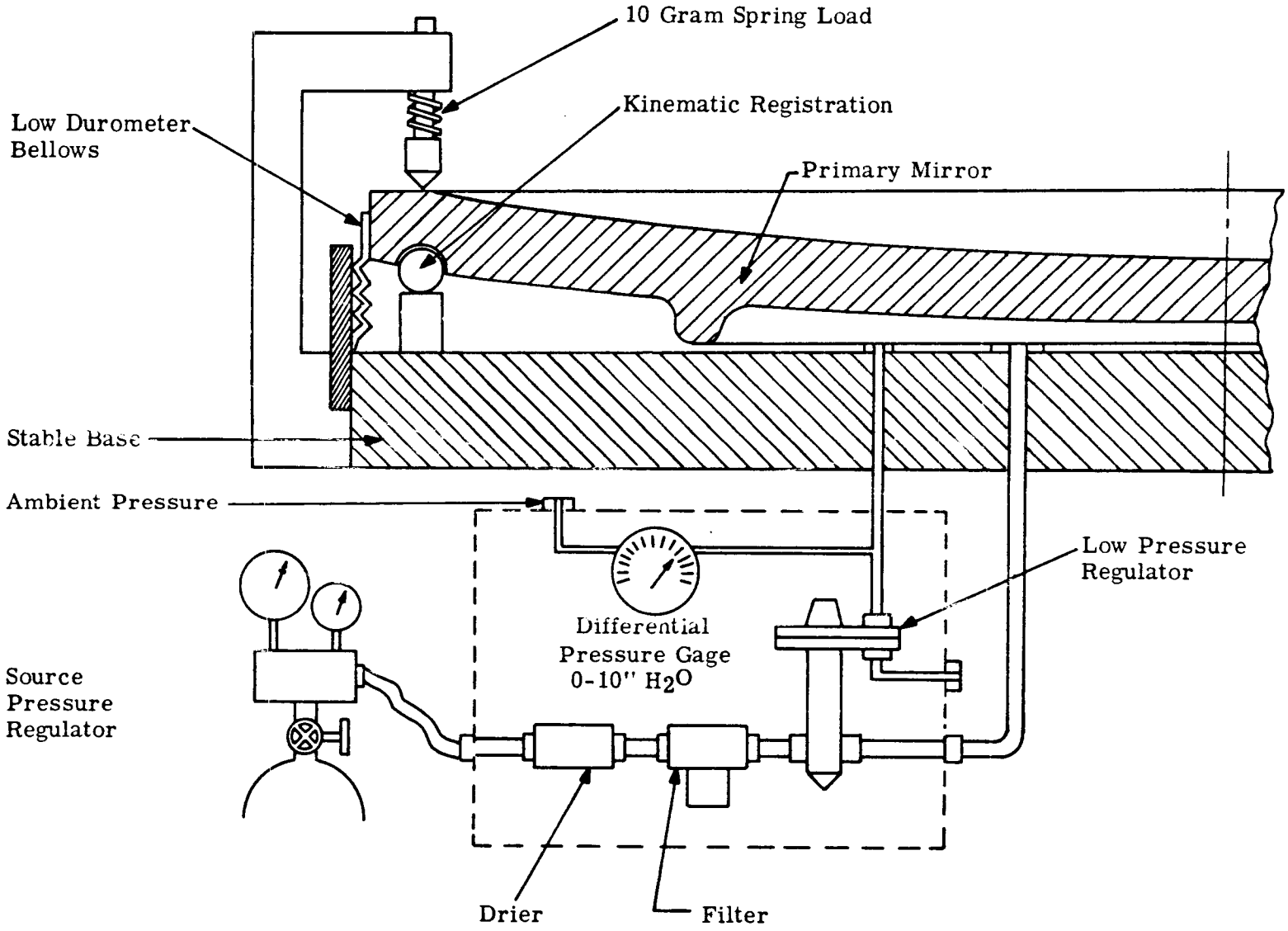


Figure 4.10-1a Zero-G Test Fixture

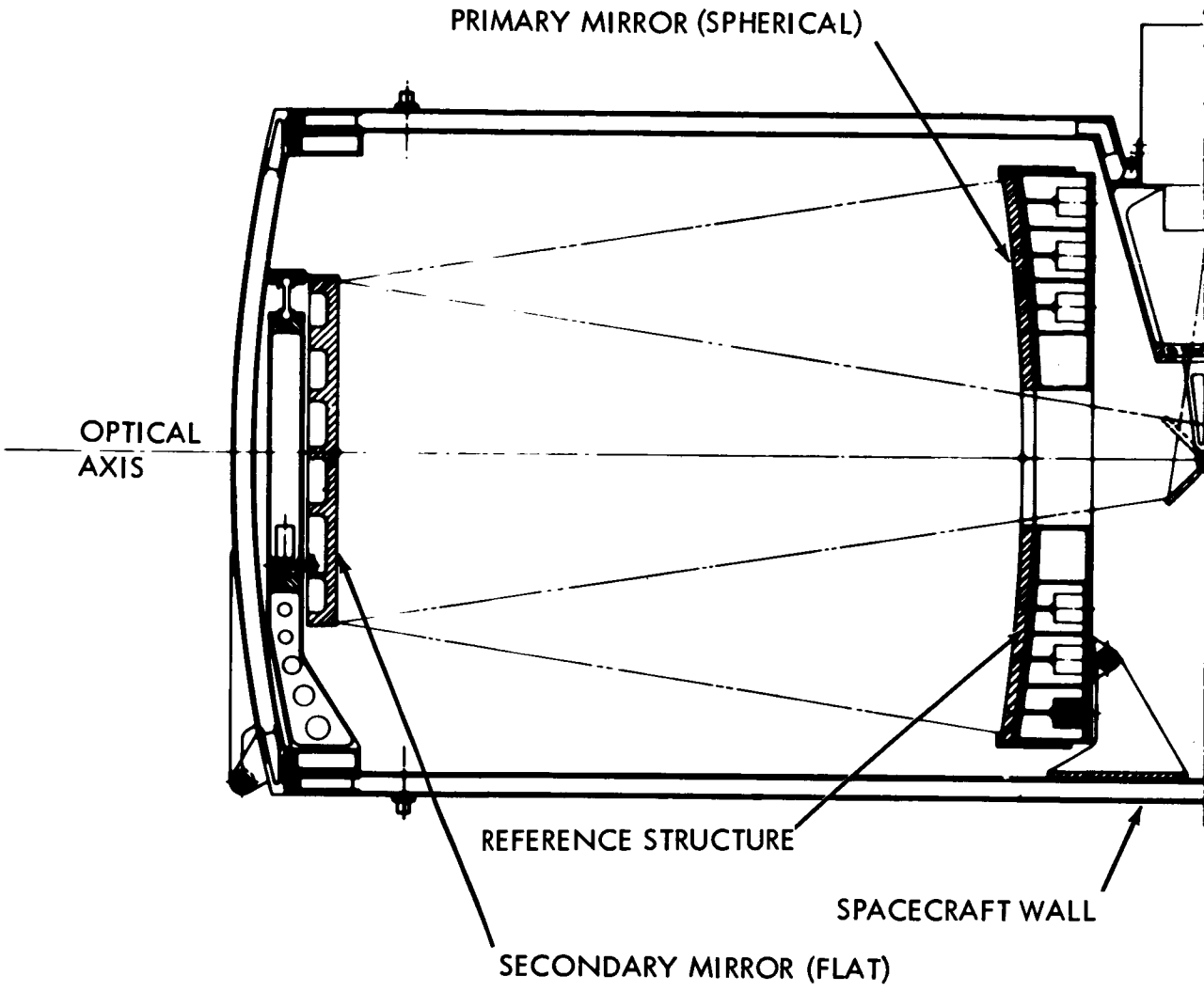
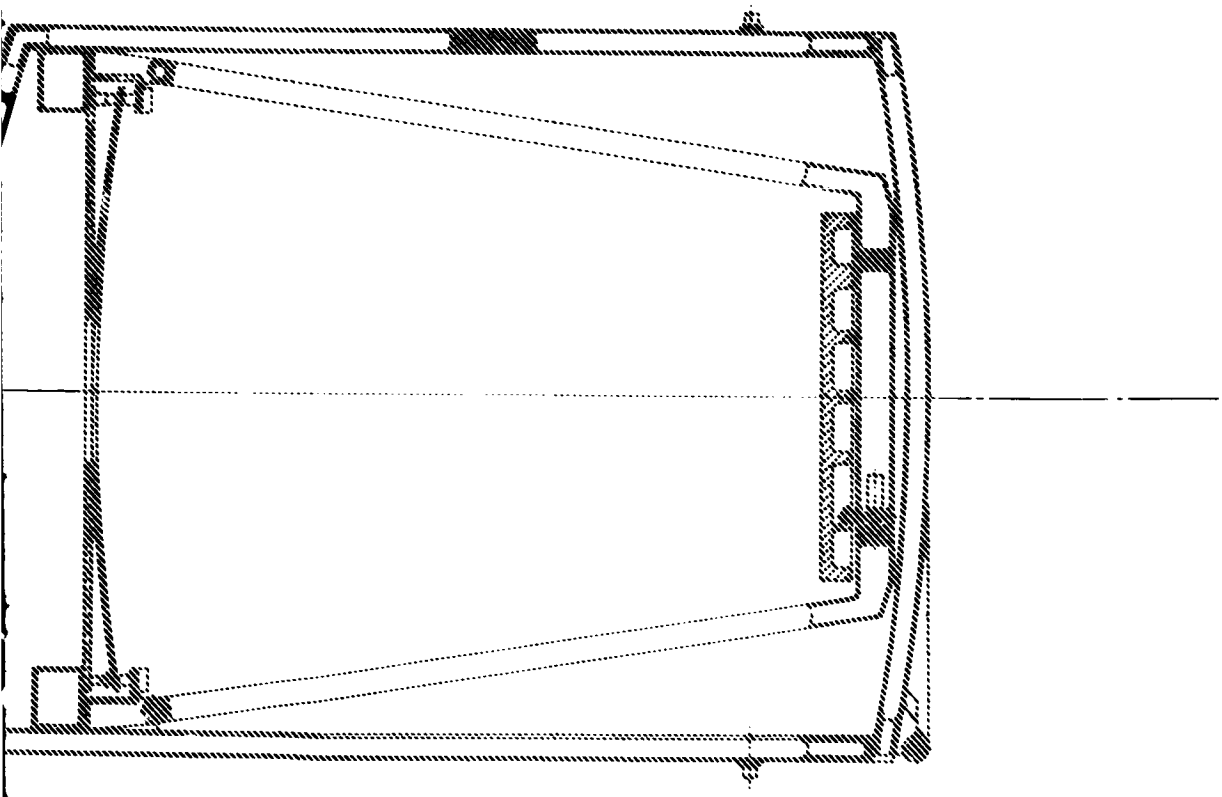


FIGURE 4.10 - Ib PRIMARY
WELL - MIRROR FIGURE TES

PRECEDING PAGE BLANK NOT FILMED.

MIRROR TESTING INSTRUMENTS



R EXPERIMENT
CORRECTION

igure 4.10-1b. Primary Mirror Experiment Well-Mirror Figure Test and Correction

4.10.4 Implementation

The chart of Figure 4.10-2 shows the major functional components and the design alternatives that were considered. In this experiment we selected a thin mirror "active-thermo-mechanical control" concept.

The chart of Figure 4.10-3 shows the steps involved in the implementation of this experiment to obtain the necessary technological data for future large thin mirror optics for space.

4.10.4.1 Experiment Design

The experiment (see Figure 4.10-1b) contains a thin spherical beryllium mirror "fixed" at selected points to a stiff light-weight reference structure.

A matrix of mechanical actuators is placed between the mirror back and the reference structure. These change the shape of the front surface by applying forces between the mirror and the reference structure. The actuators are individually controlled and capable of continuous operation for mirror surface control. The test and evaluation instruments are placed at the center of curvature of the spherical mirror as noted in Figure 4.10-1b.

The parameters to be measured are as follows:

a. Mirror figure change from earth to space environment (microns)

b. Mirror figure control with actuators only (microns/ Kg cm)

c. Mirror figure control with heaters only (microns/ΔT)

d. Mirror figure control with actuators and heaters (manual and automatic mode)

A block diagram outlining the major elements of mirror control and test is shown in Figure 4.10-4. Two modes of mirror control are presented. These are manual mode and automatic mode. The mirror figure is tested with a scatter plate interferometer that includes a fringe pattern readout. This fringe pattern is compared with a reference fringe pattern. In the automatic mode, the fringe pattern is converted to digital information by the scanner mechanism. This data is sent via telemetry to a ground based general purpose computer. A comparator compares both patterns and develops digital control signals which are transmitted to the spacecraft. These signals are used to operate the mechanical actuators which apply forces to the rear surface of the mirror to alter the figure. The temperature sensing section of the diagram depicts a secondary feedback loop for maintaining the mirror isothermal. The mechanisms shown in the diagram are discussed in more detail in subsequent paragraphs.

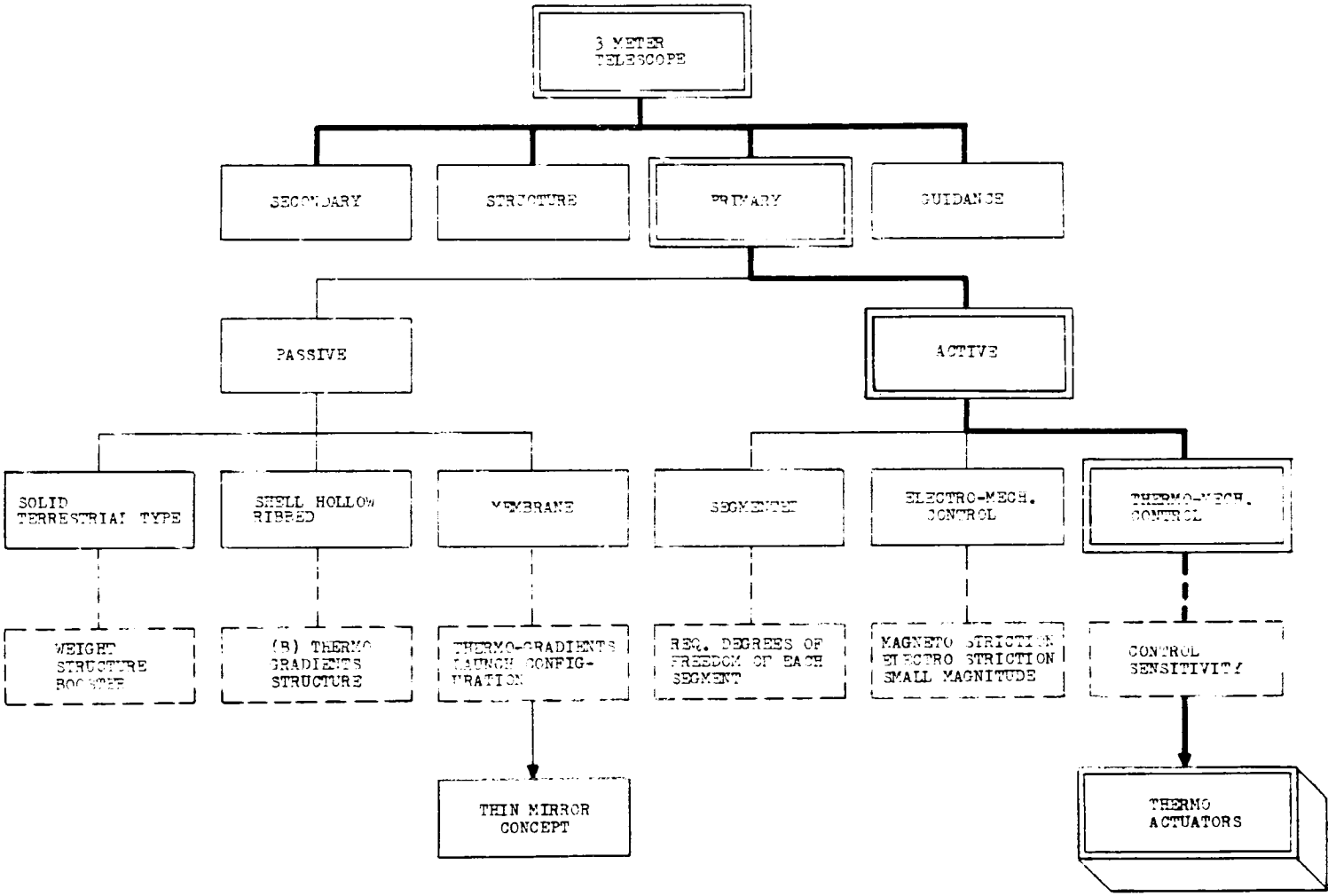


Figure 4.10-2 Design Approach

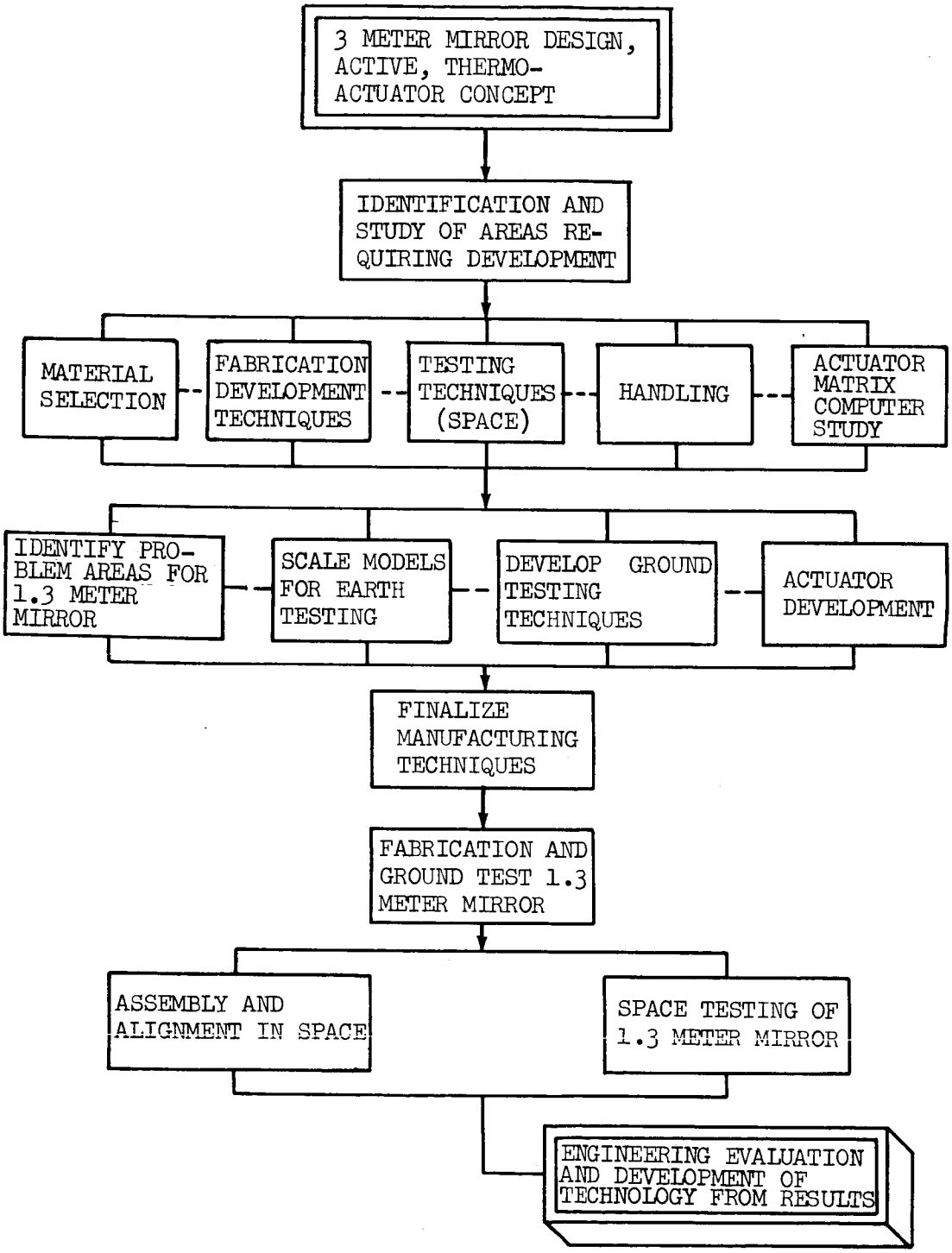


Figure 4.10-3 Experiment Plan

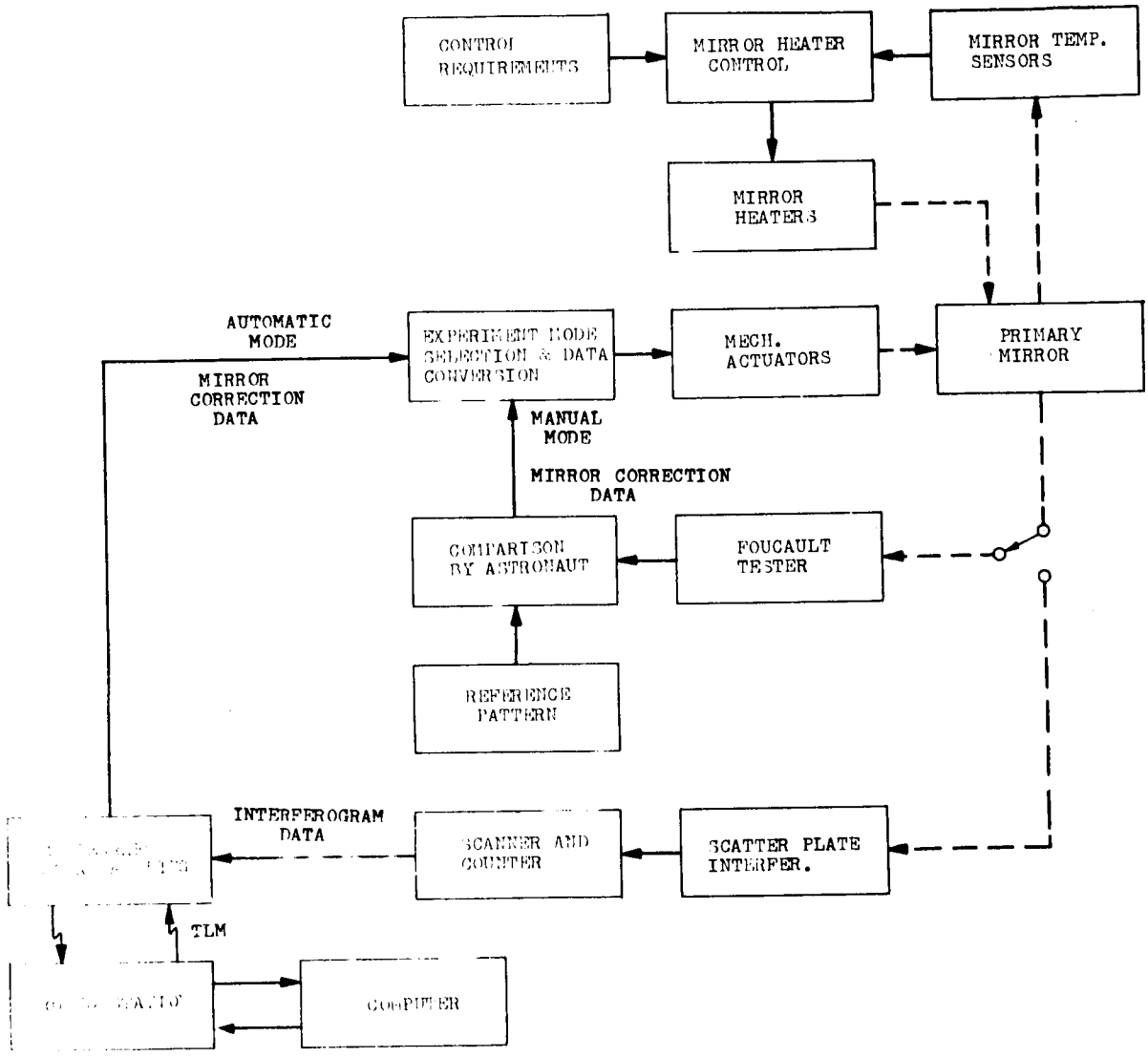


Figure 4.10-4 Design Implementation

An interferometer method has been perfected that tests a mirror at or near the radius of curvature by means of a scatter plate.(1) The scatter plate interferometer has been used to verify large aperture mirrors to tolerances of 1/50th of a light wave. The same instrument will be used during ground and space tests to eliminate instrument error. Section 4.10.5.1 describes the operation of the interferometer.

The most significant test instrument is the scatterplate interferometer. The components necessary for this type interferometer will be fabricated as per the design suggested by the inventor, J. M. Burch.

Components in the fringe counting and measurement section of the system that require developmental effort are listed below:

a. PPI scan deflection circuitry

b. Electronic blanking logic circuitry

The hardware associated with controlling the figure of the primary mirror will be development and ground tested. The fabrication of these parts are within the state-of-the-art. Circuitry associated with the interface between test and control hardware will also be designed, developed and ground tested.

The manner in which the stored fringe data is used for control of the mirror figure must be studied. The ultimate use of the data is to provide information which will serve as command signals for closed loop operation of the actuators. Considerable empirical data is necessary to obtain the relationship between feed back error signals and control signals to correct the mirror figure. Thus before a fully automatic system for figure correction can be successfully instrumented, development and ground testing is required in addition to the present KIC analysis by computer program. This will determine how combinations of actuators in the matrix are applied. Section 4.10.5.8 summarizes the computer study to date.

A schematic drawing of a 1.3 meter diameter spherical mirror was shown in Figure 4.10-1b. This mirror is a scale model of 3 meter and larger telescope designs. The thin mirror design is reviewed in section 4.10.5.2. Of interest is the table in that section tabulating mirror thickness and weight vs mirror diameter.

Since the experiment is to determine the ability to control an optical surface, the shape of the surface should permit ease of manufacture and tests. Therefore, a spherical surface has been selected taking advantage of the condition of unity magnification during mirror figure evaluation, i.e., it permits Foucault and interferometer tests to be performed at the center of

(1) "Scatter-Fringe Interferometry" by J. M. Burch, Journal of Optical Society of America, Vol.52, page 600, 1962

curvature. This is also realistic since it does not vary too much from a paraboloid and will satisfy the experiment requirements (e.g. the difference in sagittal dip between a 1.3 meter spheroid and a paraboloid each having an arbitrary radius of 6.25 meters is only 8 times 10^{-5} meters). Section 4.10.5.3 describes a comparison of shapes (spheroid vs paraboloid). Hence, the results of figure tests on a spherical mirror are most applicable to a paraboloid and the experimental results can later be applied to the common aspheric surfaces used for telescopes.

The fabrication and testing, on earth, of a thin shell primary mirror will be in a nesting fixture. Essentially, this "nesting technique" is such as to provide uniform mechanical support and thermal continuity throughout the initial manufacture of a thin shell primary, so that it is completely unstrained while in its nest. Section 4.10.5.4 describes this further.

Beryllium S-200-C was selected as the mirror material for this experiment on the basis of thermal, physical, stiffness-to-mass ratios and manufacturing considerations. Section 4.10.5.5 reviews these considerations. Of special interest is Table 4.10-3 of this section.

The reference structure is aluminum welded in an egg-crate type design with 50 millimeter (2-inch) thick plates top and bottom per Figure 4.10.5. The top plate of this reference structure will contain the actuators which are in contact with the rear surface of the mirror. The top plate curvature will match the rear surface of the mirror. However, during the polishing, figuring, and testing phase, a spherical back plate is used as a nest to uniformly support the mirror on the table of a polishing machine. Circumferential restrainers will be used to keep the mirror in position. After mirror figuring, the reference structure is used for storage and installation into the spacecraft.

Three mounting pads are located on the base plate of the reference structure. These pads are placed at a .707 radial distance per Figure 5.10-5. The top plate contains clamps around its circumference for retaining the mirror rim. It should be noted at this time that the reference structure will be designed to isolate mirror surface changes from the surrounding spacecraft structure. The most vital part of the figure control mechanism is the actuators.

These actuators are shown in Figures 4.10-13 and 4.10-14 of Section 4.10.5.6 which describe the actuators in detail.

If the mirror shape changes uniformly as a function of force or temperature, the primary effect is a change in focus without loss in image definition. Temperature effects can cause local changes which will produce aberrations or image defects. The extent of local deformation can be severe. Consider that the beryllium mirror surface will move approximately $\lambda/3$ for a temperature change of one degree C. Also, the resulting change of mirror shape will be a function of the length of the temperature gradient across the mirror. Thus, some type of thermal control may be required with at least 1/10 degree C sensitivity in order to maintain the mirror figure.

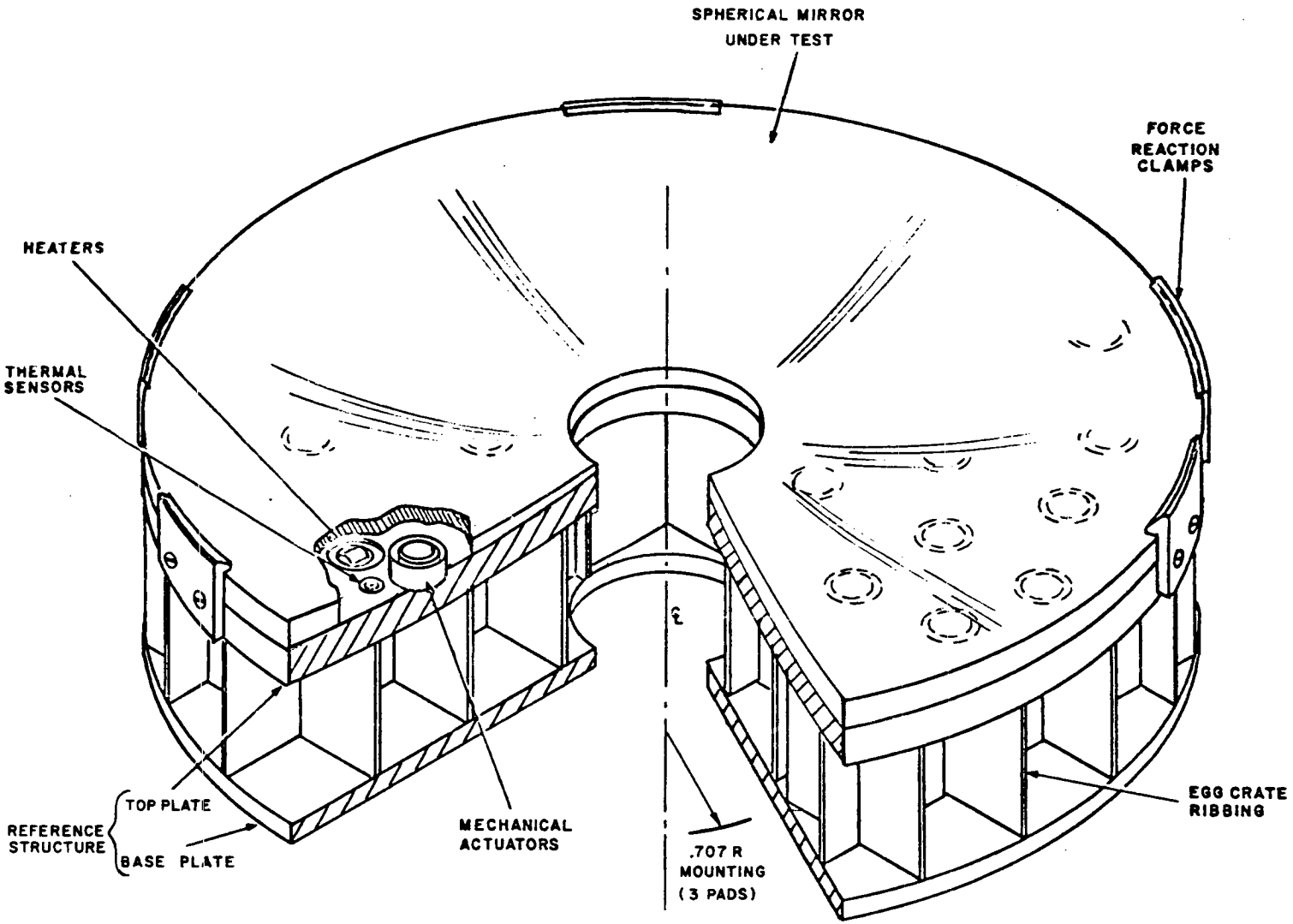


Figure 4.10-5 Test Mirror Mechanization

Since thermal control will be required, it is appropriate to use such control for stabilizing the mirror to an isothermal condition and to use thermal control for reshaping the mirror figure. The "thermal only" figure control was not fully investigated at this time. This concept requires a multi-mode analysis where the inputs are a function of variables related to the spacecraft and what the mirror "sees". Since the mirror will not support thermal gradients, the most significant means of figure control will be by means of thermo-mechanical actuators.

4.10.4.2 Operational Procedure

In view of pre-test tasks, an observer will be called upon to perform these operations. After launch and during the interval for the mirror to approach thermal equilibrium, the astronaut will need to perform some of the tasks outlined below. These tasks are divided into two categories, i.e., manned and automatic mode.

4.10.4.2.1 Set Up Time (Manned Tasks)

		Estimated Time
a.	Primary mirror is uncovered from launch configuration to test set-up. This task consists of -	
	(1) Removing pneumatic cushions and retaining straps	15 mins.
	(2) Removing protective mirror coating	15 mins.
	(3) Assuring mirror is seated	10 mins.
b.	Erecting Secondary support system and placing secondary flat in position. A tripod secondary support system is envisioned permitting the astronaut to have access to the primary mirror.	20 mins.
c.	Alignment of optics	
	(1) The flat is adjusted normal to the optical axis. An illuminated cross wire at or near the vertex of the primary will be used as the target and autocollimation from a reference location will be used.	15 mins.
	(2) Center of Curvature Established. The test equipment will be accurately located so that the knife-edge test instrument can be adjusted within.	15 mins.

(3) Final Alignment and Smoothness Evaluation. 20 mins.
Using the knife edge tester the accuracy of Focus alignment will be attained so that scatter-plate tests can be performed.

(4) Install the Scatter-plate Interferometer Module. 20 mins.
It has the same mounting configuration as the knife-edge tester. Therefore, these modules need only be interchanged without adjustments.

4.10.4.2.2 Automatic Mode

a. Obtain an Interface Pattern of the Mirror prior to operating controls. 30 mins.
This pattern may be forwarded to ground stations by energizing Auto. Mode Switch as shown in Figure 4.10-4. The Interferogram is compared to the reference pattern to obtain Mirror Figure change from earth to space environment.

b. Investigate Surface Figure as above to obtain Mirror Figure Control with actuators only. 1 hour

c. Monitor Temperature Sensors and activate heaters as required to attain isothermal mirror. Operate force actuators and investigate surface figure as above to obtain mirror figure control with heaters and actuators - (Manual Mode). 1-2 orbits
The effects on the mirror shape by various combinations of actuators and heaters will be noted by the Interference patterns obtained.

The above 3 steps should be conducted with an astronaut available to determine facts or factors not automated but of possible interest.

d. Continue to investigate surface figure as in Step 4.10.4.2-1c(4) above. The data may be stored aboard the spacecraft then transmitted to a preselected ground station for comparison. This information is relayed to the ground station via telemetry where a zone-by-zone comparison is then made by appropriate selection of data in the computer. 2-3 orbits

4.10.4.2.3 Error Averaging

Each actuator controls a fixed section of the mirror and an average error for that section can be computed. The results of that portion of the interferogram are summed in the appropriate section of the computer.

4.10.4.2.4 Control of Heaters.

Each actuator of the mirror has a corresponding coded command from the ground based computer. The coded command will actuate control circuitry wherein signals are generated and sent to the actuator control mechanism. The signals will be based on the average error computed for that zone and will dictate the quantity of heat necessary for correction. Thus after the experimental data are complete, they will be analyzed. The parameters of actuator quantity, location and matrix, force and heat requirements, operation patterns, etc. will be determined. Based upon this, optimum designs will be made for future large diffraction limited mirrors, with confidence levels exceeding 99% that correction to mirror figure requirements will be attained.

4.10.5 Supporting Analyses

4.10.5.1 Interferometer Measurement Analysis

Figure 4.10-6 is a schematic of the scatter-plate interferometer. A laser beam is projected by lens 1 to focus on the center of the spherical mirror at point E. A scatter-plate intercepts this beam (Point A) so that part is transmitted undeviated to point E. Part of the beam is deviated or scattered to Point F. The mirror reflects both beams which re-combine (Point C) on the scatter-plate. A difference in length exists between A E C and A F C if the mirror is not a perfect sphere. This path length difference will create a pattern of dark interference bands or fringes. These are projected by Lens 2 onto the electronic scanner. The scanner reads out the pattern to a ground station.

The intensity distribution for these interference bands is given by the following relationship:

$$B_R = 1 + B \cos \left[\frac{2\pi (R-Ro)}{\Delta R_i} \right] \qquad (1)$$

For an average brightness value of unity, maxima are obtained where $B_R = 1 + B$, for $R = R_1 \ldots R_n$. The distance, R_i, is the separation between successive fringe brightness peaks and will be a function of the mirror contour, scatter plate aperture, and focal length of the mirror. The scanner should be automated to solve this equation.

The electronic scanner sweeps across the fringe pattern and generates a signal whose waveform is the electrical analog of the brightness of the interference bands. The concentric fringe pattern obtained with the scatter plate interferometer is best displayed by a polar coordinate scanning system (see Figure 4.10-7). Thus, a radial or PPI type display which scans across fixed angular intervals can be implemented. An image dissector tube and circuitry for obtaining a linear sweep is helpful. Small departures from linearity will not significantly affect accuracy because the reference pattern is the desired interferogram.

The reference interference pattern is contained in a similar PPI scan performed with the same instruments prior to orbit. The reference scan and the test scan are fed to the comparator. This device generates a one-to-one correspondence between pattern and compares both patterns. In regions where both patterns are identically superimposed electronic blanking will become effective. Hence, the resultant pattern will collate any departures from the reference figure. Zero cross-over points and fringe counts will be measured and stored.

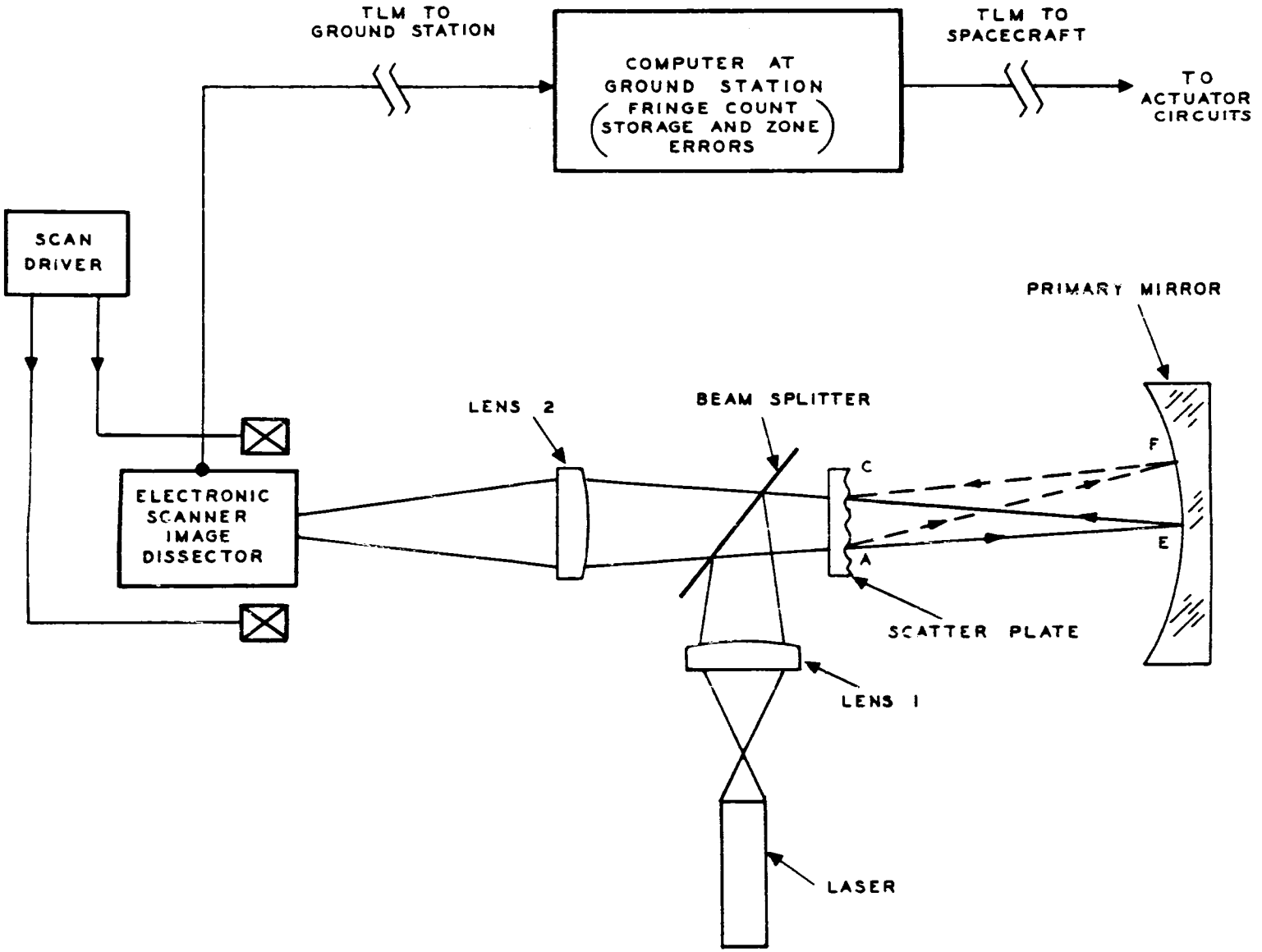


Figure 4.10-6 Scatter Plate Interferometer with Fringe Readout and Error Computation

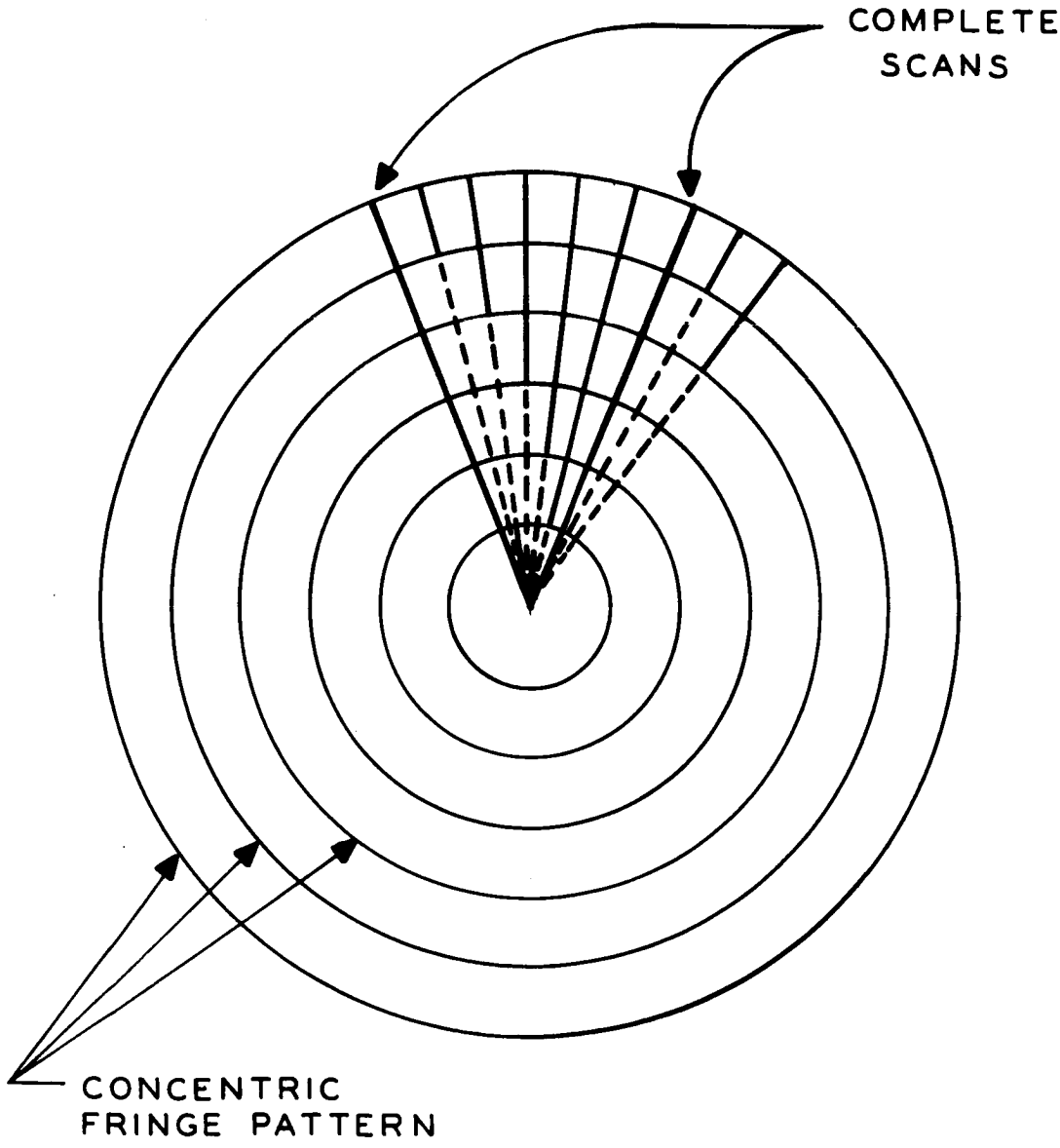


Figure 4.10-7 Radial Scan With Electronic Blanking

4.10.5.2 Mirror Thickness Evaluation

To design these mirrors, use is made of the concept of Precision Elastic Limit (P.E.L.), which is defined as the stress which produces a residual strain or deformation of one micro-inch per inch. This concept recognizes the fact that hysteresis effects or departures from Hooke's Law must be considered in very precise optical systems. For a mirror of given diameter, the criterion used for establishing the required thickness is simply that, stresses induced by handling must not exceed the P.E.L.

For analytical purposes, flat plate theory applies adequately to the present problem (the "stiffening effect" of a spherically shaped mirror blank is insignificant to the results - flat plate theory is more conservative).

A mirror made of S-200C Beryllium, a highly stress-relievable grade recommended for telescope mirror use, was selected based upon the analysis contained in Section 4.10.5.3. It has been determined by studies made for the Navy(1) that the P.E.L. stress, which will produce one to two micro-inches per inch permanent deformation, is 2500 psi. Since our confidence level is not as high as is desirable, 125 psi will be used as the maximum allowable handling stress yielding a margin of safety (MS);

$$MS = \left[\frac{2500}{125}\right] - 1 = 19$$

From the equation for radial or tangential stress for a thin plate supported at the rim with a uniformly distributed load (weight of mirror in a one g field) we can then determine that the corresponding mirror thickness is expressed by:

$$h = .0006\ a^2 \qquad (1)$$

where a is semi-diameter of mirror in inches.

Also, from the equation for deflection at the center, using the appropriate numerical values, we find that the maximum deflection for a rim supported mirror is given by

$$y = 14.5 \text{ times } 10^{-10}\left(\frac{a^4}{h^2}\right) \qquad (2)$$

- - - - - - - - - -

(1) Dr. T.J. Hughel, "An Investigation of the Precison Mechanical Properties of Several types of Beryllium" by G.M. Research Labs, 1960.

It should be noted that, for three equally spaced point supports at the rim, the analysis for maximum deflection of a beryllium mirror yields an almost identical result as in (2), except that the coefficient 14.5 must be replaced by 21.0; i.e.,

$$y = 21.0 \text{ times } 10^{-10}\left(\frac{a}{h}\right)^4 \qquad (2')$$

Table 4.10-1 lists the corresponding numerical values obtained from the equations above for several sizes of mirror

As shown in the table, the plate deflection, y, is identical in all cases. This results from the criterion of a given strain level as applied in equations (1) and (2). Inspection of the equations shows that stress is proportional to $\frac{a^2}{h}$ and that deflection is proportional to $\left[\frac{a}{h}\right]^2$.

Substitution of the appropriate constants yields a maximum deflection of a trifle over 0.1 mm. (0.0042 inch) in all cases obeying the Fractional Precision Elastic Limit as a criterion. This deflection is large enough to permit mechanical measurement by ordinary means. In the "zero g" environment of orbital testing, the mirror should return very closely to the initial mathematical figure, so that optical testing, e.g., by scatterplate interferometry will be feasible.

In order to establish a scale model to be tested for extrapolation to the three meter size, we have seen fit to stop at a minimum diameter of 32 inches for practical reasons. The practical considerations of machining and handling thin beryllium blanks establishes a minimum thickness and hence a minimum diameter. The graph, Figure 4.10-8 shows the relationship between mirror thickness and diameter for a range of diameters from 5 inches to 120 inches for the scaling model. As can be seen from the graph, the mirrors become extremely thin for diameters under 32 inches. Our experience with beryllium, especially with respect to its brittleness and notch sensitivity, inclines us to the view that the machining and handling of this material in mirror blanks where the thickness falls below 0.2 inches presents serious practical problems. A model, approximately 50 inches in diameter and 0.38 inches thick, should prove useful and would still be within range of many available Draper grinding and polishing machines.

4.10.5.3 Shape Variation-Sphere vs Paraboloid

Figure 4.10-9 shows the geometry of a paraboloid and a sphere. The eccentricities at various points have been calculated and tabulated in Table 4.10-2. These eccentricities are within interferometric measurement techniques.

TABLE 4.10-1

THIN SHELL MIRROR

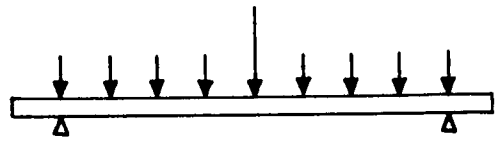
MARGIN OF SAFETY

PEL. ALLOW 2500

PEL. USED 125

$MS = \left(\frac{2500}{125} - 1\right) = 19$

CIRCULAR FLAT PLATE
UNIFORMLY SUPPORTED AT
RIM. LOAD IS ITS OWN WEIGHT.



THICKNESS

$h = .0006\ a^2$ (1)

h = thickness
a = half-diameter
y = deflection

DEFLECTION

for rim supported mirror

$y = 14.5\ (10)^{-10}\ \frac{a^4}{h^2}$ (2)

for 3 point support at edge

$y = 21\ (10)^{-10}\ \frac{a^4}{h^2}$ (2')

DIAMETER (2a)	THICKNESS (h)	DEFLECTION (y)	WEIGHT (W)
32 inches	.156 inch	0.0042 inch	8.4 lbs
50	.38	"	49.8
60	.54	"	103
80	.96	"	323
100	1.50	"	788
120	2.13	"	1615

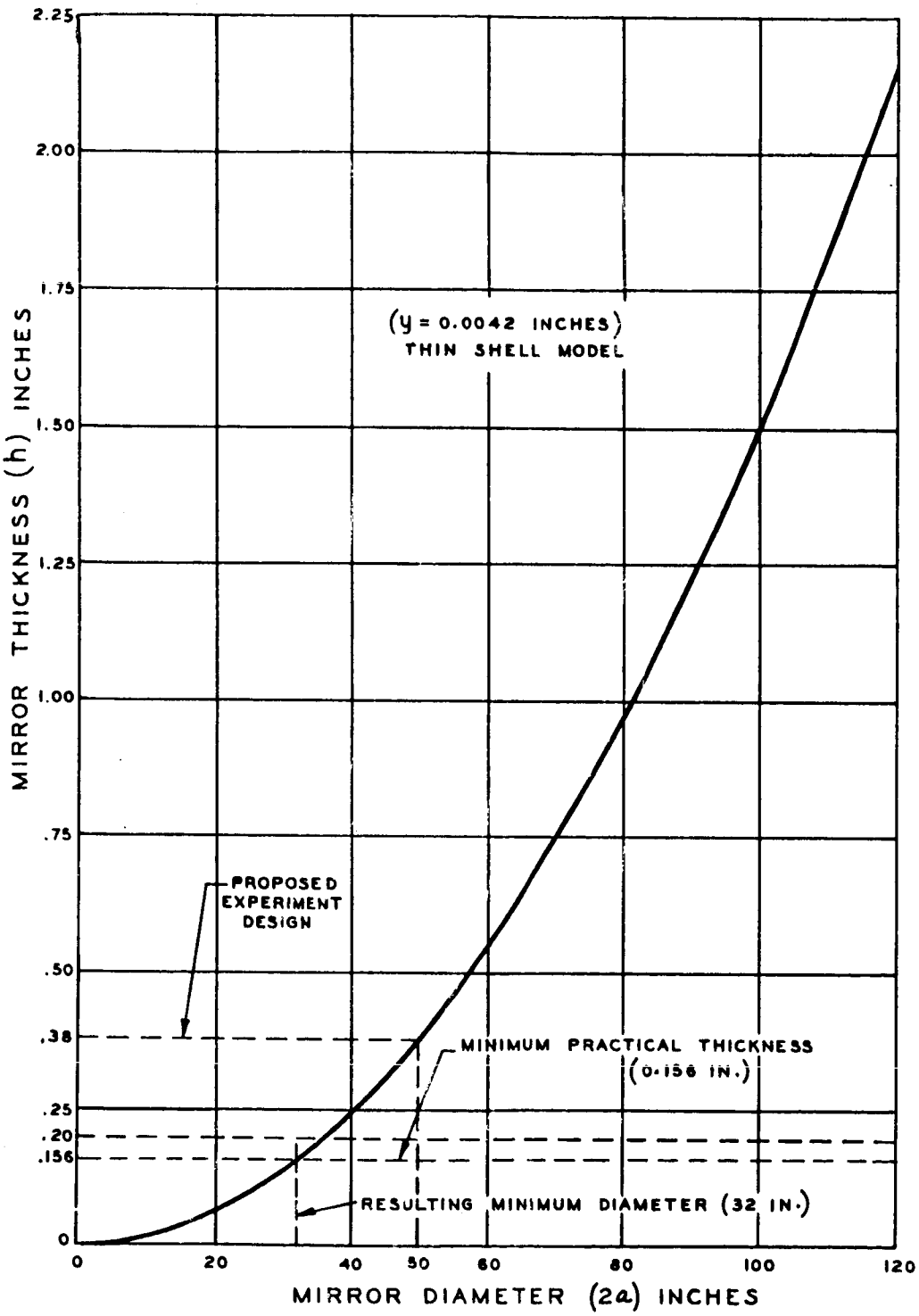
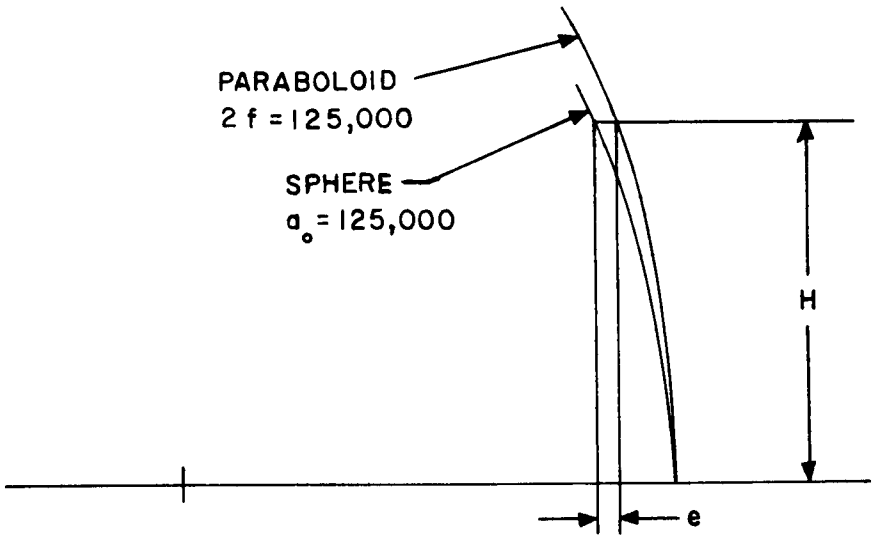


Figure 4.10-8 Mirror Thickness vs. Diameter (Thin Shell)



The eccentricity at height H from the center

$$e = \frac{1}{64}\left(\frac{H^4}{f^3}\right)$$

where f = focal length = $a_o/2$

Figure 4.10-9. Geometry of a Paraboloid and a Spheroid

TABLE 4.10.-2

ECCENTRICITY OF A PARABOLOID RELATIVE TO A SPHERE

h	e
1	.000 000 06
2	.000 001
3	.000 005
4	.000 016
5	.000 040
6	.000 082

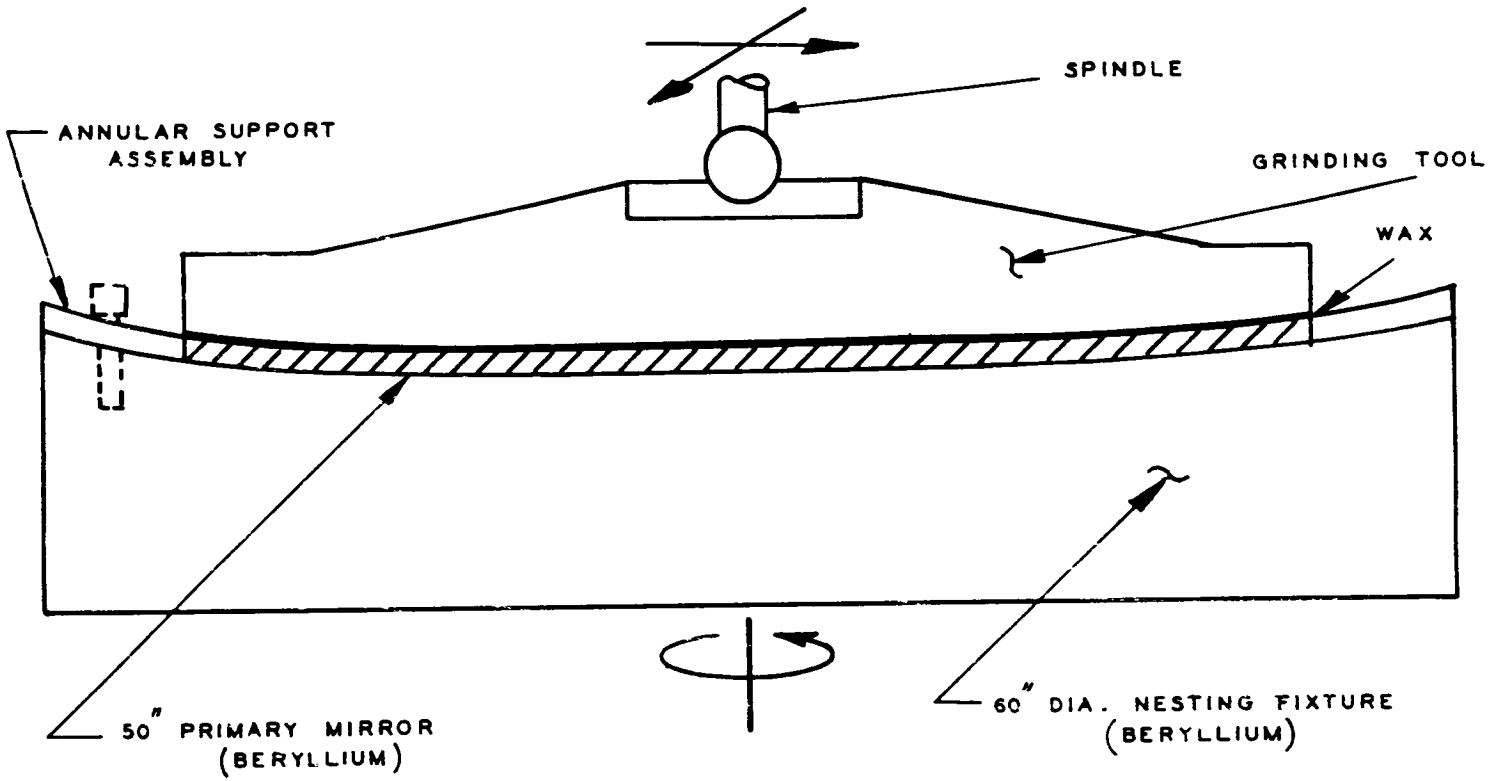
4.10.5.4 Fabrication and Nesting Techniques and Evaluations

The manufacture of a large thin mirror presents the problem of supporting the element during fabrication. The local effects of the polishing tool and the strains resulting from the mirror's own weight in a one-g earth environment dictates a complete and uniformly distributed support of the mirror during all manufacturing operations. A uniformly distributed support can be designed as a nest wherein the mirror can be fitted to the nest with a wringing fit. In this way, total support for the thin mirror can be obtained. The same material as the mirror (Beryllium S-200-C) is recommended for the "nest". The nesting technique calls for the back of the mirror to be ground to form a spherical seat. The nest is then ground and polished to obtain a precise spherical fit with the mirror. See Figure 4.10-10. If may be necessary to coat the nest with Kanigen or equivalent material to minimize seizing between the mating surfaces. Both nest and mirror would be thoroughly strain relieved to remove stress concentrations induced by the nesting. After the spherical fit is obtained, the mirror can be retained in the nest by vacuum. This thin mirror will remain in the nest for all (1 g environment) manufacture and testing. The major manufacturing sequence for the mirror is grinding, polishing, front surface figuring, aluminizing, then a final overcoat of silicon monoxide.

After manufacture and tests the mirror must be removed from its nest and assembled to the remaining optics. The manner in which the mirror is removed becomes complex in view of the wringing fit between mating surfaces. A wringing fit introduces large resistive forces which prevent separation. The magnitude of these forces need to be determined. The quantitative values will affect the method of surface separation. As a result, a survey is outlined which shows the magnitude of forces involved and a method is recommended that will permit separation of surfaces.

When two surfaces are in intimate contact, there are two forces that act on those surfaces. Molecular cohesion is one force. Solid surfaces regardless of optical quality make intimate contact only at the tops of their surface roughness. Under pressure and without contaminants, cold welding may occur. Such adhesion involves the tensile strength of the regions in actual contact. Friction is the second force. When one surface slides on the other, the force resisting motion depends on the shear strength of the regions in actual contact. Hence, the strength of materials in contact and the area in contact affect cohesion and friction.

In air, hard and clean surfaces may show appreciable friction or cohesion at the regions of metal to metal contact. Under special conditions, a thin film can produce strong cohesion. Such cohesion is the result of surface tension due to the film. For example, surface tension is the major cause for cohesion between two gauge blocks "wrung" together. Under normal stress, cohesion increases due to a growth in contact area.



- SPHERICAL MATING SURFACES
- UNIFORM HEAT SINK AND SUPPORT
- THIN SHELL INTEGRAL WITH NEST THROUGHOUT MANUFACTURE AND TESTING

Figure 4.10-10 Thin Mirror Mfr. (Nesting Technique)

Consider that any sliding action between dry surfaces produces plastic deformation at the high spots such that the mean surfaces sink closer together. Therefore, the contact area increases. It has been shown that at any stage of this deformation, the normal stress, p, and the tangential stress, s, are related by $p^2 + \alpha\ s^2 = p_o^2$. (1) The symbol, α, is a constant (approx. 3) and p_o is the mean pressure at each contact point. See Figure 4.10-11.

The normal load on a surface in close contact is W = pA and the tangential or sliding force is F = sA. By substitution in $p^2 + \alpha\ s^2 = p_o^2$, the relation for W and F becomes $W^2 + \alpha\ F^2 = A^2 p_o^2$. If the normal force W is a constant, then F increases linearly with A, the area in contact.

The loads F and W are also related by the coefficient of friction from $k = \frac{F}{W}\left[\cos \Theta\right]$. The coefficient of friction varies for some materials according to the environment as explained in NASA Report TN-D-3399. However, the coefficient of friction is considered constant herein. For the condition where loads are normal to the mating surfaces, the angle of contact (Θ) is Zero degrees and cos Θ is one. Hence F = kW. In addition, for very small velocities and clean surfaces sliding friction and static friction are approximately equal.

Optical surfaces flat to 1 wavelength (green light) have a mean variation in height across the surface of 22 times 10^{-6} inches or 550 x 10^{-7} or 550 millimicrons. Two surfaces in contact exhibiting 1 wavelength of flatness will have a separation of 5500 times 10^{-8} cm. Quality optics can be held to better than 1/5 wavelength. In contact, these surfaces will have a gap of 1000 times 10^{-8} cm. The mean free path of nitrogen (air) molecules at standard temperature and pressure is 940 times 10^{-8} cm. Surfaces flat to 1/5 wavelength will permit 2 molecules of gas (height only) to exist during contact. This implies that when two surfaces are wrung together a near vacuum exists between them. In addition, the pressure differential between mating surfaces equals the barometric pressure (normal stress, p.).

(1) D.D. Elay, Adhesion, Oxford Press, London, 1961 - Chap.5

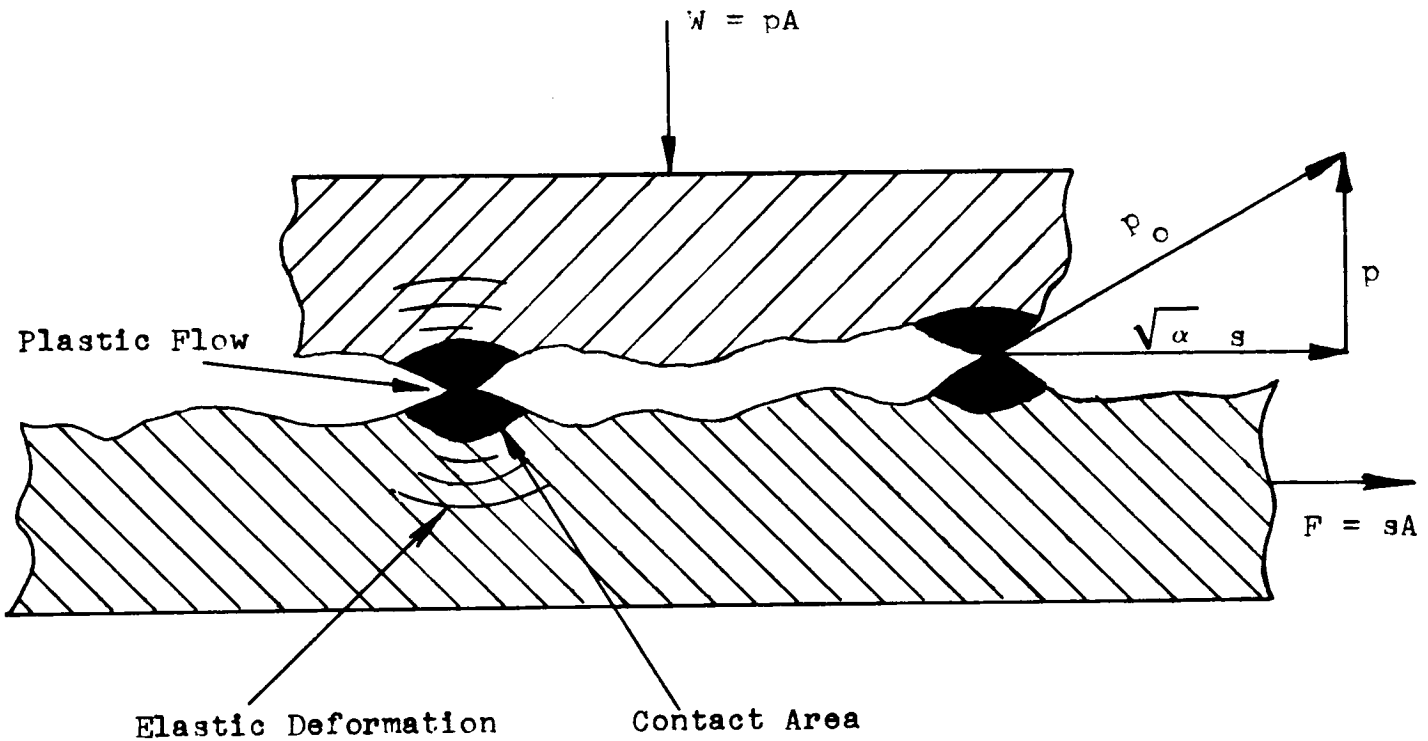


Figure 4.10-11 Contact Between Surfaces

Substituting this value in the previous equation, $W = pA$, one gets $W \text{ lbs} = \frac{15 \text{ psi}}{\text{in}^2}$ times Area in^2. From $F = kW$, $F = k\,(15\,A)$. Assuming a static friction of 0.2, then $F \text{ lbs} = 3 \text{ psi } (A \text{ in}^2)$. For these conditions and by substitution in $A^2p_o^{\,2} = W^2 + \alpha F^2$, $p_o^{\,2} = \frac{(15A)^2}{A^2} + 3\,\frac{(3A)^2}{A^2}$ or $p_o = (225 + 27)^{1/2}$ and $p_o = 15.9$ psi. This value is the combined stress between mating surfaces.

In this report, it is desirable to isolate normal loads from tangential loads and obtain surface separation. Therefore, W and F will be treated independently and compared. By simple substitution, F is some factor of W (assumed at 0.2). Hence, F equals 3A. For a wringing fit between surfaces at or near zero fringes, the area in contact can be considered the total surface area. For a 50 inch diameter surface, the value of W in lbs = 15 psi (π times 25^2, in^2) or 15 tons for separation due to adhesion. The sliding force, $F = 3$ (π times 25^2) or 6000 pounds due to friction.

The above values need to be corrected for the following:

a. Additional forces due to dead weight of the material and the gravitational loads on the dead weight due to attitude.

b. Change due to reflective overcoating to the base metal.

c. Changes in friction coefficient due to optical quality.

Since no data on the above appears available, corrections to W and F loads cannot be supplied.

The method for surface separation is directed towards thepath of least resistance, i.e., sliding forces (F). The maximum allowable handling stress that should be imposed on a Beryllium mirror is 125 psi(1). If one considers a 50" dia. thin shell mirror of 3/8" thickness, the maximum sliding force to be applied as a uniformly distributed load is 3/8 times 50 times 125 or 2300 pounds. Consequently sliding separation cannot be achieved directly in view of 6000 pounds of friction.

- - - - - - - - - - - - - -

(1) KIC Study - OTES Program Experiment

One method to reduce friction forces is to decrease k or W since F = kW. The normal load, W can be reduced by reducing the pressure acting on the surfaces in contact. This is the barometric pressure and an evacuated chamber is necessary to significantly reduce "p". In addition, remote handling devices need to be used during evacuation to obtain surface separation. This method may become fairly complex for large mirrors (50" dia. and over) and needs to be reviewed in greater detail.

An alternate method is to decrease the pressure differential between mating surfaces. This is equivalent to lowering the barometric pressure between surfaces in contact. This can be accomplished by forcing compressed air or a fluid between mating surfaces. This method reduces W by decreasing p. Also, a fluid film between surfaces is equivalent to boundary lubrication and thereby lowers "k" and friction forces should decrease. A uniformly distributed pressure of 15 psi between mating surfaces should lower the differential pressure, lower F and permit sliding separation.

The mechanics of providing a pressure differential between surfaces can be achieved with existing techniques. The surfaces in contact may be shaped such that the lower surface supports the upper mirror on a cellular configuration. This contour permits a wringing fit between surfaces in contact and permits entrance of a fluid film to obtain separation.. However, the width between cellular supports cannot exceed the deflection criteria of the mirror surface. In addition, the supports should be arranged to comply with an equal area or equal weight distribution.

The optical quality of the mirror figure needs to be maintained at all times. The channels introduced for separation permit an unsupported mirror section across each one and these sections may affect mirror figure. It becomes necessary to determine the maximum unsupported mirror span or channel width that can be tolerated.

4.10.5.5 Thermal Considerations in the Selection of Mirror Materials

The thermal effects encountered by mirrors in space is a major consideration in the selection of a mirror material. To this end an index, called the Thermal Warpage Index, has been used and tabulated for evaluating the thermo-physical merits of optical and structural materials. This index is independent of geometric configuration and is purely a function of the physical properties of the materials.

4.10.5.5.1 Thermal Warpage Index

The Thermal Warpage Index, TWI, is a qualitative measure of the ability of a material to resist a change in its dimensions with a temperature gradient applied across the material. The TWI is the ratio of the coefficient of expansion to the thermal diffusivity or;

$$TWI = \frac{\alpha C_p \rho}{k} \quad (1)$$

where:

coefficient of expansion = α (2)

thermal diffusivity = $\frac{k}{C_p \rho}$ (3)

k = thermal conductivity

C_p = specific heat

ρ = density

Thus the TWI is proportional to the coefficient of expansion, specific heat, density and inversely proportional to the thermal conductivity. A derivation of formula (3) may be found in texts on heat transfer such as "Elements of Heat Transfer and Insulation" by Jacob and Hawkins.

The values of TWI for various materials are listed in Table 4.10-3 and may be compared numerically. The materials having the lower TWI will have less of a tendency to support temperature gradients and will stabilize quicker; therefore, they are more desirable.

This is as important in the fabrication stage as in application and use. During fabrication, one of the time consuming factors is the stabilization required between figuring and testing, i.e., the material must be dimensionally stablized before a measure of mirror figure can be made.

Figure 4.10-12 is a photograph of a large light weight beryllium mirror (38" diameter, 1-1/2" thick). Experience with this mirror and others has shown that the time required to stabilize and test beryllium as compared to quartz was significantly less and resulted in a more favorable manufacturing time cycle.

4.10.5.5.2 Comparison of Materials

Material properties and dimensions measured at initial assembly vs. those after long term usage have been known to change. Thus proper material selection and consideration of these possible changes is very important. The material selected for each mirror must be evaluated by metallurgical and radiographic tests to assure the required homogeneity, internal microstructure, surface conditions, etc. Proper stress relief control must be maintained in order to control and effectively eliminate the effects of aging and creep.

TABLE 4.10-3

COMPARISON OF MIRROR MATERIAL

Group	Material	Coefficient of expansion α x 10^{-6} (in/in^{o}F)	Density ρ (lbs/in^3)	Specific Heat Cp (Btu/lb^{o}F)	Thermal Conductivity k (Btu-in./ ft^2 hr ^{o}F)	Young's Modulus E x 10^6 (lb/in^2)	(1)Thermal Warpage Index TWIx10^{-12} (hr ft^2/^{o}F in^4)	(2)Stiffness to Mass ratio E/ρ x 10^6 (psi/lb/in^3)
A	Beryllium	6.4	.066	.46	1040	42.0	187	636
	Aluminum 356A-T6	11.9	.097	.23	1056	10.3	253	106
	Invar (36% Ni) (anneal)	0.80	.290	.12	93.5	21.0	298	72.5
	Quartz (fused)	0.30	.082	.18	9.7	10.0	450	122
	Pyrex	1.8	.081	.20	6.7	9.3	4400	115
B	Pyroceram (9609)	0.10	.095	.185	25.2	17.3	69	182
	Cervit-C-100	0.05	.091	.20	6.7	13.3	135	146
C	Beryllium oxide	4.4	.109	.24	1500	45	77	412
	Copper (pure)	9.0	.322	.094	2760	12	97	37.3
D	Meehanite GA	6.87	.268	.13	350	21	680	78.3
	416 SS (anneal)	5.50	.28	.11	174	29	980	103
	Inconel	6.1	.286	.10	90	31	1940	108
	Monel (as cast)	9.17	.312	.13	186	23	2000	74
	303 SS	9.6	.29	.12	112	28	2980	96.5

(1) Thermal Warpage Index ($TWI = \frac{\alpha \rho C_p}{k}$)

(2) Stiffness to mass ratio (E/ρ)

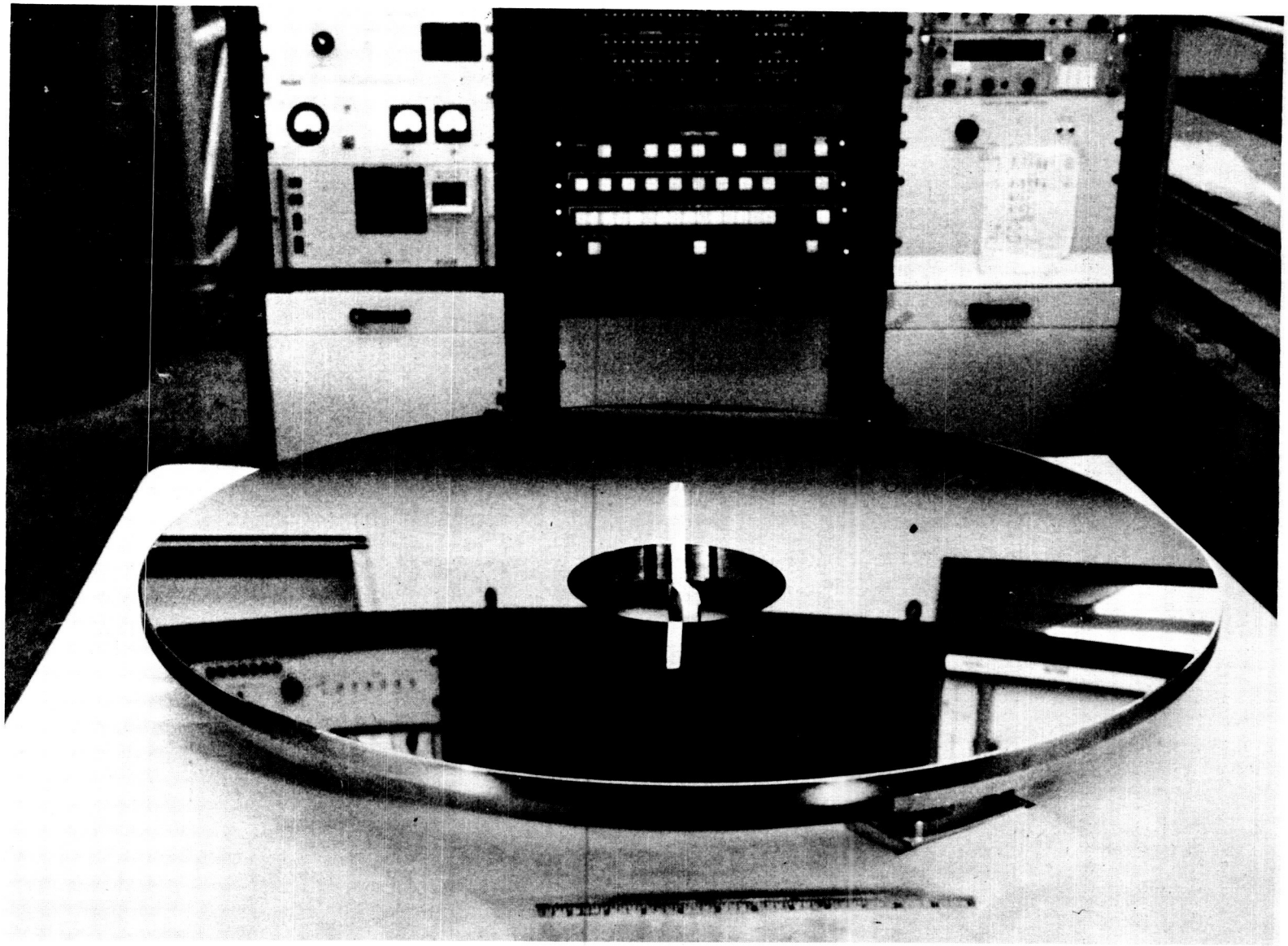


Figure 4.10-12. 38" Beryllium Mirror (Space Application)

Thus, a complete history must be maintained of the mirror material from ingot or press, thru manufacture-assembly and on thru its useful life. This history will be the basis for an accurate quality control of mirror figure as well as providing much needed data for future designs of better and larger mirrors.

Table 4.10-3 tabulates four groups of materials investigated as candidates for mirror material.

Group A lists the materials that will be considered for mirror fabrication based upon availability, practicality, experience and desirability. These materials, headed by beryllium, are ranked in order of lowest TWI. A column indicating the stiffness to mass ratio is also included,

$$\text{stiffness to mass ratio} = \frac{E}{\rho} \tag{4}$$

where:

E = Young's Modulus

The higher the stiffness ratio the more desirable the material is, in that a lighter weight mirror can be fabricated with equal stiffness.

From the consideration of TWI and E/ρ beryllium seems to be the better selection for mirror material.

Group B lists two new "glass" materials with very low coefficients of expansion. The TWI index is very favorable. However, at the present time we cannot consider these materials for large mirrors. The present technology has not produced mirrors over 16 inches in diameter, hence production of a large mirror, say 120 inches, represents a tremendous technological advance. It is also noted that the E/ρ ratio is relatively good except when compared to Beryllium.

Group C lists two additional non-ferrous metals. These have been excluded from Group A because of fabrication problems with the materials and the E/ρ ratio indicates Beryllium will produce a much lighter mirror.

Group D lists several members of the iron-steel family. Their exclusion from Group A is readily apparent when considering the TWI values. In fact, previous experimental efforts with these materials have demonstrated the lack of desirable properties for the manufacture of mirrors.

In conclusion the major desirable properties required of a good thin mirror material are:

a. High modulus of elasticity

b. Low density

c. High conductivity and thermal diffusivity

d. Dimensional stability of mirror figure

e. Machinability

Based upon this and the foregoing analysis, beryllium most satisfies the material requirements for large thin mirror fabrication.

4.10.5.6 Thermal Actuator Design Approach

Figures 4.10-13 and 4.10-14 illustrate how force will be applied to the rear of the mirror via an actuator. An aluminum tube is shown with a wire heater inside and insulated on the outside by 20 layers of aluminized mylar. All surfaces are in contact before heat is applied to the rod. The top plate described will be stiffer than the mirror and can be considered as the reference plane. The expansion of the thermal-actuator will transmit a force to the rear of the mirror and deflect it in proportion to the spring constants of the two materials and the heat applied.

The mirror is attached to the top plate at its outer edge. Therefore, the force required per centimeter deflection will vary with the change in location of the applied force. The outer edge supports are considered as pinned joints and cannot transmit a moment. A preliminary calculation of forces required shows that a .45 kilogram force will produce an 8.0×10^{-7} cm deformation at a point near the axial region of a test mirror that is simply supported at its outer edges. The required sensitivity for controlling the thermal actuators will be established through analysis and pre-tests. The change in the mirror figure before and after orbit is not expected to exceed 2 fringes (one wavelength) or about 50×10^{-6} centimeters. Further, for the measuring or correcting to one wavelength, instruments sensitive to 1/2 wavelength are required. The surface tolerance is 1/32 wavelength and instruments sensitive to 1/60 wavelength are needed. These requirements are within the practical limits of optical measuring instruments.

The coefficient of thermal expansion of the aluminum in the actuator is linear within the anticipated temperature range of actuator operation. The aluminum in the actuator is equivalent to a 1 inch rod which will elongate 12×10^{-6} in when its temperature is raised 1.0 degree F. A temperature control to 0.1°C will be required to obtain elongations within the optical tolerances previously specified.

4.10.5.7 Mirror Figure Tolerance Requirements

It is necessary to establish the precision required for modifying mirror figures and the required mirror tolerances.

When a perfect optical system forms an image of a point source, a diffraction pattern occurs. In this annular ring pattern, 84% of the total energy is concentrated in the central region (the Airy disc) and 16% is spread among the adjacent diffraction rings. The conventional "Rayleigh Limit" is based on the fact that a wavefront which departs

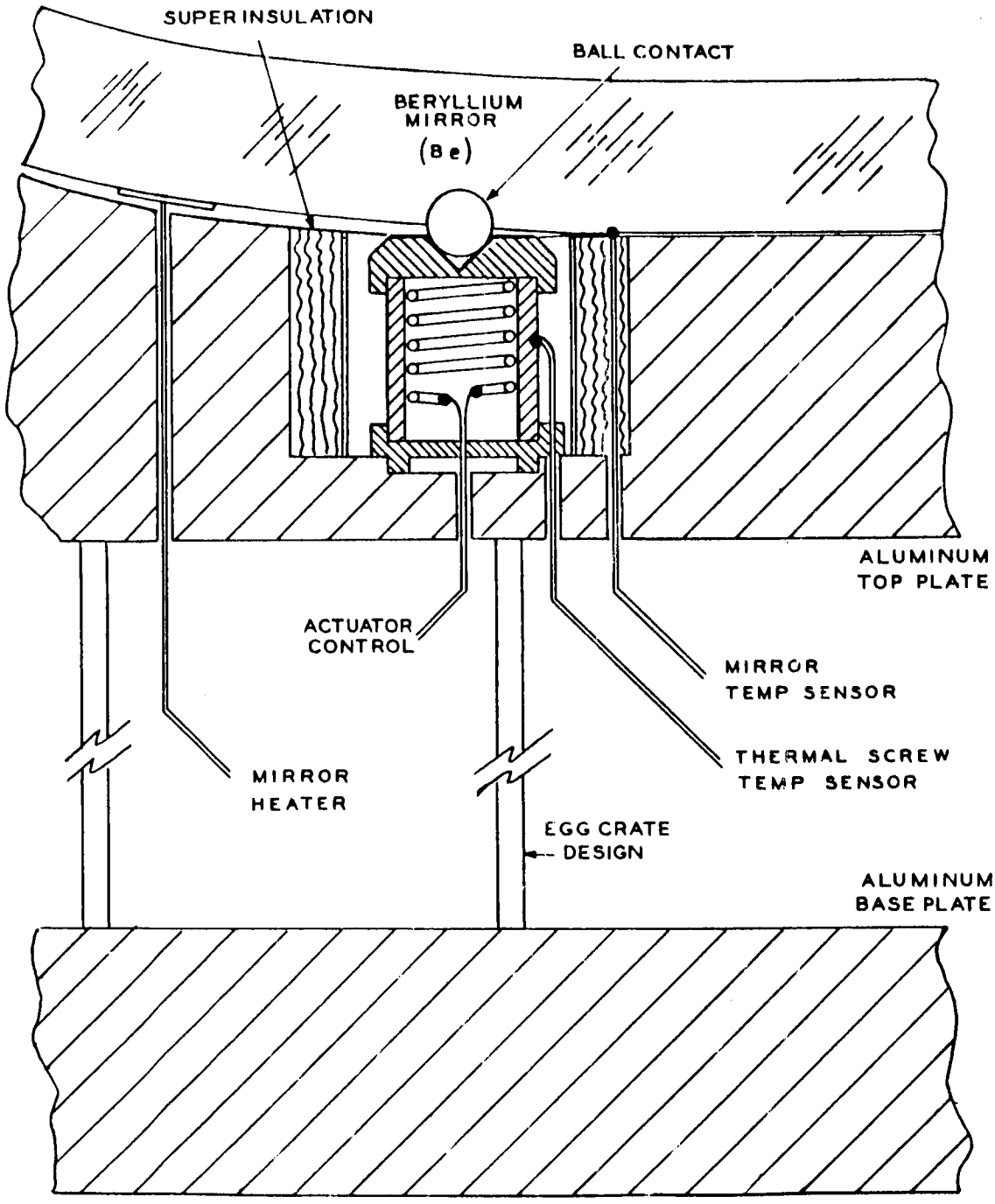


Figure 4.10-13 Unidirectional Actuator Schematic

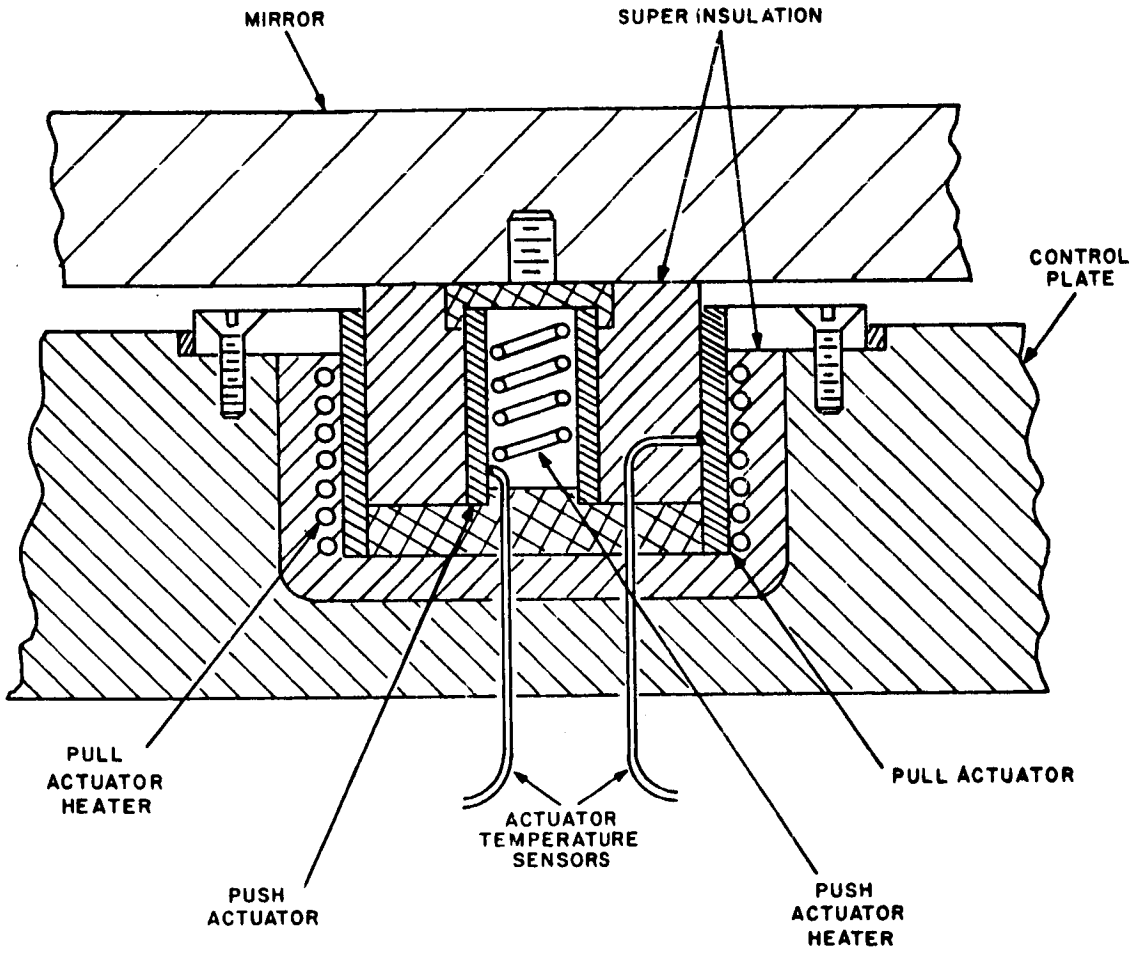


Figure 4.10-14 Bidirectional Actuator Schematic

by $\frac{\lambda}{4}$ from the ideal spherical shape creates a noticeable redistribution of the diffraction pattern relative to the theoretical one, to the extent of a reduction of about 20% in the total intensity of the central Airy disc. For most purposes, this has been considered a reasonable tolerance; however, for many astronomical applications, fractional portions of the Raleigh Limit are deemed preferable.

If the Raleigh Criterion is adhered to, the energy in the Airy disc could conceivably fall to 80% of 84% = 67% of the total incident energy, and this may represent an appreciable degradation. For this reason, it is usually preferable[3] to tighten tolerances to 1/4 of the nominal Rayleigh Limit. This implies that mirror surface should be figured to an accuracy of $\pm$ (1/2) (1/4) $(\frac{\lambda}{4}) = \pm \frac{\lambda}{32}$ (about .55 micro inches) since a mirror doubles the wave-front error. This tolerance will permit the mirror to perform near its diffraction limit or maximum efficiency.

Means of defining these optical specifications are important. One parameter that is useful is a value of the root-mean-square (RMS) value for the deviation of the surface.[4] This quantity can be statistically related to the amount of energy distributed outside the diffraction image. From the exact relations as specified by Shack [5] the following values are found:

2% outside diffraction pattern = 1/50 λ RMS

10% outside diffraction pattern = 1/20 λ RMS

50% outside diffraction pattern = 1/8 λ RMS

In the case of near diffraction performance, interference in the wavefront near the focus redistributes the energy per the above and there need be no concern about the actual values of the maximum residual slope errors of the surface. This information can be obtained directly from error patterns of the interferometer tests.

(1) Hardy and Perrin, "Principles of Optics", p. 128.
(2) Conrady, "Applied Optics and Optical Design".
(3) Southall, "Mirrors, Prisms and Lens", p. 713.
(4) A.B. Meinel, "Introduction to the Design of Astronomical Telescopes".
(5) R.V. Shack, "Applied Optics", 1966.

4.10.5.8 Mirror Correction Analysis

An analysis has been performed on the 50 inch primary mirror to establish the optimum arrangement of actuators for correcting possible error patterns of the mirror. The maximum error in the pattern is assumed to be 1 λ or 20 times 10^{-6} inches. It is desired to correct the mirror so that the maximum distortion at any point is less than $\frac{\lambda}{30}$ = 0.8 times 10^{-6} inches.

The analytical technique used for the mirror correction analysis is discussed in detail in Section 4.10.5.8.1. This technique was programmed for a digital computer for this study.

Two error patterns were considered; a paraboloid error pattern and sinusoid-paraboloid error pattern. The limitation in the number of cases considered was the delay resulting from initial problems in developing a workable digital computer program.

The results indicate that the array of four actuators, shown in Figure 4.10.-18 will reduce the maximum distortion of the mirror to 1.1 times 10^{-6} inches $\left(\frac{(\lambda)}{18}\right)$ for the case of a parboloid error pattern. For the actuator cases considered, the best correction of a sinusoid-paraboloid error pattern was - 2.95 times 10^{-6} inches $\left(\frac{(\lambda)}{7}\right)$, produced by the actuator array shown in Figure 4.10-17.

Although cases were considered involving 4, 8 and 12 actuators, it is felt that further work is necessary on this problem to fully evaluate the possible actuator arrays that could be considered in a study of this nature.

4.10.5.8.1 Analytical Procedure

The purpose of this study has been to minimize the deflections of a circular mirror, resulting from an induced error pattern, with the application of restoring force actuators. The method of obtaining the values of these restoring forces as well as determining the resulting deflections of the plate is described below:

Consider a circular plate simply supported at the outer boundary as shown in Figure 4.10-15(a). This represents an idealization of the mirror configuration considered in this analysis, but the following discussion is applicable to any support condition. The positive X, Y axes are as shown, with the origin of coordinates being the center of the plate. The Z axis is the direction of plate deflection and has the positive direction shown in Figure 4.10-15(a).

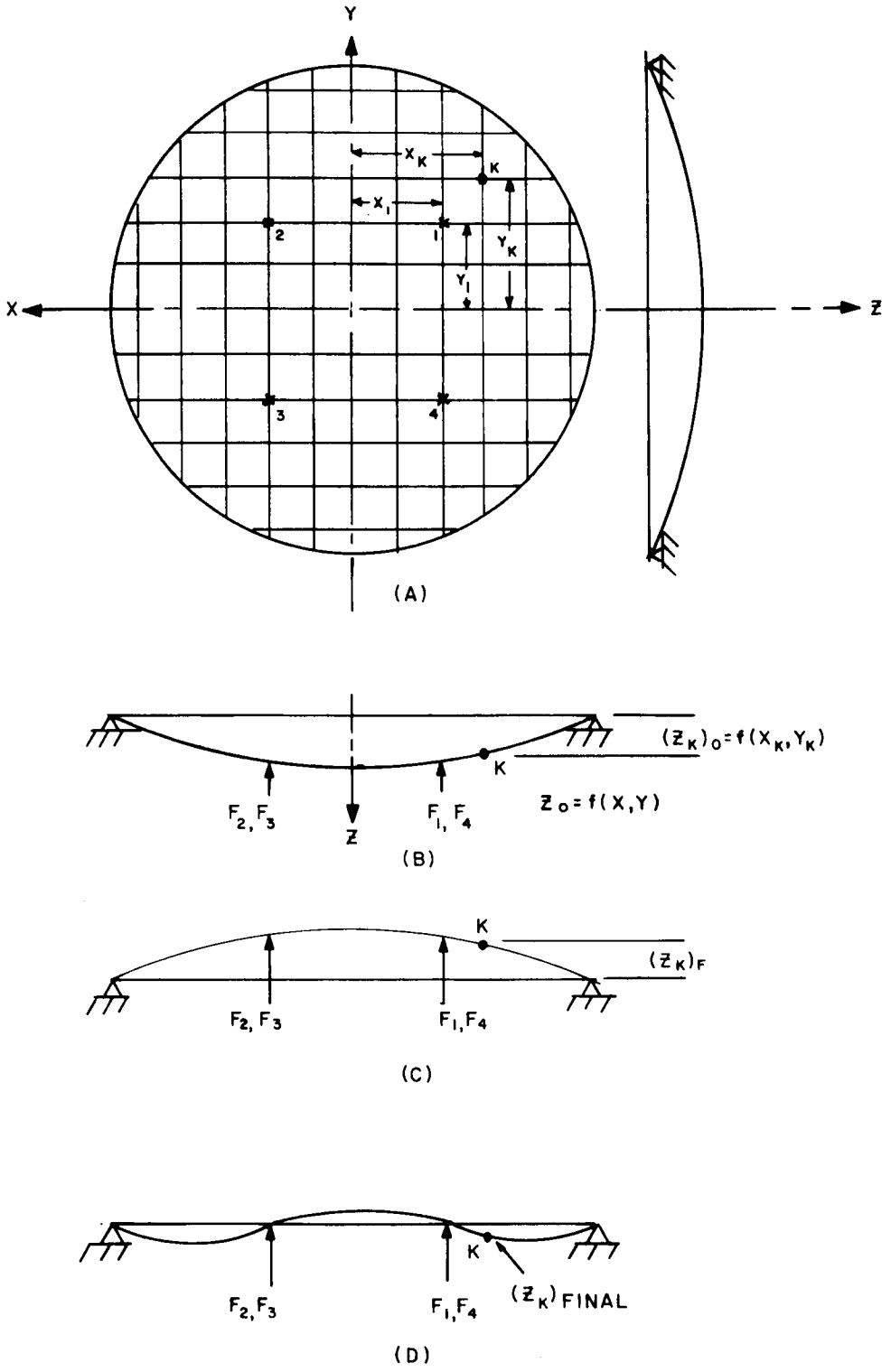


Figure 4.10-15 Rim Supported Circular Plate

If the plate has an initial deflection pattern Zo = f (x, y), the deflections at all points on the plate indicated by the coordinates (x, y) will be defined by this function. A method of reducing the deflections of these points, from those defined by the function Zo = f (x,y) is to force one or more points on the plate to a reduced value of deflection. Usually restraint forces are applied opposite to the direction of initial deflection such that the displacements at the location of these forces are reduced to zero. The deflections at the remaining points on the plate are computed by subtracting the deflection at these remaining points, resulting from the applied (restraint) forces, from the values of the initial deflections Zo at these points using the principle of superposition.

To aid this approach the plate is divided into an array of discrete points, as indicated by the gridwork intersections shown in Figure 4.10-15(a). Supposing there are m discrete points on the plate, n of which are the locations of the restoring (restraint) forces. For explanatory purposes let n = 4, where the locations of the forces are as indicated in Figure 4.10-15(a). It is required that the displacements at the coordinated (x_1, y_1), (x_2, y_2), (x_3, y_3) and (x_4, y_4) be reduced to zero.

The deflections of $(Z_i)_F$ of the n = 4 force application points, due to the n = 4 applied forces F_j, can be written as a set of simultaneous equations in the following manner;

$$
\begin{aligned}
(Z_1)_F &= \alpha_{11} F_1 + \alpha_{12} F_2 + \alpha_{13} F_3 + \alpha_{14} F_4 \\
(Z_2)_F &= \alpha_{21} F_1 + \alpha_{22} F_2 + \alpha_{23} F_3 + \alpha_{24} F_4 \\
(Z_3)_F &= \alpha_{31} F_1 + \alpha_{32} F_2 + \alpha_{33} F_3 + \alpha_{34} F_4 \\
(Z_4)_F &= \alpha_{41} F_1 + \alpha_{42} F_2 + \alpha_{43} F_3 + \alpha_{44} F_4
\end{aligned}
\qquad (1)
$$

where the α_{ij} (i = 1, 4; j = 1, 4) are influence coefficients, defined as the deflection at a point i due to a unit force applied at a point j.

Equation (1) can be written in the reduced matrix form

$$\begin{Bmatrix} (Z_1)_F \\ (Z_2)_F \\ (Z_3)_F \\ (Z_4)_F \end{Bmatrix} = \begin{bmatrix} A \end{bmatrix} \times \begin{Bmatrix} F_1 \\ F_2 \\ F_3 \\ F_4 \end{Bmatrix} \qquad (2)$$

where $\begin{bmatrix} A \end{bmatrix} = \begin{bmatrix} \alpha_{11} & \alpha_{12} & \alpha_{13} & \alpha_{14} \\ \alpha_{21} & \alpha_{22} & \alpha_{23} & \alpha_{24} \\ \alpha_{31} & \alpha_{32} & \alpha_{33} & \alpha_{34} \\ \alpha_{41} & \alpha_{42} & \alpha_{43} & \alpha_{44} \end{bmatrix}$ = influence coefficient matrix for the force application points

To reduce the deflections at points i = 1, 4 to zero, the displacements $(Z_i)_F$ caused by the applied forces at these points must be equal to the initial displacements $(Z_i)_o = f(x_i, y_i)$; in this case

$$\begin{aligned} (Z_1)_F &= (Z_1)_o = f(x_1, y_1) \\ (Z_2)_F &= (Z_2)_o = f(x_2, y_2) \\ (Z_3)_F &= (Z_3)_o = f(x_3, y_3) \\ (Z_4)_F &= (Z_4)_o = f(x_4, y_4) \end{aligned} \qquad (3)$$

Substituting equations (3) into equation (2) for $(Z_i)_F$,

$$\begin{Bmatrix} (Z_1)_o \\ (Z_2)_o \\ (Z_3)_o \\ (Z_4)_o \end{Bmatrix} = \begin{bmatrix} A \end{bmatrix} \times \begin{Bmatrix} F_1 \\ F_2 \\ F_3 \\ F_4 \end{Bmatrix} \tag{4}$$

To solve for the values of the restraint forces F_j both sides of equation (4) are pre-multiplied by the inverse $\begin{bmatrix} A \end{bmatrix}^{-1}$ of the matrix $\begin{bmatrix} A \end{bmatrix}$. The restraint forces F_j are equal to the product of $\begin{bmatrix} A \end{bmatrix}^{-1}$ and the initial deflection column matrix $\begin{Bmatrix} (Z_i)_o \end{Bmatrix}$; that is,

$$\begin{Bmatrix} F_1 \\ F_2 \\ F_3 \\ F_4 \end{Bmatrix} = \begin{bmatrix} A \end{bmatrix}^{-1} \times \begin{Bmatrix} (Z_1)_o \\ (Z_2)_o \\ (Z_3)_o \\ (Z_4)_o \end{Bmatrix} \tag{5}$$

The restoring forces are opposite in direction to the initial displacement pattern $Z_o = f(x, y)$ as shown in Figure 4.10-15(b). Therefore, the effect of these forces will result in deflections of the plate in the negative Z direction as shown in Figure 4.10-15(c).

If the deflection of an arbitrary point K on the plate is considered, the initial deflection of this point is

$$(Z_K)_o = f(x_K, y_K) \tag{6}$$

The deflection of the point K due to the restoring forces F_j is as follows:

$$(Z_K)_F = - \left[\beta_{K1} F_1 + \beta_{K2} F_2 + \beta_{K3} F_3 + \beta_{K4} F_4 \right] \qquad (7)$$

where the β_{Kj} $(j = 1, 4)$ is the deflection of the arbitrary point K due to a unit applied restraint force F_j. Since the values of F_j have been computed by equation (5), these values are substituted into equation (7) for the deflection $(Z_K)_F$.

The final deflection $(Z_K)_{FINAL}$ at the point K is given by the sum of equations (6) and (7), using the principle of superposition.

$$(Z_K)_{FINAL} = (Z_K)_o + (Z_K)_F$$

$$(Z_K)_{FINAL} = f(x_K, y_K) - \left[\beta_{K1} F_1 + \beta_{K2} F_2 + \beta_{K3} F_3 + \beta_{K4} F_4 \right] \qquad (8)$$

A typical final deflection pattern is shown in Figure 4.10-15(d), where the deflections at the force application point are shown to be zero. The forces F_j will be felt as reactions by supports at these zero deflection locations.

In the general case there can be m discrete points and n force application points; therefore a summation of this analytical technique will be given in the general sense;

Computation of restraint forces:

a. $$\left\{ Z_i \right\}_F = \left[A \right] \left\{ F_j \right\} \quad ; (i = 1, n; \; j = 1, n)$$

where

$$\left[A \right] = \begin{bmatrix} \alpha_{11} & \alpha_{12} & \cdots & \alpha_{1n} \\ \alpha_{21} & \alpha_{22} & \cdots & \alpha_{2n} \\ \vdots & & & \\ \alpha_{n1} & \alpha_{n2} & \cdots & \alpha_{nn} \end{bmatrix}$$

= influence coefficient matrix for force application points (n x n)

The matrix symbol $\{\ \}$ indicates a column matrix of elements.

b. Condition of zero displacement at force application points

$$\left\{(Z_i)_F\right\} = \left\{(Z_i)_o\right\} = \left\{f(x_i, y_i)\right\}$$

NOTE: It is sometimes advantageous not to reduce the displacement at the force application point to zero, but to some arbitrary value ΔZ_i. For this case the above relationship is modified as follows:

$$\left\{(Z_i)_F\right\} = \left\{(Z_i)_o\right\} \pm \left\{\Delta Z_i\right\} ,$$

which reduces to the above relationship for $\Delta Z_i = 0$

c. Solution for restraint forces

$$\left\{F_j\right\} = \left[A\right]^{-1} \left\{(Z_i)_o\right\}$$

or, as noted in step b.

$$\left\{F_j\right\} = \left[A\right]^{-1} \left\{(Z_i)_o \pm \Delta Z_i\right\}$$

Computation of final plate deflections:

a. Initial deflections of all discrete points K on plate

$$\left\{(Z_K)_o\right\} = \left\{f(x_K, y_K)\right\} \ ; \ (K = 1, m)$$

b. Deflections due to restraint forces F_j

$$\left\{(Z_K)_F\right\} = - \left[B\right] \left\{F_j\right\} \ ; \ (K = 1, m; \ j = 1, n)$$

where:

$$\left[B\right] = \begin{bmatrix} \beta 11 & \beta 12 \cdots \beta 1n \\ \beta 21 & \beta 22 \cdots \beta 2n \\ \vdots & \\ \beta m1 & \beta m2 \cdots \beta mn \end{bmatrix} = \text{influence coefficient matrix deflections of m discrete points due to n applied unit restraint forces } F_j$$

c. Final deflections of plate

$$\left\{(Z_K)_{FINAL}\right\} = \left\{(Z_K)_o\right\} + \left\{(Z_K)_F\right\}$$

$$\left\{(Z_K)_{FINAL}\right\} = \left\{f(x_K, y_K)\right\} - \left[\bar{B}\right] \left\{F_j\right\}$$

4.10.5.8.2 Mirror Correction Analysis

For the mirror correction analysis the OTAES 50 inch mirror was idealized as a uniform thickness circular plate, simple supported at the outer boundary. The plate was divided into a set of discrete points corresponding to possible location of the force actuators, both of the push-pull and push only types, as shown in Figure 4.10-17. These points also define the final deflection pattern of the plate for the different force actuator arrays considered in this study.

Two error deflection patterns were considered in this study; paraboloid and sinousoid-paraboloid. The paraboloidal deflection pattern shown in Figure 4.10-16(a) is given by the function

$$(Z_i)_o = 20 \times 10^{-6} \left[1 - \frac{r_i^2}{a^2}\right] \qquad (1)$$

where: $r_i^2 = x_i^2 + y_i^2$

x_i, y_i = coordinates of discrete points

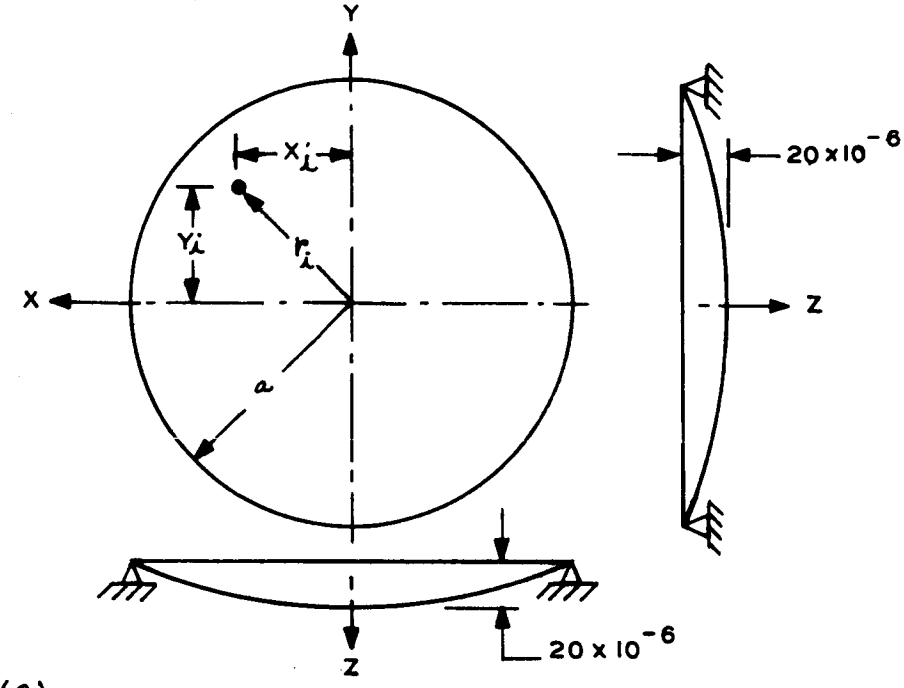
a = radius of the plate

The sinousoid-paraboloid deflection pattern shown in Figure 4.10-16(b) is given by the function

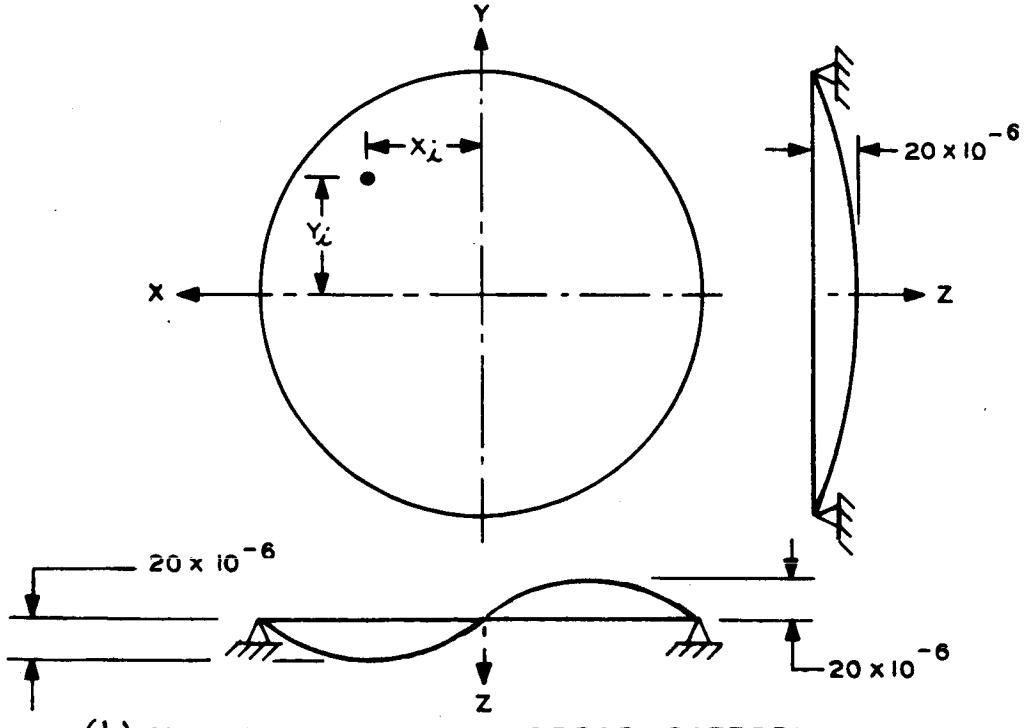
$$(Z_i)_o = 20 \times 10^{-6} \left[1 - \frac{y_i^2}{a^2 - x_i^2}\right] \sin \frac{x_i}{\sqrt{a^2 - y_i^2}} \qquad (2)$$

The equation defining the deflections of a uniform thickness simply supported circular plate due to discrete applied forces, was obtained from reference[1]. This equation applies for a uniform plate without a hole in the

(1) Raymond J. Roark,"Formulas for Stress and Strain", Third Edition, 1954, pl95 (Case 4).



(a) PARABOLOID ERROR PATTERN



(b) SINUSOID - PARABOLOID ERROR PATTERN

Figure 4.10-16 Error Patterns

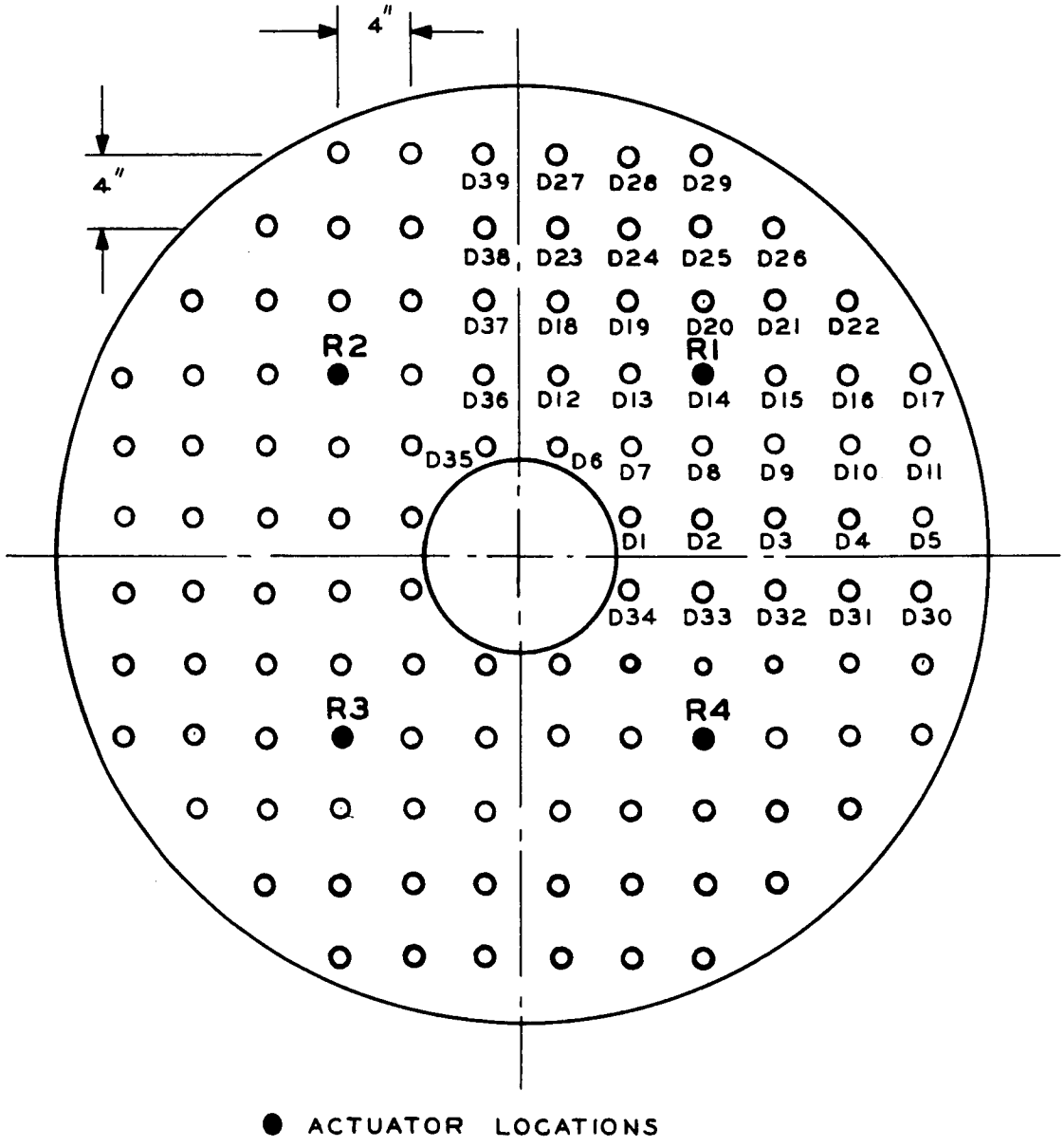


Figure 4.10-17 Schematic of 50" Mirror Showing Actuator Locations - Case 1

center. Although the plate analyzed has a hole in the center, it is anticipated that the errors incurred by using this formula will not affect the accuracy necessary to evaluate the best force actuator array for minimizing the deflections resulting from the initial error pattern. The deflection equation in Reference[1] is used for obtaining the influence coefficients of the force actuator points, which are included in the [A] matrix, (see Section 4.10.5.8.1), and the influence coefficients of the deflection points due to the actuator forces which are included in the [B] matrix (see Section 4.10.5.8.1).

4.10.5.8.3 Computer Analysis

Both the analytical procedure discussed in Section 4.10.5.8.1 and the deflection equation given in Reference [1] were programmed for the digital computer. The program has been written in Fortran II for the SDS 930 digital computer which has a core memory of 8000 bits. Due to core memory limitations the maximum number of force actuators which could be considered was n = 12. The maximum number of points which could be used to define the final deflection pattern was m = 50. To facilitate the deflection analysis, force actuator arrays were selected to be symmetric with respect to the x and y axes so that a single quadrant of m = 39 points could be used to describe the deflection pattern of the restrained circular plate. In this manner, the deflection patterns in the remaining quadrants are defined using the results obtained in the single quadrant. This is discussed further in Section 4.10.5.8.4.

The initial computer runs performed to check out the computer program indicated a sensitivity in the inversion of the [A] matrix (see Section 4.10.5.8.1) for greater than n = 5 force actuators. That is, the computer program sub-routine for matrix inversion based on the Count matrix inversion technique, treated any [A] matrix greater than a size 5 by 5 as a singular matrix, indicating that a solution for the forces either did not exist or was not unique. This was possible due to rounding off errors in the computer computation of the matrix inversion. The sensitivity was apparent since the elements of the [A] matrix were not well separated, resulting in a determinant solution $|A|$ which was small, but not near zero as would be the case in a singular matrix.

To achieve a solution for the actuator forces the matrix equation given by equation 4 in Section 4.10.5.8.1 was treated in expanded form as a set of linear simultaneous equations which were solved using the relaxation method

(1) Raymond J. Roark,"Formulas for Stress and Strain", Third Edition, 1954, P195 (Case 4).

described in Reference [2]. This method is not as sensitive to rounding off errors in computing the actuator forces and allows a larger number of force actuators to be considered.

The following numerical quantities were used in the mirror correction analysis.

a = radius of plate = 25 inches

t = thickness of plate = 0.5 inches

E = modulus of elasticity = 42×10^6 psi

ν = Poisson's ratio = .02

In one typical case for which a computer solution was obtained, force actuators were assumed located at points (-6, 6), (6, 6), (6, -6), (-6, -6) (i.e., n = 4) where the terms in the parenthesis are the x and y locations (in inches) of the force actuators. This case is shown in Figure 4.10-18 where the actuator points are labeled R1, R2, R3, R4 and the m = 39 deflection points are labeled D1, D2, ... D39. The influence coefficients of the actuator points and the deflection points due to applied unit loads F_J^* (J = 1, 4) at the actuator locations, were computed. The solution for the actuator forces in this case is $F_1 = F_2 = F_3 = F_4 = .0775$ lbs. Finally, the solution for the final plate deflections was computed.

4.10.5.8.4 Results

In the computer study, arrays of 4, 8 and 12 push-pull actuators were considered to minimize the paraboloid and sinusoid-paraboloid error patterns. The results of this study are tabulated in Table 4.10-4, 4.10-5, and 4.10-6. Each of the cases in the tables corresponds to an actuator array indicated by the appropriate figure number. For instance, case (2) in Table 4.10-4 corresponds to the actuator array shown in Figure 4.10-18. Both the paraboloid (P) and Sinusoid-paraboloid (S-P) error patterns are considered in each case. The actuator forces (F_1, F_2 ....) required to create a zero deflection at the actuator locations are given. The actuator locations (R_1, R_2 ....) are shown in the appropriate figure. Also included in the tables are the maximum positive and negative deflections of the plate due to the restraint of a particular actuator array, and the points in the appropriate figure where these deflections exist.

(2) M.G. Salvadori and M.L. Baron, "Numerical Methods in Engineering", Second Edition, 1961, p 36.

TABLE 4.10-4

NUMBER OF ACTUATORS = 4

Case	Error Pattern	Figure	Actuator Forces (lb)				Maximum Pos. Deflection		Maximum Neg. Deflection	
			F_1	F_2	F_3	F_4	Point	Value (In)x10^{-6}	Point	Value (In)x10^{-6}
1	P	4.10-17	0.115	0.115	0.115	0.115	21	0.61	34	-1.685
	S-P		-0.842	0.842	0.842	-0.842	32	2.87	24	-2.95
2	P	4.10-18	0.078	0.078	0.078	0.078	4	1.1	34	-0.4
	S-P		-0.867	0.867	0.867	-0.867	22	1.8	24	-3.33
3	P	4.10-19	0.16	0.16	0.16	0.16	24	0.68	34	-2.5
	S-P		-0.8	0.8	0.8	-0.8	22	1.85	24	-3.31
4	P	4.10-20	0.071	0.071	0.071	0.071	20	1.26	34	-0.045
	S-P		-0.474	1.34	0.474	-1.34	22	1.66	24	-3.32

TABLE 4.10-5

NUMBER OF ACTUATORS = 8

Case	Error Pattern	Figure	Actuator Forces (lb)								Maximum Pos. Deflection		Maximum Neg. Deflection	
			F_1	F_2	F_3	F_4	F_5	F_6	F_7	F_8	Point	Value (In)x10^{-6}	Point	Value (In)x10^{-6}
5	P	4.10-21	.564	.554	.55	.556	-.218	-.189	-.191	-.207	23	3.03	33	-2.4
	S-P		-.869	.861	.87	-.862	.205	-.20	-.21	+.204	22	1.85	24	-3.31
6	P	4.10-22	1.094	1.178	1.095	1.09	-0.48	-0.58	-0.5	-0.5	18	4.34	3	-2.63
	S-P		-1.116	1.115	2.773	-2.773	0.19	-0.19	-2.316	2.316	22	1.84	34	-3.33

TABLE 4.10-6

NUMBER OF ACTUATORS = 12

Case	Error Pattern	Figure	Actuator Forces (lb)												Max. Pos. Defl.		Max. Pos. Defl.	
			F_1	F_2	F_3	F_4	F_5	F_6	F_7	F_8	F_9	F_{10}	F_{11}	F_{12}	Point	Value x10^{-6}	Point	Value x10^{-6}
7	P	4.10-23	9.5	7.49	9.62	7.44	9.53	7.56	9.43	7.61	-10.74	-10.73	-10.72	-10.75	10	.64	12	-.83
	S-P		25.	-63.5	63.3	-24.5	-35.	73.6	-73.2	34.4	0	0	0	0		-		-

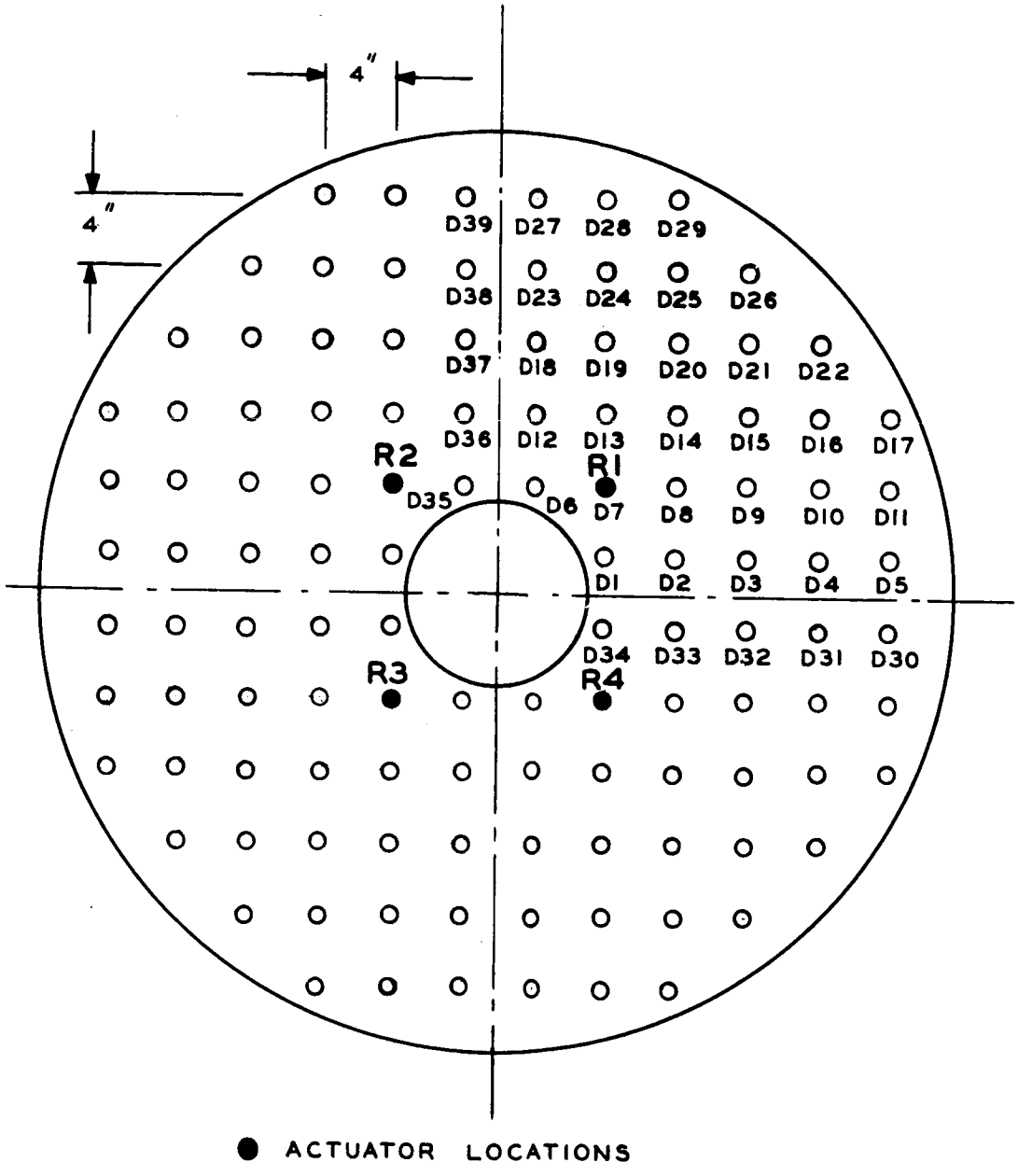


Figure 4.10-18 Schematic of 50" Mirror Showing Actuator Locations - Case 2

Deflection contour plots (showing lines of constant deflection) for cases 2, 5 and 7 are shown for a single quadrant in figures 4.10-24 thru 4.10-28. For the paraboloid error pattern symmetry of the contour plot exists across both the x and y axes. For the sinusoid-paraboloid error pattern symmetry exists across the x axis and asymmetry exists across the y axis.

The analytical results indicate that a mirror correction for the paraboloid error pattern near $\lambda/30 = 0.8$ times 10^{-6} inches can be achieved with four actuators corresponding to case (2) in Table 4.10-4. The maximum deflection of the plate is 1.1 times 10^{-6} inches which is obtained by applying 0.078 lbs at each of the actuator locations shown in Figure 4.10-18. The deflection contour plot shown in Figure 4.10-24 indicates the distortion pattern of the 50 inch mirror when the force actuators are applied to correct for the paraboloid error pattern. A reduction in the deflections of the plate to less than $\frac{\lambda}{30}$ can also be achieved with twelve actuators as indicated in Table 4.10-6. The actuator forces required are of the order of 10 pounds, resulting in a maximum deflection of - .83 times 10^{-6} inches. However, it was expected that the actuator forces F_1 thru F_8 would be nearly equal as are F_9 thru F_{12}. This inequality suggests that the computer solutions for the actuator forces did not converge exactly. However, it is expected that an increase in the number of computer iterations can converge the solutions to more exact values. A study of the effect of the number of iterations on convergence will be performed at a later date. The maximum error correction of - .83 times 10^{-6} inches, as shown in the approximate contour map in Figure 4.10-28, can at best be taken as an order of magnitude of the solution due to the present uncertainty of this solution. However, the error correction due to the four actuators shown in Figure 4.10-18, has a high confidence level.

The best correction for the sinusoid-paraboloid error pattern with the limited number of actuator arrays considered was -2.95 times 10^{-6} inches with an actuator array as shown in Figure 4.10-17. This corresponds to case 1 of Table 4.10-4, which requires actuator forces of $F_1 = F_4 =$ -.842 lbs. and $F_2 = F_3 = .842$ lbs. However, all the cases considered using four and eight actuators, resulted in approximately this maximum deflection as indicated in Tables 4.10-4 and 4.10-5. It is anticipated, that of these cases only case 7, Table 4.10-6, could have resulted in a smaller deflection. However, the results in this case were uncertain at this time, since the solutions for the actuator forces did not converge. Typical contour plots of the actuator corrected deflection pattern are shown in Figures 4.10-25 and 4.10-27, for the case of the sinusoid-paraboloid error pattern.

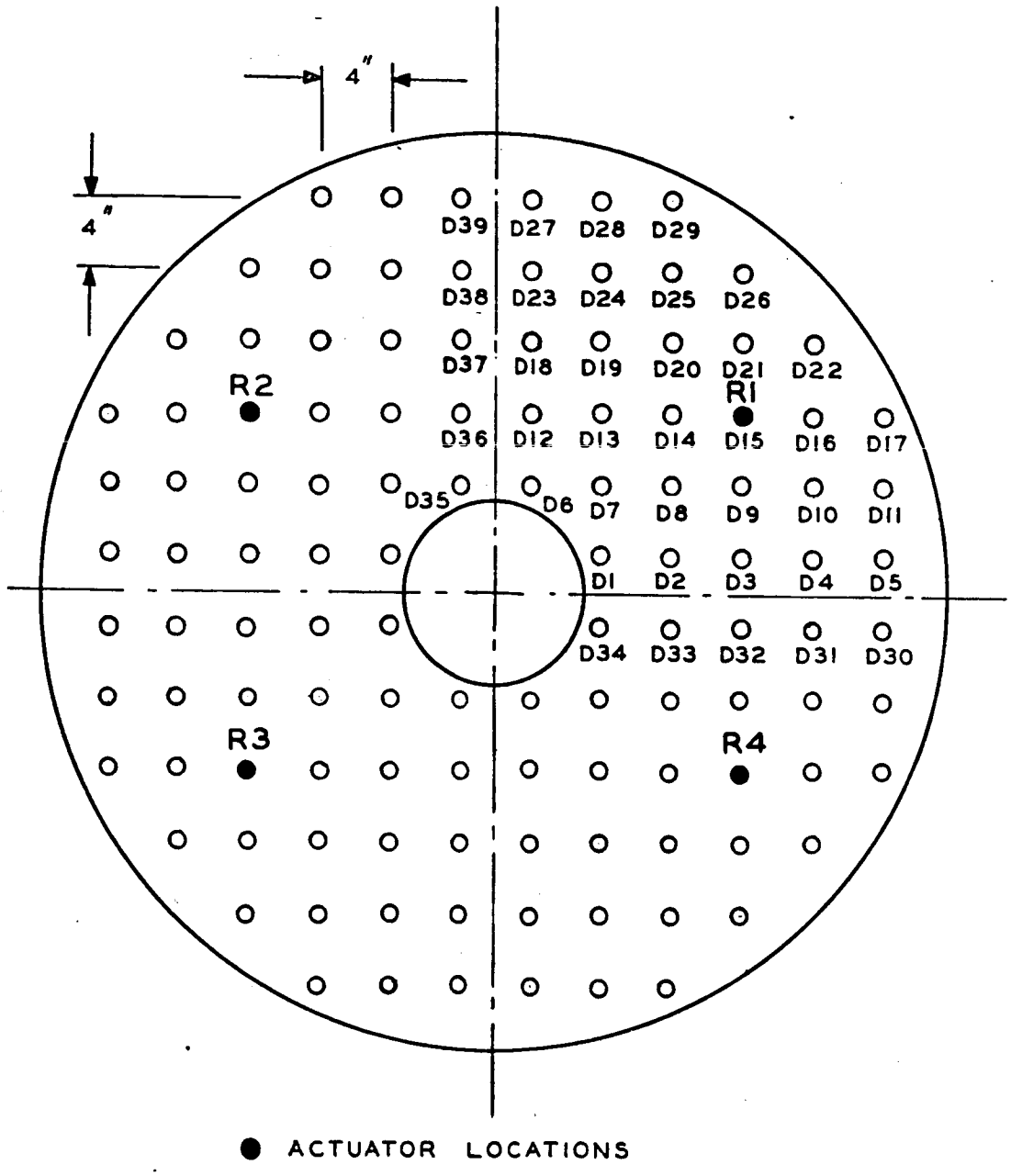


Figure 4.10-19 Schematic of 50" Mirror Showing Actuator Locations - Case 3

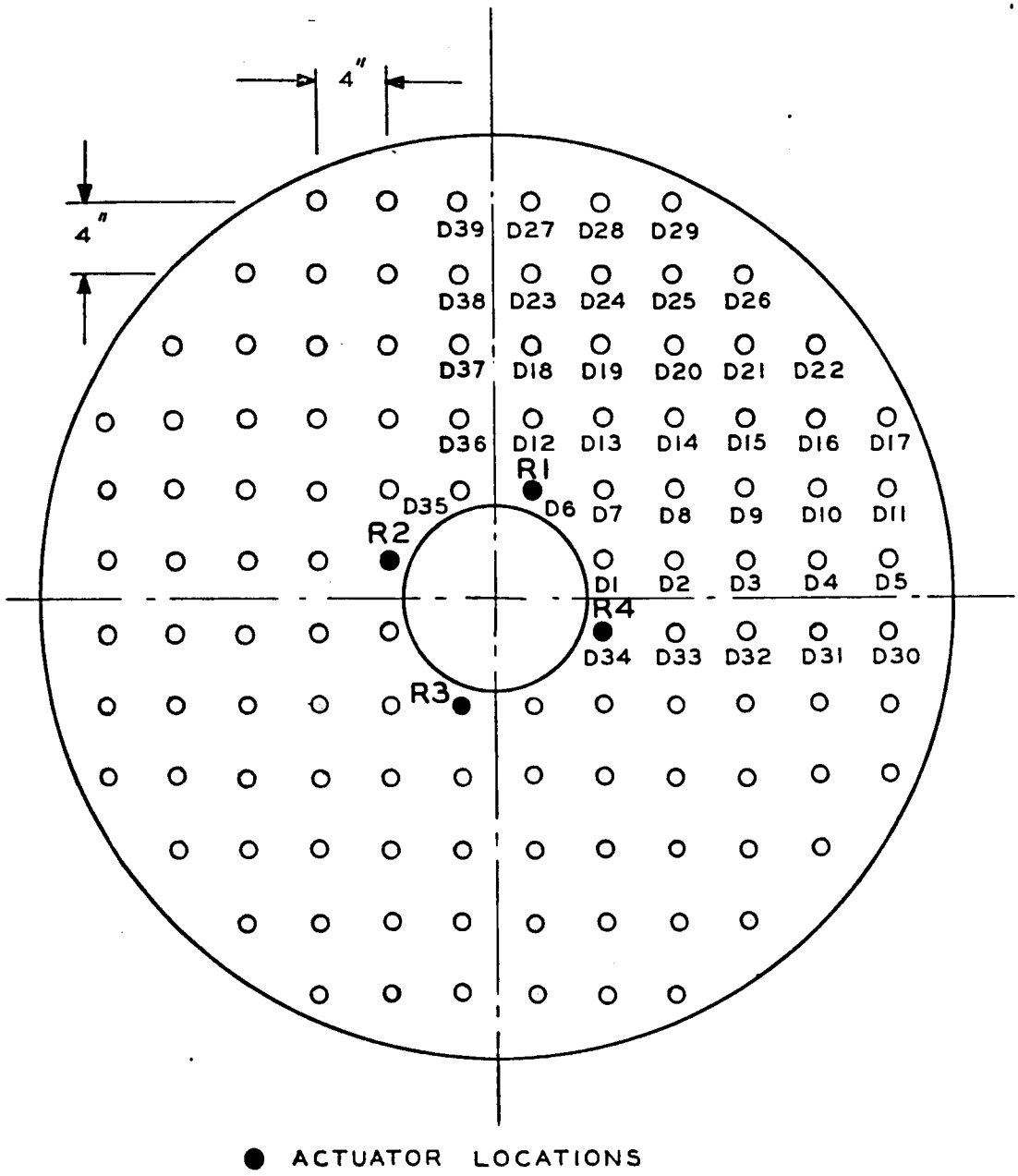


Figure 4.10-20 Schematic of 50" Mirror Showing Actuator Locations - Case 4

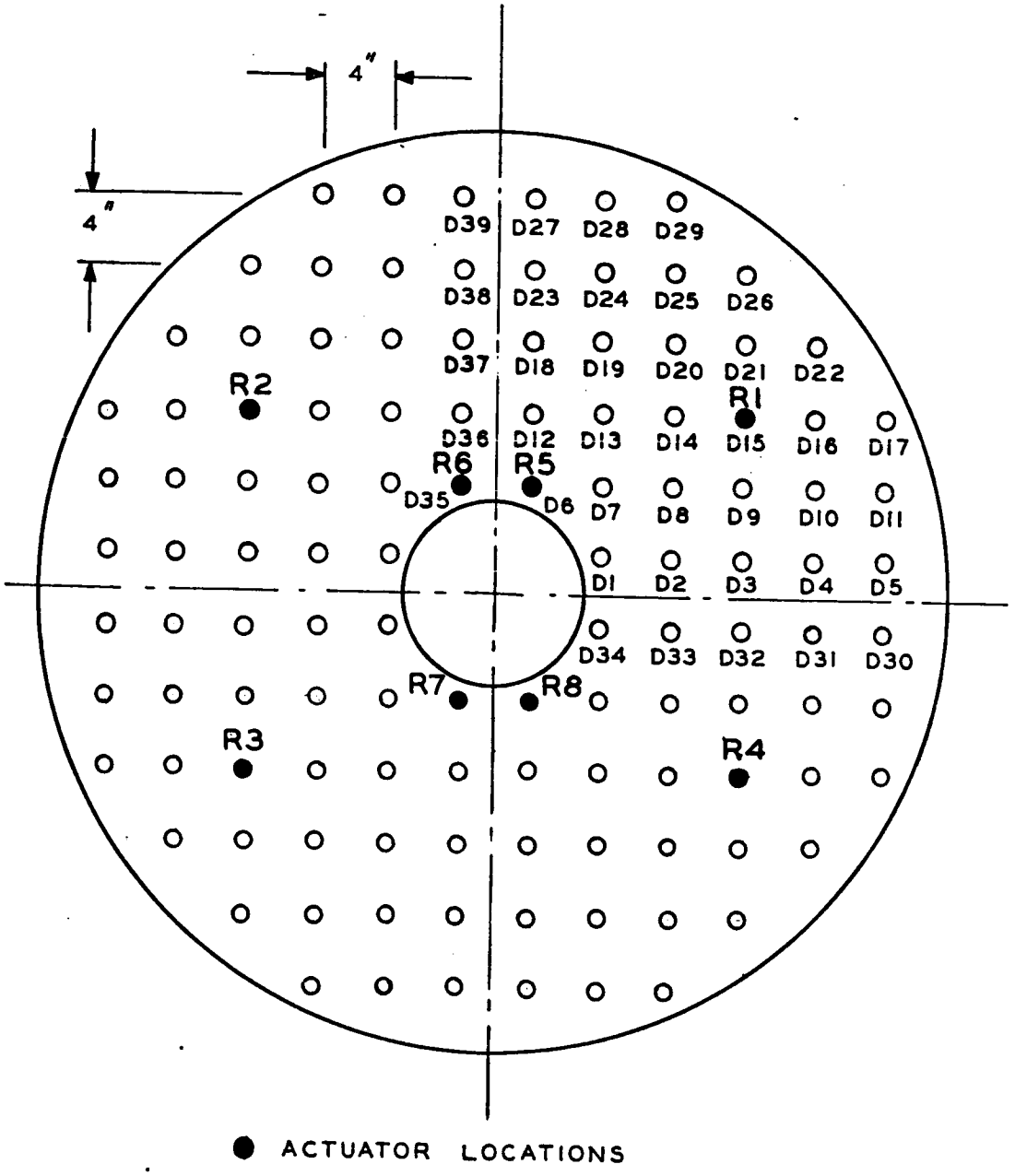


Figure 4.10-21 Schematic of 50" Mirror Showing Actuator Locations - Case 5

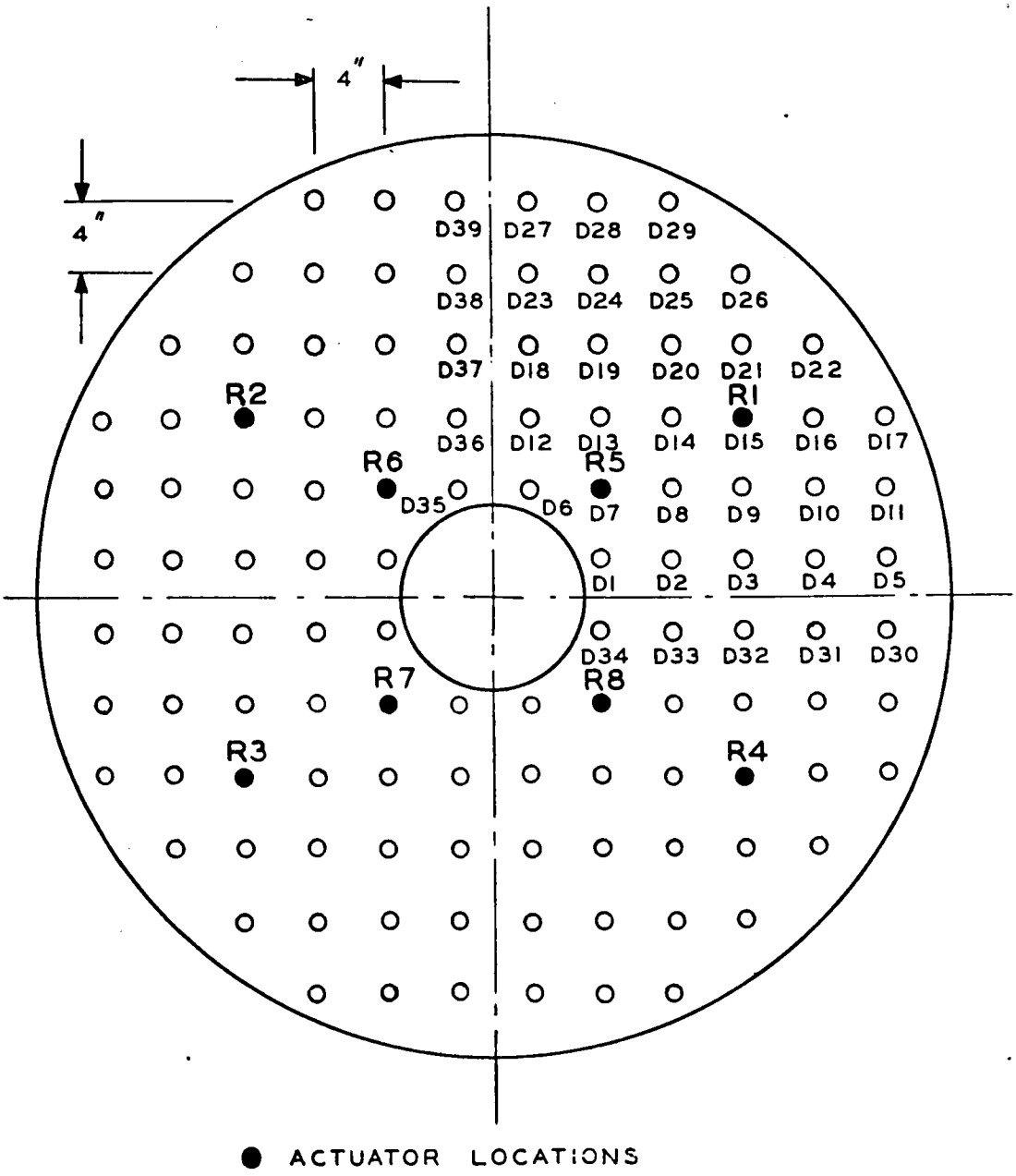


Figure 4.10-22 Schematic of 50" Mirror Showing Actuator Locations - Case 6.

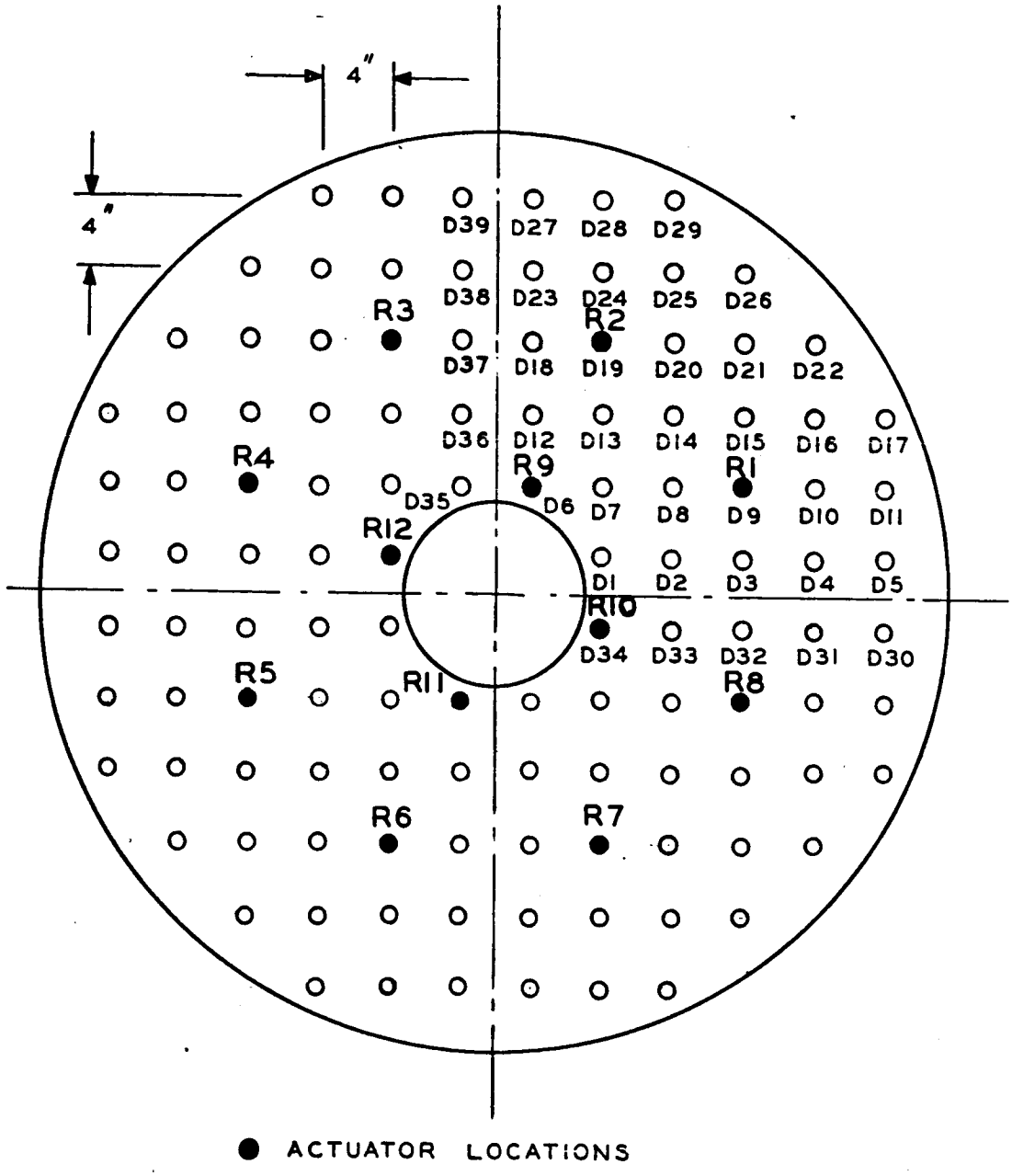


Figure 4.10-23 Schematic of 50" Mirror Showing Actuator Locations - Case 7

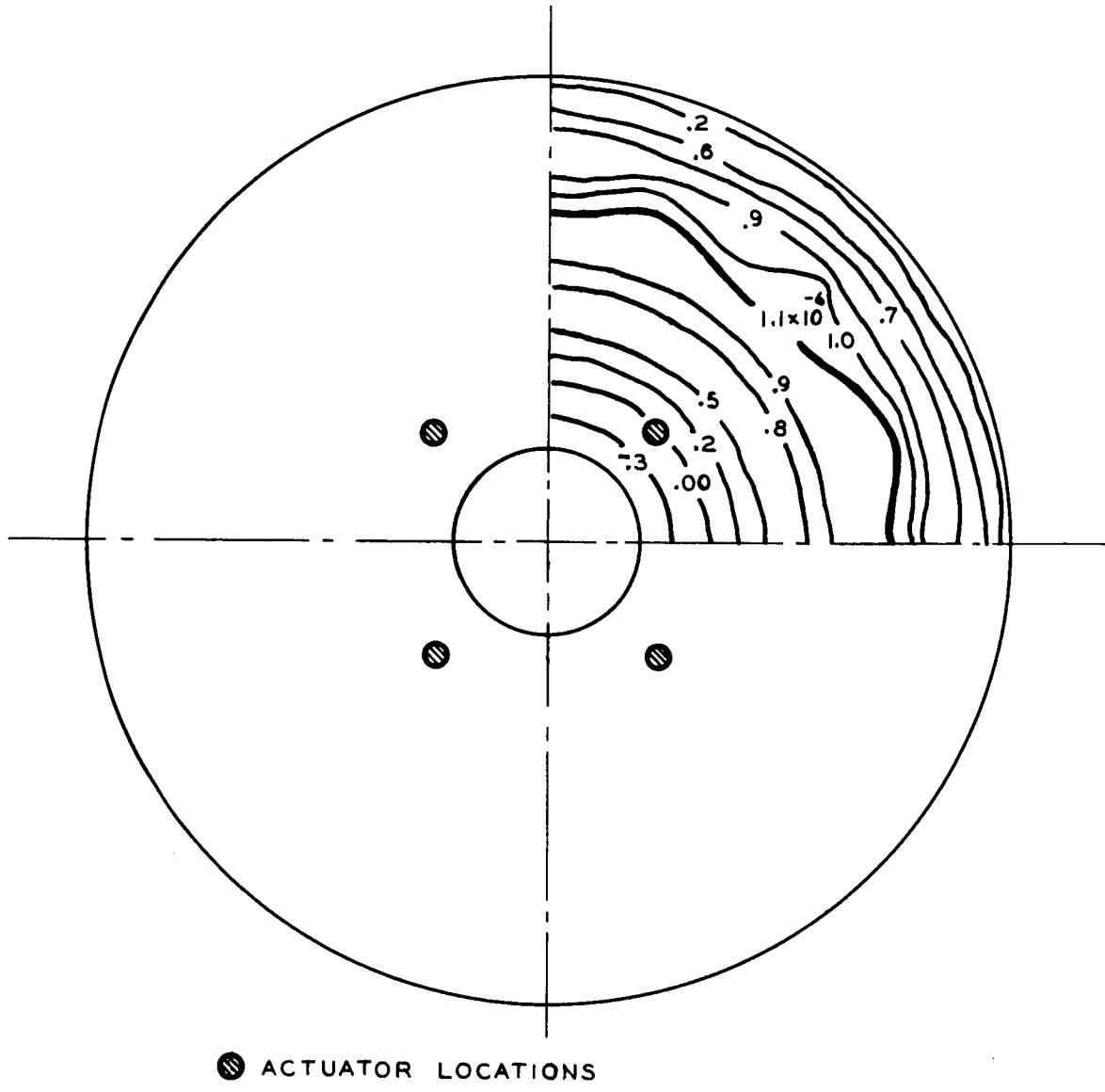


Figure 4.10-24 Deflection Contour Plot of Correction to Paraboloid Error Pattern - Case 2

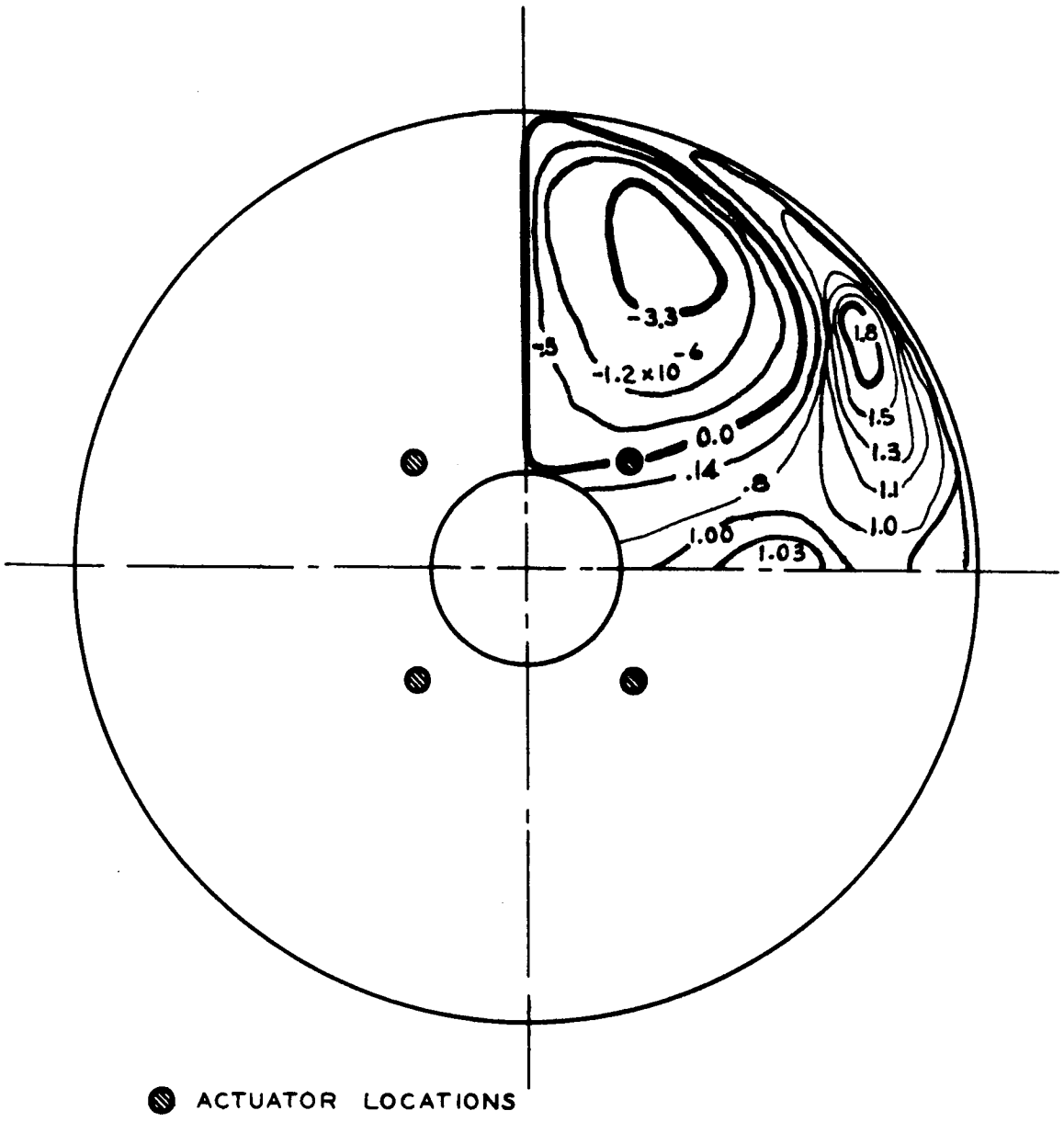


Figure 4.10-25 Deflection Contour Plot of Correction to Sinusoid Error Pattern - Case 2

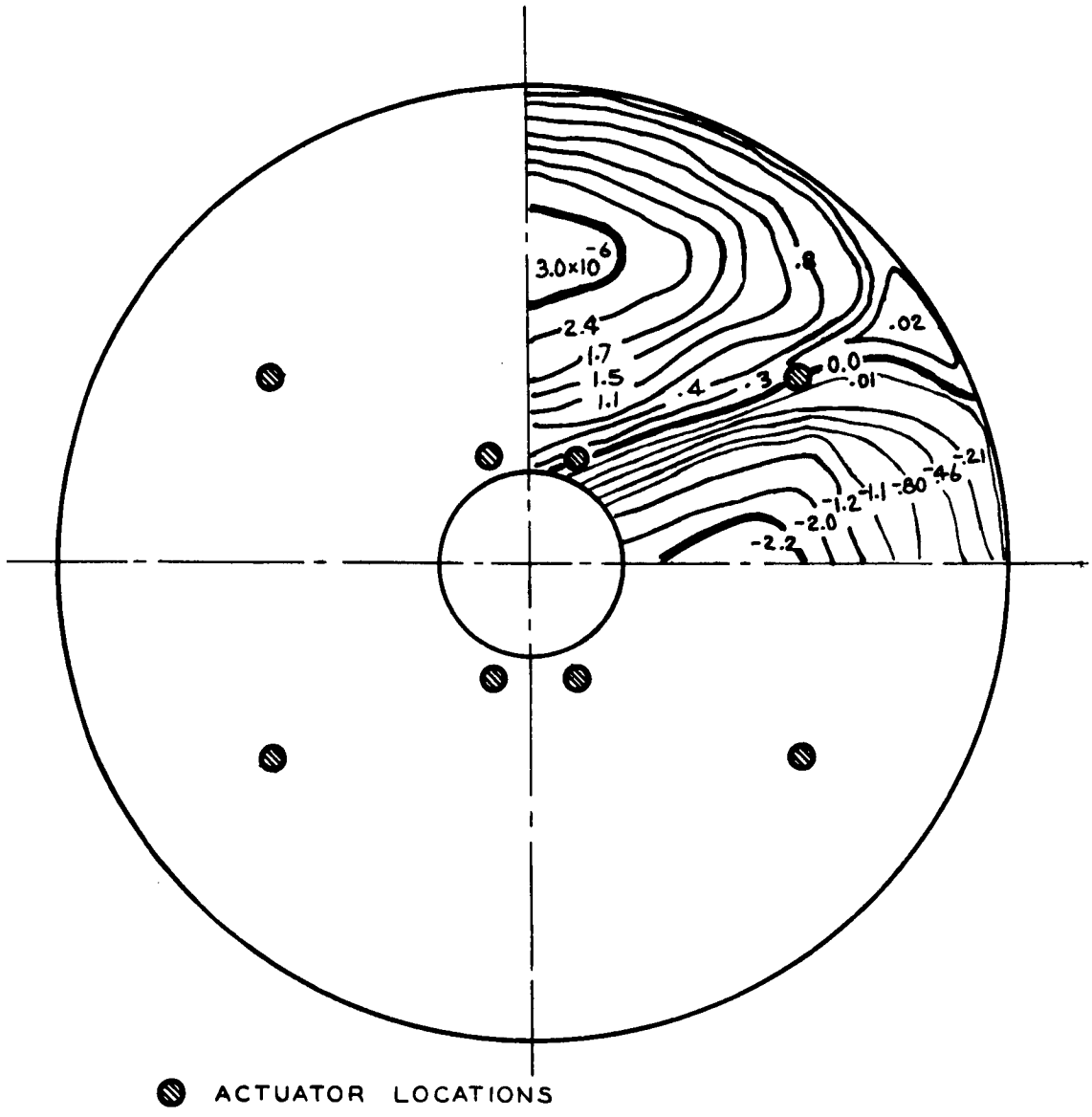


Figure 4.10-26 Deflection Contour Plot of Correction to Paraboloid Error Pattern - Case 5

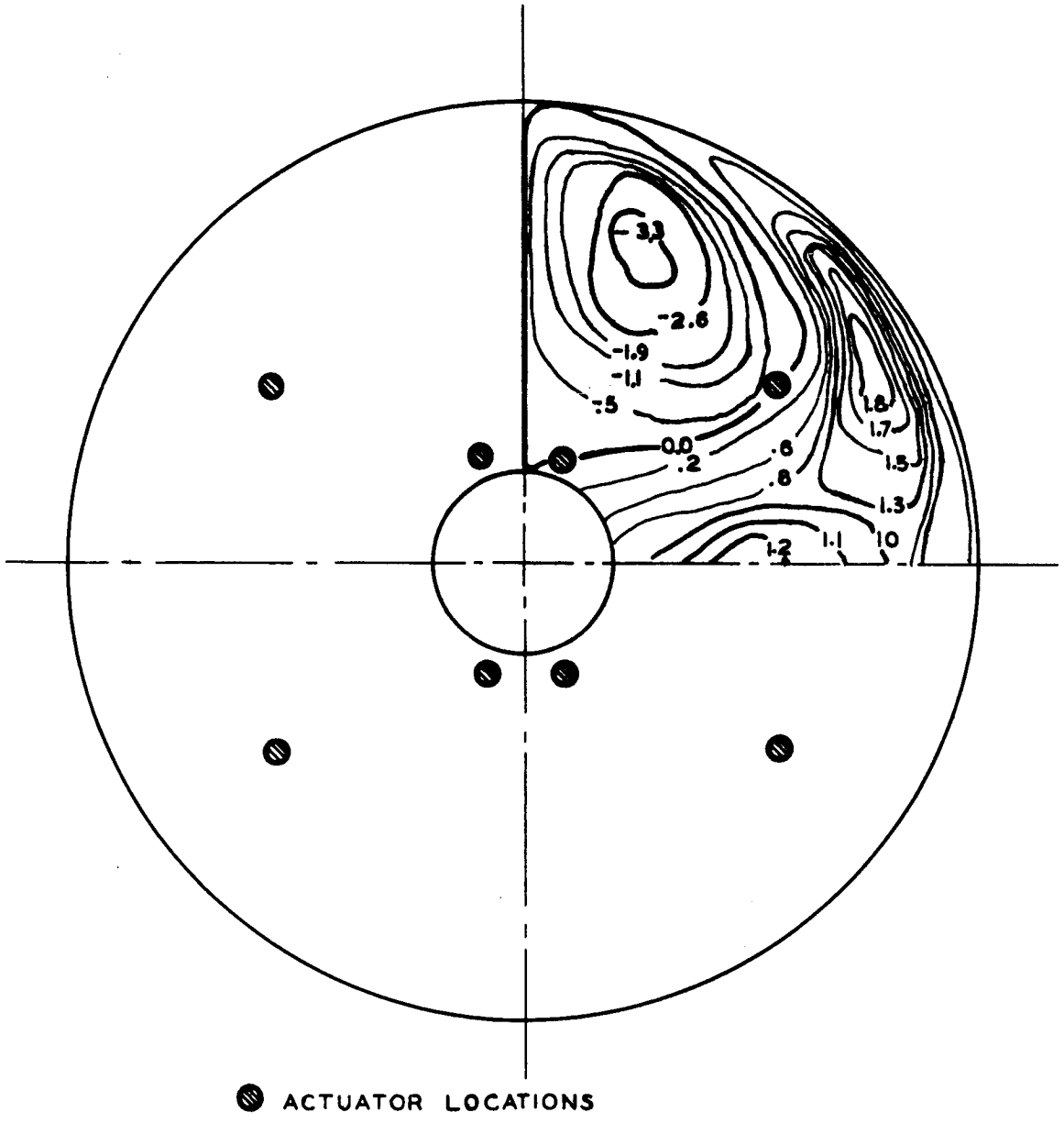


Figure 4.10-27 Deflection Contour Plot of Correction to Sinusoid Error Pattern - Case 5

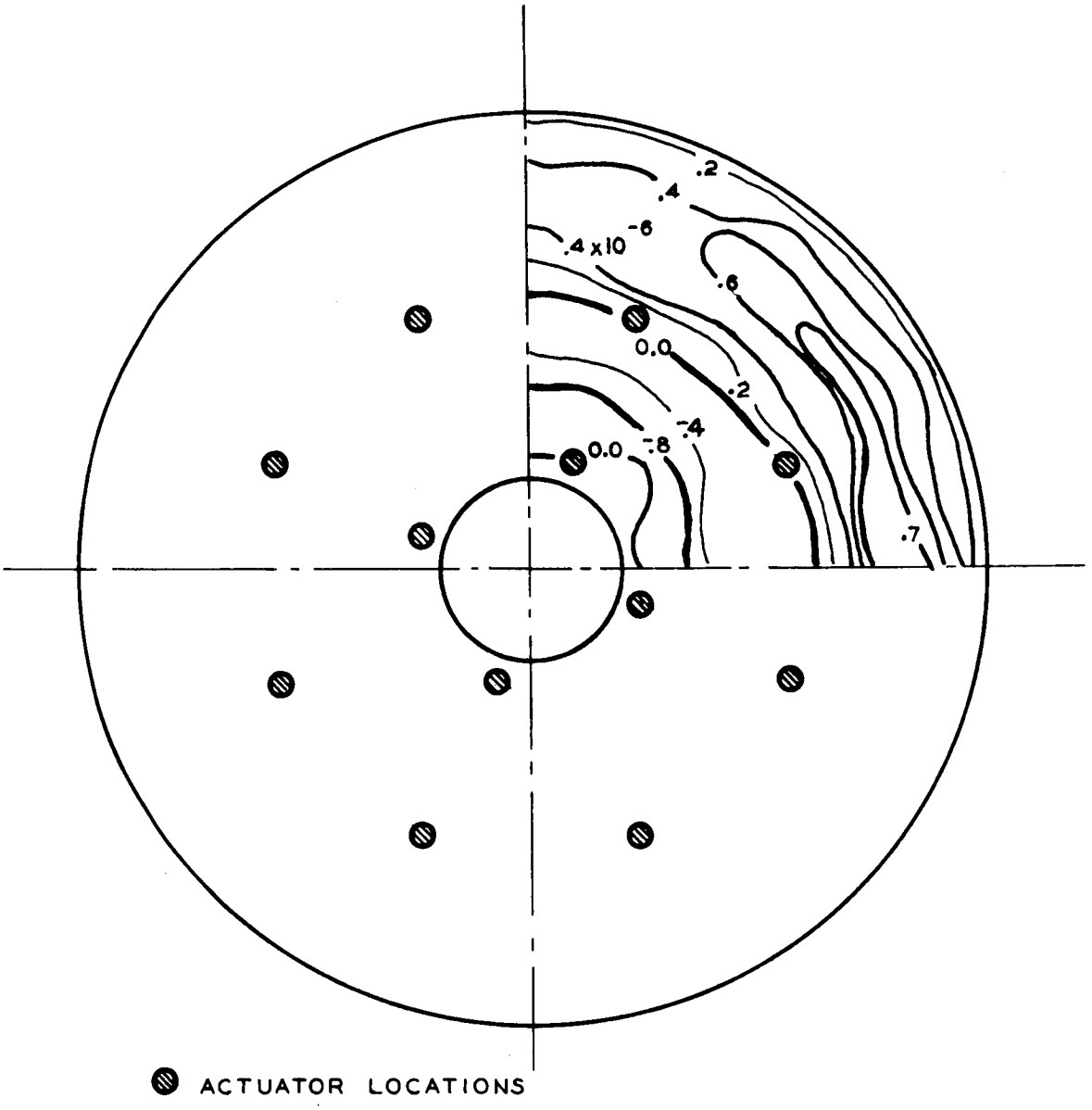


Figure 4.10-28 Deflection Contour Plot of Correction to Paraboloid Error Pattern (Approx.) - Case 7

4.10.5.8.5 Conclusions

As a result of the matrix inversion problem discussed in Section 4.10.5.8.2, which delayed a more complete study, a limited number of error patterns and actuator arrays were considered. From these results certain conclusions and trends have been established, which encourage further work in this area.

For example, as the size of the actuator arrays become large, the solution for the actuator forces, using the relaxation method (Reference (2) becomes sensitive to the number of iterations or successive approximations to the solution. That is, an increased number of iterations are required to converge on the solution for the actuator forces. This is indicated in Tables 4.10-5 and 4.10-6 where the solutions for the actuator forces have not quite converged to the actual values. A study should be performed to establish convergence limitations of the computer analysis.

The results also indicate that as the error pattern becomes more complicated, such as an increased number of waves in the pattern, the amount of force required by the actuators will increase. Depending on the error pattern, this will also be the case if a large number of actuators are involved. It therefore seems plausible that mirror correction should be achieved with a minimum number of force actuators.

It has been established that the array of four actuators shown in Figure 4.10-18 can correct the paraboloid error pattern to about $\frac{\lambda}{30}$.

Since the maximum positive deflection is 1.1 times 10^{-6} inches and maximum negative deflection is -0.4 times 10^{-6} inches, as shown in Table 4.10-4, the maximum deflection in the plate can be further reduced by forcing the displacements at the actuator locations to values other than zero. An increase in the deflection of the actuator locations to 0.4 times 10^{-6} inches decreases the maximum deflection of the plate to about 0.9 times 10^{-6} inches.

To ascertain whether the sinusoid-paraboloid error correction can be reduced from the value of -2.95 times 10^{-6} inches attained by case 1 of Table I, requires further investigation. Since the study was limited by development of a workable computer program, it is felt that additional work is necessary to evaluate the effects of other actuator patterns for mirror correction.

4.11 THIN MIRROR NESTING PRINCIPLE AND ERECTION AND ALIGNMENT OF LARGE OPTICS IN SPACE

4.11.1 Summary

The resolution of an optical system is proportional to its aperture and modified by the quality and uniformity of each optical element. Light gathering power increases as the square of the aperture. The speed and resolution of optical systems can be increased by using larger and higher quality optics. Various astronomers have indicated that certain astronomical observations, not achievable with earth observatories or within the capability of the OAO series, require 2.5 to 5 meters (100 to 200 inch) aperture telescopes with diffraction-limited resolution ability. It is agreed that this size and class of optical systems, if used in space will provide scientific data on heretofore undetectable and unmeasurable astronomical bodies and phenomena. However, the weight and volume required by systems of this size impose severe requirements even on the more advanced launch systems.

One means for alleviating these weight constraints is to configure a very thin mirror. This, of course, has the attendent problems of support during manufacture, handling and launch. Manufacture and test of a very thin mirror in a "nest" where the mirror is uniformly supported at all times simulates, in effect, the zero gravity condition of space. This also permits the construction of such a mirror on earth so that it will perform under the weightlessness conditions of space.

It has been established that in order to maintain performance specifications in precision systems, an exact determination of proportional limit must be made. Minute permanent deformations occurring in materials below the conventional proportional limit now require a new limit. This limit has been termed as P.E.L. (Precision Elastic Limit) and is defined as "the stress which produces a residual strain or deformation of one micron per meter (or one micro inch per inch)". This strain is a permanent set in the material and is sufficient in magnitude to change the power of an optical element. These minute permanent deformations in a large mirror will impart an exceedingly small additional deflection when compared to the effect of gravity (ratio greater than 1000:1) and is therefore not reliably measured on earth.

The purpose of this experiment is to investigate the theory and develop the technology so that very thin mirrors fabricated on earth in a "nest" (so as to negate the distorting force of gravity) can be handled, launched and erected in zero "g" space and that they will retain their figure when deployed in this zero "g" environment where stresses induced by gravity are removed. A thin mirror will be manufactured, handled, launched and inserted into orbit while limiting all applied stresses by a factor of 1/19 of the Precision Elastic Limit.

In this experiment, a scale model telescope employing a thin 1.3 meter (50-inch) diameter beryllium mirror will be erected, aligned and tested in space. During orbit, the astronaut will erect and align the mirror to the optical tolerances associated with earth-bound observatories. The evaluation of the mirror figure will be accomplished by interferograms. Mirror figure patterns will be obtained prior to and during orbit. These patterns will be compared. The results of this experiment will serve as a guide for the design and fabrication of a 2.5 to 5 meter (100 to 200 inch) reflector type telescope for orbital use.

4.11.2 Objective

This experiment will determine the safe design stress and space alignment techniques to be employed in the design of 3 meter (120 inch) or larger, thin shell primary mirrors for future space borne telescopes.

The primary objective is to gather technological data on the Precision Elastic Limit (P.E.L.) i.e., the stress at which permanent deformations due to strain will place the mirror out of figure tolerance when used in space. These data, which will be obtained from a scale model of the ultimate 3 meter mirror, will permit determination of required design parameters that will be most sensitive to extrapolation.

The secondary objective of this experiment investigates the ability of man to assemble, align and test a large optical system in orbit. Techniques for future space replacement of degraded components (e.g., a primary mirror) may be evolved.

4.11.3 Experiment Justification

According to basic physical concepts, a thin membrane (shell mirror) can be figured to optical tolerances in a strain free supporting nest while in the gravitational field of one "g". Once removed from the nest for assembly in a telescope, gravitational effects will distort the mirror figure. However, when placed in orbit (zero "g"), the mirror will revert to the strain free condition thereby returning to the perfect optical figure that was attained on earth.

There is however one attendant problem. It is well known that a material experiences a permanent set or deformation when its elastic limit is exceeded. Accordingly, "hardware" has been designed to operate at stress levels below the elastic limit of the component materials. However, in precision instrumentation, it has been found that even when designs have been engineered to within a substantial percentage of the elastic limit, unexplained errors have occurred.

It has been established that in order to maintain performance specifications in precision systems, an exact determination of proportional limit must be made. Minute permanent deformations occurring in materials below the conventional proportional limit now require a new limit. This limit has been termed P.E.L. (Precision Elastic Limit) and is defined as "the stress

which produces a residual strain or deformation of one micron per meter (or one micro inch per inch)". This strain is a permanent set in the material and is sufficient in magnitude to change the power of an optical element. These minute permanent deformations in a large mirror will impart an exceedingly small additional deflection when compared to the effect of gravity (ratio greater than 1000:1) and is therefore not reliably measured on earth.

4.11.3.1 Contribution and Need

The need for large Diffraction Limited Mirrors in space has been discussed in Optical Technology Needs (Paragraph 3.0 of this report). The astronomical and scientific community (Woods Hole Report 1965) have stressed the importance of penetrating deeper into the universe. The space borne telescope will not be resolution limited by the atmosphere and a significant reduction in terrestrial telescope film exposure for dim objects will be achieved. The major contribution of this experiment is the determination of the maximum stress a mirror may experience and still remain within figure tolerance for diffraction limited performance. Thus, this maximum stress level (or P.E.L.) will be determined with a satisfactory confidence level so that with appropriate factors of safety thin diffraction limited mirrors may be designed, manufactured and launched into orbit.

The secondary contributions will be the confirmation of and/or indication of new techniques for orbital assembly and alignment.

The advantage and contribution of the thin mirror concept is basically a lower unit mass and weight than is possible with any other design. Some of the more important benefits which will be derived from this are as follows:

a. Ease of handling and erection. This will also permit mirror replacement in a space-borne telescope while in orbit if, after a few years usage, the optical surface has been degraded to the point of reduced efficiency.

b. Conservation of booster thrust requirements. Since the mirror has smaller mass, the supporting structure will be lighter in weight resulting in a smaller payload or allowing weight for additional instrumentation.

c. Guidance control will be easier. The lighter mass permits more responsive and faster slew rates. Less energy will be expended in control.

d. Reduced thermal gradients in mirror. The gradients parallel to the optical axis will be eliminated and, with the proper thermal design, can be practically eliminated in the radial direction (There will be no deleterious thermal effects due to rib structures).

4.11.3.2 Need For Space Testing

The necessity of gathering technological data from this experiment in the space environment is evident since the original premise is based upon the zero "g" environment (for measurements).

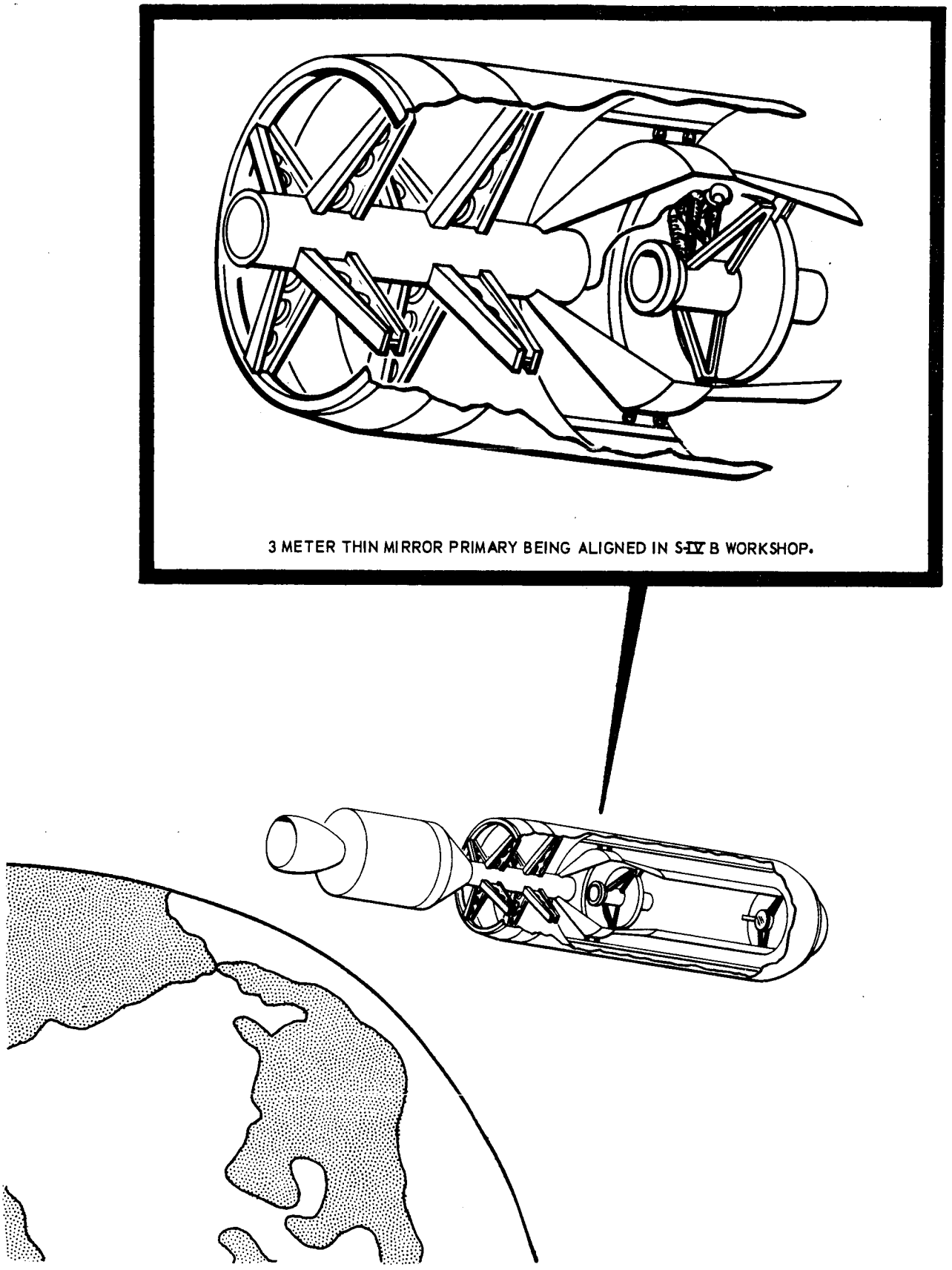


Figure 4.11-1. Mirror Alignment In Orbit

In order to clearly define the thickness-to-diameter ratio for large thin mirrors, it is necessary to eliminate the initial uncertainty of the physical constants. The uncertainty in this experiment is the determination of the maximum stress level that will not impart detrimental strains to the mirror. Accuracies required for diffraction limited performance restrict deformations to the order of magnitude of 0.02 microns. The deflections in a one "g" environment of the mirror due to its own weight are on the order of magnitude of 20 microns. Thus, at better than 1000 to 1 ratio the permanent deformations are not accurately measurable in the environment of earth. A method of determining and evaluating the maximum stress level is discussed in Section 4.11.5.8. Thus once the P.E.L. or maximum stress level is determined with a satisfactory confidence level, appropriate factors of safety may be applied to thin mirror design and fabrication.

A study was made of various methods for simulation of a zero "g" environment on earth. Each approach reviewed had serious drawbacks resulting in a need for space testing.

An earthbound simulated space lab to test optical mirrors for ultimate use in space should have a zero gravity or a uniform support pressure capability. Changes in pressure and gravity are changes in applied loads on the mirror and alter its characteristics. These parameters must be nullified on earth to duplicate a space environment. Some approaches to compensate for these loads and their merits are reviewed:

It is assumed that the mirror to be tested has a uniform section; (e.g. 10 millimeters (3/8 inch) thick, mirror material is Beryllium, 1.3 meters [50 inches] in diameter). For a mirror with a spherical shape and a radius of 3.2 meters [125 inches], the sagittal dip is approximately 6.35 cm [2 1/2 inches]. The weight of this dish at 1 g is 22.6 kilograms [50 pounds]. The surface area is 12,600 cm^2 [1960 in^2]. The temperature and relative humidity of air are maintained constant.

a. Water Flotation Method

The mirror may be floated on water with its reflective surface up and central aperture closed. The test instruments are rigidly supported above and independent of the mirror. The surface figure is tested as the mirror free-floats below.

The mirror and test instruments alignment will be difficult to maintain in a paraxial focus condition:

(1) The free-floating mirror will shift due to seismic tremors.

(2) The mirror is subject to bending at the unsupported ends for the section above the water-level.

b. Mercury Flotation Method

The mirror is floated on a mercury pool as in "a" above. Stability between test instruments and mirror surface cannot be obtained because:

(1) Seismic tremors will shift mirror axis with respect to test instruments and a stable interferogram cannot be obtained for 1/20 λ or better.

(2) Mercury will support the mirror over a smaller area than water and permit a larger mirror overhang, since Mercury has a specific gravity = 13.6 and beryllium has a specific gravity = 1.85. This increases the bending moment at the unsupported ends.

NOTE: Attaching the test apparatus to the mirror to offset item 1 aggravates item 2.

c. Submersion Method

Ideally, the mirror should be totally submerged in a fluid whose specific gravity is equal to that of the mirror (1.85). A review of known fluids does not indicate any fluid near the specific gravity of Beryllium which would also be clear enough for satisfactory light transmission.

d. "Zero-g" Aircraft Method

Zero-g aircraft tests can be achieved for periods up to about 1 minute. The time required to obtain a good interferogram study is about 1 hour. The one minute test time available in airborne tests is inadequate to obtain satisfactory results.

e. Pneumatic Floatation Methods

The mirror is floated on a cushion of air similar to the method outlined in Figure 4.11-2. Except for the loads of the 10 gram limit stops, the mirror is essentially free from the effects of gravity.

(1) The degree of uncertainty of obtaining 90% zero-g for the test period is about 50% since the control of the pressure support must be on the order of 81 $\pm$ 0.51 millimeters of water.

(2) The temperature of the supporting gas must be uniform.

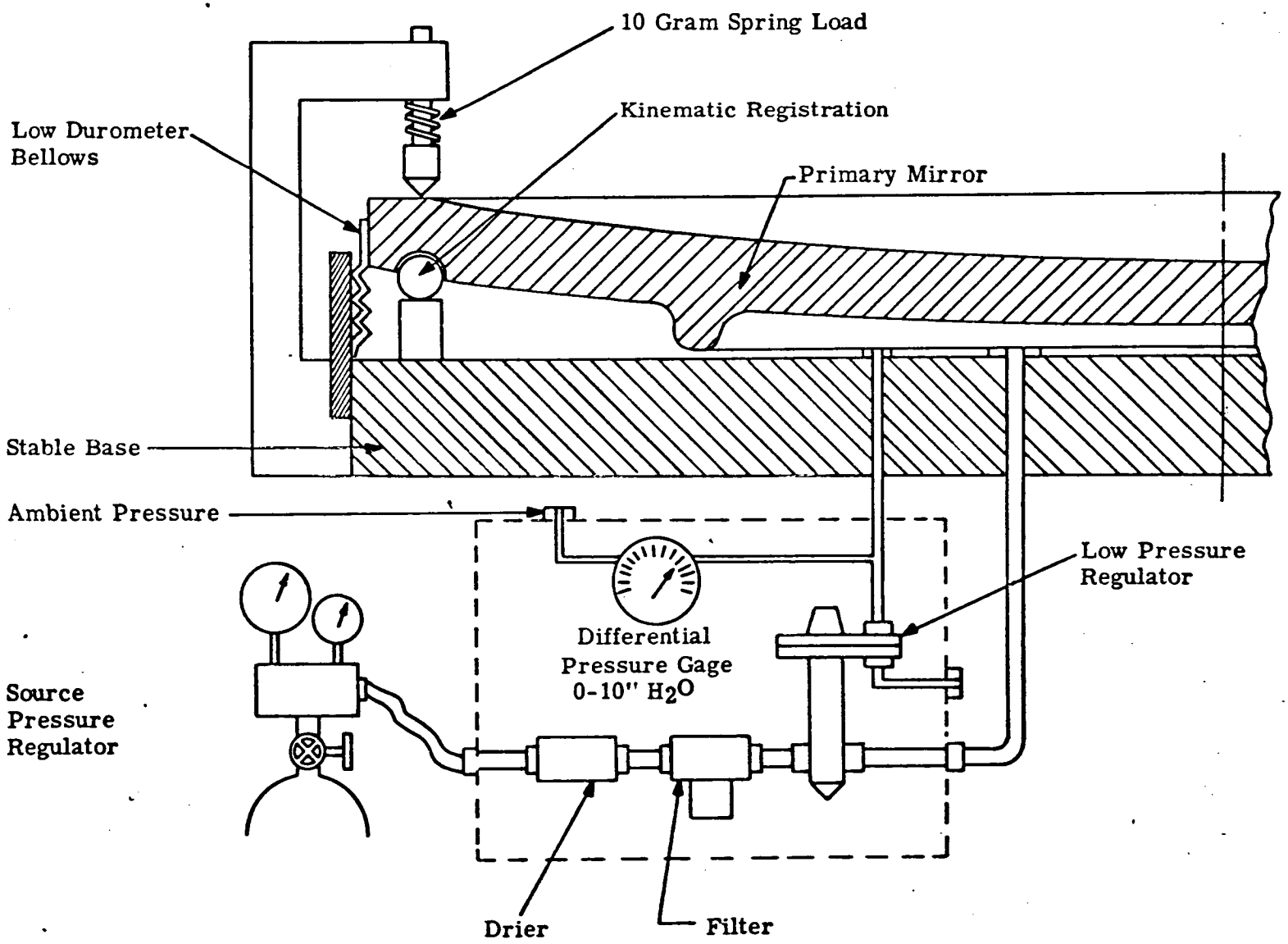


Figure 4.11-2 Zero-G Test Fixture

4.11.3.3 Feasibility

There are many major and varied problems which must be solved in order to successfully accomplish this experiment. These will be discussed in the text following. However, it should be understood that most of these problems are of complexities normally encountered in any development program and will be solved by techniques within the present "state-of-the-art".

The technological areas which must be advanced are:

a. Determination of the P.E.L.

b. Thin Mirror Design

c. Thin Mirror Fabrication

d. Space Testing Techniques for Mirror Figure

Preliminary studies of each area have been made and are described in the following text. The results of these studies indicate, with a high degree of confidence, that this experiment can be successfully engineered, implemented and executed.

This experiment also evaluates the advantages and problems encountered in the erection, alignment and testing of a large optical system (thin mirror design) in space. The design of such a system is shown schematically in Figure 4.11-3. The life of this system is expected to be far greater than the experiment requirements.

4.11.4 Implementation

The chart of Figure 4.11-3 shows the major functional components and the design alternatives that were considered. In this experiment we selected the thin mirror or "passive membrane" concept.

The chart of Figure 4.11-4 shows the steps involved in the implementation of this experiment to obtain the necessary technological data for future large thin mirror optics for space.

4.11.4.1 Experiment Design

Figures 4.11-5 and 4.11-6 are schematic sketches of the imaging system proposed for this experiment. This structure will maintain its dimensional stability with a minimum of weight.

The primary mirror is located against a reference frame by means of a modified kinematic mount, employing a ball-groove-flat three point constraining principle.

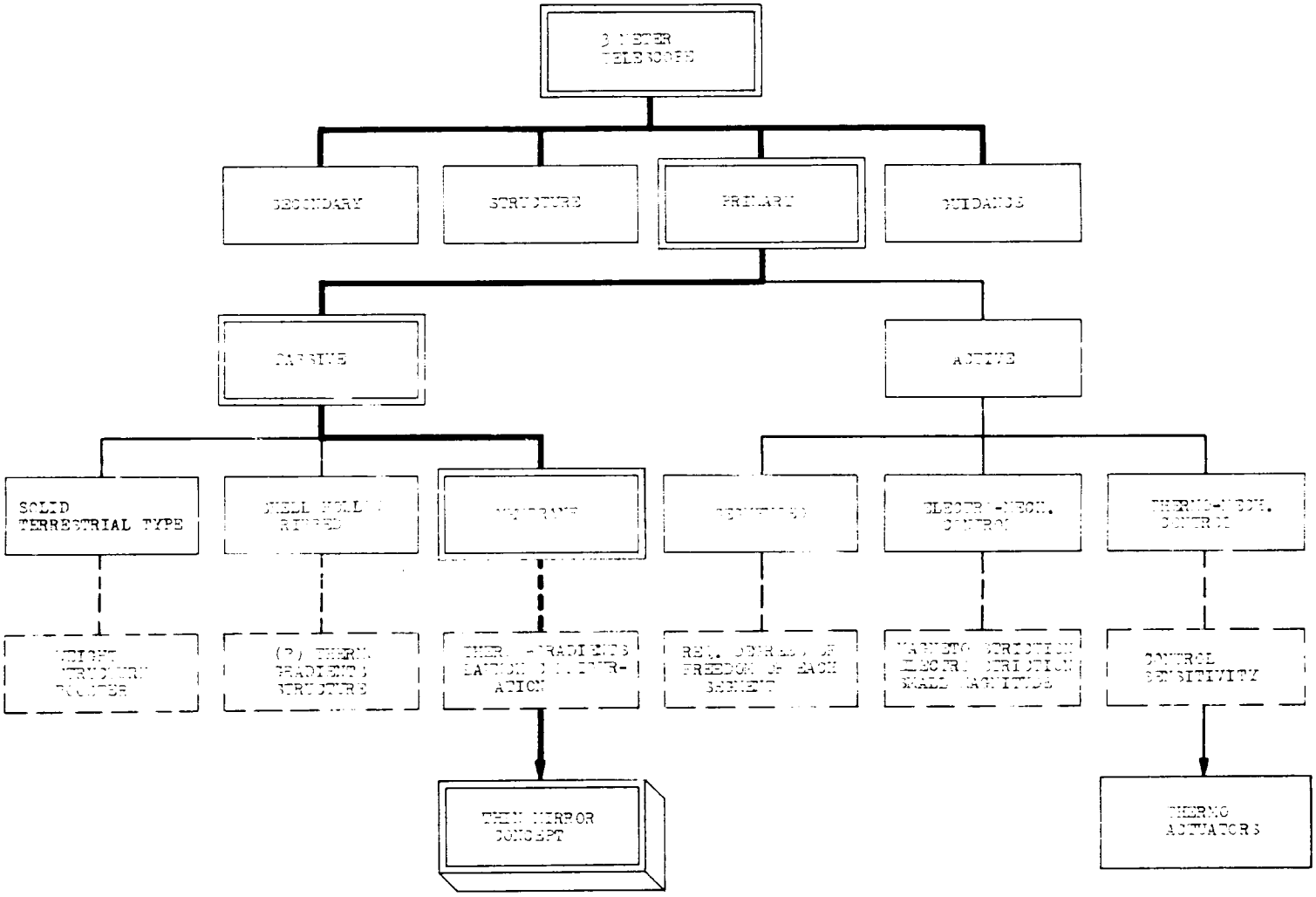


Figure 4.11-3 Design Approach

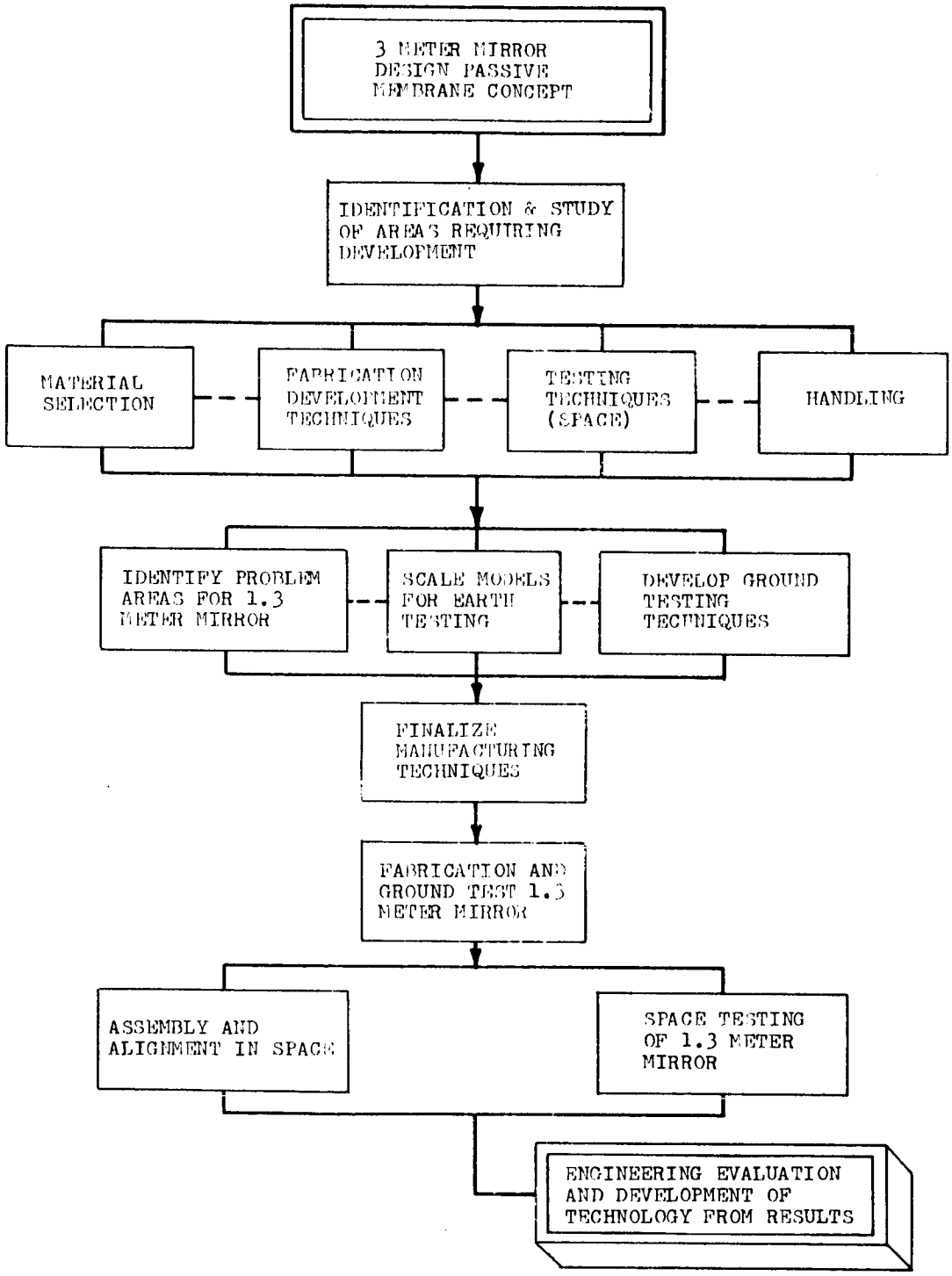


Figure 4.11-4 Experiment Plan

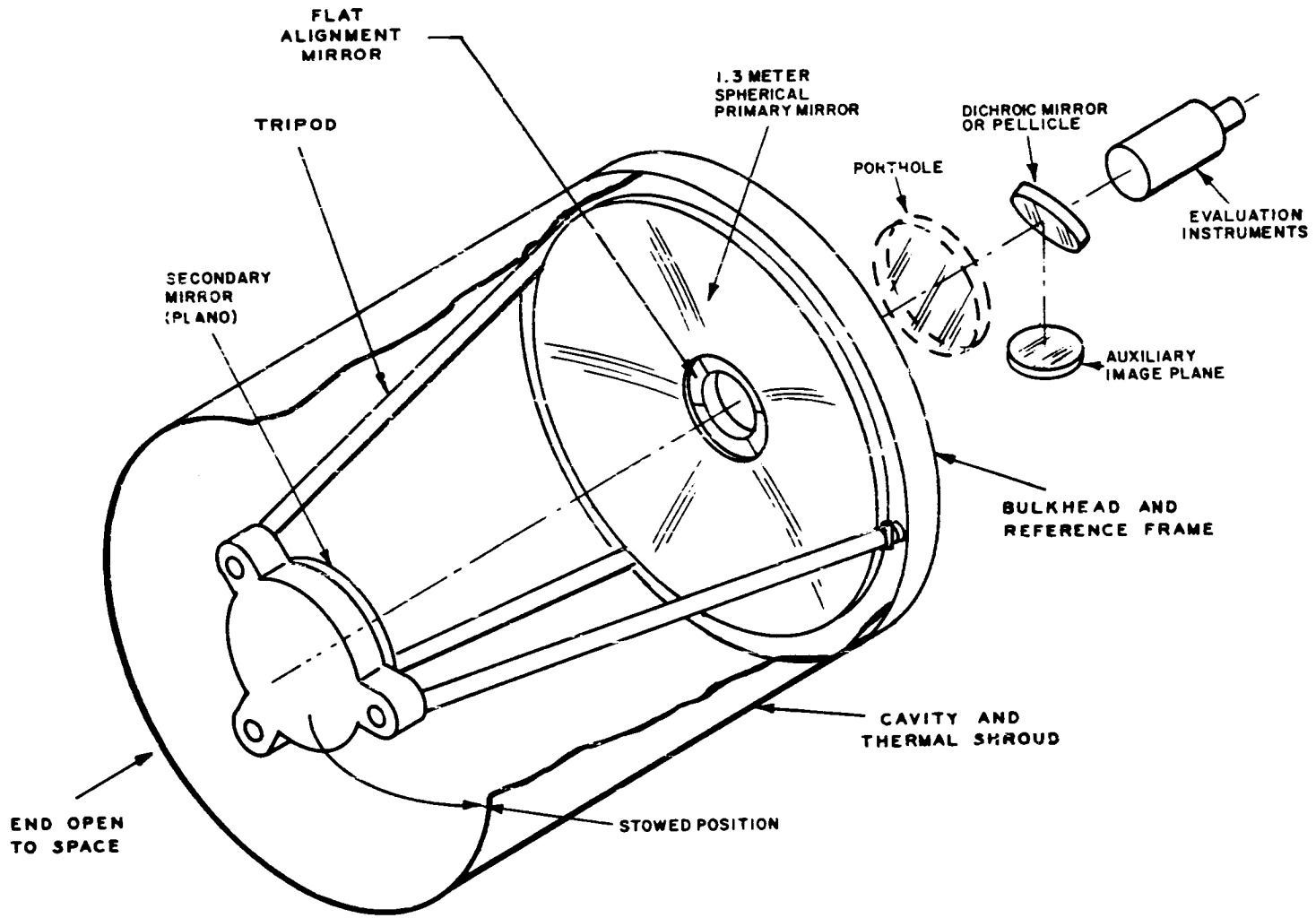
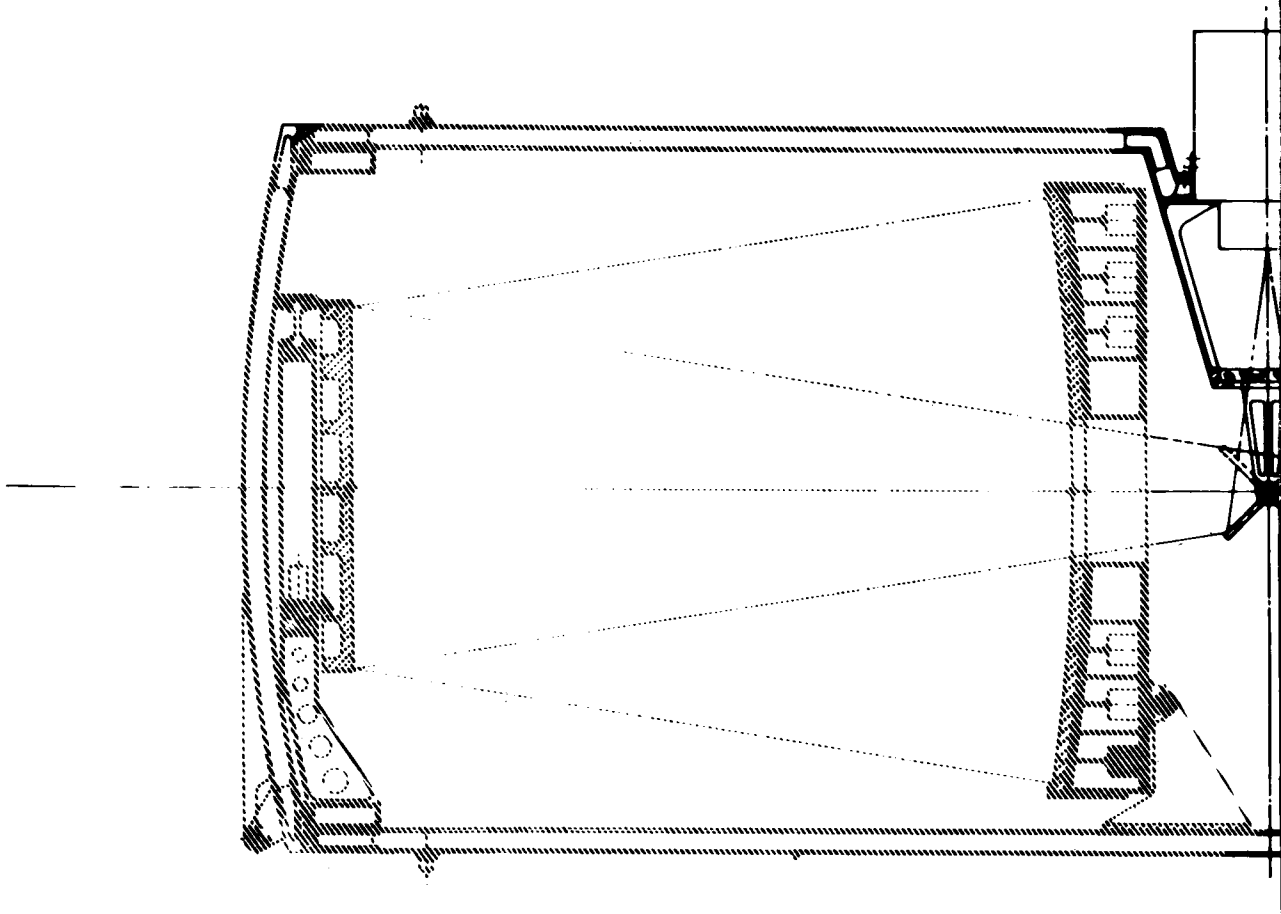


Figure 4.11-5 Imaging Reflector with 1.3 Meter Aperture



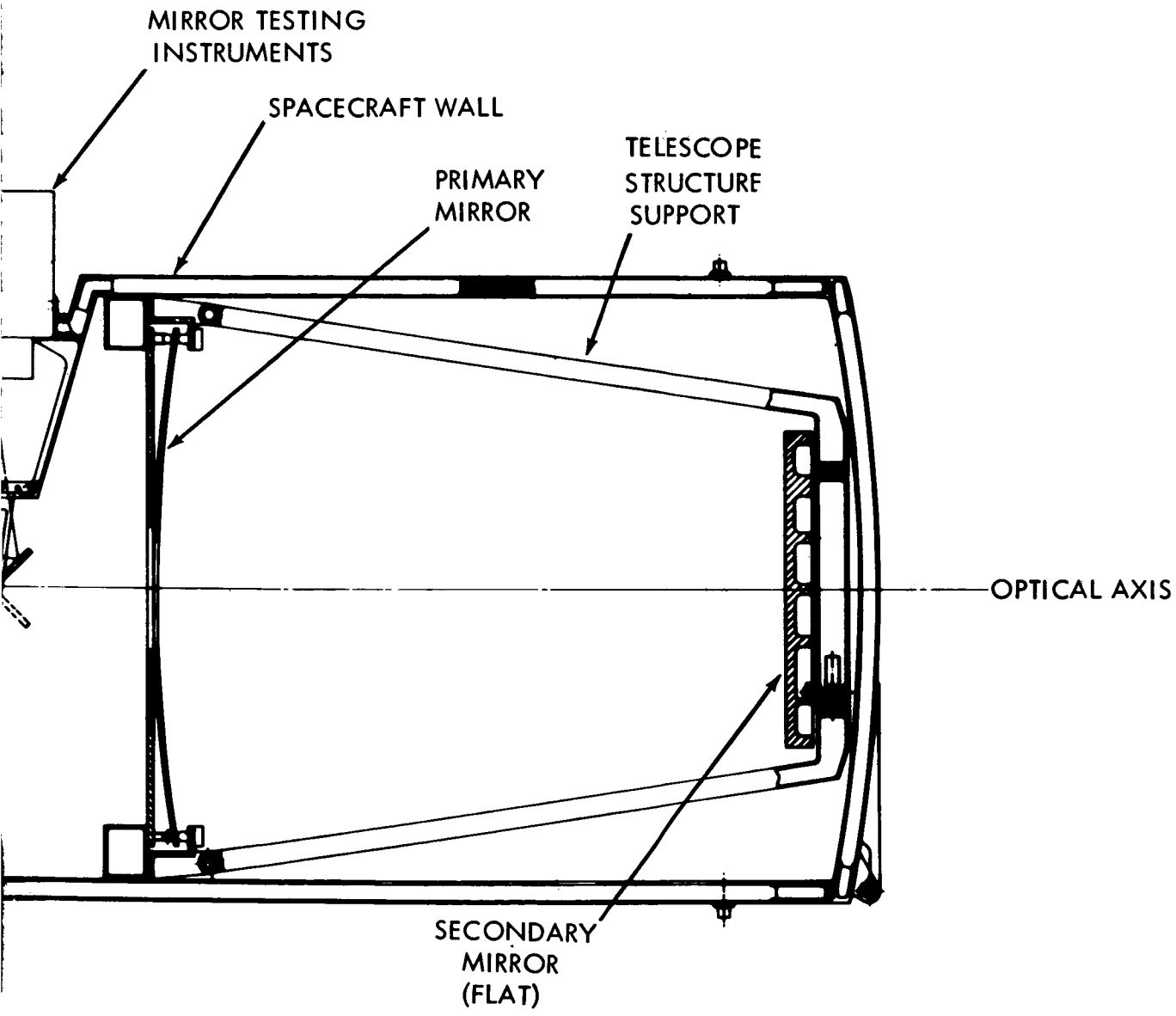


Figure 4.11-6. Primary Mirror Experiment Well-Thin Mirror Nesting Principle

The secondary mirror is mounted on a tabular tripod referenced to the primary mirror.

The cylindrical cavity shown surrounding the structure serves to block and absorb stray light and to act as a thermal isolating shroud. The cylinder is structurally separate from the optical system and may be shaped as necessary to allow access ports, exit windows and perhaps the ingress of an astronaut.

A camera interferometer or other instrumentation may be adapted and adjusted with respect to the same reference frame holding the kinematic mount for the primary.

4.11.4.1.1 Design Approach

Studies of the precision elastic limit have been made. Perhaps the most applicable to our purpose is the study conducted for the Navy (1) in 1960. This study verified that minute deformations were occurring in materials below the conventional proportional limit.

The standard used in this study was the stress at which the permanent deformation of one millionth of an inch per inch was evidenced. Since even this much strain can be detrimental to diffraction limited performance of a mirror, new limits must be experimentally determined for our application.

Thus the objective of this experiment is to determine the safe P.E.L. (i.e., stress vs. an allowable permanent deformation) to be used in the design of large diffraction limited mirrors for space applications. It is necessary to test the deformation vs. stress to determine the acceptable P.E.L.; resulting in an increase in the confidence level in using this P.E.L. Thus, we can safely design large mirrors of minimum thickness, thereby deriving all the benefits of weight saving, ease of replacement, cost, etc.

At any selected P.E.L., a family of mirrors may be designed for various diameters with minimum thickness. Since the primary purpose of this experiment is to determine the P.E.L. more precisely than is presently known, a factor of safety of 19 will be used in this experiment. After determining the P.E.L. allowable by means of this experiment more realistic factors of safety permitting even thinner mirrors will be possible. Section 4.10.5.2 develops the means of determining the mirror thickness vs. diameter. Of particular interest is Table 4.10.1 in that section tabulating mirror thickness and weight vs. mirror diameter.

---

(1) Dr. T.J. Hughel, "An Investigation of the Precision Mechanical Properties of Several types of Beryllium", G.M. Research Labs, 1960.

Based upon this, a recommended mirror size for an experiment is 1.3 meters (50 inches) and thickness of 10 millimeters (0.38 inches) of Beryllium S-200-C.

Since the same P.E.L. or maximum stress allowable is used for each mirror diameter, the following relations hold true:

a. The maximum deflection of each mirror is the same.

b. The stress value and variation from the center to the outer edge is the same for each diameter when comparing stress vs. the ratio of r/a where r is the radius from the center to the point of measurement and a is the maximum radius of the mirror (one half the diameter). For a description of stress variation across the mirror see Section 4.11.5.1.

Beryllium S-200-C was selected as the mirror material for this experiment on the basis of thermal, physical, stiffness-to-mass ratios and manufacturing considerations. Section 4.10.5.5.2 reviews these considerations. Of special interest is Table 4.10.3 of that section.

The fabrication and stress relieving of this mirror will be carefully planned and executed so that all handling and manufacturing stresses imparted to the mirror will have been within 1/20 of the P.E.L. (or 8.75 kg/cm^2). Thus we may have a high confidence level that the mirror has not experienced any stresses near or beyond the selected P.E.L. of 175 kg/cm^2 (2500 psi).

The shape best suited and selected for manufacturing in this experiment is a sphere. It is much simpler to figure than an aspheric surface. In addition, a spherical form may take advantage of the condition of unity magnification during mirror figure evaluation, i.e., it permits Foucault and interferometer tests to be performed at the center of curvature. This is also realistic since it does not vary too much from a paraboloid and will satisfy the experiment requirements. Section 4.11.5.3 describes a comparison of shapes (spheroid vs. paraboloid).

The fabrication and testing, on earth, of a thin shell primary mirror will be in a nesting fixture. Essentially, this "nesting technique" is such as to provide uniform mechanical support and thermal continuity throughout the initial manufacture of a thin shell primary, so that it is completely unstrained while in its nest. Section 4.11.5.4 describes this further.

Prior to launch, the mirror will be rim mounted and under controlled conditions will be subjected to a uniform load in order to stress the mirror to 175 kg/cm^2 P.E.L. This load will then be relieved and the mirror prepared for launch.

Section 4.11.5.1 describes and reviews the stressing effects of this load.

Careful consideration will be made to protect the mirror from the environment of launch and insertion into orbit. A feasibility study, "OTAES-Mirror Support Analysis" (See Section 4.11.5.6), has been made to show that the mirror may be protected from the forces of vibration and shock in all directions (i.e., translation and rotation of mirror surface, and translation parallel to the mirror surface) as well as from the fundamental "free-free" mirror resonance (existing at a frequency of approximately 75 hz).

The means of protection envisioned is the placement of pneumatic bladders on the front and rear surfaces of the mirror and a toroidal bladder about the rim. The spring constants and requirements of these bladders are described in Section 4.11.5.6. Thus it can be assumed to an acceptable high confidence level that the stresses applied to the mirror during launch and insertion into orbit will also be safely below the P.E.L. (or below 8.75 kg/cm^2).

Once the mirror is in orbit it will be unpacked, aligned and focused as described in Section 4.11.5.7.

The mirror will then be tested for "figure" by interferometric means. Section 4.11.5.8 outlines how the mirror figure will be determined by this method. The interferometer data will be used to determine the mirror shape and hence how far from the manufactured shape it has gone. After determining the new shape, the strain induced by the controlled stressing at the P.E.L. of 175 kg/cm^2 can be calculated and plotted as a function of radius from the center. The stress is calculated as it varies from a maximum of 175 kg/cm^2 at the center to a lesser value at the rim (a function of the radius also). Then the deformations may be directly compared to the stress. Thus by reviewing the results and comparing with the maximum allowable deformation for a diffraction limited mirror, a maximum P.E.L. can be established. This P.E.L., with an appropriate safety factor, will then be used in the design of large diffraction limited mirrors.

Of interest are the weight savings resulting from these designs. Section 4.11.5.9 describes a comparison of designs for the launch weight of a rigid (GEP metal mirror system) system designed to be built and launched in a one "g" environment vs. a zero "g" design. Table 4.11.7 of this section shows that the savings in weight of large optics are expected to exceed 80% of the rigid design. Thus the larger the optics the more desirable the thin shell approach becomes.

4.11.4.2 Operational Procedure

After launch and insertion into orbit, the telescope must be assembled and aligned before the experiment can be performed. The following steps are necessary.

4.11.4.2.1 Erection in Orbit

A pneumatic suspension system as described in Section 4.11.5.6 has protected the primary mirror. This will be automatically deflated and stowed with an astronaut observing. The kinematic locators will be inspected.

EVA TASK ESTIMATE 10 MINUTES

The primary mirror kinematic mounts will be activated and the primary secured. The mirror surface will be inspected for surface defects.

EVA TASK ESTIMATE 30 MINUTES

The secondary mirror will be removed from stowage and deployed (coarse positioning) on the tripod. Remote drive controls for fine alignment will be inspected.

EVA TASK ESTIMATE 30 MINUTES

4.11.4.2.2 Alignment

The alignment may be accomplished within the protection of a space cabin. An autocollimator will be removed from stowage and secured in position on a mount provided. The autocollimator will be used to align the secondary to it and establish a preliminary optical axis.

ASTRONAUT TASK ESTIMATE 30 MINUTES

The autocollimator will then be used to sight onto the central flat and crossline of the primary mirror. The secondary mirror and autocollimator will be adjusted to center cross line of the primary with autocollimator reticle. This will establish axial alignment.

ASTRONAUT TASK ESTIMATE 60 MINUTES

4.11.4.2.3 Image Plane Check

The autocollimator will be detached and stowed. The eyepiece will be removed from storage and positioned in the autocollimator mount near the calculated focal plane. A point light source will be positioned at an alternate image plane. The astronaut will then sight through the eyepiece and reposition the secondary mirror for maximum target definition (best focus). Since the image will be inverted and reverted, any off-axis translations will also be reversed, i.e., left will be right and top will be bottom.

ASTRONAUT TASK ESTIMATE 20 MINUTES

4.11.4.2.4 Mirror Evaluation

The eyepiece will be removed and stowed. A Foucault tester will be positioned on the autocollimator mount at the established image plane. The primary mirror surface will be illuminated with a light source within this tester. The astronaut shall sight through this tester and reposition this unit axially until the entire mirror surface appears to darken uniformly. The mirror surface should be divided in zones and deviations from uniform darkening should be tabulated by zones. This tabulation which is equivalent to a contour map or shadowgraph of the mirror surface could be supplemented with photographs taken via the Foucault tester. Two astronauts required (observer relaying data to recorder).

ESTIMATED TIME 30 TO 60 MINUTES

Remove Foucault test apparatus and autocollimator mount from bulkhead and stow. Attach scatter-plate interferometer to bulkhead and align interferometer to optical axis of telescope.

ASTRONAUT TASK ESTIMATE 20 MINUTES

Interferometer scan is activated by manual or remote control to sweep across primary surface. The data is generated and transmitted to earth in real time or stored (several scans) for later transmission. Astronaut is not required for this portion.

With the above procedures the experiment has been put into operation. The necessary data collected from the interferograms will be used to determine the mirror shape, the strains and location of these strains. From this a maximum stress will be found within which the mirror will retain its figure to a prescribed tolerance (e.g. $1/32\lambda$).

The experiment mirror was fabricated with a factor of safety of 19 because our confidence level in our knowledge of the safe P.E.L. was less than 50% Now, we may design future large diffraction limited mirrors using much lower factors of safety with a confidence level exceeding 99.9%.

4.11.5 SUPPORTING ANALYSES

4.11.5.1 Variation of Stress Across the Mirror As a Function of Radius

For analytical purposes, flat plate theory applies adequately to this problem in spite of the stiffening effect encountered in a spherical shape. Shell theory is more complex computationally and yields results differing insignificantly from the following discussion.

The mirror is a thin plate supported at the rim with a uniformly distributed load. (See Fig. 4.11.7a). The formulas (1) for stress and deflection are:

Radial Stress

$$S_r = -\frac{3W}{8\pi m h^2}\left[(3m+1)\left(1-\frac{r^2}{a^2}\right)\right] \qquad (1)$$

Tangential Stress

$$S_t = -\frac{3W}{8\pi m h^2}\left[(3m+1) - (m+3)\frac{r^2}{a^2}\right] \qquad (2)$$

Deflection

$$y = \frac{-3W(m^2-1)}{8\pi Em^2h^3}\left[\frac{(5m+1)a^2}{2(m+1)} + \frac{r^4}{2a^2} - \frac{(3m+1)r^2}{m+1}\right] \qquad (3)$$

Max. stress at center $S_r = S_t$

$$S_r = S_t = -\frac{3W}{8\pi m h^2}(3m+1) \qquad (4)$$

Max. deflection at center

$$y = -\frac{3W(m-1)(5m+1)a^2}{16\pi Em^2h^3} \qquad (5)$$

(1) Roark, "Formulas for Stress and Strain"

$$W = w \pi a^2$$

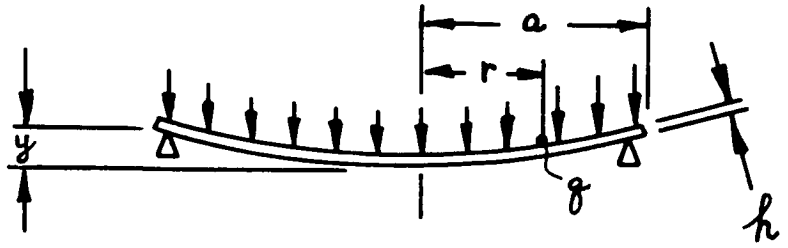


Figure 4.11-7a Uniformly Loaded Thin Plate Supported at the Rim

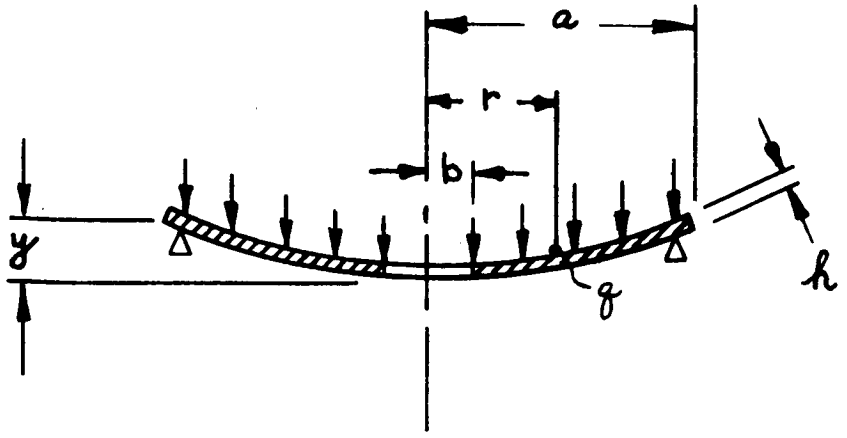


Figure 4.11-7b Uniformly Loaded Thin Plate with Hole in Center and Supported at the Rim

W = total weight ..... lb

w = unit applied load ..... lb/in^2

a = radius or half diameter ..... in

y = deflection ..... in

S_r = radial stress ..... psi

m = reciprocal of Poissons ratio (50 for Beryllium)

h = thickness ..... in

r = distance from center to any point q

S_t = tangential stress ..... psi

E = Youngs Modulus ..... psi

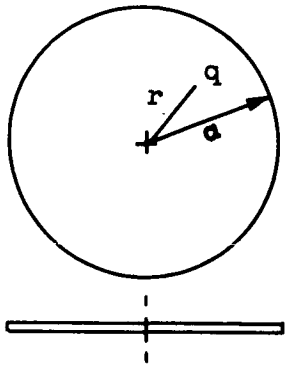
q = any point considered

It is shown in section 4.11.5.2 that a family of mirrors may be designed with a factor of safety of 19 or a P.E.L. of 125 psi. These mirrors of Table 4.10.1 may then be subjected to a uniform load in addition to their own weight to attain a maximum stress of 2500 psi (the P.E.L. to give a permanent strain of one to two micro inches per inch). By using equation (4) the applied load to obtain 2500 psi can be determined.

From formulas (1) and (2) it is seen that the stress is a function of the ratio r/a; i.e., a ratio of the radius at the point of consideration to the half diameter of the mirror. Table 4.11.2 tabulates the calculated stresses using formulas 1 and 2 for maximum stresses of 125 psi (as manufactured due to the mirrors own weight) and 2500 psi (the P.E.L. to which the mirror will be stressed once prior to launch). The maximum deflections for 125 psi and 2500 psi are found to be 0.0042 and 0.0840 respectively. If all the load were removed, all deflection would also be removed except for the minute residual deflection due to the expected deformation of the mirror material of one to two millionths of an inch per inch in the radial direction. However, because the effects of earth's gravity upon the mirror mass cause a deflection many times the expected permanent deflection due to the stressing at 2500 psi, it is not a measurable quantity except in a zero "g" environment.

TABLE 4.11-2

CALCULATED STRESSES (USING FORMULAS (1) AND (2))



Beryllium γ = .02 (Poissons ratio)

m = 50 $(1/\gamma)$

ρ = .066

a, t = see Table 4.10.1

S_r = eq (1) Sec. 4.11.5.1

S_t = eq (2) Sec. 4.11.5.1

y = eq (5) Sec. 4.11.5.1

r = radius from center to point q

	STRESS			
	(Max. stress 125 psi)		(Max. stress 2500 psi)	
r/a	S_r psi	S_t psi	S_r psi	S_t psi
1	0	81	0	1620
.8	25	90	500	1800
.6	50	99	1000	1980
.4	75	107	1500	2140
.2	100	116	2000	2320
0 (center)	125	125	2500	2500

It is noted that the proposed design will be a mirror with a hole in the center approximately 1/5 the diameter (see figure 4-11-7b). Careful review shows that the formulas for the stress and deflection will vary from those in (1) to (5). However, these deviations can be taken into account and scaled for proper results.

For instance, using flat plate theory again, we see the more complex (computationally) formulas for stress and deflection are:

Max. stress

$$S_{max} = S_t = \frac{3W}{4\pi m h^2 (a^2-b^2)2} \left[a^4(3m+1) + b^4(m-1) - 4ma^2b^2 - 4(m+1)a^2b^2 \log \frac{a}{b} \right]$$

Max. deflection

$$Y_{max} = \frac{3W(m^2-1)}{\pi 2m^2Eh^3(a^2-b^2)} \left[\frac{a^4(5m+1)}{8(m+1)} + \frac{b^4(7m+3)}{8(m+1)} - \frac{a^2b^2(3m+1)}{2(m+1)} + \frac{a^2b^2(3m+1)}{2(m-1)} \log \frac{a}{b} - \frac{2a^2b^4(m+1)}{(a^2-b^2)(m-1)} \left(\log \frac{a}{b} \right)^2 \right]$$

where:

S_t = tangential stress psi

W = $\pi w(a^2-b^2)$ lb

w = unit load psi

a = half O.D. in.

b = half I.D. in.

h = thickness in.

m = reciprical of Poissons ratio (50 for Beryllium)

E = Youngs modulus

When the final shape is determined the proper stress variations with a maximum stress of 2500 psi at the I.D. (radius b) can be determined and applied as previously described.

4.11.5.2 Mirror Thickness Evaluation

(See subsection 4.10.5.2)

4.11.5.3 Shape Variation - Spheroid vs. Paraboloid

(See subsection 4.10.5.3)

4.11.5.4 Fabrication and Nesting Techniques and Evaluation

(See subsection 4.10.5.4)

4.11.5.5 Thermal Considerations in the Selection of Mirror Materials

(See subsection 4.10.5.5)

4.11.5.6 Mirror Support Analysis - Launch Environment

When the mirror is removed from its nest and installed into a spacecraft, it experiences a variety of stresses, chiefly those from handling. Proper design and careful handling will keep these stresses at an appropriate low level.

When the mirror is launched into orbit it must also be protected from detrimental stressing. Thus it must be supported by a separate elastic support suitably retained.

By far the most pormising type support is that of contained pneumatic cushioning, i.e., sectional gas filled bladders, principally because of light weight and minimal EVA in space for positioning and inspection of the primary mirror.

Figure 4-11-8 shows this arrangement in schematic form. The segmented cushion supporting the entire second surface of the mirror may be retained by a metal membrane or the bulkhead. The segmented toroidal cushion supports the periphery of the mirror and is in intimate contact with the other cushions.

The first surface of the mirror is supported by cushions affixed to the hinged doors; these doors serving the dual purpose of holding the mirror during launch and of protecting the primary whenever work is being done in the area of the primary. Protection of the surface of the primary is recognized as a problem area. The solution may be in the use of a "peel coat", removable as part of the erection procedure.

Means such as bleed valves may be employed for each section of the pneumatic suspension system in order to vent pressure during the boost to altitude. In this way, a uniform force would retain the mirror during its ascent to orbit.

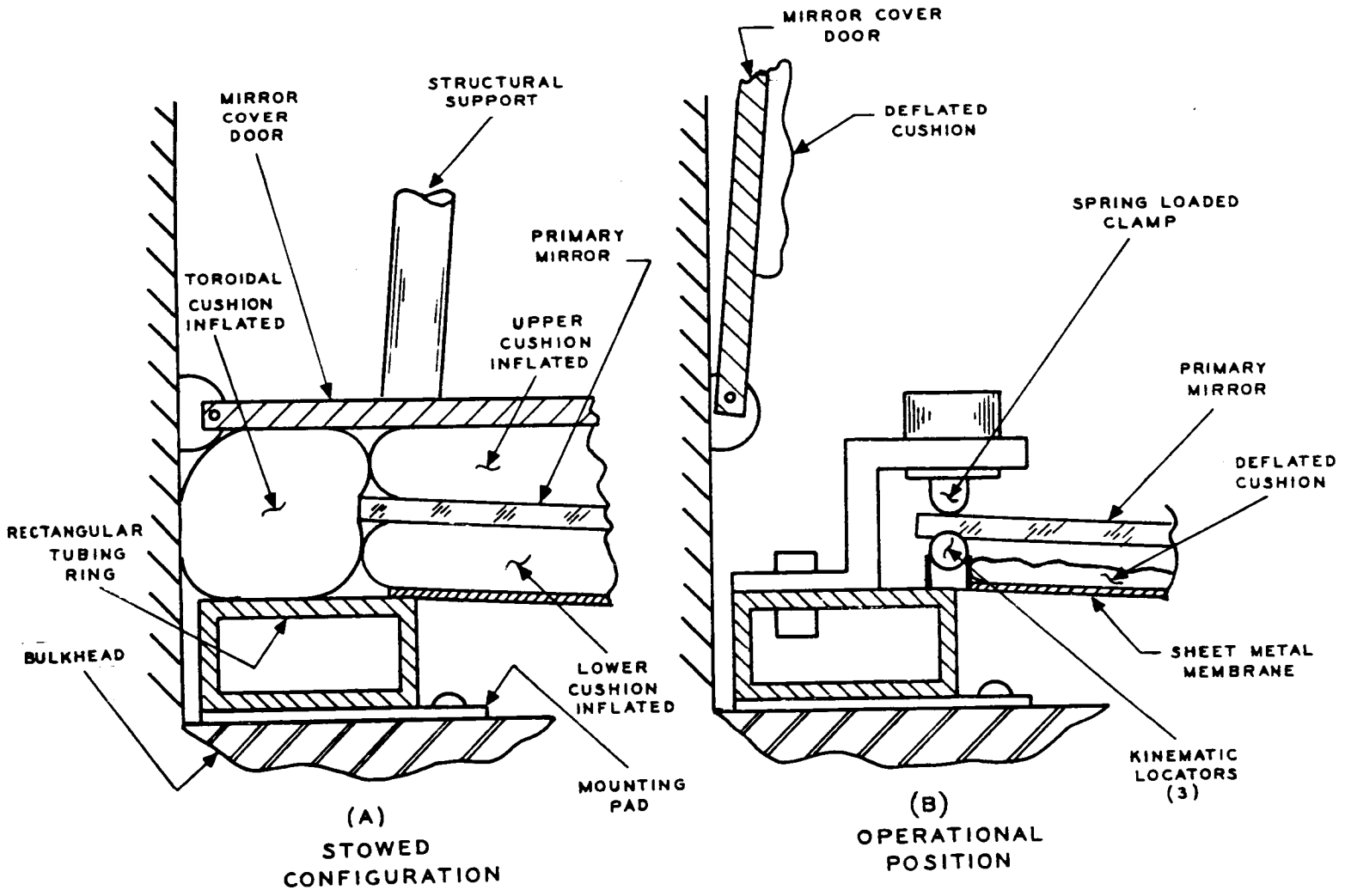


Figure 4.11-8 Primary Mirror Mounting

The following is a preliminary dynamic analysis of this "bladder supported" mirror subjected to launch environment.

Figure 4-11-9 shows a mirror supported on its two faces and its edge. This support system may exhibit three modes of dynamic response as shown in the figure. The spring constants K_1, K_2 are used to represent the stiffnesses of the face bladders, assumed linear. K_3 (y) is a non-linear spring rate.

The three modes of vibration are translation and rotation of the mirror surface and translation parallel to the mirror surface.

The coupled equations of motion for the first two modes are:

$$m\ddot{x} + (K_1 + K_2)\, x - (K_1 \ell_1 - K_2 \ell_2)\, \theta = 0 \qquad (1)$$

$$I\ddot{\theta} - (K_1 \ell_1 - K_2 \ell_2)\, x + (K_1 \ell_1^2 + K_2 \ell_2^2)\, \theta = 0 \qquad (2)$$

Assuming $K_1 = K_2 = K$

$$\ell_1 = \ell_2 = \ell$$

Equations (1) and (2) are uncoupled and the translational and rotational natural frequencies become:

$$\omega_t = \sqrt{2K/m} \qquad (3)$$

$$\omega_r = \sqrt{\frac{2K\ell^2}{I}} \qquad (4)$$

For the 50 inch Beryllium mirror (.38 thick):

$m = .126$ lb sec^2/in

$I = 19.69$ lb sec^2 in

$\ell = 12.5$ in

Therefore:

$$\omega_t = \left[(15.87K)^{1/2} \text{ rad/sec}\right] \qquad (5)$$

$$\omega_r = \left[(15.87K)^{1/2} \text{ rad/sec}\right] \qquad (6)$$

A desirable situation will be to isolate the mirror from the fundamental "free-free" resonance existing as a frequency of 75 Hz. A fundamental mirror-bladder frequency of approximately 10 Hz would be ideal for this case. This would be equivalent to a spring constant of $K = 250$ lb/in. The equivalent bladder pressure can then be computed.

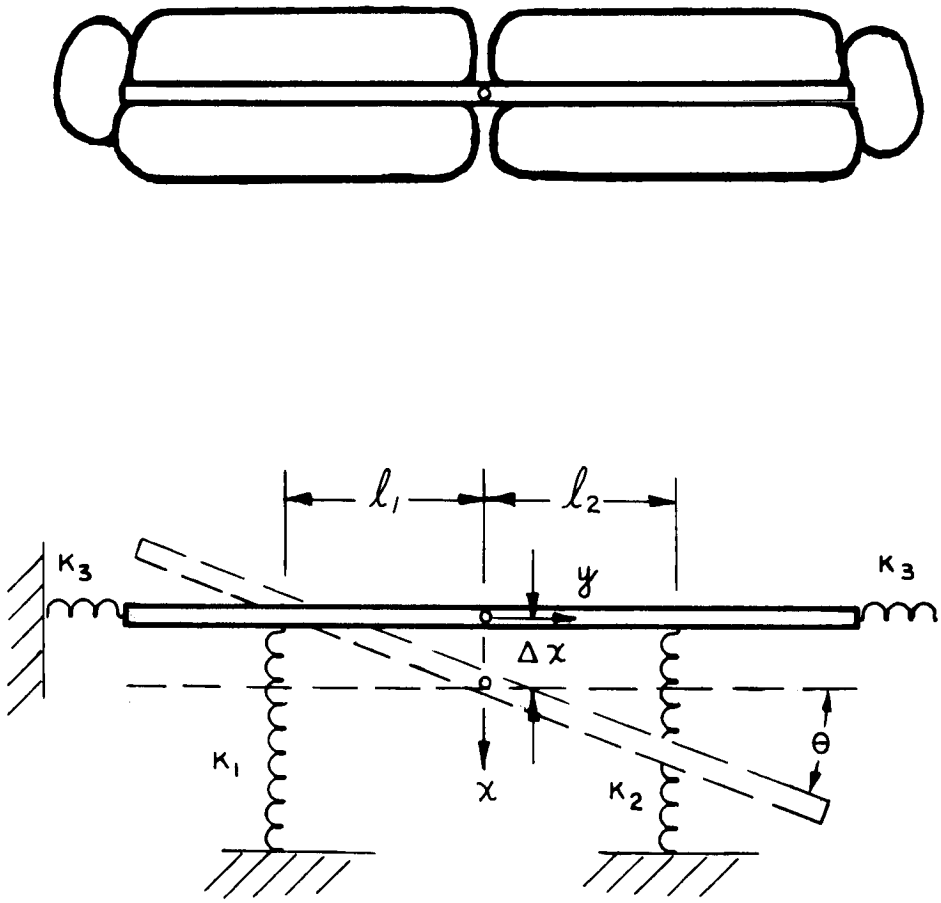


Figure 4.11-9 Bladder Supported Thin Mirror

Analysis of the in-plane vibration in the y direction (shown in Figure 4.11-9) is complicated by the distortion of the bladder which is non linear. Thus more detailed analysis of this also will be made to ascertain the bladder characteristics and hence the requirements for this mode of vibration.

The procedure for mounting the primary mirror after reaching orbit would consist of: deflation and automatic stowage of the pneumatic cushions, inspection to affirm that the kinematic locators are in position, activation of kinematic locators. Removal of the mirror protective coat would not occur until that point in the erection and alignment routine when the optical surface was actually required.

4.11.5.7 Alignment Considerations

After launch and during orbit, an astronaut by EVA will mount the thin mirror and erect the prealigned (coarse alignment) secondary mirror. This secondary mirror assembly is capable of remote longitudinal and 2 axis tilt adjustment. The secondary mirror is positioned in front of the primary by a 3-vane spider anchored to the tripod. This telescope construction is designed to bring the optical elements into a coarse alignment upon assembly. Final optical alignment is achieved with the aid of auxiliary equipment and the exercise of specific degrees of freedom on the elements themselves.

The Cassegrain type of Figure 4.11-10 may then be aligned as follows: After the deployment of the primary and secondary mirrors, an autocollimator is centralized behind the primary mirror. It is capable of angular tilt in elevation and azimuth with respect to the observer's body. The observer autocollimates from the secondary mirror and thereby establishes a line of sight between autocollimator and secondary mirror.

The cross-line in the central region of the primary is selected as the target. The line-of-sight is extended from secondary to primary mirror. The secondary mirror is indexed about two angular axes by remote control and the autocollimator is re-oriented manually until primary mirror alignment is achieved. In this fashion, fine alignment of optical elements are obtained and an optical axis is established.

After this alignment is obtained, a focus check for image location is required. The collimator is replaced with a modified "Gauss" occular or eyepiece and a point source is projected into the primary. The secondary mirror is adjusted along the optical axis previously established until best image definition is obtained within the control region of the field of view.

When the image check is completed, a Foucault or knife-edge test is performed to obtain a rapid evaluation of the primary mirror figure.

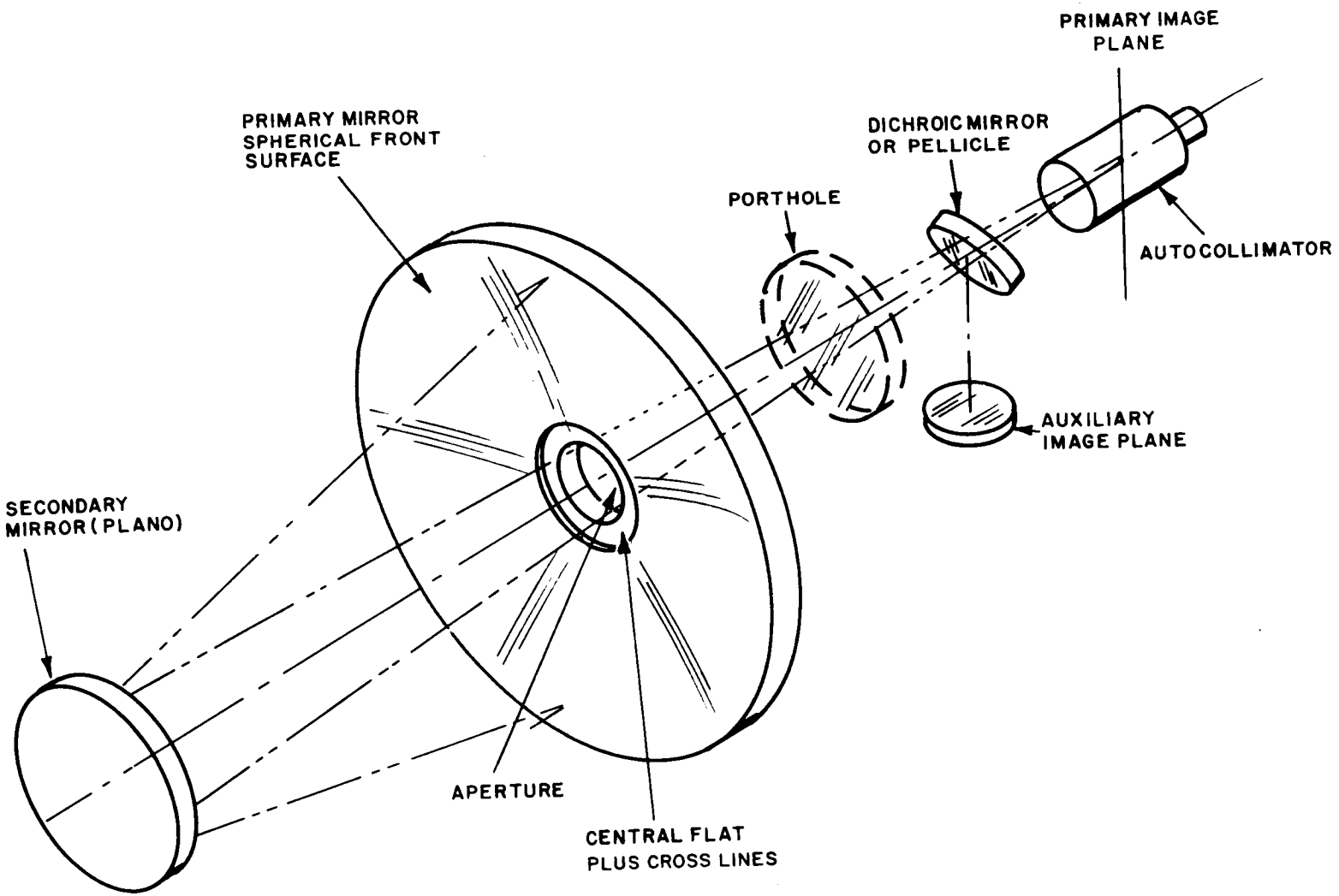


Figure 4.11-10 Modified Cassegrain

In a zero-g and vacuum environment, the effects of differential pressures and loading changes due to altitude are eliminated. However, severe thermal effects may alter the mirror figure and if so a precise control of this thermal degradation will be required in the final designs of large optic systems in order to perform near or at the diffraction limit. To determine the extent of and the effects of these thermal gradients, the primary in this experiment will be instrumented with a mosaic pattern of temperature sensors. The pattern selected will be capable of indicating thermal gradients across the mirror as well as imbalances in local areas where variations may exist. Data will be acquired indicating the thermal conditions as they vary as a function of telescope attitude in space.

When integrated with the Foucault and interferometer test data, later evaluation and further ground tests will establish the need for and consequently the means of determining the optimum configuration for temperature control of the final optical designs.

4.11.5.8 Measurement of Mirror Figure by Interferometers

Figure 4.11-11 schematically shows a mirror spherical shape of constant radius a, as manufactured. Due to the application of a uniform load, producing a maximum stress of 2500 psi at the center, a new shape is expected as a direct result of the permanent strains induced in the material. Since the expected strain is a function of stress and the stress varies as a function of the radial distance from the center it is sure to produce an aspheric surface as a final product. (Shown in Figure 4.11-11 as a_o , a_1 ----------a_n).

Thus a method of determining the radii a_{o-n} at every point on the mirror must be used. It is expected that the radius value will change very slightly although mirror figure may be affected measurably.

The proposed mirror is a 50 inch diameter sphere of 125.00 inch radius of curvature. Figure 4.11-12 shows the geometry of the sagittal and radius of curvature. From this the equation for the sagittal is:

$$a^2 = (a - S)^2 + H^2$$

or

$$H^2 = 2\ aS - S^2 \qquad (1)$$

For chords that are short in comparison with the radius, S^2 will be negligibly small with respect to 2 aS and the length of the sagittal becomes:

$$S = \frac{H^2}{2\ a} \qquad (2)$$

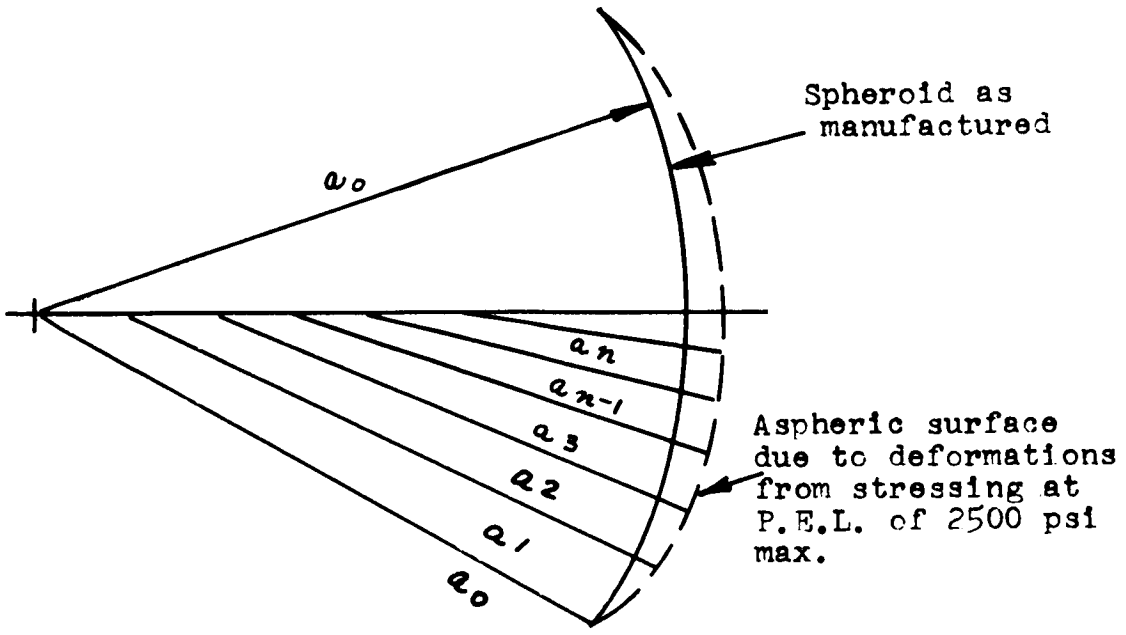


Figure 4.11-11 Mirror Figure Before and After Stressing

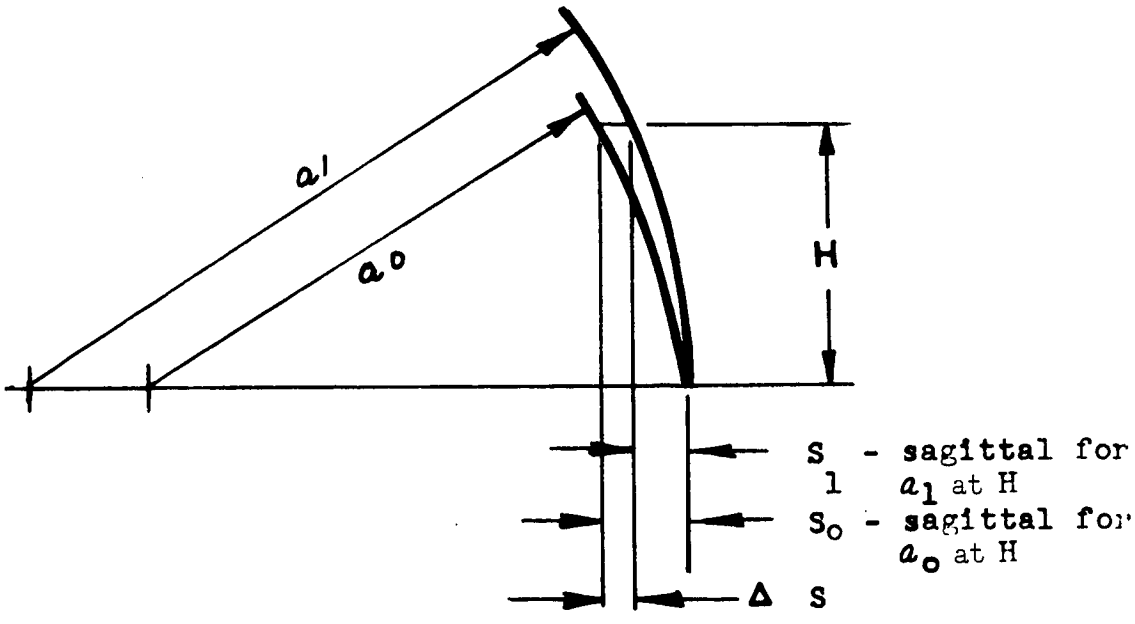


Figure 4.11-12 Geometry of the Sagittal and Radius of Curvature

Because of the accuracies required in this case the S^2 term cannot be ignored in the final analysis. However, for study purposes since the order of magnitude in the error is small, and formula (1) is more complex computationally, formula (2) has been used to obtain the data for Table 4.11-3.

Table 4.11-3 is a tabulation of sagittal distances at various chord lengths (H = half chord) for values of H from 1 to 6 and for radii variation from the nominal 125.000 (124.80 to 125.20).

The radius of the mirror can be determined in its nest when manufacturing is complete and mirror figure requirements are satisfied. The exact mirror figure can be determined by interferometric means and related to index markers on the mirror surface.

After launch, insertion into orbit and alignment of the mirror system, the interferometer will again be brought into focus. However, since an aspheric surface is expected, minute radial changes will be found across the diameter of the mirror. If all factors other than the controlled stressing to 2500 psi max, are held constant, the expected change in figure will be found as annular rings of different radii of curvature.

To appreciate the order of magnitude of radial change, assume that the increase in arc length is 2 micro inches/inch across the mirror and the subtended angle Θ is constant. Figure 4.11-13 shows the geometry and computations indicating a new radius of 125.000248. (A change of 2 1/2 ten thousandths.) Therefore, Table 4.11-3 well covers the range to be encountered.

The spherical area in focus with the interferometer will appear as a uniform surface. The areas that are aspheric will be detected by the interferometer and indicated by light fringes.

Referring to Figure 4.11-12, if the interferometer is at radius a_o and an area of height H is at radius a_1, there is a change in sagittal, ΔS as follows:

$$S_o = \frac{H^2}{2 a_o} \tag{3}$$

$$S_1 = \frac{H^2}{2 a_1} \qquad \text{but } a_1 = a_o + \Delta a \tag{4a}$$

and

$$S_1 = \frac{H^2}{2 (a_o + \Delta a)} \tag{4b}$$

TABLE 4.11-3

SAGITTAL DISTANCES AT VARIOUS CHORD LENGTHS

SAGITTAL $S = \frac{H^2}{2a}$ (See Formula (7))

R	H / H^2 / 2 R	1	2	3	4	5	6
		1	4	9	16	25	36
124.80	249.6	.004006	.016024	.036054	.064096	.100150	.144216
124.85	249.7	.004004	.016019	.036043	.064076	.100120	.144172
124.90	249.8	.004003	.016012	.036028	.064051	.100080	.144115
124.95	249.9	.004001	.016006	.046014	.064025	.100040	.144057
125.00	250.0	.004000	.016000	.036000	.064000	.100000	.144000
125.05	250.1	.003998	.015993	.035985	.063974	.099960	.143942
125.10	250.2	.003997	.015987	.035971	.063948	.099920	.143884
125.15	250.3	.003995	.015980	.035956	.063923	.099880	.143827
125.20	250.4	.003994	.015974	.035942	.063976	.099840	.143769

$$\text{Sin } \theta = \frac{25}{125}$$

$$\theta = .2013 \text{ rad.}$$

$$\ell = \theta r = 25.1625000 \text{ inches}$$

$$\ell = \ell + \Delta \ell$$

$$\Delta \ell = \ell \ (.000002) = .000050$$

$$\ell' = 25.162550$$

With θ constant

$$\frac{\ell}{\ell'} = \frac{r}{r'} \qquad \text{or} \qquad r' = \frac{r \ell'}{\ell}$$

$$r' = \frac{125.000 \ (25.162550)}{25.1625}$$

$$r' = 125.000248$$

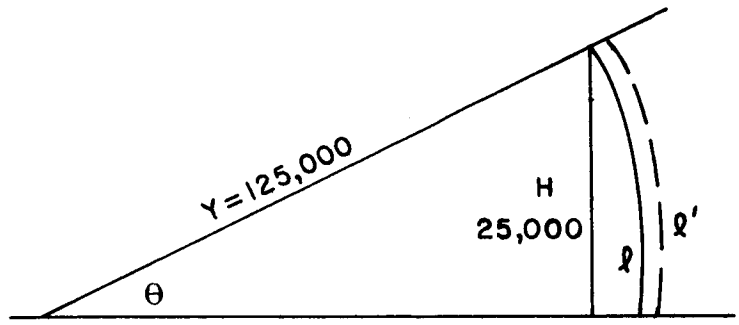


Figure 4.11-13
Effect of Radial Change

Thus $\Delta S = \frac{H^2}{2}\left[\frac{1}{a_o} - \frac{1}{a_o + \Delta a}\right]$ (5)

The new radius a_1 can now be determined by using equation (5) and solving for Δa. We may do this because the other quantities are known or determined as follows:

H is determined by the index markers on the mirror surface which give scale to the interferogram.

a_o is the initial radius of the spheroid.

ΔS can be determined from the interferogram and light fringes. For example if H were 5 and a_o was 125.000 inches, Table 4.11-4 can be derived from Table 4.11-3 data. Table 4.11-4 shows ΔS as a function of Δa values. These values are seen to vary from 0 at a = 125.000 in.

(Δa = o), to .000160 at a = 125.200 or 124.800 in.

(Δa = .200 in.).

If light of a wavelength = 5000 $\mathring{A}$ is used, a fringe for each 0.000010 inch Δa should be detected. Thus, at Δa of 0.100 (say a_1 = 124.9 or 125.1), the ΔS of 0.000080 is 8 fringes. This is a measurable quantity. Thus by counting the fringes in the interferogram the ΔS and subsequently the shape of the mirror may be accurately determined. From this data, the point at which strain deformations take the mirror out of figure tolerance can be readily determined and a proper P.E.L. selected for mirror manufacture.

4.11.5.9 Weight Saving Considerations

The launch weight of a large optical system complete with infinity imaging capabilities is a function of the design approach. For example, compare the launch weight of a rigid design capable of withstanding the rigors of launch and one g environment, to that of a thin mirror designed for a zero "g" environment. Full cognizance can be taken of the fact that the equipment need be aligned and operating only when weightless or during orbital flight. The astronaut may assemble and set up the operating conditions.

4.11.5.9.1 One "g" Design

A weight estimate for a rigid system may be realistically approached by starting with values derived from the OAO Goddard Experiment Package modified to achieve diffraction limited performance. Table 4.11-5 shows the resulting weights for a 38-inch diameter telescope and values corresponding to 50- and 120-inch optics having the same general configuration.

TABLE 4.11-4

ΔS AS A FUNCTION OF Δa

a_1	ΔS for $a_1 - a_o$ when $a_o = 125.000$ & $H = 5$	# fringes (light $\lambda = 5000$ Å)
124.80	.000150	15
124.85	.000120	12
124.90	.000080	8
124.95	.000040	4
125.00	-	-
125.05	.000040	4
125.10	.000080	8
125.15	.000120	12
125.20	.000160	16

The estimates shown in Table 4.11-5 assume the following conditions:

a. The imaging system incorporating such optics must survive the stresses of launch without losing its surface figure or coarse alignment.

b. Camera weight is excluded.

c. Extrapolation to the larger (50 and 120-inch) telescopes is made in accordance with specific rules for weight growth, designated at the bottom of Table 4.11-5 and discussed at the end of this section.

4.11.5.9.2 Zero "G" Design

Deferring final erection and alignment of an imaging system until orbit is reached permits new major considerations with respect to optics fabrication, structural design, in-orbit alignment techniques, and human factors; the latter being accentuated by the increase of total duties and the introduction of new skills to the astronaut. Further study of these skills as a bi-product of this experiment will be facilitated by the initial tests on a

TABLE 4.11-5
WEIGHT SUMMARY OF RIGID (PRE-ASSEMBLED) SPACEBORNE IMAGING SYSTEMS

TELESCOPE WEIGHTS FOR GROUND ASSEMBLY AND ALIGNMENT MINIMAL ADJUSTMENT IN ORBIT					
Primary Dia (Inches)	Primary Weight (Pounds)	Secondary Weight Beryllium (Pounds)	Secondary Weight Quartz (Pounds)	Structure and Mech. Weight (Pounds)	Total Weight (Pounds)
38 *	290		15	370	680
50 ** 50 **	850 850	- 15	50 -	800 800	1700 1665
120 ** 120 **	27000 27000	- 500	1500 -	11800 11800	40300 39300
BASIS OF SCALING	4 Dia	1/3 Quartz	4 Dia	3 Dia	
GEP (Present hardware)	130	-	15	185	330

NOTE:

* Numerical values in this row obtained by modifying present GEP (last row) to achieve Diffraction Limited performance.

** Numerical values obtained by scaling numbers in first row in accordance with BASIS OF SCALING row.

*** All telescopes F/5

"model" system. The choice of test parameters and the incorporation of simulated tasks will enhance the success of the orbital alignment of a diffraction limited telescope. The results revealed by such a "model" system will provide the information needed for later large optics systems.

An "imaging" system or telescope "kit" may be designed having the optical characteristics appropriate for high optical quality, structural integrity and economy in weight. Estimates made of the weights contributed by the optical elements, their supporting structure and the ancillary features of the system, are presented in Table 4.11-6.

As has been forecast in the prior analysis of the rigid system, the weight saving is to be expected from a redesign of the optical elements (for zero g), specifically a reduction in the mirror thickness and supporting structure.

The weight advantage gained by designing the optical system for a zero-g environment may be most directly appreciated by its comparison with a rigid, pre-assembled system designed to similar performance requirements. The last column of Table 4.11-6 shows these savings.

The governing parameter used in establishing the weight growth equations for the optical elements is the Rayleigh criterion that "the optical path length over the entire aperture of the element must not vary more than a quarter wavelength". For a specific optical surface this imposes the restriction that any deflection caused by the element's own weight and other earth environment forces should not exceed a small fraction of the wavelength. Thus, the mirror must be designed to have the same deflection regardless of diameter. Applying this constraint to the deflection equation results in a weight growth as the fourth power of the diameter.

A different criterion has been applied to the structure supporting the optical elements; namely, that the buckling stress remain constant as the size increases. Using this premise, the weight of the structure increases as the cube of the diameter.

The relation between the weight of an element and the material of which it is made was also investigated. It was found that the weight varies with the three-halves power of the density and inversely as the one-half power of the modulus of elasticity. For beryllium and quartz, the materials which are of interest in construction of secondary mirrors, it was found that a beryllium secondary would weigh approximately one-third as much as a quartz secondary of equal stiffness and size.

An examination of Table 4.11-6 highlights the large influence of the optical elements on the weight of the telescope portion of an imaging system, and upon the system itself.

TABLE 4.11.6

WEIGHT SUMMARY OF SPACE ASSEMBLED IMAGING SYSTEM

THIN PRIMARY AND LIGHTWEIGHT STRUCTURE							
Primary Dia. (Inches)	Primary Weight (Pounds)	Secondary Weight (Pounds)	Structure Weight (Pounds)	Alignment Equipment (Pounds)	Approximate Stowage Equipment (Pounds)	Total Weight (Pounds)	Savings From 1 "g" Design *
50	50	15	400	150	30	645	1020 #
120	1615	330	2200	720	180	5045	34,255 #

NOTE:

1. Telescope Assembled and Aligned in Orbit

   * Launch weight savings

4.12 FINE GUIDANCE

4.12.1 Summary

Large manned diffraction limited astronomical telescopes for application in earth's orbit, where atmospheric disturbances, are absent, are in the planning stage. In order to fully utilize the freedom from atmospheric disturbances the orbiting telescope will require a high degree of pointing accuracy and, even more so, pointing stability.

The Fine Guidance experiment will serve the purpose of space development and testing of a highly stable star pointing system, applicable to large telescopes (at least 100 inches). For this experiment (24 inch primary) the comparable performance is a pointing system stable to one one-hundredth of one second of arc when guiding on dim stars (+10 mag A0 star) against different background brightnesses.

Although earthbound testing must be performed on space equipment, the sought after stability performance in the proposed experiment will be lacking or at least masked by such testing. Transmission of microseisms (0.1 to 10 Hz) through the mount of an optical bench and flexing of the mount itself under 1 g earth conditions can each be comparable to or larger than the desired pointing accuracy and stability. Image dancing due to atmospheric turbulence might be eliminated by testing in a vacuum chamber; however, the distortion of a 100 foot long seismic block supporting an optical bench due to the change in pressure load arising from the chamber evacuation may be of the same order as the desired performance. Air bearing table facilities for dynamic stability tests to hold .01 arc-seconds for six hours do not exist and the degrading effects of turbine torques, torques due to mass shifts, magnetic torques and other air bearing disturbances make it questionable whether the desired performance can be obtained on the ground. The desired performance will be difficult to achieve in space; in the presence of earth's degrading influences the performance may never be achieved.

The requisite testing and data gathering (of the proposed experiment) essential to the design of a large telescope fine guidance system include: evaluating the pointing stability as a function of star color temperature and magnitude; evaluating (at least) two types of fine sensors; testing reacquisition and fine guidance on consecutive half orbits (which is important in near earth orbit missions), and evaluating different fine beam deflectors.

The experiment will consist of a Fine Guidance telescope whose optical axis is initially pointed by the spacecraft towards the line of sight to a selected target star with a ±1 degree accuracy. The 2-axis star trackers are programmed to acquire and track two selected bright stars. The errors detected by the two star trackers are transformed into coarse telescope pointing errors in pitch and yaw; and the telescope attitude is controlled until the intermediate error sensor, which uses only the primary mirror,

acquires the fine pointing target star and takes over the telescope pointing correction. The pointing capability of the telescope in the intermediate mode will be 0.5 second of arc, which is within the ±1.0 second of arc field of view of the fine error sensor. Fine pointing will be obtained using a small light beam deflection element inside the telescope. Based on signal-to-noise and servo analyses, this fine pointing correction is expected to provide pointing errors in the order of 0.01 second of arc.

4.12.2 Experiment Objective

The prime objective of this space flight experiment is to gather technological data essential for 0.01 sec of arc guidance design applicable to large astronomical telescopes of which long term pointing stability is required. In particular the experiment shall measure limits of fine pointing and error sensing resolution in a test free from ground disturbing effects and in actual working ambient exposures.

The experiment has a 0.01 second of arc pointing objective for on-axis target stars down to +10 magnitude. For fainter on-axis targets the same order of pointing is achieved by use of a bright off-axis guide star (> +10 mag).

Detailed experiment objectives are:

a. Pointing stability evaluation as a function of target star type (color temperature) and magnitude.

b. Pointing stability as a function of background intensity (function of target position change from galactic plane through the galactic pole).

c. Dynamic pointing stability investigation i.e. transfer from coarse to medium and from medium to fine guidance. Two sensor types which are considered for this application have different field of view-to-linear range ratios. The one with a higher ratio and a corresponding higher error gradient is expected to offer better pointing provided that limit cycling (bang-bang condition) does not occur.

d. Target reacquisition time and fine guidance settling time measurement on consecutive half orbits, both important in a near-earth orbit whenever the target is obscured by earth.

e. Evaluation of approaches to beam deflection, applicable to large optical telescopes for fine pointing. Two methods are considered suitable at this time for the postulated experiment goal, others require technological development.

f. Evaluation of the off-axis guidance concept.

g. Evaluation of fine pointing as a function of internal and external disturbance torques for various suspension systems.

h. Evaluation of fine pointing as a function of error sensor and fine pointing actuator temperature and thermal gradients using both active and passive gradient controls and temperature sensors placed in critical points.

4.12.3 Experiment Justification

4.12.3.1 Contribution and Need

The contribution offered by the fine guidance experiment is the advancement of telescope pointing technology of at least one order of magnitude above the known existing designs. This is illustrated in Figure 4.12-1, where the present pointing capability for a +2 mag star is given as 0.1 sec of arc (Fine guidance specification for the Princeton Experiment for the Orbiting Astronomical Observatory-C, Curve A). Even this level of pointing was not tested dynamically to date (scheduled for February, 1967) and the Grumman air bearing table capability after a two year improvement period is inadequate for above requirements. On the other hand the Goddard Experiment Fine Guidance Sensor built by Kollsman for the OAO-B has met the specified pointing stability of 1.0 sec of arc for a +2 mag star in a dynamic test. An improved version with a sensor designed for 0.02 sec of arc shot noise limited error resolution has been built and is awaiting dynamic tests.

In comparison with above systems the OTAES Fine Guidance Experiment (0.61 meter collecting aperture) is expected to provide pointing of 0.002 sec of arc for +2 mag star and 0.01 sec of arc for a +10 mag star, both for on-axis guidance as shown in Figure 4.12-1, Curves B and C for two sensor types. As the interest in astronomical research shifts towards fainter celestial targets (quasars) the gathered photon flux is not high enough to maintain the experiment pointing stability through longer exposure periods (required for the fainter targets), and the application of off-axis pointing is considered. The sensitivity threshold between on- and off-axis guidance is a function of pointing error and for the 0.01 sec of arc goal indicated in Figure 4.12-1, this threshold will be approximately a +10 magnitude star. For the future three meter collecting aperture a +12th magnitude threshold will be obtained. Space evaluation will yield the selection of the most suitable fine guidance components, limits of space guidance capabilities, and the effects of measured parameters listed in subsection 4.12.1, which will permit a design of fine guidance for the future large, diffraction limited orbiting astronomical observatory.(1) The pointing accuracy goals

(1) Space Research - Directions for the Future, Part Two, Space Science Board, National Academy of Sciences, National Research Council, Washington, D.C. January, 1966.

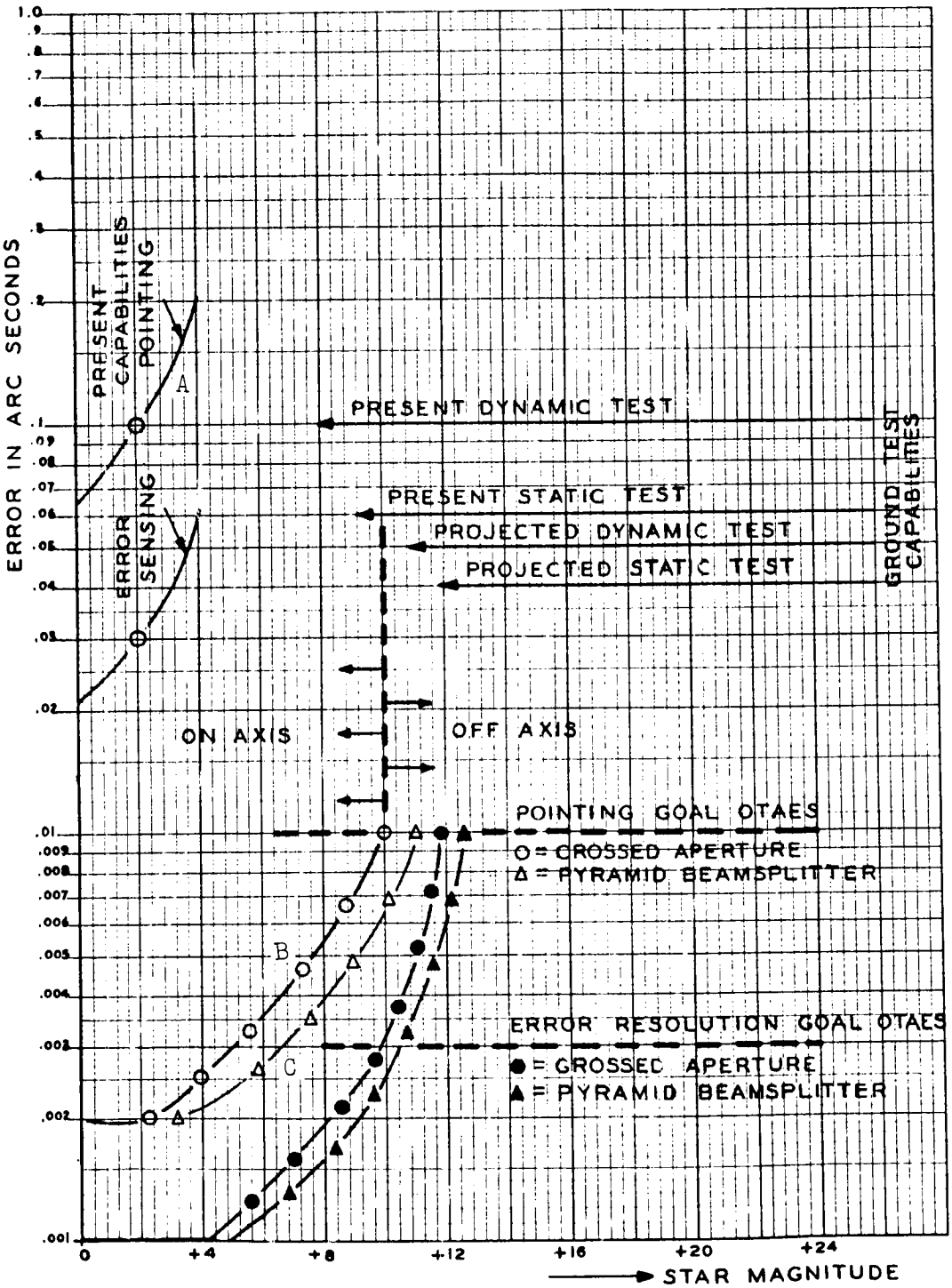


Figure 4.12-1 Fine Guidance Error vs Star Magnitude

established here are based on the ultraviolet resolution of the prospective large telescope (2) and the assessed pointing requirements for various astronomical experiments in conjunction with this telescope.(3)

4.12.3.2 Need for Space Testing

Technological data listed in subsection 4.12.2 has to be obtained under actual or simulated ambient conditions for the fine pointing error sensor and the fine pointing actuator. This need exists in order to properly design and predict the stability of a fine guidance system for future large astronomical space telescopes, assuming its requirements will be one or two orders of magnitude more severe than any system developed to date.

Two problems arise:

a. Ground test facility stabilities and error resolution are inadequate for this application.

b. Some of the ambient coefficients like magnetic coupling coefficients and man generated disturbance torques coupled through the suspension system are either not accurately known or cannot be simulated in a ground test facility.

Optimum present and projected extreme future static and dynamic test facility limits are shown in figure 4.12.1 against the projected fine guidance requirements. It is evident that only a 50% improvement over what is claimed as today's state-of-the-art in the fine guidance pointing limit will be possible in the future ground test facilities (next 10 years), if we assume that the outstanding technological data will be obtained through other space experiments. This is a factor of five short of the requirement goal of the OTAES fine guidance experiment not counting the customary requirement that test equipment stability exceed the unit under test by a factor of five to ten.

Following are the listings of dynamic test facilities, known also as air bearing tables, used in this report for generation of present and projected capabilities in Figure 4.12-1:

(2) Feasibility Study of a 120-inch Orbiting Astronomical Telescope, J.W. Fecker Division, American Optical Company, Pittsburgh, Pa. Under Contract NAS 1-1305-18, 1963 to NASA, Langley.

(3) A System Study of a Manned Orbital Telescope - The Boeing Company Seattle, Wash. Under Contract NAS 1-3968, prepared for NASA - Langley Research Center, Oct. 1965.

a. Grumman Aircraft Engineering Corporation, Bethpage, New York

b. General Electric Company, Valley Forge, Pennsylvania

c. The Boeing Company, Seattle, Washington

These air bearing tables use a sphere diameter in the 0.3 to 0.5 meter range with the table mounted on a cup which closely matches the sphere. Compressed air pumped between the sphere and the cup provides a low friction bearing. All inputs to and outputs from the air bearing table are processed through digital and analog telemetry. With the power source in the form of batteries aboard the air bearing table no lead connections are used.

Present air bearing table facilities exhibit the following problem:

a. Drag due to ambient air

b. Drag due to ball shape distortion under load

c. Turbine effect in the air bearing

d. Mass unbalance due to temperature gradients, due to battery discharge and due to variation in magnetic coupling.

Limiting or saturation can occur in the fine and intermediate pointing range, and require jet unloading approximately every 10 minutes. The jet induced disturbance causes the fine pointing sensors loss of the target star due to the limited field of view ($\pm$1 second of arc) and between two to five minutes elapsed time until target is reacquired. With additional time needed for nulling a total of 10 minutes useful data time was obtained during a six hour air bearing test.(4)

The best known present air bearing capability is in the order of 0.2 second of arc (0.1 second of arc being claimed).

Based on the past improvement rate of above test facilities the projected dynamic ground test capability will be 0.05 second of arc.

Capabilities of a 30 meter long optical bench were evaluated based on experimental data measured at Kollsman on a 15 meter optical bench and microseismic vibration of the ground base. For a 30 meter object-to-image

(4) Test Report Stabilization and Control Subsystem Orbiting Astronomical Flight B, Grumman Aircraft Engineering Corporation, No. AV252R-189.0 Vol I, May 14, 1965.

distance air turbulence caused 0.05 arc second image dancing in a 0.3 meter aperture F/15 telescope.(5) Image deterioration for the larger size optical bench will increase unless the optical bench is evacuated. However, under this condition another factor will remain; this is the microseismic vibration coupled through the ground.

The computation in subsection 4.12.5 shows that the errors induced in a telescope on a 30 meter bench due to microseismic disturbances amount to 0.05 second of arc without using the possible magnification due to the resonance condition of 8 to 50.

Based on the projected extreme static and dynamic ground test facility capabilities in the next 10 years, it clearly can be concluded that only space comparison of components, technological data gathering in space, and space testing of a complete fine guidance experiment will offer the knowledge needed for fine guidance design to the postulated performance goals.

4.12.4 Implementation

4.12.4.1 Experiment Design

The fine guidance experiment will investigate in a space test, the long term star pointing stability limits for various fine guidance error sensing and pointing correction component types. Further, pointing stability will be measured as a function of variable target and background luminance, as a function of thermal gradients, magnetic gradients, and torque disturbances. thermal gradients, magnetic gradients, and torque disturbances. Influence parameter measurements will be instrumented during these tests and the stability will be evaluated from pitch and yaw error recording for ence system. Remote visual monitoring using a microscope and a TV link will be compared against direct viewing through a microscope. For comparison the image position will automatically be photographed at fixed time intervals in respect to a fixed reference.

4.12.4.1.1 Acquisition

The fine guidance experiment will provide a pointing to null correction of the line of sight to a point-form celestial target located within the fine pointing sensor's narrow circular field of view, with a conceptual size of one second of arc half-angle. Associated with the fine pointing system are the coarse and the intermediate pointing systems, both serving the purpose of reducing the initial pointing error to enable target acquisition by the fine pointing system.

(5) Fine Pointing Sensor Evaluation - Company sponsored project, Kollsman Instrument Corporation, July, 1966.

Table 4.12-1 shows the error sensing and pointing in the individual modes of operation. The block diagram in figure 4.12-2 presents the simplified configuration. The fine guidance telescope roll pitch and yaw attitude control within a one degree half angle from the null position is provided. This accounts for initial spacecraft pointing errors from the selected target. Two (or more) coarse star trackers mounted rigidly on the fine guidance telescope provide error signals used for its pointing correction. Each star tracker has a separate telescope mounted on two gimbals each with $\pm 45^{\circ}$ freedom of travel about two orthogonal axes both normal to the tracker optical axis. The tracker provides a circular instantaneous field of view with one degree half-angle which can be pointed at any target within the articulation range of its two gimbals. An auxiliary bright star is used for coarse guidance. The tracker generates error signals denoting deviation of the actual pointing to its target from the command target coordinates. Transformation of tracker error readouts into fine guidance telescope pointing correction angles is provided.

The telescope suspension, although physically associated with the fine guidance telescope and using the fine pointing sensor as readout, is treated as a separate experiment in subsection 4.13.

The conceptual servos for the fine guidance telescope position correction in roll, pitch and yaw use six control moment gyros, two for each axis, respectively.

The signal flow in the coarse mode of operation is shown in the detailed block diagram figure 4.12-3.

Working in the +1 to +4 star magnitude range the star tracker with a four inch aperture will provide a minimum error detection capability of ±15 second of arc, and the fine guidance telescope coarse pointing accuracy will be ±30 second of arc.

With this telescope pointing correction the target star enters the field of view of the intermediate pointing error sensor. This sensor picks up 10-30% of total light energy collected by the fine guidance 0.61 meter aperture. Using only the primary mirror, the intermediate error sensor, located in its focal plane, furnishes a ±1 minute of arc active field of view in which it can acquire the target star. The star presence signal generated by the intermediate pointing error sensor provides automatic switching of the input to telescope position servos from coarse star trackers to intermediate error signals. With the conceptual intermediate error signal minimum resolution of 0.2 sec of arc for a +10 mag. target star, telescope pointing correction to 0.5 sec of arc will be obtained. This pointing assures the target star acquisition by the fine pointing sensor which has a field of view of one second of arc half-angle for the optical system described in subsection 4.12.4.1.3.1.

TABLE 4.12-1

OTAES FINE GUIDANCE EXPERIMENT: MODES OF OPERATION AND CONCEPTUAL PERFORMANCE*

	Coarse	Intermediate	Fine
	Two Star Trackers Individual Optics and Gimbals w. ±45° travel	Fine Guidance Telescope 10-30% of energy collected by the 0.61 m (using primary mirror only)	Fine Guidance Telescope 0.61m aperture 50-90% of collected energy
ERROR SENSING	Tilt and Crosstilt- with coordinate transformation into roll, pitch and yaw	Pitch and Yaw	Pitch and Yaw
	Field of View: ±1° Resolution: ±15 arc sec Star Magnitude: +1 to +4 mag	Field of View: 1 min of arc Resolution: +0.2 sec of arc Star Magnitude: +10 mag	Field of View: ±1 sec of arc Resolution: ±003 sec of arc Star Magnitude: +10 mag
POINTING	Fine Guidance Telescope in roll pitch and yaw axis Actuators 6 CMG's	Fine Guidance Telescope in pitch and yaw axis using CMG's	Pitch and Yaw Axis using Diasporameters or Cantilever on Tertiary mirror
	Error: ±30 sec of arc	Error: ±0.5 sec of arc	Error: ±0.01 sec of arc

* Spacecraft Control stable to one degree half-angle each axis, roll, pitch and yaw

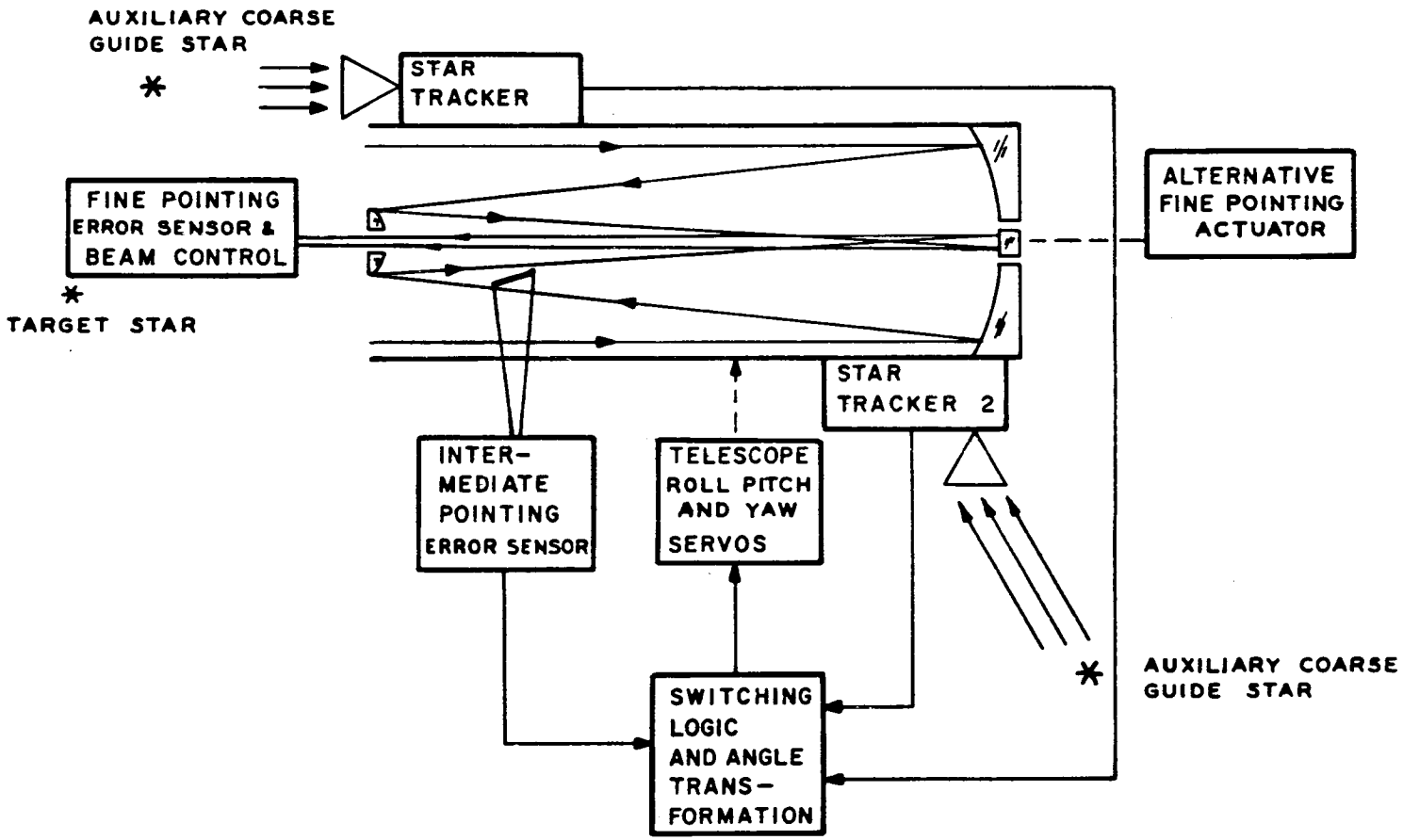


Figure 4.12-2 Fine Guidance Simplified Block Diagram

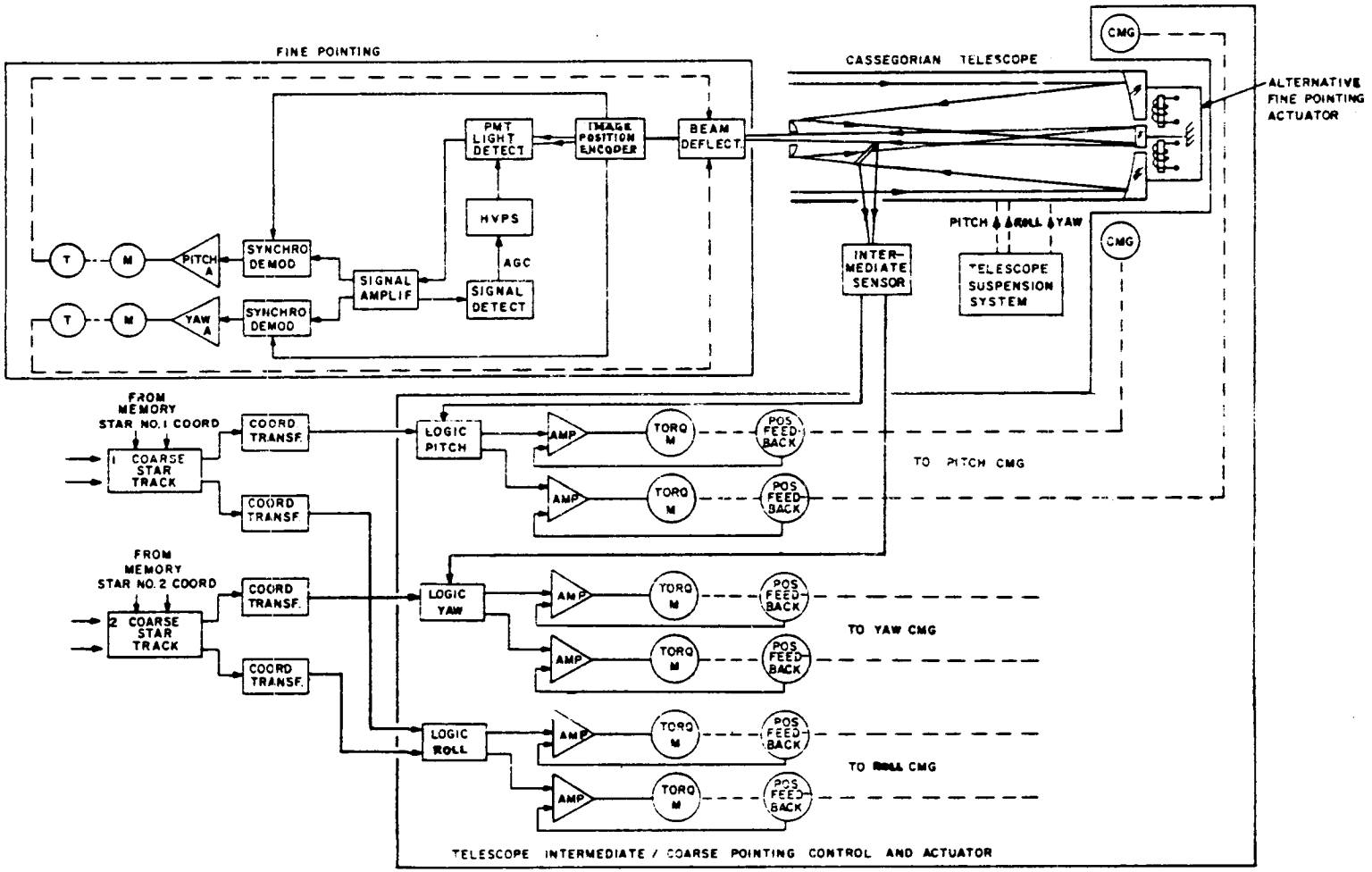


Figure 4.12-3 Fine Guidance Detailed Block Diagram

4.12.4.1.2 Telescope Coarse-Intermediate Actuators

It was assumed for this study that the spacecraft attitude control system will initially point the experiment to an accuracy of 0.5 to 1.0 degree. Therefore coarse, intermediate and fine pointing is required to achieve 0.01 second of arc experiment pointing capability. For the coarse and intermediate pointing, error signals developed by star trackers and by the intermediate error sensor will have to control auxiliary torquers to obtain telescope pointing accuracy down to 0.5 second of arc.

The spacecraft analysis will indicate the disturbance torque levels and likely vehicle rates. Although the suspension system for the telescope has not been definitely selected, the leaning is toward a soft or an active semi-soft type. Both suspension types will be evaluated in an associated experiment, described in subsection 4.13.

A number of torque producing devices can be considered for this application: reaction wheels, reaction sphere, control moment gyros, magnetic torquers.

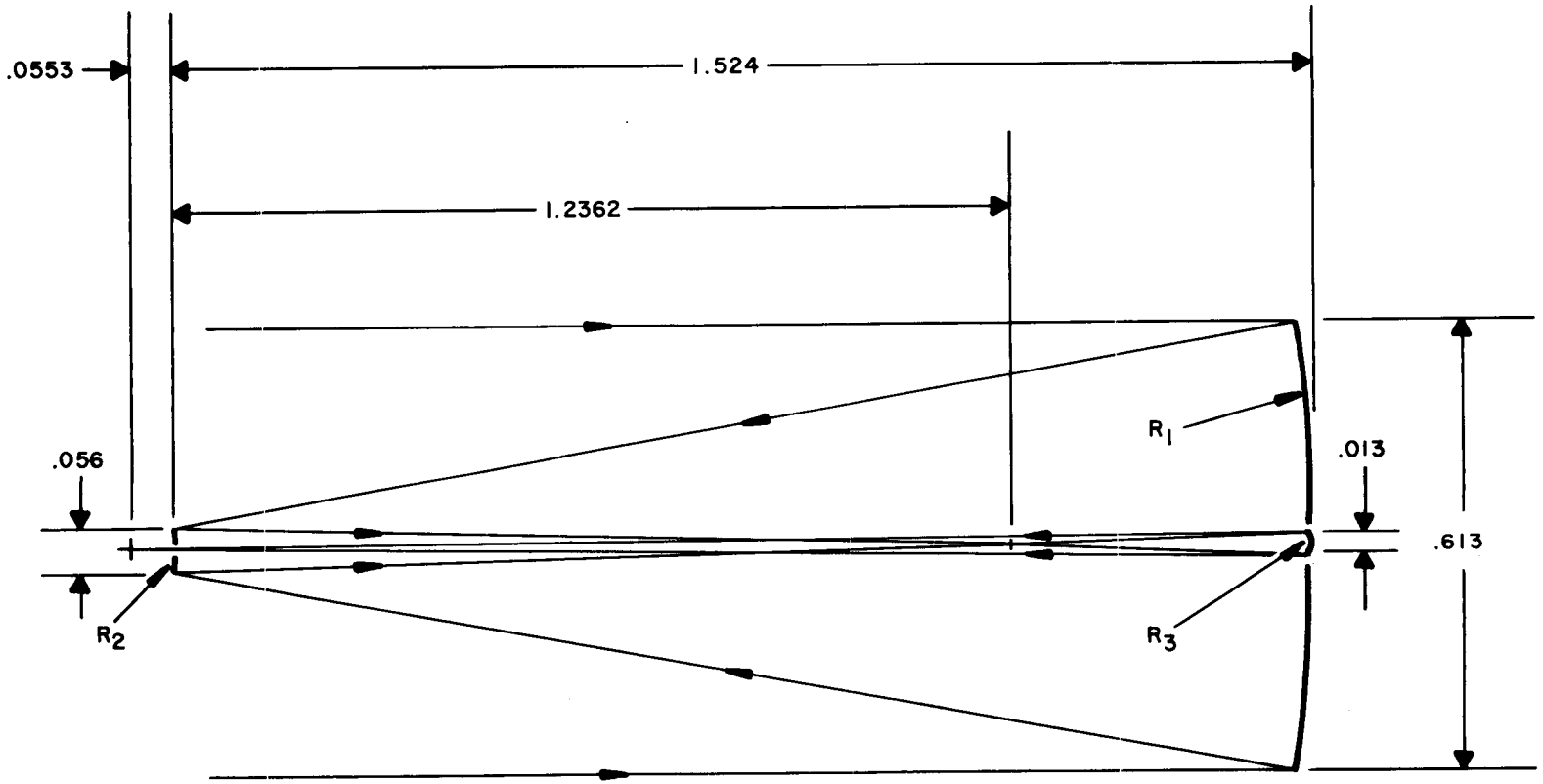
Reaction wheels (with cold gas unloading) are commonly used in satellites. Motor torque, accelerating or decelerating the wheel, is transmitted through the mounting pads of the unit to the telescope to maintain telescope attitude in the presence of disturbance torques. In effect, the reaction wheel is absorbing the angular momentum the disturbance would apply to the telescope.

The wheel motor can continue to apply torque (and absorb momentum) until a maximum (saturation) speed is reached. The wheel must then be unloaded or returned to a speed in the neighborhood of zero by the application of an opposite torque to the telescope; e.g., by cold gas reaction jets.

The advantages of the reaction wheel are its ability to provide intermediate telescope pointing control and to compensate for cyclic disturbance torques without the expenditure of (cold gas) propellant, however, gyroscopic cross coupling effects exist when three wheels are used.

Like the reaction wheel system, the reaction sphere is an inertial torquing device for controlling the attitude of a space vehicle. At the same time, the reaction sphere eliminates gyroscopic cross coupling effects which exist when three wheels are used. Three stators surround the sphere in the orthogonal axes; these may be excited singly, or in combination to induce a torque to accelerate the sphere in any desired direction. The reaction to the applied torque accelerates the vehicle. When the component of the sphere speed in the plane of a stator reaches its maximum value, the sphere is "unloaded" in that plane through the application of an opposite torque to the vehicle, e.g., by reaction jets. The unit incorporates velocity sensors in each stator plane for initiating this action.

Use of a gyro as a torquing device is another inertial control concept. Like the reaction wheel, the gyro operates on the principle of conservation of momentum and, as such, is a momentum transfer device. In the



NOTE:
DIMENSIONS IN METERS

Figure 4.12-5 Three Mirror Optical System (Cassegorian)

which scribes the total available field in a Lissajou pattern, based on the two drive frequencies. The single axis error transfer function for the crossed aperture image position encoder is shown in figure 4.12-8.

A four-alkali type photomultiplier tube with a near U-V window is considered in conjunction with this image position encoder. Change to a solid state multiplier will be considered when the quality of this device approaches the tube multiplier.

The electro-mechanical aperture motion can be replaced by an image dissector tube with a square aperture for which the derived equations will also apply. The question of null stability, however, will have to be resolved before a final decision. From available information the electromagnetic dissectors provide a stability in the order of 1% cathode size and the electrostatic dissectors 0.1%. None is adequate for this application and technological development is needed.

TABLE 4.12-3

OPTICAL SYSTEM COMPONENTS

Surface	Radius (m)	Diameter (m)	(inch)	Surface	Separation (m)	(inch)
1	R_1=3.3570164	0.613	24.0	Paraboloid $\theta^2 = 1$	1.524	60
2	R_2=0.3531565	0.056		Hyperboloid $\theta^2 = 1.653$	1.524	60
3	R_3=0.486893	0.013		Spherical		

EFFECTIVE FOCAL LENGTH EFL = 73.692 m

BACK FOCAL LENGTH BFL = 1.579 m

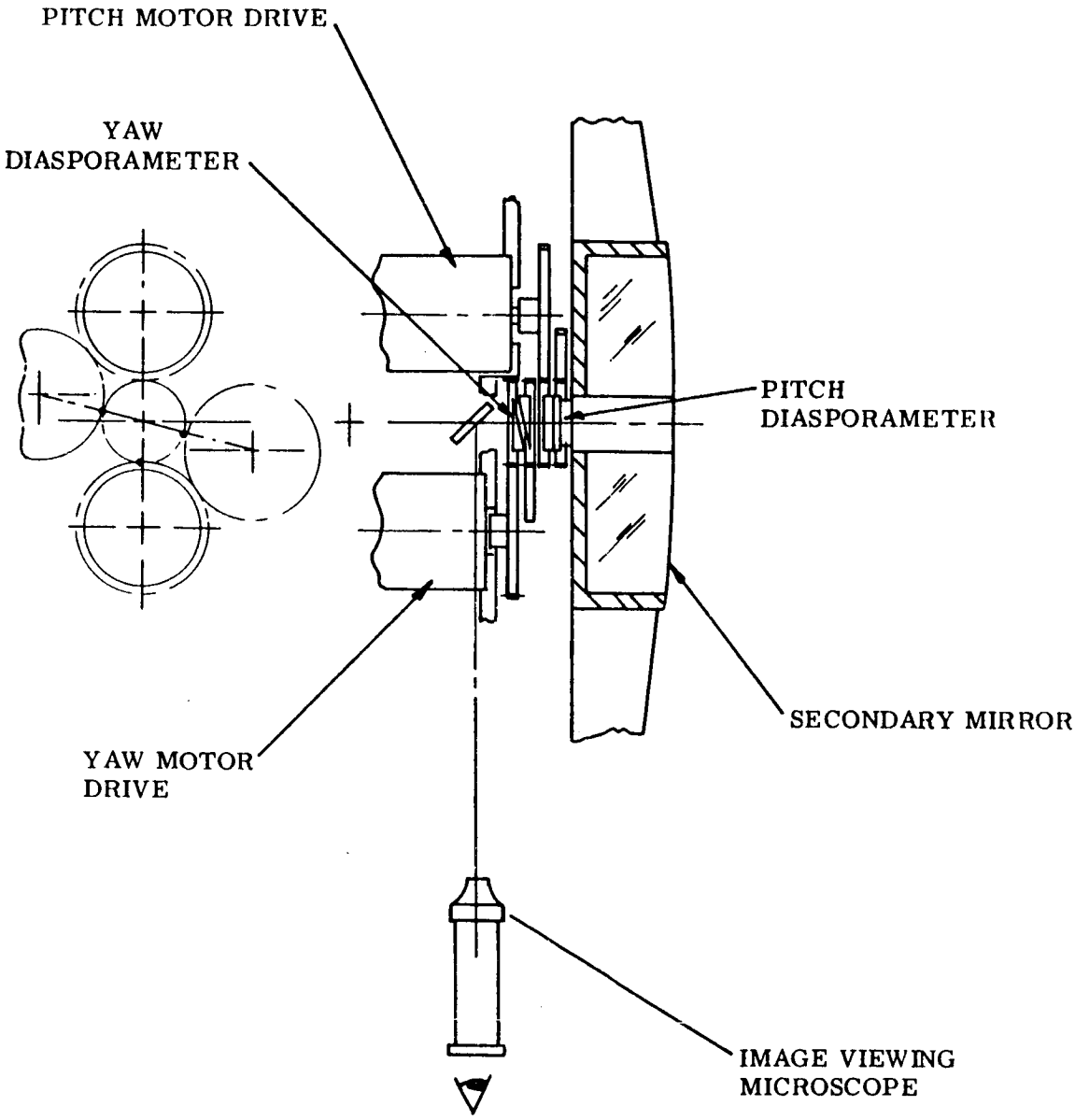


Figure 4.12-10 Fine Pointing Actuator

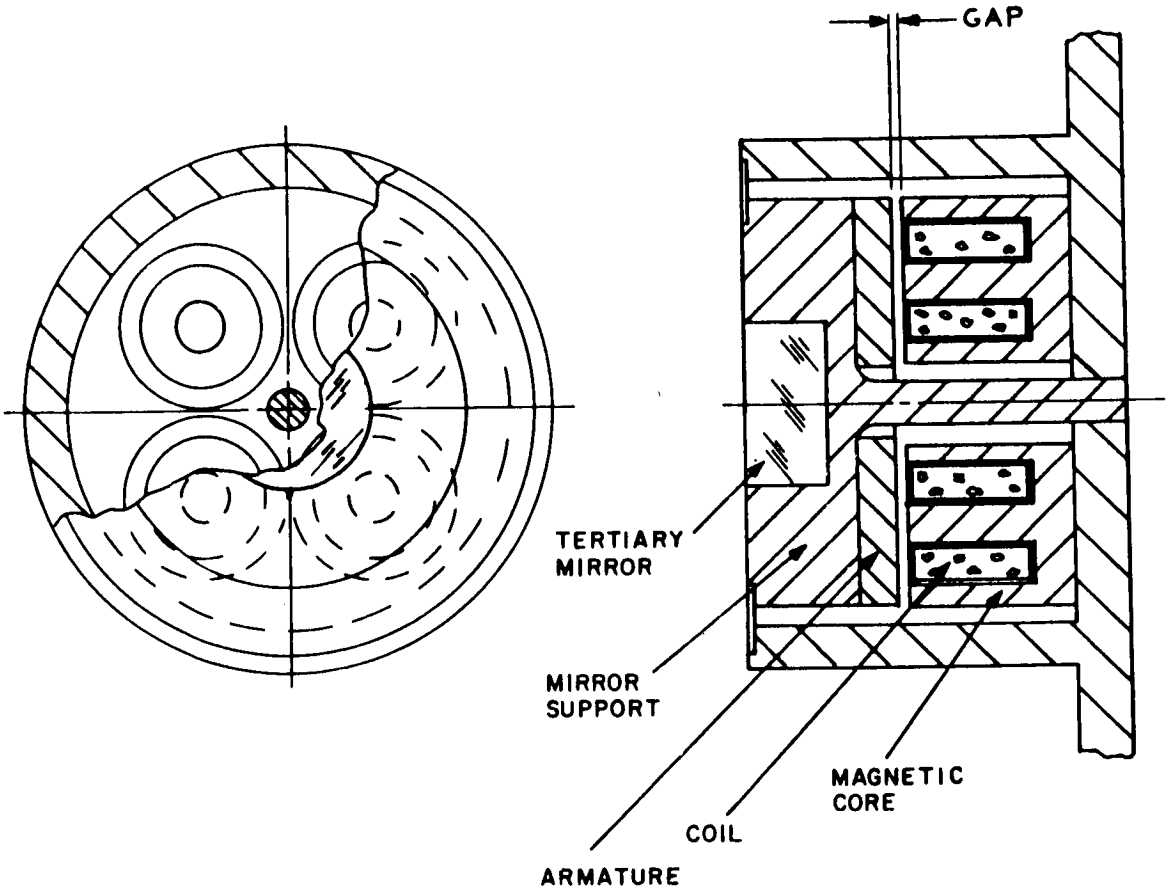


Figure 4.12-11 Fine Guidance Experiment, Tertiary Mirror Cantilever Mount

Flux density of B = 0.53 Weber/m^2 obtains for the configuration shown. For a gap of 2.5 X 10^{-4} meters the required power is P = 0.32 watt per coil. Thus a low power deflector was conceptually designed which does not use rotating components and appears very desirable for space applications.

4.12.4.2 Operational Procedures

The fine guidance experiment is divided into three phases, the first dealing with initial alignment, and the second concerned with evaluation of the two fine sensing methods, the two fine pointing methods, and the selection of the best suitable combination. These first two phases will require a manual operator for:

a. Initial optical alignment

b. Electronics and protect shutter checkout

c. Selection of the most stable fine sensor-actuator combination for image stability

The third phase will be concerned with the quantitative tracking capability evaluation as a function of:

a. Star magnitude

b. Star galactic latitude (background luminance level)

c. Star color temperature

d. Disturbance torque upon the spacecraft

e. Temperature and temperature gradients

f. Magnetic field

4.12.4.2.1 Initial optical alignment

a. Close telescope light cover

b. Apply power to star light simulator

c. Apply power to fine guidance system

d. Observe star image position with respect to reticle in viewing microscope

e. Compare intermediate error readout with fine error readout and the observed image

f. Repeat steps d and e using a remote TV link in place of direct viewing

g. Repeat steps d and e and photograph the image each time through the microscope

4.12.4.2.2 Electronics and protect shutter checkout

a. Check voltage on all electrical test points

b. Change simulator intensity to planet level

c. Observe the functioning of the protect mode

4.12.4.2.3 Selection of the most suitable combination of fine error sensor-fine pointing actuator for pointing stability.

a. Interconnect one fine error sensor type (one out of two) with one fine pointing actuator. Measure the pointing stability for a +10 magnitude star.

b. Replace the fine error sensor with the alternative type. Repeat test a.

c. Replace the fine pointing actuator with its alternative design. Repeat test a.

d. Replace the fine error sensor by the unit used in test a. Repeat test a.

e. Evaluate test results in a, b, c and d and select the most stable combination of the error sensor and pointing actuator.

4.12.4.2.4 Measure pointing stability as a function of star magnitude and star color temperature.

4.12.4.2.5 Measure pointing stability as a function of background intensity by selecting equivalent stars at various galactic latitudes.

4.12.4.2.6 Measure pointing stability as a function of disturbance torques.

a. Repeat test a using the alternative fine error sensor

b. Replace the original fine error sensor.

4.12.4.2.7 Offset tracking capability evaluation

a. Select a +10 magnitude star as a target and a second +10 magnitude star (off axis star) with an angular separation angle of 0.5 degree from the target star. Track target star to null and correct off-axis tracking mirror for a null error in the alternative fine error sensor. Monitor the error signals from:

1. the active fine pointing system

2. the alternative fine error sensor

3. monitor visually and photographically the image stability

b. Repeat test a for an offset angle of one degree between the on-axis target star and the off-axis star.

c. Repeat test a for brighter stars (magnitudes to be determined)

4.12.4.2.8 Measure pointing stability as a function of temperature of active fine guidance components (temperature measured at predetermined points).

4.12.4.2.9 Upon re-entry from the light to the dark side of the earth measure the following:

a. Elapsed time needed to acquire various star magnitudes

b. Additional elapsed time required to obtain fine pointing for these stars.

4.12.4.2.10 Repeat tests from 4.12.4.2.4 to 4.12.4.2.9 upon departure of the crew from the spacecraft using telemetered error signal readouts as a pointing stability measurement.

4.12.5 Supporting Analyses

4.12.5.1 Computation of Optical Bench Errors Due to Microseismic Activity

4.12.5.1.1 Introduction

In the following evaluation, alignment errors of a large optical bench caused by microseismic activity are computed. The telescope under test is mounted on one end of a 30 meter long seismic block and the star simulating collimating mirror on the other end, with its light source (in the mirror focal plane) located in front of the telescope. The seismic block rests on compacted sound. Both constitute a resonance system.

4.12.5.1.2 Conclusion

It can be shown that even without accounting for magnification at resonant frequency of the foundation-block combination, the desired system accuracy of .003 arc second maximum mirror rotation will not be met. Magnification between eight and fifty is possible at resonance.

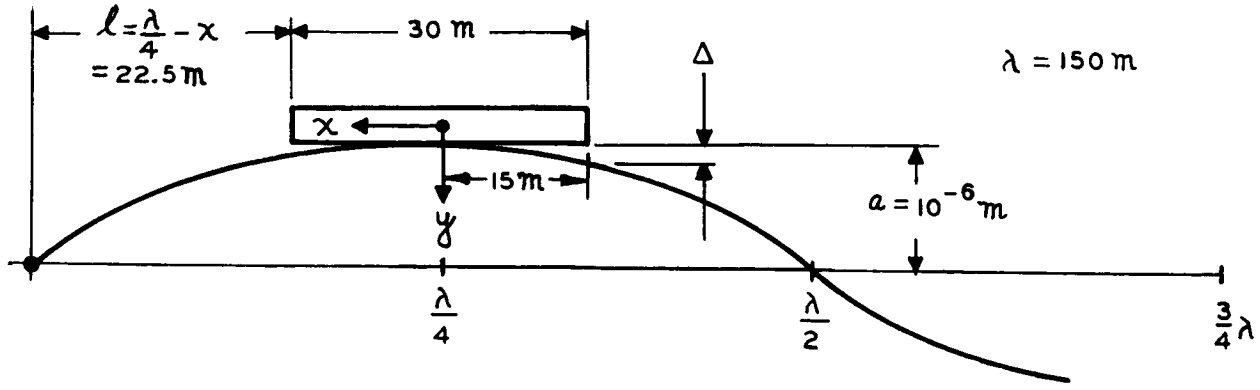
4.12.5.1.3 Discussion

To substantiate the above conclusion a numerical evaluation was performed and is presented here.

From measurements listed in the Survey of Microseismic Activity[6] it can be seen that the period of micro seismic waves varies from 0.03 - 9 seconds with amplitudes varying from 0.5 to 5.0 microns. Using representative figures of 0.05 second for the period and 1 micron (1×10^{-6} meter) for the amplitude, the input frequency $f = \frac{1}{0.05} = 20$ Hz. Since the wave velocity e given in Ref. (1) is V = 3000 meter/sec, the wavelength corresponding to 20 Hz is $= \frac{V}{f} = \frac{3000}{20} = 150$ meter.

(6) L.M. Murphy: "A Survey of Microseismic Activity", Earthquake Notes Vol. XX No. 3, 1949.

Assume that the 30 meter block rests on the crest of the halfwave:



The wave amplitude in inches

$$a = (39.37)\ (10^{-6})$$

Then

$$\frac{22.5}{37.5} = 0.6 = \frac{X^{o}}{90^{o}}$$

$$X^{o} = 54^{o}$$

$$\sin 54^{o} = 0.80902$$

and the deviation of the wave from the crest at the extremities of the block is

$$\Delta = (1 - 0.80902)\ (39.37)\ (10^{-6}) = 7.55 \times 10^{-6} \text{ inch}$$

The angular deviation from the horizontal at the same point on the wave is now obtained as follows:

With

$$\ell = \frac{\lambda}{4} = 37.5 \text{ m}$$

$$y = a \sin \frac{\pi x}{2\ell}$$

$$y' = a\left(\frac{\pi}{2\ell}\right) \cos\frac{\pi x}{2\ell}$$

With

$$\frac{\pi x}{2\ell} = 54^\circ, \quad \cos 54^\circ = 0.588$$

$$y' = \tan = \frac{(1 \times 10^{-6})\ \pi\ (0.588)}{(2)\ (37.5)} = 2.48 \times 10^{-8}$$

For small angles, the tangent is the same as the angle, therefore

$$\theta = 2.48 \times 10^{-8} \text{ radians} = 0.0051 \text{ arc second}$$

This angle θ represents the deviation of the mirror from the vertical; thus the light beam is turned through an angle 2θ by this means.

The telescope and light source at the other end of the block also turn through an angle θ, producing a rotation of the beam relative to the telescope of 2θ, if the mirror had remained stationary, and a total relative rotation of 4θ including the mirror rotation. After a half period $t = \frac{T}{2}$ the angle θ reverses and an overall relative rotation of 8θ results, excluding and magnification factor.

$$\chi = 8\theta = (8)\ (0.0051) = 0.0408 \text{ arc seconds}$$

It is obvious that χ is much larger than the desired error resolution of 0.003 arc second shown in figure 4.12-1.

It remains to be shown that the foundation-block combination follows the motion of the seismic wave. This is done by computing the resonant frequency of the foundation block combination and comparing it with the input frequency of the seismic wave.

According to DEGEBO studies[7] using 6000 lb (3T) with a contact area of 10.7 ft^2, the measured and computed resonant frequency of non uniform compacted sand

$$f_n = 26.7 \text{ Hz}$$

The foregoing test was based on a bearing pressure

$$P = \frac{6000 \text{ lb}}{10.7 \text{ ft}^2} = \frac{3 \text{ T}}{10.7} = \frac{0.28 \text{ T}}{\text{ft}^2}$$

(7) G.P. Tschebotarioff, Solid Mechanics Foundations & Earth Structures, McGraw Hill, N.Y. 1951.

whereas, the proposed block produces a bearing pressure

$$p = \frac{(10)(100)(10)(150)}{(10)\quad(100)} = \frac{1500\ lb}{ft.^2} = \frac{0.75\ T}{ft.^2}$$

Using the method outlined by Tschebotarioff (pp. 586-587), the equivalent resonant frequency of the foundation - block (fn) is obtained

$$fn' = \frac{fnr}{\sqrt{P}} = 26.7 = \frac{fnr}{\sqrt{0.28}} = \frac{fnr}{0.53} = 1.88\ fnr$$

$$fnr = \frac{26.7}{1.88} = 14.2$$

$$fn = \frac{fnr}{\sqrt{0.75}} = \frac{14.2}{\sqrt{0.75}} = \frac{14.2}{0.86} = 16.5\ Hz.$$

Where, fnr denotes the resonant frequency based on a unit bearing pressure $(1\frac{T}{ft^2})$

The resonant frequency of the proposed foundation-block combination is 16.5 Hz and is therefore in the same range as the seismic wave inpuy frequency of 20 Hz.

An extended examination of means to minimize disturbances caused by microseisms will be performed in phase two of the OTAES study. It will encompass two directions:

a. Determination of localities with minimum microseismic transmission (mountain areas) and optical bench stability computation for them.

b. Decoupling of the seismic block from its supporting soil element using supports which will filter out the predominant microseismic frequency. For this configuration the optical bench stability will also be computed, taking into consideration magnification due to resonance.

4.12.5.2 Dual Aperture Light Modulator

4.12.5.2.1 General

The light modulator provides a means of accurate image position deviation measurement from a stable and repeatable null position. The high stability of the modulator and the AC characteristic of the generated signals which permit stable amplification and phase discrimination constitute the main advantages of this fine error sensing method.

In this system, two elongated apertures are sinusoidally oscillating at different frequencies about two orthogonal axes (pitch and yaw) as shown in figure 4.12.5.2-1. The dual aperture light modulator was derived from a dual fork scanner assembly, each fork operating with its electronic circuitry in a self-starting oscillator configuration, compensated for

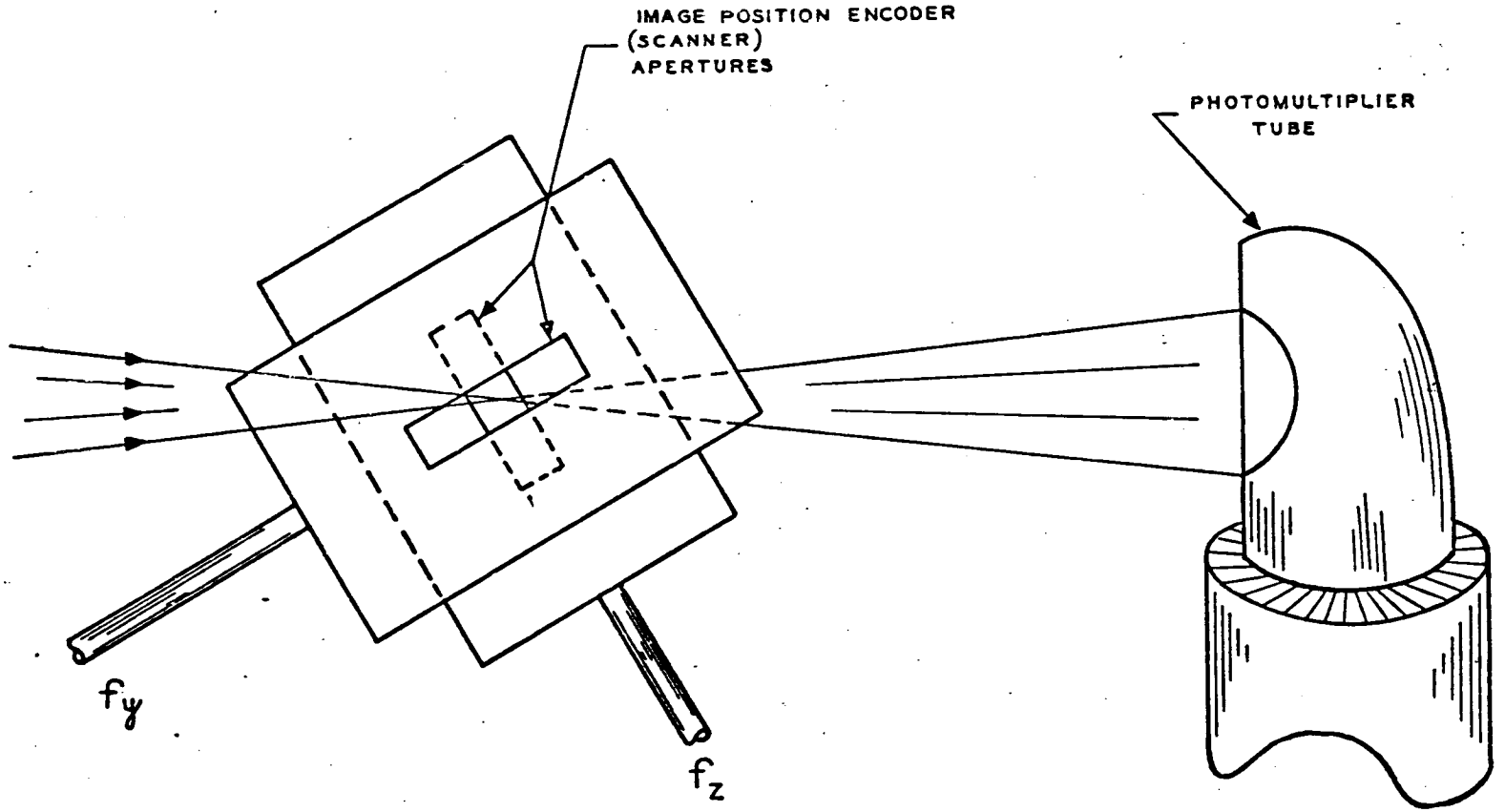


Figure 4.12.5.2-1 Dual Aperture Light Modulator and Sensor

amplitude and frequency change with temperature. The following description and analysis also applies to an image dissector tube wherein the electromagnetic or electrostatic electron beam deflection in two axes across one stationary square aperture substitutes for the two mechanical aperture motions.

When a star image appears in the field of view, the aperture encodes two-axes position information upon the emerging star light. This modulated light signal is then converted by the photomultiplier tube (see figure 4.12.5.2-1) into electrical signals for use in the error detection circuit. The light modulator also generates electrical reference signals, f_y and f_z, for use in the synchronous demodulation of the corresponding errors, pitch (y) and yaw (z), respectively.

The required 1.0 X 1.0 second-of-arc field of view for the fine pointing system will be derived from the following parameters:

- Optics, EFL $\cong$ 2900 inch, (discussed in Section 3.1).
- Light modulator aperture width, W = 0.014 inch.
- Scanner double amplitude deflection, 2 A = 0.020 inch.
- Scanner frequencies, f_y = 350 Hz and f_z = 450 Hz.

4.12.5.2.2 Analysis

Useful tracking and recognition signals can be derived from the dual scanning technique. This technique uses two superimposed, elongated slits, oscillating about two axes at 90 degrees to each other in the focal plane of the tracker telescope. The two frequencies f(y) and f(z) are chosen to be non-integral multiples of each other so that the sum and difference terms of the signal generated, as shown in the following Fourier analysis (figure 4.12.5.2-2), can be kept outside the pass bands of the tracker narrow band amplifiers. The light flux that passes through one aperture is a function of the time frequency and the image position with respect to the center of oscillation.

The developed waveforms for one axis are shown in figure 4.12.5.2-2 for the star position in three discrete regions.

The displacement of the slot, measured from the center of oscillation, is given by:

$$d = A \sin \omega_y t$$

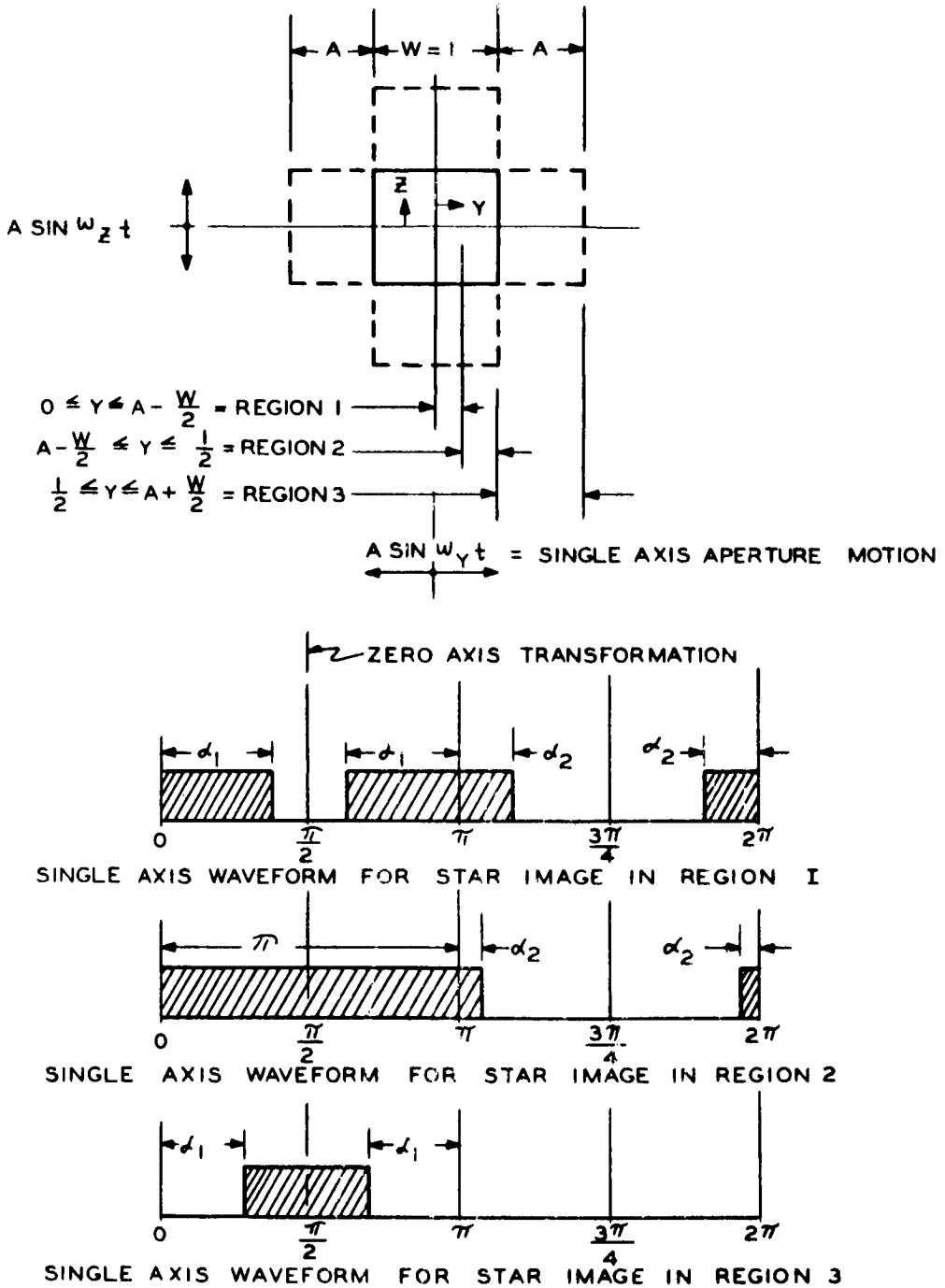


Figure 4.12.5.2-2 Single Axis Waveforms

In region 1:

$$\alpha_1 = \sin^{-1} \frac{(y + 1/2)}{A}$$

$$\alpha_2 = \sin^{-1} \frac{(1/2 - y)}{A}$$

In region 2:

$$\alpha_2 = \sin^{-1} \frac{(1/2 - y)}{A}$$

In region 3:

$$\alpha_1 = \sin^{-1} \frac{(y - 1/2)}{A}$$

By axis transformation the developed signal waveforms, shown in Figure 4.12.5.2-2, represent an even function having the Fourier series:

$$\tau_y(t) = f_o(y) + f_1(y) \cos \omega_y t + f_2(y) \cos 2\omega_y t + \ldots$$

where:

$f_o(y)$ = dc component of transmitted energy

$f_1(y)$ = fundamental coefficient

$f_2(y)$ = second harmonic coefficient

$\tau_y(t)$ = displacement of the star image from null measured along the y axis, with respect to time

The motion of the z axis is superimposed upon the light flux energy ϕ in the same fashion as described for the y axis. Proper selection of ω_y and ω_z enables coordinate transformation of the z axis to coincide with the y axis such that both the y and z functions become even.

Therefore:

$$\tau_{yz}(t) = \tau_y(t) \cdot \tau_z(t)$$

$$\tau_{yz}(t) \quad f_o(y) f_o(z) + f_o(z) f_1(y) \cos \omega_y t$$

$$+ f_o(z) f_2(y) \cos 2\omega_y t + f_o(y) f_1(z) \cos \omega_z t$$

$$+ f_o(y) f_2(z) \cos 2\omega_z t$$

$$+ \text{sum and difference terms}$$

The significant flux components that pass the narrow band limitation in y and z are:

		Signals used for
$f_o(y)\ f_o(z)$	average flux	
$f_o(y)\ f_1(z) \cos \omega_z t$	= z axis	position and recognition
$f_o(y)\ f_2(z) \cos 2\omega_z t$	= z axis	recognition
$f_o(z)\ f_1(y) \cos \omega_y t$	= y axis	position and recognition
$f_o(z)\ f_2(y) \cos 2\omega_y t$	= y axis	recognition

The results of this Fourier analysis for the signal components are given in Table 4.12.5.2-1. Figure 4.12.5.2-3 indicates the plot of the d-c fundamental and second harmonic components as a function of star displacement (y) using a single aperture.

Superposition of the two apertures, one for each axis, modifies this response as shown in Figure 4.12.5.2-4.

A study of the second harmonic component in region 1, reveals that its maximum occurs at a reed amplitude: $A = \frac{1}{\sqrt{2}}$.

For identical apertures of a width w oscillating in a plane of two orthogonal axes with an amplitude A, the coverage in each axis is 2A + W; this is also the length of the complementary aperture. A total field of (2A + w) x (2A + w) is successively scanned by an instantaneous field opening w x w.

4.12.5.3 Signal To Noise Analysis

The object of the Fine Guidance Experiment is to test telescope pointing capabilities of 0.01 arc second using target stars of +10 magnitude or brighter. This technology will be required for the 3 meter diameter (or larger) future space telescope. The following analysis will establish the collecting aperture needed for noise limited resolution of 0.003 sec of arc using the scanning and detection method previously described. This analysis, when applied to the 3 meter telescope will provide a higher sensitivity with resolution capability comparable to the Fine Guidance experiment.

The experiment telescope described in Subsection 4.12.3.2.1 will provide a $\pm$ 1 arc sec. field of view using the scan method analyzed in Subsection 4.12.5.2 with aperture dimensions W = 0.32 x 10^{-3}m and scan double-amplitude 2A = 0.46 x 10-3m.

TABLE 4.12.5.2-1

FOURIER ANALYSIS RESULTS OF SINGLE AXIS MODULATION

	Region 1	Region 2	Region 3
Limits	$C \leq y \leq A - \frac{W}{2}$	$A - \frac{W}{2} \leq y \leq 1/2$	$1/2 \leq y \leq A + \frac{W}{2}$
DC Signal	$\text{SIN}^{-1} \frac{1/2 - y}{A\pi} + \text{SIN}^{-1} \frac{y + 1/2}{A\pi}$	$1/2 + \text{SIN}^{-1} \frac{1/2 - y}{A\pi}$	$1/2 - \text{SIN}^{-1} \frac{y - 1/2}{A\pi}$
Fundamental Component	$\frac{2}{\pi}\left[\sqrt{1 - \frac{(1/2 - y)}{A^2}} - \sqrt{\frac{(1/2 + y)^2}{A^2}}\right]$	$\frac{2}{\pi}\sqrt{1 - \frac{(1/2 - y)^2}{A^2}}$	$\frac{2}{\pi}\sqrt{1 - \frac{(y - 1/2)^2}{A^2}}$
Second Harmonic Component	$\frac{2}{\pi}\left[\frac{y + 1/2}{A^2}\sqrt{1 - \frac{(y + 1/2)^2}{A^2}} + \frac{1/2 - y}{A}\sqrt{1 - \frac{(y - 1/2)^2}{A^2}}\right]$	$\frac{2}{\pi}\left[\frac{1/2 - y}{A}\sqrt{1 - \frac{(1/2 - y)^2}{A^2}}\right]$	$\frac{2}{\pi}\left[\frac{1/2 - y}{A}\sqrt{1 - \frac{(1/2 - y)^2}{A^2}}\right]$

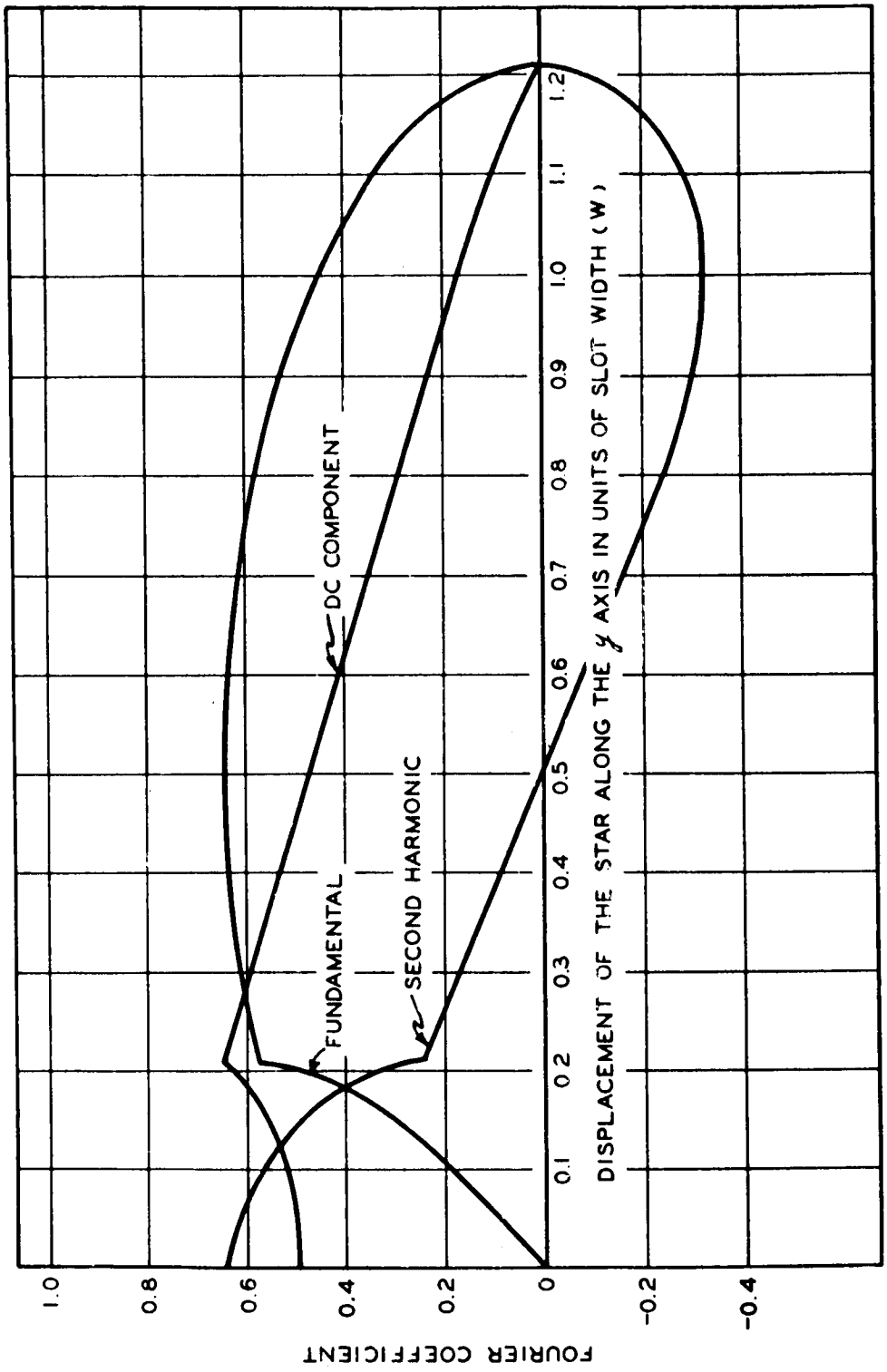


Figure 4.12.5.2-3 DC, Fundamental and Second Harmonic Amplitudes, Single Axis

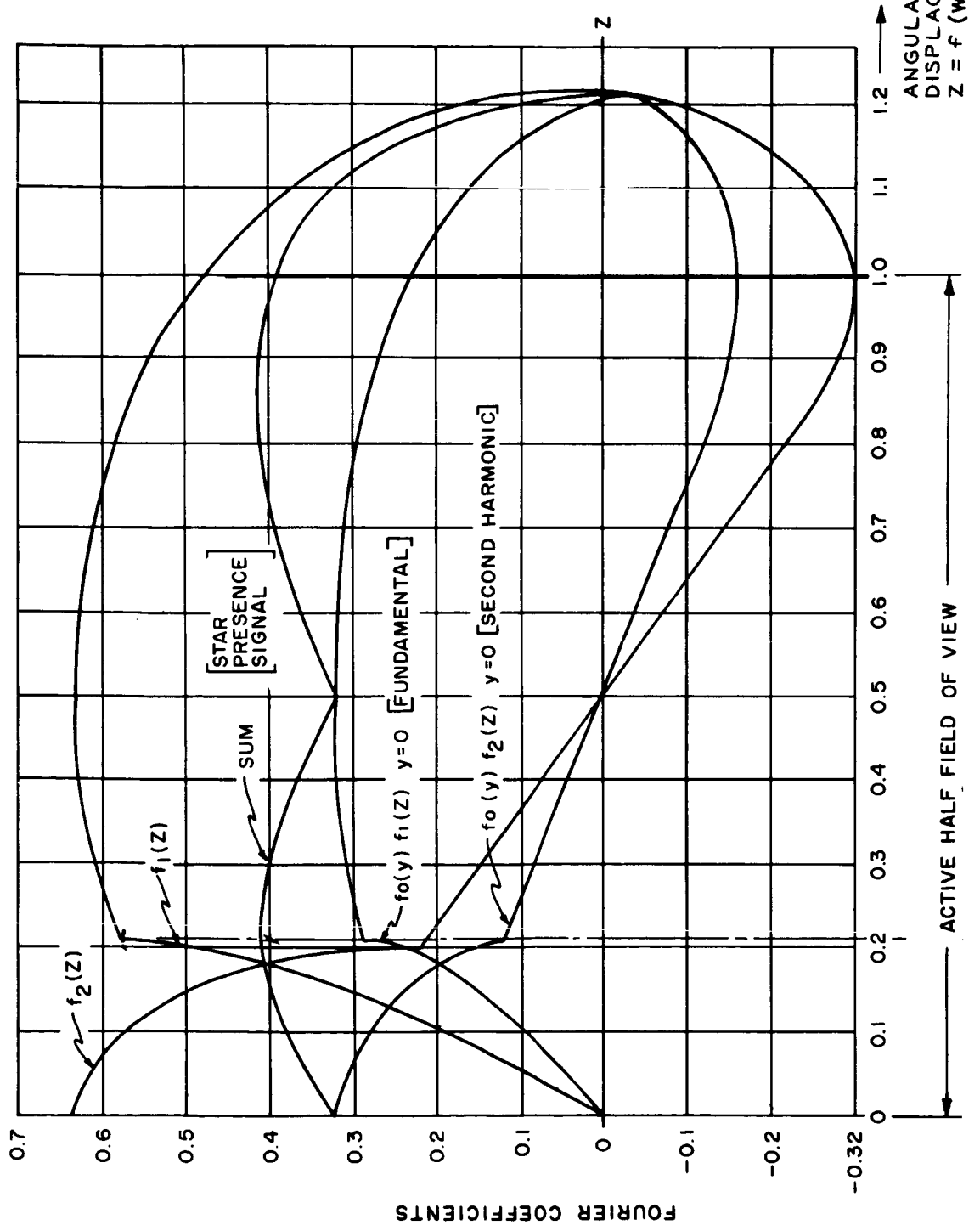


Figure 4.12.5.2-4 Two Axis Scanner, Waveform Amplitudes

Actual transfer functions for the +1 and +10 mag stars as shown in Figure 4.12-8 were obtained by scaling down the field size in the Kollsman built Fine Guidance for the Goddard Experiment Package which was designed for the Orbiting Astronomical Observatory B.

For our computation the linear approximation of the transfer function as shown in Figure 4.12.5.3-1, will be used. It shows a linear error range from -0.2 arc sec. to +0.2 arc sec. and is comparable to the theoretical transfer characteristic shown in Figures 4.12.5.2-3 and 4.12.5.2-4 in subsection 4.12.5.2. At an error E = 0.2 arc sec the signal current I_s is maximum and the signal to noise ratio S/N is also maximum. It is desirable to have a one sigma resolution limit of ϵ resol = 0.003 arc sec., for which the signal to noise ratio S/N = 1. This requires a maximum signal to noise S/N max = 67.

The S/N max. will be computed for an A0 spectral class star ($T \cong 11{,}000$ K), and a four-alkali (extended S-20) photomultiplier tube with a UV transmitting window Photocathode spectral response $\sigma_K(\lambda)$ is shown in Figure 4.12.5.3-2.

$$S/N \text{ max} = \frac{I_{s \text{ max rms}}}{\sqrt{2\, e\, \Delta f \Sigma I_{dc \text{ noise}}} + I_{tn \text{ rms}} \sqrt{\Delta f}}$$

where

$I_{s \text{ max rms}}$ = maximum photocathode ac error signal output

$e = 1.6 \times 10^{-19}$ (coulombs), electron charge

Δf = 1 Hz system closed loop bandwidth

$\Sigma I_{dc \text{ noise}} = I_{dc \text{ sn}} + I_{dc \text{ bn}}$ Noise generating current due to signal and due to background

$I_{tn \text{ rms}}$ = Photomultiplier tube noise

Signal Current

Calculated for a +10 magnitude star

$$I_{s \text{ max rms}} = \frac{A_e}{\sqrt{2}} A \eta \; P_{\max} \int_0^\infty \left[P(\lambda)/R(\lambda)_{\max}\right] d\lambda \int_0^\infty \sigma_K(\lambda) d\lambda$$

where A_e = 0.29 is the modulation coefficient as described in subsection 4.12.5.2.

A = collecting area of the Fine Guidance Experiment telescope assigned to fine pointing (cm^2).

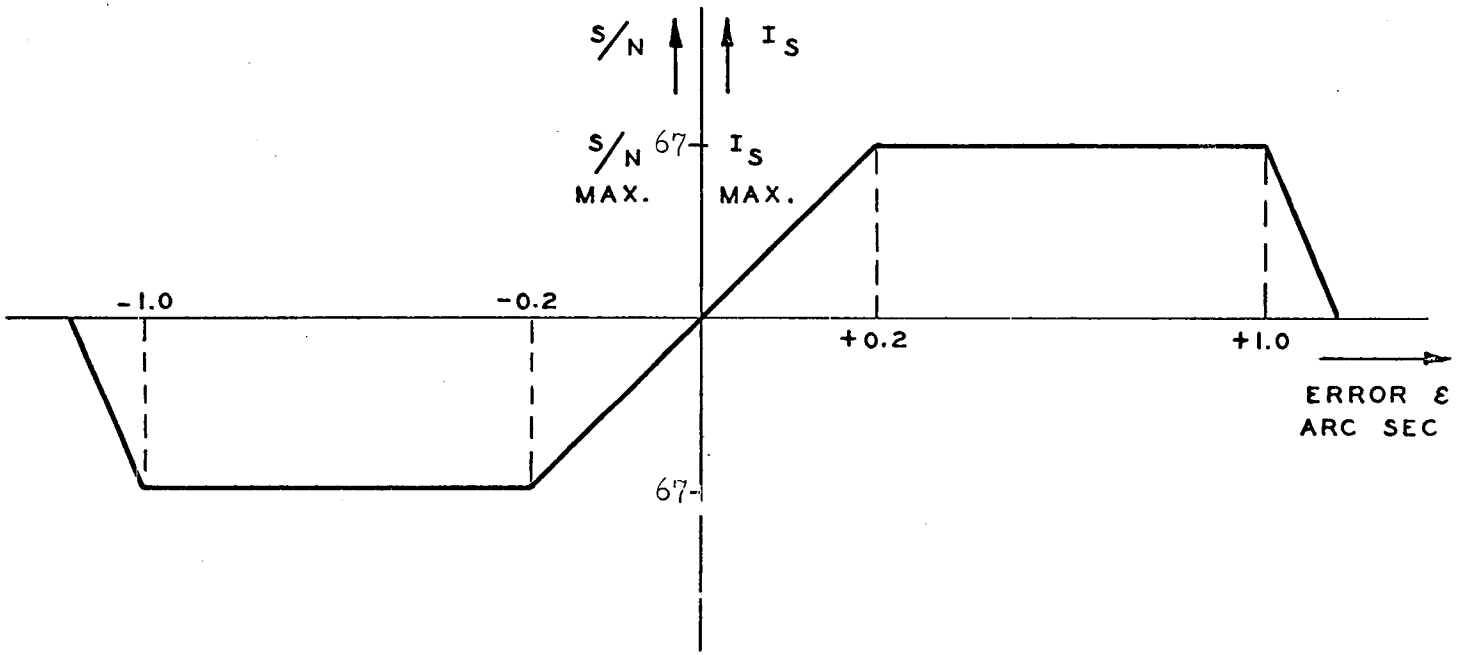
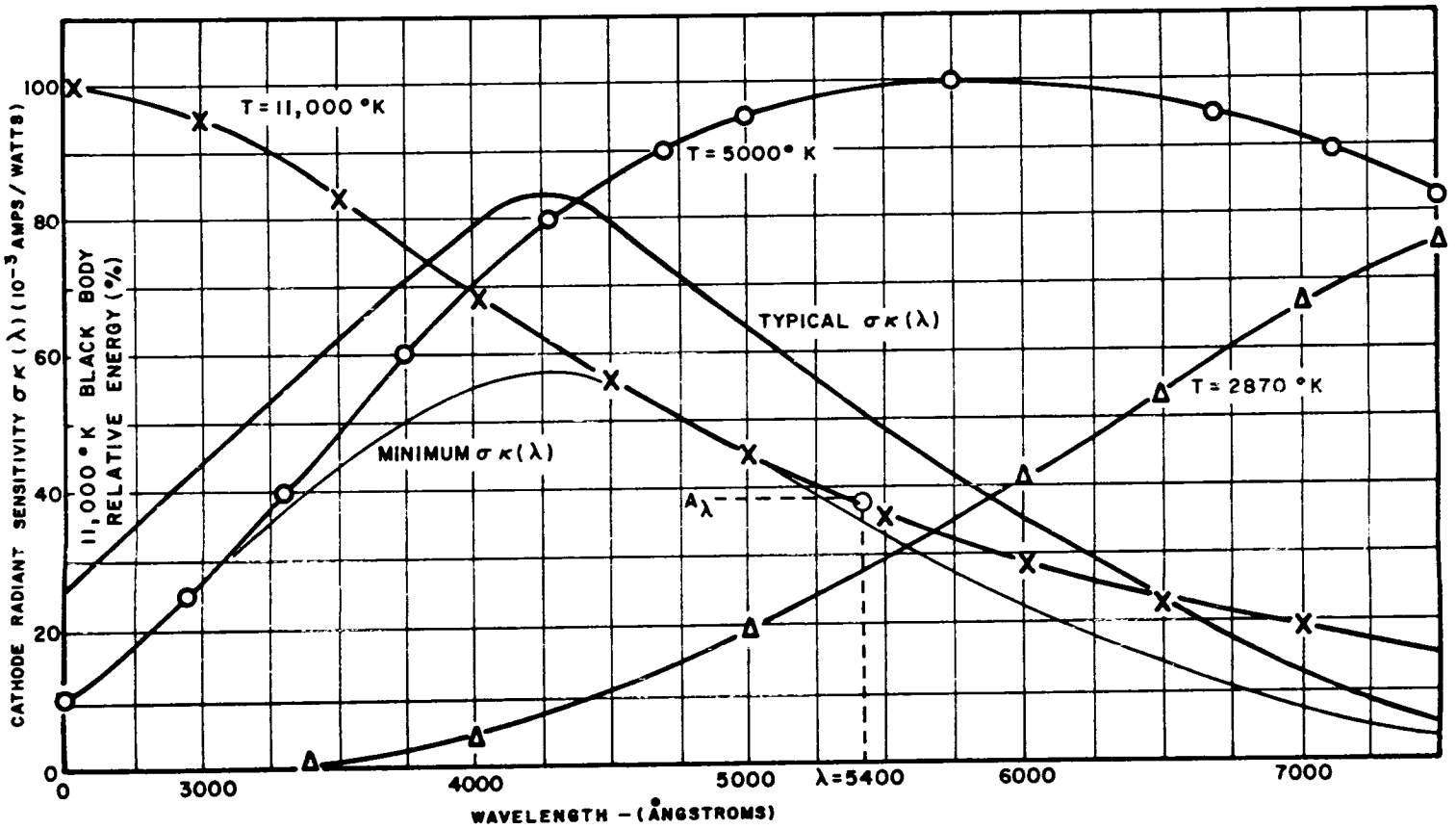


Figure 4.12.5.3-1 Linear Approximation of Error Transfer Function



P_λ/P_λ Max. Black Body Radiation vs. Wavelength

X-X T = 11,000 °K
O-O T = 5,000 °K
Δ-Δ T = 2,870 °K

Figure 4.12.5.3-2 Photomultiplier Spectral Response

$\eta = 0.8$ average efficiency of the telescope

$P_{max} = \frac{1}{A_\lambda} \times P_\lambda$ peak black-body star radiation

A_λ = 0.39 coefficient for 11,000°K star (see Figure 4.12.5.3-3) at $\lambda = 5400$ Å

for $\lambda = 5400$ Å, $P = 3.8 \times 10^{-7}$ (erg/cm^2/sec/100A) for a 0 mag star outside earth atmosphere

for a + 10 mag star $P_\eta \simeq 1.9 \times 10^{-17}$ (W/cm^2/500Å)

$P_\lambda / P_{\lambda\ max}$ i.e. the A0 star black body radiation as a function of wavelength is plotted in figure 4.12.5.3-2.

$\sigma_K(\lambda)$ is the photomultiplier cathode spectral response (see Figure 4.12.5.3-2, for Type 641E EMR tube). For this calculation the typical values were used.

A graphical summation of $P_{(\lambda)} / P_{(\lambda)\ max}\ \Delta\lambda \times \sigma_K(\lambda)\Delta\lambda$ was performed in place of the integration, using a

$\Delta\lambda = 500$Å:

$$\sum_{\lambda = 2500\text{Å}}^{\lambda = 7500\text{Å}} P_\lambda / P_{\lambda\ max}\ \Delta\lambda \times \sigma_K(\lambda)\Delta\lambda = 0.116 \text{ amps} \times 500\text{Å/watt}$$

Thus,

$I_{s\ max\ rms} = 0.9A \times 10^{-18}$ (Amps)

where A is the collecting area in Cm^2

$$I_{dcs} = I_{s\ max\ rms} \sqrt{2 \times \frac{Aav}{Ae}}$$

$$I_{dcs} = 1.75\ A \times 10^{-18} \text{ (Amps)}$$

Background Illumination Noise

A background illumination impinging upon the photocathode generates a dc current:

$$I_B = B\omega A\eta\sigma k\,(5000\text{Å})$$

$$I_B = 0.2\ A \times 10^{-25} \text{ amps with A in } CM^2$$

where

ω = solid angle subtended by the Fine Pointing Sensors

$\omega = 0.8 \times 10^{-14}$ (steradian)

Using the star distribution graph in Figure 4.12.5.3-3 the mean background star class was established. Using the Herzsprung diagram in Figure 4.12.5.3-4 this mean spectral class indicated an equivalent black body radiation at T - 5000°K. For which σ_K - 35 x 10^{-3} A/W.

Star Noise

Noise contribution of star current is a function of the dc value of the star signal. This dc signal is computed in the Fourier analysis of the light modulator in subsection 4.12.5.2. From the graph in Figure 4.12.5.2-4 the average star flux factor A_{av} = 0.4.

$B = 9.1 \times 10^{-12}$ (8) $\left[\text{Watt/Sterad/cm}^2\right]$ mean space background radiation

Tube Noise

The photomultiplier tube equivalent noise input (ENI) is defined as the luminous flux input at 2870 K chopped on and off (50% duty cycle) at a low audio frequency, which will produce a signal of the same rms value, in a 1 H_Z bandwidth, as does the noise. This noise is a function of PMT current amplification and ambient temperature.

$P_{\text{noise at } 4200\text{Å}} = 3.5 \times 10^{-16}$ $\left[\text{Watt}\right]$ for Δf - 1 $\left[\text{Hz}\right]$, for 10^6 current amplification at 20 $\left[^{o}\text{C}\right]$.

(8) Computed from C.W. Allen: ASTROPHYSICAL QUANTITIES, The Athlone Press, London, 1963.

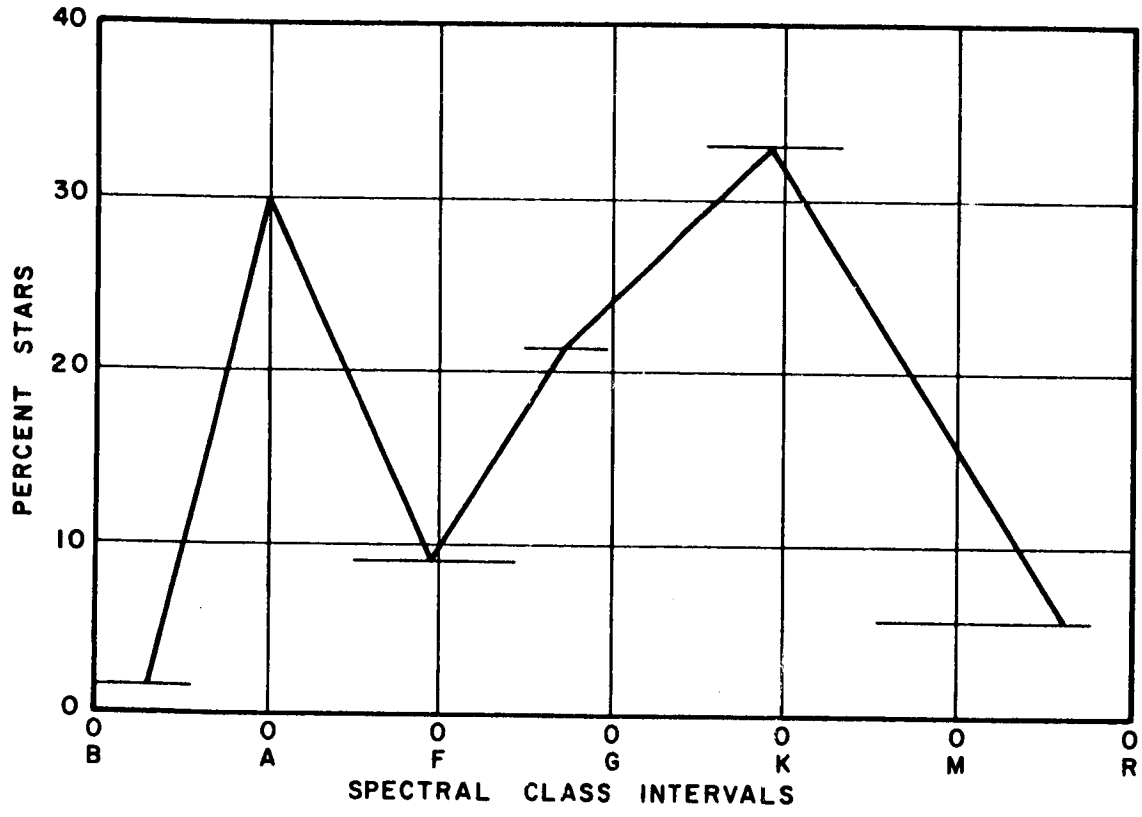


Figure 4.12.5.3-3 Star Distribution as a Function of Spectral Classes (Based on Henry Draper Catalogue - Using 222, 750 Brightest Stars)

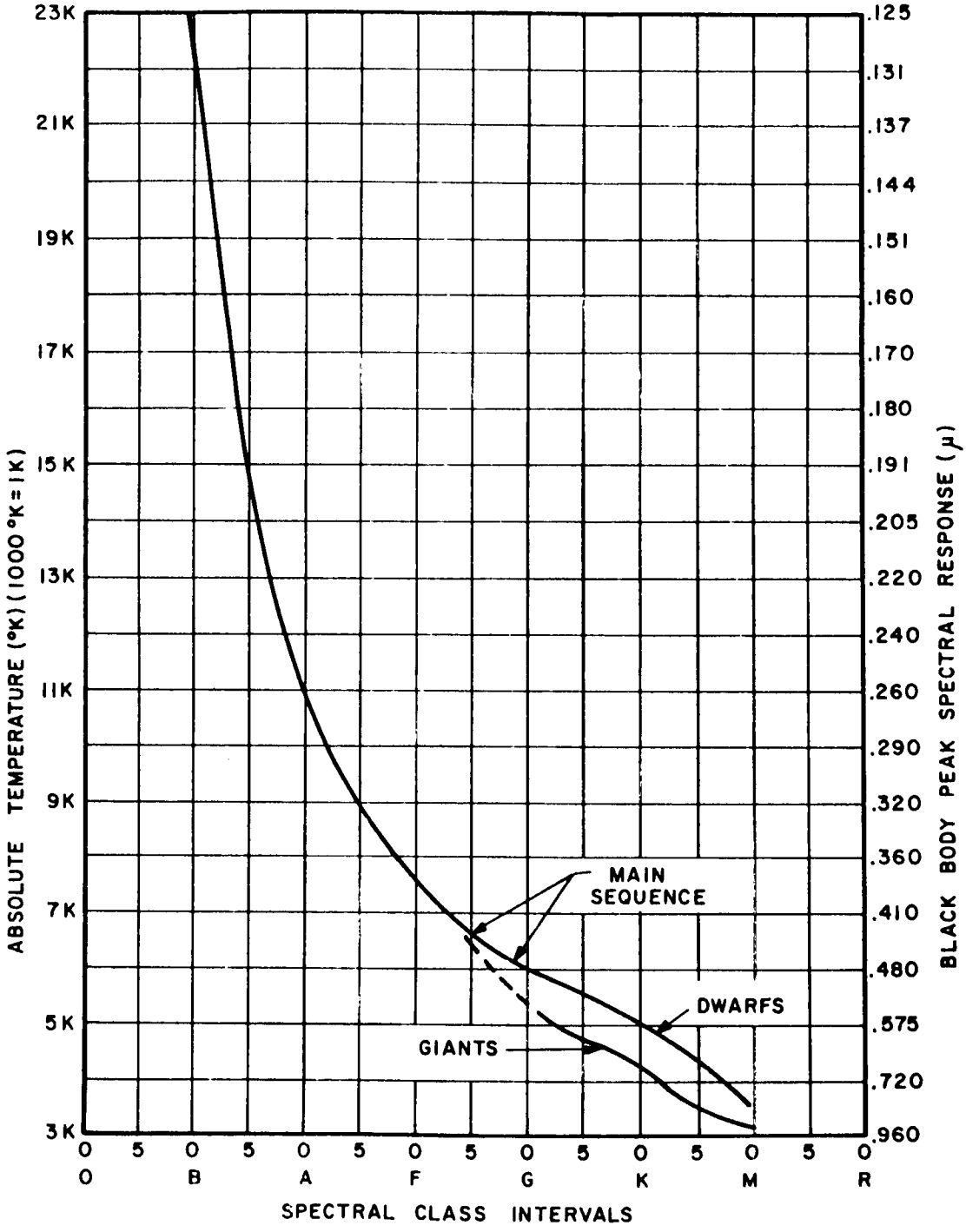


Figure 4.12.5.3-4 The Color Temperatures of the Stars

(From: Astronomy by Russel, Stewart and Dugan, Vol.II, Rev. Ed. 1955)

STEPS	HUMAN FUNCTION / BODY SEGMENT MOVEMENT	HEAD MOTION	HEAD FORCE	HEAD DURATION	RIGHT ARM MOTION	RIGHT ARM FORCE	RIGHT ARM DURATION	RIGHT FOREARM MOTION	RIGHT FOREARM FORCE	RIGHT FOREARM DURATION	RIGHT HAND MOTION	RIGHT HAND FORCE	RIGHT HAND DURATION
	ACTIVITY: PERIODIC MAIN CONTROL PANEL SYSTEMS STATUS CHECK/CREWMAN IN VENTED SPACE SUIT.												
1	REACH TOGGLE SWITCH TASK — UPPER ARM/FOREARM/HAND MOTION; FOREARM/HAND MOTION; UPPER ARM/FOREARM/HAND MOTION	SNV 20°			SEV 60°; TEV 10°		50 SEC	SEV 60°					
2	MANIPULATE TOGGLE SWITCH FROM CENTER TO UP POSITION — UPPER ARM/FOREARM/HAND MOTION				SEV 1°	40 OZ.	.75 SEC						
3	SCAN MAIN CONTROL PANEL DISPLAYS .20 SEC												
4	MANIPULATE TOGGLE SWITCH TO DOWN POSITION — UPPER ARM/FOREARM/HAND MOTION				SIV 2°	40 OZ.	.75 SEC						
5	SCAN MAIN CONTROL PANEL DISPLAYS .20 SEC												
6	MANIPULATE TOGGLE SWITCH TO CENTER POSITION — UPPER ARM/FOREARM/HAND MOTION				SEV 1°	40 OZ.	.75 SEC						
7	REACH FOR SECOND TOGGLE SWITCH ONE INCH TO RIGHT — UPPER ARM/FOREARM/HAND MOTION				TIV 2°		.50 SEC						
8 TO 12	REPEAT 2 TO 6												
13	REPEAT 7 FOR THIRD TOGGLE SWITCH ONE INCH TO RIGHT												
14 TO 18	REPEAT 2 TO 6												
19	RETURN TO STARTING POSTURE — UPPER ARM/FOREARM/HAND MOTION; FOREARM/HAND MOTION; UPPER ARM/FOREARM/HAND MOTION	SPV 20°			TIV 6°; SIV 60°		.50 SEC	S V 60°					

LEGEND:

SNV – SAG–NEG–VECTION
SEV – SAG–E–VECTION
TEV – TRANS–E–VECTION
SIV – SAG–IN–VECTION
TIV – TRANS–IN–VECTION
SPV – SAG–POS–VECTION



INDICATES MOTION OF DISTAL BODY SEGMENT BEING INCLUDED IN MOTION OF PROXIMAL BODY SEGMENT.

Figure 4.13.3.1.1-1. Typical Body Movements Matrix

TABLE 4.13.3.1.1-1

TYPICAL RANGE OF MAN-PRODUCED DISTURBANCES

Crew Motion	Movement Time-Sec	Angular Excursion-degree	Maximum Torque ft - lb	θ_m deg
Push-off	5	-	125	1°
Head, neck, and trunk (bend forward at waist)	0.4	45°	281.0	0.95 arc min
Lateral motion of full extended arm about shoulder, elbow stiff	0.2	45°	65.1	5.05 arc min
Lateral motion of forearm and hand about elbow	0.174	43.2	18.9	0.72 arc sec
Head (turn)	0.1	45	14.2	0.18 arc sec
Rotation of hand	0.1	180	1.92	0.025 arc sec

Such a disturbance function is illustrated in figure 4.13.3.1.1-2. Each pulse is caused by a different limb movement, but each movement requires the same period of time. This means that the time function jumps discontinously, as indicated in the figure. If the mean value of the disturbance momentum is H_m and the characteristic movement time is T_1, the power spectral density function as shown in section 4.13.5 is

$$\Phi_{11} = H_m \left(\frac{\sin \frac{\omega_a T_1}{2}}{\omega/2} \right)^2$$

and is sketched in figure 4.13.3.1.1-3.

4.13.3.1.2 Spacecraft Attitude Control Considerations

In deriving the spacecraft motion caused by the disturbance environment, the spacecraft was assumed uncontrolled. This section will look briefly into artificailly stabilizing the spacecraft attitude against man-produced disturbances. First it should be clear that, unless man is to put himself into a permanent spin, he will induce no net momentum into the spacecraft. Any movement on his part which puts the spacecraft into motion must be followed by a reverse movement which stops the spacecraft. The result will be a net change in the attitude of an uncontrolled spacecraft. This is illustrated in figure 4.13.3.1.2-1 where for convenience the disturbance is taken as an impulse. The area under the velocity curve is the angular excursion of the spacecraft. That is, without control, no net momentum is induced into the spacecraft. With control the momentum must be handled twice-at the initiation of the disturbance and at its termination.

This might appear to be an obvious point, but is one worth emphasizing. At the initiation of this study, the control philosophy was to make no attempt to stabilize the spacecraft against man-produced disturbances, in which case the momentum storage capabilities required would be only that caused by external torques and slewing requirements. Subsequently, to simplify the design of the suspension systems considered in this experiment, it has been decided to partially stabilize the spacecraft to ± 6 arc minutes.

Figure 4.13.3.1.2-2 shows the weight penalty for limiting the excursion shown in figure 4.13.3.1.2-1. The derivation of this curve, which is discussed in section 11.4, is based on the maximum control torque required to limit the maximum angular excursion θ_m and on the weight of the control system (actuators only) to produce this torque. Also shown is the required bandwidth of the control system. The curves in figure 4.13.3.1.2-2 are derived for an impulse of 7.05 Kg-M-sec. As discussed previously there is a trade-off between the constraints placed on man, the maximum altitude excursion, and the control system weight.

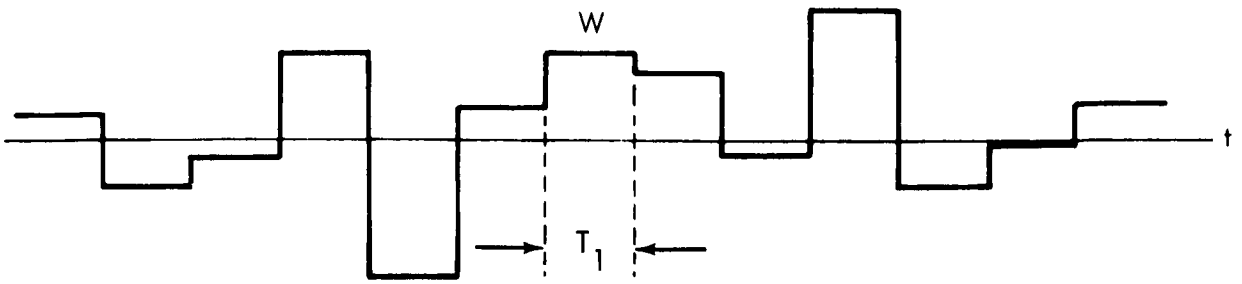


Figure 4.13.3.1.1-2. Disturbance Model

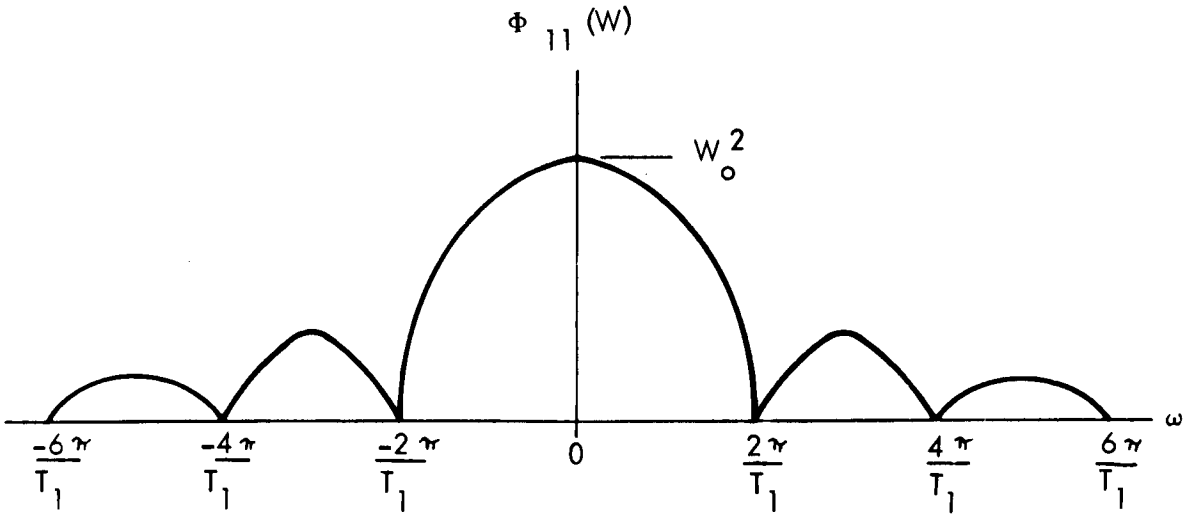


Figure 4.13.3.1.1-3. Disturbance Spectrum

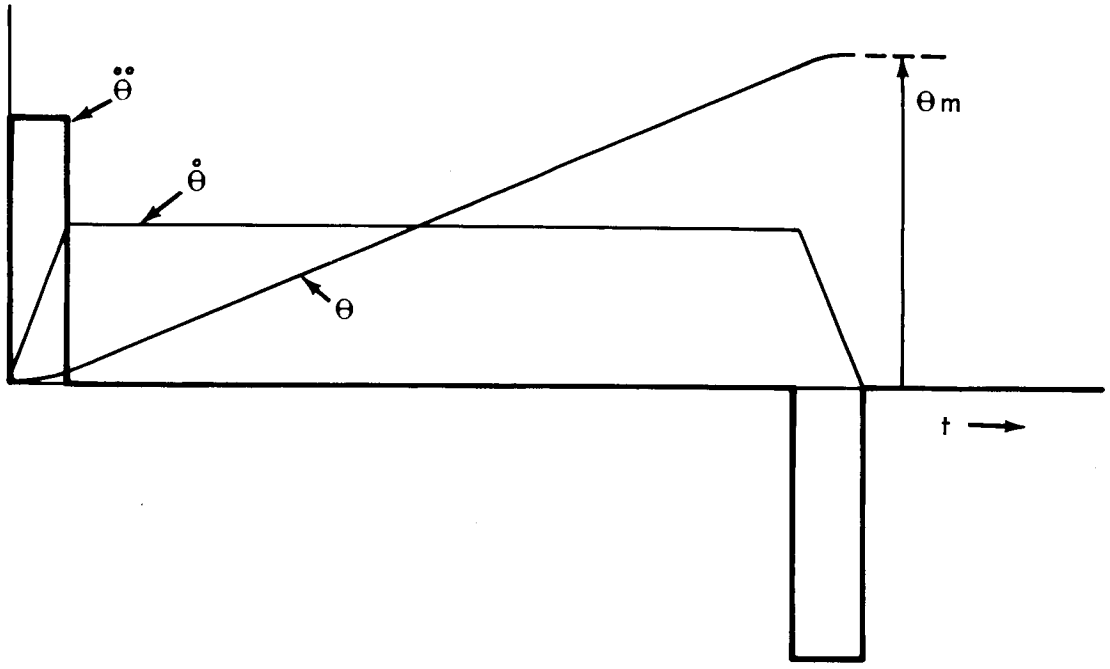


Figure 4.13.3.1.2-1. Uncontrolled S/C Response to An Impulsive Disturbance

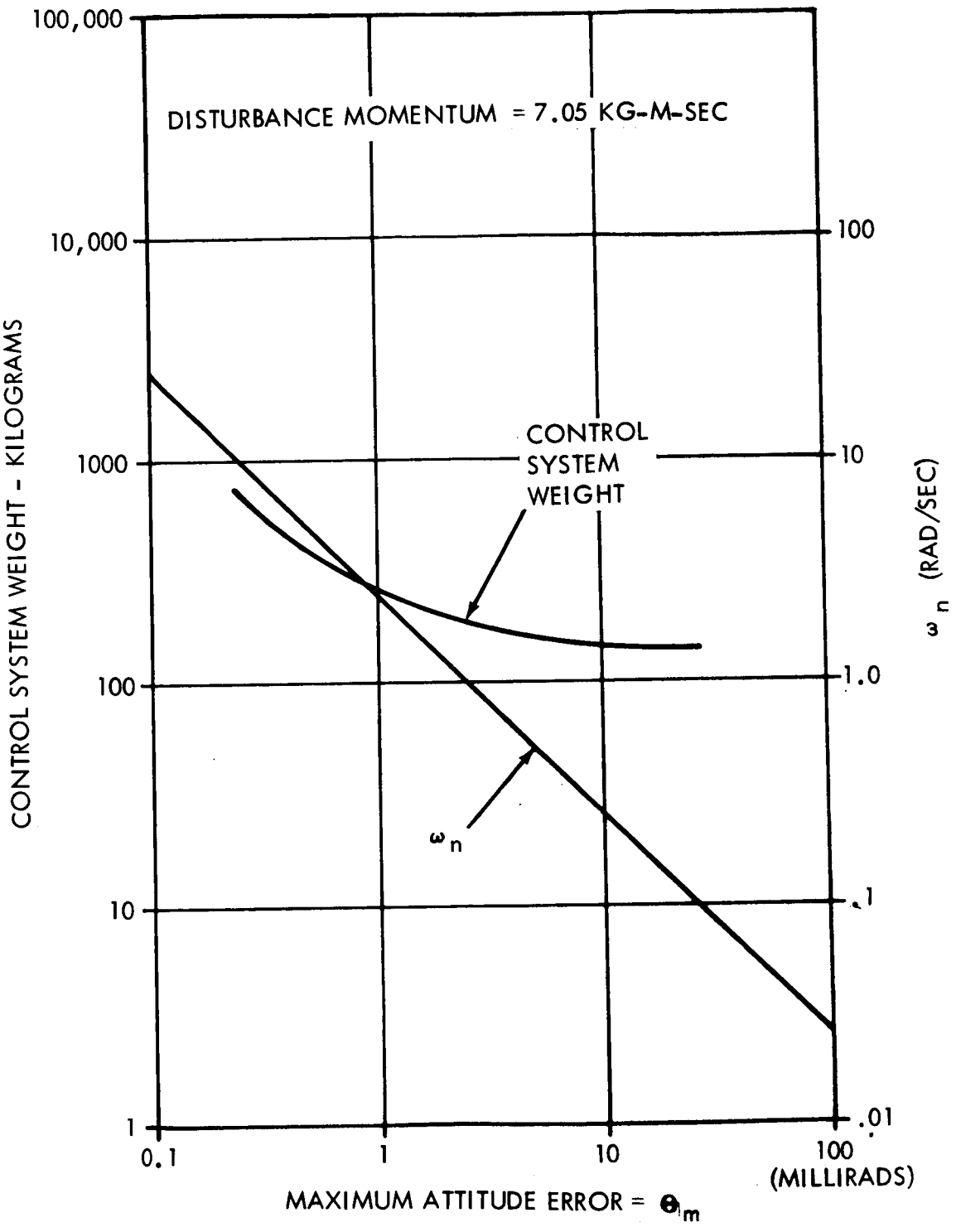


Figure 4.13.3.1.2-2. Weight & Bandwidth Control System vs θ_m

4.13.3.1.3 Stabilization Requirements

It is the purpose of this section to examine particular astronomical applications to determine the optical resolution requirements and how image stability requirements are related to resolution requirements.

Image Stability Requirements

Typical space optics applications might include spectrometry, star field photography, and optical communications.

The requirement for spectrometry is to direct the incoming light through a narrow slit. The effect of mispointing is to increase the exposure time. For high-dispersion work stability requirements have been given as(1) pitch- $\pm$ 0.02 arc second 70 per cent of the time and $\pm$ .03 arc second 95 per cent of the time; yaw - 0.1 arc second 70 per cent and 0.15 arc second 95 per cent of the time and roll - $\pm$ 180 arc second 95 per cent of the time. These are the actual stability requirements or excursions from the initial position. In addition, to direct the light through the slit, an absolute pointing accuracy of about $\pm$ 0.01 and 0.1 arc second for pitch and yaw, respectively, is required. To determine the stability requirements for photography, the characteristics of the film must be considered. First, it should be clear that the required absolute pointing accuracy is determined by off-axis aberrations and should be no more stringent than a few arc seconds in pitch and yaw with no preferred roll orientation.

The stability requirements, on the other hand, are determined by the photographic smear that can be tolerated. The exposure characteristics as a function of time, for a constant light intensity, is shown in figure 4.13.3.1.3-1 for a typical film. To expose a given element of the film above the fog level, minimum integrated exposure time is required. This means that a certain number of the impulsive type disturbances are discussed in the previous section can be tolerated during a given exposure period, providing the accumulated dwell time in the annulor region surrounding the image airy disk does not exceed a certain percentage of the total exposure time. In general, the image will be stabilized by a control system whose error response to an impulsive disturbance is typified by the graph in figure 4.13.3.1.3-2. In this figure, θ_m is the maximum error reached as a result of the disturbance, and T_1 and T_2 are the times required for the beam to traverse the boundary circle of the airy disk upon leaving and returning to the origin, respectively.

(1) A System Study of a Manned Orbital Telescope, The Boeing Company, 1965.

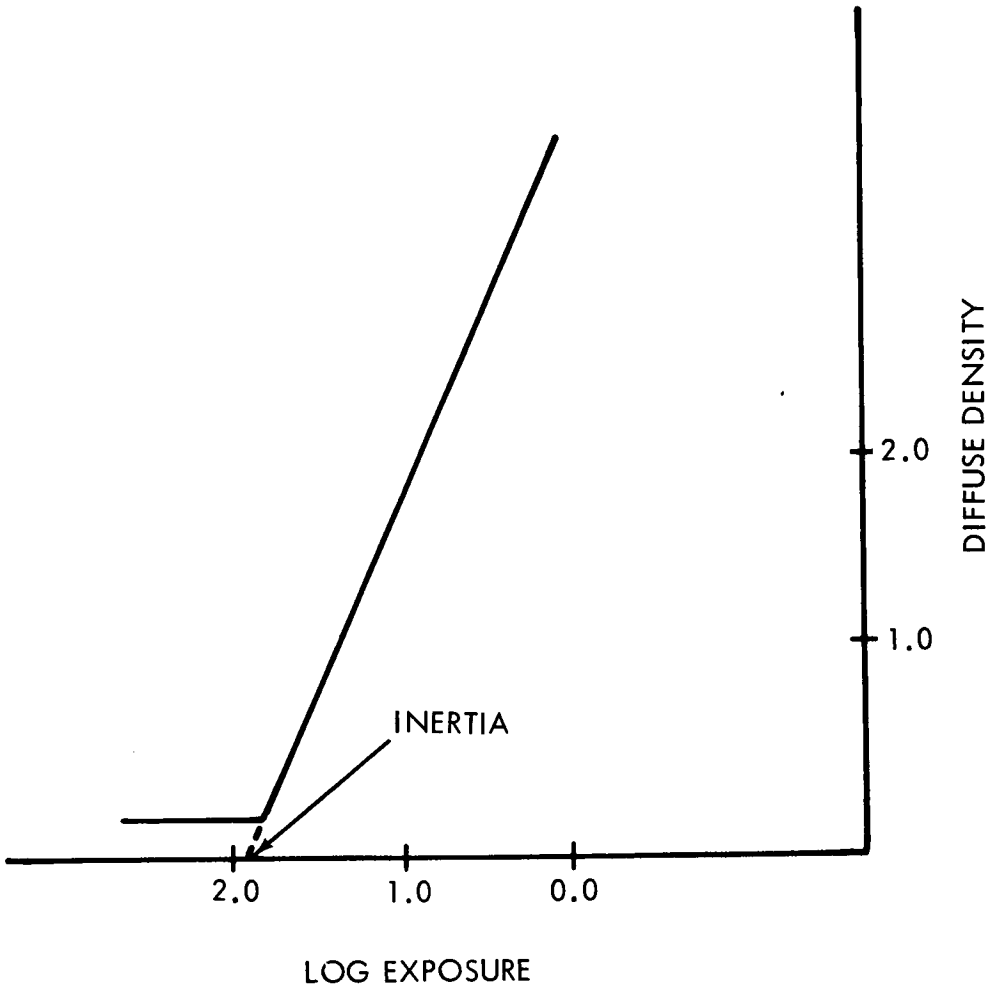


Figure 4.13.3.1.3-1. Linearized Exposure Characteristics

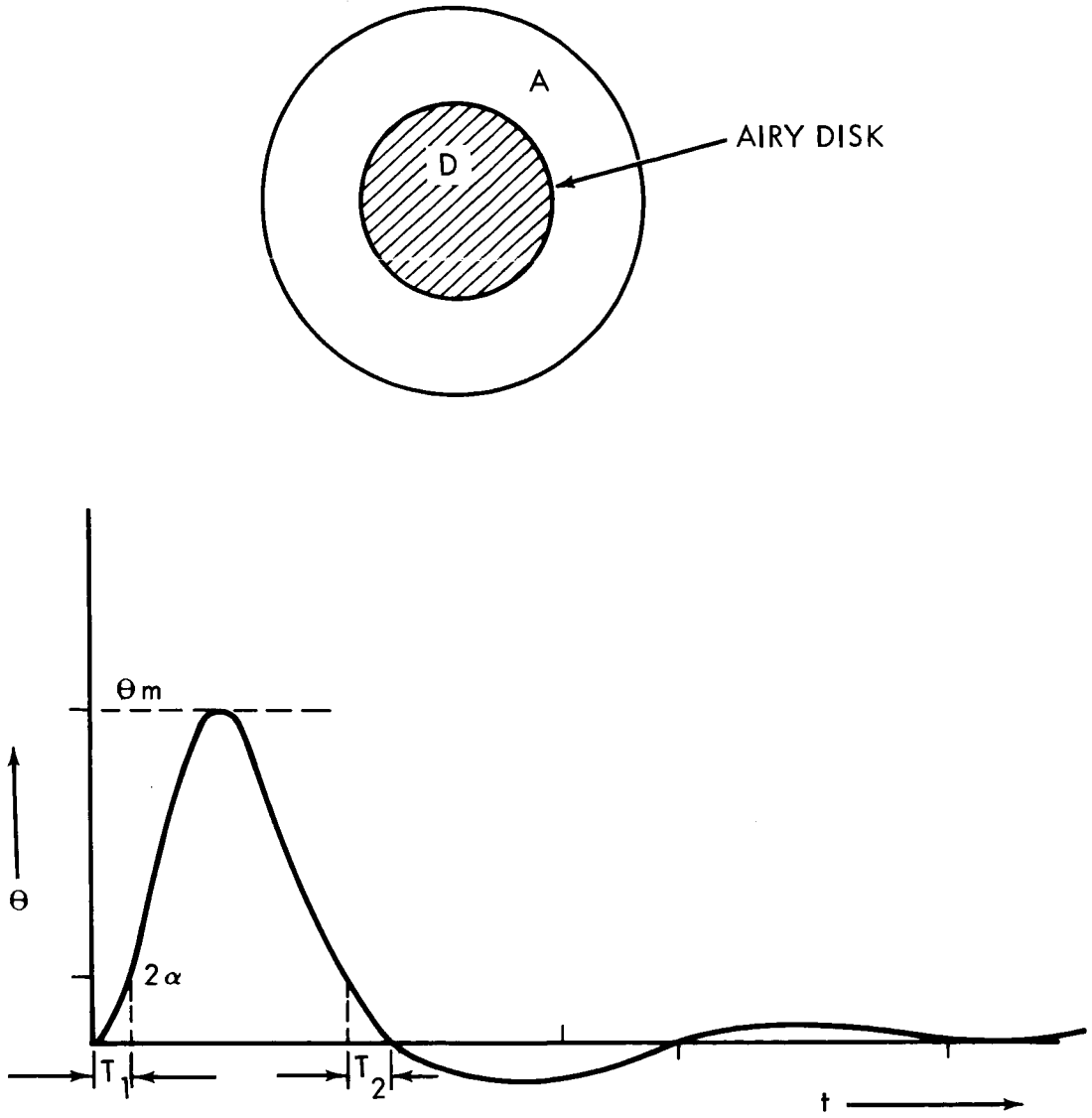


Figure 4.13.3.1.3-2. Time Response of Control System to An Impulsive Disturbance

As derived in section 4.13.5, the number of disturbances per exposure period that can be tolerated is given by.

$$N = \frac{E_r \, \theta_m \, \omega_n \tau}{2\alpha \left[\exp\left(\frac{-z}{\sqrt{1 - z^2}} \cos^{-1} z \right) + \exp\left(\frac{z}{\sqrt{1 - z^2}} \left(\pi - \cos^{-1} z \right) \right) \right]}$$

where

E_r = percentage of exposure period that the beam may dwell in the annular region A before degrading the contrast

θ_m = maximum error, radians

ω_n = control frequency, rad/sec

α = Airy disk radius, radians

z = damping ratio

τ = Exposure period

This equation only holds for reasonable damping (50 to 100 per cent) and disturbances impulses ($2\alpha \leq \theta_m \leq 10\alpha$).

Typical values for these parameters are as follows: E_r = 4 per cent; $\theta_m = 10\alpha$; ω_n = 5 rad/sec; z = 70 per cent. This gives N to be less than about 5 disturbances per minute.

For impulsive disturbances then, the following is concluded. For spectral studies where the objective is to pass light through a narrow slit, impulses have the effect of increasing the exposure time and the exact number that can be tolerated depends on operational considerations, but obviously occasional disturbance of this type are acceptable. For photography, the above analysis indicates no practical limitations on occasional impulsive movements.

Next consider the effect of random motion of the image on film exposure. The same film characteristics are assumed as before. The results, which are derived in section 4.13.5, are shown in figure 4.13.3.1.3-3 where a cross-section of the exposure density is shown.

The edge exposure of the central disk at radius $r - 1.5\ r_o$ has about 80 per cent of the exposure of the annular ring of radius $r = 2.5\ r_o$. Therefore, it is questionable that the central disk can be distinguished as such, which means that in effect the rms amplitude of random motion must be added directly to other contributions such as optical resolution and film resolution in determing the system resolution. Therefore, the image stability requirements for this kind of disturbance is at least as stringent as the resolution requirements.

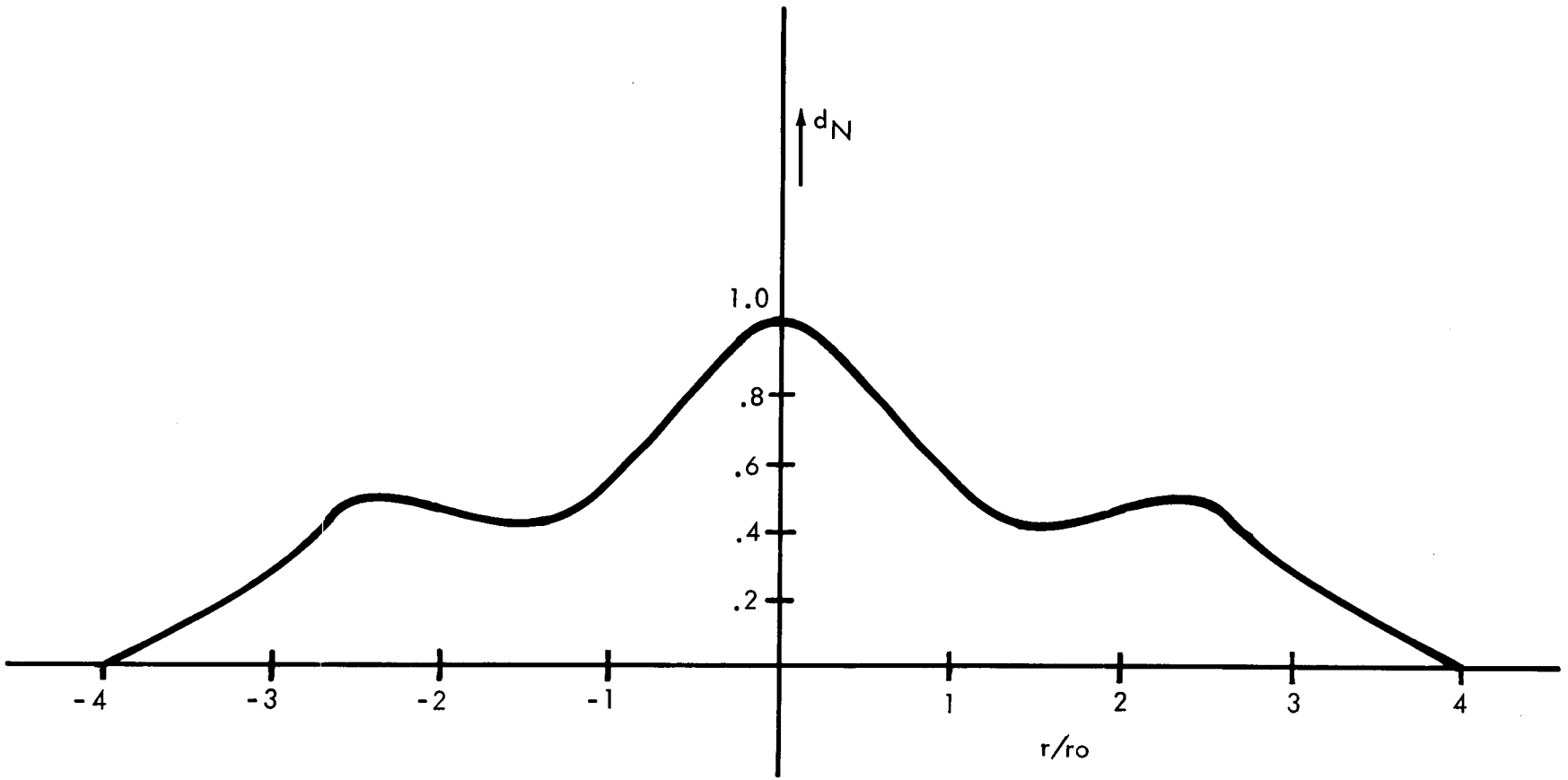


Figure 4.13.3.1.3-3. Cross-Section of Exposure Density

The image stability requirements can be summarized as follows. For both spectrometry and photography occasional impulsive disturbances as would be caused by a sudden movement of the upper body of a constrained man or a mild push-off maneuver of an unconstrained man can be tolerated. Random or sinusoidal image motion comparable in magnitude to the resolution requirements cannot be tolerated for either application.

The stability requirements for the optical communication application are discussed in detail in Section 4. and will not be covered here. However, it should be pointed out that generally they are not as stringent as the astronomy requirements because the power of the ground-based transmitter allows for a high signal to noise ratio and therefore greater control bandwidth and the operating frequency allows for the design of fine guidance loops to utilize the larger bandwidth in practical configurations.

4.13.3.1.4 Isolation Requirements

The purpose of the isolation system is to attenuate the magnitude of disturbances transmitted from the spacecraft to the telescope. The amount of attenuation required is dependent on the disturbance environment, the telescope control dynamics, and the image stabilization requirements. In order to establish a reference requirement on which the design and analysis of candidate suspension system can be based, the following assumptions are made.

a. The disturbance environment is random and is characterized by the power spectrum sketched in figure 4.13.3.1.1-3 with $\bar{H}_m = 3$ ft-lb-sec.

b. The image stability requirements for this type disturbance are 0.01 arc sec in accordance with the analysis in a previous section.

c. The control system consists of a coarse control loop and a fine guidance loop as shown in figure 4.13.3.1.4-1. The fine loop is much faster than the coarse loop and effectively governs the response of the system.

d. Disturbance torques are transmitted to the telescope as unbalance torques, due to the acceleration of the telescope support.

e. The criterion for establishing the attenuation requirements is the mean square error.

Under these assumptions the required attenuation is determined as follows:

$$H_{T/S} = K' H_{S/C} \qquad (1)$$

where

$$K' = \frac{M_{T/S}\ ld}{I_{S/C}} \qquad (2)$$

$H_{S/C}$ = disturbance momentum into the spacecraft.

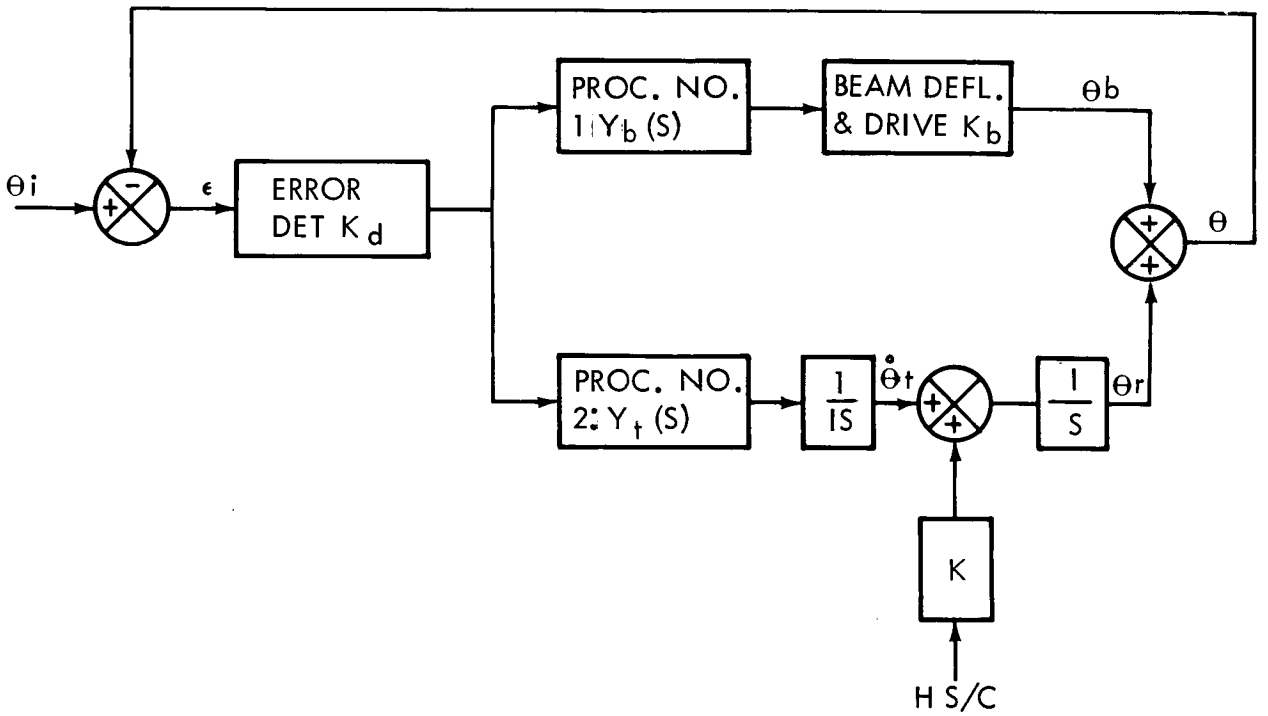


Figure 4.13.3.1.4-1 Dual-Tracker Analytical Model

$H_{T/S}$ = disturbance momentum into the telescope.

$M_{T/S}$ = telescope mass

l = distance between telescope support and rotation axis of spacecraft.

d = distance between telescope support and telescope center of mass.

The mean square error is determined as follows. The beam deflector can be represented as an integrator (see section 4.5) so that the open-loop transfer function is

$$G = \frac{K_{vb}}{S} \tag{3}$$

$$\theta(S) = \frac{K}{K_{vb} + S} \; H_{S/C}(S) \tag{4}$$

As shown in section 4.13.5.1.1.4, the disturbance spectrum is given as

$$\Phi_{ll}(jw) = \frac{\bar{H}_m^2}{T_l} \left(\frac{\sin \omega T_l/2}{\omega/2} \right)^2 \tag{5}$$

Thus the mean square error is

$$\bar{\theta}^2 = \frac{1}{2\pi} \int_{-\infty}^{\infty} \left| \frac{K}{K_{vb} + j\omega} \right|^2 \frac{\bar{H}_m^2}{T_l} \left(\frac{\sin \omega T_l/2}{\omega/2} \right)^2 d\omega \tag{6}$$

Carrying out the integration gives

$$\bar{\theta} = \frac{K \bar{H}_m}{K_{vb}} \left\{ 1 - \frac{1}{K_{vb} T_l} \left[1 - e^{-K_{vb} T_l} \right] \right\}^{\frac{1}{2}} \tag{7}$$

where

$\bar{\theta}$ = rms error

$K = \frac{K'}{I_{T/S}}$

$I_{T/S}$ = telescope moment of inertia

K_{vb} = velocity constant of the fine guidance loop

$\bar{H}_m$ = mean value of the disturbance momenta

T_l = characteristic period of disturbance

In choosing numerical values for the above parameters, the following points should be made. The spacecraft inertia is fixed, for a given system and so are the telescope inertia and the distance l between the center of mass of

the spacecraft and the telescope support. The distance d between the telescope center of mass and support is not certain and may vary under actual operating conditions because of shifting mass (e.g., film) in the telescope. The effective bandwidth of the fine guidance loop K_{vb} is limited by signal to noise ratio and is determined primarily by the fine guidance error sensor. The disturbance period T_1 is determined by rapidity with which movements in a space environment are naturally executed and should range from about 0.5 to 1 second. The mean value of the disturbance $\bar{H}_m$ may range from 1 to 5 ft-lb-second depending on the type of tasks being performed by the crew.

Therefore, to establish the isolation requirements, the following numerical values are assumed.

$\bar{\theta}_m$ = 0.01 arc-second

$I_{T/S}$ = 300 slug-ft^2

K_{vb} = 5 rad/second

$\bar{H}_m$ = 3 ft-lb-seconds

T_1 = 1 second

$M_{T/S}$ = 30 slugs

$I_{S/C}$ = 12,000 slug-ft^2

l = 10 feet

d = 1 inch

Substituting for these numerical values gives a required attenuation factor of about 0.01.

This is taken as the isolation requirements. That is, at a frequency of 1 CPS, the force transmissibility of the isolation system should be down 40 db.

The contribution that this experiment makes toward advancement of the optical technology is summarized as follows. The isolation that must be afforded a space telescope depends on the disturbance environment which is to be isolated, the spacecraft control system, the telescope control system, the fine guidance loop, the actual image stability requirements, and the capabilities of existing isolation technology, namely, gimbal mounts. All these factors and their interrelationships have been investigated and it is concluded that further isolation must be provided and the performance of a frequency dependent isolation system should provide 40 db attenuation at a frequency of 1 Herz.

4.13.3.2 Need for Space Testing

It has been shown in previous sections that a need for advancing the technology space telescope isolation exists. The purpose of this section is to

determine whether space testing is required to effect this advancement. To show that space testing is essential, it is necessary to show that the space properties of interest to this experiment cannot be simulated closely enough on Earth to give meaningful experimental results.

These properties are high vacuum and low-g conditions, and the latter is by far the most important to the performance of this experiment. First, although experiment design has not yet been discussed, it should be obvious that a space isolation system bears some resemblence to an isolation system used on the ground, a device with which everyone has some familiarity. An important design parameter for an isolator is the static deflection, and it is evident that a spring isolator which will support the weight of a telescope with a reasonable static deflection will not be effective in isolating the disturbances encountered in space.

Therefore, to obtain test information on the ground for design of an isolation system in space, it is mandatory that the low-g conditions of space be simulated. And to simulate the space environment it is necessary, of course, to know what this environment is. This section is conveniently divided into two parts. Analysis of the space environment and investigation of ways to simulate it.

Before going into these two facets in detail, one other point should be made, which is reiteration of the relationship of the Fine Guidance experiment to the present one. As discussed previously, the isolations experiment is performed in conjunction with the fine guidance experiment, and it is to support the stability requirement that isolation is needed in the first place. This means that the discussion in section 4.12 relative to the need for space testing and the ground-based development limitations for that experiment is largely applicable to the present experiment also and is omitted here only to avoid duplication. However, the need for low-g simulation for the present experiment is in addition to the requirements discussed there.

4.13.3.2.1 Space Environment

The space environment is not truly zero-g. Gravity-gradient forces, local-g forces, and impact forces such as aerodynamic and solar radiation all combine to produce a varying low-g environment. A very extensive analysis of this environment was performed as part of this study. This analysis was performed primarily in support of experiment design. A number of the isolation schemes considerd, particularly the diamagnetic bearing, can support only very weak static forces, and all depend on a low-g environment for proper operation.

Therefore, it was deemed desirable to do a detailed analysis of the orbital forces that would act on the isolation systems. The results of this analysis is important here also, since it is this environment that is to be simulated.

This analysis deals with the description of the forces that act between two bodies in nearly similar orbits around the earth with constraints on the orientation and relative positons of the two bodies. The two bodies are assumed to be joined together so that they cannot move relative to each other. The complete system is either assumed to have fixed orientation with respect to an inertial frame of reference, or to be fixed re-

lative to an orbital frame of reference. Also the two parts of the space system can either be separated in space, or one section can be contained within the other so that it is shielded from solar and aerodynamic pressures. Of primary interest in this study are the forces that must be exerted by the restraining devices holding the two sections of the space system apart.

The results are detailed in section 4.13.5. Briefly, they are summarized as follows. For low earth orbit, gravity-gradient, aerodynamic, and rotational inertial (for an earth-oriented system) dominate and are on the order of 10^{-3} lbs each. For synchronous altitude, all the forces may be comparable in magnitude (about 10^{-5} lbs) and may add or subtract along particular spacecraft axes. For purposes of simulation, a force as low as 10^{-5} lbs and variable over two orders of magnitude should be available.

4.13.3.2.2 Space Environment Simulation

The isolations comparison experiment is to be performed in conjunction with the five guidance experiment, or at least certain of the functions and hardware of the latter is essential to the performance of the former. This means that any simulation facility to develop the suspension systems should also include the capability to test the fine guidance systems. Also, most of performance limitation of ground systems as discussed in section 4.12 apply here. However, the simulation of low-g conditions is essential to the present experiment but may be only incidental to the fine guidance test laboratory.

There is no known way to completely simulate the low-g orbital environment. Since the high stability required depends in a fundamental way on removing the stresses and strains caused by the 1-g field, space experiments are required. However, even to develop the space experiments a certain amount of ground testing is essential. Therefore, most of discussion which follows is slanted toward ground-based development of space experiments, as being an essential element in the overall OTAES experiments program.

It is essential that any simulation scheme prevent the 1-g support forces from coupling into the axes which are to be tested at the psuedo orbital conditions. This includes isolation from vibration and other disturbances, from direct coupling of the support forces, and from friction introduced by the support system.

Several candidate schemes are available for simulation of low-g conditions in one or more axes of rotation and translation.

These include:

a. Pendulum or wire suspension.

b. Floatation on a liquid.

c. Ball bushing.

d. Air cushion vehicle.

The first type is illustrated in figure 4.13.3.2.2-1. The telescope is suspended vertically by a wire along the optical axis. This allows freedom of movement in the horizontal plane. The telescope well is constructed around the telescope with the isolation system between well and telescope. The dynamics of the spacecraft system is simulated with a forcing function into the well. Obvious deficiencies of this scheme include (a) only translational motion is possible. Attempts to circumvent this problem by the use of gimbals will introduce large friction torques because of the loading of the bearings.

Also, because of imperfect balance additional torques are introduced. If, for example, the C.G. offset is 0.01 inches, the unbalance torque is about 10-inch-lbs which is a couple of magnitudes larger than friction torques expected in space.

Similarly for identical friction coefficients, the friction torque itself will be close to two magnitudes greater than that is space. (b) Only small translational movements are possible if the space environment is to be simulated. For example, if the movement from vertical is 2 inches and the suspension height is 100 feet, the transverse loading is 1.67 lbs. This is about the practical limit in static force capable of the spring and active suspension systems. Therefore the dynamic effects would be swamped by the g-field component. (c) Only the one or two axes of motion can be simulated in this way. As shown in section 4.13.4.1.3 there is important coupling between the optical axis translation and pitch and yaw rotations. This aspect of the dynamic problem would be lost.

The next apparent simulation technique is flotation. Practical problesm with this scheme include the viscous damping in the fluid and imperfect flotation conditions which will introduce torques and forces.

If for example, the telescope and isolation system are perfectly balanced but there occurs a change in temperature, the result will be a static loading determined approximately as follows.(2)

Let

F = centering force required to offset lack of neutral buoyancy

W = weight of the telescope and isolation system = 1000 lbs

β = volumetric coefficient of thermal expansion of fluid = 800 X 10^{-6} per degree centigrade

α = volumetric coefficient of thermal expansion of the telescope and isolation system = 72 X 10^{-6} per degree centigrade

Δt = 1° C

(2) Savet, P. H. Gyroscopes: Theory and Design, McGraw-Hill, 1961.

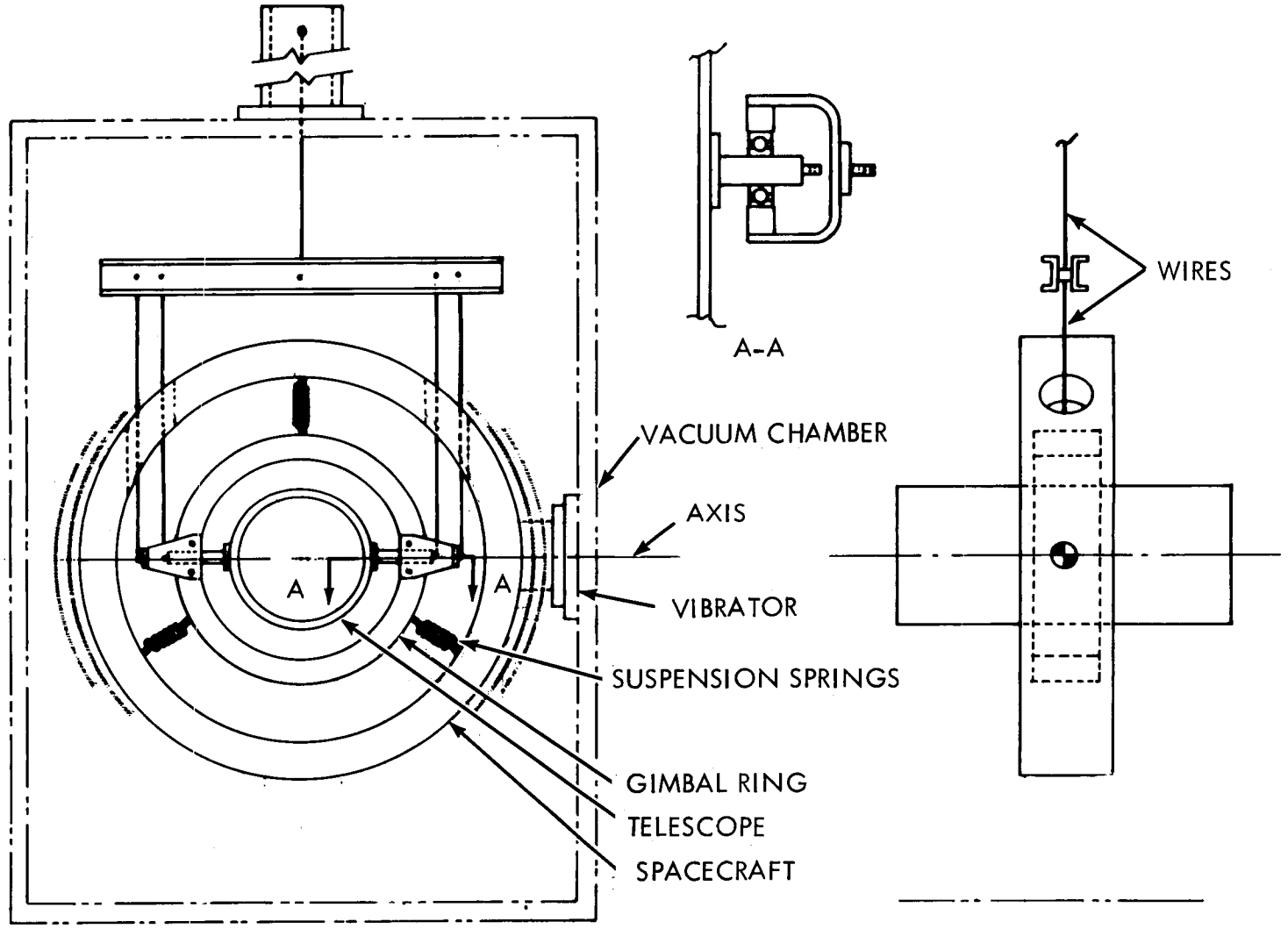


Figure 4.13.3.2.2-1. Suspension Scheme for Simulation of Low-g Environment

Then

$$F = W(\beta - \alpha)\Delta t$$

$$= 1000\ (728 \times 10^{-6})\ 1$$

$$= 0.728 \text{ lbs}$$

The most promising low-g simulation scheme is air cushion vehicle, illustrated in figure 4.13.3.2.2-2* A granite table is kept level to within a fraction of an arc-sec by a servo controlled mount, if foundation disturbances make servo-control necessary. The payload is mounted on an air bearing to give two degrees translation and one rotation. Thus, one axis of the fine guidance loop can be tested simultaneously with the suspension system, to partially include the cross-coupling effects. Direction and magnitude of the orbital forces can be simulated as a function of time through programmed tilt of the table.

More degrees of freedom can be simulated by mounting the telescope on a ball air bearing which in turn rests on the air cushion. By placing the entire apparatus in a vacuum chamber, the true orbital environment is more closely approached. Of course, the facility then becomes extremely complex so that it might be cheaper to perform the development testing in space. A cost analysis of this type is beyond the scope of the present study.

Need for space testing may be summarized as follows. It does not appear possible to completely simulate low-g orbital conditions. But several schemes are available to partially simulate these conditions in one or two axes of translation and rotation. Of these, the air cushion vehicle is the most promising. The extent to which the orbital environment is a function of cost and complexity of the simulation facility. Since the performance of the suspension system depends in a fundamental way on removing the stresses and strains of the 1-g field, space experiments are recommended. However, certain ground-based testing is required in support of these experiments. It is recommended that such a ground development program be initiated.

4.13.4 Implementation

4.13.4.1 Experiment Design

It is the purpose of this section to conceptually design the isolations comparison experiment. The basic reference by which the other isolation techniques are compared is the hard mount or mechanical gimbals. There are several reasons for this, the most important one being reliability. Mechanical gimbals is a well developed technique for providing a mount with angular freedom relative to the structure to which it is mounted, and is widely used in ground, airborne and space applications. Since, as will be discussed in a later section, the isolation system is used to support other experiments on the same telescope, elementary reliability considerations dictate that the capability of locking out the isolation system should be provided.

---

* Debra's paper.

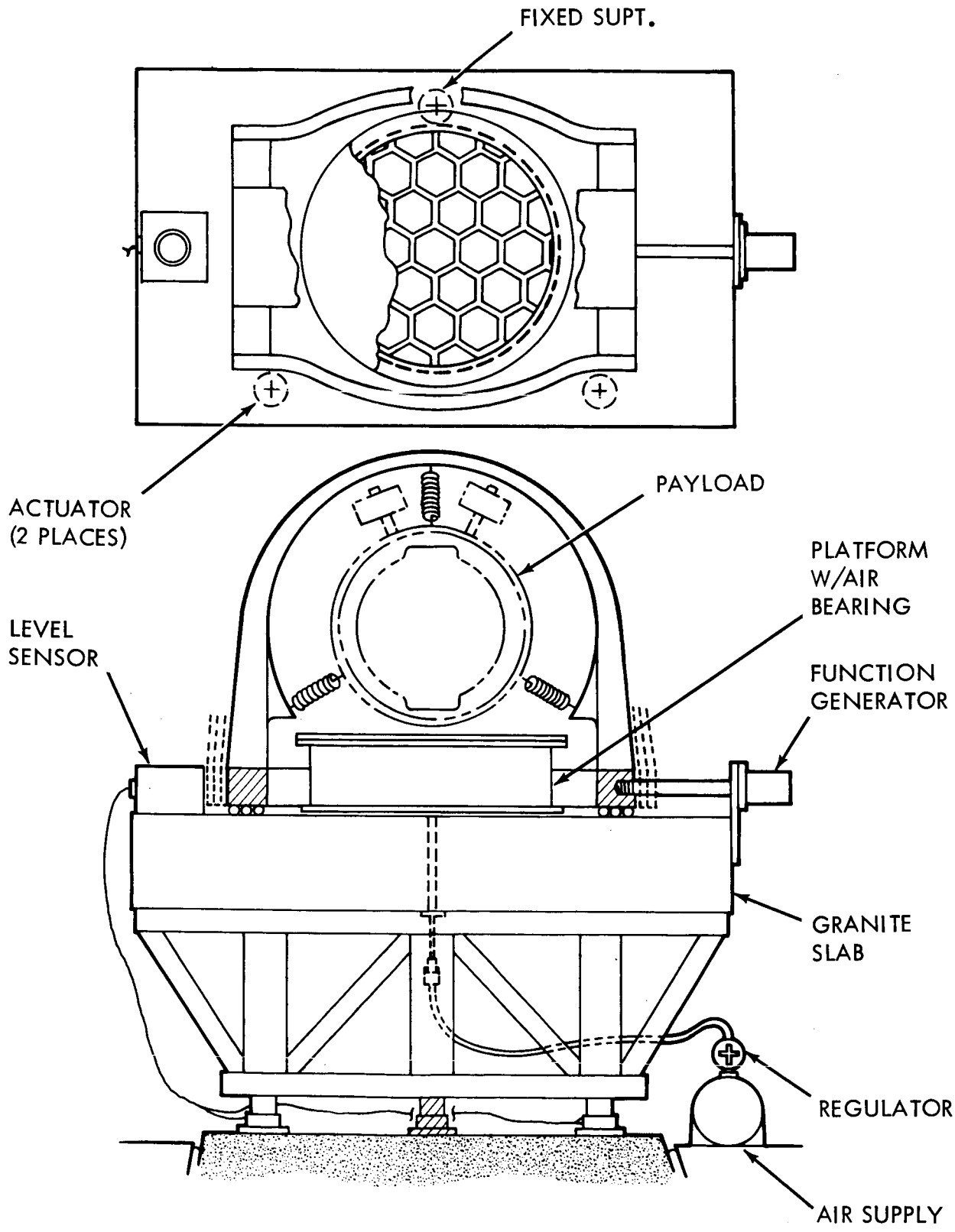


Figure 4.13.3.2.2-2. Air Bearing Simulation Scheme

At the same time the hard mount is used as a reference by which to compare the performance of the other isolation schemes.

Basically, three types of isolation schemes have been investigated: a spring mount, an active suspension system, and the diamagnetic suspension system. Greatest effort was directed toward a detailed analysis of higher-order effects in the spring suspension, which is considered the simplest and most reliable technique that will perform adequately for all space environments that may be encountered. The diamagnetic technique is reliable but requires much ground-based development and is marginal in performance at low altitudes where orbital separation forces approach the static force capability of a practical diamagnetic configuration.

4.13.4.1.1 Hard Mount

Early in the study it was decided that the hard mount would be used with the LASER telescope and as a basic reference for comparison of other isolation techniques. Therefore, much effort was directed toward optimizing the performance of the hard mount and preliminary design of the optimized configuration. The basic problems with a hard mount are listed below:

a. Friction and commutation in the torquer.

b. Non-linear friction and stiction in the bearings.

c. Inertial torques caused by imperfect balance of the mount.

d. Lead torques caused by draped leads across the gimbals.

e. High frequency vibrations which may degrade the optics.

Each of these problems was investigated in some detail before preliminary design of the mount was undertaken. The results are summarized below.

The friction and commutation problem may be solved by the use of brushless permanent magnet torquers. These devices have infinite resolution and zero friction, and, for applications requiring limited travel, are nearly ideal. A typical torque linearity curve is shown in figure 4.13.4.1.1-1.

Nonlinear bearing friction may be reduced by the use of flex bearings. During the course of this study, several types of flex bearings have been investigated.

The one tentatively chosen for the hard mount is the Bendix Free Flex Pivot illustrated in figure 4.13.4.1.1-2. Operation of this bearing is predictable and well behaved. There are a couple of problems, however. The center of the bearing unit shifts with rotation. With a clearance between stator and rotor of the torques of only a few thousandths of an inch, very little shift can be tolerated.

The problem of inertial reaction torques caused by mount unbalance can be solved by dynamically balancing the mount. A technique using servo controlled weights is well developed for ground test airbearing platforms. The problem with doing this under space operating conditions is sensing the very small unbalance inertias involved. A possible solution is to accelerate the spacecraft to provide artificial gravity.

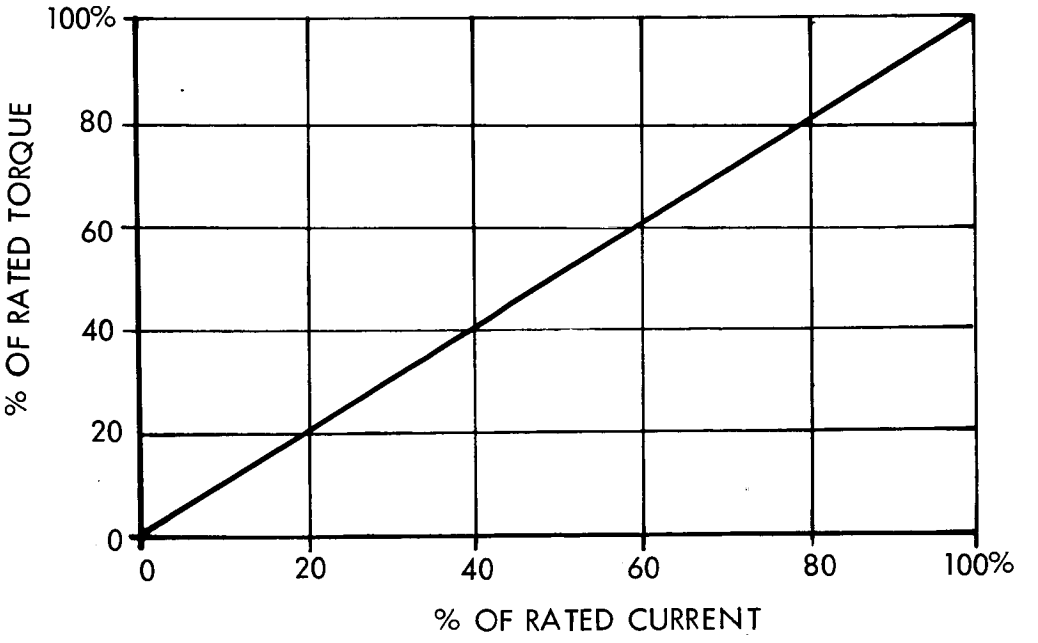


Figure 4.13.4.1.1-1. Torque - Current Characteristics of a Permanent Magnet Brushless Torquer

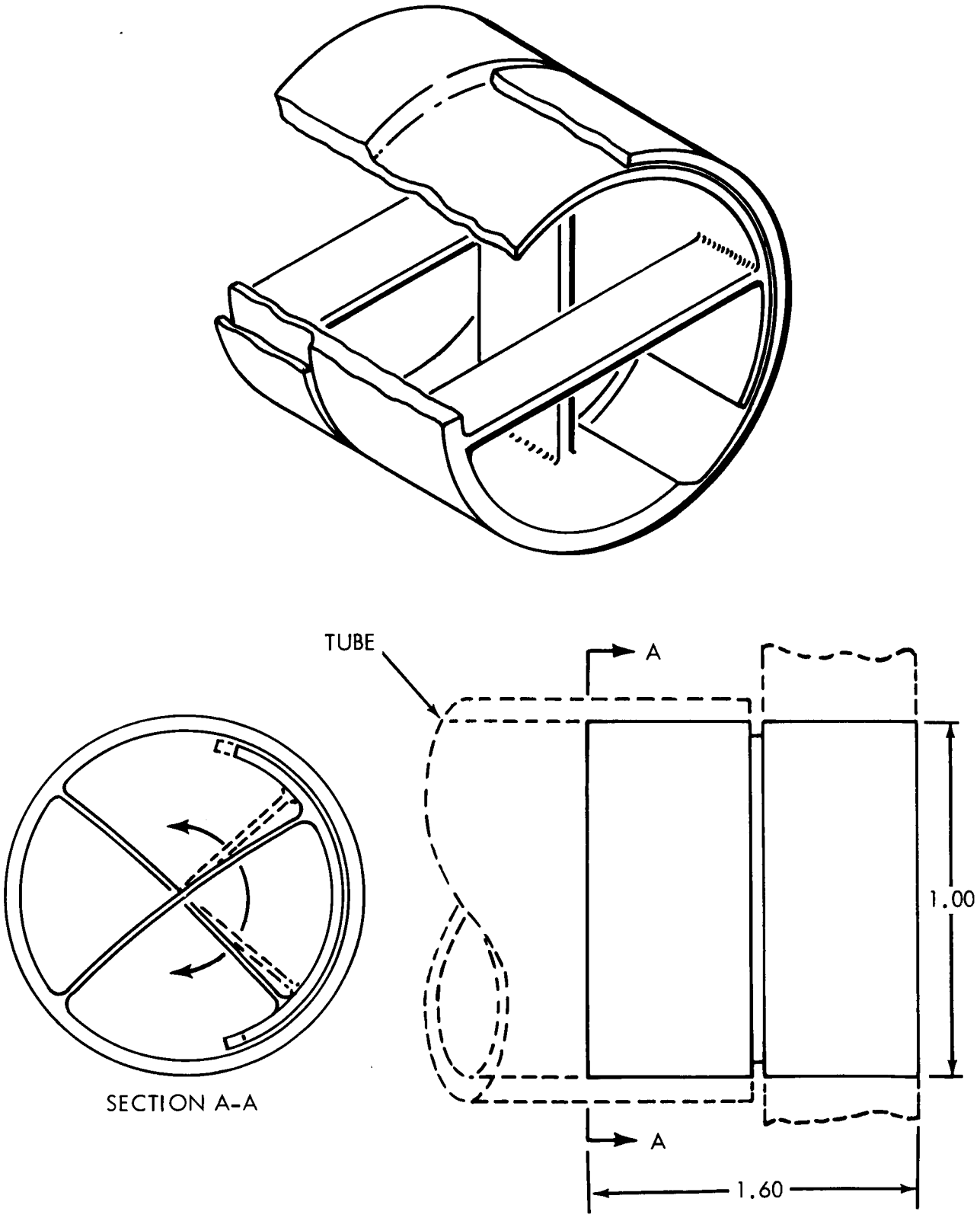


Figure 4.13.4.1.1-2. Bendix Free-Flex Bearing , Cantilever Type

The problem of minimizing the torques associated with draped leads is a difficult one. Not the least of the problems is predicting the torques that are experienced. A solution which both minimizes the torques and provides for predictable operation is to use the electro-bridge developed by Aeroflex Corporation. Illustrated in figure 4.13.4.1.1-3, the electro-bridge uses copper-berylium strips for conducting power and data between the spacecraft and the telescope. A single unit can incorporate as many as 69 conducting leads with a total restraining torque of less than .0035 m-n.

General Design Criteria

Mass: 1000 #m

Moments of Inertia: I_x - 3836 kg m^2 (about optical axis)
I_y - 18,085 kg m^2 (about outer gimbal axis)
I_z - 18,073 kg m^2 (about inner gimbal axis)

Freedom of Rotation: Max Pitch angle - .087 rad
Max Yaw angle - .087 rad
Roll Angle - 0 rad

Torquer Specifications: Continuous Torque: 34 cm - KgF
Angular Freedom: $\pm$ .17 rad
Size O.D.: 23 cm
Thickness: 4 cm
Input power: approximately 45 watts

General Control Requirements

Slew Rates: $1.7X10^{-4}$ rad/sec
Accuracy: $\pm$ 30 arc sec
Stability: $\pm$ 30 arc sec
Maximum Control Torque: 68 cm kg

The torque calculations are based on ground test conditions. It is assumed the center of gravity of the telescope is .025 cm from the gimbal axis and the bearings have a coefficient of friction of 0.002, which is considered conservative.

This gives a friction torque of about .3 n-m on earth.
For 0.01 inch offset, the unbalance torque is 1.1 n m

An Aeroflex brushless d.c. motor in the TQ82 series was selected to meet the torque requirements. This is a 4 pole motor that is capable of 3.4 n-m continous torque and can be peaked to approximately 8.5 n m. Assuming bearing friction to be the same in outer space as it is on earth, this motor provides a safety factor of 2 on earth and a factor of 10 under "zero-g" conditions. Since this factor of safety is based on the motor operating at the continuous torque level, it can be more than doubled by the application of a peak input to the motor.

The type and size of the ball bearing was chosen to meet earth testing requirements and docking loads. On earth the bearings would have to withstand

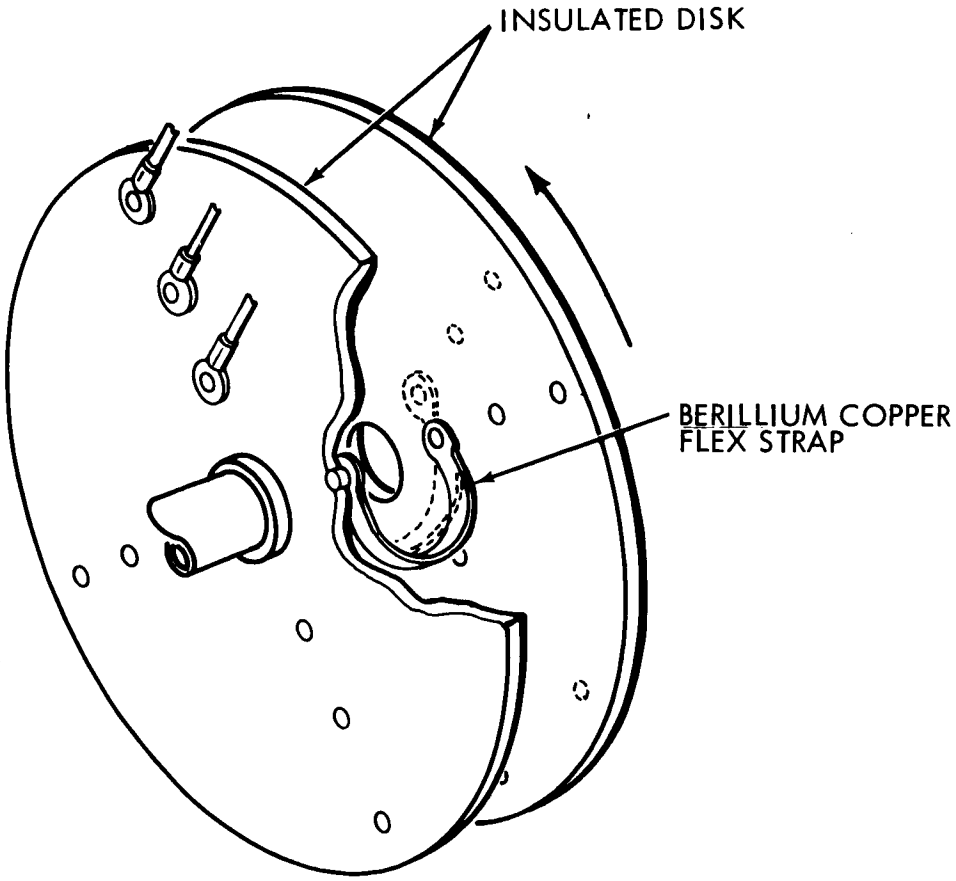


Figure 4.13.4.1.1-3. Electro-Bridge for Data and Power

a radial load of 270 kg and a thrust load of 540 kg. Docking requirements would be one and a half (1.5 g) times this. These loads would be static loads due to the low slew rate requirements and small angular motion.

Other bearing requirements are: (a) high precision, (b) large bore bearing so that a hollow shaft could be used for data bridge use.

The bearing selected in a New Departure type 3000, Conrad, ball bearing. Its load capabilities are 4,714 kg thrust and 3,380 kg radial. Its dimensions are 6.50 cm bore, 12 cm outer diameter and 2.3 cm width.

There are 10 balls with a diameter of 5.9^2 cm (see figure 4.13.4.1.1-4).

The space use requirements for this bearing are: (a) a space lubricant (b) a low bearing friction. The bearing friction was computed using a coefficient of friction of 0.002. The problem of a space lubricant would be handled by using a low vapor pressure lubricant and sealing the bearing by bonding a corrugated rubber seal to the bearings inner and outer race (see figure 4.13.4.1.1-5).

This sealing will be done by injecting the lubricant into the bearing at a pressure of 1 times 10^{-6} mm H_g. The added torque due to this synthetic rubber seal will be held within the capability of the torque motor and will be determined by test. The differential pressure on earth will not substantially increase the bearing torque since the lubricant is essentially noncompressable. The bearing torque is essentially the same in space since the differential pressure here is only 1 times 10^{-6} mm H_g.

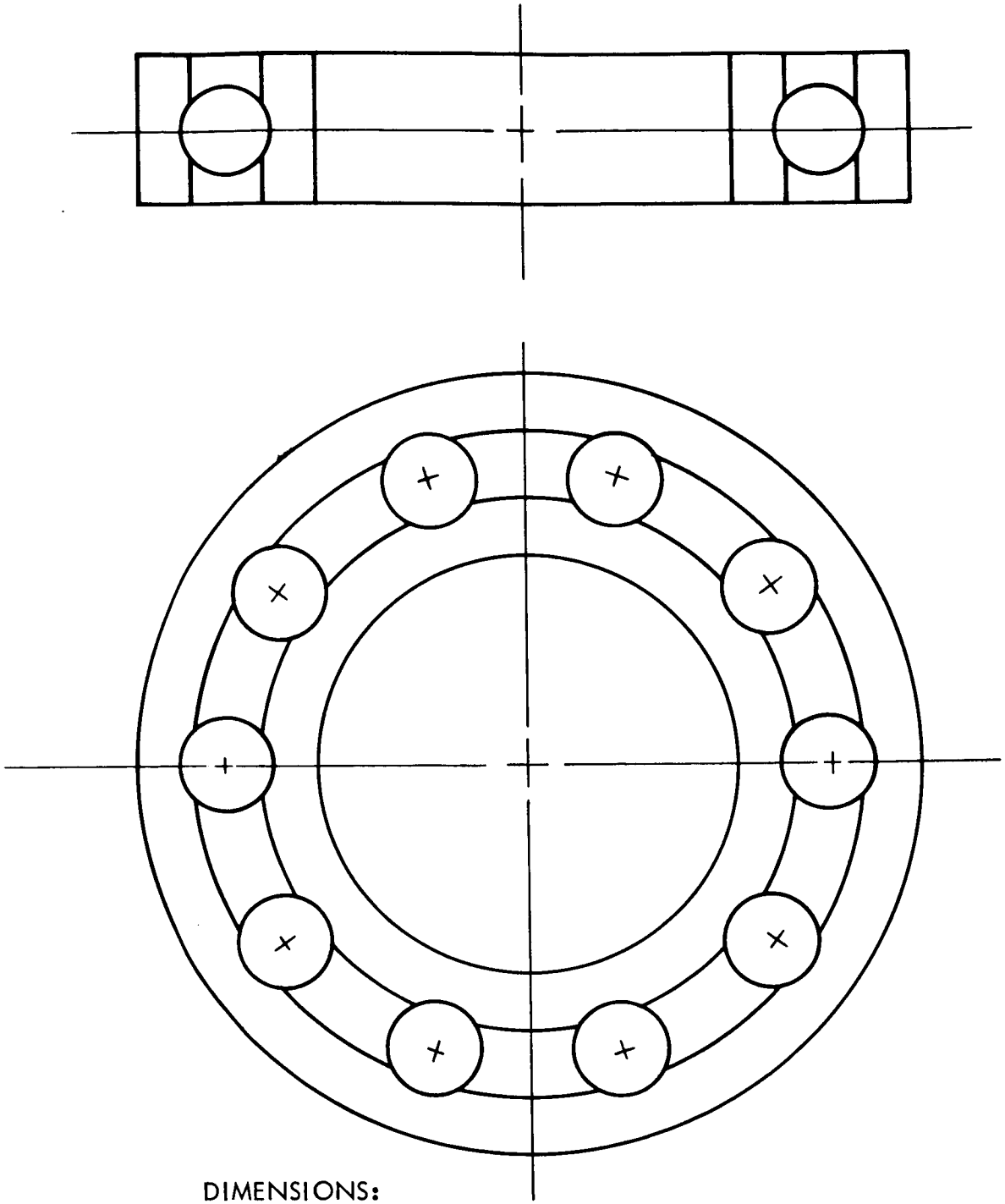
The OTAES program imposes extreme conditions on lubricants, namely, long life requirements, radiation heavy impact loads and a hard vacuum. With these conditions in mind, several methods of lubrication were investigated.

A solid lubricant is usually the most acceptable type to use in a hard vacuum because the problem of vaporization which occurs with oils and greases is practically eliminated. However, solid lubricants did not prove to be feasible in this case because of the severe impact loads and limited rotational movement.

These lubricants tend to permanently deform and therefore increase the rolling friction tremendously.

One of the most popular approaches to a vacuum lubrication problem is the use of a sealed bearing with a low vapor pressure oil or grease. Since conventional sealed bearings would not be reliable for the long period of time involved, new methods of sealing were studied. The method best suited for small angles of rotation is to use a thin rubber seal between the bearing races. The rubber must not be affected by radiation. For dual protection, a low vapor pressure grease such as versilube G-300 or aeroshell 15 should be used.

Several other lubricants are being investigated but limited test data makes their selection difficult. One such lube is teflon-based and was developed by Wright-Patterson Air Force Material Lab for hard vacuum, high temperature use. The optimum design will incorporate a lube which will sustain long periods in space without deterioration, with a bearing sealing device incorporated as a redundant measure.



DIMENSIONS:

DEPTH: 0.9055
BORE: 2.5591 IN.
O.D.: 4.7244
BALLS: no. 10 dia. 21/32 = .656
GROOVE: RADIUS .52 D = 0.341
DEPTH .20 D = 0.1315

Figure 4.13.4.1.1-4. Ball Bearing Design

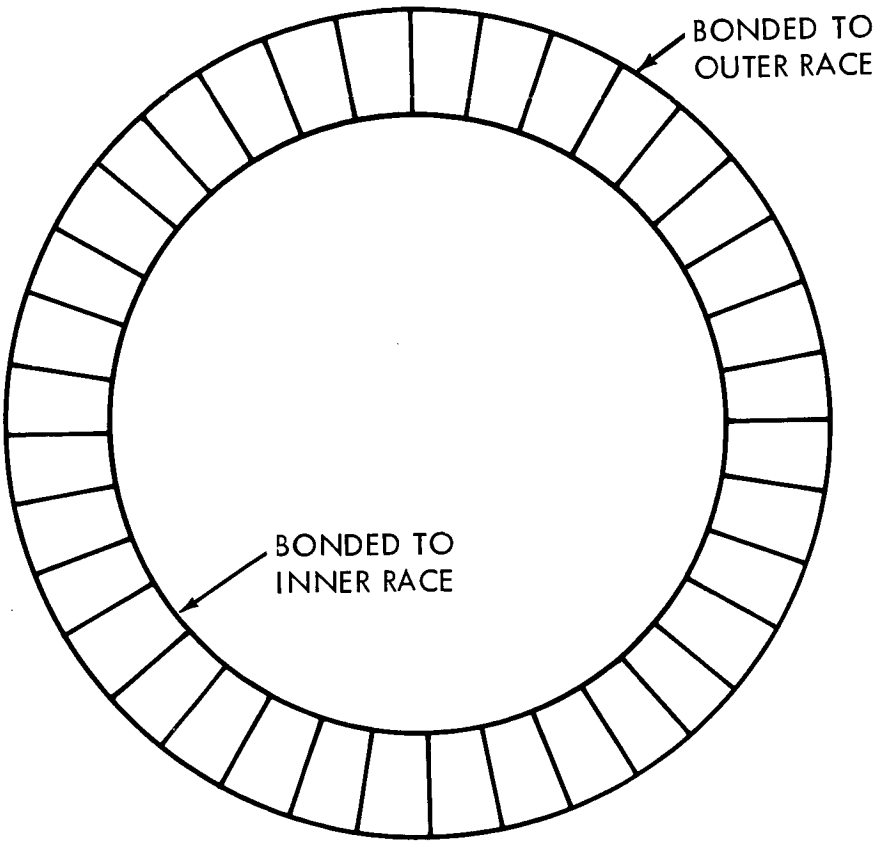


Figure 4.13.4.1.1-5. Bearing Seal

Ring stress and deflections were calculated at various points on the gimbal ring. The loads imposed was in plane loading at $1\frac{1}{2}$ g conditions. The attitude of the ring was taken at its worst condition. Three types of loads were assumed: (a) point load of 810 kg at 0 radians, (b) point loads of 405 kg at $\pi/2$ and $3/2\ \pi$ radians, (c) 4000 n-m moments at $\pi/2$ and $3/2\ \pi$ radians. Cross sections at various points are shown in figure 4.13.4.1.1-6.

The greatest stress was found to be where the trunion cross section reduces to the ring cross section. The stress here was 9000 psi. The assumption of $1\frac{1}{2}$ g conditions in ultra conservative in that this is only a momentary condition when docking and stresses and deflections are soon relieved. The types of loads are also very conservative since in the true case one bearing will not be subjected to the entire force of 810 kg.

The Aeroflex Electro-Bridge is a low torque device for maintaining electrical continuity across two members which rotate relative to each other.

A data bridge was chosen which can accomodate 65 channels with a $\pm\ \pi/18$ radians rotary displacement. Two of these are parallel stacked thus increasing the number of channels to 130. Its dimensions are 12.7 cm by 14.2 cm by 2.54 cm.

The inductosyn is a space proven precision data element for accurate angular measurement of small angular displacement. Its operation principle is similar to an electrical resolve or selsyn. The Inductosyn chosen for this application has a 17.8 cm diameter and 256 pole-s. Its accuracy is $\pm$ 5 arc seconds; repeatability 0.6 arc seconds and sensitivity of 0.15 arc seconds. The manufacturer is Farrand Controls Inc.

The caging device, illustrated in figure 4.13.4.1.1-7, utilizes a high torque, low speed gearmotor in conjunction with a spring loaded pin to lock the gimbal ring and telescope.

The gearmotor is mounted to the telescope well and when activated linearly advances a screw driven drive pin into the gimbal ring. The drive pin then drives a spring loaded pin into the telescope.

The engineering drawing, figure 4.13.4.1.1-8, incorporates the design features discussed above.

4.13.4.1.2 Hard Mount with Flex Bearing

The provision for comparing a flex bearing with a ball bearing is incorporated into the experiment. Friction of the flex bearing is lower than for ball bearings and is predictable. However, the flex bearing will not support the telescope weight on Earth, and provisions for ball bearing operations must be included. The hard mount with flex bearing is essentially the same as the ball bearing mount except for the mechanism for coupling between one bearing and the other.

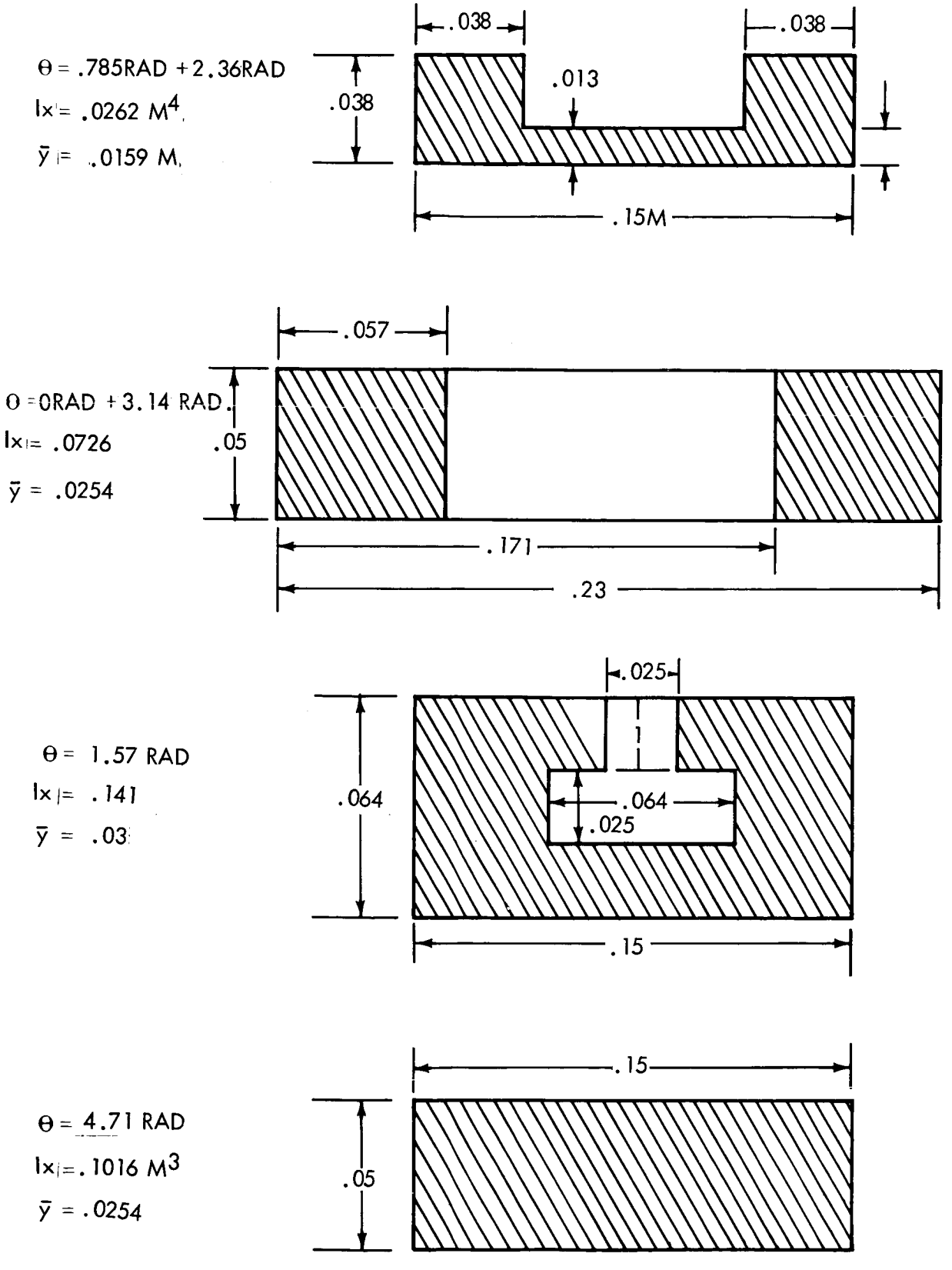


Figure 4.13.4.1.1-6. Primary Ring in Plane Cross-Section

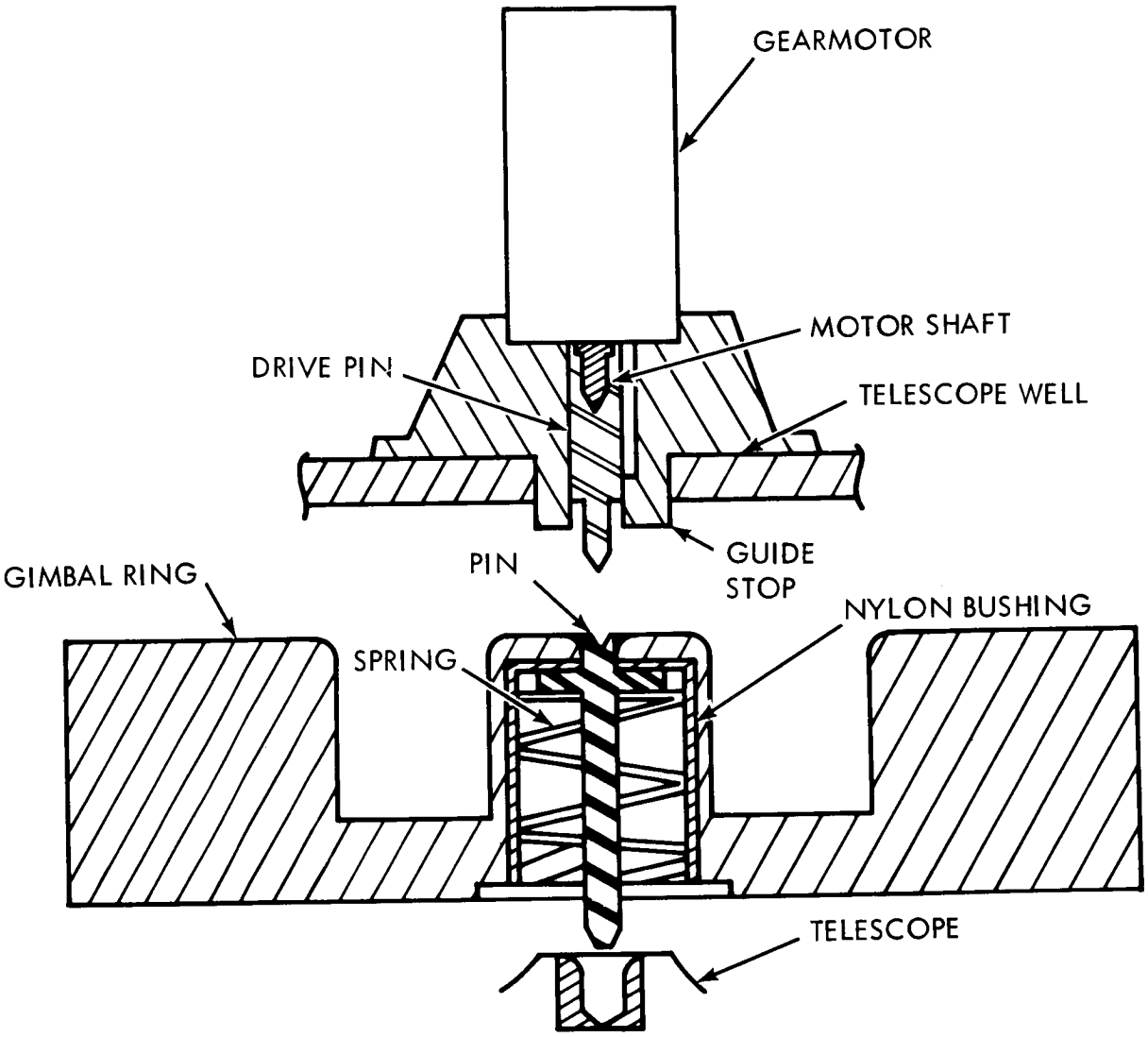


Figure 4.13.4.1.1-7. Telescope Caging Mechanism

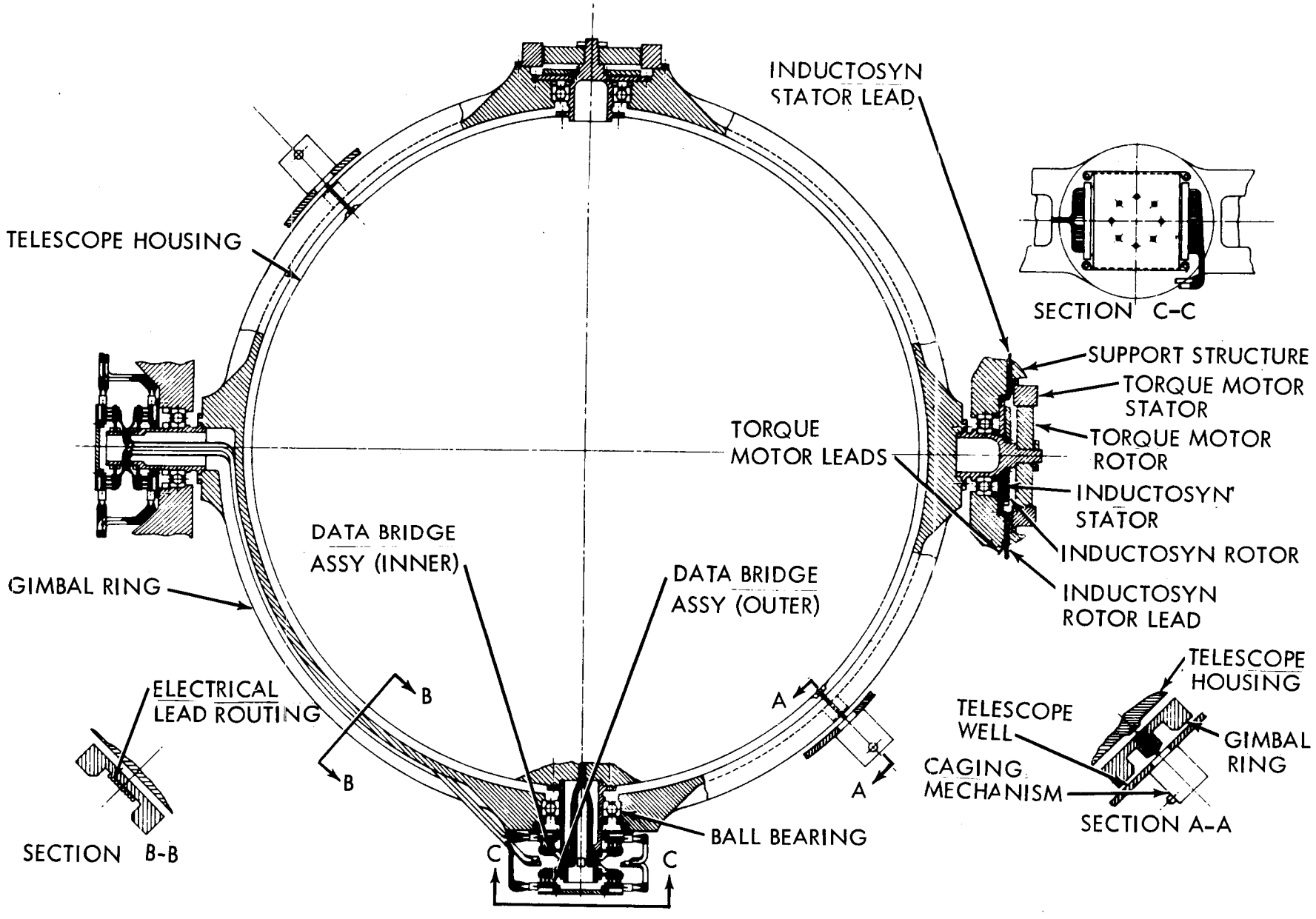


Figure 4.13.4.1.1-8. Hard Gimbal Suspension System

The design of the flex bearing and the coupling mechanism is covered below.

Ball Bearing:

Manufacturer:	New Departure
Type:	Conrad type 3000
Load Ratings:	Thrust 261 kg
	Radial 192 kg
Dimensions:	Bore 5.0 cm
	Diam 9.0 cm
	Width 2.3 cm
	Balls 11 17/32 Diam

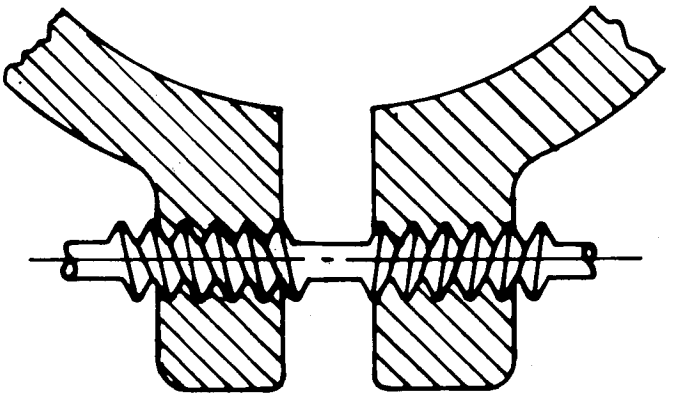
Flex Bearing:

Manufacturer:	Bendix Corporation
Type:	Cantilever Standard Pivots
Number:	5032-6000
Load Ratings:	V_c = 31.8 kg
	V_r = 101 kg
	deflection $\pm \pi/6$ rad max
Dimensions:	Diameter: 2.54 cm
	Length: 4.06 cm
Load:	13.5 kg
Rate:	1.2 n-m/rad .087 rad - .1 n-m)
Angle of Deflection $\pm 5°$	$\pm$0.08727 rad
No Load Center Shift	0.000927 cm
Hysterysis:	max. = 0.000209 rad.
	au. = 0.00002 rad = 0.36 arc min
	= 216 arc sec

For ball bearing coupling a compound screw driven by a high torque low speed D. C. Motor is used to couple the bearings outer race to the gimbal ring or to the telescope well. When activated the outer race is held by a torque of about 14.0 in-lb. The flex bearing is now disconnected from the shaft and the telescope is supported by the ball bearing. The compound screw is shown in figure 4.13.4.1.2-1 and the motor description is given in figure 4.13.4.1.2-2. The flexure pivot used is of the cantilever type. The back of the pivot is always held fixed while the front is connected by a shaft which is coupled to the main shaft for use and uncoupled for ball bearing support. Coupling is obtained from a magnetic clutch brake (see figure 4.13.4.1.2-3) which produces a static torque of 4.0 n-m min.

Shaft stresses and deflections dictated the order in which the ball bearing, torque motor, Inductosyn, and flex bearings were mounted on the shaft. Minimum stress is obtained when largest shaft diameter is the ball bearing bore diameter and when the ball bearing is located closest to the shaft.

Stresses and deflections in the gimbal ring were calculated. Loads were assumed under 1.5 g conditions and telescope attitude at its worse conditions.



MATERIAL: SCREW - STEEL
COLLAR - BRONZE

Figure 4.13.4.1.2-1. Compound Screw

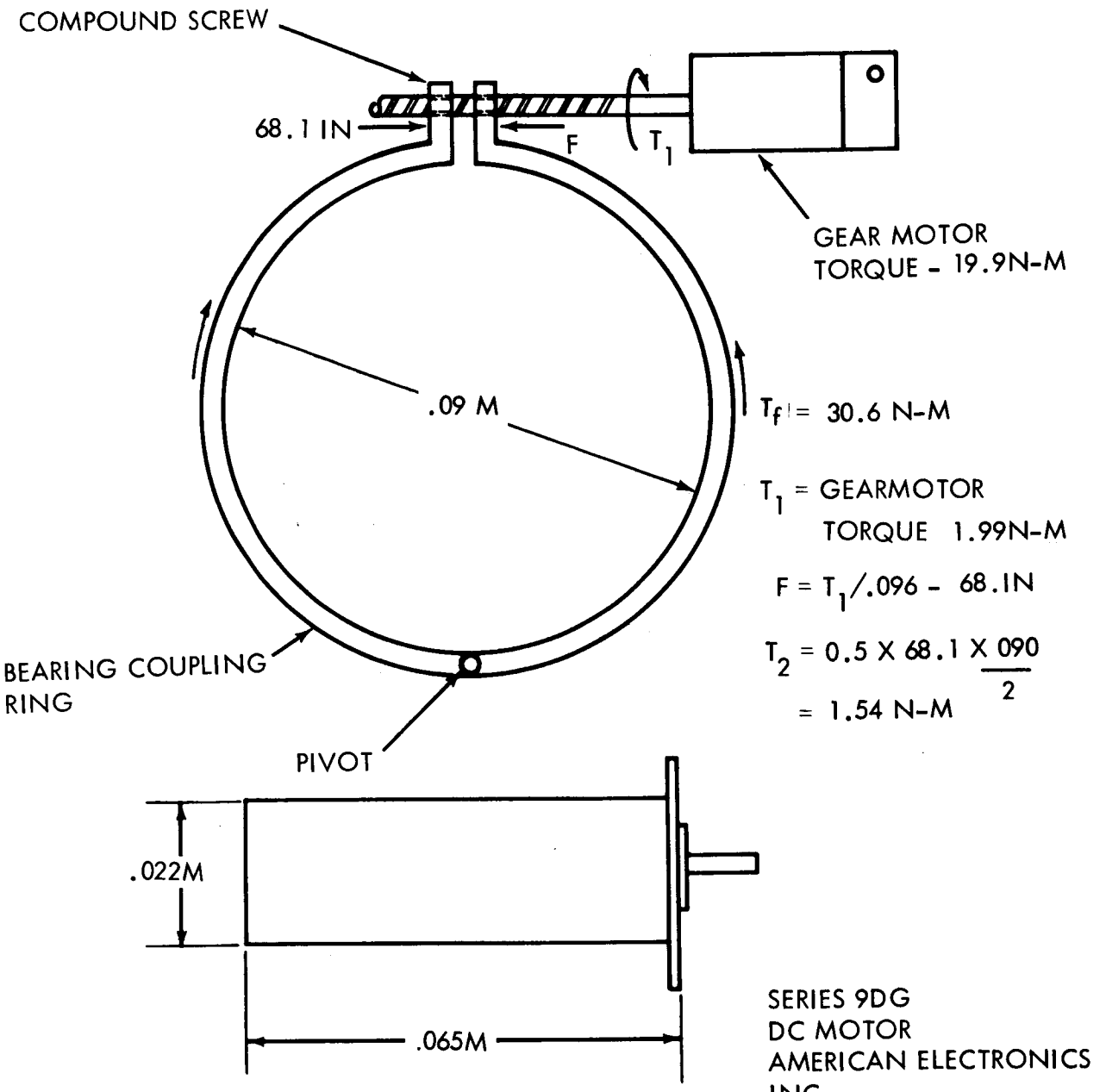
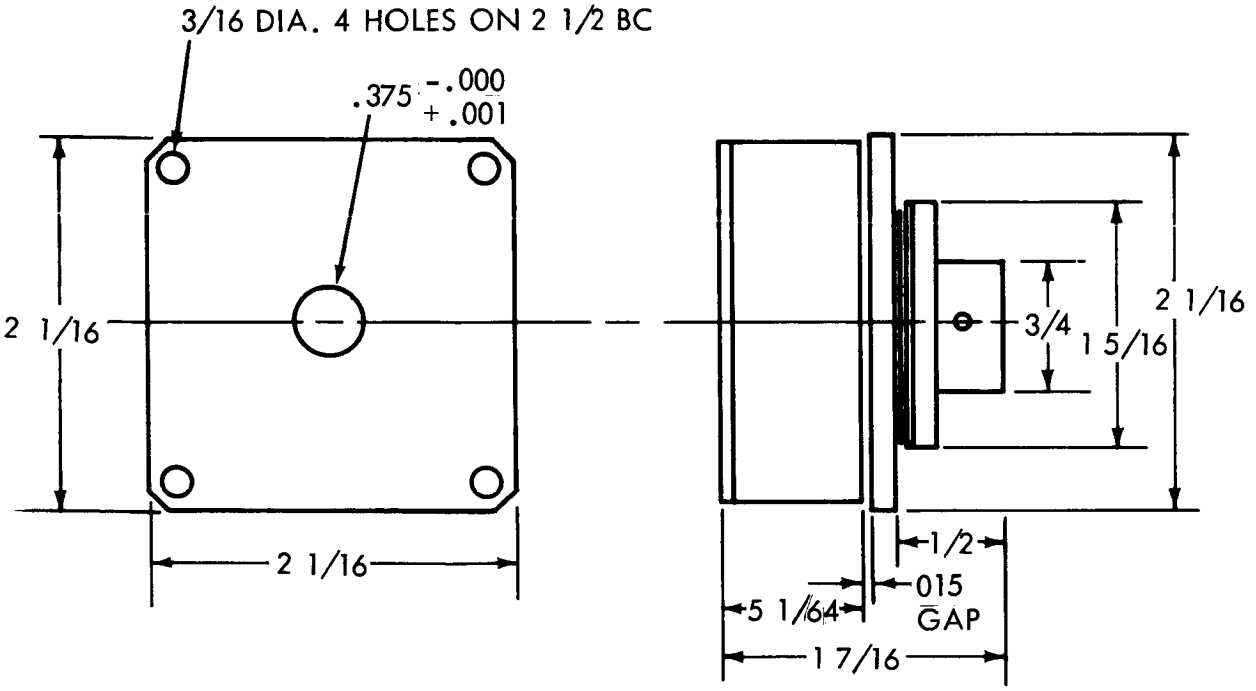


Figure 4.13.4.1.2-2. Drive Motor



DIAL PRODUCTS CO. SAB-212 TYPE 2
STATIC TORQUE: 4NM (MIN)
POWER CONSUMPTION: 3.36 WATTS (28 VOLTS D. C.)

Figure 4.13.4.1.2-3. Magnetic Clutch Brake

Stresses and deflections in the trunions are negligible due to the very high section moments of inertia, small loads and small radius.

Stresses in the ring were in the order of 2600 psi with deflection around 0.0064.

Gimbal Torque Motor

Man:	Aeroflex TQ52W Series
Torque:	.16 n-m
Input:	80 watts
Dimensions:	5.125 OD
	0.75 ID
	1.30 width

Inductosyn

Manufacturer:	Farrand Controls	
Size:	3 in D 360 poles	
Dimensions:	Stator:	OD - 9.35 cm
		ID - 2.95 cm
		Width - 0.465 cm
		Separation - 0.005 + 003

Data Bridge

Manufacturer:	Aeroflex Electrobridge
Channels:	65
Torque:	.007 n-m
Dimensions:	12.7 cm x 14.2 cm by 2.54 cm thick

A drawing of the hard mount with flex bearings is shown in figure 4.13.4.1.2-4.

4.13.4.1.3 Spring Mount

The basic concept of a spring mount is illustrated in figure 4.13.4.1.3-1. The telescope is attached to the spacecraft by a set of springs distributed symmetrically about the optical axis. By making the springs very weak, the spacecraft can move relative to the telescope in response to crew movements, and only a minimum of this motion is transferred to the telescope. Slow movements, however, will be transmitted to the telescope, e.g., those caused by the orbital forces derived in subsection 4.13.3. Some basic problems in mechanization include the following:

a. Behavior of the spring system is very complex and difficult to predict analytically.

b. Designed specifically to operate in a zero-g environment, its operation will be difficult to prove in a ground-based test program.

c. This technique will operate only under quiescent conditions for the telescope. Initially, the telescope must have nearly zero momentum with respect to the orbit.

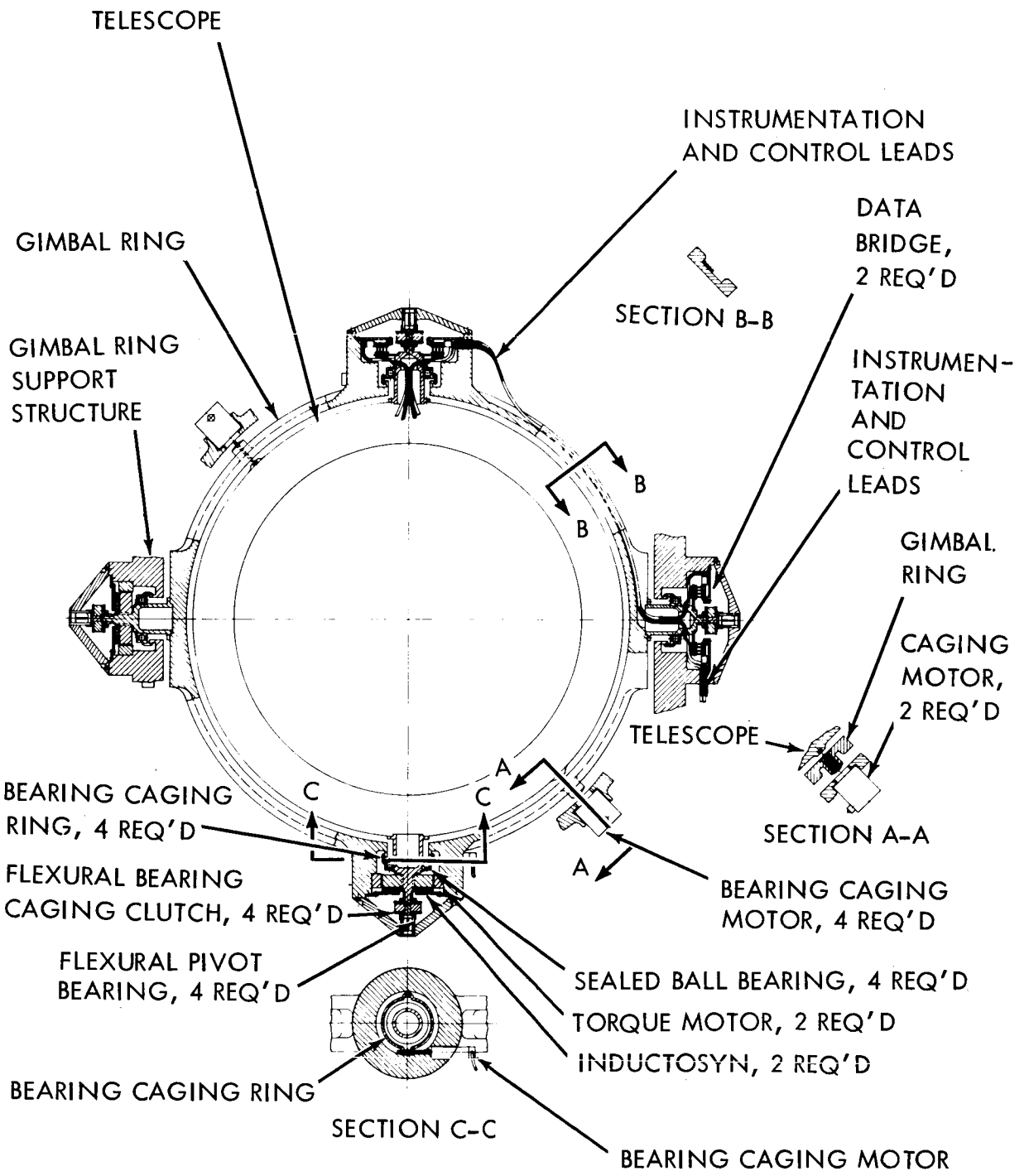


Figure 4.13.4.1.2-4. Hard Mount with Flex Bearings

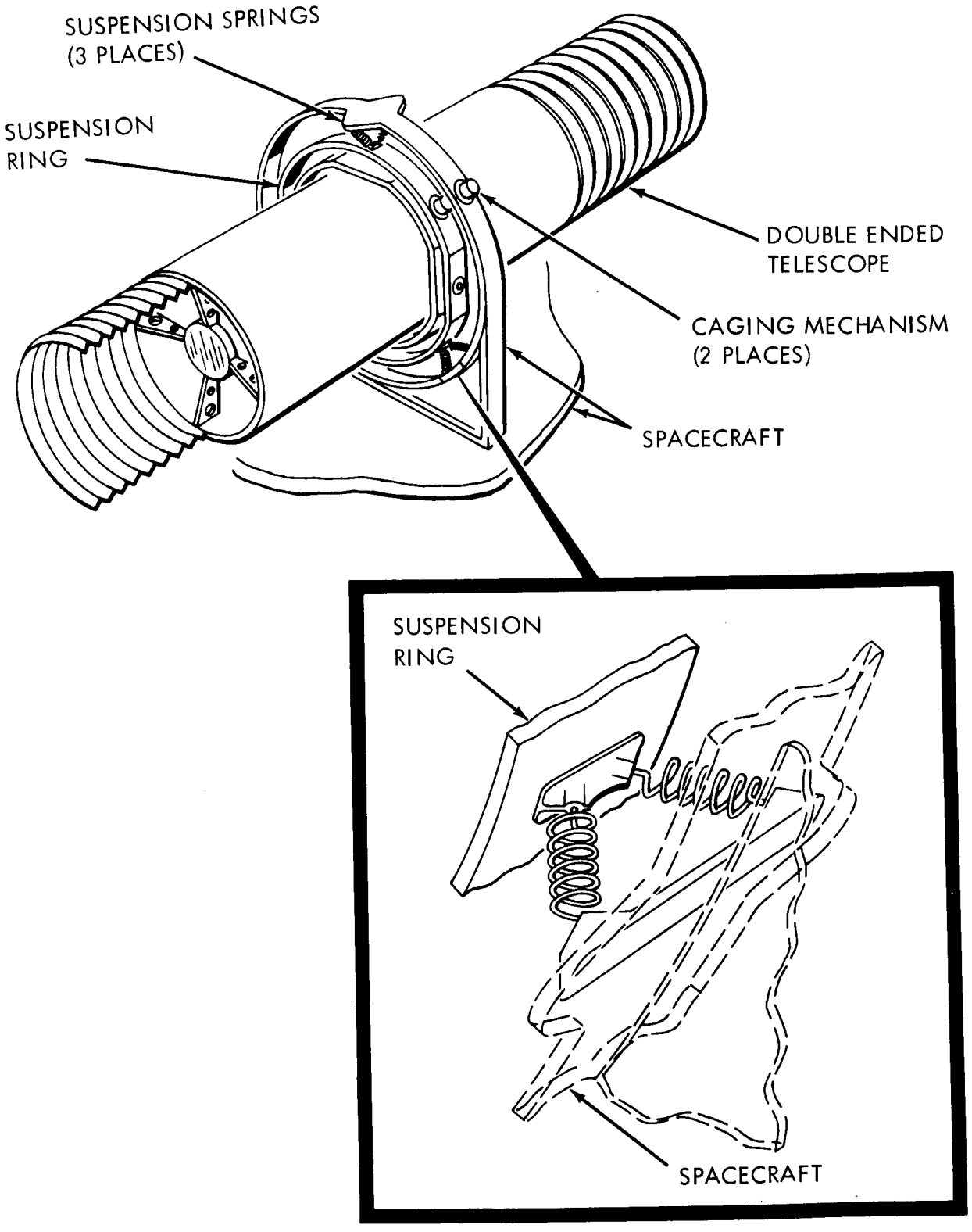


Figure 4.13.4.1.3-1. Spring Isolation

d. The only damping available is between the telescope and the spacecraft. Such damping will couple disturbances, especially impulsive disturbance, across the springs, thus tending to defeat the isolation objective.

e. Drive for the telescope cannot be coupled across the springs. Momentum storage devices on the telescope will couple with the spring action, creating a very complex dynamic system.

f. Conducting leads between spacecraft and telescope will tend to by-pass the springs.

g. Attitude of the telescope relative to the spacecraft must be sensed in order to provide an error signal to the spacecraft control system. There is not a well developed and simple technique available for doing this.

4.13.4.1.3.1 Analysis

The arrangement of springs discussed above will evidently meet the attenuation requirements as long as the springs behave ideally. Most of the analysis of this section is concerned with the departure of the spring system from the ideal.

This includes a geometric analysis to determine how the force varies in magnitude and direction with position of the telescope relative to the spacecraft spring attach points, an analysis of the coupling between translation and rotation, an analysis of standing wave effects and an investigation of damping problems.

Three pairs of springs equally spaced around the circumference of the telescope well are used, each pair arranged to give stiffness radially and axially. (See figure 4.13.4.1.3.1-1.) With initial tension in these springs, the arrangement will offer stiffness to rotation about the telescope axis.

For the arrangement of springs shown in figure 4.13.4.1.3.1-1, the effective axial spring constant K_a = (net) and the effective radial spring constant K_r = (net) are

$$K_a = (\text{net}) = 3\ K_a = 6\ K \sin^2 \phi,$$

and

$$K_r = (\text{net}) = 3\ K \cos^2 \phi$$

where K is the stiffness of an individual spring.

Since the tension in the spring does not alter the individual spring constants, the following static analysis assumes that initial tension is zero for calculations involving K_a and K_r.

The effective spring constants will in general vary during motion of the system. However, for displacements along the axis of the telescope the ef-

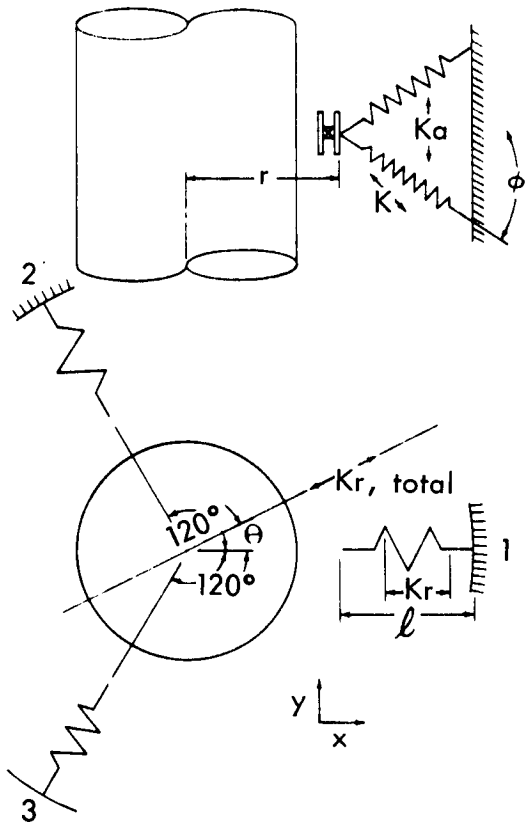


Figure 4.13.4.1.3.1-1. Spring Geometry

fective spring constant is essentially constant, i. e. for $0 \leq \Delta \leq 0.5$, $K_a = K_{oa} \pm 5\%$, where K_{oa} is the axial spring constant for infinitesmal displacements. Because of the anisotropy of the supports the effective radial spring constant will be a function of both the magnitude and direction of the radial displacement.

For radial displacement Δ made at an angle ϕ, the net force and torque exerted by the spring on the telescope are given by,

$$F = (\text{net}) = \left[\left(\sum_{i=1}^{3} F_{ix} \right)^2 + \left(\sum_{i=1}^{3} F_{1y} \right)^2 \right]^{\frac{1}{2}}$$

$$= r F_{iy} - \tfrac{1}{2} (F_{2y} + F_{3y}) + \frac{3}{2} (F_{3x} - F_{2x})$$

r = radius of telescope

F_{ij} = $j^{\underline{th}}$ (x or y) component of $i^{\underline{th}}$ spring force

$$F_{ix} = K (1 - 1/\ell_1) (1 - \Delta \cos\theta)$$

$$F_{iy} = K (1 - 1/\ell_1) (-\Delta \sin\theta)$$

$$F_{2x} = K (1 - 1/\ell_2) (-\tfrac{1}{2} - \cos\theta)$$

$$F_{2y} = K (1 - 1/\ell_2) (3/2 - \sin\theta)$$

$$F_{3x} = K (1 - 1/\ell_3) (-\tfrac{1}{2} - \Delta\cos\theta)$$

$$F_{3y} = K (1 - 1/\ell_3) (-\sqrt{3/2} - \Delta \sin\theta)$$

$$\ell_1 = (1 + \Delta^2 - \Delta 2 \cos\theta)^{\frac{1}{2}}$$

$$\ell_2 = \left[1 + \Delta^2 - 2\Delta\cos(120 - \theta)\right]^{\frac{1}{2}}$$

$$\ell_3 = 1 + \Delta^2 - {}^{2}\Delta\cos(120 + \theta)^{\frac{1}{2}}$$

If one expands $1/\ell_i$ by means of a Taylors series one obtains a second order expression for K_r (net) which is valid for Δ 0.1:

$$K_r (\text{net}) = K_r \left[2.25 + 3.375\Delta (1 - 4 \sin\phi^2) \cos\phi\right]^{\frac{1}{2}}$$

Table 4.13.4.1.3.1-1 gives the ϕ dependence K_r (net) /K for Δ = 0.1.

With the assumption of zero tension in the springs when the telescope is in its equilibrium position, the restoring torque τ about the telescope axis is negligible (See figure 4.13.4.1.3.1-2). A second order approximateion of this torque is identically zero.

TABLE 4.13.4.1.3.1-1

	K_r (net)/K_r
0 radians	1.6
$\pi/6$	1.5
$\pi/12$	1.4

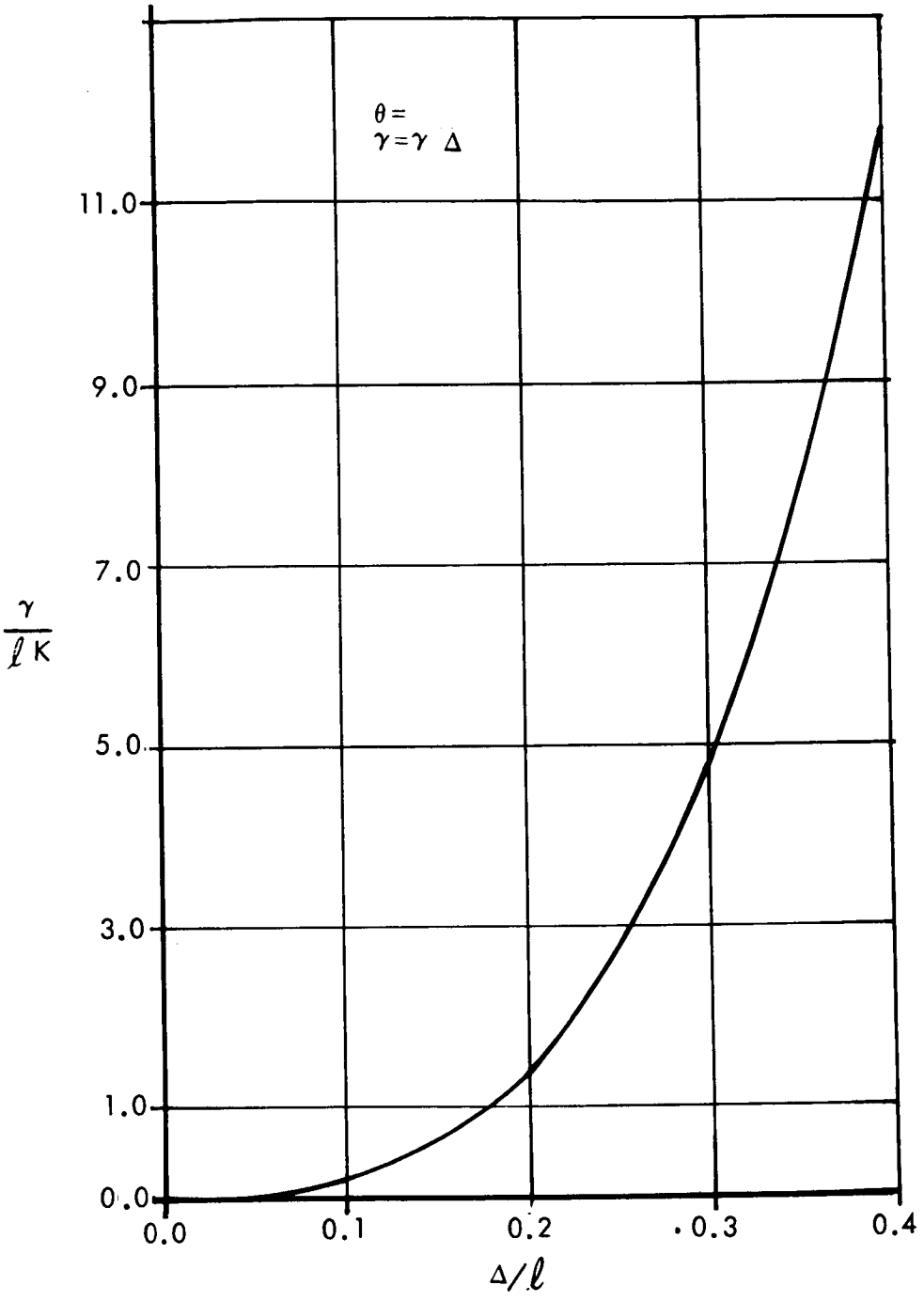


Figure 4.13.4.1.3.1-2. Roll Axis Restoring Torque

For larger displacements, the restoring torque about the telescope axis is proportional to Δ 2.82, where Δ is the linear displacement. (See figure 4.13.4.1.3.1-3). If one assumes initial tension in the springs, an angular displacement of the telescope about its axis produces a restoring torque $\tau = K_\phi r^2 \phi$, where K_ϕ is given by,

$$K_\phi / K_\Delta = 3 \quad \frac{\ell(1 - \cos\phi) + r(1-\cos\phi)}{\ell + r(1 - \cos\phi)} \quad \frac{\sin\phi}{}$$

,

See figure 4.13.4.1.3.1-4. In the absence of such initial tension, K_ϕ for infinitesmal rotations is zero.

Because of the anticipated control of rotation about the axis of the telescope, the analysis of the coupled modes is primarily concerned with the coupling of translational motion and rotation of the telescope axis about the center of mass of the telescope. Thus the motion of the system (sketched in figure 4.13.4.1.3.1-5) was investigated.

The solutions of the coupled equations of motion are $\beta = C_\beta \cos \omega_x t - \cos \omega_\beta t$

$$x = C_x \cos \omega_x t$$

where:

$$\omega_x = \sqrt{K/m}$$

$$\omega_\beta = \sqrt{K r^2 / I}$$

$$C_\beta = \frac{X_o \delta}{r^2 - \rho^2}$$

$$C_x = x_o$$

I = moment of inertia

ρ = radius of gyration

δ = axial separation of the center of mass and center of force.

Therefore the ratio of vertical rotation frequency to translational frequency, ω_β / ω_x, is 0.529 and the maximum vertical rotation amplitute is

$$\frac{x_o \delta}{249}$$

where δ is the axial separation of the center of mass and center of force. A similar analysis for the case of a radial δ was made and the results are identical to those given above.

When the forcing frequency becomes large compared to the natural frequency of the system; the assumption of a negligible inertial for the spring becomes progressively poorer. The finite inertial mass of the spring allows for resonant standing wave modes in the spring. These modes in the limit

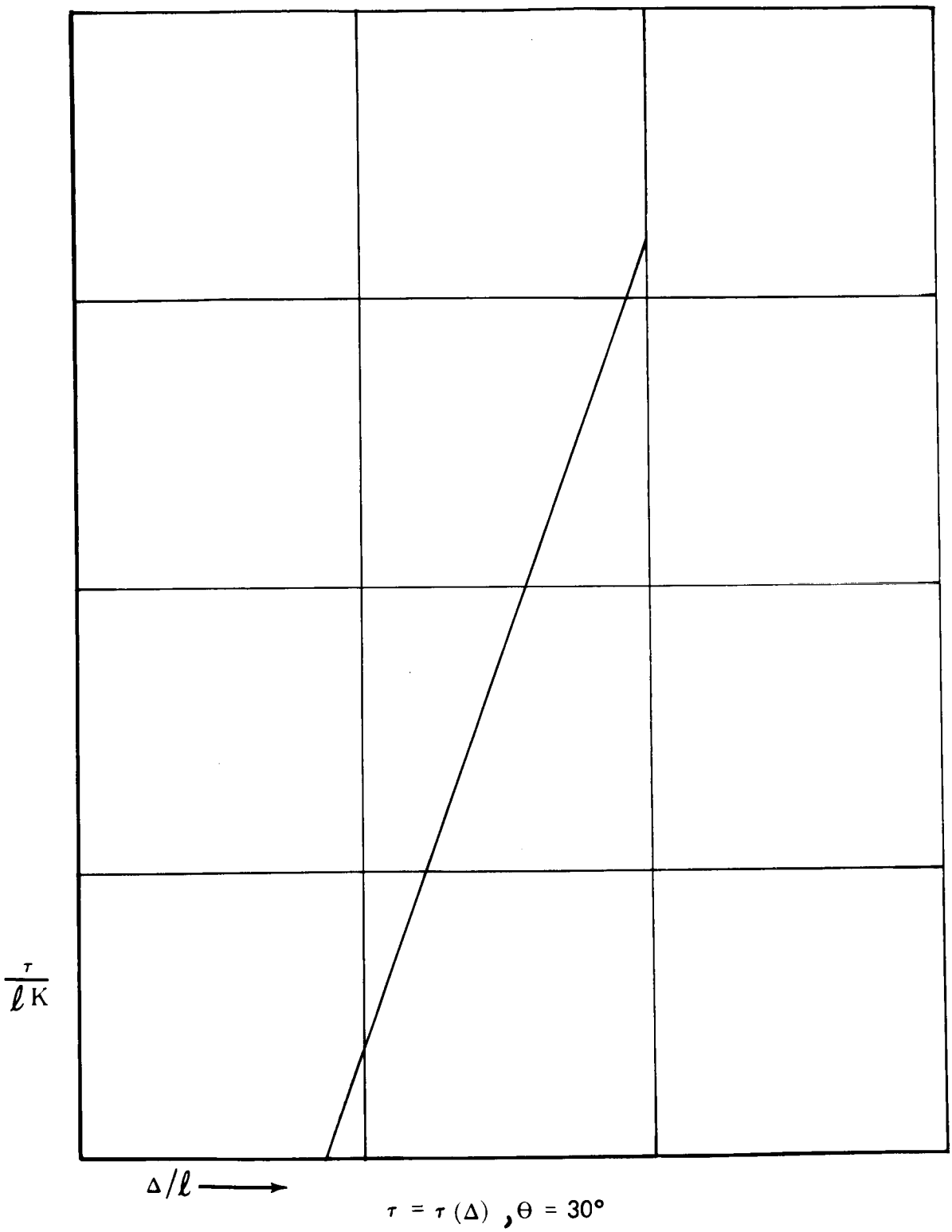


Figure 4.13.4.1.3.1-3. Restoring Torque (Log-Log Plot)

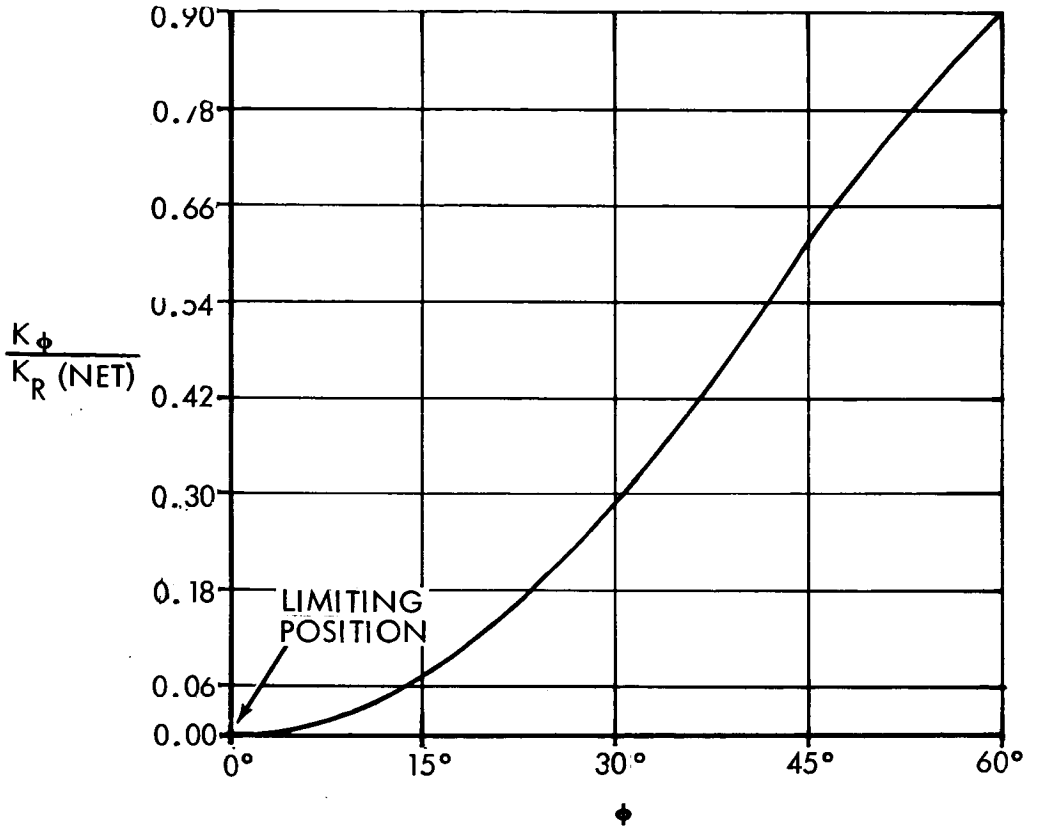


Figure 4.13.4.1.3.1-4. Restoring Torque (Initial Tension)

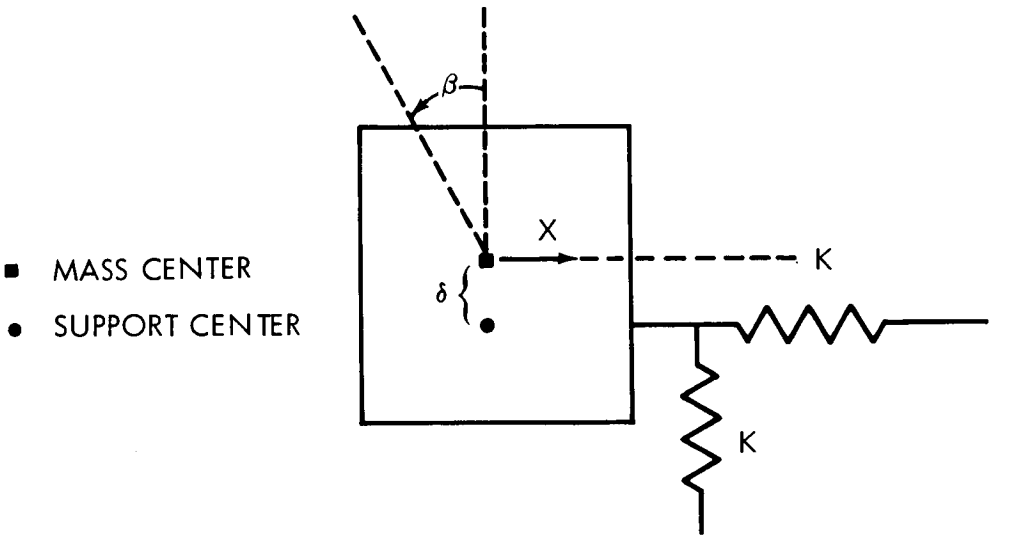


Figure 4.13.4.1.3.1-5. Dynamic Model

of zero internal and external damping cause the absolute transmissibility x_o/μ_o, to approach unit. x_o and μ_o are the amplitudes of motion of the isolated mass and support respectively.

The expression for the transmissibility in the undamped case is given below:

$$\frac{x_o}{\mu_o} = \frac{1}{\left[\cos^2\left(\frac{f}{f_o}\sqrt{\frac{m_I}{m}}\right)+\left(\frac{f}{f_o}\sqrt{\frac{m}{m_I}}\right)^2 \sin^2\left(\frac{f}{f_o}\sqrt{\frac{m_I}{m}}\right)\right]^{\frac{1}{2}}}$$

Where m_I is the mass of the isolator, m is the mass of the isolated system and f_o is the natural or resonant frequency of the isolator plus system. It is seen that resonant standing wave frequencies for which $\frac{x_o}{\mu_o} = 1$ are given by

$$\frac{f_{sw}}{f_o} = n\pi\sqrt{\frac{m}{m_I}}, \quad n = 1, 2, 3$$

Also one can see that for $f > f_o\pi\sqrt{\frac{m}{m_I}}$ the attenuation of the transmitted motion in the intervals between resonance goes as f^{-1} rather than f^{-2} which is the case for the inertialess isolator.

The presence of internal and external damping attenuates these modes and hence reduces the transmissibility. For high quality spring metal in a low strain state, the internal damping is negligible. Figure 4.13.4.1.3.1-6 illustrates the transmissibility for two cases: $\xi = 0$ and $\xi = 0.3$ where ξ is the fraction of the critical damping coefficient, $2\sqrt{K_m}$. These curves have been calculated assuming a mass of the suspended object (telescope) of 30 slugs and an effective spring mass of 1/16 slug.

Damping of the spring mount is an especially difficult problem because of the low frequencies at which the damping is to be effective. Also there is a mechanical problem in mechanizing a damper between the telescope and spacecraft with relative freedom in six degrees.

The tentative choice is eddy current damping using permanent magnets and thin rectangular plates.

The damping coefficient is given as

$$C = \frac{\sigma\beta^2 V}{2}$$

where

σ = electrical conductivity of the plates = $(1.7 \times 10^8 - \text{cm})^{-1}$

β = magnetic flux density = 0.1 webers/m^2

V = volume of damping plate within the magnetic field

= 3×10^{-4} m^3

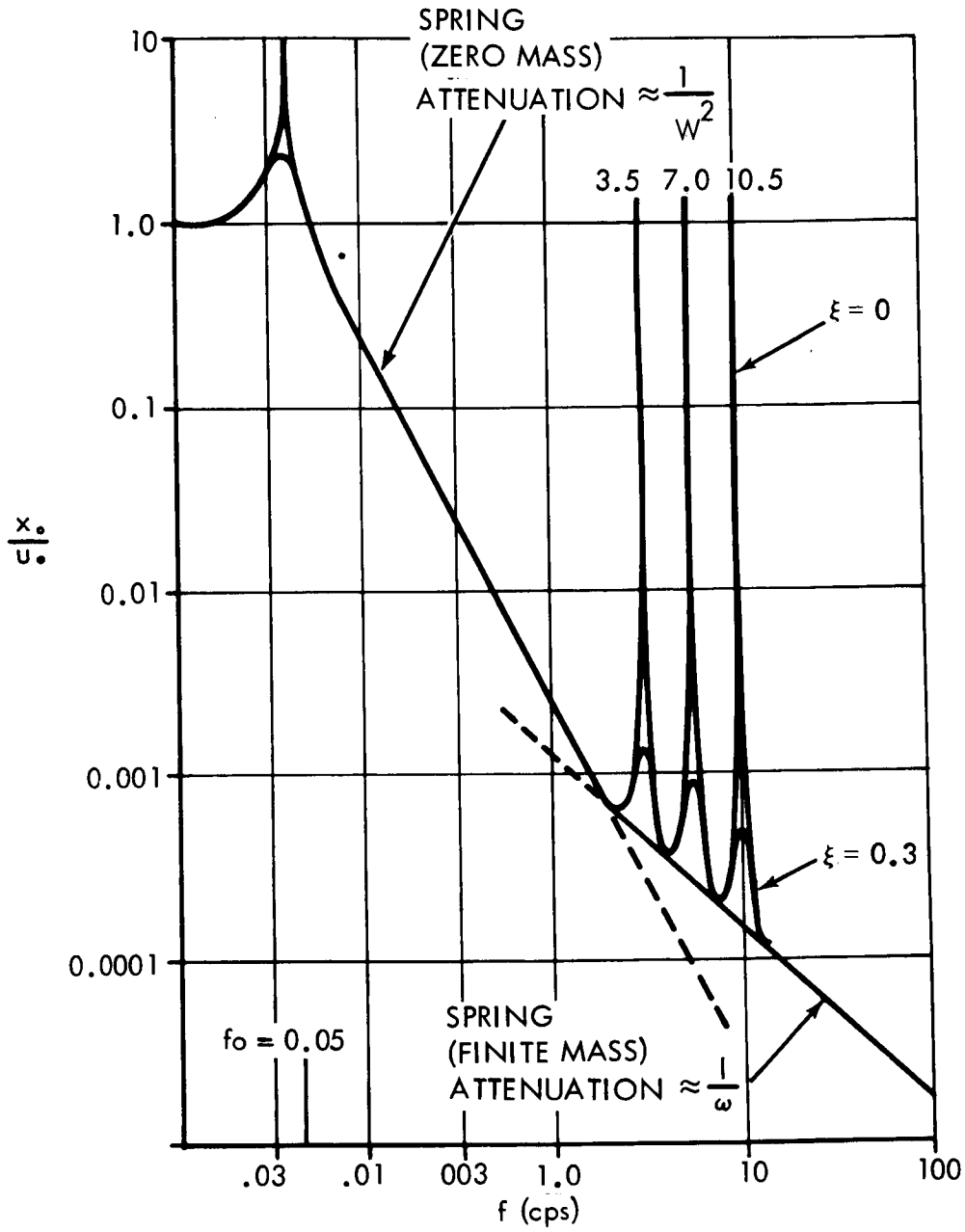


Figure 4.13.4.1.3.1-6. Transmissibility Curve for Case of Standing Waves

For the indicated values of the above parameters the damping coefficient C is 91 newton-sec/m. For a telescope with a mass m = 455 Kg (1000 lb) suspended by a spring with an effective spring constant K = 41 nt/m (0.1 lb/in), such damping could constitute a damping function = 0.34 of critical damping.

4.13.4.1.3.2 Design

The previous analysis shows that for small relative displacements, the departure of the spring system from the linear is essentially negligible. Also, as discussed in some detail in earlier sections, the relative movement between the telescope and the spacecraft is determined by crew movements and the amount of spacecraft stabilization that is provided. With an uncontrolled spacecraft and an unconstrained crew, this movement might be as much as three inches (for the baseline spacecraft considered here). This requirement can be relaxed by constraining man, by stabilizing the spacecraft, or both. The type of movements (uninhibited pushoffs) that cause large movements occur infrequently. Generally, during operational periods, the disturbance environment will consist primarily of random impulses distributed in time such that large excursions never occur. This means that most of the time the motion of the telescope support will be low amplitude, say, less than 0.5 inch.

Therefore, operation of the spring mount for the most part will be in the linear region, with occasional large swings. Because of this, the springs are designed for a working length of 12.7 cm and are installed under tension. The effective spring constant is chosen to be .035 Kg per M to meet the isolation requirements (factor of 100 attenuation at 1 cycle per second).

The design expression for the spring constant of a helical, round wire spring is given by:

$$K = \frac{G\ d^4}{8\ D^3\ N}$$

where:

K = spring constant = 0.1 lb/in

D = coil diameter = 1 inch

d = wire diameter

N = number of active coils = 25

G = torsion modulus of the material

With G = 11.5 x 10^6 psi for steel and 6 x 10^6 psi for beryllium copper, the required d is .109 cm for beryllium copper and .091 cm for steel. Thus K_a = (net) = K_r = (net) = .035 kg/m and the natural frequency f of the system is

$$f = 1/2\pi \sqrt{(0.2/m)} = 0.045 \text{ cps.}$$

For the two materials considered, an average solid height of 2.54 cm and an average coil weight of 5.4×10^{-4} Kg is assumed. Taking 1 inch for terminal connections and a working length of 12.7 cm, the tension in the spring is .135 kg. The lateral stiffness is estimated to be 1.75×10^{-3} kg/cm. Thus the maximum vertical deflection that results in a one-g environment when the spring is extended to its working length in a horizontal position is

$$\Delta = \left[W/N\ (0.01) \right] \left[N/2 \right] = 0.06 \text{ in.} = .15 \text{ cm}$$

where:

W = weight of one coil
N = (0.01) = lateral stiffness of one coil

The catenary sag for the same length and tension is 0.165 cm

A drawing of the spring mount as proposed in the experiment is shown in figure 4.13.4.1.3.2-1.

The telescope is mounted first in a set of mechanical gimbals to give two degrees of freedom. The outer gimbal is attached to a suspension ring, which in turn is suspended from the spacecraft structure by three pairs of springs to provide 6 degrees of freedom of the telescope relative to the spacecraft.

The system depicted incorporates a hard mount also. As discussed previously, reliability considerations and the requirement for a comparison reference dictate that the hard mount capability be provided. A locking mechanism is used to remotely engage/disengage the suspension ring on command from the spacecraft.

The springs are shown recessed into cups in the spacecraft structure, to conserve space in the telescope well. Subsequently, when integrating the experiment, it was decided to mount the telescope on which the suspension system is used (fine guidance telescope) outside the spacecraft with no provision for a pressure well.

The problem of power and data transmission across the telescope-spacecraft interface without interfering with the operation of the springs has not been solved. An attractive solution is to use the springs as electrical conductors. This will work in both principle and practice (See, for example, the electrobridge used on the hard mount), but the simple arrangement shown in figure 4.13.4.1.3.2-1 does not provide enough capability. Addition of more springs reduces the required size of each spring which also limits its current-carrying capability.

The maximum capability does not meet the requirements for all future applications. It is estimated that a laser telescope, for example, may require as many as a hundred conductors between the spacecraft and the telescope. Several alternate configurations to increase the power and data transmission capabilities were investigated. But each was discarded for one reason or another, and basically this is still a problem to be solved for the spring mount.

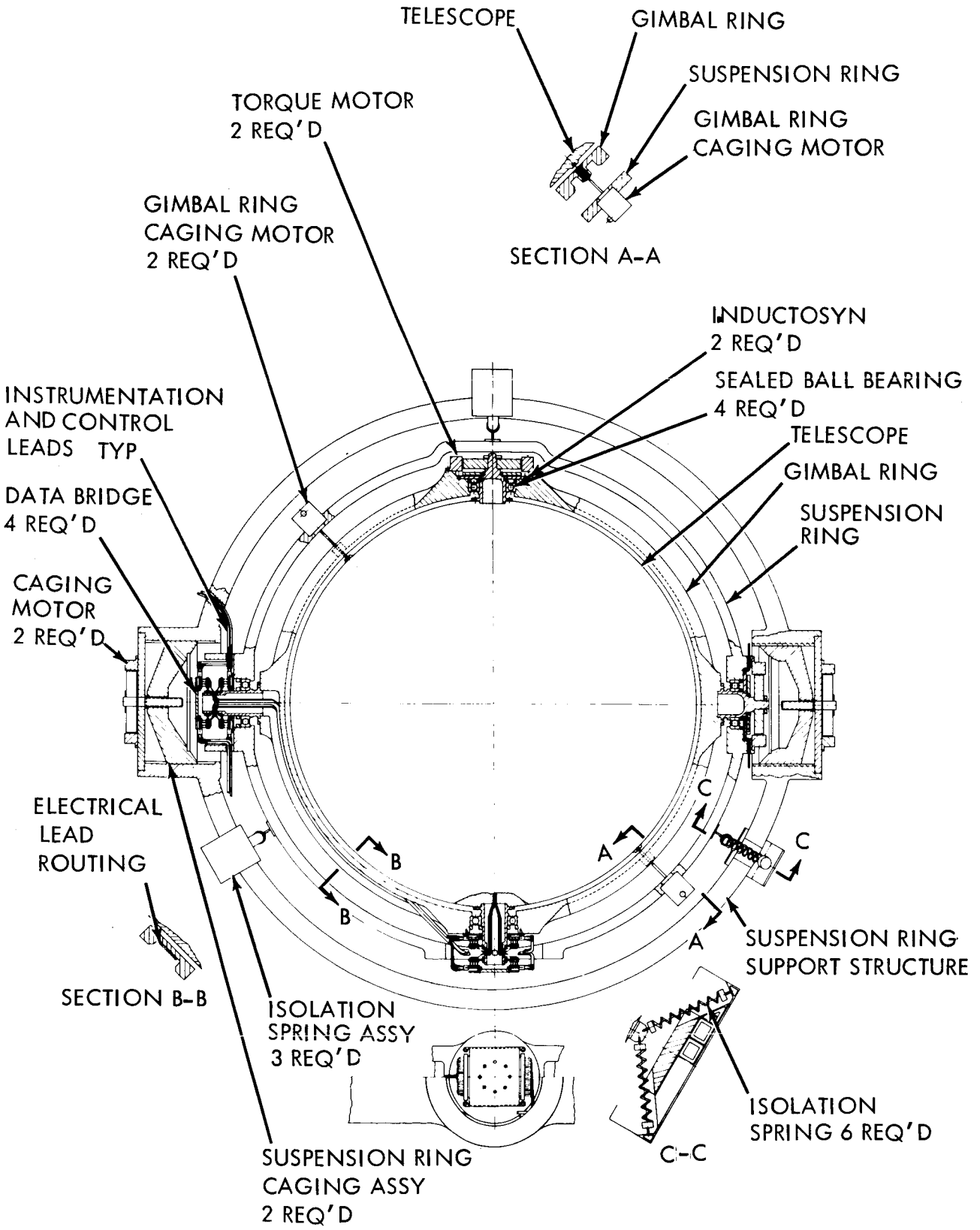


Figure 4.13.4.1.3.2-1. Spring Suspension

4.13.4.1.4 Diamagnetic Suspension

Operation of the diamagnetic bearing as a telescope mount suspension is illustrated in figure 4.13.4.1.4-1. An oval-shaped slug of diamagnetic material is suspended in a magnetic field which is created either by permanent magnets or electro-magnets. The field is configured such that a minimum flux density occurs at the geometric center of the bearing. Since a diamagnetic material tends to seek the field minimum the shaft tends to stay centered.

Operation of the bearing is similar to that of the spring mount. The magnetic force lines may be thought of as a continuium of spring distributed around the shaft. The diamagnetic bearing has certain advantages relative to the spring mount. It has no moving parts and by use of permanent magnets can be made completely passive. Therefore its operation should be very reliable. Also, since the "springs" are massless, many of the secondary characteristics of lumped springs discussed in section 4.13.4.1.4 need not be considered. Actual operation of the bearing will then more nearly approach ideal operation and is therefore more predictable.

However, considered objectively, it still has the disadvantages of an ideal spring system, the principal one of which is the problem of transmitting power and data across the telescope/spacecraft interface. The principal limitation of the diamagnetic suspension is the maximum restoring force that can be achieved with a practical bearing configuration. This is a fundamental limitation that may prevent use of the bearing, especially in low orbits where the space operating environment departs appreciably from zero-g conditions.

Because of the limited load bearing capabilities of the diamagnetic bearing, considerable effort was directed to analysis of the orbital environment in which the bearing will operate. This analysis is covered in detail in section 4.13.3.2. There it is shown that a realistic value for the "static" bearing load may be as great as 10^{-3} lbs.

Theoretical and experimental work were performed for the diamagnetic bearing. The purpose of both was to determine the magnitude of the static force capability. The configuration chosen for laboratory tests was dictated by the availability and cost of components and is shown in figure 4.13.4.1.4-2.

A typical test run is shown in figure 4.13.4.1.4-3. The maximum force obtained with this set up for any of the runs was less 0.2 grams. Though this is a rather crude experimental setup, and far from optimum, the results indicate a fundamental limitation of the bearing which is the low magnitude forces that can be obtained. As shown previously, the maximum orbital forces for low orbits is about 10^{-3} lbs. At synchronous altitudes this is reduced to about 10^{-5} lbs.

The configuration chosen for theoretical analysis was dictated by the practical difficulties of analyzing a magnetic field. The problem is approached as follows.

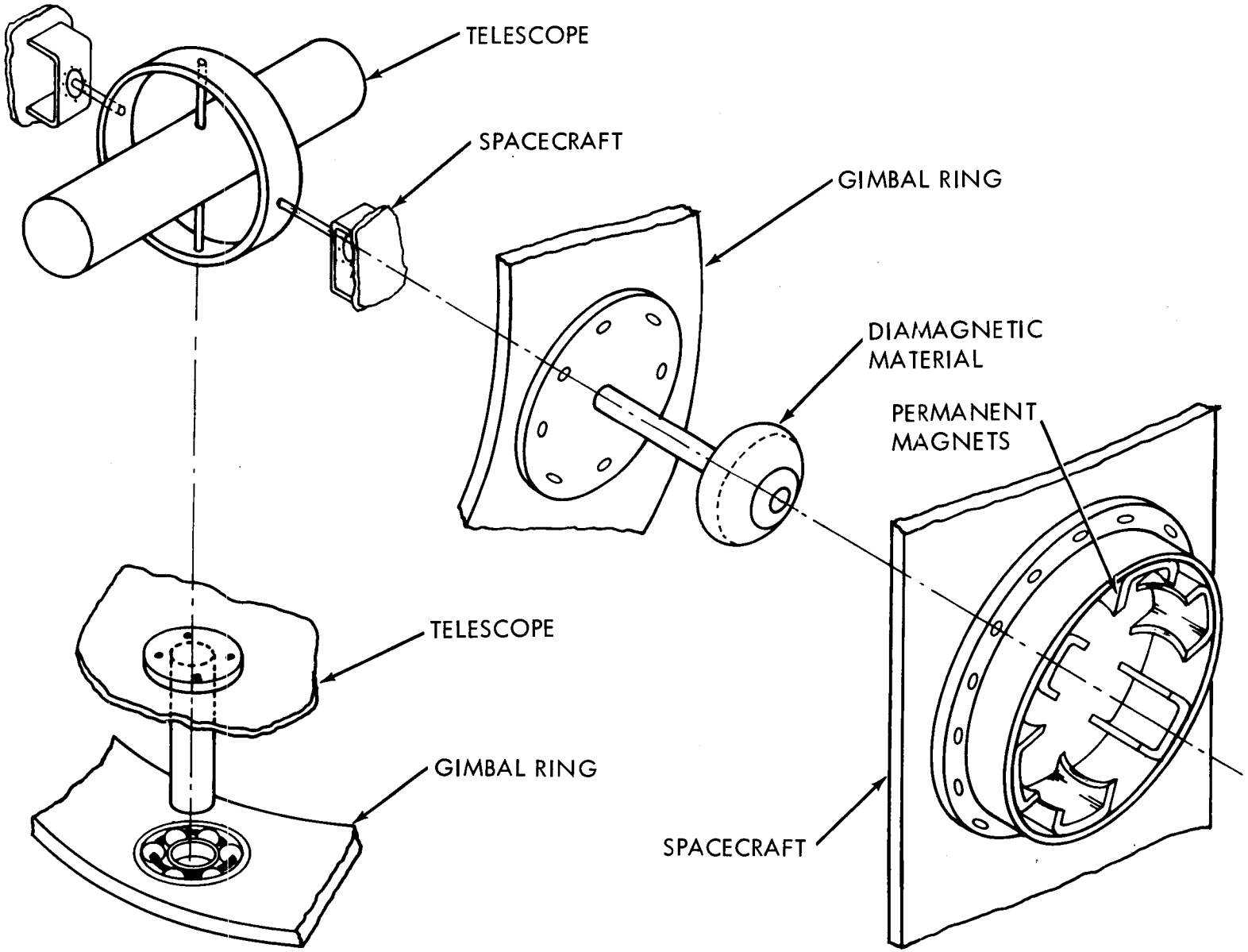
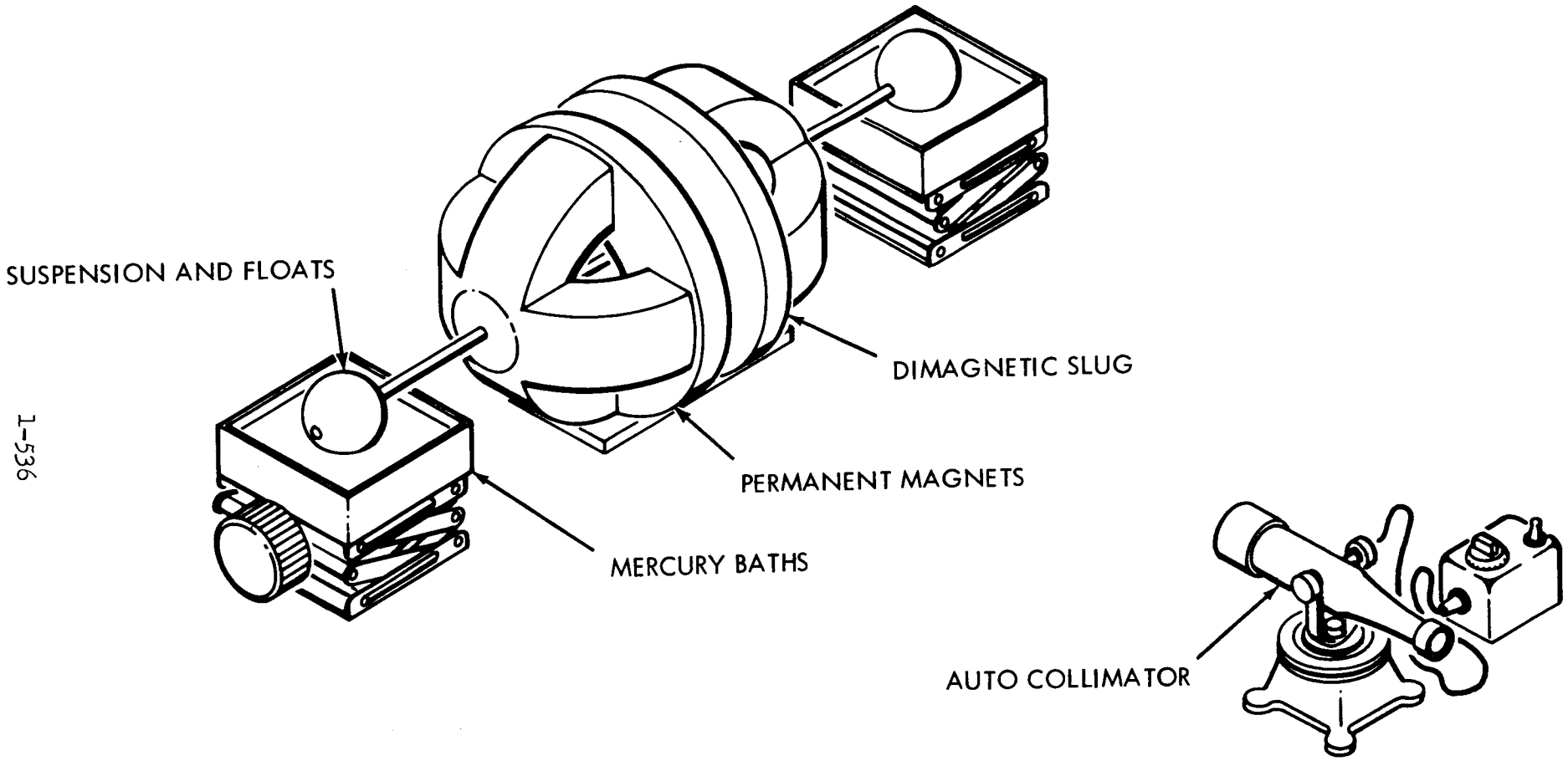


Figure 4.13.4.1.4-1. Diamagnetic Bearing Suspension



1-536

Figure 4.13.4.1.4-2. Diamagnetic Bearing Test Set Up

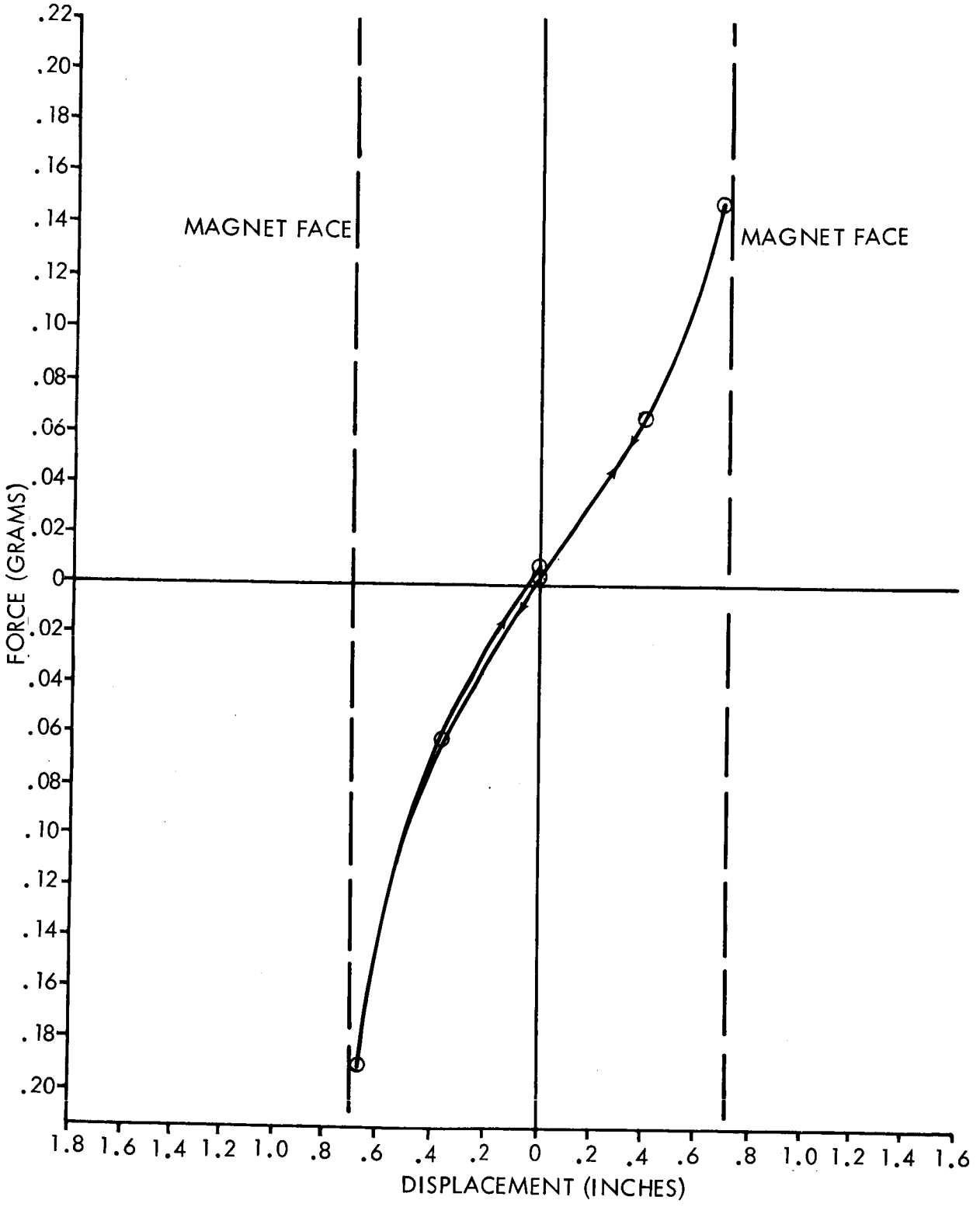


Figure 4.13.4.1.4-3. Typical Experimental Force Curve

If the field density is B_o and the permeability μ_o inside a volume ΔV, then the potential energy of the field inside the volume is

$$E_o = \frac{1}{2} \frac{B^2_o}{\mu_o} \Delta V \qquad (1)$$

If the volume is replaced with a material of permeability μ, the change in energy is

$$\Delta E = \frac{1}{2} B^2_o \left(\frac{1}{\mu} - \frac{1}{\mu_o} \right) \Delta V \qquad (2)$$

The factor $\frac{1}{\mu} - \frac{1}{\mu_o}$ can be expanded in powers of $\mu - \mu_o$ as

$$\left(\frac{1}{\mu} - \frac{1}{\mu_o} \right) = \frac{\mu - \mu_o}{2_o} + \frac{(\mu - \mu_o)^2}{2 \mu^3_o} + \cdots \qquad (3)$$

Retaining only the linear approximation since $|\mu - \mu_o| << 1$ and recognizing $\mu - \mu_o = x$ as the magnetic susceptibility

$$\Delta E = \frac{1}{2} \frac{x}{\mu 2_o} B^2_o \Delta V \qquad (4)$$

The total energy in the diamagnetic slug is obtained by integration over the volume

$$E = \frac{1}{2} \frac{x}{\mu 2} \int B^2_o \, dv \qquad (5)$$

and the force in the x-direction is given by

$$F_x = \frac{\partial E}{\partial x} \qquad (6)$$

The basic difficulty of theoretical analysis is analytically describing the field for a practical configuration and carrying out the integration. It was found that the only practical approach is to choose a configuration which gives spherical symmetry and expand the field in a series of Legendre polynominals. The configuration shown in figure 4.13.4.1.4-4 was analyzed in this way.

Along the z axis,

$$B_z = B_s \sum_{n=0,2,4,\cdots}^{\infty} {}^{n} \Big[(\mu_1 \; P_{n+1} (\mu_1) - \mu_2 \; P_{n+1} (\mu_2) + P_{n+2} (\mu_2) - P_{n+2} (\mu_1) + (\mu_4 \; P_{n+1} (\mu_4) - \mu_3 \; P_{n+1} (\mu_3) + P_{n+2} (\mu_4) + \cdots + (\mu_N - 1 \; P_{n+1} (\mu_N - 1) - \mu_N \; P_{n+2} (\mu_N) + P_{n+2} (\mu_N) - P_{n+2} (\mu_N) - P_{n+2} (\mu_{N-1}) \qquad (7)$$

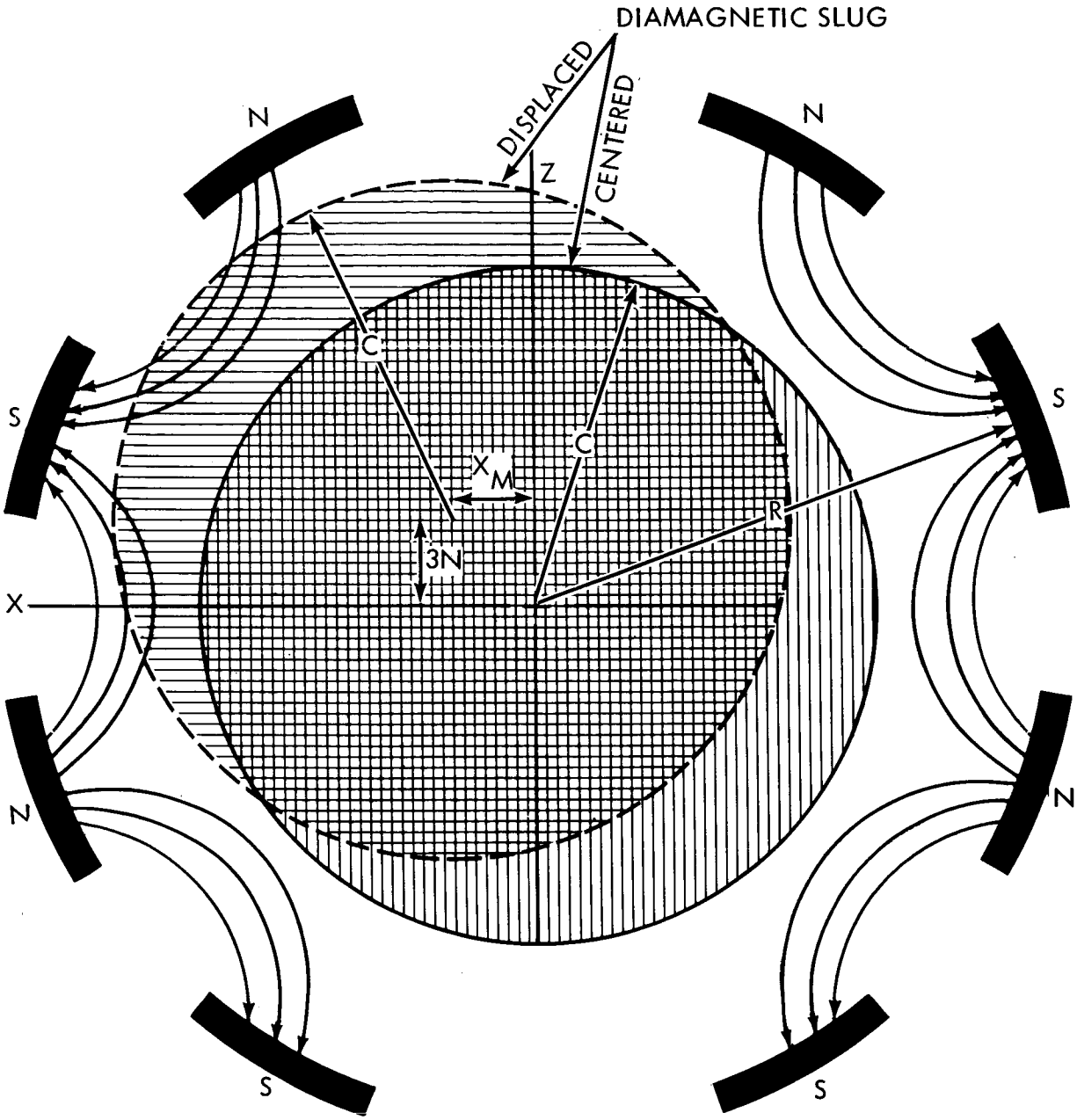


Figure 4.13.4.1.4-4. Cross-Section of the Magnetic Configuration Used in Analysis

where B_s is the pole-face intensity, $\rho = z/R$, R is the magnet radius, z is the point on the axis where the field is being calculated, and N is the number of poles. $P_n(\mu)$ is the Legendre Polynominial defined as

$$P_n(\mu) = \sum_{s_i=0}^{m} (-1)^s \frac{(2n-2s)!}{2^n (s!)(n-s)!(n-2s)!} \mu^{n-2s} \tag{8}$$

where $m = \frac{1}{2}n$ or $\frac{n-I}{2}$ whichever is an integer

and,
$$\mu_1 = \cos\left(\frac{\pi}{2N+1}\right)$$
$$\mu_2 = \cos\left(\frac{2\pi}{2N+1}\right) \tag{9}$$
- - - - - - - - - -
$$\mu_N = \cos\left(\frac{N\pi}{2N+1}\right)$$

Rewrite the above equation as

$$B_z = B_o + B_2 P^2 + B_4 P^4 + - - - - + B_\ell P^\ell \tag{10}$$

where B_ℓ is the last coefficient to be calculated and shouls satisfy $\left|B_\ell \rho^\ell\right|^\ell << B_o$, say, the last term should not affect the sum in the third siginificant digit.

Once the series, has been determined for a given N, the field at any point (r,ϕ) may be determined as

$$B(r,\phi) = B_o + B_2 P_2(\cos\phi)\left(\frac{r}{R}\right)^2 + B_4 P_4(\cos\phi)\left(\frac{r}{R}\right)^4 + ---+ B_\ell P_\ell (\cos\phi)\left(\frac{r}{R}\right)^\ell \tag{11}$$

The Legendre Polynominals $P_n(\mu)$ can be taken from a table or can be calculated using the recurrence formula

$$n P_{n-1} + (n+1) P_{n+1} = (2n+1)\mu P_n \tag{12}$$

A number of configurations, including the one shown in figure 4.13.4.1.4-4 was analyzed on a digital machine. Generally, the analytical work confirms the experimental. The maximum force for a practical permanent magnet configuration is considerably less than one gram. This can perhaps be increased by one order of magnitude by optimizing a configuration. By going to electromagnets, the maximum force capability might further be increased by a factor of 5. Still, the static force capability of the diamagnetic is marginal for the worst orbital environment that might be encountered in low orbits.

Therefore, no effort was made to design an actual experiment which incorporates the diamagnetic bearing. This is not to say, however, that effort in this area should be discontinued. The diamagnetic bearing or suspension system has several properties which make it nearly ideal for this type of application. In addition to the simplicity, reliability, long life and low cost, the field of the magnets can be shaped so as to obtain a spring constant which increases sharply with displacement from the equilibrium position. This means that the bearing can provide nearly perfect isolation under normal operating conditions but still prevent both telescope-spacecraft separation under the influence of orbital forces and telescope-spacecraft collision caused by crew activity. Because of these advantages more effort should be expended on ways to increase the static-force capability. Also. a detailed operational procedure should be performed for a baseline mission. The analysis of the external environment given in section 4.13.5 is very detailed but fairly general with no attempt to analyze the forces on each axis as a function of time.

Such an analysis for a specific configuration might show that the diamagnetic bearing actually exhibits enough static support capability for use as a telescope isolation system.

4.13.4.1.5 Active Suspension System

An active suspension system is one that requires electrical power for its operation and consists of some form of electromagnetic support. The basic principle of magnetic support can be used in several distinct ways to achieve the desired isolation between the telescope and the spacecraft. These include the electromagnetic bearing of magnesyn, the electromagnetic soft mount, and the electromagnetic servo suspension.

The electromagnetic bearing would be used in a hard mount (as magnesyns are used to support the float in one type of floated inertial-grade gyroscopes.) Such a bearing will support both the static and dynamic loads encountered in most space optics applications of the type considered in this study. However, this will eliminate only one source of pointing disturbance, namely, stiction and coulomb friction associated with ball bearings. This does not solve the problem of how to pass conducting leaks between the spacecraft and the telescope. Neither does it solve the problem of unbalance torques. As shown in section 4.13.4.1, even with a friction-free bearing some attenuation of man-produced disturbances is still required. Therefore, this particular bearing was not studied in any detail here. That is, it was assumed that such a bearing, even if feasible and perfect, would not meet the requirements under the guidelines established.

This does not mean, however, that further study of this bearing should not be pursued. If,for example, the electro-bridge or a similar device can be used with this bearing to solve the power and data transmission problem without introducing too much restraining torque and some means of automatic balancing the mount during operation can be devised, the magnesyn support might effect the required isolation between the telescope and the spacecraft.

This is one approach that definitely should be pursued in the overall problem of isolating a telescope from spacecraft-induced disturbances. There was not enough time to pursue it any further in the present study.

The electromagnetic soft mount uses the magnesyn principle but in a different mode of operation.

In the bearing application discussed above, the rotor and stator of the magnesyn are separated by a very small airgap, and the bearing must support the full dynamic loads encountered in operation. In the configuration to be discussed now, about a half-inch clearance is maintained between the stator and rotor, and the rotor, which is attahced to the telescope, is allowed to the spacecraft. In other words, the magnesyn soft support operates very much like the spring suspension and the diamagnetic suspension. Much of the discussion and analysis presented for the springs applies here also. The analysis presented below is concerned mostly with establishing feasibility of the approach by showing that the required spring constant can be obtained with a practical configuration.

The microsyn magnetic suspension was originally developed at the Instrumentation Laboratory, MIT, by Dallas Draper and associates as a nearly frictionless axial support for floated gyros and accelerometers.* A schematic of a four pole a.c. microsyn is shown in figure 4.13.4.1.5-1. Each pole is wound with an energizing coil which is connected in series with a capacitor C. This is illustrated in figure 4.13.4.1.5-2a. The frequency of the energizing current I is chosen such that when the central rotor or keeper is in its equilibrium position, the inductive reactance L is greater than the capacitive reactance 1/ c. In fact, to expedite the calculations, the upper 1/2 power point is generally chosen as the equilibrium operating point as is indicated in figure 4.13.4.1.5-2b.

It should be pointed out that in general this is a case of unstable equilibrium since the forces exerted by each pole on the keeper are attractive and become unbalanced with the slightest motion of the keeper away from the magnetic center. It is only the presence of the capacitor in this reactive circuit that produces dynamic stability. If the keeper suffers a displacement such as that shown in figure 4.13.4.1.5-1, the inductance of coils 1 and 4 increases and correspondingly, that of coils 2 and 3 decreases. Because of the choice of operating frequency, I_1 and I_4 decreases and I_2 and I_3 increases, thereby lessening the attractive force of poles 1 and 4 and increasing the attractive force of poles 2 and 3 for the keeper. This is illustrated in figure 4.13.4.1.5-2b. In effect there results a net restoring force toward the magnetic center.

In order to illustrate the above qualitative discussion, we include an outline of the calculation of the restoring force for a multipole microsyn suspension and also numerically calculate an effective spring constant.

The radial attractive force, F_r, exerted by each pole on the keeper is simply given by

$$F_r = \frac{\partial W_g}{\partial g} \qquad (1)$$

* Air Space and Instruments ed. Sidney Lees, McGraw Hill, 1963 pps. 312-333.

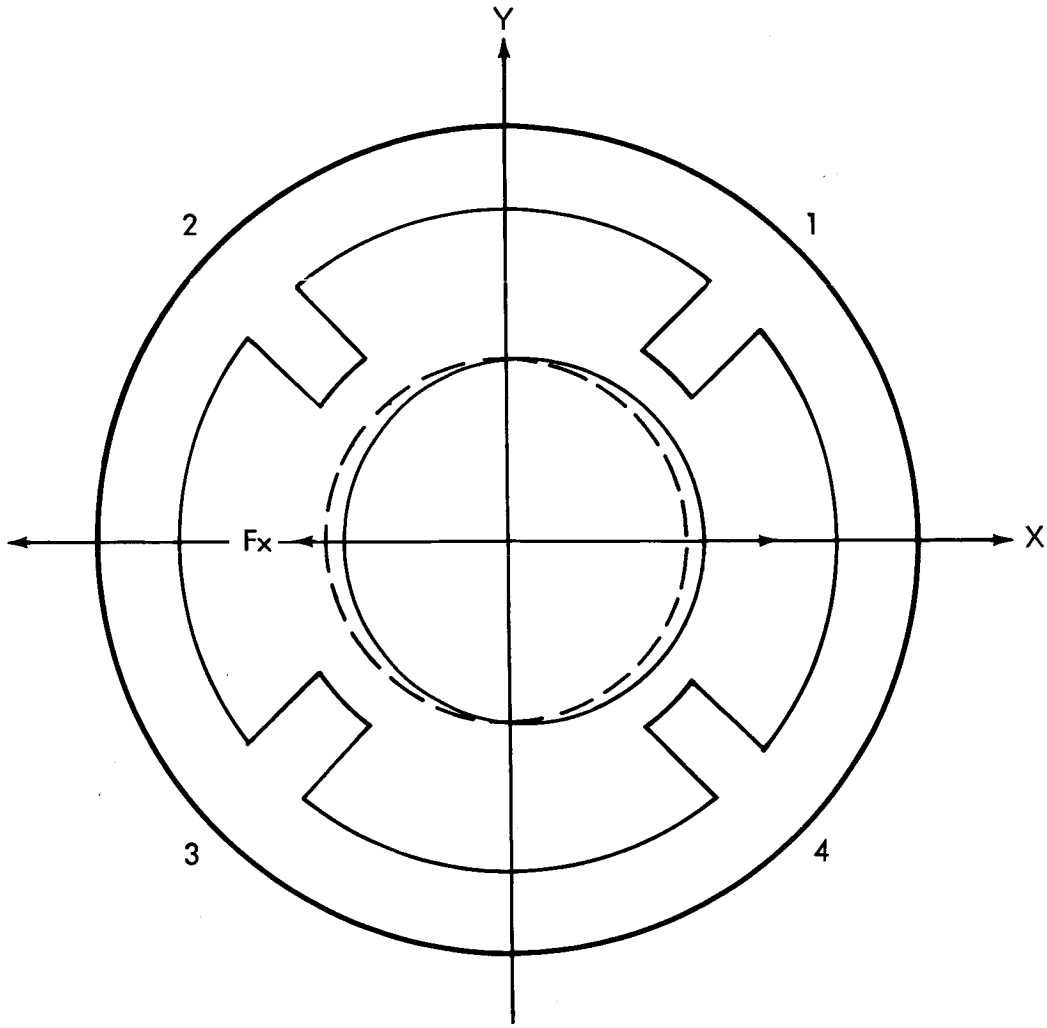


Figure 4.13.4.1.5-1. Four-Pole Microsyn

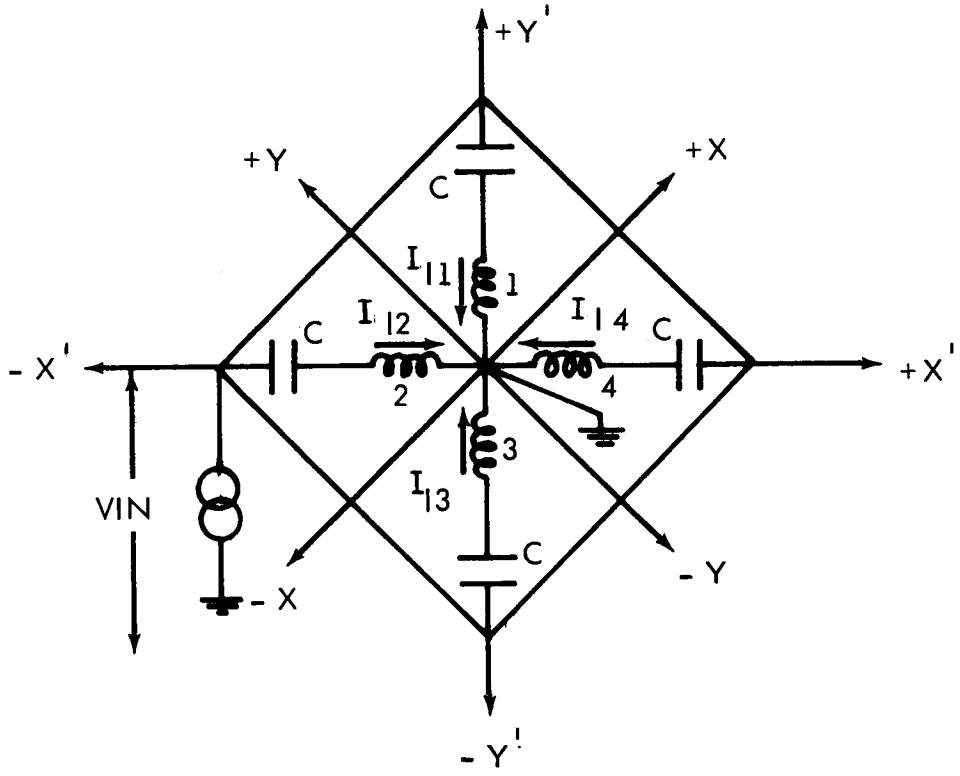


Figure 4.13.4.1.5-2a. Circuit Diagram

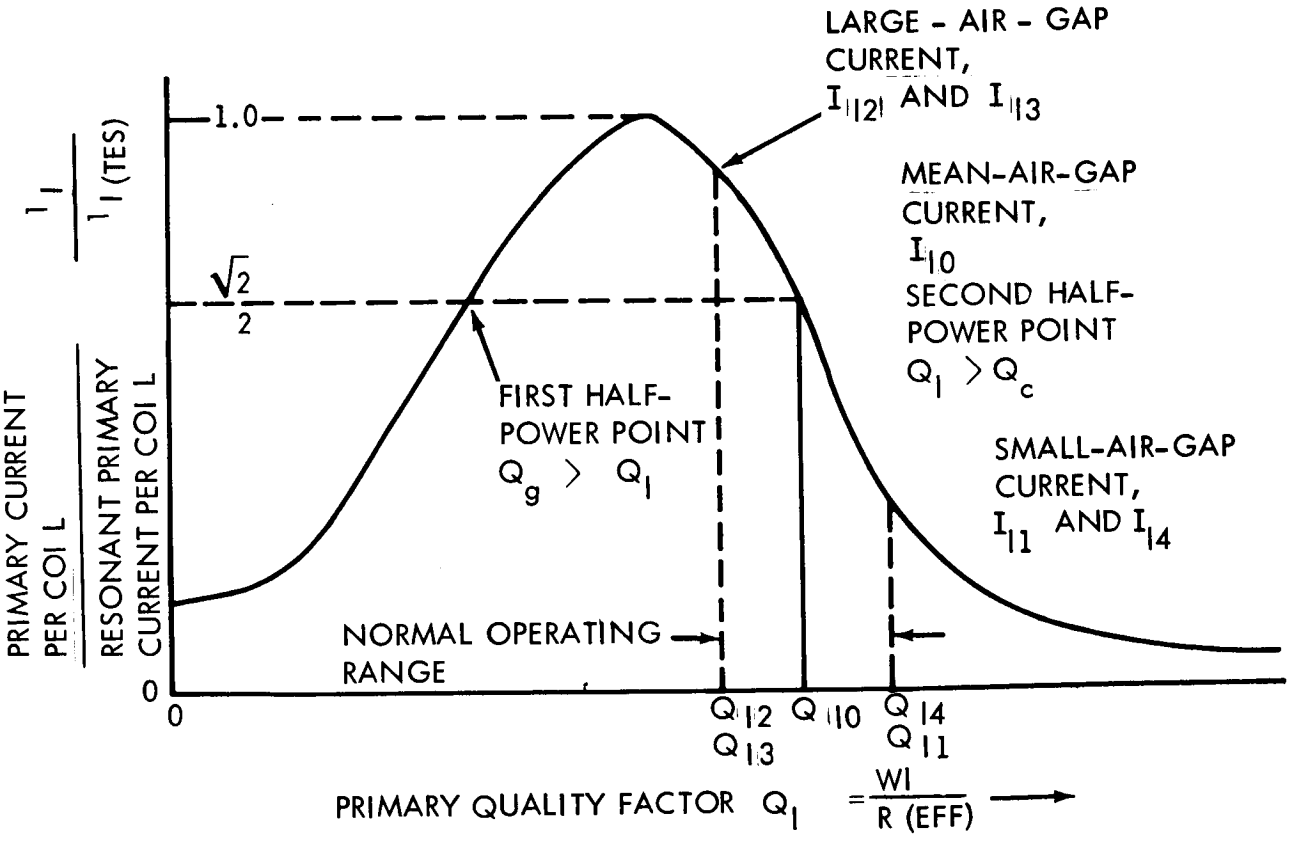


Figure 4.13.4.1.5-2b. Coil Current

where

W_g = magnetic energy in the air gap

g = air gap length.

Further, W_g may be written as,

$$W_g = 1/2\ (mmf)^2_g\ P_g \qquad (2)$$

where $(mmf)_g$ = air gap magnetomotive force

P_g = air gap permeance.

In the approximation that the reluctance of the flux path through the iron is negligible.

$$(mmf)_g = NI \qquad (3)$$

and

$$P_g = \frac{\mu_o\ \pi\ a^2}{g} \qquad (4)$$

where NI is the ampere turns of the coil, a is the radius of the pole face and μ_o is the permeability of free space, $4\pi \times 10^{-7}$ $\frac{\text{webers}}{\text{amp-meter}}$,

Hence,

$$\left|F_r\right|_i = \tfrac{1}{2} \left(\frac{NI}{g}\right)^2_i \mu_o \pi a^2 \ ; \ i = 1,2,3,4 \qquad (5)$$

The ratio of the current I to its resonant value, ie.e., where

$L\omega_{res} = \frac{1}{\omega_{res}\ C}$ is given by

$$\frac{I}{I_{res}} = \frac{1}{1 + j\ (Q_L - Q_C)} \qquad (6)$$

Where $Q_L = \frac{\omega L}{R_{eff}}$

$Q_c = \frac{1}{C\ R_{eff}}$

ω = excitation frequency = $\omega + 1/2$

C = capacitance of series capacitor

R_{eff} = the effective power dissipation coefficient of the circuit (which includes core losses)

Figure 4.13.4.1.5-2b is a graphical illustration of equation (6). Under optimum conditions $R_{eff} = 2\ R_{dc}$ where R_{dc} is the dc coil resistance.

For positive x displacements of the keeper,

$$Q_{L1} = Q_{L4} = \frac{1}{1 - x/g_o \cos \pi/4} Q_{Lo}$$

$$Q_{L2} = Q_{L3} = \frac{1}{1 + x/g_o \cos \pi/4} Q_{Lo} \qquad (7)$$

Where g_o is the equilibrium gap width.

It should also be noted that at $\omega = \omega + 1/2$, $Q_L = Q_c + 1$. In the linear approximation it is easily shown that the net restoring force is given by

$$F_x \text{ (net)} = - \left(\frac{N I_o}{g_o} \right)^2 P_o \ (Q_{Lo} - 2) \ x \qquad (8)$$

Similarly for a small arbitrary radial displacement

$$F_r \text{ (net)} = - \left(\frac{N I_o}{g_o} \right) P_o \ (Q_{Lo} - 2) \ r \qquad (9)$$

For an eight pole suspension the analysis produces essentially identical results except for a factor $2 \cos^2 (\pi/8)$ which multiplies the right hand side of equation (9).

From an examination of equation (9) one can see that the quality factor of the coil serves as an amplification factor for the restoring force and for a stable suspension system must exceed 2. Hence one would be tempted to design a system with a large Q_{Lo}. However, one finds that for large displacements, i.e., in the non-linear approximation, there is a "softening" of the effective spring constant and in fact the restoring force reaches a maximum value at a relative displacement r/g_o for which $\omega L' = \frac{1}{\omega c}$ where L' is the inductance of the coil(s) withe a widening gap. This displacement is roughly given by

$$r/g_o \cong \frac{1}{(Q_{Lo} - 1)} \qquad (10)$$

With a further increase in radial displacement, the net force then decreases to zero and may become positive before the keeper comes to rest against the near poles. This unstable behavior for large displacements occurs only when $Q_{Lo} \gtrsim 5$.

Therefore one must employ a system with a relative low QLo value (between 2 and 5) in order to have a stable suspension system over the full range of relative displacements.

Figure 4.13.4.1.5-3 illustrates the full restoring force versus displacement curve for a circuit with a $Q_{Lo} = 2.54$. The small-displacement spring constant given by the initial slope is $K = 18 \frac{nt}{m} \cong 1 \frac{lb}{in}$.

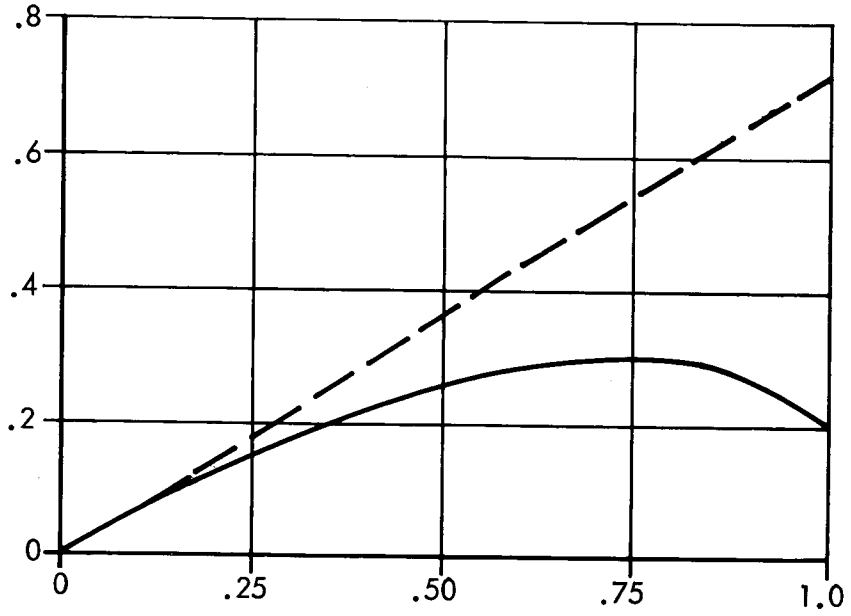


Figure 4.13.4.1.5-3. Restoring Force Versus Displacement

Below are given the other values for the pertinent parameters:

P = power dissipated per coil = 50 watts

ρ = resistance/meter = 1Ω (approximately 20 gauge wire)

N = 3280 turns

L_o = 1.73 henries

$\omega + \frac{1}{2}$ = 2500 rad/sec.

a = g_o = 0.04 meters

C = 0.158 μfa rads.

This suspension system for motion in the plane of figure 4.13.4.1.5-1 is stable over the entire range of allowed displacements and its initial effective spring constant has approximately the same value as that of the previously discussed mechanical suspension system which utilized helical springs.

Like the other suspension systems previously considered, achieving the required damping is a particular problem. In the more conventional application of this type support in floated gyros, radial viscous damping is provided by the fluid. For this application the straight-forward approach is again to use eddy current damping as discussed for the spring mount. The damping coefficient C is given by

$$C = A \bar{B}^2 \sigma V$$

where

A = dimensionless constant of about unity.

$\bar{B}$ = average flux density within the conducting medium

V = Volume of the conducting medium

σ = electrical conductivity.

The quadrapole configuration of a magnesyn suspension supplies the spatially varying field that is required, and the soft iron keeper should adequately serve as the conducting medium.

The magnesyn as analyzed above would behave similarly to the spring mount but without some of the second-order effects associated with the mechanical springs. It also has the same disadvantages as for example the power and data transmission problem. The third type of active suspension considered here, the servo-controlled suspension, is designed to solve that problem.

First, as discussed in section 4.13.4.1.1, the disturbances primarily enter the telescope as accelerations and are transformed to torques by the dynamic unbalance of the telescope and mount. Therefore, if these accelerations can

be sensed and nulled through a servo system, this type of disturbance will be eliminated. That is the purpose of the servo-controlled suspension. Ultra-sensitive accelerometers sense the linear acceleration of the telescope along each axis. The accelerometer outputs drive linear actuators which drive the sensed acceleration to zero.

The equations of motion are derived from the sketch in figure 4.13.4.1.5-4. The equation that describes the telescope motion relative to the combined center of mass is

$$\ddot{\bar{r}} = \bar{A}_p + \frac{\bar{F}^c}{M_T}$$

where,

M_T = telescope mass

$\bar{F}c$ = control forces

and

A_p equals the sum of the accelerations of the entire system due to external forces (other than gravitational), the negative of the external forces acting on the telescope alone and the gravity gradient forces.

In choosing a control law, $\ddot{\bar{r}}$ should be emphasized, as it is this quantity that is to be minimized. The position of the telescope relative to the spacecraft should play a role, but a minor one, since it is not desired to maintain this distance a constant. The same reasoning will show that the damping term should not be derived from the rate of change of relative position, but should be derived from the accelerometer output.

These considerations lead to a simple law of the form

$$F^c = -K_1(s)A - K_3 X$$

where,

$K_1(S)$ = gain of the accelerometer and includes a frequency dependent compensation term.

s = Laplace variable

X = a change in relative position.

K_3 = weighting gain of X.

and

A = accelerometer output.

The accelerometer output will be of the form

$$A = \frac{F^c + F^{ext}}{M_T} - \frac{F^e}{m}$$

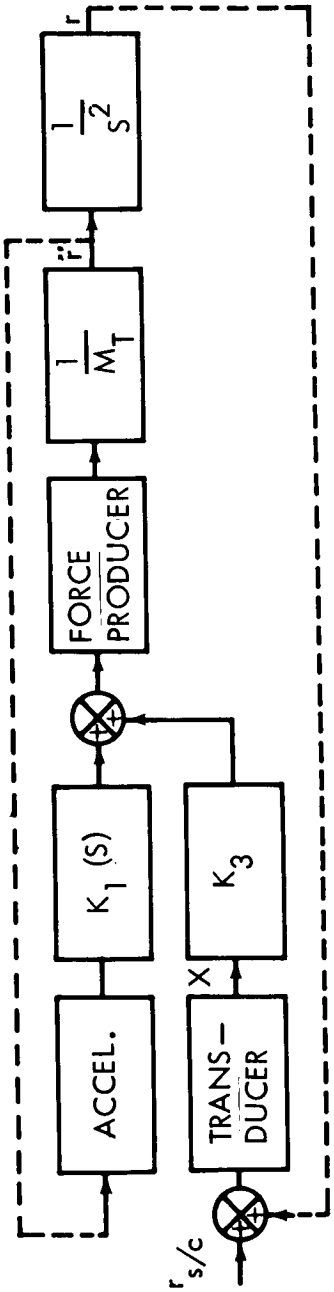


Figure 4.1?.4.1.5-4. Schematic Diagram of Servo Mount

where,

F^e = error forces

m = proof mass.

Combining the above equations gives

$$r = \frac{Ap\ (MT + K_1) - K_3\ rs/c}{S^2\ (M_T + K_1) + K_3}$$

This equation shows that the effect of the accelerometer is to artificially increase the mass of the telescope. The effect of the relative position gain is to provide a suspension with effective spring constant K_3. By choosing K_1 large and K_3 small, the system behaves as a large mass suspended by weak springs, which is of course what is desired. Gain of the accelerometer loop is limited by noise. Performance of the system is limited by the noise threshold of the accelerometers, by the threshold of the linear actuators and by the maximum force capability of the actuators. The system is unitable as presented but can be stabilized by loop compensation. This is another advantage of the servo-controlled suspension. The damping can be made dependent on the telescope velocity in inertial space. All the other suspension systems considered obtain damping between the spacecraft and the telescope, which provides an alternate path for impulsive disturbances.

To get an idea of the sensitivity required of the accelerometers, it is assumed that the disturbance is sinusoidals of a frequency somewhat below the control frequency (of the telescope pointing system) so that input torques are followed with a steady-state error determined by control system gain. The maximum acceleration is given by

$$A = \frac{\theta_m\ K}{M_t/s^d}$$

where

θ_m = maximum of the sinusoidal error
K = attitute control gain
M_t/s = telescope mass
d = telescope support offset from center of mass of telescope.

Choosing θ_m equal to 0.01 arc-sec, taking K to be 16,320 n.m./rad as typical for a 445 kg telescope with a 1 cycle per second bandwidth, and assuming a 2.54 cm offset, the maximum acceleration is about 1.2×10^{-4} m/sec^2. Vibrating-string accelerometers are available in reasonable sizes with thresholds of 10^{-7} g and three orders of magnitude operating range. Thus, the sensors should present no particular problem.

Several types of linear actuators were investigated. The requirements are low threshold, a clearance between moving and stationary members of at least a half-inch in both directions, and a maximum capability of about 0.1 to 1 lb depending on the specific configuration.

A type which appears to meet the requirements is a modification of the magnesyn magnetic support considered earlier. (See figure 4.13.4.1.5-5). The poles of the stator are wound for both a.c. and d.c. The a.c. circuit is used for position readout just as for the magnesyn. The d.c. is used for actuation, the advantage being that a greater support force can be obtained with the wide air-gaps that are required. However, the force provided by the magnesyn can also be servo-controlled, and there is good possibility the the required support forces can be obtained in this way, i.e., with an all-a.c. system.

4.13.4.2 Experiment Procedure

As discussed in detail in the previous section, several alternate concepts for an isolation system were investigated in this study. None was judged clearly superior to the others. Each has its advantages and disadvantages, and more analysis and much ground testing needs to be done before a choice is actually made. However, to obtain a baseline from which orbital analysis, experiment integration and system analysis could be carried out, it was decided that one of the concepts being considered would be chosen for conceptual design and integration with the other experiments and the spacecraft. On this basis the spring mount was and is tentatively chosen for comparison under actual operating conditions with the hard mount.

The purpose of the isolation system is to support the fine telescope stabilization system, and the best direct measure of the isolation provided is by the fineness of stabilization achieved. Another experiment in this program is the fine guidance experiment described in section 4.12, where the objective is to compare the effectiveness of several guidance components in achieving a pointing stability of 0.01 arc second. To achieve this stability in the first place will require isolation, either by an isolation system or by removing man's presence from the spacecraft during operation. Therefore, it is natural that the isolation techniques comparison experiment be closely integrated with the fine guidance experiment.

A drawing of the fine guidance telescope is shown in figure 4.13.4.2-1. This telescope is actually used for several experiments. On the figure, however, components not associated with the isolation experiment or the fine guidance experiment are crosshatched. The fine guidance components are left dark to emphasize the relationship between that experiment and this one.

In fact, the fine guidance system is used as the sensor and data gathering agent for the isolation experiment. Therefore, most of the procedure outlined in section 4.12.4.2 is applicable here also. The exception is in the comparison of fine guidance components. It would be desirable to use one error sensor, for example, with one isolation technique and another sensor with another technique. Instead, the performance of the hard mount should be checked first with the most reliable fine guidance configuration that is available. Then, using the same configuration, the isolation system is checked out. After its performance has been proven, the various fine guidance configurations are evaluated, using

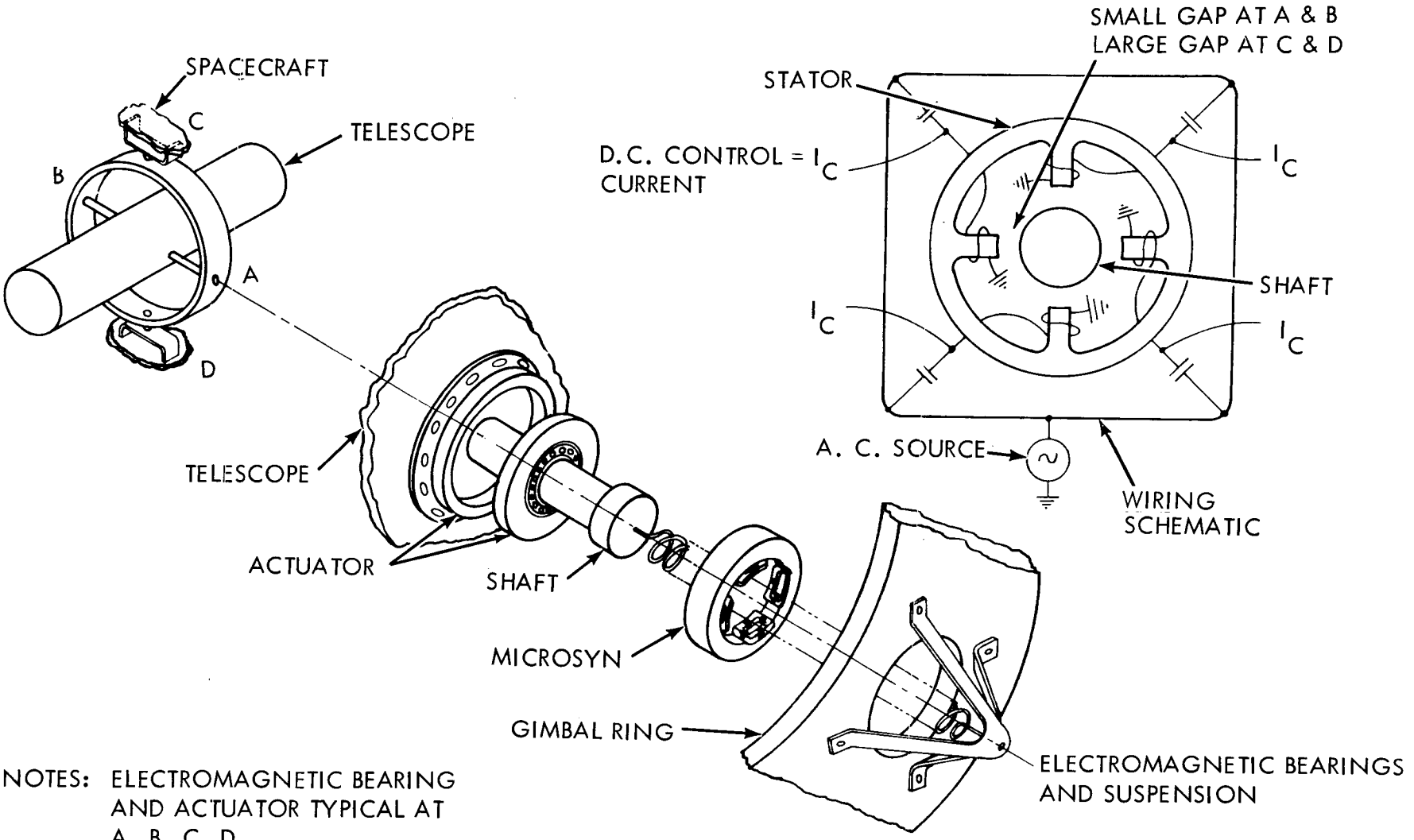
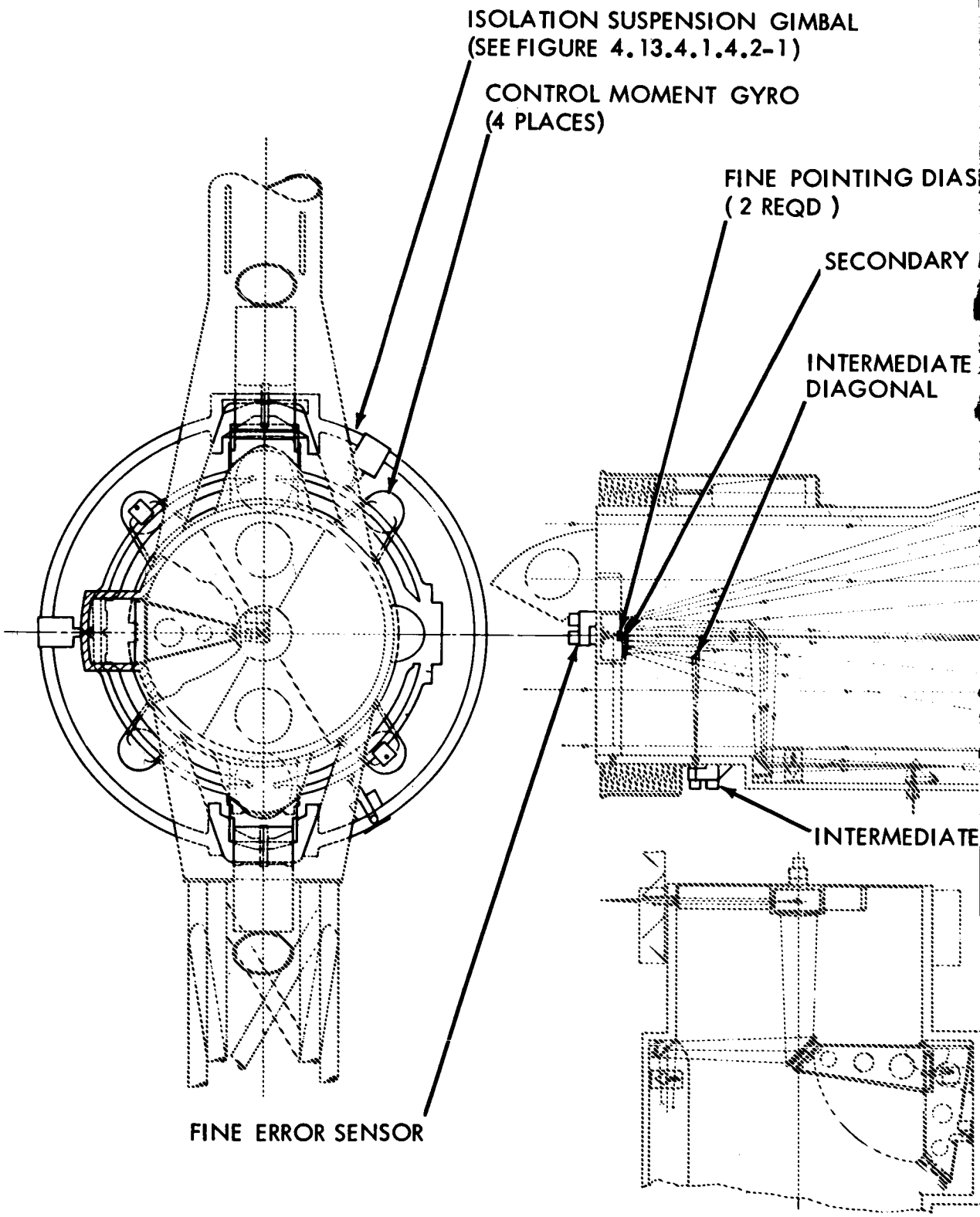


Figure 4.13.4.1.5-5. Possible Actuator for Use in the Servo Mount



PRECEDING PAGE BLANK NOT FILMED.

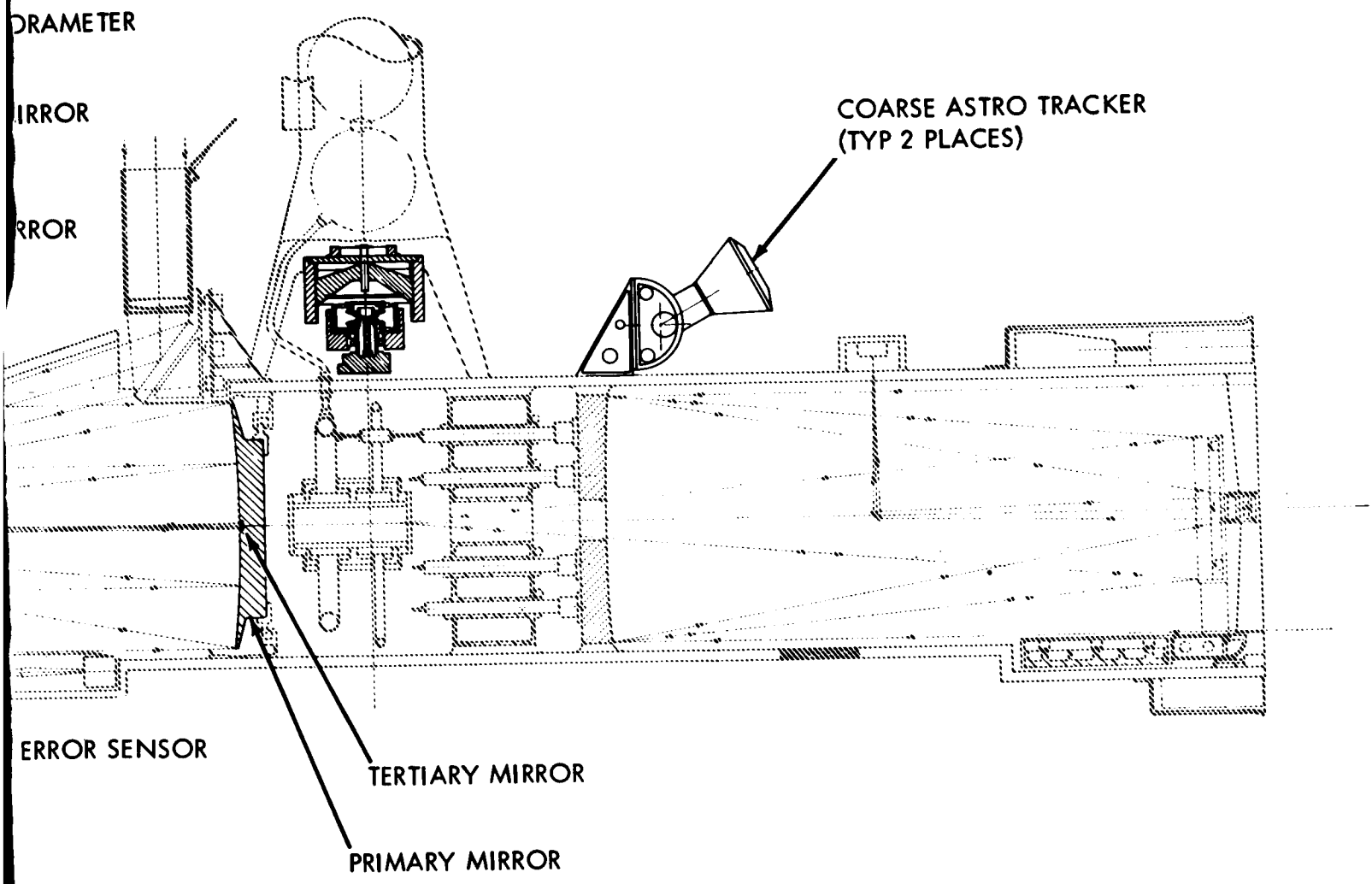


Figure 4.13.4.2-1. Fine Guidance Telescope Gimbal

this single isolation system. Later, after the preferred fine guidance configuration has been determined, the isolation comparison experiment would be repeated using this configuration.

As the experiment is now defined, the procedure consists basically in first comparing the operation of the hard mount with ball bearing with the hard mount with flex bearing, then comparing whichever of the above techniques is deemed best with the spring mount.

Both the suspension ring for the spring mount and the flex bearing are provided with locking mechanisms which are energized on command from the crew station. The procedure is outlined as follows:

a. Choose and install the initially preferred fine guidance configuration.

b. Proceed through acquisition procedure as described in section 4.12.

c. Unlock gimbals of hard mount and proceed with hard mount evaluation.

   (1) First period. Crew performs normal tasks thereby creating a random distribution of disturbances. Accelerations of the telescope are measured as a function of time and the data recorded. Error signals from the fine guidance loop are monitored and recorded.
   (2) Second period. Starting from acquired condition, crew goes through programmed movements. For example, 5 minutes of quiet time, 5 minutes of limb movements (arms, head, etc.), 5 minutes of body bending while restrained, 5 minutes of unrestrained body translation about each axis with varying soaring speeds, distances and times. During acceleration of spacecraft, error voltages from fine sensor are monitored and recorded as before. In above steps, any loss of acquisition is noted (if it occurs) and this will represent terminal condition of experiment.

d. Cage gimbals, lock ball bearings, unlock flex bearing. Repeat (1) and (2).

e. On the basis of the monitored error signal, choose either the ball or the flex bearing and proceed to the next step.

f. Initiate quiet made in spacecraft, allow time for spacecraft control system to completely absorb momentum of spacecraft.

g. Unlock suspension ring, allow transient to damp out. Reacquire guide star, if necessary.

h. Repeat (1) and (2).

i. Initiate formal evaluation of alternate fine guidance configuration and choose one.

j. Repeat as much of steps c. through h. as is deemed desirable by the astronaut experimenters.

In concluding the procedure, it should be pointed out that although the isolations comparison experiment depends somewhat on the fine guidance experiment, the reverse is not true. One reason the hard mount is included in its present configuration is to avoid having another experiment depend on an untried technique. There is really no way to avoid having the isolation systems depend on the fine guidance experiment as they are to be evaluated under actual operating conditions. Something similar to the fine guidance experiment must be provided in any case. However, to increase the reliability, at least one fine guidance technique developed to a high-confidence level will be included. Then the provision for multiple fine guidance configurations will actually enhance reliability. Also, a backup mode using highly sensitive accelerometers on the telescope is provided. This will allow the correlation of spacecraft acceleration, telescope acceleration, and fine guidance error signals.

4.13.5 Supporting Analysis

This section contains discussions considered too detailed for inclusion in the main body of the experiment but which should be included for completeness. Generally, the disturbance environment analyses, for both internal and external disturbances, some detailed derivations of the stabilization requirements, and a few other miscellaneous analyses are included.

4.13.5.1 Disturbance Environment

4.13.5.1.1 Internal Disturbances

The effect of crew motions on spacecraft stability is not a problem peculiar to OTES. The problem arises in all manned-satellite applications in which some experiment subsystem must be controlled to a high angular stability. (1) (2) (3) (4) (5) Consequently, CCSD has had a continuing effort in this area. Most of the results are applicable to OTES and are summarized in the following paragraphs.

---

(1) J. C. Riles, Effect of Mass Shifts on Spacecraft Stability, TB-AE-66-346, Chrysler Corporation Space Division, New Orleans, La.

(2) J. G. Wohl, Anticipated Coupling Effects of Human Body Motion Upon the Rotation of a Manned Satellite, Contract NOB-30564, Dunlap and Associates, Inc., Darien, Connecticut, December 9, 1965.

(3) J. G. Wohl, On the Nature of Disturbance Torques Generated by Human Body Motions in Manned Spacecraft, Contract NOB-30564, Dunlap and Associates, Inc., Darien, Connecticut, December 30, 1965.

(4) P. Ireton, On the Dynamic Motion of an Orbiting Vehicle From Man-Produced Disturbances, TN-AE-66-145, Chrysler Corporation Space Division, New Orleans.

(5) E. P. Hanavan, Jr., A Mathematical Model of the Human Body, AMRL-TR-102, Aerospace Medical Research Laboratories, Wright-Patterson Air Force Base, Ohio, October, 1964.

4.13.5.1.1.1 Inertial Properties of the Human Body

The dynamics of the living human body is not susceptible to general analytical treatment. The body must be represented as composed of a finite number of rigid parts, each part free to move relative to its neighbors under specified constraints. In this way, a model of the body can be constructed. The sophistication of the model is dependent on the number of parts and the care with which the parts and the constraints themselves are modeled.

One such model, due to Hanavan,[5] is shown in figure 4.13.5.1.1.1-1. The body is divided into 15 parts, the division being effected along commonly accepted lines. That is, the head, hands, and feet are each a single part, while the trunk, the arms, and the legs are each divided into two parts. The upper arms, fore arms, upper legs, lower legs, and feet are frustra of right circular cones; the head is a right circular ellipsoid of revolution, the upper and lower torso are right elliptical cylinders; and the hands are spheres. Each segment is assumed homogeneous, with the mass of each segment determined by regression equations.

Each movable part is assumed to have two degrees of freedom relative to a coordinate system fixed at the center of mass of the body. Two Euler angles are used to describe the angular position of each part, which pivots at the extremities of the part. In Hanavan's model, only the limbs are moveable. For the general model being developed at CCSD, and described later, this restriction is removed.

4.13.5.1.1.2 Dynamic Model of a Constrained Man

That the human body is an imperfect machine should be evident to anyone having done physical labor. A model that does not include energy-dissipative elements is incomplete from the standpoint of velocities and accelerations achieved by the various members. However, to connect the individual parts with motors and dampers is to introduce more complexity than is either feasible or warranted. The principal effects of damping are to increase the chemical energy expended in the performance of tasks and to limit the speed of movement of individual members. From the standpoint of man-produced disturbances, it is the velocity (not the expended energy) which determines the angular momentum imparted to the spacecraft. Therefore, a most feasible and realistic approach to the dynamic modeling is to consider the motion of individual parts as forcing functions and depend on empirical data to define these functions.

Most of the available empirical data is for one-g conditions. However, the available zero-g data show that maximum accelerations are about the same as for the one-g case but that velocities are lower. When only the body inertia is available for reaction, maximum forces will be sustained for less time. In practical terms, this means that the use of one-g empirical data to predict the angular momentum impacted in a zero-g environment gives conservative results.

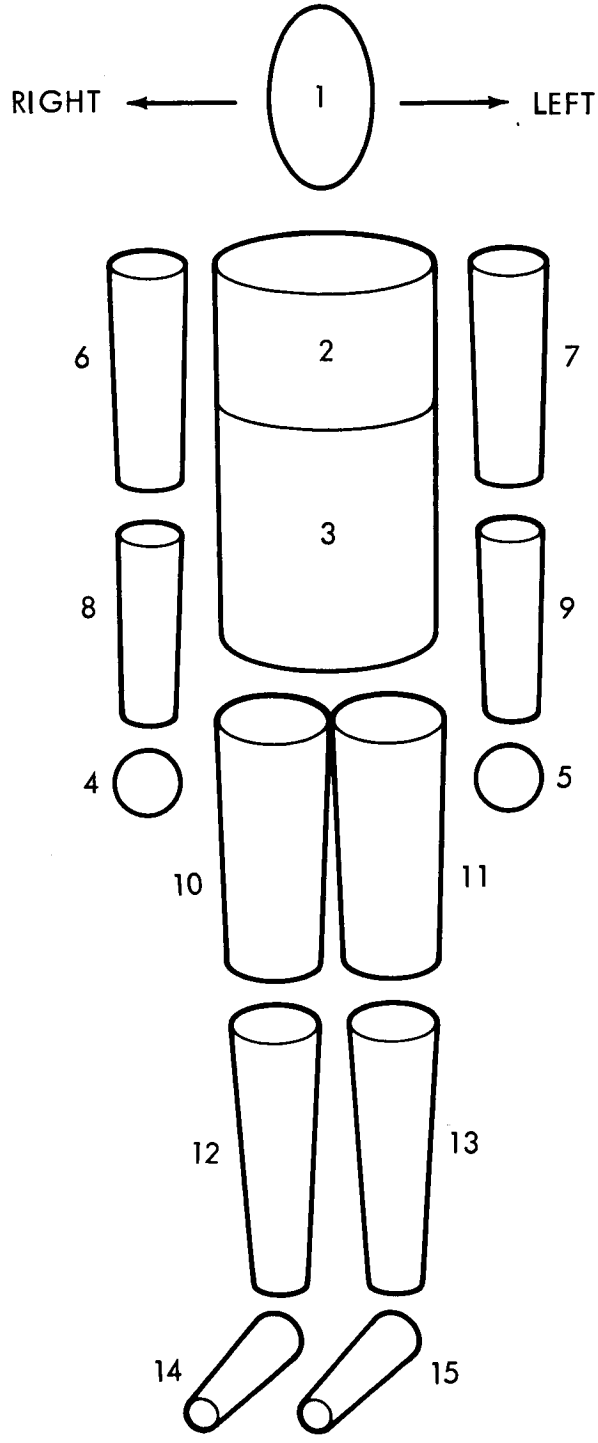


Figure 4.13.5.1.1.1-1. Model of the Human Body

Some of the most useful empirical data is from Taylor and Birmingham.[6] In one set of experimental tasks, the subjects were required to move a lever, in a controlled manner, a distance of 9 inches. Typical results are shown in figure 4.13.5.1.1.2-1. These results indicate that limb motions are non-ballistic in nature; that is, motions are characterized by smooth, near-sinusoidal variations in accelerations and velocities, with no time-increment of constant velocity. Other researchers (7) have found that under certain conditions (such as moving objects from one position to another) limb motions are characterized by an impulse of acceleration, a constant velocity period, then an oppositely-directed acceleration impulse to remove the velocity. This type of motion is illustrated in figure 4.13.5.1.1.2-2.

From the practical viewpoint of spacecraft disturbances, these two types of motions have virtually the same effect. The time involved is measured in fractions of a second, and a spacecraft control system with this type of response is impractical. Only the spacecraft inertia is available to limit the net excursion, which is the same for both types of motion. Therefore, the model developed by Taylor and Birmingham will be used here.

The experimental velocity curves from Taylor and Birmingham are closely approximated by the following expression:

$$\omega = \omega_{max} \sin^2 \left(\frac{\pi t}{T}\right) \qquad (1)$$

where,

ω = instantaneous angular velocity in rad/sec
ω_{max} = maximum value of ω

T = duration of the movement in seconds
t = time in seconds

Integrating equation (1) gives angular position as:

$$\theta = \omega_{max} \left[\frac{t}{2} - \frac{T}{4\pi} \sin \left(\frac{2\pi t}{T}\right)\right]$$

Other researchers have independently derived functions of the same form.[8] Differentiating equation (1) to obtain acceleration gives results which agree

(6) F. V. Taylor and H. P. Birmingham, Psychological Studies of Tracking Behavior Part II, A Study of the Acceleration Pattern of Quick Manual Corrective Responses, NRL Report R-3249, Naval Research Laboratory, Washington, D. C., March 3, 1948.

(7) G. de Montpellier, Note on Acceleration in Voluntary Hand Movements, Arch. Psychol. Geneve, 26, pp. 181-197. 1937.

(8) L. Slote and G. Stone, "Biomechanical Power Generated by Forearm Flexio," Human Factors, Vol. 5, No. 5, pp. 443-452, October 1963.

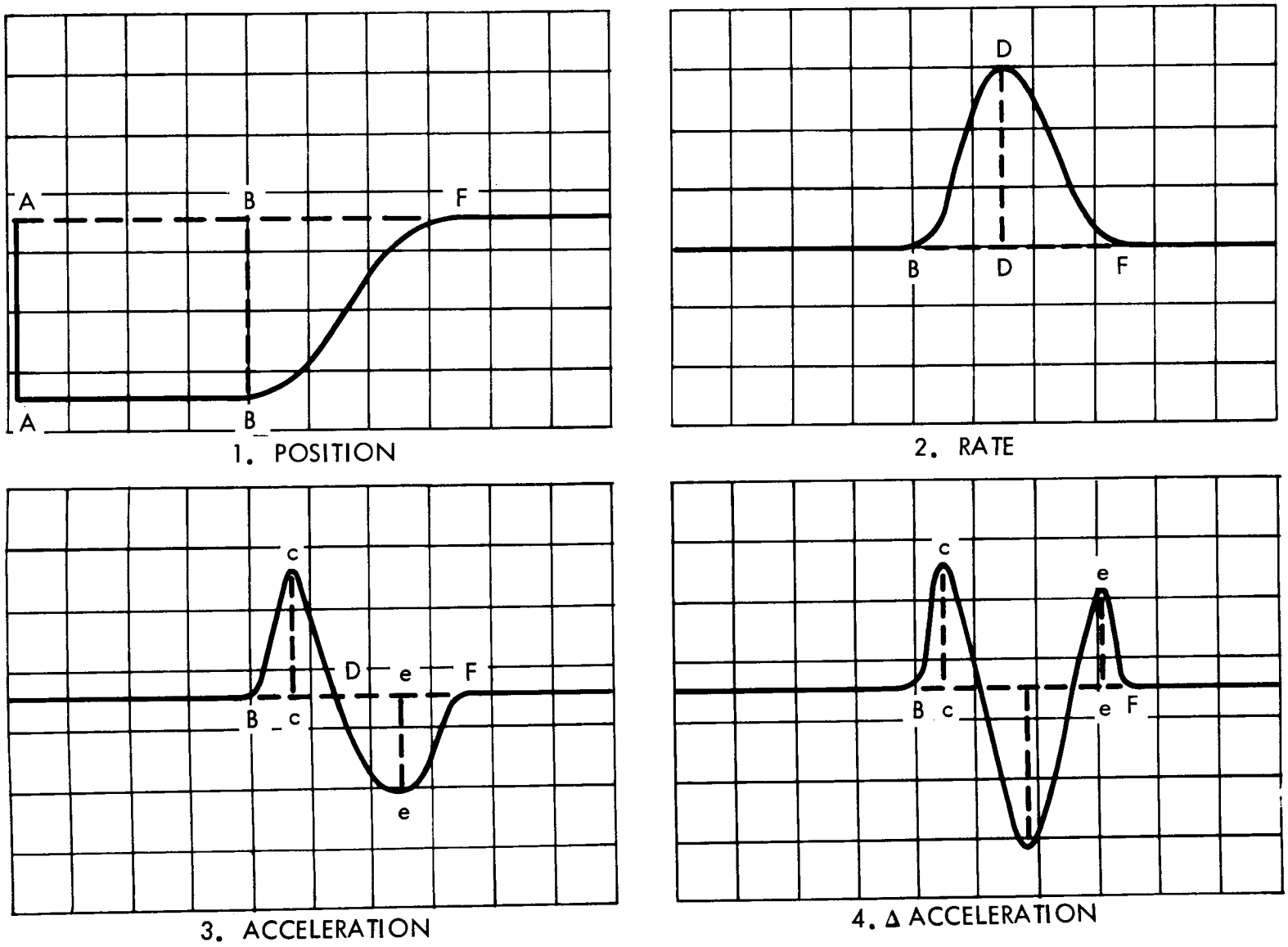


Figure 4.13.5.1.1.2-1. Experimental Response Curves

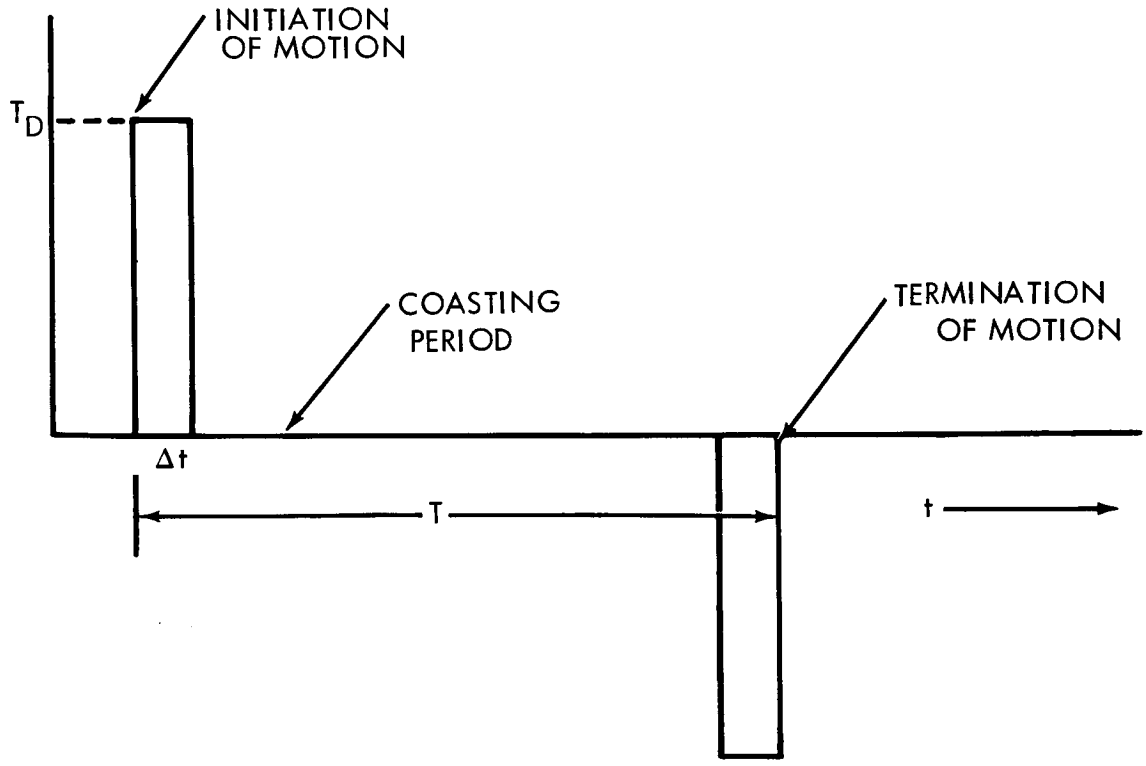


Figure 4.1?.5.1.1.2-2. Simplified Model for Man-Produced Disturbance

to within a few per cent of the experimental data. Using this model, and worst-case experimental data developed by others,(9) gives maximum forearm rates of about 500 degrees per second and maximum accelerations of about 18,000 degrees per second.^{2}

Very little experimental data is available for the general body motions of interest in determining spacecraft disturbances. Informal observations show that a quick rotation of the head through $\pi/4$ radians takes 70 to 100 milliseconds; bending the trunk forward from the waist through $\pi/4$ radians, using a seat belt as a constraint, takes 350 to 400 milliseconds; and moving the entire arm through $\pi/4$ radians about the shoulder pivot takes 150 to 200 milliseconds. This data is for worst-case, uncontrolled motions and is of value only in making rough approximations of worst-case disturbances.

Using this data in the models previously developed, the following estimates are obtained:

a. For a stiff-elbow arm motion of $\pi/4$ radians in 200 milliseconds, maximum angular velocities and accelerations are 2π radians per second and $5\pi \times 10$ radians per second^2.

b. Rotating the head through $\pi/4$ radians in 100 milliseconds, produces maximum velocities and accelerations of 5π radians per second and $3.17\pi \times 10^2$ radians per second^2.

c. A $\pi/4$ radians trunk motion in 400 milliseconds gives maximum velocities and accelerations of 1.25π radians per second and $2\pi \times 10$ radians per second^2.

4.13.5.1.1.3 Unconstrained Man

A man free of all constraints in a zero-g environment can move the various parts of his body relative to one another, but because of momentum conservation, can induce no net angular momentum into his body and cannot shift the center of mass of the combination. These movements will induce no disturbances into the spacecraft and are of no further interest here. However, to initiate the unconstrained state, and also to terminate it, the spacecraft inertia may be used as a reaction base. Such action, potentially the source of greatest spacecraft disturbances, is very much of interest.

Similar to the constrained case, the parameters of primary interest are: (a) the time profile of application of the push-off force; (b) the maximum velocity and acceleration achieved; (c) inertial model of the body under this motion, and (d) the duration of "soaring" before the maneuver is terminated.

These parameters are determined not only by man's capability, but also by the safety constraints that must be imposed on this freedom of movement. Again the model must be developed largely on the basis of empirical data, with liberal extrapolations where experimental data is scant. Experiments under zero-g conditions indicate an upper limit of 4.8 meters per second on

(9) R. H. Deupree and J. R. Simon, "Reaction Time and Movement Time as a Function of Age, Stimulus Duration, and Task Difficulty," Ergonomics, Vol. 6, No. 4, pp. 403-411, October 1963.

man's push-off velocity capability.(10) (11) However, safety considerations place a limit of 1.5 meters per second on the soaring velocity of man for a "reasonably-sized" cabin space.(3) For the OTES configurations developed in this study, the maximum safe velocity is reduced to .3 to 16 meters second.

Though no empirical data is available for the time profile of force applications for a push-off maneuver, it is reasonable to assume that the model developed for the arm motion holds here also.

$$F(t) = M \; A_{max} \sin^2 \left(\frac{\pi t}{T}\right)$$

or (1)

$$F(t) = F_{max} \sin^2 \left(\frac{\pi t}{T}\right)$$

Using this model and worst-case empirical data and a 7.5 kg man gives a maximum theoretical force of 3300 kg. Returning from worst-case data to what is considered realistic for OTES applications reduces the maximum force to 225 to 450 kilograms.

Another parameter of interest is time between push-off and termination of the maneuver. This is determined directly from the maximum safe velocity and space available for soaring which are not independent. Since the safe velocity increases with soaring distance up to a maximum of 1.5 meters per second, the duration of the maneuver remains relatively constant at 3 to 5 seconds for small to medium soaring volumes.

4.13.5.1.1.4 Disturbance Torques

Given a time history of the experimental tasks that man will perform and static and dynamic properties of the human body, the next step is to determine how these are transmitted into spacecraft disturbance torques. Very little data, either experimental or theoretical, is available in this area. Most previous studies related to manned spacecraft, in which man-produced disturbances are of interest, have assumed that man is a mass particle; that his instantaneous motion is related to the spacecraft instantaneous motion by the ratio of the inertias; and that his acceleration is an impulse, either mathematical or of finite duration. For preliminary feasibility studies, where worst-case possibilities are of primary interest, this approach not only gives good results, but is the only one practical. However, for the OTES experiments, in which the effect of man's presence is

---

(10) J. C. Simons and W. Kama, A Review of the Effects of Weightlessness on Selected Human Motions and Sensations, AMRL Memorandum P-36, 6570th Aerospace Medical Research Laboratories, Aerospace Medical Division, Wright-Patterson Air Force Base, Ohio, May 1963.

(11) D. D. Mueller and J. C. Simons, Weightless Man: Single-Impulse Trajectories for Orbital Workers, AMRL-TDR-62-103, Behavioral Sciences Laboratory, 6570th Aerospace Medical Research Laboratories, Wright-Patterson Air Force Base, Ohio, September 1962.

a critical factor, this simple approach is considered adequate only for Phase I of the study in which gross effects are to be determined. For use in Phase II, a general program to give spacecraft motion as a function of the motion of individual parts of the body is in development.

Before discussing the status of the general program and the spacecraft model on which it is based, a further word about the man/spacecraft interface is in order. An implicit assumption in the following work is that if N parts of the body are in motion, the other 15-N become parts of the rigid structure. This is not completely realistic. Man is, in fact, a "suspension system" himself, with eleasticity and damping. No zero-g information is available on man's mechanical impedance. But Caermann has investigated the impedance of man under one-g conditions. Some typical results from his work are shown in figure 4.13.5.1.1.4-1. This shows that man has a resonant frequency of about 5 cycles per second and a damping of about 6 per cent. The resonant frequency is within the range previously determined for man motions. However results obtained under one-g conditions and for a single frequency must be used with caution, since man's impedance is likely to be highly nonlinear.

The general approach to determine man-produced disturbances is as follows:

a. Using Hanavan's model, the inertial properties of a stationary man is a specified position is known.

b. Human factors analysis for experimental tasks will show which limb and body motions predominate.

c. The dynamic model previously developed gives the time pattern of these motions.

d. A general computer program to relate the motion of the parts to spacecraft motion is developed.

In developing the general program to give spacecraft motion as a function of man's motion, the problem is divided into two parts. Each part is solved separately; super-position of the solution gives the total motion. First it assumed that motion of parts takes place with no exchange of momentum (only at rest, this will produce no disturbance at all. Next, the reaction of the spacecraft to man's motion is determined. Then the results are added together to give the total disturbance.

The details of the derivation are given in reference (4). The result is

$$I^j \cdot \dot{\vec{w}} + \vec{w} \times [\dot{I}_v^j - I^j] \cdot \vec{w} = T^{jo} \sum_{K=1}^{15} T^{jk} + R^j \times \vec{F}$$

$$(J = 1 \cdot \cdot \cdot \cdot N_f) \qquad (1)$$

where,

I^j = Inertia Matrix of j^{th} part
w = Angular velocity of vehicle (dot indicates angular acceleration

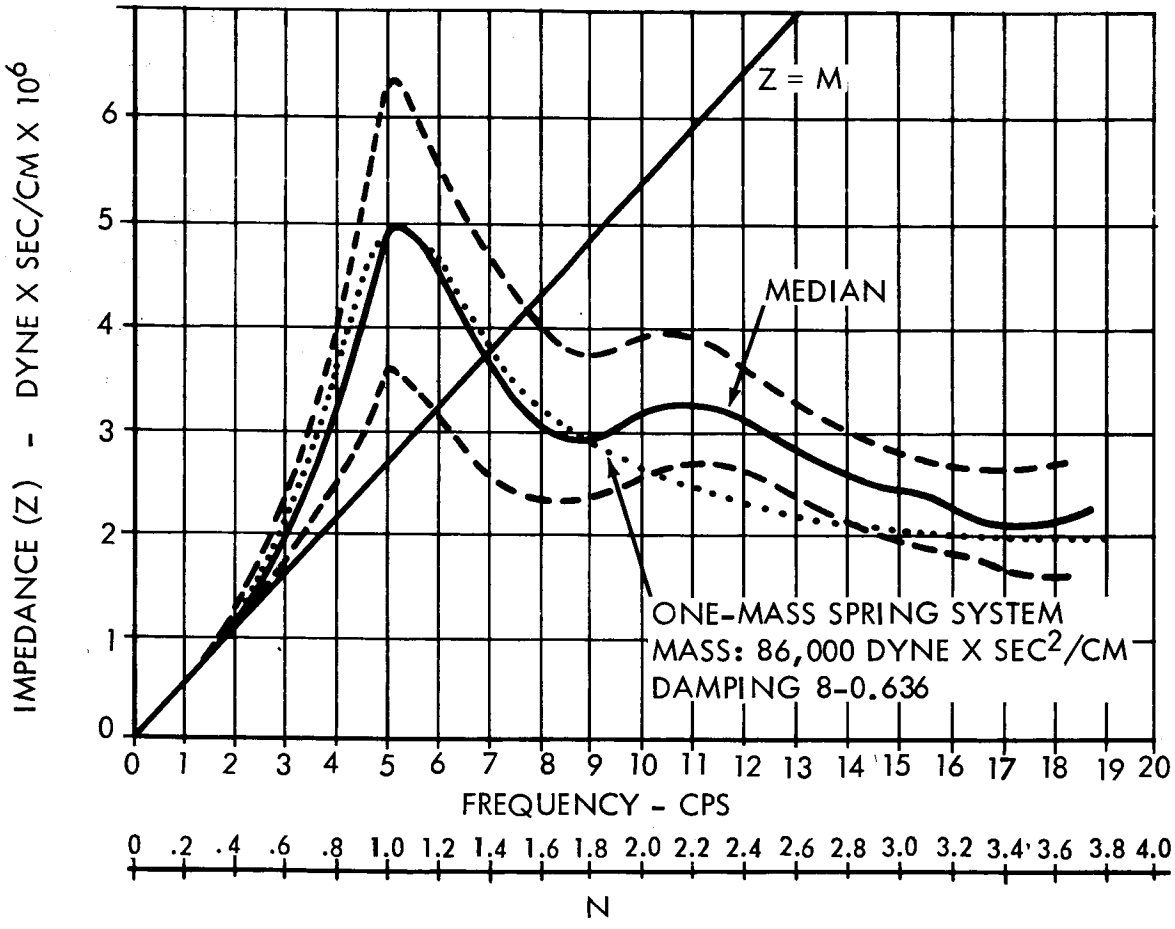


Figure 4.13.5.1.1.4-1. Low Frequency Mechanical Impedance of the Human Body

Coermann, Rolf R. " The Mechanical Impedance of the Human Body in Sitting and Standing Position at Low Frequencies," Human Factors, Volume 4, Number 5, pp. 227--253. October 1962.

I_v^j = Rate of charge of the inertia matrix of j^{th} part that moved
Tjo = Torque applied to vehicle by j^{th} part
Tjk = Torque applied to k^{th} part by j^{th} part
Rj = Distance of center of mass of jth part from vehicle center of mass
F = Control force (independent of j^{th} part)

This equation gives the motion of a spacecraft in terms of the rates of change of the moving parts of man. The inertia values are found from a computer program based upon Hanavan's mathematical model. The values of T^{jo} and T^{jk} are found by using the model in the program. This model, together with the vehicle geometry, gives 15 constraint equations. Obviously, not all of man's parts can move simultaneously without losing contact with the vehicle. With man constrained in some working position, any number of parts less than 15 can be moved. Presently, this general model is being programmed for the IBM 7094 digital computer.

Also planned for this program is a numerical analysis routine which determines the disturbance auto-correlation function and power distribution as a function of frequency. Until the program is ready a heuristic approach to the problem is taken. One such approach is to assume a distribution as follows (See figure 4.13.3.1.1-2). The angular momentum $H_{s/c}$ induced into the spacecraft is constant for an interval T_1 sec and jumps discontinuously and randomly at the end of this period, the magnitudes obeying a poisson distribution.

The autocorrelation function is

$$\phi_{11}(\tau) = \begin{cases} \bar{H}_m^2 \left(1 - \left|\frac{\tau}{T_1}\right|\right), & |\tau| < T_1 \\ 0, & |\tau| > T_1 \end{cases}$$

Where $\bar{H}_m$ is the mean value of the random variable $H_{s/c}$.

The power-density spectrum is given by

$$\Phi_{11}(j\omega) = \int_{-\infty}^{\infty} \phi_{11}(\tau) \cos\omega\tau \, d\tau$$

Carrying out the integration gives

$$\Phi(j\omega) = \frac{\bar{H}_m^2}{T_1} \left(\frac{\sin \omega T_1/2}{\omega/2}\right)^2$$

While the general program is being developed and checked out, the simpler technique illustrated in figure 4.13.5.1.1.2-2 is used to predict the effect of man-produced disturbances. At the initiation of a maneuver, man applies a constant torque, T_d, for a time increment, Δ_t. This produces an angular momentum into the spacecraft given by the produce T_d t. After the coast period, T_1, an opposite torque is applied to terminate the maneuver.

Here, it is assumed that the same kind of disturbance results whether the man is constrained or unconstrained. If man is unconstrained, the disturbance represents a push-off; if constrained, it represents motion of one of the 15 parts, while the others remain parts of the rigid structure. This model is used to derive the disturbances used in the simulation described in subsection 11.4.4.

4.13.5.1.2 External Disturbance

4.13.5.1.2.1 Simplified Analysis

To determine the feasibility of the soft suspension concept, it is necessary first to determine the static and dynamic forces that the bearing must support and the damping characteristics it must possess. Static forces arise because of the fact that two satellites of different geometrical and inertial configurations and orbiting in slightly different orbits will experience different accelerations. This is caused by unbalanced aerodynamic and solar forces and by gravity-gradient forces. The aerodynamic and solar forces are eliminated by placing the telescope in a well.

This leaves only gravity-gradient forces as the static bearing load. A simplified analysis of these follows. Let two masses m_1 and m_2 be orbiting at nominal radius, r_o as illustrated in figure 4.13.5.1.2.1-1. Their center line makes an angle θ with the local vertical. Due to the gradient of the gravitational field, and the constraint of identical angular velocity, there will be a stress in the rod conncecting the masses given by(15)

$$\Delta F_s = -\frac{3}{2} \frac{\mu d \cos^2 \theta}{r_o^2} (m_1 + m_2) \qquad (24)$$

where,

ΔF_s = gravity-gradient stress, the μ = earth gravitational constant, ft^3/sec^2

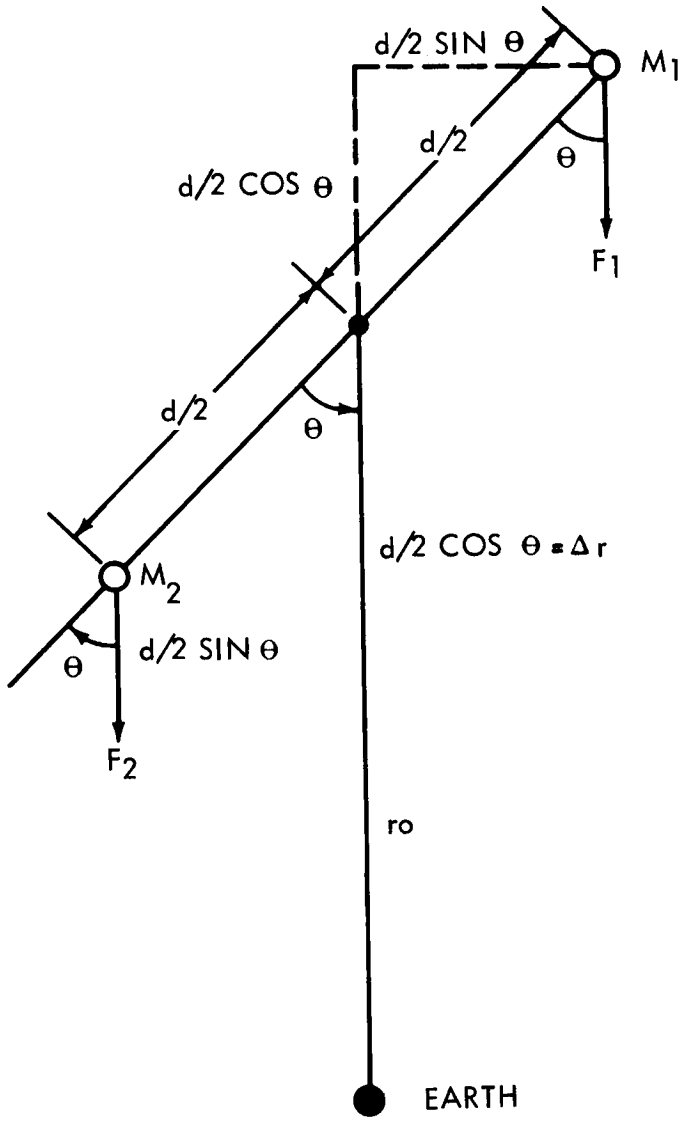
d = separation distance, ft.

m_1, m_2 = masses, slugs

r_o = orbit radius, ft.

This force is plotted as a function of d in figure 4.13.5.1.2.1-2, for several altitudes. Though very small by ordinary standards, these forces, if not counteracted, will cause considerable separation during an orbital

(15) J.C. Riles, Gravity-Gradient Stresses, TB-AE-66-350, Chrysler Corporation Space Division, New Orleans, Louisiana.



18326

Figure 4.13.5.1.2.1-1. Geometry for Calculating Gravity-Gradienl Stresses

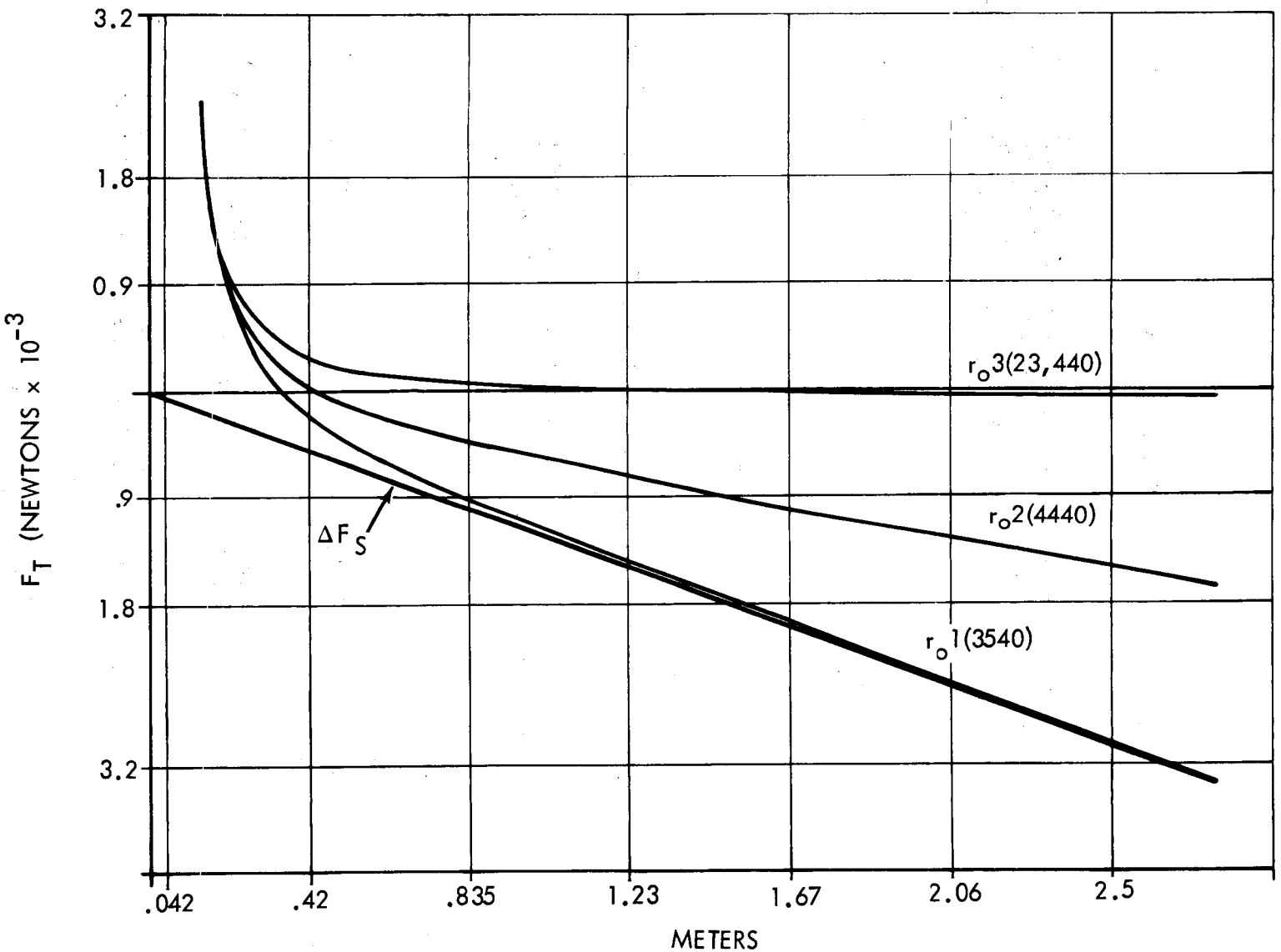


Figure 4.13.5.1.2.1-2. Gravity-Gradienl Stresses as a Function of Separation

period. However, since the forces are small, the local g-field may become important. An approximation of these forces is given by:

$$F_g = G \frac{m_1 m_2}{d^2} \tag{25}$$

The total force F_T is the sum:

$$F_T = G \frac{m_1 m_2}{d^2} - \frac{3}{2} \frac{\mu d \cos^2}{r_o^3} (m_1 + m_2) \tag{26}$$

The total force is also plotted as a function d in figure 4.13.5.1.2.1-2. For very small separations, the local field dominates. But as the separation increases, the gravity gradient force becomes dominate. The equilibrium distance d_o is determined by setting equation (24) to zero and solving for d. The result is

$$d_o = \left[\frac{2}{3}\left(\frac{m_r}{m_e}\right)\right]^{1/3} r_o \tag{27}$$

where,

m_r = reduced mass = $m_1 m_2/m_1 + m_2$, slugs

m_e = earth mass, slugs

The equilibrium distance is plotted as a function of orbital altitude for the two telescope sizes in figure 4.13.5.1.2.1-3.

At synchronous altitude, a separation distance of five feet, which is reasonable for some of the configurations covered in subsection 11.1, the static forces woul theoretically disappear.

4.13.5.1.2.2 Detailed Analysis

4.13.5.1.2.2.1 Acceleration Field

In a moving reference frame, X, Y, Z the acceleration of a particle p is (see figure 4.13.5.1.2.2.1-1)

$$\bar{a} = \bar{a}_o + \frac{\partial^2 \bar{r}}{\partial_t 2} + \frac{\partial \bar{\omega}}{\partial t} \times \bar{r} + 2\bar{\omega} \times \frac{\partial \bar{r}}{\partial t} + \bar{\omega} \times (\bar{\omega} \times \bar{r}) \tag{1}$$

An orbital reference frame was chosen with the Z axis pointed at the geocenter and with the x axis in the orbit plane and pointed as shown in figure 4.13.5.1.2.2.1-2.

$$\bar{R}_o = \bar{R}_o (-k), \quad \bar{\omega} = \omega (-j) = \frac{d\gamma}{dt} (-j)$$

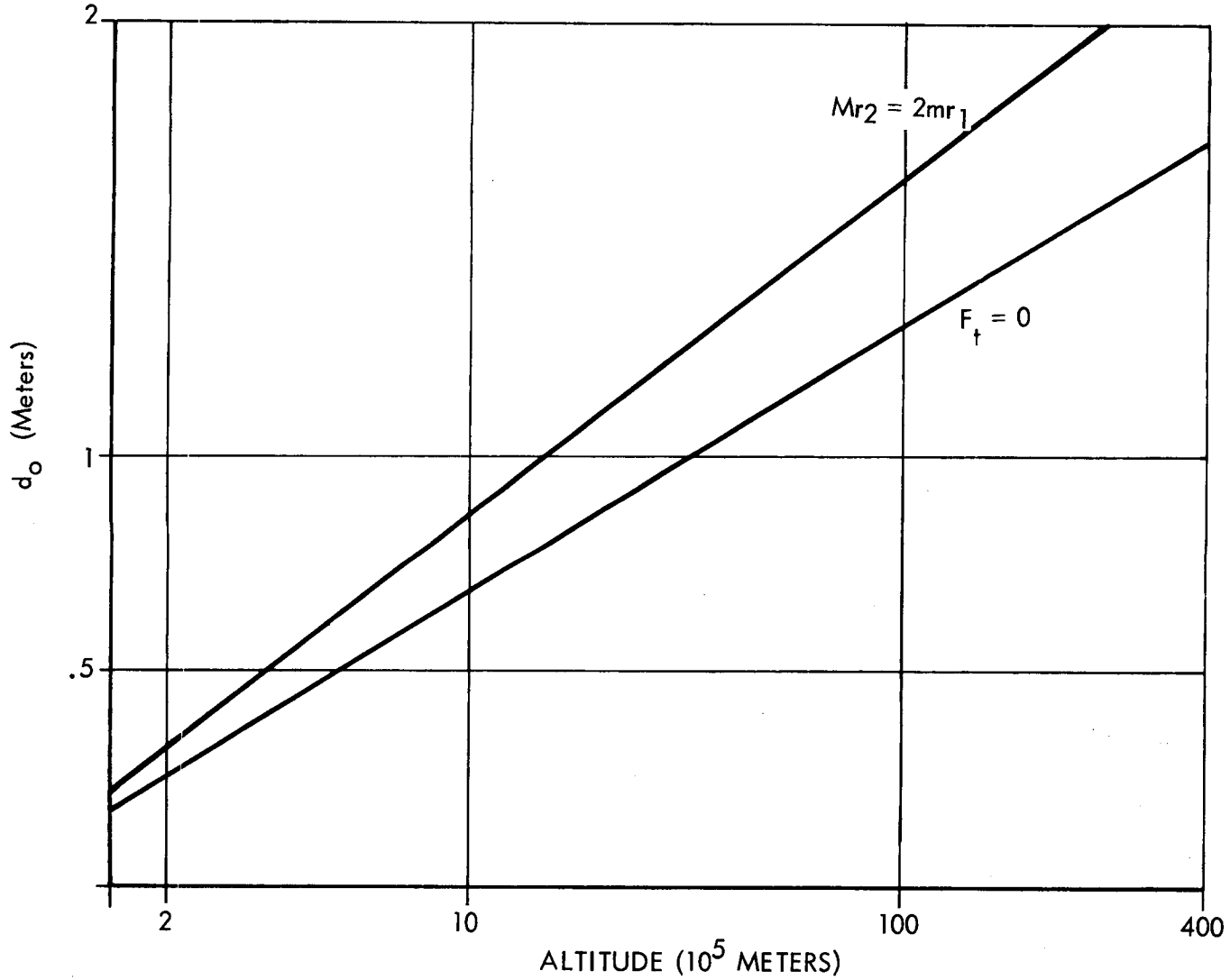


Figure 4.13.5.1.2.1-3. Equilibrium Separation as a Function of Altitude

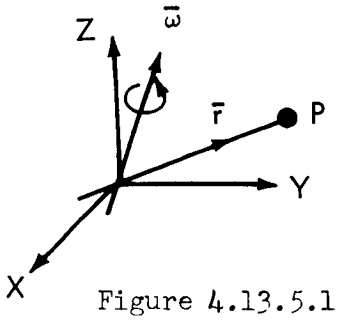


Figure 4.13.5.1.2.2.1-1

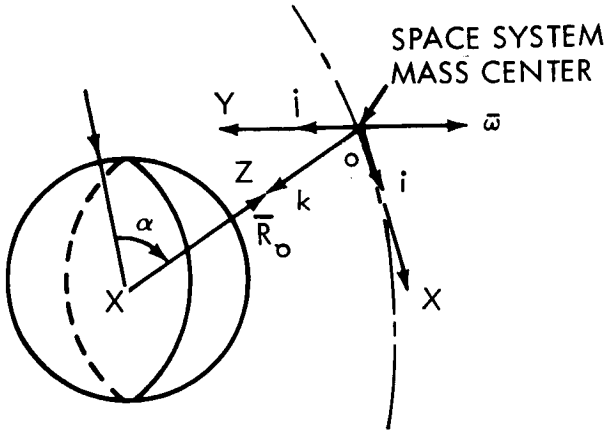


Figure 4.13.5.1.2.2.1-2

The scalar components of acceleration from equation (1) are:

$$\begin{aligned} a_X &= a_{o_X} + \ddot{X} - \dot{\omega}Z - 2\omega\dot{Z} + \omega^2 X \\ a_Y &= a_{o_Y} + \ddot{Y} \\ a_Z &= a_{o_Z} + \ddot{Z} + \dot{\omega}X + 2\omega\dot{X} - \omega^2 Z \end{aligned} \qquad (2)$$

If the satellite system is fixed with respect to the X, Y, Z axes then $\dot{X} = \dot{Z} = \ddot{X} = \ddot{Y} = \ddot{Z} = 0$, and equation (2) become

$$\begin{aligned} a_X &= a_{o_X} - \dot{\omega}Z - \omega^2 X \\ a_Y &= a_{o_Y} \\ a_Z &= a_{o_Z} + \dot{\omega}X - \omega^2 Z \end{aligned} \qquad (3)$$

Another case of interest is that of the satellite system fixed in orientation with respect to an inertial reference frame, that is, rotating about the center of mass with a rate of rotation ωj with respect to the X, Y, Z axis.

Hence,

$$\begin{aligned} a_X &= a_{o_Y} \\ a_Y &= a_{o_Y} \\ a_Z &= a_{o_Z} \end{aligned} \qquad (4)$$

In vector form equations (3) and (4), respectively, become

$$\bar{a} = \bar{a}_o + \dot{\omega}(X\,k - Z\,i) - \omega^2(Z\,k + X\,i) \qquad (5)$$

and

$$\bar{a} = \bar{a}_o$$

4.13.5.1.2.2.2 Gravity Gradient Forces

In the coordinate system X, Y, Z a mass dm, which is a distance $\bar{r}$ from the mass center of the satellite system and distance R from the geocenter, has a gravitational attraction to the earth given by: (see figure 4.13.5.1.2.2.2-1)

$$d\bar{F} = \mu \frac{\bar{R}\,dm}{R^3} \qquad (1)$$

where

$$\bar{R} = \bar{R}_o + \bar{r} = R_o\,(-k) + \bar{r}, \quad \mu = 1.404 \times 10^{16}\ \frac{ft^3}{sec^2}$$

$\frac{1}{R^3}$ can be approximated by $\frac{1}{R^3} \simeq \frac{1}{R_o^3}\left[1 + \left(\frac{3\,\bar{r}\cdot k}{R_o}\right)\right]$ (2)

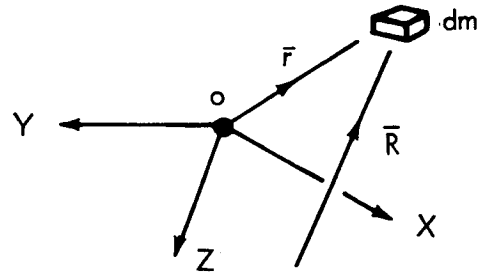


Figure 4.13.5.1.2.2.2-1

which allows equation (1) to be written as

$$d\bar{F} = \frac{-\mu}{R_o^2}\left[\left(1 + \frac{3\ r\cdot k}{R_o}\right)(-k) + \left(1 + \frac{3\ \bar{r}\cdot k}{R_o}\right)\frac{\bar{r}}{R_o}\right] dm$$

or

$$d\bar{F} = -g_o\left[\left(1 + \frac{3Z}{R_o}\right)\left(\frac{\bar{r}}{R_o} - k\right)\right] dm \qquad (3)$$

where $g_o = \frac{\mu}{R_o^2}$ is the gravitational acceleration of the earth at point O.

The components of equation (3) are

$$\left.\begin{aligned} dF_X &= -g_o\left[\frac{X}{R_o}\left(1 + \frac{3Z}{R_o}\right)\right] dm \\ dF_Y &= -g_o\left[\frac{Y}{R_o}\left(1 + \frac{3Z}{R_o}\right)\right] dm \\ dF_Z &= +g_o\left[1 + \frac{2Z}{R_o} - \frac{3Z^2}{R_o^2}\right] dm \end{aligned}\right\} \qquad (4)$$

A further simplification, but still accurate approximation, can be made by linearization of equations (2), that is, by assuming that the products

$$\frac{3XZ}{R_o^2}, \frac{3YZ}{R_o^2} \text{ and } \frac{3Z^2}{R_o^2} \text{ are small.}^{(1)}$$

---

(1) B. Etkin - Dynamics of Gravity-Oriented Orbiting Systems with Application to Passive Stabilization. AIAA Journal, Vol. 2, No. 6, June 1964.

Therefore

$$dF_X = -g_o\left(\frac{X}{R_o}\right)^{dm}, \quad dF_Y = -g_o\left(\frac{Y}{R_o}\right)^{dm}, \quad dF_Z = +g_o\left(1 + \frac{2Z}{R_o}\right)^{dm} \qquad (5)$$

For a mass M, distance $\bar{r} = Xi + Yj + Zk$ from the mass center of the complete space system, the integration of equation (5) gives

$$F_X = \frac{-g_o X}{R_o}M, \quad F_Y = \frac{-g_o Y}{R_o}M, \quad F_Z = g_o\left(1 + \frac{2Z}{R_o}\right)M \qquad (6)$$

In vector form (6) is

$$F = -g_o\left[\frac{\bar{r}}{R_o} - k\left(1 + \frac{3Z}{R_o}\right)\right]M \qquad (7)$$

4.13.5.1.2.2.3 Impact Forces - Aerodynamic and Solar Wind Forces

The aerodynamic and solar wind forces were analyzed concurrently. At the start it was recognized that, at the high altitudes of interest, the aerodynamic force is the result of molecular impact and therefore can be treated in the same way as the solar wind forces, which are the consequence of photon impact.

The character of the impact pressure is dependent upon the type of molecular or photon reflection that occurs at the surface. A diffuse reflection causes both a normal and tangential (or shearing) force, whereas, a pure specular reflection creates only a normal force. For this analysis only the normal force contribution was considered; and to obtain the most conservative, or highest, estimate of aerodynamic and solar pressures for the numerical examples dealt with, a specular reflection was assumed. In fact, the actual process is a combination of the two types of reflection.

The analysis was carried out for bodies of revolution only, as follows.(2)

From simple Newtonian Impact theory the normal pressure applied to the surface element ds can be written as

$$dp = kf\cos^2\eta \qquad (1)$$

where; η is the angle between the velocity vector $\bar{V}$ or $\bar{c}$ and the normal $\bar{n}$ to the surface element ds.

$\frac{f}{2} = \frac{\rho V^2}{2}$ = dynamic pressure for aerodynamic analysis

(2) G. Grimminger, E. P. Williams, and G. B. W. Young - Lift on Inclined Bodies of Revolution in Hypersonic Flow. Journal Aeronautical Sciences Vol. 17, No. 11, November 1950.

$f = \frac{E}{c}$ = for solar wind pressure analysis (9.56×10^{-8} lbs/sq.ft.)

E = solar incident power (Assumed equal to 94 ft.lb/ft^2 sec.)

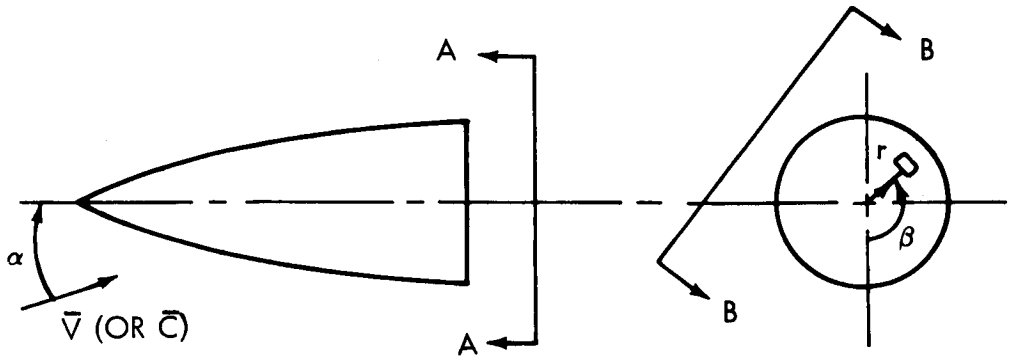
c = velocity of light (9.83×10^8 ft/sec.)

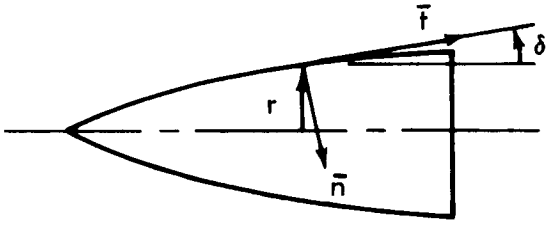
k = 1 = for diffuse reflection or photon absorption

k = 2 = for specular reflection

Furthermore,

$$\cos\eta = \cos\alpha \sin\delta + \sin\alpha \cos\beta \cos\delta \qquad (2)$$





VIEW B-B

n̄ IS A UNIT, INWARD, NORMAL VECTOR.

t̄ IS A TANGENTIAL, UNIT VECTOR, FORMING ANGLE δ WITH THE AXIS OF REVOLUTION.

Figure 4.13.5.1.2.2.3-1

Equation (1) is valid only over surfaces that can "see" the flow. In the "shadow" region, shielded from molecular or photon impacts, dp is assumed equal to zero.

The boundary of the shadow coincides with $\cos \eta = 0$ and is defined by

$$\cos \beta_u = - \frac{\tan \delta}{\tan \alpha} \qquad (3)$$

a. Circular disk (See figure 4.13.5.1.2.2.3-2)

Radius r, $\delta = \frac{\pi}{2}$, $\cos \eta = \cos \alpha$

Chord Force (Axial Force)

$$C = kf \, (\pi r^2) \cos^2 \alpha \qquad (4)$$

Normal Force

$$N = 0$$

b. Cylindical Afterbody (Neglect fore-body or flat face at the front of the body) (See figure 4.13.5.1.2.2.3-3)

Length = L

Radius = r, $\delta = 0$, $\cos \eta = \sin \delta \cos \beta$

$$\beta_u = \pm \frac{\pi}{2}, \text{ or } dp = 0 \text{ for } \frac{\pi}{2} \leq \beta \leq \frac{3}{2}\pi$$

$$N = \int_{\sigma}^{L} \int_{\beta = -\frac{\pi}{2}}^{\frac{\pi}{2}} ds \, dp \cos \beta, \; ds = r \, d\beta \, dl, \; dp = kf \sin^2 \delta \cos^2 \beta \qquad (5)$$

Which gives

$$N = \frac{4}{3} kf \, rL \sin^2 \alpha \qquad (6)$$

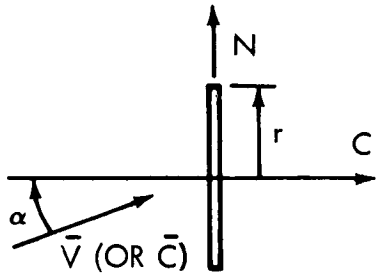


Figure 4.13.5.1.2.2.3-2

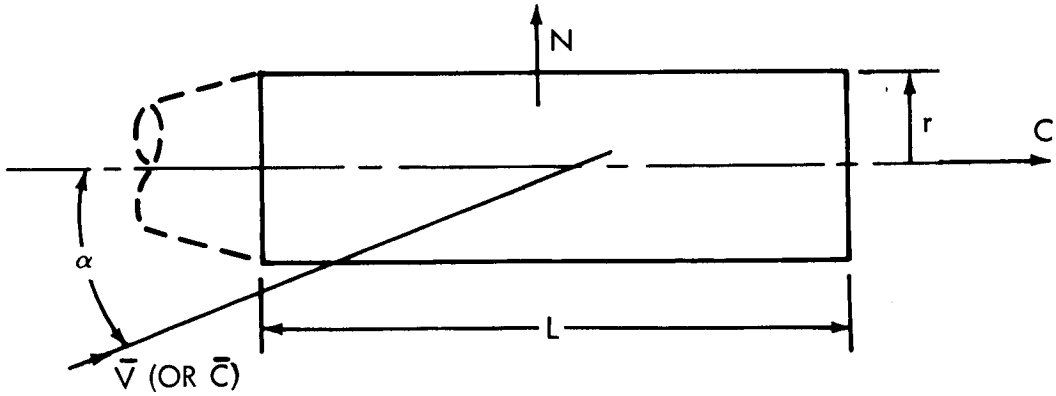


Figure 4.13.5.1.2.2.3-3

Also

$$C = \int_{\sigma}^{L} \int_{\beta=-\frac{\pi}{2}}^{\frac{\pi}{2}} ds\, dp \sin\delta = 0 \qquad (6)$$

c. Cone (See figure 4.13.5.1.2.2.3-4)

Base radius = r_b

Length = L_c

For the cone two special cases are recognized;

Case (i) $\alpha \geq \delta$

$$N = \int_{0}^{L_c} \int_{\beta=0}^{2\pi} kf\,(\cos\alpha \sin\delta + \sin\alpha \cos\beta \cos\delta)^2\, r \cos\beta\, d\beta\, dL \qquad (7)$$

$$N = kf \frac{\pi r_b^2}{2} \cos^2\delta \sin 2\alpha \qquad (8)$$

and

$$C = kf \frac{\pi r_b^2}{2} \left[2\sin^2\delta + \sin^2\alpha\,(1 - 3\sin^2\delta)\right] \qquad (9)$$

Case (ii) $\alpha \geq \beta$

In this case the integration over β is $-\beta_u \leq \beta \leq \beta_u$, giving

$$N = kf \frac{\pi r_b^2}{2} \cos^2\delta \sin 2\alpha \left\{\frac{\beta_u}{\pi} + \frac{1}{3\pi} \sin\beta_u\,(\cot\alpha \tan\delta + 2 \tan\alpha \cot\delta)\right\} \qquad (10)$$

and

$$C = kf \frac{r_b^2}{2} \beta_u \left[2\sin^2\delta + \sin^2\alpha(1 - 3\sin^2\delta)\right] + \frac{3}{8} kf\, r_b^2 \sin\beta_u \sin 2\alpha \sin 2\delta \qquad (11)$$

with β_u in radians

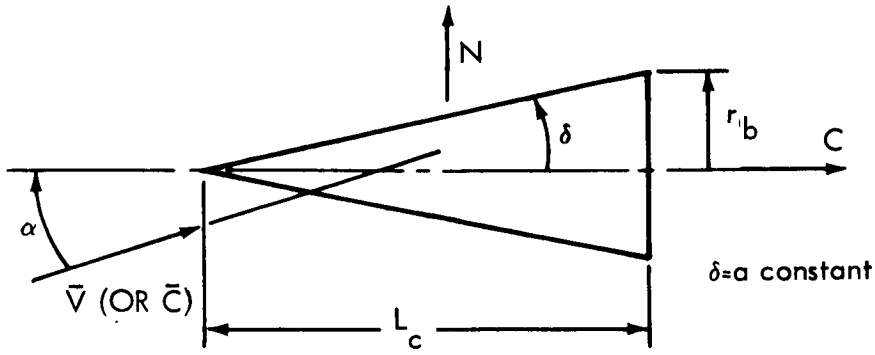


Figure 4.13.5.1.2.2.3-4

The impact forces for the geometrical combinations of interest in this study can be derived by simple addition of the appropriate equations given in (4) to (11). The numerical example chosen (see section 4) consists of a space vehicle with a cone-cylinder configuration and a telescope which was idealized as a flat faced cylinder. The ratio of aerodynamic (or solar) forces to the product kf, versus angle of attack (or impact) from 0 to $\pi/2$ rad, are presented in figure 4.13.5.1.2.2.3-5 and 4.13.5.1.2.2.3-6. Figure 4.13.5.1.2.2.3-5 describes the behavior of the normal and chord forces, while figure 4.13.5.1.2.2.3-6 gives the lift and drag as a functions of the angle of impact. The lift and drag are defined as the forces perpendicular and parallel, respectively, to the velocity vector or solar wind vector. The most significant impact force is obviously the normal force acting on the spacecraft at $\alpha = \pi/2$ rad.

In the calculation of impact forces referred to the axis system X, Y, Z, it is convenient to transform the normal and chord forces into the directions $\bar{v}$ and $\bar{a}$, as shown in figure 4.13.5.1.2.2.3-7.

$\bar{a}$ is a unit vector in the direction of the longitudinal axis. $\bar{v}$ is a unit vector in the direction of $\bar{V}$ (or $\bar{c}$).

The unit vector $\bar{\eta}$ is given by

$$\bar{\eta} = \frac{\bar{a} \times (\bar{v} \times \bar{a})}{\sin \alpha} = \frac{\bar{v}}{\sin \alpha} - \bar{a} \tan \alpha \qquad (12)$$

and

$$\alpha = \cos^{-1} (\bar{v} \cdot \bar{a})$$

The vector impact force is

$$\bar{F}_I = N \bar{\eta} + C \bar{a} \qquad (13)$$

which becomes

$$\bar{F}_I = \frac{N \bar{v}}{\sin \alpha} + (C - N \tan \alpha) \bar{a} \qquad (14)$$

The calculation procedure is

1) $\alpha = \cos^{-1} (\bar{v} \cdot \bar{a})$
2) N and C from equations (4) to (11)
3) $\bar{F}_I$ from equation (14)

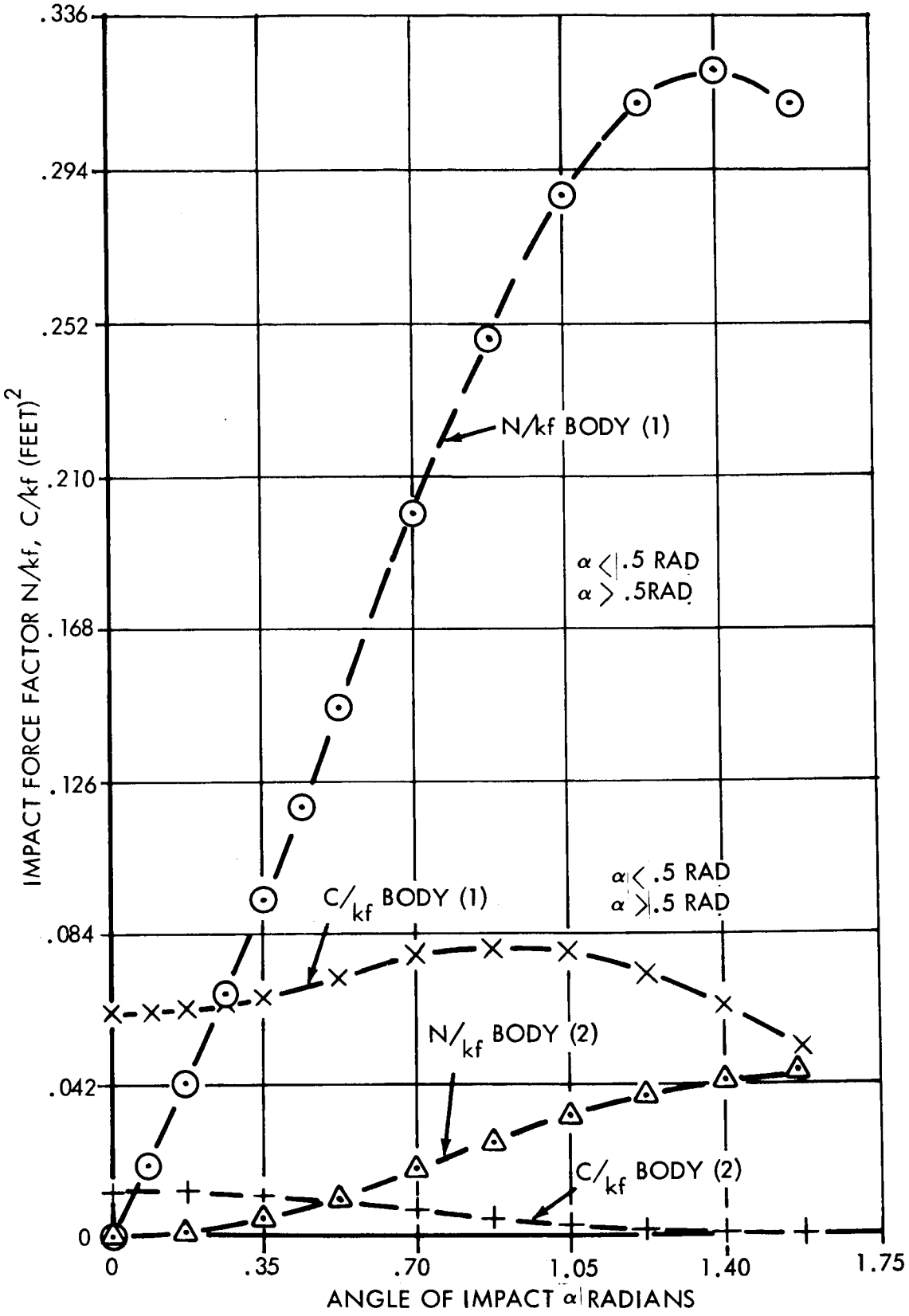


Figure 4.13.5.1.2.2.3-5. Impact Normal and Chord Forces

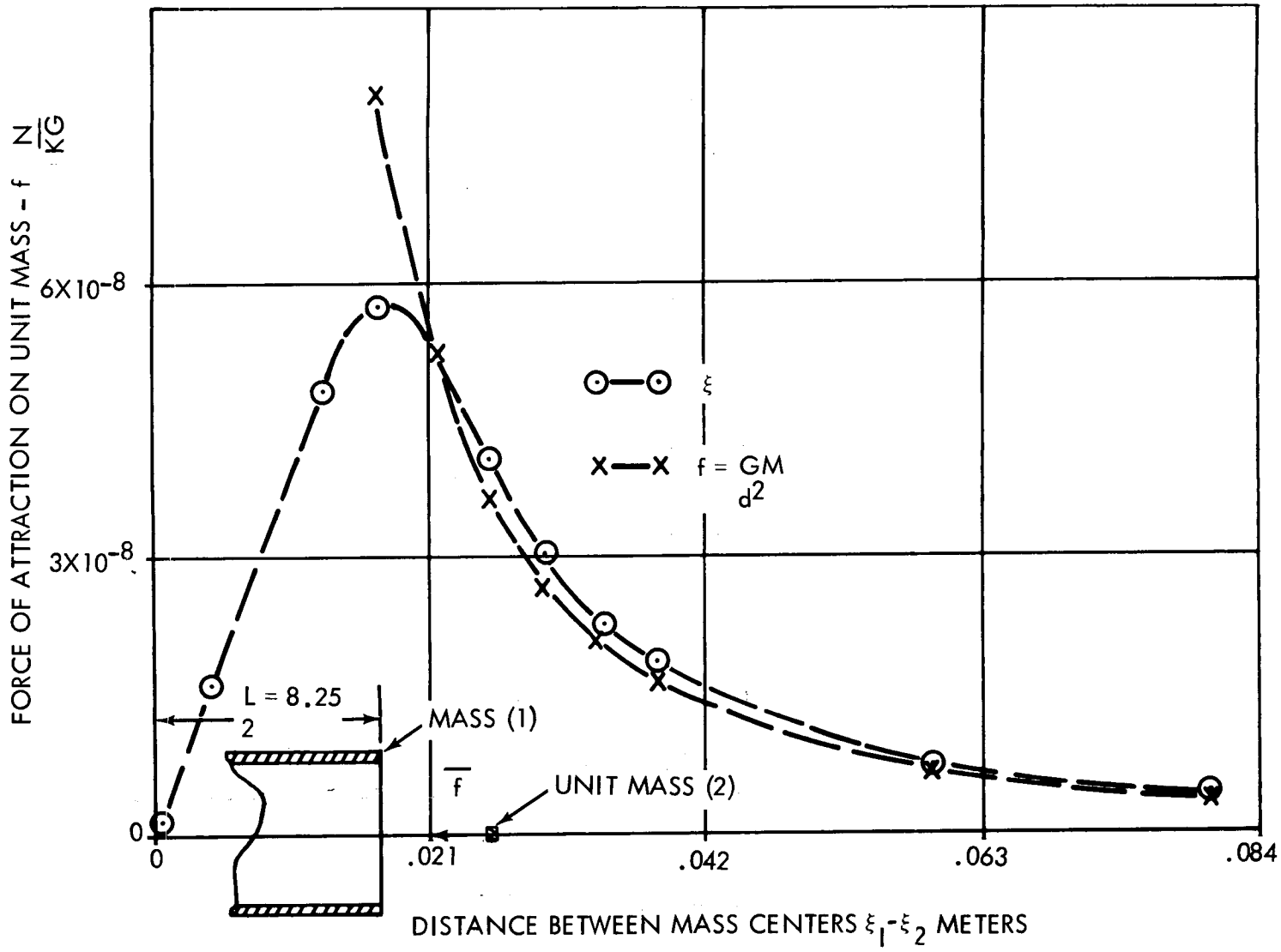


Figure 4.13.51.2.2.3-6. Impact Lift and Drag Forces

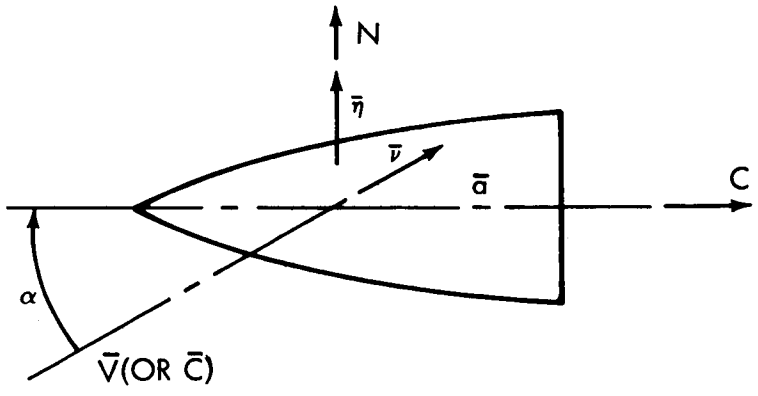


Figure 4.13.5.1.2.2.3-7

4.13.5.1.2.2.4 Mutual Attraction Forces

The analysis of the mutual attraction forces between the two sections of the space system was primarily concerned with the estimation of the error involved in using the universe square attraction law. This law is exact only for point mass objects or for spherically symmetrical bodies.(3) In calculating the mutual attraction for other types of bodies, the inverse square law is assumed to be exact for the attraction between elemental mass components. The mutually attractive force is then obtained by integration over each body. The details of the procedure are described as follows: (see figure 4.13.5.1.2.2.4-1)

The force excited on unit mass at point p is

$$d\bar{f} = -\int_M \frac{G\,\bar{r}\,dm}{r^3} \qquad \text{where G is the constant of gravitational attraction} = 3.44 \times 10^{-8} \frac{(ft)^3}{slug} \qquad (1)$$

It is sometimes easier to evaluate the potential field, that is

$$\phi = \int_M \frac{G\,dm}{r} \qquad (2)$$

The force field is then obtained from

$$\bar{f} = \Delta\phi \qquad (3)$$

The present analysis is restricted to bodies of revolution, with axial mass symmetry. This is the approximate general configuration of the components of the space system. For these types of bodies, it was found that there is no advantage to calculating the potential field first as in equation (2). Thus the force field was calculated directly according to equation (1). The mutual attraction force between mass M_1 and a mass M_2, inserted into the force field $\bar{f}$, is derived by integration of $\bar{f}$ over M_2. The integration of the force field due to mass M_2, performed over itself, is zero, of course, because this field is a system of internally balanced forces.

The integration of the apparently simple equation (1) is surprisingly difficult, and usually can be evaluated only by an approximation of the factor $1/r$.(3) See figure 4.13.5.1.2.2.4-2.

---

(3) J. A. Stratton - Electromagnetic Theory. McGraw-Hill Book Company, Inc., New York, London 1941.

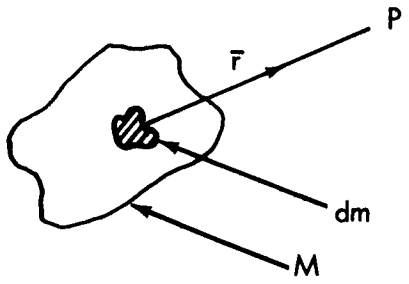


Figure 4.13.5.1.2.2.4-1

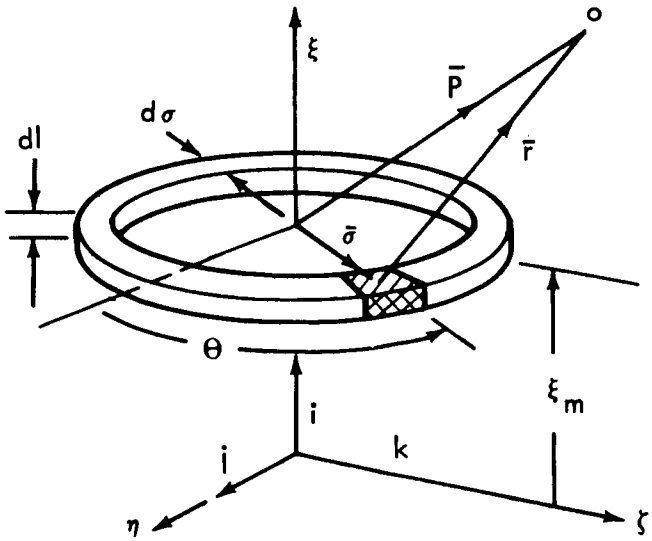


Figure 4.13.5.1.2.2.4-2

$$P\ (\xi_p - \xi_m,\ \eta_p,\ \xi_p)$$

$$\bar{r} = \bar{p} - \bar{\sigma}, \quad \bar{p} = (\xi_p - \xi_m)\ i + \eta_p j + \zeta_p k$$

$$= \xi^1\ i + \eta_p j + \zeta_p k$$

$$\xi^1 = \xi_p - \xi_m$$

$\frac{1}{r}$ can be written as

$$\frac{1}{r^3} = \frac{1}{(p^2 + \sigma^2)^{3/2}} \left[1 - \frac{2\ (\bar{p} \cdot \bar{\sigma})}{p^2 + \sigma^2}\right]^{-3/2} \qquad (4)$$

The binominal expansion of this expression is convergent if $\left[\frac{2\ \bar{p} \cdot \bar{\sigma}}{p^2 + \sigma^2}\right] < 1$.

This is true for every point in space for which $\bar{p} + \bar{\sigma}$. Thus, only on the circle $\bar{p} = \bar{\sigma}$ is the above binomial expansion not convergent.

As a first approximation

$$\frac{1}{r^3} \quad \frac{1}{(p^2 + \sigma^2)^{3/2}} \quad \left[1 + \frac{3\ \bar{p} \cdot \bar{\sigma}}{p^2 + \sigma^2}\right]$$

Also let $dm = \rho\, \sigma\, d\, \sigma\, d\, \phi$ where ρ is the density of the material.

Then

$$f \simeq -G\rho \int_L \int_\sigma \frac{\sigma d\ \sigma dL}{(P^2 + \sigma^2)^{3/2}} \int_\sigma^{2\pi} (\bar{P} - \bar{\sigma})\ (1 + \frac{3\ \bar{p} \cdot \bar{\sigma}}{p^2 + \sigma^2}\ d\theta \qquad (5)$$

In the above integration

$$\bar{\sigma} = \sigma \left(\cos\theta\ (j) + \sin\theta\,(k)\right), \int_\sigma^{2\pi} \bar{\sigma} d\ \theta = 0$$

$$\int_\sigma^{2\pi} (\bar{p} \cdot \bar{\sigma})\ d\ \theta = 0, \int_\sigma^{2\pi} \frac{3\ \bar{p}\ (\bar{p} \cdot \bar{\sigma})}{(p^2 + \sigma^2)}\ d\ \theta = 0 \qquad (6)$$

giving

$$\bar{f} \simeq - \pi G\rho \int_L \int_\sigma \frac{\sigma d\ \sigma dL}{(p^2 + \sigma^2)^{3/2}} \left[2\bar{p} - \frac{3\sigma^2 (j\eta p + k\zeta p)}{p^2 + \sigma^2} \right] \quad (7)$$

Thin-walled cylinder, see figure 4.13.5.1.2.2.4-3,

Wall thickness = t

σ = a constant

Let,

$$D^2 = \eta_p^2 + \zeta_p^2 + \sigma^2$$

= constant for a fixed field point p and constant σ.

Equation (7) becomes

$$\bar{f} = \pi G\rho\sigma t \int_{\xi_a^1}^{\xi_b^1} \left[\frac{}{(D^2 + \xi^{12})^{3/2}} - 3\sigma^2 \frac{(j\eta p + k\zeta p)}{(D^2 + \zeta^{12})^{5/2}} \right] d\zeta^1 \quad (8)$$

where

$$\xi^1 = \xi_p - \xi_m \quad \text{and} \quad d\xi^1 = - d\xi_m$$

and when integrated gives

$$f = \pi G\rho\sigma t \left[2_1 \left(\frac{1}{\sqrt{D^2 + \xi^1{}_a{}^2}} - \frac{1}{\sqrt{D^2 + \xi^1{}_b{}^2}} \right) \right.$$

$$+ \frac{(j\eta p + k\zeta p)\ (\xi_b{}^1)}{D^2 \sqrt{D^2 + \xi^1{}_b{}^2}} \left(2 - \frac{\sigma^2}{D^2 + \xi^1{}_b{}^2} - \frac{2\sigma^2}{D^2} \right) \Bigg\} \quad (9)$$

$$\left. - \frac{(j\eta p + k\zeta p)\ (\xi_a{}^1)}{D^2 \sqrt{D^2 + \xi^1{}_a{}^2}} \left(2 - \frac{\sigma^2}{D^2 + \xi^1{}_a{}^2} - \frac{2\sigma^2}{D^2} \right) \right]$$

The field along the longitudinal axis and in the bisecting, transverse plane of Body (1) of the numerical example is shown in Figures 4.13.5.1.2.2.4-4 and 4.13.5.1.2.2.4-5. In these graphs, Body (1), which is a cone-cylinder,

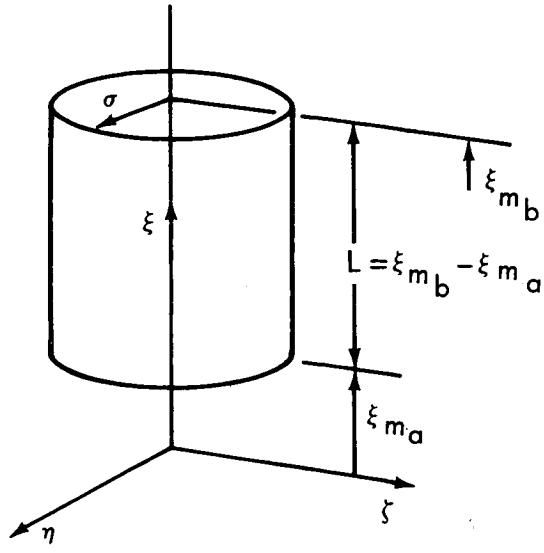


Figure 4.13.5.1.2.2.4-3

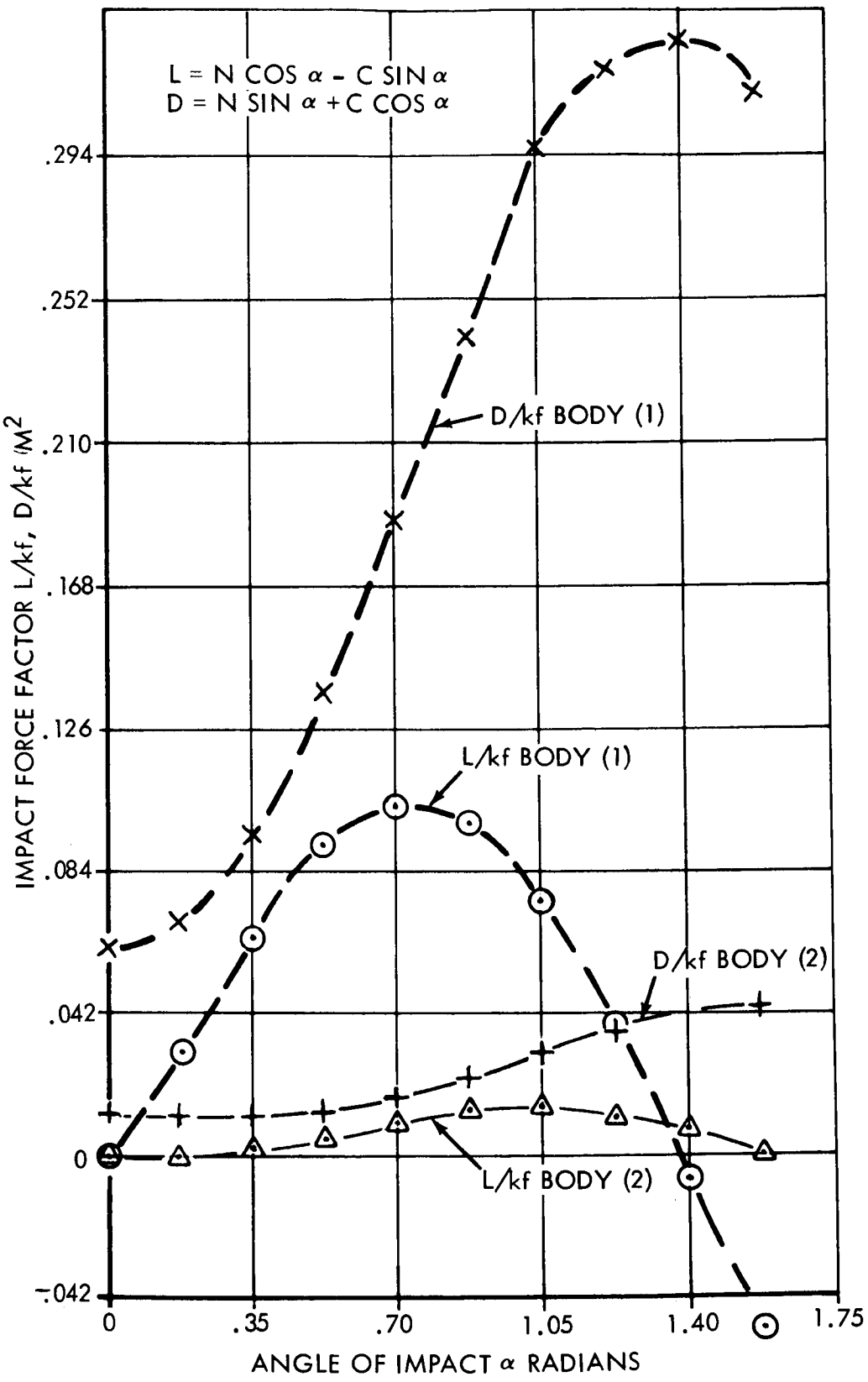


Figure 4.13.5.1.2.2.4-4. Axial Mutual Attraction Force Field

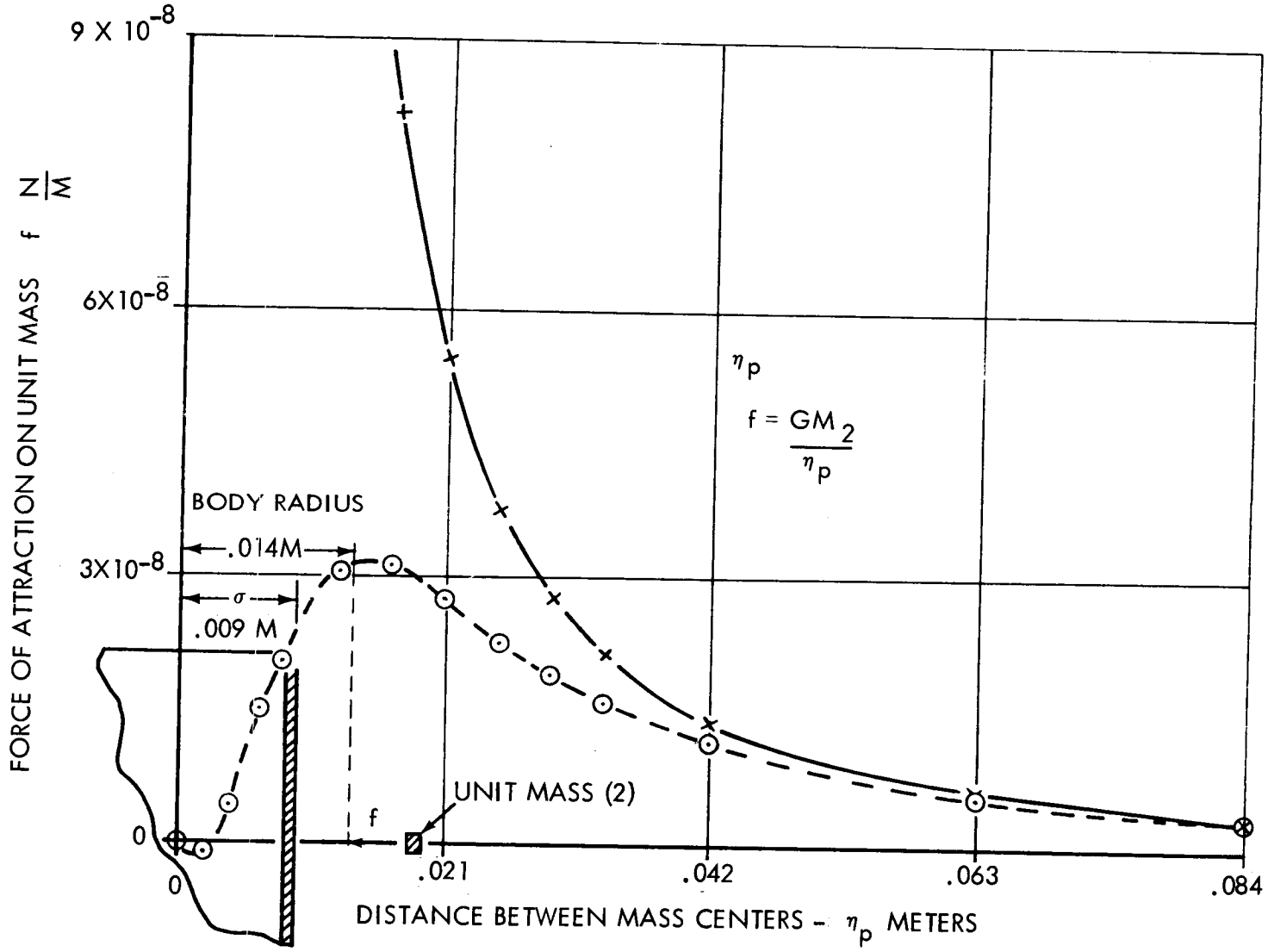


Figure 4.13.5.1.2.2.4-5. Transverse Mutual Attraction Force Field

was idealized as a cylinder 5 meters long. This length was chosen as twice the distance from the flat end to the center of mass of the body. In applying equation (1), the factor $\pi G \rho \sigma t$ was written as $\frac{M}{2L}$, and the effective radius σ was defined as $\sigma \simeq \frac{2}{3} r_b$, where r_b is the radius of the cylinder.

Figure 4.13.5.1.2.2.4-4 shows the force on unit mass on the longtudinal axis. A comparison with the inverse square law shows that beyond 10 feet distance from the center of the cylinder, and along its axis, the inverse low appears to be a good approximation. Within the cylinder, however, the approximation is not valid. The expected behavior of the attraction is satisfied in that it falls to zero as the unit mass approaches coincidence with the mass center of Body (1).

The correspondence between the equation (9) and the inverse square approximation in the bisecting, transverse plane of the cylinder is not as good as in the longitudinal direction. The approximation appears to be good beyond a distance of 9 meters from the mass center of Body (1). In the numerical example, Body (2) is a distance of 11.5 feet away from Body (1). Figure 4.13.5.1.2.2.4-5 indicates that the inverse square approximation will be about 1.7 times too large, if Body (2) can be idealized as a point mass. Of course, a truer picture of the force of attraction on bodies that are not point masses is obtained if equation (9) is integrated over Body (2). This was attempted, but, in the time available, could only be accomplished where Body (2) was either a disk or another cylinder with its axis of revolution coincident with the same axis of Body (1).

Another interesting facet or figure 4.13.5.1.2.2.4-5 is that for points close to the mass center of Body (1), the force is "repulsive". At first, this behavior seems to be illogical, but possibly it is actually a force of attraction pulling the point mass closer to the inner wall of Body (1). To prove this unusual prediction, additional terms in the binominal expansion of $\frac{1}{r^3}$ (equation (4)) shoule be incorporated into the integration.

Time has not permitted this to be done in this study.

Figures 4.13.5.1.2.2.4-4 and 4.13.5.1.2.2.4-5 give a comparison, which is reververdly called quantitative, of theerror involved in using the inverse square law in the present study. More accurate estimation requires additional information about the physical properties of the bodies under study, and possibly machine computation to deal with the difficult integrations.

As mentioned previously, the final integration was performed over Body (2), idealized as a cylinder or disk, with its axis of revolution coincident with the axis of Body (1).

For two cylinders the result is

$$F = 4\pi^2 G\sigma_1\sigma_2\rho_1\rho_1 t_1 t_2 \left[\left(\sinh^{-1} \frac{\xi_1^1}{D_1} \right)_{\xi_{a_1}}^{\xi_{b_1}^1} - \left(\sinh^{-1} \frac{\xi_2^1}{D_2} \right)_{\xi_{a_1}}^{\xi_{b_1}^1} \right] \quad (10)$$

where

$$D_1^2 = \eta_p^2 + \zeta_p^2 + \sigma_1^2, \quad D_2^2 = \eta_p^2 + \zeta_p^2 + \sigma_2^2$$

In this integration, the terms $(j\eta_p + k\zeta_p)$ in equation (9) are cyclic in θ, and hence contribute nothing when integrated from $\theta = 0$ to 2π.

For two disks

$$F = 4\pi^2 G\rho_1\rho_2\ell_1\ell_2\xi^1 \left[\sqrt{\xi^{1\,2} + \sigma_1^2 + \sigma_2^2} - \sqrt{\xi^{1\,2} + \sigma_1^2} - \sqrt{\xi^{1\,2} + \sigma_2^2} + \xi^1 \right] \quad (11)$$

where,

ℓ is the disk thickness.

ξ^1 is the disk spacing.

In the limit as $\sigma_1 \to \sigma_2 \to 0$, with the mass of each disk remaining constant, it is easy to show that this expression approaches the point-mass, inverse square approximation.

For a cylinder-disk combination

$$F = 4\pi^2 G\rho_1\rho_2\sigma_1 t_1 \ell_2 \left[\sqrt{\xi_a^{1\,2} + \sigma_1^2 + \sigma_2^2} - \sqrt{\xi_a^{1\,2} + \sigma_1^2} - \sqrt{\xi_b^{1\,2} + \sigma_1^2 + \sigma_2^2} + \sqrt{\xi_b^{1\,2} + \sigma_1^2} \right] \quad (12)$$

where ξ_a^1 and ξ_b^1 are the values of $\xi^1 = \xi_p - \xi_m$ at each end of the cylinder and t_1 is the wall thickness of the cylinder.

4.13.5.1.2.2.5 Orbit Calculations

Three orbits were chosen for the numerical analysis of the restraining forces:

a. 3.2×10^5 meter altitude, circular orbit.

b. 1.6×10^7 meter altitude, circular orbit.

c. 3.2×10^5 meter perigeen, 1.5×10^7 meter apogee, elliptical orbit.

The rate of rotation of the earth was neglected in the analysis.

Orbits (1) and (2) are intended to show the effect of altitude on the aerodynamic forces and gravity gradient. Orbit (3) was chosen primarily to demonstrate the magnitude of the rate of change of angular rotation, $\dot{\omega}$, on the restraining forces. This term is zero for a circular orbit.

The equations used in the evaluation of the important orbit characteristics are:(4)

Transverse force equation

$$R_o\dot{\omega} + 2\dot{R}_o\omega = 0 \qquad (1)$$

Radial Force equation

$$\ddot{R}_o - R_o\omega^2 = -g_o = -\frac{\mu}{R_o^2} \qquad (2)$$

where R_o = orbit radius, g_o is the gravitational attraction at distance R_o from the geocenter.

$$\frac{1}{R_o} = \frac{\mu}{h^2}(1 + e\cos\ ), \quad h = R_o^2\omega = \text{a constant} \qquad (3)$$

where e orbit eccentricity (see figure 4.13.5.1.2.2.5-1).

The velocity V of the space system is given by: (see figure 4.13.5.1.2.2.5-2)

$$V^2 = \dot{R}_o^2 + (R_o\omega)^2 \qquad (4)$$

The angle is given by

$$\tan\ = \frac{\dot{R}}{R} = \frac{\sin}{1 + e\cos} \qquad (5)$$

The maximum value of $\dot{\omega}$ for orbit (3) was obtained by solving for ω from equations (1), (2) and setting $\frac{\partial\omega}{\partial\gamma} = 0$.

The orbit characteristics are given in the following table. Included is the air density ρ and the product ρV^2. The eccentricity for orbit (3) was calculated as e = 0.54.

(4) W. T. Thomson - Introduction to Space Dynamics. John Wiley & Sons, Inc. New York, London, 1961.

Orbit Characteristics

ORBIT	ORBIT POSITION γ	ALTITUDE	RADIUS R_o	ω	$\dot{\omega}$	λ	AIR DENSITY ρ	V	ρV^2
	radians	meters	meter	rad/sec.	rad/sec.^{2}	radians	kg/m^3	m/sec	n/m^2
(1)		3.2×10^5	6.70×10^6	1.15×10^{-3}	0	0	2.5×10^{-11}	7.7×10^3	1.47×10^{-3}
(2)		1.6×10^7	2.25×10^7	1.87×10^{-4}	0	0	9.0×10^{-20}	4.2×10^3	1.59×10^{-12}
(3)	$\gamma = 0$ (Perigee)	3.2×10^5	6.7×10^6	1.43×10^{-3}	0	0	2.5×10^{-11}	9.6×10^3	2.27×10^{-3}
(4)	$\gamma = \pi$ (Apogee)	1.6×10^7	2.25×10^7	1.24×10^{-4}	0	0	9.0×10^{-20}	2.8×10^3	7.0×10^{-13}
(5)	$\gamma = \pm .27\pi$ ($\dot{\omega} = \dot{\omega}_{max}$)	8.8×10^5	7.26×10^6	1.19×10^{-3}	$\pm 8.32 \times 10^{-7}$	$\pm .09\pi$	3.5×10^{-15}	9.0×10^3	2.86×10^{-7}

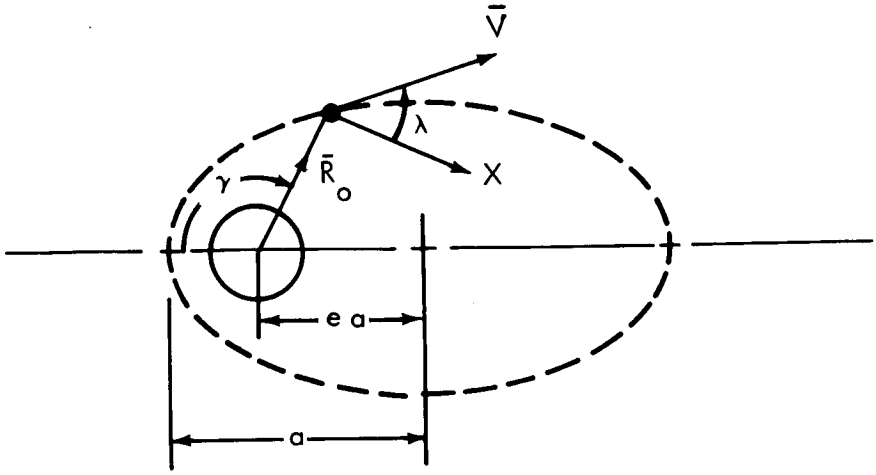
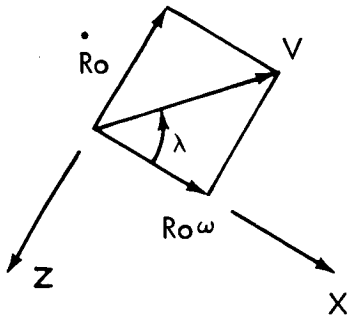


Figure 4.13.5.1.2.2.5-1



THE ANGLE λ IS GIVEN BY

$$\text{TAN}\,\lambda = \frac{\dot{R}}{Rw} = \frac{e\,\text{SIN}\,\gamma}{1 + e\,\text{COS}\,\gamma}$$

Figure 4.13.5.1.2.2.5-2

4.13.5.2 Analysis of Stabilization Requirements

4.13.5.2.1 Effect of Sinusoidal Disturbances on Film Resoultion

It is assumed that with no disturbances to the beam, a disk r_o is exposed as indicated in the top of figure 4.13.5.2.1-1. The intensity of the light is uniform over the disk, equal to I_o. The image is initially at rest at the origin of an x-y coordinate system. But before exposure commences, the image starts to swing sinusoidally with time along the x-axis with amplitude a_m and frequency.

If the light is constrained to move along the x-axis, the exposure function will be as indicated in the bottom of figure 4.13.5.2.1-1. For the two-dimensional case, where the light beam moves sinusoidally along every line in the x-y plane, the integrated effect for each element must be considered.

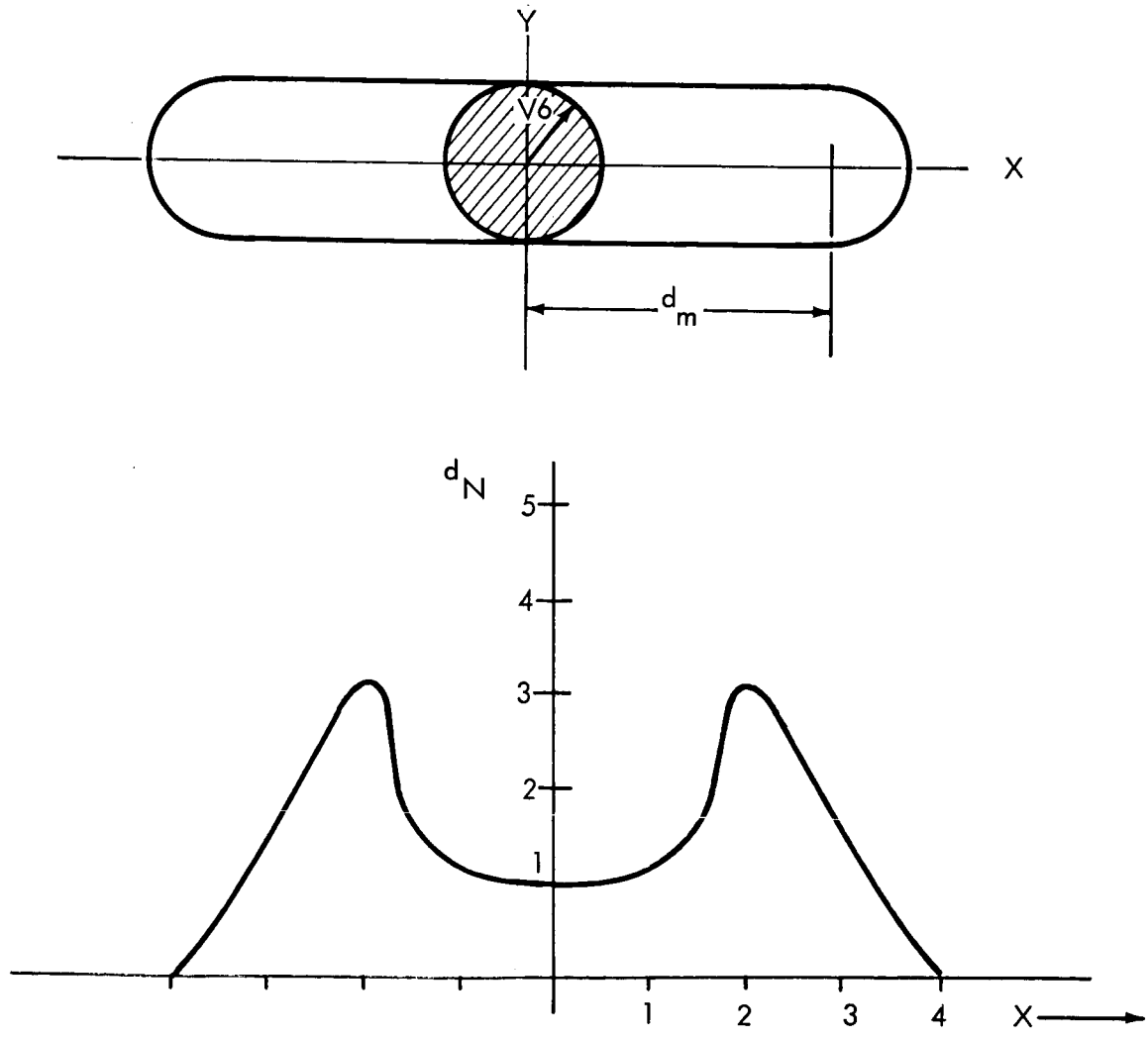


Figure 4.13.5.2.1-1. Effect of One-Dimensional Motion

The equation of the circle bounding the disk is,

$$(x - a)^2 + y^2 = r_o^2 \qquad (1)$$

where the displacement of the center is given by,

$$a\,(t) = a_m \sin A \qquad (2)$$

The circle will enclose a point (x,y) during the time $T = t_2 - t_1$. For each cycle,

where

$$t_1 = \frac{1}{\omega}\left[\sin^{-1}\left(\frac{x}{a_m} - \frac{\sqrt{r_o^2 - y^2}}{a_m}\right)\right] \qquad (3)$$

$$t_2 = \frac{1}{\omega}\left[\sin^{-1}\left(\frac{x}{a_m} + \frac{r_o^2 - y^2}{a_m}\right)\right] \qquad (4)$$

a result obtained by combining (1) and (2)

For analysis purposes the exposure characteristics of the film is idealized as shown in figure 4.13.3.1.3-1.

Light of uniform intensity impinging on photographic film produces exposure.

$$d = \frac{I_o^{\gamma}}{i^{\gamma}}\,(t')^{\gamma} \qquad (5)$$

where t' is the exposure period, i is the film inertia, and γ is the film gamma.

In our case,

$$t' = \frac{1}{\pi}\,(t_2 - t_1) \qquad (6)$$

Therefore, at the point P (x,y)

$$d\,(x,y) - I_o \left(\frac{1}{\pi}\right)^{\gamma} \sin^{-1}\left(\frac{x}{a_m}\ \frac{\sqrt{r_o^2 - y^2}}{a_m}\right) - \sin^{-1}\left(\frac{x}{a_m} - \frac{\sqrt{r_o^2 - y^2}}{a_m}\right) \qquad (7)$$

For the general case in which the motion is just as likely in one direction as another, the total exposure contained in the strip s defined by,

$$-(a_m + r_o) \leq x \leq a_m + r_o$$

$$-r_o \leq y \leq r_o$$

will be spread throughout the disk defined by $o \leq r \leq a_m + r_o$ such that elements of area equi-distant from the origin have the same exposure density.

That is, the exposure density will be a function of r only, and the total exposure will remain the same. The required expression is obtained by writing Equation (7) as a function of the polar coordinates r and θ and, for each $x = r$, integrating between the boundaries of s; and dividing the result by half the circumference of the circle defined by r. Or mathematically,

$$d_n(r, \theta) - \left[\sin^{-1}\left(\frac{\cos\theta}{a_m} + \frac{\sqrt{r_o^2 - r^2\sin^2}}{a_m}\right) p \sin^{-1}\left(\frac{r\cos\theta\sqrt{r_o^2 - r^2\sin^2}}{a_m}\right)\right] \quad (8)$$

$$d'_n(r) - \frac{2}{\pi}\int_o^{\alpha} d_n(r,\theta)\, d\theta \quad (9)$$

where

$$\alpha = \sin^{-1}\frac{r_o}{r}, \quad r_o \; r$$

$$\alpha = \frac{\pi}{2}$$

$$o < r < r_o$$

The integration in Equation (9), which cannot be handled analytically, is evaluated numerically in figure 4.13.3.1.3-3. It is apparent that the averaging effect of a random distribution is to reduce the exposure density proportional to distance from the origin while leaving the density at the origin the same.

4.13.5.2.2 Effect of Impulses on Film Resoulution

It will be assumed that the beam is controlled by a second order control system characterized by a control frequency $_n$ and a damping ration ζ . The error time response of the system is given by the following equation.

$$\theta(t) = \frac{\dot{\theta}_o}{\omega_n \sqrt{1 - \zeta^2}} e^{-\zeta\omega_n t} \sin \omega_n \sqrt{1 - \zeta^2}\, t \qquad (1)$$

where

$\dot{\epsilon}_o$ = induced error rate, rad/sec, and other quantities are defined above.

The film, it will be assumed, is represented by the exposure characteristics shown in figure 4.13.3.1.3-1. A certain amount of integrated dwell time is required to expose a given element of the film above the fog level. Now consider a beam of light represented by its Airy disk of radius α as depicted in the upper part of figure 4.13.3.1.3-2.

If the beam is perfectly stable, only the disk D of the film will be exposed. Disturbances will cause the annular region A outside the disk to be exposed. The purpose of the present analysis is to determine how many disturbances may occur per exposure period and still maintain the required contrast between regionals D and A.

The time response, equation 1, is plotted in figure 4.13.3.1.3-2. At the initiation of the disturbance the beam traverses the region A in time T_1, and upon returning the time to traverse is T_2.

For reasonable damping in the control system (50 to 100 percent), only the first cycle need be considered. Therefore the total exposure time for region A per disturbance is T_1 plus T_2, and for N identical disturbances the total exposure time for A is $T_A = N (T_1 + T_2)$. To maintain the proper contrast between regions A and D, T_A must be less than some fraction of the exposure period τ. That is,

$$T_A \leq E_r \tau \qquad (2)$$

where E_r is taken from the film characteristic in figure 4.13.3.1.3-1.

To determine T_1 and T_2, Equation 1 is expanded in a series about t = o, and t =

$$\frac{\pi}{\omega_n \sqrt{1 - \zeta^2}} \qquad (3)$$

to give

$$T_1 = \frac{2\alpha}{\dot{\theta}_o} \text{ sec.}$$

$$T_2 = T_1 \exp. \left(\frac{\xi}{\sqrt{1-\xi^2}}\right) \tag{4}$$

$$T_A = N(T_1 + T_2) = \frac{2N\alpha}{\dot{\theta}_o} \left[1 + \exp\left(\frac{\xi}{\sqrt{1-\xi^2}}\right)\right] \tag{5}$$

Also, by equating the derivative of equation (1) to zero, the relationship between the initial velocity $\dot{\theta}_o$ and the maximum error θ_m is determinted to be.

$$\theta_m = \frac{\dot{\theta}_o}{\omega_n} \exp(-1) \left(\frac{\xi}{\sqrt{1-\xi^2}} \cos^{-1}\xi\right) \tag{6}$$

Combining equations (5) and (6) and using the inequality (2) gives for the final result

$$N = \frac{Er \quad \tau\theta_m \quad \omega_n}{2\alpha \exp\left[\left(-\frac{\xi}{\sqrt{1-\xi_2}} \cos^{-1}\xi\right) + \exp\left(\frac{\xi}{\sqrt{1-\xi^2}} \pi - \cos^{-1}\xi\right)\right]}$$

where

N = number of disturbances per exposure period.

Equation (7) holds only for reasonable values of disturbance ($2\alpha \leq \theta_m \leq 10\alpha$) and control damping ($\xi$ = 50 to 100 per cent). Generally larger values of θ_m will saturate the control system so the Equation (1) no longer describes its response.

4.13.5.3 Eddy Current Damping

The problems of passively damping the motion of a spring-supported telescope are considerably increased in an orbital environment. However, one technique that should be unaffected by the orbital environment is electromagnetic or eddy current damping.

Figure 4.13.5.3-1 shows an idealized version of such a damper. One can regard the conducting plate and the magnet as being rigidly attached to a spacecraft and telescope which are weakly coupled by helical springs.

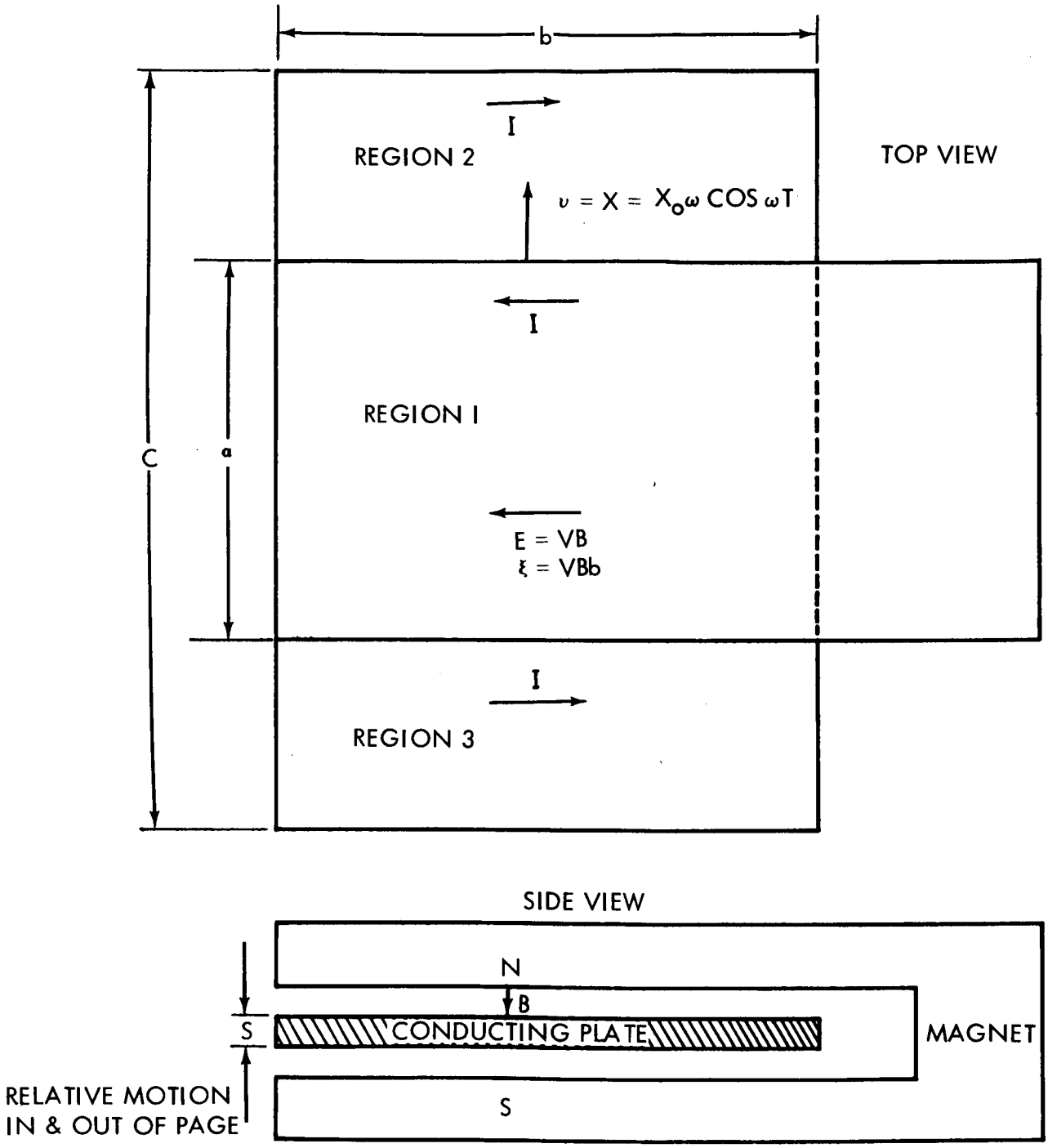


Figure 4.13.5.3-1. Schematic of an Eddy Current Damper

The initial assumptions and outline of the calculation of the damping factor follows:

a. The relative motion of the telescope and spacecraft is simple harmonic.

b. The magnetic field, B, is uniform in the gap of the permanent magnet and goes sharply to zero at the pole face boundaries.

c. The angular frequency, , is sufficiently low such that attenuation of B in the interior is negligible. In cases where this assumption is invalid one can replace the thickness of the conducting plate, S, by an effective thickness $\bar{S}$ (S) which is directly calculable.

The seat of emf of the induced eddy current, I, lies in region 1 which is defined as that portion of the damping plate that lies between the poles of the magnet, M, which produces a flux density $\bar{B}$ directed into the paper, as shown in figure 4/13.5.3-1.

Although it is realized that the current I swirls about in smooth area, as a calculational expediency it is assumed that the distribution of current is as shown in figure 4.13.5.3-1, i.e., in region 1 the current flows to the left and in regions 2 and 3 flows to the right.

We may write the emf, ϵ, as,

$$\epsilon = E \cdot dl = E\ b = \dot{x}Bb = x_o wBb\cos\omega t. \qquad (1)$$

The power dissipated in the plate is

$$P = \frac{\epsilon^2}{R} \qquad (2)$$

where R is the effective resistance of the plate.

We may express R for the assumed distribution as,

$$R = R_1 + \frac{R_2 R_3}{R_2 + R_3} \qquad (3)$$

Where R_1, R_2, R_3 are the electrical resistance of regions 1, 2 and 3, respectively.

Therefore, $R = \frac{1}{\sigma}\left(\frac{1}{a} \quad \frac{1}{c-a}\right)$

(for $a < c$) where σ is the electrical conductivity and a, b, and c are linear dimensions given by figure 4.13.5.3-1.

In order to maximize P we must minimize R. The minimizing condition given by $\frac{dR}{da} = 0$ is that $c = 2a$. Hence,

$$R = \frac{1}{\sigma} \quad \frac{b}{S} \quad \frac{2}{A} . \tag{5}$$

We now have

$$P_{max} = \frac{B^2 bsa \ \sigma}{2} \quad x_o^2 w^2 \cos^2 wt. \tag{6}$$

And the energy dissipated per cycle is given by

$$W_d = \int P_{max} \, D^t = \frac{B^2 \, bsa \, \sigma \, x_o^2 w}{2} . \tag{7}$$

We recall that for a damping force of the form $F_d = c\dot{x} = cx_o\omega\cos\omega t$, where c is the damping coefficient, the energy dissipated per cycle is

$$W_d = c \pi x_o^2 W.$$

Therefore the effective damping coefficient c for the configuration shown in figure 4.13.5.3-1 is

$$C = \frac{B^2 \sigma \, sab}{2} , \tag{9}$$

or

$$C = \frac{B^2 V}{2} \tag{10}$$

Where V is the volume of the conducting plate in which the magnetic field is non zero. The critical damping coefficient for a spring system is given by

$$C_c = 2\sqrt{Km} = 2 w_n \ m.$$

For wn = 0.3 rad/sec and m = 30 slugs = 455 kg,

$$C_c = 286 \frac{Kg}{sec} .$$

We consider $\xi = \frac{c}{c_c} = 0.3$ to be the lower limit for effective damping. Hence we assume the following values for the parameters in equation 9a,

$B = 1000$ gauss $= 0.1$ webera/m^2

$\sigma = (1.7 \times 10^8)^{-1}$

$S = 0.02m$

$a = 0.1$ m

$b = 0.15$ m

and thus we have,

$$C = 91 \ \frac{Kg.}{sec}$$

hence $\xi = 0.34$.

4.13.5.4 Inertial Unbalance Effects

To determine the effect of gimbal pivot point offset from the telescope center of mass, consider the configuration shown in figure 4.14.5.4-1. The position of the pivot point in telescope coordinates is $\bar{r}_o$. The position of the pivot point in spacecraft coordinates is $\bar{\ell}$. The acceleration of the pivot point is $\bar{A}p$. If the motion of the telescope relative to the spacecraft is neglected, the torque acting on the telescope is

$$\bar{T}_{DT} = \bar{r}_o \times M_T \bar{A}_p \qquad (1)$$

where

M_T = telescope mass.

Ap is expressed in terms of the spacecraft motion as

$$\bar{A}p = \bar{A}_o + \omega_x \bar{r} + 2\bar{\omega} \times \bar{V} + \bar{\omega}_x (\bar{\omega} \times \bar{r}) \qquad (2)$$

where,

$\bar{A}_o$ = acceleration of the spacecraft coordinate system

$\bar{V}$ = velocity of the pivot point in spacecraft coordinates

$\bar{\omega}$ = angular rate of the spacecraft

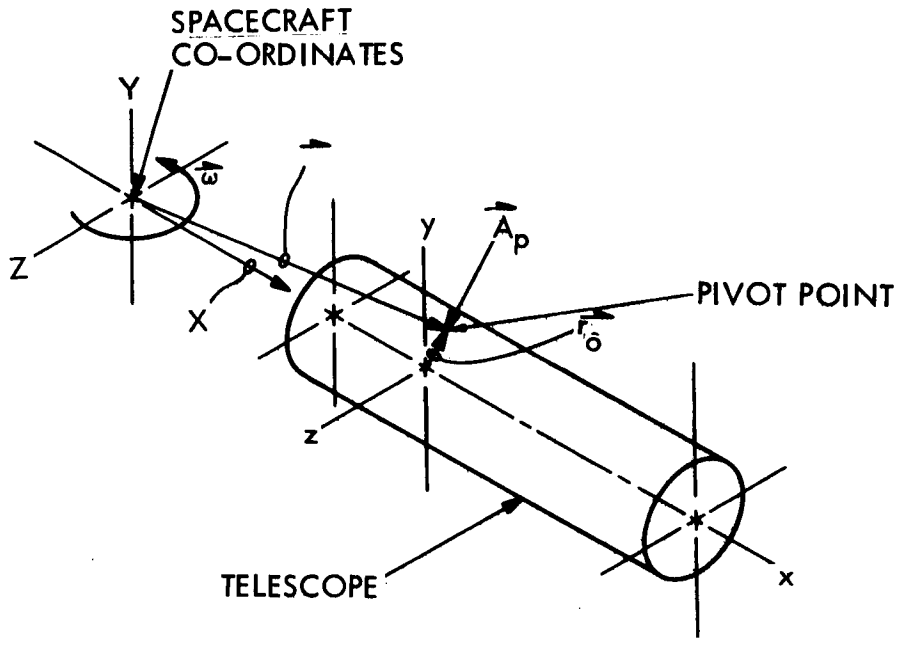


Figure 4.1?.5.4-1. Geometry For Determining Unbalance Effects

Here, V = 0, and the centrifugal acceleration is negligible. This leaves only the linear and angular accelerations of the spacecraft

$$\bar{A}p = \dot{\omega}_x \bar{r} + \bar{A}_o \tag{3}$$

Substituting back into equation (3) and resolving into components gives

$$T_{DX} = M_T \left[(\ell_y y_o + \ell_z z_o)\ \ddot{\phi}_x - \ell_x y_o\ \ddot{\phi}_y - \ell_x z_o\ \ddot{\phi}_z + y_o\ \ddot{X} - z_o \ddot{y}\right] \tag{4}$$

$$T_{DY} = M_T \left[(\ell_z z_o + \ell_x x_o)\ \ddot{\phi}_y - \ell_y z_o\ \ddot{\phi}_z - \ell_y x_o\ \ddot{\phi}_x + z_o\ \ddot{X} - x_o \ddot{z}\right] \tag{5}$$

$$T_{DZ} = M_T \left[(\ell_x x_o + \ell_y y_o)\ \ddot{\phi}_z - \ell_z x_o\ \ddot{\phi}_x - \ell_z y_o\ \ddot{\phi}_o + x_o\ \ddot{Y} - y_o \ddot{x}\right] \tag{6}$$

where, $\ell_x, \ell_y, \ell_z = \bar{\ell}$ components

$x_o, y_o, z_o = \bar{r}$ components

$x, y, z = \bar{A}_o$ components

$\phi_x, \phi_y, \phi_z = \bar{\dot{\omega}}$ components

This last relationship assumes that the body angles are small so that body rates are equal to the angle rates. For most OTES configurations discussed in subsection 11.1, ℓ_x will be several feet, whereas ℓ_y, ℓ_z, x_o, y_o, z_o will all be in inches. Also, for the present analysis, only two axes of rotation are considered. That is, T_{DY} and T_{DZ} are of interest, and ϕ_x is neglected. For these conditions the disturbance torque equations reduce to

$$T_{DY} = M_T\, x_o\, \ell_x\, \ddot{\phi}_y + M_T\, (z_o \ddot{x} - x_o \ddot{z}) \tag{7}$$

$$T_{DZ} = M_T\, x_o\, \ell_x\, \ddot{\phi}_z + M_T\, (x_o \ddot{y} - y_o \ddot{x}) \tag{8}$$

Or redefining,

$$T_{DY} = I_e\, \ddot{\phi}_y + M_T\, (z_o \ddot{x} - x_o \ddot{z}) \tag{9}$$

$$T_{DZ} = I_e\, \ddot{\phi}_z + M_T\, (x_o \ddot{y} - y_o \ddot{x}) \tag{10}$$

where,

$$I_e = M_T\, x_o\, \ell_x$$

is a "disturbance inertia".

As discussed in subsection 11.4 a general program to give the angular and translational disturbances as a function of man's motions is in development. However, for present purposes highly simplified versions of these are used, in which translational motion is uncoupled from rotational motion. Under these assumptions, spacecraft translational disturbances cause telescope disturbance torques which are independent of the control loop dynamics.

4.14 STELLAR INTERFEROMETER DEVELOPMENT EXPERIMENT

4.14.1 Summary

One astronomical goal is to measure stellar diameters and binary separations. The stellar interferometer is used to measure angular diameters through interpretation of interference patterns. Stellar interferometers were constructed and operated successfully by Michelson, Pease, Anderson, and others before Pease's death in 1930. Much useful data on stellar diameters and binary separations was derived with the 20 ft. interferometer, but the 50 ft interferometer built in 1930 proved to be a disappointment. F. G. Pease worked with the instrument at Mount Wilson, but as evidenced by the conspicuously small mention given the interferometer in the annual reports of the thirties, he was plagued with beam vibration and atmospheric turbulence effects.

A stellar interferometer stationed in earth orbit, where these effects can be minimized, will be a valuable tool for increasing our knowledge of stellar and galactic dimensions, Cepheid characteristics and mechanics of stellar systems, to name a few applications. Recommendation #5 in Orbital Astronomy of the Space Science Board Meeting at Woods Hole in 1965 called for the development of optical stellar interferometers, citing the importance of stellar diameter measurements.

The technology necessary for placing such an instrument in orbit and maintaining it there does not exist at present. This technology must be developed through analytical and experimental programs on earth in conjunction with experiments conducted in space on the pointing and stabilization of long beams in space. A large interferometer structure cannot be properly tested and hence developed entirely by earth-based programs.

As a developmental experiment program on OTES, it is proposed to design, orbit, and deploy a 50 foot stellar interferometer system to meet the most rigid performance criteria, and to monitor environmental effects on performance. Even under the best of conditions, operation of the interferometer is a painstaking proposition, and astronaut/instrument interface data will be useful in the planning of missions for manned orbiting observatories.

4.14.2 Experiment Objective

The stellar interferometer is an extremely sensitive tool of astrometry for which technological development ceased in 1938 because of difficulties encountered with vibration and image deterioration by atmospheric effects. This experiment has as its basic objective, the development and evaluation of a space technology necessary to the extension of the principles of stellar interferometry to an instrument designed to function out of range of these constraints. Information gained will be used to support development of an orbital stellar interferometer. Specific objectives of the experiment are:

a. Identification of beam stability problems.
b. Evaluation of a pointing and control system compatible with interferometer requirements.
c. Evaluation of mirror adjustment techniques.
d. Determination of adverse effects of geocentric parallax and orbital motion, if any.
e. Trial and comparison of narrow-band techniques in the UV with conventional wide-band observations.
f. Estimation of size requirements for subsequent instruments.
g. Evaluation of astronaut performance.

4.14.3 Experiment Justification

The stellar interferometer is a device which applies the theory of interference to two incoherent beams of light to the measurement of small angles subtended by astronomical bodies. A double-slit arrangement with variable slit separation is used to produce interference fringes. The behavior of these fringes as slit separation is varied is a function of the physical characteristics of the source. The physical and mathematical relationships involved were derived by A. A. Michelson,(1) who was responsible for the design and operation of stellar interferometers which verified his theory and produced some practical measurements.

The stellar interferometer has thus far been neglected in scientific space programs. However, now that large payloads are becoming available for applications other than man-in-space experiments, there is an opportunity to develop models of this instrument and others of similar complexity to function in space, where their operation is most useful. Since only a limited number of stellar diameters and binary separations have been successfully measured on earth, an orbit-based instrument will have a bountiful supply of subjects. Problems with beam flexure and atmospheric disturbances inhibit the usefulness of a terrestrial instrument of baseline greater than 20 feet. However, absence of atmosphere and gravity makes it feasible to achieve in space Michelson's ambitions of instruments with baselines in excess of 100 feet.

Recommendation #5 in Optical Astronomy of the Space Science Board Meeting at Woods Hole in 1965,(2) called for the development of optical stellar interferometers, citing the importance of stellar diameter measurements.

The evolution of a Stellar Interferometer for space can be broken down into four developmental areas in which engineering research, design, and testing are needed.

a. Optical elements - Optical elements must be chosen and designed such that they will function unchanged through prolonged exposure to the space environment. This involves materials research and

(1) Philosophical Magazine, July 1890, Vol. 30., No. 182, p. 1, Astrophysical Journal, June 1920, Vol. 51, No. 5, p. 257.
(2) Space Research, Directions of the Future, Space Science Board, National Academy of Sciences - National Research Council, 1965.

testing to identify or develop the optimum type of glass from the standpoint of transmission characteristics after prolonged irradiation, thermal performance, and ease of fabrication. All effects can be thoroughly treated on the ground, both analytically and experimentally. Suitable materials exist today and no critical problems are foreseen in space qualification of the optical components and associated shielding.

b. Outboard Mirror Drive System - Coarse positioning of the outboard mirrors along the beam can be accomplished with existing technology. Environmental component testing of drive motors and linkage will require only moderately sized space simulation chambers (6 ft^3).

c. Fine Adjustment Systems - Precision required in the alignment of the Stellar Interferometers of the Michelson or the Fabry-Perot type. These instruments are aligned with relatively sophisticated worm reduction gears or differential screws. Because of potential problems with cold welding of materials other adjustment techniques should be studied such as thermal actuators. Again the facilities required for developmental experiments and tests are presently available.

d. Deployable Beam - Vibrational stability of the beam for extended periods of time represents the critical design constraint for the Stellar Interferometer. The tolerances on motion are optical, that is, to be operable the beam must be completely damped to amplitudes of less than one micron. This rigid constraint can be met simply by employing sufficient thickness in the construction, however only at the cost of a significant weight penalty. Analytical studies are needed for various lightweight beam concepts in order that a choice can be made with sufficient knowledge of the inevitable trade-offs between performance/reliability and weight/cost. Detailed studies are need comparing implementation and performance of telescoping structures vs. rigid, fixed-length booms assembled by astronauts.

   Implicit response of the beam to known disturbance torques can be analyzed mathematically and vibration amplitudes predicted within a few percent. Since the operating environment is ideal from an analytical standpoint, inaccuracies in prediction will result mainly from errors in disturbance assumptions. Experiments aimed at collecting accurate data on disturbances and their propagation must be conducted in space in order to establish firmly the disturbances for continuous station-keeping and the complex propagation of internal disturbances.

OTES offers an opportunity to experiment with beam deployment, mirror adjustment techniques, parallax effect of orbit, vibration effects, and the use of filters and ultraviolet for increased resolution. In addition, the tedious adjustments required in operating the interferometer may warrant the use of automation where possible to satisfy human factors constraints.

4.14.3.2 Need for Space Testing

It is estimated that for potential scientific measurements in the next ten to twenty years an interferometer will be required with a baseline of 50 to 100 feet. Extreme performance requirements combined with necessarily imposed weight and space restrictions rule out single, brute strength approaches to the stability problem. New, sophisticated ideas must be conceived, developed and tested before an instrument can be placed in orbit with any reasonable confidence in its successful operation. In space, environmental tests are needed to supplement component testing on earth because certain information on the environment and its effect on the instrument cannot be obtained on earth nor can they be adequately simulated in the presence of gravity. In particular, while transverse oscillations of a complex beam can be analyzed mathematically with a high degree of accuracy, the longitudinal propagation of disturbances and their effect on the stability of the beam are not amenable to rigid analysis programs. Data is also needed on the combination and transmission of the many disturbances as inputs to a beam analysis model. Data is needed on the effect of continuous station-keeping and continuous fine pointing requirements. Comparison of beam concepts must be accomplished in space.

It is necessary to make practical and accurate measurements of the adverse effects of the totality of factors affecting the performance of the interferometers such as thermal deformation, vehicle and rotation, parallax of orbit, orbital motion, etc., before including the instrument or an orbital laboratory at an operational level. Although small instruments can be fairly thoroughly subjected to many of the deleterious aspects of the space environment they cannot be subjected to all of the conditions at once. Performance of small models can be extrapolated to predict the behavior of large ones in which the effects are magnified, but the total effect of the orbital environment on a 50 or 100 foot interferometer cannot be fully assessed on earth.

4.14.3.3 Feasibility

Critical components in the experiment are:

a. Deployable beam.
b. Optics.
c. Mirror Drive Systems.
d. Fine Adjustment Systems.

None of the above present lifetime problems for a 45 day mission. The main consideration is packaging, deployment and stability.

4.14.4 Implementation

4.14.4.1 Experiment Design

An interferometer system with a nominal beam length of 50 feet will be deployed in two stages and subjected to stability and operational tests.

Vibration and thermal deformation will be monitored with sensors and by measuring displacements of the fringe pattern as the system is pointed and adjusted. Object stars which have been used with ground based interferometers will be used as targets. An equipment block diagram is shown in figure 4.14.4.1-1.

A schematic of the interferometer experiment optics and major components is shown in figure 4.14.4.1-2. The major components are the Beam, Outer Mirror Assembly, Inner Mirror Assembly, Imaging Assembly and the Telescope Cover and Positioning Mechanism. The preliminary design assembly drawing illustrating major component designs, is shown in figures 4.14.4.1-3 and 4.14.4-1-4.

At least two beam concepts will be compared and used in the acquisition of environmental impact data. Potential designs will be carried in ground development and test programs and the most promising types included in the experiment. Several alternative configurations for the optical design of the inner components will be considered. These elements, while critical to the performance of the interferometer, can be developed with existing knowledge and technology, and the experiment configuration will be chosen on the basis of convenience and integration considerations.

4.14.4.1.1 Beam

The requirements imposed on the interferometer beam design are:

a. The beams extend on both sides of the telescope to a distance of 10 feet from the telescope centerline for the first mode of operation. For the second mode of interferometer operation, the beam length is 25 feet from the telescope centerline.

b. The beams are mounted to the telescope (rather than the telescope well).

c. It is preferable to mount the beams at the telescope center of gravity in order to accomodate the control and stabilization systems.

d. The deflections from inertial, solar pressure and gravity gradient loads must be kept to a very low value.

e. The dynamic response must be kept within required limits.

f. The outboard mirrors must be able to be positioned to within 0.1 arc seconds of angle at any position along the beam.

g. The beam will be assembled to the telescope by EVA.

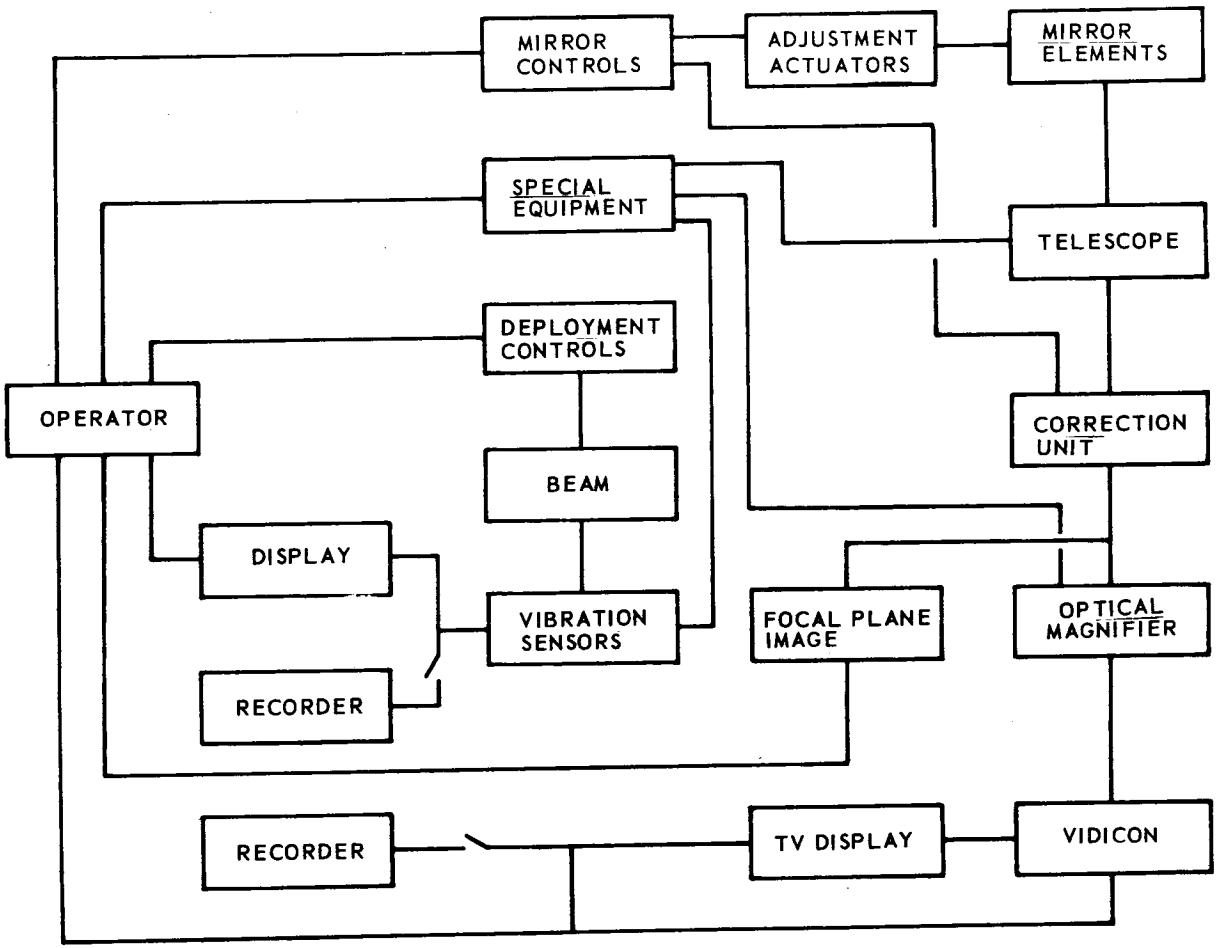


Figure 4.14.4.1-1. Equipment Block Diagram

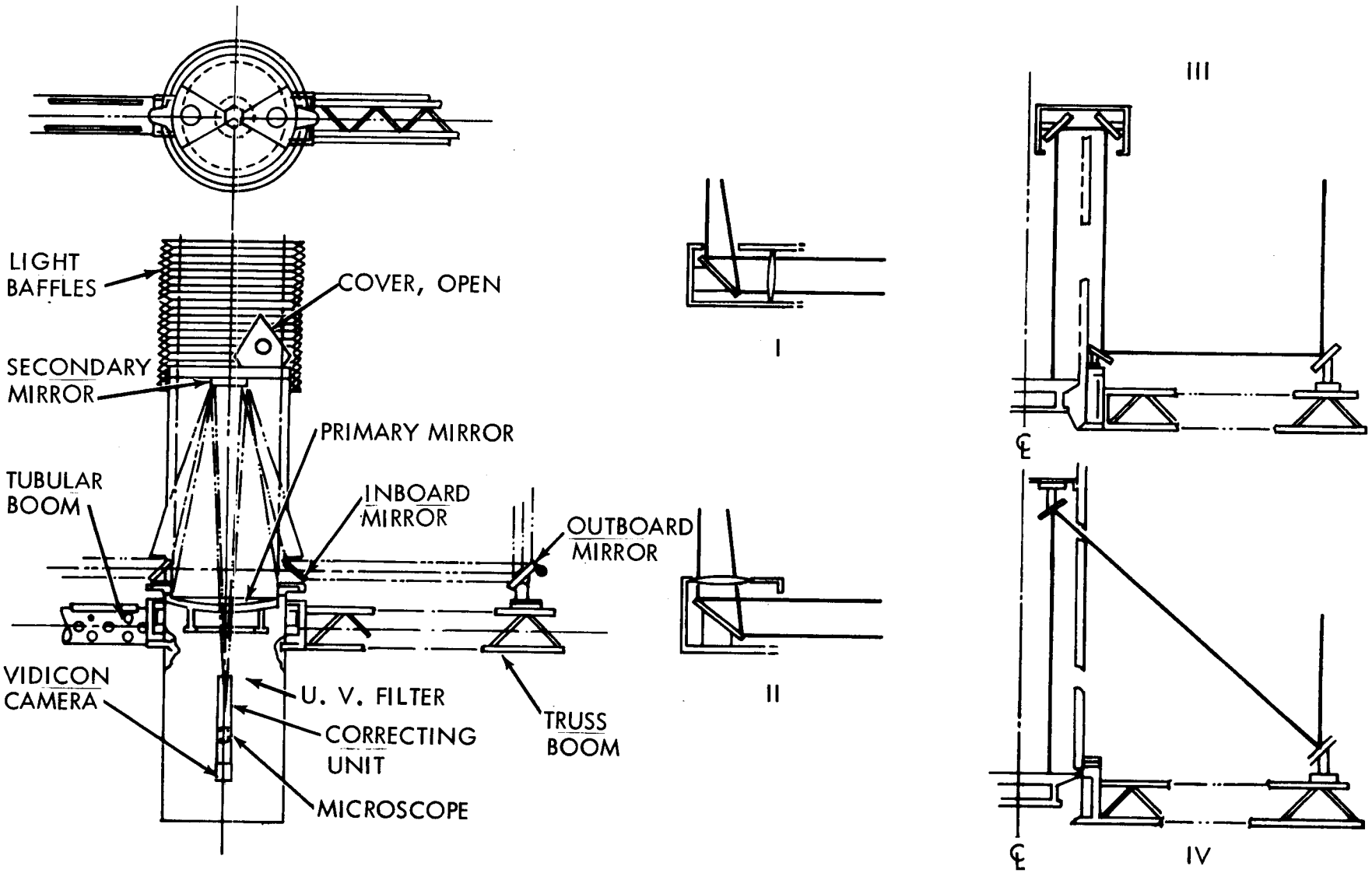
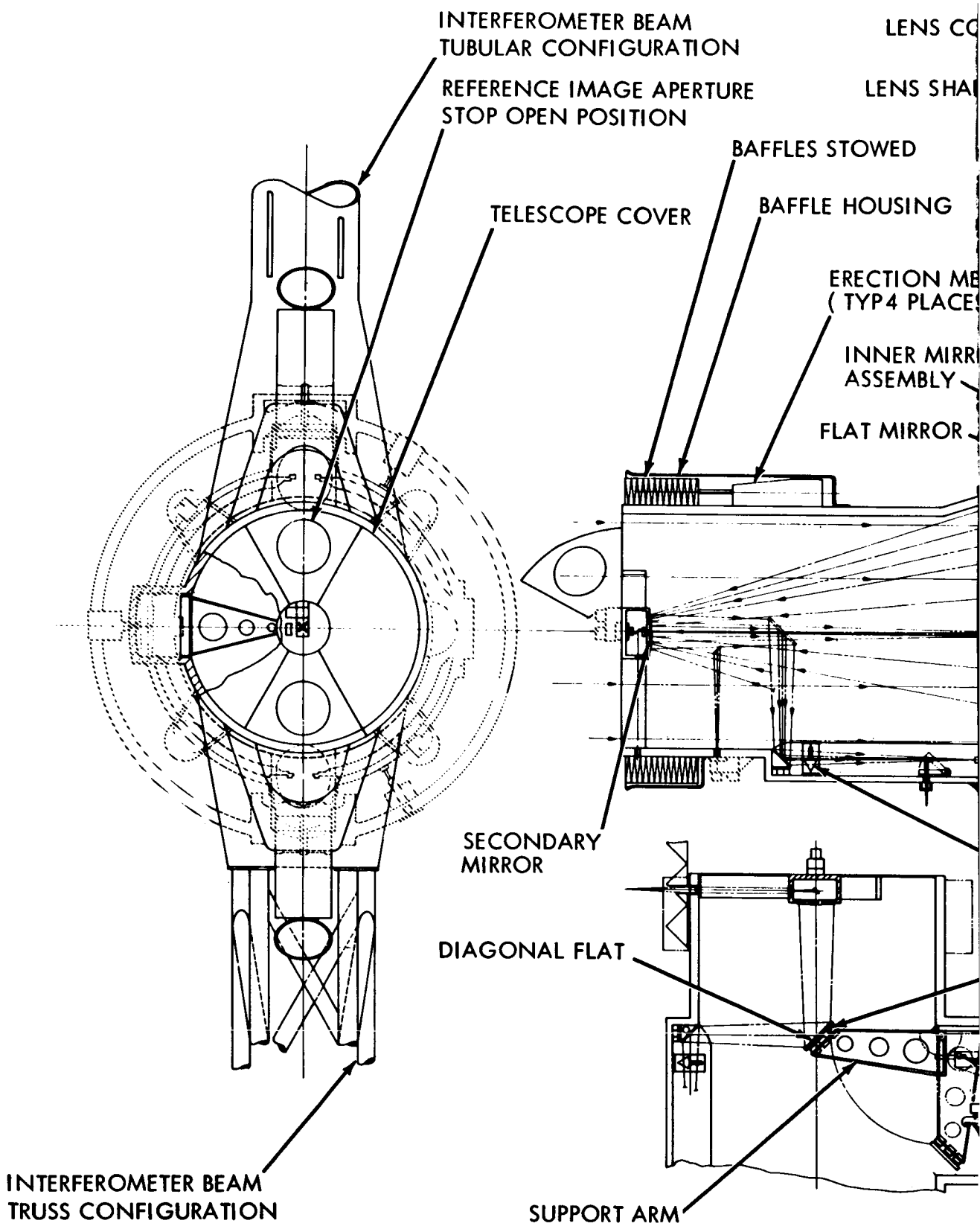
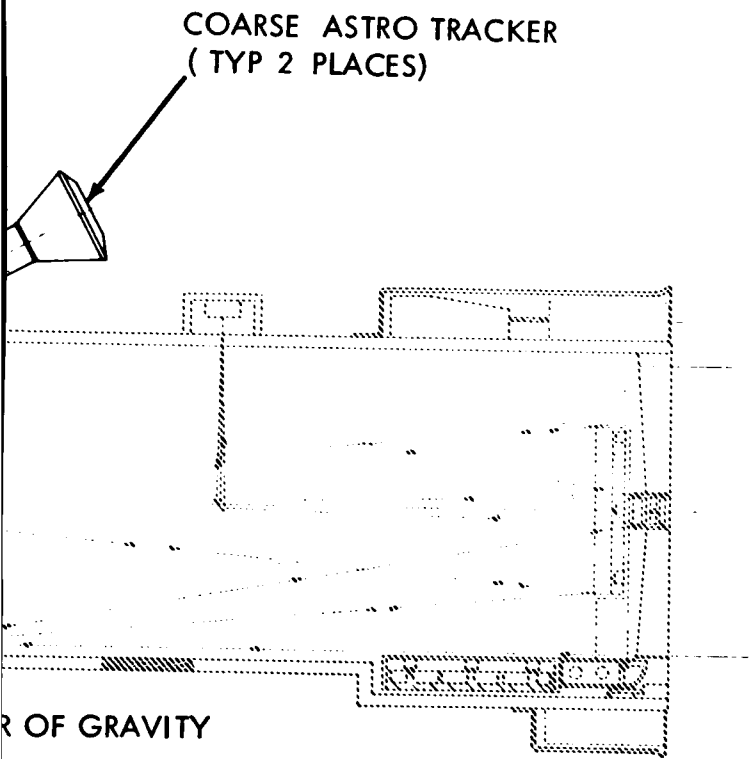


Figure 4.14.4.1-2. Conceptual Interferometer Design


INTERFEROMETER BEAM
TUBULAR CONFIGURATION
REFERENCE IMAGE APERTURE
STOP OPEN POSITION
LENS CO
LENS SHA
BAFFLES STOWED
BAFFLE HOUSING
TELESCOPE COVER
ERECTION ME
(TYP4 PLACES
INNER MIRR
ASSEMBLY
FLAT MIRROR
SECONDARY
MIRROR
DIAGONAL FLAT
INTERFEROMETER BEAM
TRUSS CONFIGURATION
SUPPORT ARM

OBJECTIVE LENS

MECH



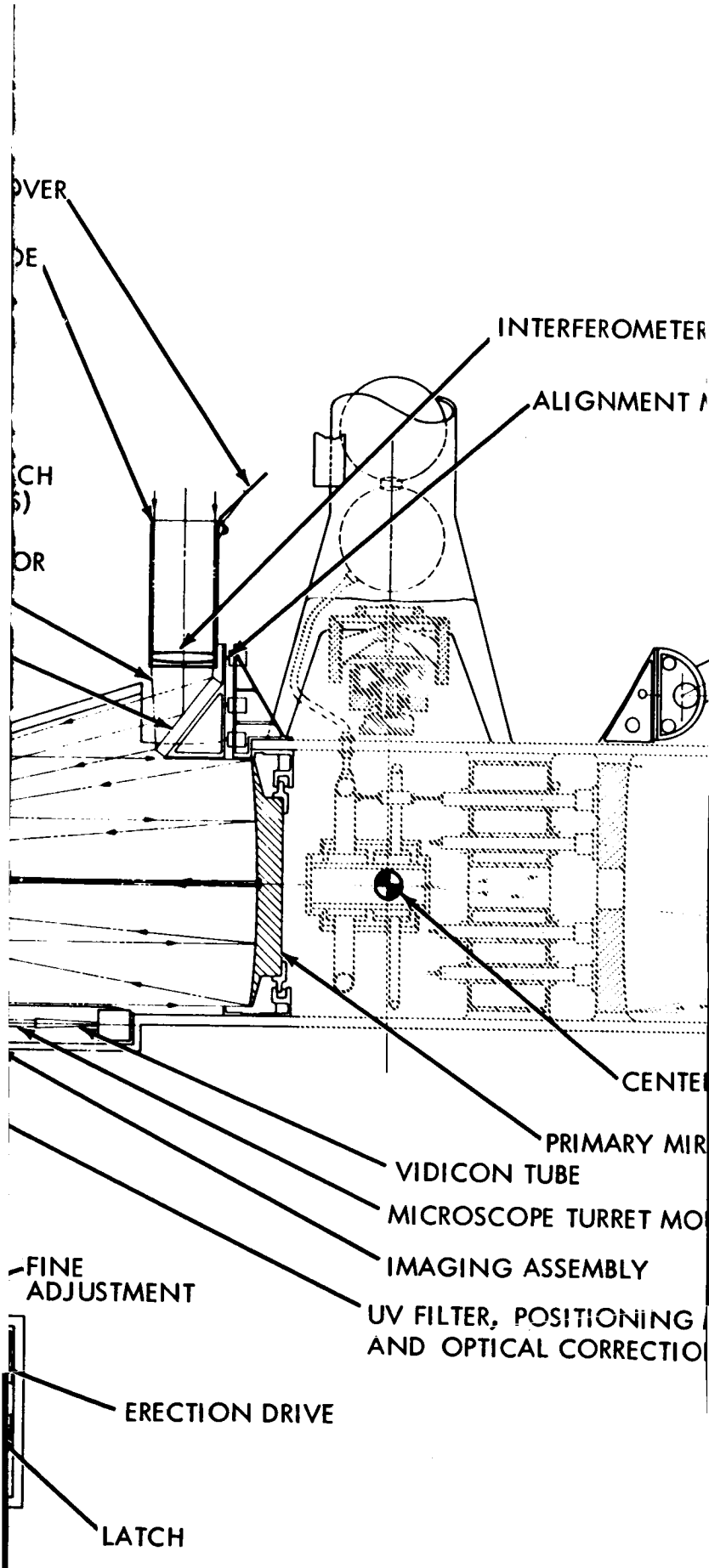
R OF GRAVITY

ROR

UNTED

MECHANISM
N UNIT

Figure 4.14.4.1-3.


VER
E
CH
S)
OR
INTERFEROMETER
ALIGNMENT
CENTE
PRIMARY MIR
VIDICON TUBE
MICROSCOPE TURRET MO
IMAGING ASSEMBLY
FINE ADJUSTMENT
UV FILTER, POSITIONING
AND OPTICAL CORRECTIO
ERECTION DRIVE
LATCH

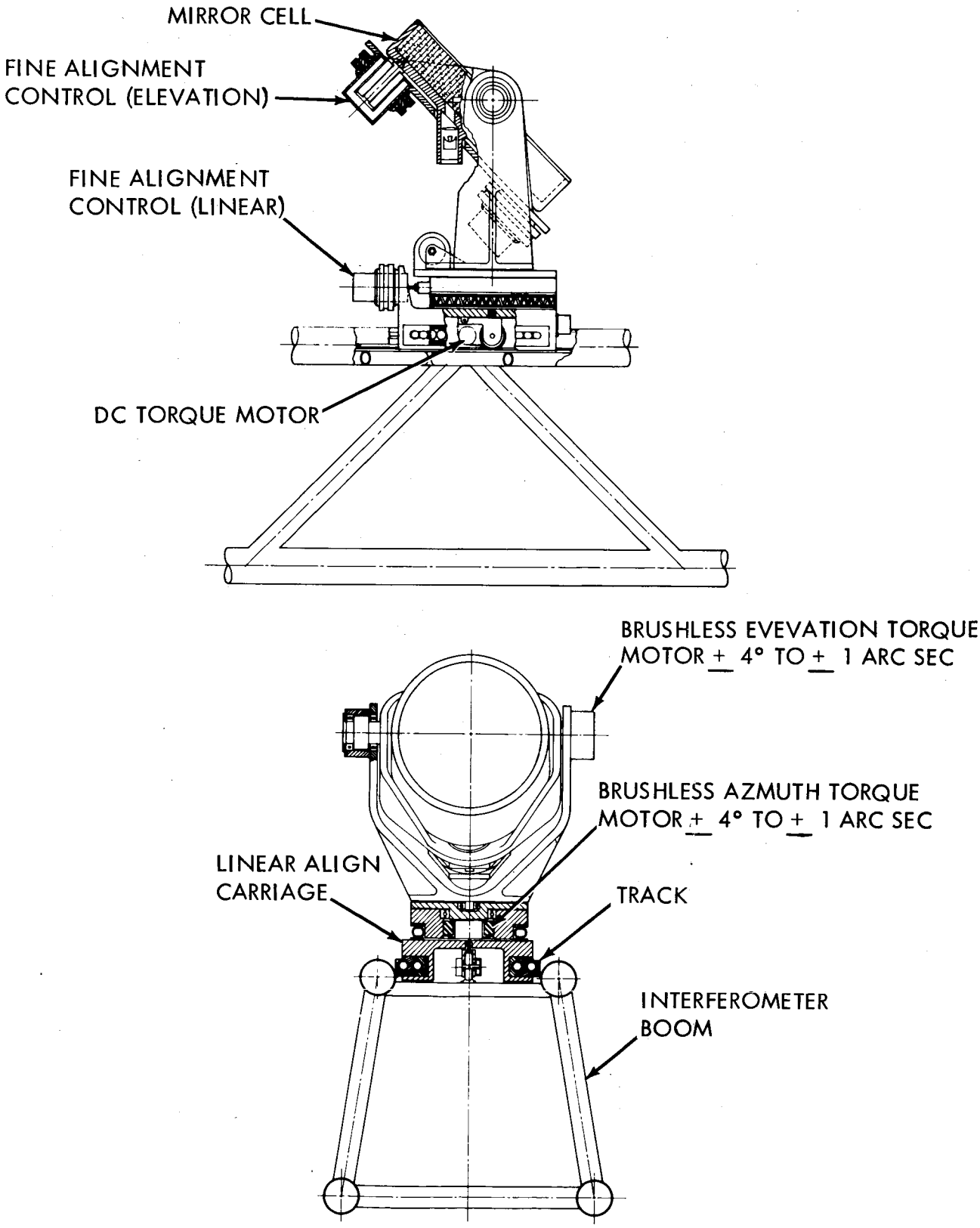


Figure 4.14.4.1-4. Outboard Mirror & Beam Design

Two separate beam designs are presented in figure 4.14.4.1-2. Each beam consists of two separate sections; an inboard section and outboard section. The inboard sections are attached by EVA to the telescope for the first mode of experiment operation. For the second mode of operation, the outboard sections are attached by EVA to the end of the inboard section. During launch and when not in use, all beam sections are conveniently stored on the spacecraft as shown in figure 4.14.4-1-3. During storage the outboard mirror assembly remains attached to the inboard section. The track which allows the outboard mirror to traverse the beam length is an integral part of the beam assembly as shown in figure 4.14.4.1-4. By simple keying of the two beams at assembly, a continuous track at the beam joint is obtained. Accelerometers are positioned along both beam sections for monitoring beam stability during both modes of experiment operation.

A remotely deployable beam not utilizing EVA is also feasible. If the remote deployment method is selected rather than the EVA assembly, it is recommended that the first mode of this experiment be eliminated. (The first mode of operation requires a shorter beam length than the final mode.) It is felt that a remotely operated variable length beam requirement is not compatible with the mirror positioning accuracies. A two section hinged beam is recommended to meet the overall mirror position requirements.

The space truss type beam configuration is fabricated of thin wall aluminum tubing. A minimum thermal gradient across the section of the beam is achieved by orienting the angular struts such that a minimum of shadowing is caused on the struts located behind the struts closest to the sun. That is, the struts on the non-sun illuminated side of the beam receive a minimum of shadow from the struts on the sun side. In like manner, the longerons are positioned such that only one at a time will be shadowed.

The tubular type beam is designed with a configuration to minimize thermal gradients across the beam section. This beam design has a pattern of small circular holes through out the surface to allow sunlight to heat the inner surface of the non-sun side of the tube. The thermal bending is minimized by designing the tube with a one to one ratio of the projected area of the holes to the projected tube area and by positioning the holes for maximum internal sun reflection, i.e., minimum sunlight passing through the beam. The resulting minimum thermal distortion of the beam is compensated for by oversizing the outboard mirror.

4.14.4.1.2 Outer Mirror Assembly

The function of the outer mirror is to direct the subject incident light toward the inboard mirror to a pointing accuracy of 0.1 arc seconds. The outer mirror assembly is presented in figure 4.14.4.1-4. The device is designed to allow the mirror to travel the full beam length by means of a coarse positioning drive motor. A linear thermal actuator allows for fine

positioning along the beam. Coarse and fine positioning at two right angles to the beam is achieved with torque motors and thermal linear actuators. The thermal actuator is similar to the device proposed for the Bidirectional Mirror Correction Device Experiment. Energizing the inner coil will cause it to heat up, which will heat the push actuator. The incremental increase in length of the push actuator will produce a pushing force on the mirror force is resulted on the mirror mount thereby tilting the mirror in the opposite direction.

A guide light is mounted in the mirror base for initial alignment of the mirror. A spring loaded take-up reel mounted to the telescope end of the beam provides the variable length electrical leads to the mirror assembly.

4.14.4.1.3 Inner Mirror Assembly

The function of the inner mirror is to align the incident light to the imaging assembly by reflection off the telescope secondary mirror. Fine positioning of the mirror is by means of linear thermal actuators similar to the units described above. The two inner mirrors are placed at a center distance of 16 inches from the telescope centerline and pointed to an accuracy of 0.1 arc seconds.

4.14.4.1.4 Imaging Assembly

The imaging assembly is illustrated in figure 4.14.4.1-2. It is rigidly mounted behind the telescope primary mirror. Its major components are: UV filter and positioning mechanism; optical correction unit; turret-mounted microscopes; vidicon tube.

4.14.4.1.4.1 UV Filter and Positioning Mechanism

The UV pass band filter (Type I-D) is mounted to a positioning mechanism which positions it in the beam path, near the focus for convenience, when required.

4.14.4.1.4.2 Optical Correction Unit

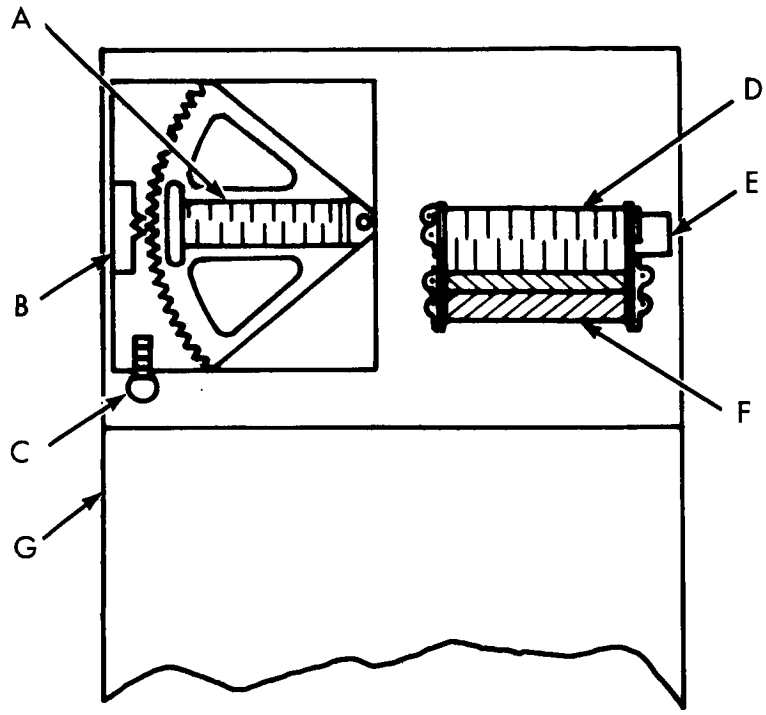
The optical correction (figure 4.14.4.1.4.2-1) unit contains a plane parallel plate and a variable wedge. Both are made from fused silica or a glass with comparable transmission characteristics such as Vycor.

4.14.4.1.4.3 Microscopes

Two microscopes are turret mounted for use as required. The optical elements are also made from fused silica or Vycor and have a linear magnification of 30 x to 50 x.

4.14.4.1.4.4 Vidicon Tube

The vidicon tube has a range of focus of about 10 mm.



A - PARALLEL PLATE (10mm THICK)

B - HORIZONTAL ADJUSTMENT MECHANISM

C - VERTICAL ADJUSTMENT MECHANISM

D - MOVABLE WEDGE

E - MOVABLE WEDGE ADJUSTMENT MECHANISM

F - FIXED WEDGE

G - MOUNTING TUBE (ATTACHES TO TELESCOPE OR TURRET)

Figure 4.14.4.1.4.2-1. Optical Correction Unit

4.14.4.1.5 Telescope Cover and Positioning Mechanism

The telescope cover has two fixed circular apertures. When the telescope cover is in operating position (deployed to cover the telescope), the circular images of light are superposed at the center of the field.

The positioning mechanism as shown in figure 4.14.4.1-1 allows the cover to be hinged accurately in place over the well so that no fine adjustment is required once in place.

4.14.4.2 Operational Procedure

The experiment is divided into two phases, the first dealing with deployment and stabilization of the rigid beam, the second concerned with operational performance. Experiment phases are arranged as follows:

a. Beam Stability
   (1) Short Beam
      (a) Vibration Monitor
      (b) Image Quality
   (2) Long Beam
      (a) Vibration Monitor
      (b) Image Quality
b. Interferometer Operation
   (1) Short beam
   (2) Long Beam
   (3) UV Imaging

a. Beam Stability

Although the problem of image deterioration and motion due to atmospheric turbulence has been eliminated by placing the instrument in orbit, the critical problem of beam vibration is, if anything, magnified. The required rigidity of the instrument is dictated by the size of that characteristic of light basically responsible for interference phenomena, the wavelength.

Hence, when working with visible light vibrations amplitudes on the order of a micron can be intolerable, and this degree or rigidity and stabilization must be assured in an operational instrument. This part of the experiment will subject a prototype beam to disturbing influences, measure the resulting beam motion, and observe the effect on image quality. These tests are made in white light with the beam partially deployed, then fully deployed.

The short beam experiments are conducted with the beam deployed for a total separation of the outer mirrors of about 20 feet. Vibration sensors along the beam are used to monitor the activity of the beam as the spacecraft is pointed at the first target and subjected to rotational torque and simulated random-type internal disturbances. Vibrational activity of the beam is recorded for various methods of positioning, i.e., different thrust functions, different turning rates. The data is stored and transmitted to earth at a convenient time.

After completion of the disturbance program, the images from the two interferometer pencils are focused near each other in the field of view. The first target is used as an object, and closed-circuit TV is used for fine pointing. The smallest circle of confusion is achieved as the spacecraft is stabilized. Excursions of the images are noted as slight changes in telescope attitude are effected.

Long beam experiments are conducted in a similar fashion with the beam fully deployed.

OPERATIONAL TASKS

First Series - Beam Stability

a. Electronics checkout.
b. Deploy inboard focusing elements.
c. Assemble and deploy short section beam.
d. Align inboard focusing elements.
e. Position outboard mirrors at 30 ft. separation.
f. Activate vibration sensors, display and recorder.
g. Acquire first target and adjust spacecraft attitude; wait for vibrations to damp.
h. Program of rotations about telescope axis. Several angular rotations of 20-30°, using a different thrust function each time, wait for vibrations to damp after each rotation.
i. Position outboard mirrors to acquire first target star.
j. Align outboard mirrors for coincidence of interferometer images.
k. Program of internal spacecraft disturbances.
l. Program of small angular rotations (2-5°), image motion recorded on videotape.
m. Deactivate sensors and TV.
n. Assemble and deploy complete beam, increase outboard mirror separation to 48 feet.
o. Activate vibration sensors, display and recorder.
p. Acquire second target and adjust spacecraft attitude; wait for vibrations to damp.
q. Program of rotations about telescope axis. Several angular rotations of 20-30°, using a different thrust function each time; wait for vibrations to damp after each rotation.
r. Position outboard mirrors to acquire second target star.
s. Align outboard mirrors for coincidence of interferometer images.
t. Program of internal spacecraft disturbances.
u. Program of small angular rotations (2-5°), image motion recorded on videotape.
v. Deactivate sensors and TV.

b. Interferometer Operation

In addition to determining the structural rigidity of the system, the interferometer is subjected to a series of operational tests. The information

derived from these tests will be used to assess the general performance of the instruments and the functioning of man in the system, and to identify specific problem areas where improvements will increase the efficiency of the instrument or the man/instrument system. The lengthy and tedious adjustments inherent in the operational procedure indicate that the human factor will be a major source of guidelines for design of later stellar interferometers.

The operational tests are performed with the beam fully deployed. Two stars are to be chosen for the tests as targets. One target will be of such size as to produce fringe disappearance at a mirror separation of approximately twenty feet, such as α Bootis (Arcturus). The second target will be selected for brightness and small size, such that the interference fringes will be visible even with maximum mirror separation. One known star of this type is α Aql (Altair). Final selection of the targets will depend on the type of orbit and the time of flight. The targets must be visible to the spacecraft continuously for 3 to 10 hours. Figure 4.14.4.2-1 shows the positions of the above target stars.

First Target (Short Beam)

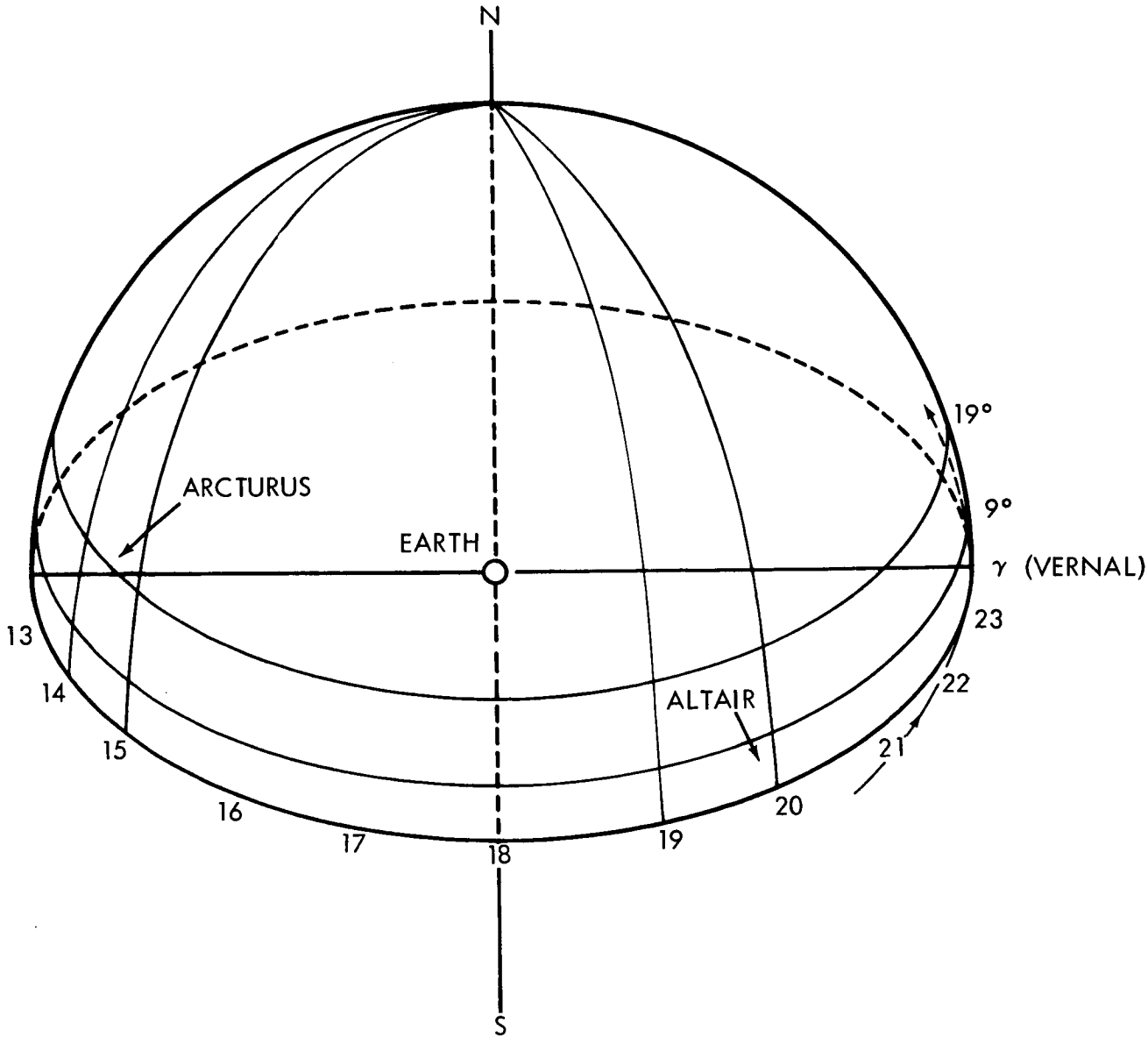
The spacecraft and telescope are pointed and the first target star brought to the center of the field of view. The telescope cover is deployed (with its two fixed circular apertures) and the circular (reference) images from these pencils superposed near the center of the field by adjusting the position of the telescope cover and the plane-parallel plate.

With the outer mirrors deployed about 20 feet apart, the focusing elements are moved into position in front of the telescope primary mirror. The focusing elements are adjusted until the two images formed by the interferometer pencils fall alongside the reference image in the field of view.

When the reference image and interferometer image are in the center of the field, the optical magnification unit and TV camera are inserted behind the focus. Subsequent adjustments are made with the aid of the TV viewing system.

A set of reference fringes is produced by adjusting the reference pencils for coincidence and path equality with the plane-parallel plate and the movable wedge.

The interferometer pencils are brought to coincide alongside the reference image by minute adjustment of the outer mirrors. Interferometer fringes are obtained by moving the wedge to equalize optical path in the two pencils. As the wedge is moved the reference fringes will disappear. A count is kept on the displacement of the wedge required to bring the interferometer fringes into view, and one of the focusing elements is repositioned slightly to compensate. After several trials, both sets of fringes should be clear.



NORTHERN CELESTIAL HEMISPHERE. SHOWING LOCATION OF TARGET STARS BY RIGHT ASCENSION (HOURS) AND DECLINATION (°) FROM VERNAL EQUINOX (MARCH 21) TO AUTUMNAL EQUINOX, THE SUN IS BEHIND THE EARTH WITH RESPECT TO STARS WITH RIGHT ASCENSIONS BETWEEN 14 HRS. AND 22 HRS.

Figure 4.14.4.2-1. Northern Celestial Hemisphere

The separation of the outer mirrors is increased two feet and the process repeated. Greater separations are used until fringes can no longer be obtained. Photographs or videotapes are of the fringe patters at the various stages of adjustment, and a visual-scale visibility assigned to the fringes at each separation.

When the point of zero visibility has been reached, the UV filters are put in place, and the fringe system obtained. The preceding procedure is repeated in reverse, decreasing the mirror separation in know increments and assigning a visibility to the fringes at each separation.

Second Target (Long Beam)

The second target is acquired by the telescope and the reference image obtained as with the first target.

The separation at the outer mirrors is increased to 30 feet and interferometer fringes obtained. Separation is increased by 4 foot increments and visibility values assigned at each separation.

Second Series - Interferometer Operation

a. Deploy special telescope cover (with aperture for reference pattern).
b. Acquire and fix on first target star.
c. Activate vibration sensors and wait for damping.
d. Reduce separation of outboard mirrors to 20 feet.
e. Bring the interferometer pencils into the field of view by adjusting alignment of outboard mirrors.
f. Insert correction unit and vidicon.
g. Check alignment.
h. Insert optical magnification unit.
i. Bring reference pencils with plane-parallel plate.
j. Adjust for equality of path length with double wedge.
k. Adjust for coincidence of interferometer pencils with outboard mirrors.
l. Adjust for equality of path length in interferometer pencils, noting the displacement of the movable wedge required to accomplish this.
m. Reposition inboard focusing element to compensate the indicated path difference.
n. Repeat steps l and m until both images are corssed with fringes.
o. Scan the pattern for intensity profile and record.
p. Separate outboard mirrors two feet.
q. Repeat steps k through p until no fringes can be obtained.
r. Insert UV filters.
s. Repeat steps p and q, decreasing mirror separation.
t. Increase outboard mirror separation to 30 feet and repeat steps k through p.
u. Optional data collection. Record intensity profiles for several separations for selected "average" object stars.

Optional Observations

Once it has been established that the instrument is functioning properly, routine observations are made on several selected small stars, whose dimensions are such that fringe disappearance will not occur for mirror separations of less than 60 or 70 feet. Using a visual scale from 0 to 10, the visibility functions will be estimated by sampling at several separations. Photographs or videotape records are made for further analysis on the ground.

It is estimated that a total of 8 hours will be required for Part a. This allows 2 hours for each of the four tasks. Each of the tasks in Part b will require 3 hours.

4.15 SEGMENTED OPTICS

4.15.1 Summary

Because of the deleterious effects of the earth's atmosphere, further improvement in astronomical telescope resolution can be achieved only by placing the telescope above the atmosphere. However, a conventional telescope cannot exhibit diffraction limited performance in the space environment, and techniques must be devised to overcome the environmental effects. Promising solutions to this problem are mirror segmentation and thin mirror correction. (The latter technique is discussed in another experiment in section 4.10.) There is, at present, insufficient information on which to base a choice between these two techniques. This information must be obtained by an experimental program, and the last part of this program must be carried out in space, free from the earth's atmosphere and from gravity-induced mirror deflections. This experiment uses a primary mirror made of three segments which will be of the same type as would be used in a large observational telescope, as determined by ground-based experiments, and evaluates its performance in space.

4.15.2 Experiment Objective

The objective of this experiment is to gather information on which a decision can be based as to the optimum means for obtaining diffraction limited performance from a large orbiting or lunar based telescope.

4.15.3 Experiment Justification

4.15.3.1 Contribution and Need

The limiting factor in earth-bound telescope performance is the earth's atmosphere. For this reason, the development of space astronomy, performed above the earth's atmosphere, has been set as an important goal of the national space program. In particular, the development of a 120 inch orbiting telescope has been established by the Space Science Board as the outstanding goal in space astronomy. (1)

The space-borne telescope will result in a significant improvement only if its resolution approaches the theoretical limit, i.e., it is diffraction limited. It is known, however, that the orbiting telescope will be subjected to a harsh environment, especially in terms of temperature and temperature gradients. This environment will tend to introduce optical aberrations, e.g., through shape distortions, which will make it impossible to achieve diffraction-limited performance with conventional mirror designs.

---

(1) Space Research - Directions for the Future, Part Two, Space Science Board, National Academy of Sciences, National Research Council, Washington, D. C., January, 1966.

One of the proposed solutions to this problem is segmented optics and another is thin mirror correction, discussed in section 4.10. In the segmented optics concept, the primary telescope mirror would be made up of a number of individually adjustable segments. These segments could then be adjusted to compensate to a large extent for shape distortions of the mirror, maintaining near diffraction-limited performance. Not only could the segments be adjusted to correct for shape distortions, but, because of their relatively small size, could be made thinner and still withstand the rigors of the launch environment. These thinner segments will be less susceptible to the thermal environment.

Among the other potential advantages of segmentation are:

a. Weight-savings - the fact that segments can be made thinner than a solid mirror means that the entire assembled mirror will weigh appreciably less than a solid mirror of the same aperture.

b. Convenience - small segments will present fewer handling problems than a large solid mirror and will be easier to package in a spacecraft.

c. Prefabrication potential - an instrument can be designed so that its resolution and light-gathering power can be improved by the later addition of segments.

d. Size - through the use of assembly techniques, a telescope could be launched by several boosters, allowing a larger mirror than would otherwise be possible.

A successful conclusion of this experiment will permit the choice of either the segmented optics or the thin mirror correction principle as the method of choice for space applications. There is presently not sufficient information on which to base this choice.

4.15.3.2 Need for Space Testing

In order to realize the potential advantages of segmented optics, the segments must be thin, and thin mirrors are subject to significant deflections by the force of gravity. The gravity induced deflection of a circular plate of radius a, supported by three supports equally spaced on a circle of radius a/2, is of the form (2)

(2) Timoshenko, S., and Woinowsky - Krieger, S., Theory of Plates and Shells, Second Ed., McGraw-Hill Book Company, New York, 1959.

$$w = K \frac{\pi^2 a^6 \rho h}{D} \qquad (1)$$

where: w = deflection at the center

ρ = density

h = thickness

D = flexural rigidity (a function of Young's modulus, Poisson's ratio, and thickness)

Computations using equation (1) for several different cases are presented in table 4.15.3.2-1.

TABLE 4.15.3.2-1

DEFLECTION AT THE CENTER OF A CIRCULAR PLATE 1 IN. THICK, WITH RADIUS a, SUPPORTED AT THREE EQUALLY SPACED POINTS ON A CIRCLE OF RADIUS a/2, DUE TO 1G LOAD

a (in.)	Material	Deflection (Å)
12	Beryllium	4,940
6	Beryllium	308
3	Beryllium	20
12	Glass	30,400
6	Glass	1,900
3	Glass	120

It can be seen that these deflections represent entirely too much distortion of the mirror figure test to be valid.

During the figuring and testing of a thin solid mirror, it can be maintained in a horizontal configuration and supported at every point on its rear surface, thereby eliminating the gravity-induced deflection problem. However, the segmented mirror system cannot be supported in this fashion -- the segments must be placed on their position actuators -- and the gravity-induced deflection cannot be avoided. The segmented system must, therefore, be tested in space.

There is an additional factor which makes space testing highly desirable, and perhaps even mandatory.

In a test of telescopes intended to be used for space astronomy, it would be desirable to photograph actual astronomical bodies. On the earth's surface, however, this would require viewing through the earth's atmosphere, and it would be impossible to determine the performance limits of the telescope.

An alternative approach would be to use simulated astronomical bodies, and carry out the tests in a vacuum chamber. However, complete astronomical bodies would be difficult to simulate, and a vacuum pumping system would introduce vibrations which could be as detrimental to performance as atmospheric turbulence.

4.15.3.3 Feasibility

This experiment utilizes a three-segment mirror with manually positioned segments and a simple optical device for sensing segment position. As such, it allows fundamental checks on the concept of segmented optics. For instance, it allows the determination of the resolution of the basic segmentation configuration,which, as yet, has not been established. An active control system, while desirable for an orbiting observatory, introduces additional complexity, and, in the event of poor performance, makes it difficult to determine the reason for that performance.

Since the system proposed here is a basic one, consisting of relatively simple position actuators and sensors, no reliability problems are anticipated.

4.15.4 Implementation

4.15.4.1 Experiment Design

The effect of segmentation on a telescope's diffraction pattern, and, hence, on its resolution has not yet been established. This effect can be determined both analytically and experimentally.

The relative intensity in the diffraction pattern can be determined by the solution of the following equation: (3)

$$\frac{I}{I_o}(p, q) = \left[\frac{\int_A \int e^{-ik(p\xi + q\eta)} d\xi \, d\eta}{\int_A \int d\xi \, d\eta} \right]^2 \qquad (2)$$

where, I_o = incident light intensity

I = light intensity at the point (ρ, q) in the diffraction pattern

k = wave number of the incident light

p, q = rectangular coordinates of a point in the diffraction patterns

ξ, η = rectangular coordinates of a point in the aperture

and both integrals are to be carried out over the area of the aperture.

(3) Born, M. and Wolf, E., Principles of Optics, Second Ed., The Macmillan Company, New York, 1964.

In the case of a circular aperture the solution of equation (2) results in the familiary Airy pattern, involving Bessel functions. In the case of a more complex geometry, such as that of a segmented mirror, equation (2) would have to be solved numerically, probably with a high speed digital computer. Nevertheless, the solution would be straightforward, and should be carried out in order to determine the effects of segmentation, and the optimum size and shape segments for use in a large telescope.

The effect of segmentation on the diffraction pattern can also be determined empirically by photographing the diffraction pattern of an actual or simulated segmented mirror. This experiment should be performed to verify the theoretical results.

After the completion of these studies, the optimum segment geometry for a large telescope can be determined. A few (perhaps three) of these segments will then be assembled into a primary mirror, with appropriate position sensors and actuators, which will then be tested in space. The tests will consist of figure measurements and actual photographs.

4.15.4.1.1 Segment Positioning

A number of systems have been considered for segment positioning:

a. Cantilever beam: If a transverse force is applied at the end of a cantilever beam, every point on the beam experiences a transverse deflection which depends on the distance of the point from the end of the beam. If the motion of some point along the beam is used to position a mirror segment, and the transverse displacement at the end of the beam is controlled, a reduction of the displacement is achieved. Several configurations of steel beams were considered (figure 4.15.4.1.1-1). The results are summarized in table 4.15.4.1.1-1.

TABLE 4.15.4.1.1-1

TRANSVERSE BEAM DEFLECTIONS

Configuration (see figure 1)	Transverse deflection at P per pound of force applied transversely at end (Å/lb)
(a)	18,300
(b)	963
(c)	378

Since it is desirable to have a positioning resolution of 0.01 wavelengths, or about 50Å, it was concluded that this system probably is not adequate, especially when the difficulty in constructing a true cantilever is considered.

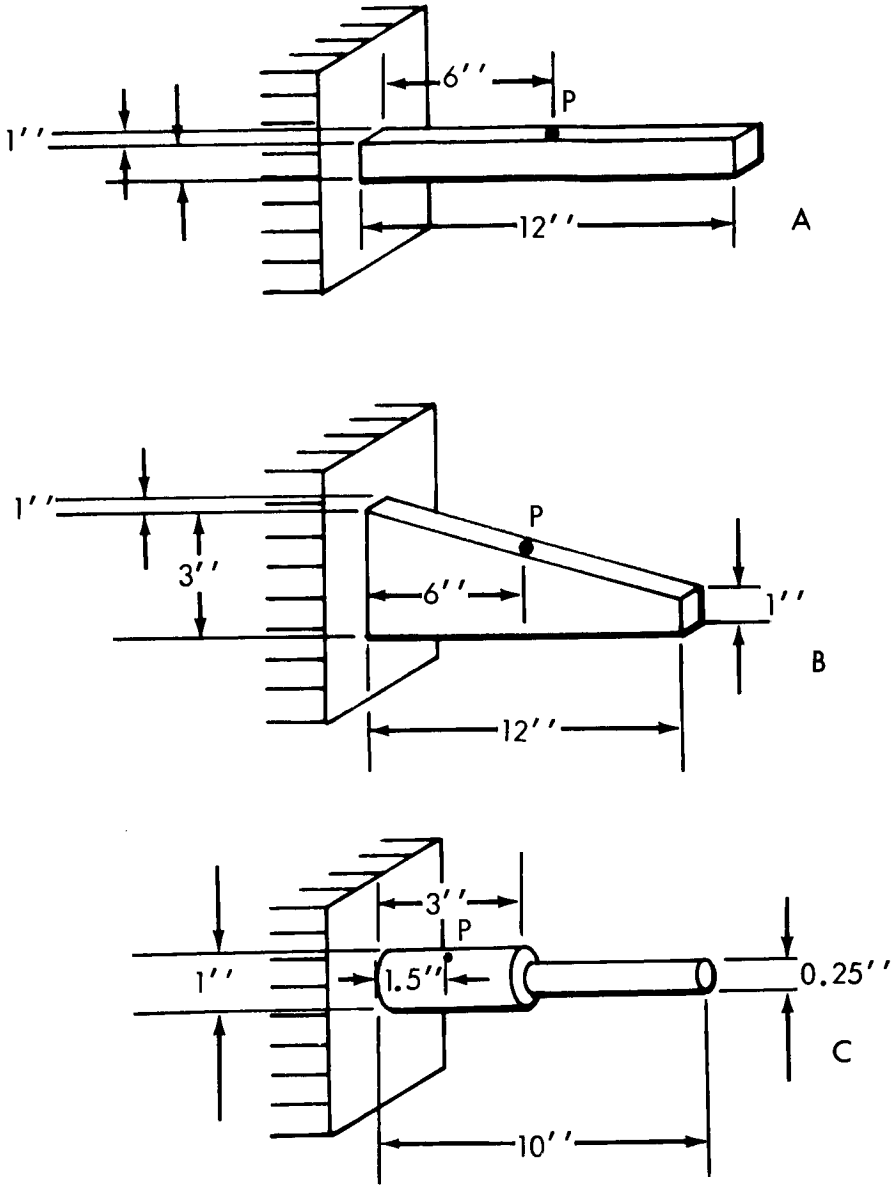


Figure 4.15.4.1.1-1. Cantilever Beams

b. Gear Train: The following gear system was considered; a worm drive with a 0.5 mm pitch driving a 5 cm diameter gear, which drives a lead screw of 0.5 mm pitch. This lead screw drives the mirror segment. With this system, a one degree rotation of the worm drive will produce 44Å of motion of the mirror segment. The feasibility of this type of system is borne out by the fact that there are commercially available Michelson interferometers using it. One of these has a least count of 1000Å on the worm drive, but according to Higgins, (4) this can be improved by perhaps an order of magnitude simply by installing a lead screw with a smaller pitch and installing a vernier readout on the worm drive. An example of a segmented mirror with this position actuator is shown in figure 4.15.4.1.1-2. Each segment has three electrically driven actuators. All three may be driven simultaneously for linear position control, or anyone of them may be driven independently for angular control.

c. Piezoelectric Effect: Piezoelectric crystals and electrostrictive crystals have the property of changing their dimensions under the influence of applied voltage. The two types of crystal differ, however, in that an electrostrictive one always expands when voltage is applied, while a piezoelectric one will either expand or contract, depending on the polarity of the applied voltage. With both types of crystal, the dimensional change is very small, but the ability to contract as well as expand makes the piezoelectric effect appear more useful in this application. A sample calculation shows that a quartz disc 1 cm in diameter and 3 mm thick will change its thickness 0.775Å per volt of applied voltage. This phenomenon, then, offers the possibility of extremely fine position control.

d. Thermal Systems: Thermal expansion and contraction offers a means of obtaining very small controllable displacements. However, a thermal system offers the disadvantages of requiring power continually, and of having an inherently long time constant.

e. Electrostatic Systems: The force between two charged conductors, according to Symthe,(5) is

$$F_p = \int_s \frac{\bar{D} \cdot \bar{E}}{2} \hat{p} \cdot \hat{n} \cdot dS, \quad (3)$$

where;

$\bar{F}_p$ = force in the direction of the unit vector $\hat{p}$
$\bar{D}$ = electric displacement
$\bar{E}$ = electric field intensity
$\hat{n}$ = unit vector, normal to the surface

(4) Higgins, L. W., Gaertner Scientific Co., Private Communication, June 28, 1966.

(5) Smythe, W. R., Static and Dynamic Electricity, Second Edition, McGraw-Hill Book Company, Inc., New York, 1950.

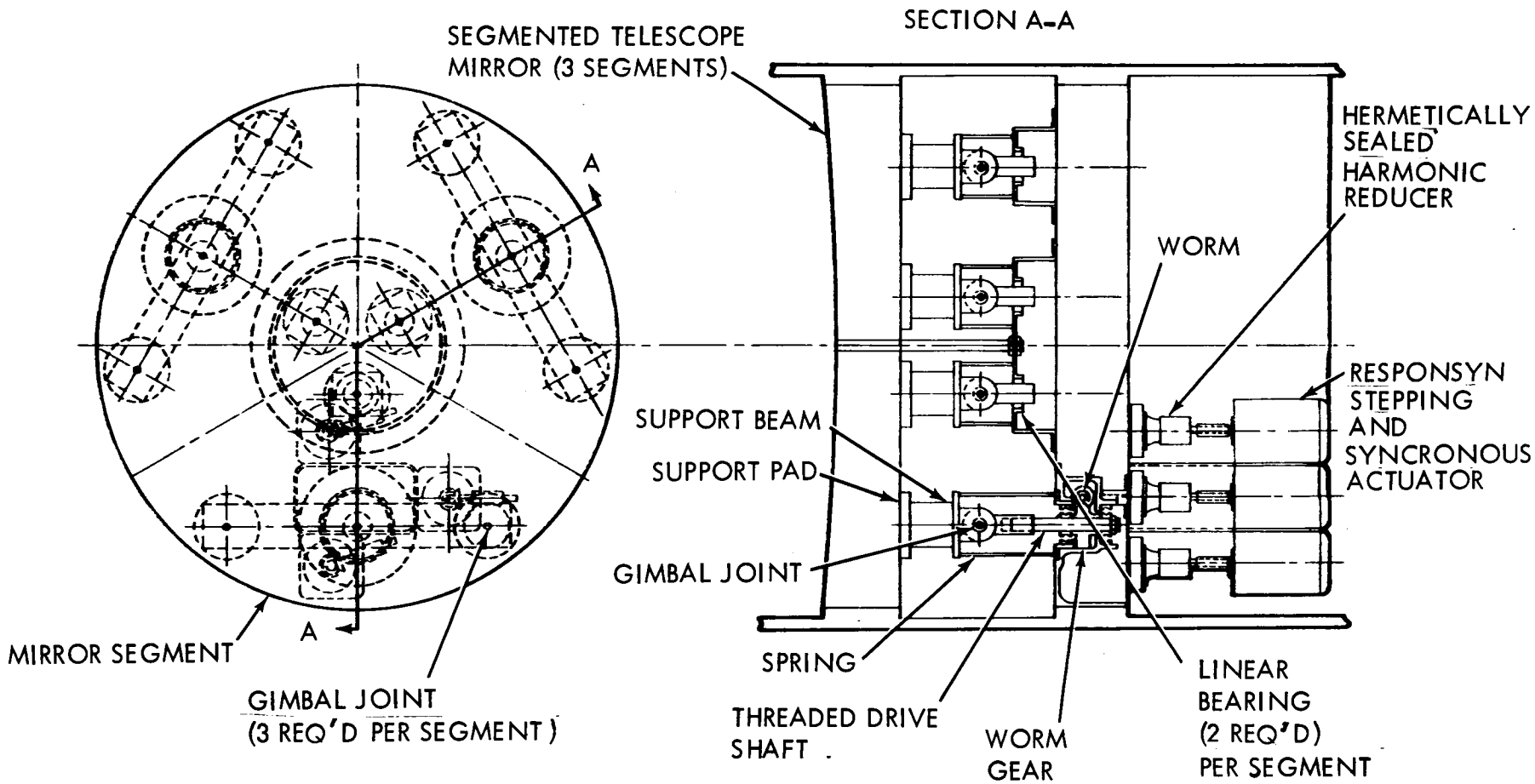


Figure 4.15.4.1.1-2. Segmented Mirror with Gear Trim Actuators

For the case of two parallel circular plates with a voltage, V, between them neglecting edge effects, the force is normal to the plates, and is given by

$$F = \frac{\overline{D} \cdot \overline{E}}{2} \int_s dS \qquad (4)$$

or, integrating over the circular area,

$$F = \frac{\overline{D} \cdot \overline{E}}{2} \quad (\pi R^2) \qquad (5)$$

But, $$\overline{D} = \epsilon \overline{E}, \qquad (6)$$

where ϵ is the capacitivity of the medium, which can be assumed to be a scaler quantity.

Therefore

$$F = \frac{\pi R^2 \quad \epsilon E^2}{2} \qquad (7)$$

But

$$E = \frac{V}{d,} \qquad (8)$$

where d is the separation between the plates, and, therefore,

$$F = \frac{\pi R^2 \epsilon V^2}{2 \quad d^2} \qquad (9)$$

It can be seen in equation (9) that the force does not depend linearly on the applied voltage, but, rather, on its square. Even less desirable, however, is the fact that the force depends inversely on the square of the plate separation. This fact implies that, for a given applied voltage, the force would vary widely, depending on the plate separation. These attributes of an electrostatic system make it undesirable, because adjustment would be difficult.

f. Magnetostatic System:

The force on a body in a magnetic field is, according to Stratton[6]

$$\overline{F} = \int_s \int \left[\mu \overline{H} \quad (\overline{H} \cdot \hat{n}) - \frac{\mu}{2} \quad H^2 \quad \hat{n} \right] \quad da \qquad (10)$$

(6) Stratton, J. A., Electromagnetic Theory, McGraw-Hill Book Company, Inc. New York, 1941.

where;

$\overline{H}$ = magnetic field intensity

μ = permeability of the body

n = unit vector normal to the surface, and the integration is carried out over the surface of the body. Equation (10) is true for paramagnetic materials or ferromagnetic materials in fields sufficientely weak so that μ does not depend on H.

For the case of a cylindrical rod of radius R inside a solenoid (with one end protruding) of length l, having N turns, and carrying a current I, equation (10) reduces to

$$F = \frac{\mu \pi R^2}{2} \left(\frac{\mu I}{l} \right)^2 \qquad (11)$$

According to equation (11), the force is dependent in the square of current in the coil, but it does not depend on the position of the rod in the coil, as long as one, and only one, end protrudes.

These characteristics, coupled with the fact that it should be possible to construct such a system having small, repeatable movements, make this system a likely candidate for a segment position actuator.

g. Pneumatic Systems:

A hollow body can be made to expand and contract longitudinally by controlling gas pressure inside it. If the body is made fairly rigid, it will have limited dynamic range, but the range can be extended indefinitely by providing clamps at both ends, which alternately open and close. This type of system has certain disadvantages (high pressure bottles, etc.) but it does offer the possibility of fine control and large dynamic range. Figure 4.15.4.1.1-3 is an example of a segmented mirror with pneumatic position actuators. Except for the operating principle of the actuators, the system is the same as that shown in figure 4.15.4.1.1-2.

In summary, then, of the seven types of position actuators discussed, the ones which seem to offer the most promise are:

a. Gear Train.

b. Magnetostatic.

c. Pneumatic.

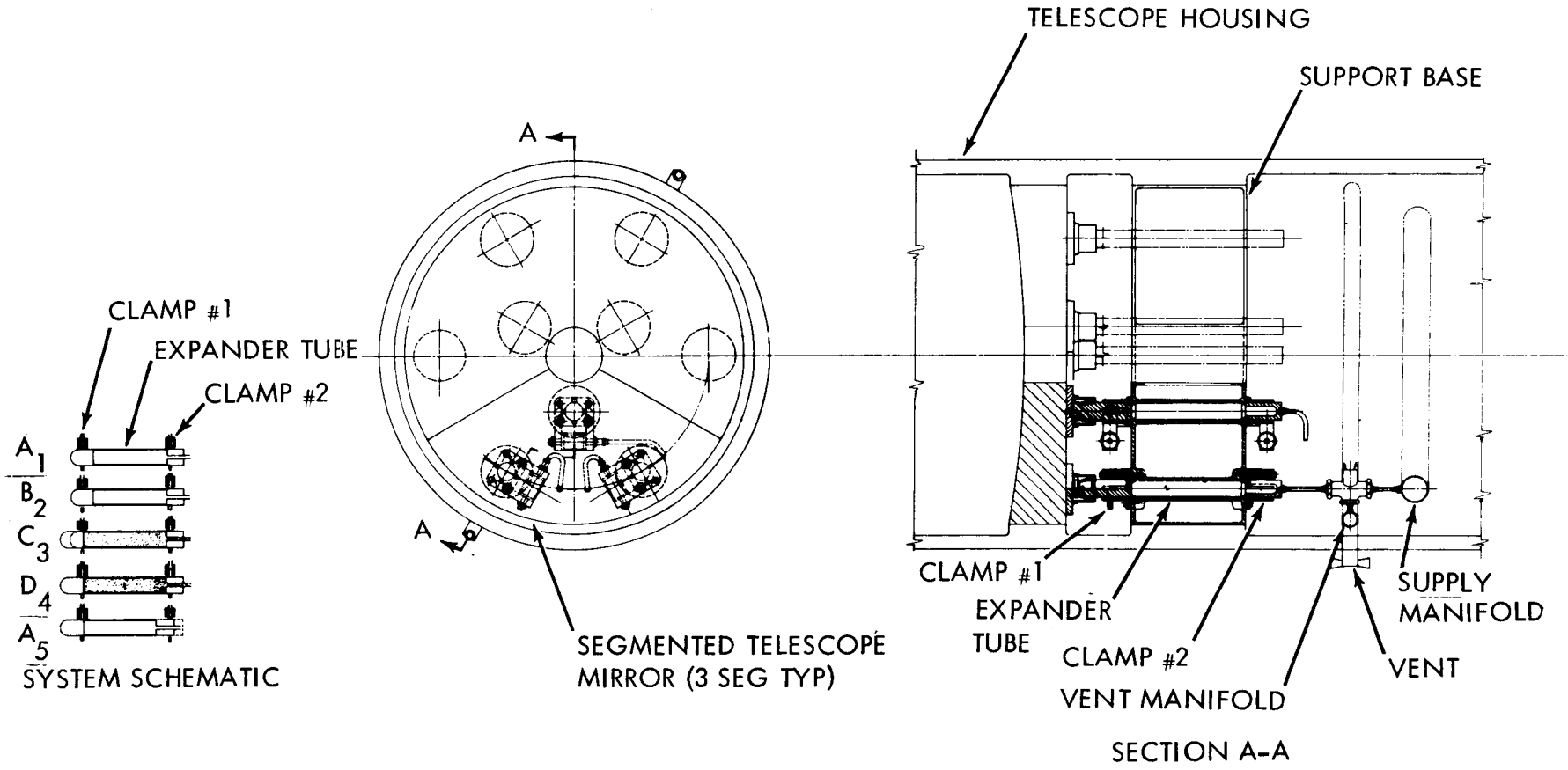


Figure 4.15.4.1.1-3. Segmented Mirror with Pneumatic Actuators

Any of these could be used in conjunction with a piezoelectric device for fine guidance.

4.15.4.1.2 Segment Position Sensing

Several systems were considered for segment position sensing.

a. Hartmann Test - The Hartmann test (7) is a photographic procedure frequently used for testing the final figure of telescope mirrors. It is an accurate method, but, unfortunately, its employment requires an elaborate series of photographs and subsequent measurement and computation. Therefore, although the test is very useful for testing the final mirror figure in an earth observatory, it is not practical for mirror figuring, especially in space.

b. Ronchi Test - The Ronchi Test(8) is an extension of the common Foucault knife-edge test, using a coarse grating rather than a knife-edge. As illustrated in figure 4.15.4.1.2-1, a grating is placed just in front of the center of curvature of the mirror vertex. A light source is placed behind the grating at one side, and the observer's eye is placed behind the grating alongside the light source. If the mirror were perfectly spherical, the observer would see a set of parallel straight lines. With a paraboloidal mirror, the display will consist of a set of parabolic lines, as depicted in figure 4.15.4.1.2-2a. If the mirror is a paraboloid in three segments, and a segment is displaced from its correct position, either linearly or in angle, the parabolic lines will be discontinuous as in either figure 4.15.4.1.2-2b or 4.15.4.1.2-2c.

c. Interferometer Tests - A number of interferometers can be adapted for mirror testing,(9) e.g., the Twyman-Green and the scatterplate interferometers. For this application, however, they do not contribute additional information and they do add additional complexity.

4.15.4.1.3 Experiment Test Subjects

In order to test the resolution of the segmented telescope it is desirable to photograph astronomical objects in addition to performing mirror figure tests.

(7) Calder, W.A., The Hartmann Test, in "Amateur Telescope Making, Book Two", Scientific American, Inc., 1963, p. 109.
(8) Kirkham, A.R., The Ronchi Test for Mirrors, in "Amateur Telescope Making, Book One", Scientific American, Inc., 1964, p. 264.
(9) Candler, C., "Modern Interferometers", Hilger and Watts, Ltd., Hilger Division, 1951.

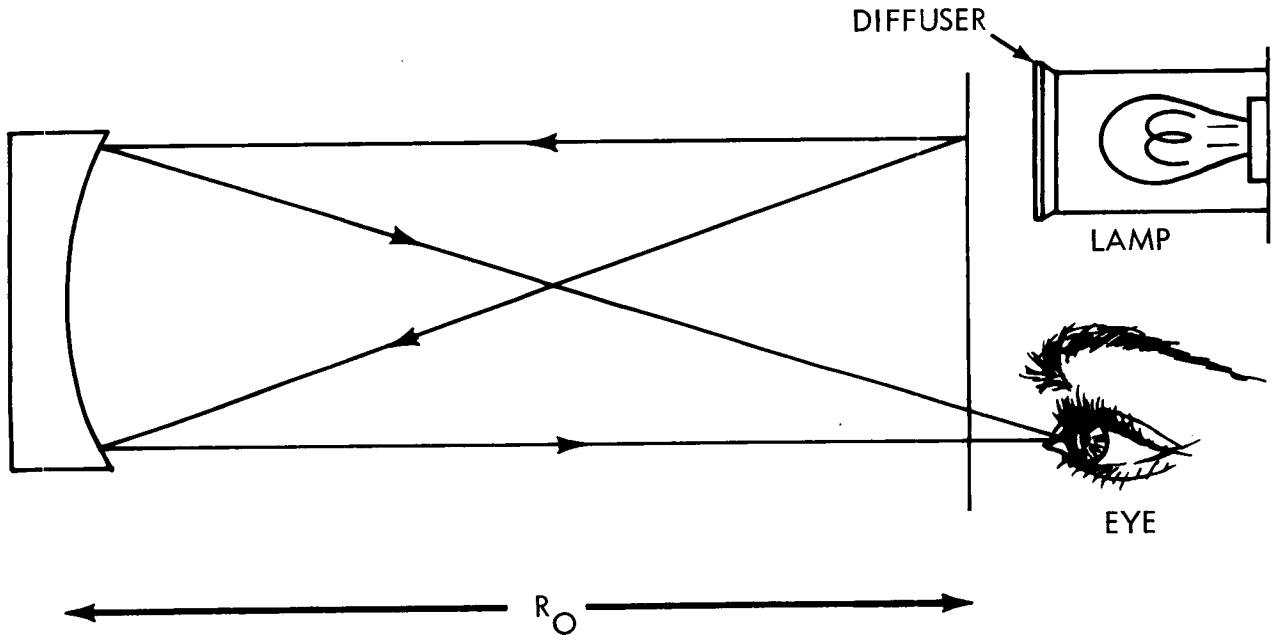


Figure 4.15.4.1.2-1. Ronchi Test Apparatus

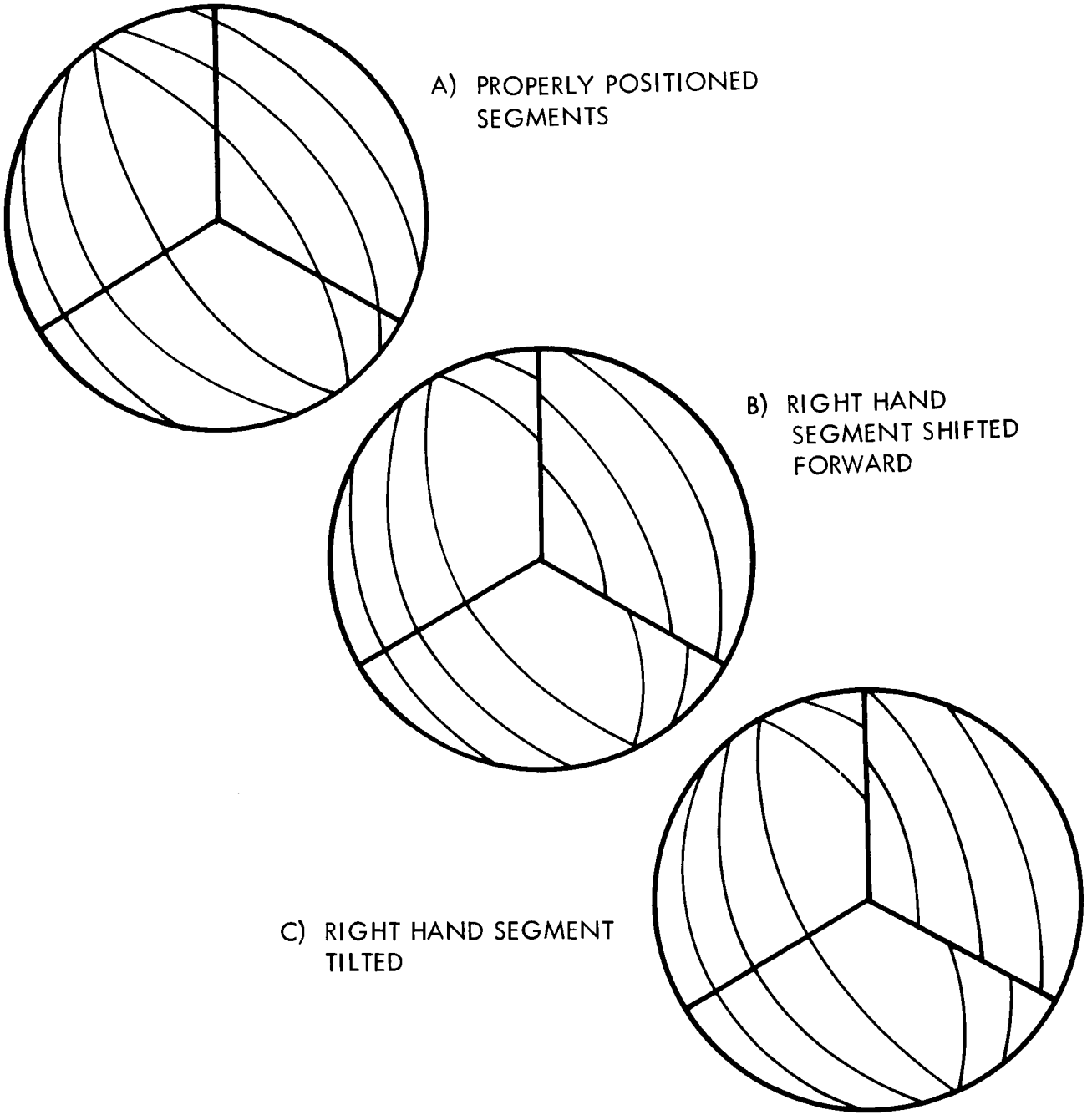


Figure 4.15.4.1.2-2. Ronchi Test Patterns

There are a number of astronomical bodies which would be useful for this purpose since they tax the telescope's capability. Several of these have been recommended for this purpose by members of the scientific community.

a. Binary stars - There are a number of binary stars whose apparent angular separation depends on their linear separation, their distance from the earth, and their orientation with respect to earth. One or more of these should be quite suitable for test purposes.(10)

b. Other binary objects - One of these is Cygnus A, the optical counterpart of the powerful source of radio-frequency radiation. The two objects in Cygnus A are believed to be colliding galaxies, both possibly large spirals. The separation between these two objects is about 0.5 arc seconds and has just barely been resolved in existing photographs. If the 24-inch segmented mirror produces the expected resolution, the two objects should be well resolved. Furthermore, because the components are believed to be galaxies, there exists the possibility of a scientific bonus in the experiment. An improved resolution in photographs of these galaxies may increase our knowledge of their structures.

c. Solar system bodies - Because of known surface features, the Moon and the planets Mars, Jupiter and Saturn are good photographic subjects for this experiment.(10)

d. Galaxies - There are two aspects of galaxies which can be used to demonstrate the resolution of a telescope.

   (1) Spiral structure: Photographs have been taken of spiral galaxies whose spiral structure is barely resolved. Two of these can be seen in the galaxy cluster in Corona Borealis. (11) A photograph taken with a two-fold increase in resolution might bring out more detail in the spiral structure, especially near the nucleus.

   (2) Photometry: The central brightness peaks in many elliptical galaxies are so sharp that the highest possible resolving power is required for their study. (12)

---

(10) Grenchik, R., Louisiana State University, Department of Physics & Astronomy, Private Communication, July 1, 1966.

(11) Hoyle, F., Astronomy , Doubleday and Company, Inc., Garden City, N. Y., 1962.

(12) King, I. R., "The Dynamics of Galaxies," in Annual Review of Astronomy and Astrophysics, Volume I., Annual Reviews, Inc. Palo Alto, Calif., 1963.

The results of Van Houten[13] show that brightness drops off one or two magnitudes in the first two seconds of radius. A potential target for this type of experiment is NGC 4278, which has been studied by Osterbrock.[14]

e. Variable stars - Cepheid variable stars pulsate in regular periods. They are important in astronomy as a means of determing distances. As it is estimated that the radius of such a star varies $\pm$ 5 per cent about a mean value, it would be interesting to compare the photographic changes during a period. The period involved need not be very long. One example of a Cepheid can be found in the Great Spiral of Andromeda, M31, with a period of 18.25 days.

4.15.4.1.4 Summary of Experiment Design

It is proposed that a ground-based program, both analytical and experimental in nature, be carried out to evaluate the performance of a segmented mirror, and to optimize the segment geometry. A ground-based program will also be necessary to choose the optimum segment position sensors and actuators. On the basis of results so far, it is felt that the Ronchi test will probably prove to provide the most useful segment position sensor, and the best position actuator will prove to be one of these three types: gear train, pneumatic, or magnetostatic, any of which may be used in conjunction with a piezoelectric crystal for fine control.

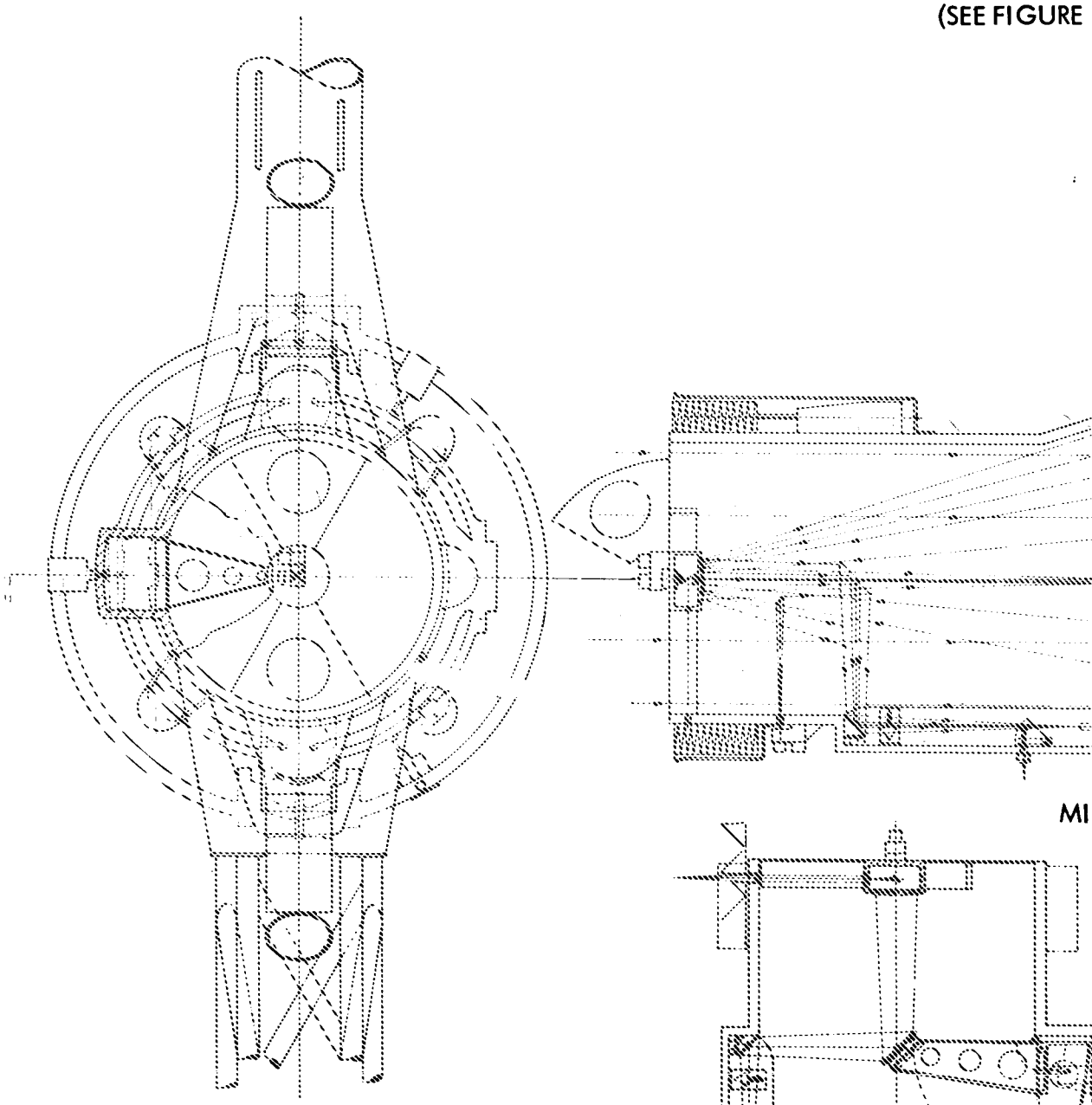
Once these ground-based programs have been completed, an experiment can be assembled, consisting of a telescope having a primary mirror composed of a few (probably three) segments of the type found to be desirable for a large observational telescope, and segment position actuators and sensors. The performance of this system will be evaluated in space by photography of astronomical objects, and by figure testing.

Figure 4.15.4.1.4-1 is an example of a possible telescope configuration. The fine guidance telescope points toward the left and a typical segmented telescope points toward the right. The segment position actuators shown are of the pneumatic type discussed above. The segmented primary mirror is of a Cassegrain type so that figure tests may be performed from a location behind it when the large flat is erected. This arrangement is necessitated by the fact that the figure tests must be performed at the center of curvature of the mirror, and it has a large radius. This configuration will require that a vidicon be used in order to transmit the figure test display to an accessible location. A diagonal flat is also shown so that, when the large flat is lowered and the telescope is used for astronomical photography, the camera can be placed at the side of the telescope tube.

The radius of curvature of the secondary will be adjusted when the focal length of the primary is ascertained so that the focal point is properly positioned.

(13) Van Houten, C. J., Bulletin of Astronomical Institute of the Netherlands, 16, 331 No. 509 (1961).
(14) Osterbrock, D. E. Astrophysical Journal, 132 325 (1960).

MIRROR ALI
(SEE FIGURE



MI

1-647

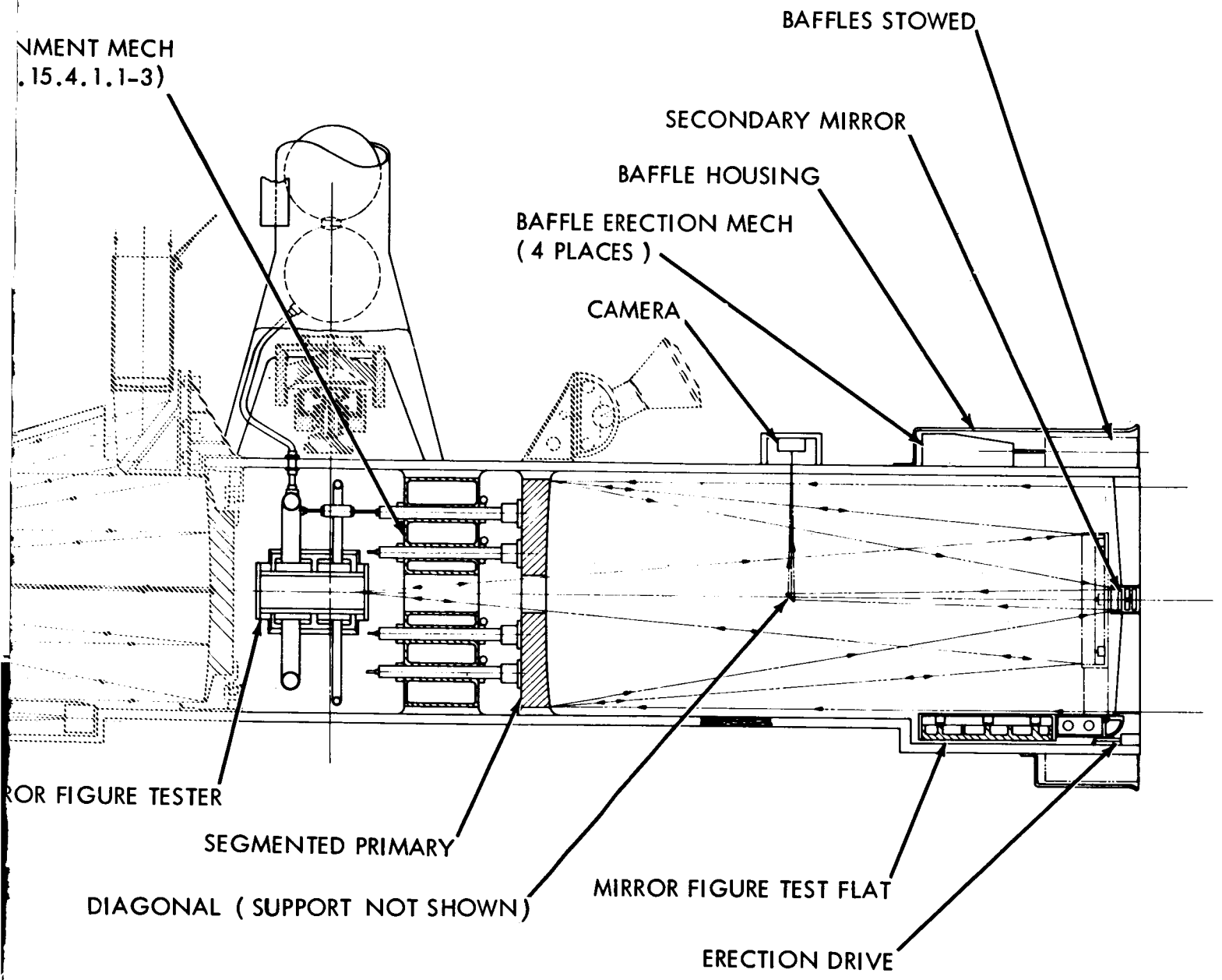


Figure 4.15.4.1.4-1. Segmented Mirror Telescope

4.15.4.2 Operational Procedures

The procedure in this experiment is quite straightforward. The segmented mirror will be aligned, pointed at the desired object, and photographs will be made on conventional materials both of astronomical objects and of the figure test display. The photographs will be subsequently returned to earth for processing and study. The alignment operation is a manned one, requiring the presence of an operator.

5.0 DISCARDED OTAES EXPERIMENTS

This section contains space experiments which were considered for OTAES but discarded in the course of the study. The optical technology development implied by the experiments is necessary for space science and as such is included in the optical technology ground development program, but the final evaluation of the experiments did not require space testing.

5.1 SPECTROGRAPH DEVELOPMENT

5.1.1 Objective

The astronomical spectrograph is one of the most important instruments used by astronomers in studying the physical nature of heavenly bodies. The spectrograph disperses the light of the stellar sources into their characteristic spectra which are then permanently recorded on an emulsion plate. These plates are then studied in detail to provide a wealth of information about the stellar sources. Since spectrographs are paramount in terrestrial observations, it is logical that they would also be fundamental instruments of large space observatories. However, terrestrial spectrographs are not designed for use in the environment of a space observatory.

It is the purpose of the experiment to develop the necessary technology required to optimize the performance of large, astronomical spectrographs in space. The technological development includes the major optical components; demonstration of system performance under space conditions; and demonstration of man's performance in aligning and operating the system in space.

5.1.2 Discussion

In general, spectrographs which are used with telescopes consist of several major components: slit, collimator, dispersive element (prism or grating), and camera. The image produced by the telescope is focused at the jaws of the slit. The light that enters the slit is rendered parallel by the collimator and falls on the dispersing element. The dispersed light is then collected by the camera objective and focused on the emulsion plate.

One of the most important considerations in designing the spectrograph is wavelength resolution, a measure of its ability to separate spectral lines of small wavelength difference. Therefore, it is always desirable to maximize the resolution, thus, the reason for the inclusion of the slit. The wavelength resolution may be increased by decreasing the slit width.

Another important consideration in spectrograph design is its speed. Just as the term implies, speed is inversely proportional to the time necessary to record the spectrum of the star of a given magnitude. It, therefore,

is desirable to also maximize the spectrograph's speed. This is especially important when recording the spectra of faint sources. However, as might be expected, both the wavelength resolution and the speed cannot at the same time be maximized. As the slit width is decreased to increase resolution, more light is lost at the jaws of the slit, thereby decreasing the speed. Therefore, there must be compromise between spectrograph resolution and speed, depending on the type of work being undertaken. This compromise may be particularly critical for terrestrial spectrographs where the size of the stellar image is determined primarily by the "seeing". For long focal length telescopes the stellar image may be quite large in comparison to the desired slit width so that only a small fraction of the image enters the slit. However, in space, where the stellar image may be quite sharp, the slit may be very narrow for high resolution and yet pass practically all of the star light so as not to reduce the speed.

The spectrograph's speed depends not only on the amount of star light entering the slit but also on the linear dispersion at the emulsion plate. Thus, for speed, spectrographs should have short cameras. However, when the slit width is very narrow to obtain very high resolution, there may be a limitation to the shortness of the camera. The camera must be long enough to produce an image large enough to be easily resolvable by the emulsion. Then since star images produced by space telescopes are very sharp, high resolution space spectrographs should have long cameras.

The space spectrographs designed for this experiment should provide for studying spectra from the extreme ultraviolet through the visible. However, two instruments are required, one for studying the visible portion of the spectrum and another for studying the ultraviolet spectrum.

The visible region spectrograph consists of several cameras and gratings to obtain various dispersions throughout the visible spectrum. The gratings which are blazed for various wavelengths throughout the visible spectrum are mounted on a turret so that they may be brought into position accurately.

The ultraviolet spectrograph which is basically like the laboratory spectrograph consists of an entrance slit, several curved gratings mounted on a turret and an emulsion plate which are all located on the Rowland circle. To span the ultraviolet spectrum the gratings are blazed for various wavelengths between 800Å and 3000Å.

Previsously, spectrograph resolution was discussed assuming that the emulsion plate and the collimator and camera mirrors are perfectly positioned, thereby, permitting the image to come to focus exactly at the emulsion plate. However, if one or more of these elements is displaced slightly, the image width is increased, thereby, causing a reduction in wavelength resolution, just as if the slit width were increased. Therefore, the tolerances in positioning these optical elements should be kept to a

minimum to afford the best possible resolution. It would be to no avail to use high quality gratings to maximize wavelength resolution when this resolution is lost because of poor positioning of the optical elements. On earth the tolerances in positioning the optical elements of the spectrograph are no greater than a few microns. If the tolerances achievable in space are this good, displacements will not affect the wavelength resolution too severely.

Thermal displacements will also cause a reduction in wavelength resolution and speed. If the spectrograph frame is constructed of one material, angles between various optical parts remains constant even though changes in temperature occur. However, a thermal excursion will cause an out-of-focus condition because of the thermal expansion of the optical bench.

Thermal excursion causes a degradation in wavelength resolution in another manner; the space between rulings of the grating changes with temperature, thereby, causing the spectral lines to shift. This effect is most critical for high dispersion instruments. The spectral lines may shift as much as 10 microns without severely affecting the resolution. Thus, for space spectrographs where the linear dispersion may be as high a 1 Å/mm, the temperature change allowable during an exposure is on the order of 1°C. For even greater dispersions, the changes in temperature permissable decrease linearly with increasing dispersion.

Rotation of the grating does not affect the resolution but will cause the spectrum on the emulsion plate to be rotated. This should not be critical because the comparison spectrum will also be rotated.

Although there are definite technological difficulties in the development of spaceborne spectrographs such as thermal and mechanical stability, they do not necessitate space testing; the space environment causing these difficulties can be properly simulated in the laboratory. Dr. Spitzer (Principla Investigator of the OAO Princeton Experiment) points out that assuming that the development of spectrographs in space could be justified technologically, the technology would most likely to obsolete before similar data gathering spectrographs could be flown.(1) He also points out that the OAO Princeton Experiment will demonstrate the technology of large (32") spectrometers which should achieve high resolution. (The best resolution for which the spectrometers are designed is 0.05Å; laboratory testing has yeilded a maximum resolution of 0.1Å).

The Woods Hole report on future areas of space research lists the development of diffraction gratings for use with spectroscopic instruments (ultraviolet) as one of the major needs in optical astronomy(2) The trend is

---

(1) Personal telephone conversation, Dr. Lyman Spitzer.
(2) Space Research, Direction of the Future, Part Two, Space Sciences Board, National Academy of Sciences, National Research Council, Washington,D.C.

towards bigger gratings with greater ruling density to achieve greater resolution. Bausch and Lomb is currently under contract by NEL to develop a high quality grating with a ruling density of 4800 grooves/mm. However, there is no particular need for space testing of these gratings in a space environment. The tests are most properly performed in a laboratory.

The sensor (e.g. film, electronographic camera, etc.) poses a very definite problem in space in so much as it is sensitive to over heating, to a hard vacuum, and to exposure to electron bombardment; although the sensor should be tested in space, this does not necessitate the presence of a spectrograph. This constitutes an individual experiment.

Also, man's role in demonstrating the operation of the spectrographs such as aligning mirrors and developing film does not justify this experiment. Man's participation may be demonstrated on other systems.

5.1.3 Recommendation

From the above discussion it is concluded that spectrographs for space use may be developed in the laboratory and as such does not constitute a valid space technological experiment.

Further, a spectrograph experiment on OTES would duplicate the efforts of the OAO spectrometer experiments.

5.2 BAFFLE SYSTEMS COMPARISON

5.2.1 Objective

This experiment was considered from the standpoint of achieving two objectives. The first objective is to compare the ability of different baffling systems to reduce noise background for various attitudes of the spacecraft relative to the sun and the earth. The second objective is to determine the quantitative effect of baffle geometry on noise reduction.

5.2.2 Discussion

Most telescope applications in which the telescope is used as receiving optics require baffling systems which serve to prevent unwanted background light from reaching the detector.

In earth orbit, there are three major components of background noise which can enter the telescope aperture. These are: sunlight, planet albedo, and Lyman airglow. Noise at the detector resulting from these background components can be reduced by extending a baffle in front of the telescope. There are two basic types of external baffles as depicted in figure 5.2.2-1. One approach typical of the OAO design involves a one-sided door which shades

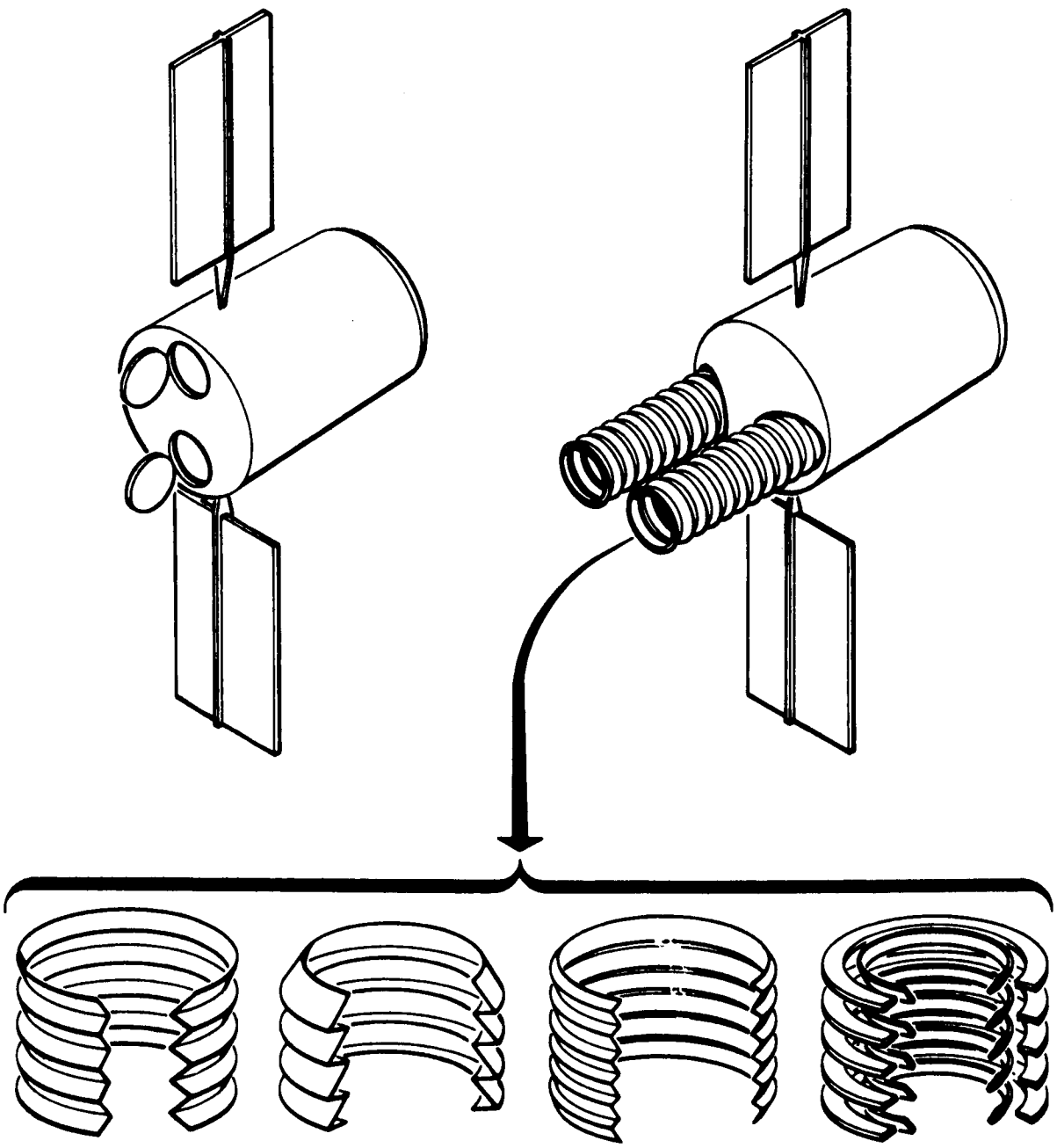


Figure 5.2.2-1. Baffle Systems Comparison

the telescope aperture. Using this technique, sunlight is prevented from entering the telescope aperture by maintaining spacecraft orientation around the telescope optical axis such that the sun is always on the door side of the aperture.

The second type baffle involves an expanding structure which is essentially an extension of the telescope well.

This approach increases the number of reflections of the scattered light prior to reaching the detector, and thus, by absorption, reduces the noise intensity. Such baffling designs can be critical to any optical application which involves detecting faint images. These applications include meteorology, planetary observations and other astronomical objectives. The following technology development is required in order to substantially improve space telescope baffles:

a. Knowledge of preferred external geometries (length to diameter ratios, deployment angle etc.) as a function of earth-sun-moon-spacecraft geometry.

b. Knowledge of preferred internal geometries as a function of earth-sun-moon-spacecraft geometry.

c. Evaluation and development of competing materials and techniques of packaging and deploying baffles.

d. Evaluation of different materials on the basis of coefficient of absorption and compatibility with deployment and packaging technique.

e. Better definition through earth orbit observations of the orbital noise background as a function of attitude.

A major parameter of the baffle is the geometry of the reflecting surfaces. The amount of scattered light reaching the detector can be decreased by designing the baffle geometry to be prejudiced against reflections toward the telescope interior. Thus, there are two aspects of baffle design which warrant experimentation; type and internal geometry. Figure 5.2.2-1 displays some internal geometrical configurations which would tend to increase the number of reflections. The purpose of this technological program would be to determine the preferred geometry and the limit of faint image detection for this geometry.

There are several means of packaging and deploying a concentric baffle. Each must be evaluated in terms of reliability and effectiveness of reducing scattered light reaching the detector. Three techniques of deployment are presented in this discussion as illustrative examples of the techniques which must be considered in a development program.

The first method, which is shown in figure 5.2.2-2 uses a bellows and the deployment is accomplished by an erectable de Havilland boom. A ring is fitted to the end of the baffle and four de Havilland booms are attached as shown before. The booms are erected simultaneously to different lengths for baffle testing. The second approach, is shown in figure 5.2.2-3. This baffle incorporates compressible foam. A foam layer with the required reflective elements in it is compressed within a small ring at the telescope well. The package ratio to expanded ratio is 1:2. Deployment is accomplished by releasing the packaged baffle and the foam's top of the baffle. Four cables are fastened to the ring and extend down to the telescope well where they attach to a ring around the telescope base. The ring is rotated, thereby winding or unwinding the cable on the ring. This will either extend or retract the baffle in different positions. Some problems might be encountered with repackaging.

The last configuration is shown in figure 5.2.2-4. This method, also packaged around the telescope well, employs a bellows-type baffle as shown in figure 5.2.2-3. Deployment is accomplished by an erectable de Havilland boom. It is deployed in definite increments and has its own frame. Upon deployment, only one increment is deployed at a time. The rest of the baffle increments are held back by their respective frames. The frame is released when the preceding segment has achieved the proper reflector element geometry. This system ensures constant reflector element geometry. The reliability of this system is impaired by its own complexity.

Each of the aforementioned technology areas was considered in terms of the need for space testing. It was concluded that a comprehensive earth-based experiment program would provide sufficient information on the relative merits of different baffle designs to support future design efforts. Such a program should consist of an analytical phase followed by a test program which faithfully simulates the light conditions of the earth-sun-moon geometry. In addition, prototype tests on materials and deployment models should be performed.

5.2.3 Recommendation

A comparison of baffle systems should be discarded as an OTES experiment. However, an earth-based research and development program should be initiated to support the development of a Manned Orbiting Telescope.

the telescope aperture. Using this technique, sunlight is prevented from entering the telescope aperture by maintaining spacecraft orientation around the telescope optical axis such that the sun is always on the door side of the aperture.

The second type baffle involves an expanding structure which is essentially an extension of the telescope well.

This approach increases the number of reflections of the scattered light prior to reaching the detector, and thus, by absorption, reduces the noise intensity. Such baffling designs can be critical to any optical application which involves detecting faint images. These applications include meteorology, planetary observations and other astronomical objectives. The following technology development is required in order to substantially improve space telescope baffles:

a. Knowledge of preferred external geometries (length to diameter ratios, deployment angle etc.) as a function of earth-sun-moon-spacecraft geometry.

b. Knowledge of preferred internal geometries as a function of earth-sun-moon-spacecraft geometry.

c. Evaluation and development of competing materials and techniques of packaging and deploying baffles.

d. Evaluation of different materials on the basis of coefficient of absorption and compatibility with deployment and packaging technique.

e. Better definition through earth orbit observations of the orbital noise background as a function of attitude.

A major parameter of the baffle is the geometry of the reflecting surfaces. The amount of scattered light reaching the detector can be decreased by designing the baffle geometry to be prejudiced against reflections toward the telescope interior. Thus, there are two aspects of baffle design which warrant experimentation; type and internal geometry. Figure 5.2.2-1 displays some internal geometrical configurations which would tend to increase the number of reflections. The purpose of this technological program would be to determine the preferred geometry and the limit of faint image detection for this geometry.

There are several means of packaging and deploying a concentric baffle. Each must be evaluated in terms of reliability and effectiveness of reducing scattered light reaching the detector. Three techniques of deployment are presented in this discussion as illustrative examples of the techniques which must be considered in a development program.

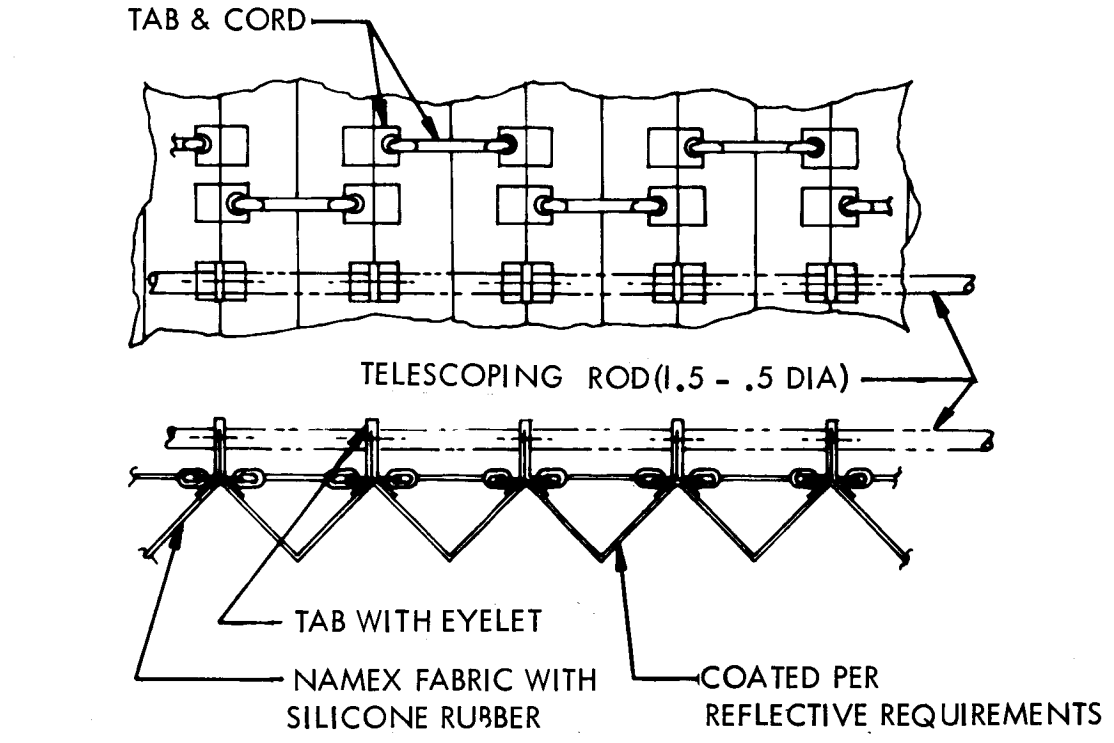
The first method, which is shown in figure 5.2.2-2 uses a bellows and the deployment is accomplished by an erectable de Havilland boom. A ring is fitted to the end of the baffle and four de Havilland booms are attached as shown before. The booms are erected simultaneously to different lengths for baffle testing. The second approach, is shown in figure 5.2.2-3. This baffle incorporates compressible foam. A foam layer with the required reflective elements in it is compressed within a small ring at the telescope well. The package ratio to expanded ratio is 1:2. Deployment is accomplished by releasing the packaged baffle and the foam's top of the baffle. Four cables are fastened to the ring and extend down to the telescope well where they attach to a ring around the telescope base. The ring is rotated, thereby winding or unwinding the cable on the ring. This will either extend or retract the baffle in different positions. Some problems might be encountered with repackaging.

The last configuration is shown in figure 5.2.2-4. This method, also packaged around the telescope well, employs a bellows-type baffle as shown in figure 5.2.2-3. Deployment is accomplished by an erectable de Havilland boom. It is deployed in definite increments and has its own frame. Upon deployment, only one increment is deployed at a time. The rest of the baffle increments are held back by their respective frames. The frame is released when the preceding segment has achieved the proper reflector element geometry. This system ensures constant reflector element geometry. The reliability of this system is impaired by its own complexity.

Each of the aforementioned technology areas was considered in terms of the need for space testing. It was concluded that a comprehensive earth-based experiment program would provide sufficient information on the relative merits of different baffle designs to support future design efforts. Such a program should consist of an analytical phase followed by a test program which faithfully simulates the light conditions of the earth-sun-moon geometry. In addition, prototype tests on materials and deployment models should be performed.

5.2.3 Recommendation

A comparison of baffle systems should be discarded as an OTES experiment. However, an earth-based research and development program should be initiated to support the development of a Manned Orbiting Telescope.


TAB & CORD
TELESCOPING ROD(1.5 - .5 DIA)
TAB WITH EYELET
NAMEX FABRIC WITH SILICONE RUBBER
COATED PER REFLECTIVE REQUIREMENTS

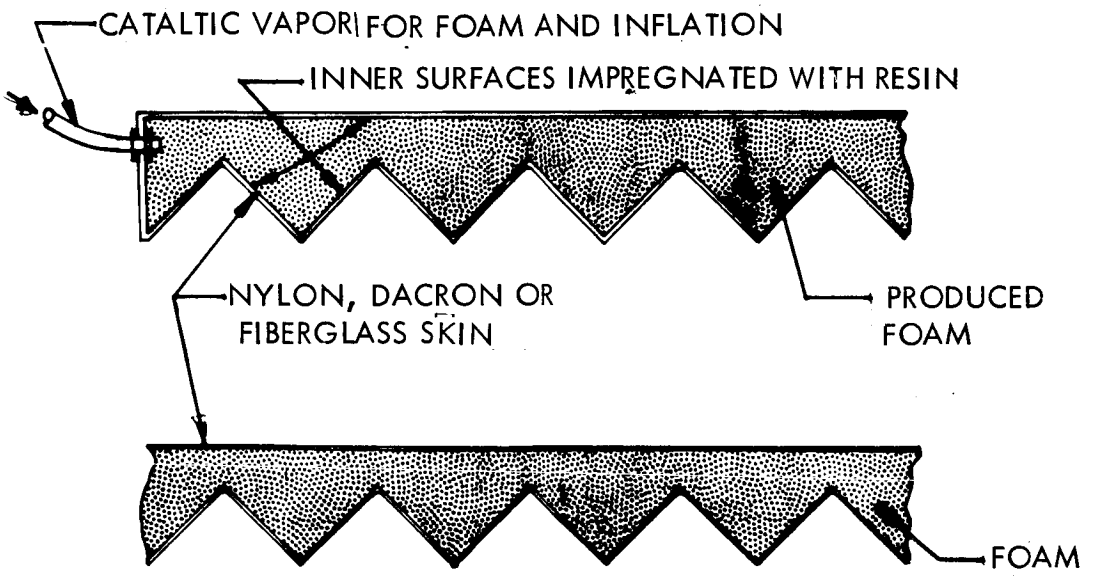

CATALTIC VAPORI FOR FOAM AND INFLATION
INNER SURFACES IMPREGNATED WITH RESIN
NYLON, DACRON OR FIBERGLASS SKIN
PRODUCED FOAM
FOAM

Figure 5.2.2-2.

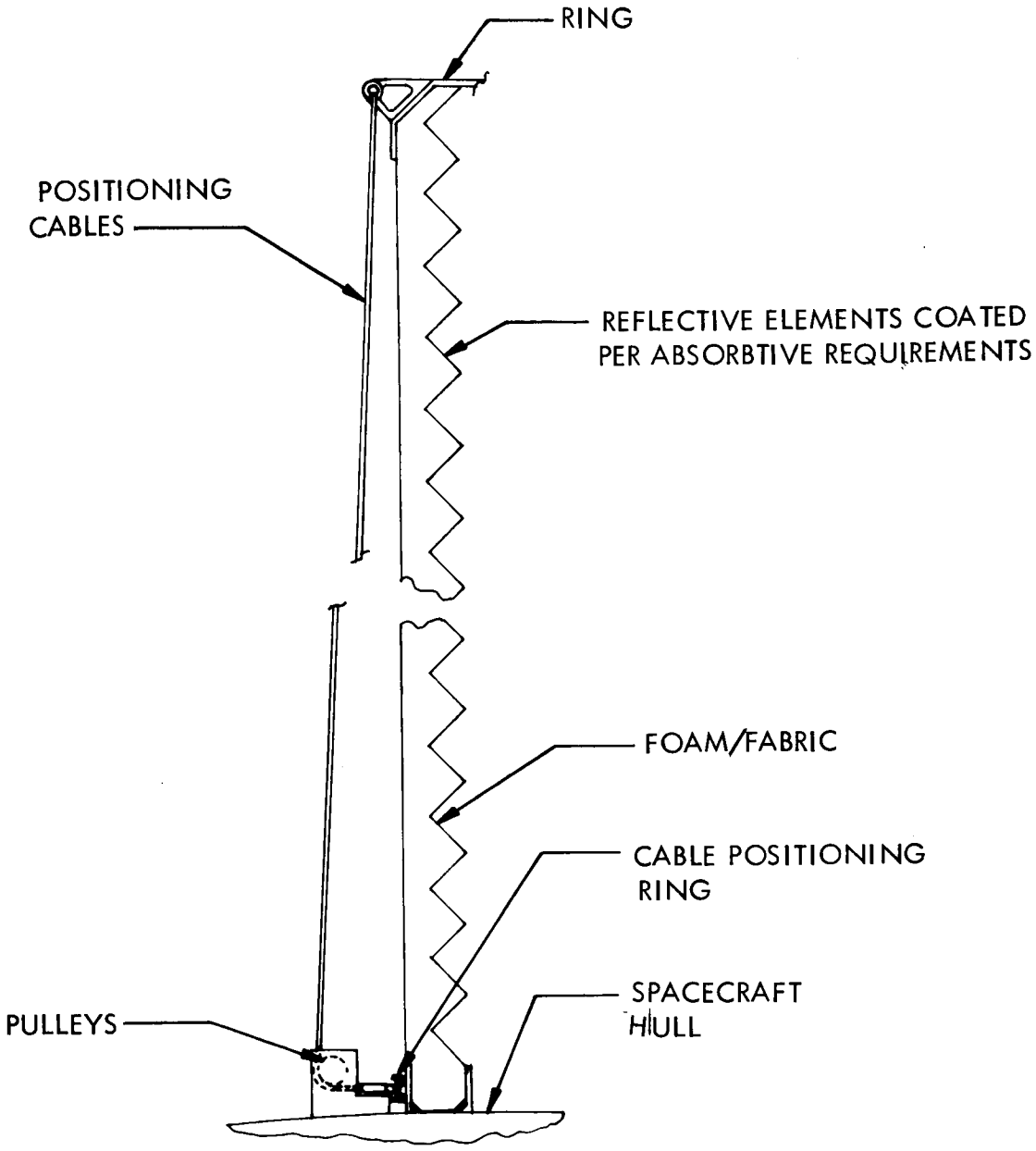
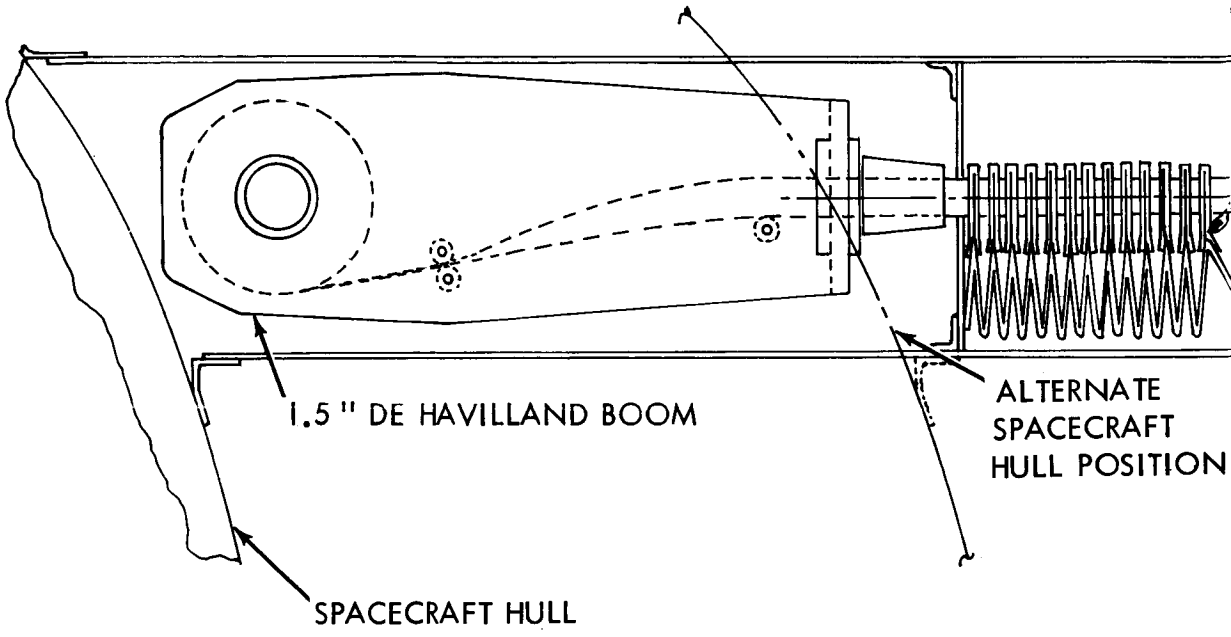
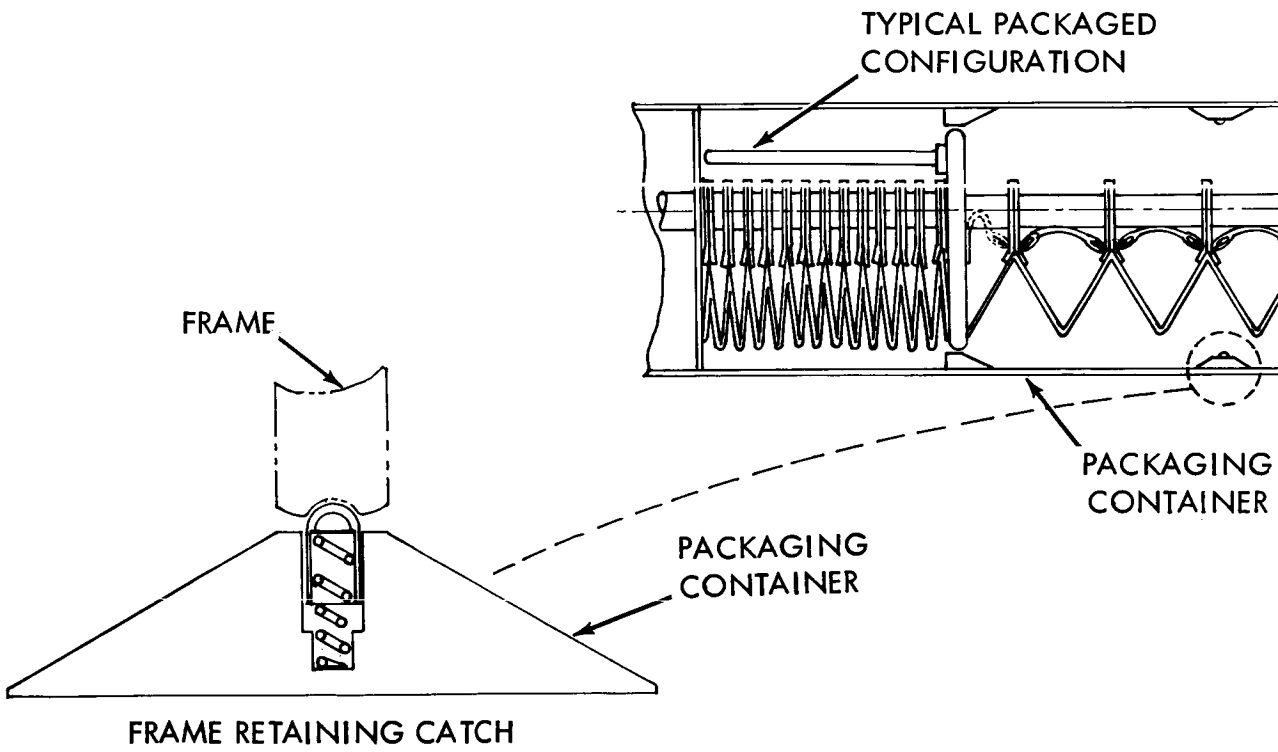

RING
POSITIONING CABLES
REFLECTIVE ELEMENTS COATED PER ABSORBTIVE REQUIREMENTS
FOAM/FABRIC
CABLE POSITIONING RING
SPACECRAFT HULL
PULLEYS

Figure 5.2.2-3.


1.5 " DE HAVILLAND BOOM
ALTERNATE
SPACECRAFT
HULL POSITION
SPACECRAFT HULL


TYPICAL PACKAGED
CONFIGURATION
FRAME
PACKAGING
CONTAINER
PACKAGING
CONTAINER
FRAME RETAINING CATCH

1-659

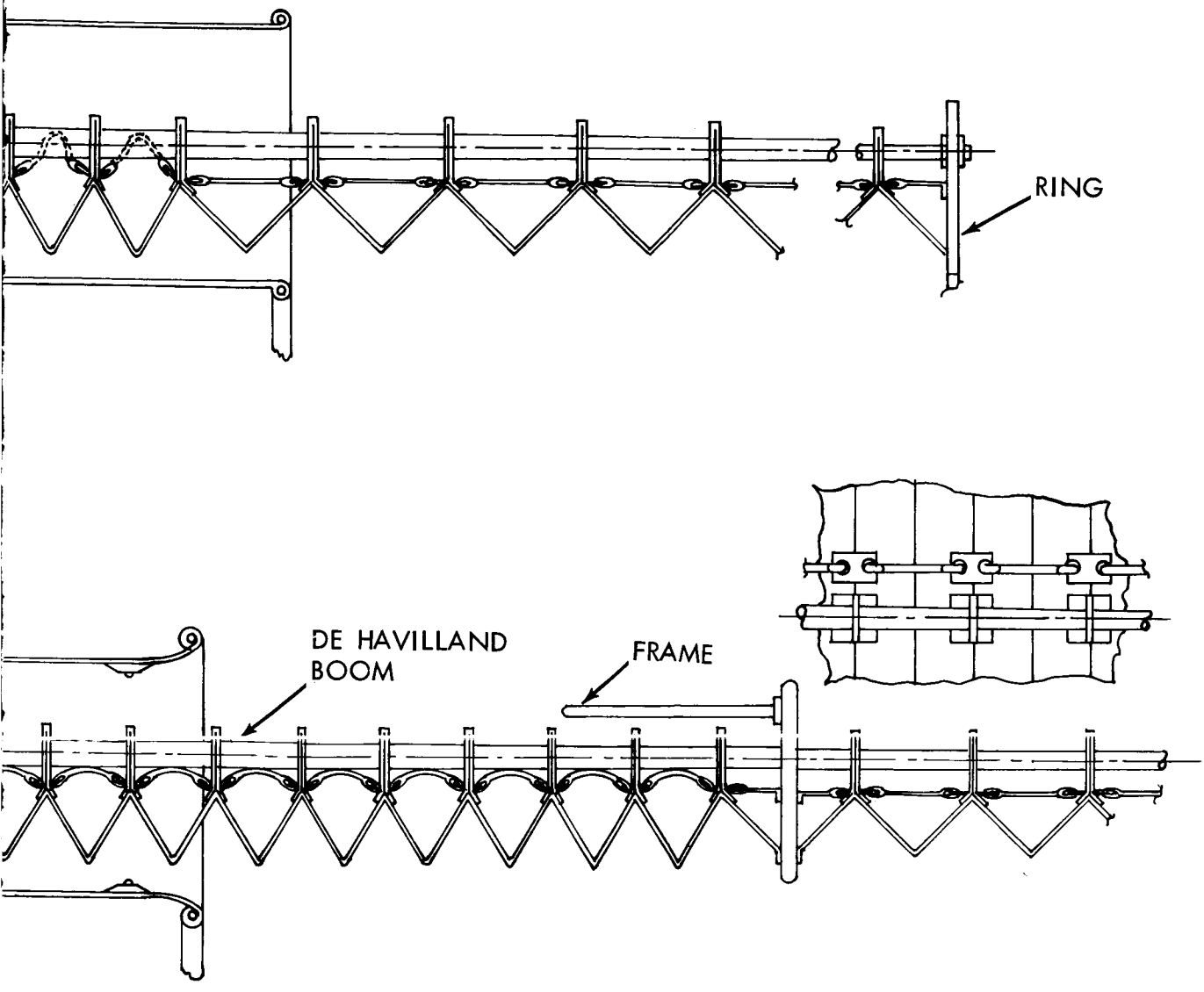


Figure 5.2.2-4.

5.3 ATMOSPHERIC ABSORPTION EXPERIMENTS

5.3.1 Objective

A number of constituents of the atmosphere can provide important information concerning the atmosphere and its circulation. Measurements of ozone, carbon dioxide, and water vapor are desirable, particularly in the region above the troposphere and below the 200 km at which a satellite can orbit. As pointed out by R. Frith of the British Meteorological Office[1], information about this region can be obtained by examining radiation that has originated in, or has passed through this region, and is received on board a satellite. Indeed, measurements of ozone content have already been made in this manner[2]. Frith states that errors arise in using the sun as a source of radiation because the sun is a distributed source. Such errors could be reduced by using a stable satellite, which used a variably restricted angle of view of the sun. The characteristics of laser transmission, particularly its monochromaticity, intensity, and spatial coherence, are attractive for measurements of this nature, and for scattering studies that have also been proposed[3]. Continuous world-wide measurements of ozone concentration would greatly assist in studies of the general circulation, especially the meridional circulation. Water vapor studies may be of even greater importance.[4] To examine the technology required to perform such measurements, an atmospheric absorption experiment was proposed.

5.3.2 Discussion

The quantitative expression for the attenuation of monochromatic radiation passing through an absorbing or scattering medium is given by[5]

$$I/I_o = e^{-(\alpha + \beta)\, x} \qquad (1)$$

where

I_o = the initial intensity
I = the intensity after passing through an absorbing layer of thickness X
α = the absorption coefficient
β = the scattering coefficient.

---

(1) R. Frith, "Meteorological Satellites, Future Research Project," World Meteorological Organization Bulletin, October 1962, p. 202.

(2) R. D. Rawcliffe, G. E. Meloy, R. N. Friedman, and E. H. Rogers, "Measurements of Vertical Distribution of Ozone from a Polar Orbiting Satellite," Journal Of Geophysical Research, Vol. 68, No. 24, December 15, 1963.

(3) G. G. Goyer and R. Watson, "The Laser and its Application to Meteorology," Bulletin American Meteorological Society, Vol. 44, No. 9, September 1963.

(4) R. Frith, Op Cit

(5) L. R. Koller, "Ultraviolet Radiation," John Wiley & Sons, Inc., New York 1952, p. 115.

If the radiation is not monochromatic, α is not a constant (near a molecular absorption line it can change very rapidly with frequency), and β is not a constant although it does not change rapidly with frequency if the scattering particles are very small, or very large compared to the wavelength used. The distance X is an equivalent optical thickness. If the scattering and absorbing particles are not uniformly distributed throughout the absorbing volume, sufficient knowledge of pressure and temperature will permit the computation of the number of absorbing and scattering particles in the path.

Note that measurement at a single frequency will only determine the total attenuation. To determine the optical thickness, two frequencies or more are used, one having a very small α compared to the β. Knowing the frequency relationship between β_1 and β_2, the latter can be calculated to permit accurate determination of the optical distance X and hence the number of particles in the path.

It is possible to obtain laser radiation sufficiently monochromatic that Eq. (1) is valid, particularly when heterodyne techniques are used. Assume also that a second frequency is available, so that the β's are readily determined. If the α's are accurately measured for a particular absorption line, X can be measured with an error that is dependent on the accuracy with which the intensity can be measured before and after passing through the absorbing medium. Let $(\alpha + \beta) = a$, which is very accurately known. Then Eq. (1) becomes

$$I = I_o\, e^{-ax} \tag{2}$$

Approximate the errors in I, I_o, X by the differential results in

$$dI = dI_o\, e^{-ax} - a\, dx\, I_o\, e^{-ax}$$

The error dx results from the independent errors dI and dI_o, which are the errors in the measurement of I and I_o. The mean square value, dx, (assuming dI and dI_o are independent) is

$$\overline{dx^2} = \frac{\overline{dI_o^2}\; e^{-2\,ax} + \overline{dI^2}}{\left(aI_o\, e^{-ax}\right)^2} \tag{3}$$

Assume that it is possible to measure the intensities to the same accuracy. Then

$$\overline{dI^2} = \overline{dI_o^2}$$

and Eq. (3) becomes

$$\overline{dx^2} = \frac{\overline{dI_o^2}}{I_o^2}\;\frac{\left(1 + e^{2\,ax}\right)}{a^2} \tag{4}$$

The mean square error of measurement is proportional to the relative error in power measurement with a proportionality factor that is a function of the attenuation coefficient. Note that when a is very large or very small, the absolute error in X rises. Dividing both sides by X, and noting that

$$ax = -\log_e {}^{I}/_{I_o} - \log_e {}^{I_o}/_{I}$$

and $e^{2\,ax} = \left(\frac{I_o}{I}\right)^2$ = reciprocal of the transmission through the sample, results in

$$\frac{\overline{dx^2}}{x^2} \Bigg/ \frac{\overline{dI_o^2}}{I_o^2} = \frac{\left[1 + \left(\frac{I_o}{I}\right)^2\right]}{\left(\log_e {}^{I_o}/_{I}\right)^2} \qquad (5)$$

The square root of this ratio is plotted in figure 5.3-1.

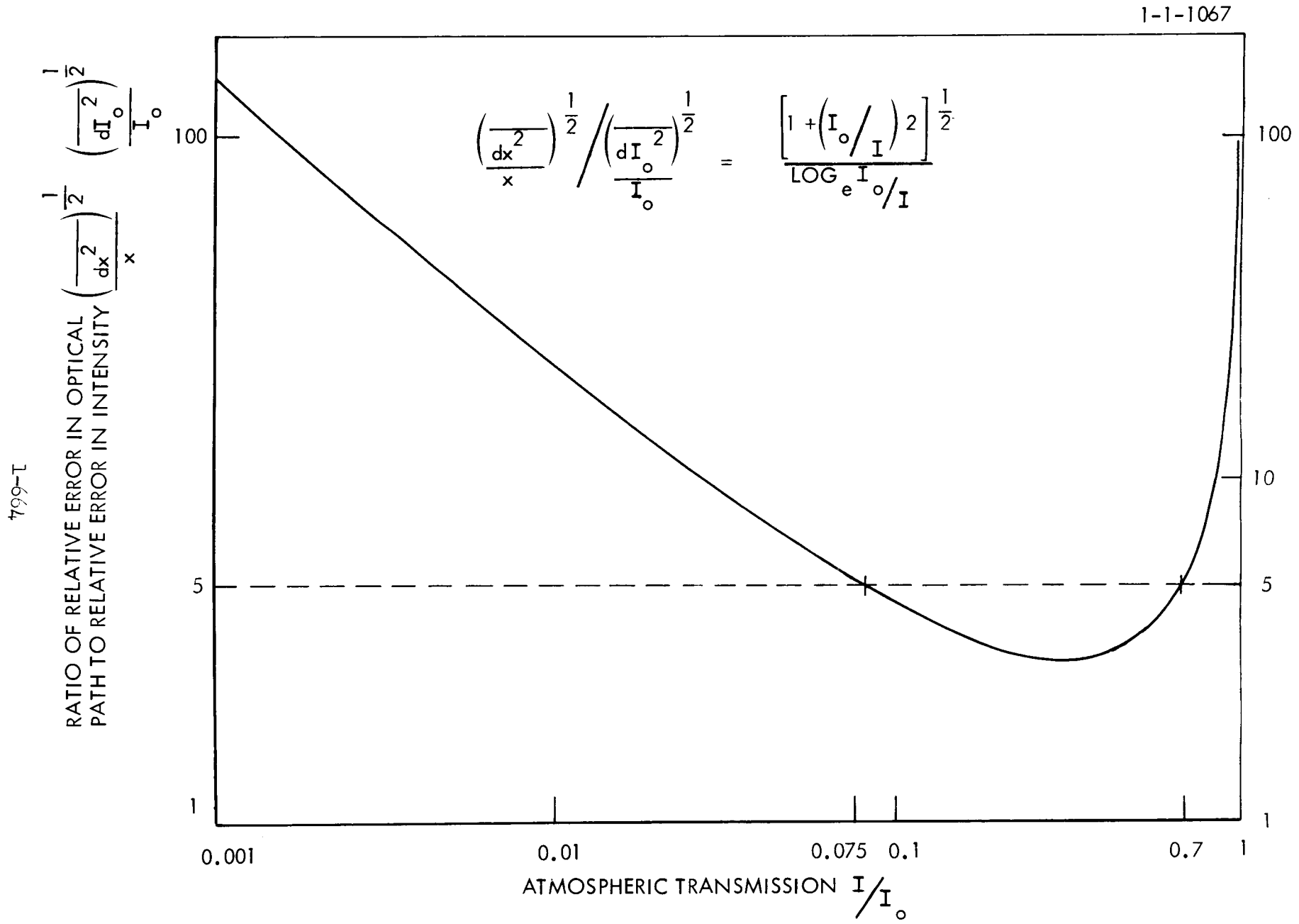
As shown in the figure, the relative accuracy with which the optical distance can be measured has an optimum value. Because the absorption coefficient is frequency dependent, there is an optimum frequency that should be used to make particular measurements. It is of interest to examine some of the known absorption bands to see what relative accuracies are attainable.

Chin and Hogg[6] have measured the attenuation of 3.392-micron radiation due to methane in the atmosphere. On the basis of their results of a measured value of 5.5 dB/kilometer, and making the reasonable assumptions that the methane is uniformly distributed through the atmosphere, and that the entire atmosphere is 5 km thick at standard temperature and pressure, (STP), the result is a total attenuation of 27.5 dB. This corresponds to $I/I_o = .00176$. In figure 5.3-1, the multiplying factor of 90 is given. Even if the transmitter power could be measured to an accuracy of 0.1%, the relative amount of methane could be measured to an accuracy of only 9 percent. Clearly it would be desirable to perform the measurement at some other frequency, which would provide an I/I_o between 0.2 and 0.5. This would be an absorption of ≈ 0.008 relative to the maximum near 3.392 microns. As shown in the curve presented by Chin and Hogg[7], the collision broadened lines of methane overlap with a minimum relative absorption of ≈ 0.35 so that there is no frequency in this region that will permit very accurate determination of the methane without putting severe measurement requirements on the incident power. At the best frequency available in this region, measurement of the methane content to 20 percent would require measurement of the incident laser power to ≈ 0.45 percent, which appears somewhat unreasonable for spaceborne applications. Note that, at the optimum total attenuation, the relative error in X can be as low as 3 times the relative error in incident power measurement.

---

(6) T. S. Chin and D. C. Hogg, "The Attenuation of 3.392 μ He-Ne Laser Radiation by Methane in the Atmosphere," BSTJ, February 1966, p. 301.

(7) Op Cit, Figure 3.



799-T

Figure 5.3-1. Normalized Error in Optical Path vs. Atmospheric Transmission.

One of the most important constituents of the atmosphere is ozone, which because of its strong optical absorption is responsible for the extinction of the ultraviolet in sunlight. As noted[8] by Rawcliffe, et al, "The ozone in a vertical column of the atmosphere amounts to only about 2 mm STP, or about one part in a million. Yet the ozone has an importance that far outweighs its concentration because of its strong optical absorption and its high chemical reactivity. Its distribution is intimately tied in with the photo-chemical and the transport properties of the upper atmosphere." There are weak absorption bands in the visible in addition to those in the ultraviolet. At 0.6328 microns the absorption coefficient is given by Inn[9] as ≈ 0.035 cm^{-1}, base 10. If a 0.2 cm layer is assumed, $I/I_o = 10^{-.007} = .984$. Although difficult to read on the graph (figure 5.3-1), the multiplying factor is approximately 90, which would require power measurement to 0.22% if 20% accuracy were desired in the ozone measurement. Clearly, accurate measurement at this frequency would also be difficult because of the difficulty of monitoring laser power to such tolerances. If the near optimum value of multiplying factor of ≈ 2.8 were chosen, $I/I_o = .34$. For the 0.2 cm layer, the absorption coefficient of 2.33 cm^{-1} is obtained at about 0.3050 microns as indicated by Inn.[10] If a laser were used at this frequency, measurement of the ozone to an accuracy of 20% would require a relative power measurement of 7.15%, which is considerably more reasonable in spacecraft applications.

Other absorption bands that would be of interest and importance are those due to water vapor and carbon dioxide. As shown in figure 5.3-1, it is necessary that the transmission through the atmosphere be between 0.075 and 0.7, if the relative accuracy of measuring the absorbing constituent is to be less than 5 times the relative accuracy of measuring the incident intensity; and it can never be less than about 2.8 times, at best. As shown in the Handbook of Geophysics,[11] there are a number of absorption bands for H_2O and CO_2 as well as O_3 in the region between 1 - 14 microns, which have transmission factors in the usable range. Lasers in this region of the infrared are under development, and the CO_2 laser at 10.6 microns has already shown great promise. However, the performance of optical components in this frequency range in space is still unproven. An important objective of the OTAES communications experiment at 10.6 microns will be to observe the effect on power transmission of infrared components in the space environment.

---

(8) R. D. Rawcliffe, G. E. Meloy, R. M. Friedman and E. H. Rogers, "Measurement of Vertical Distribution of Ozone from a Polar Orbiting Satellite," Journal of Geophysical Research, December 15, 1963, Vol. 68, No. 24, p. 6425.

(9) E. C. Y. Inn and Y. Tanaka, "Absorption Coefficient of Ozone in the Ultraviolet and Visible Regions," Journal of the Optical Society of America, October 1953, Vol. 43, No. 10, p. 870.

(10) Op Cit, Figure 2

(11) Handbook of Geophysics, U. S. Air Force, ARDC, The MacMillan Company, New York, Figure 16-6.

5.3.3 Recommendation

As discussed above, the accuracy of spectrographic experiments depends on the accuracy with which the transmitted as well as the received radiation can be measured. For a spaceborne transmitter, there will certainly be a number of optical components subsequent to the power monitor, as well as the spreading loss that will be subject to error because of the difficulties in determining the far-field antenna pattern. In order to measure an atmospheric constituent to 2%, a relative transmitted intensity measurement of less than 1% is required. In some cases this will be less than 1/2 percent. In the ultra-violet as well as the infrared, unproven optics and incalculable spreading loss errors will contribute this much error in the present state-of-the-art. The monitoring of transmitted power in the desired frequency range will also be subject to error. These factors, combined with the fact that lasers are not available in all the desired frequency bands, lead to the recommendation that the absorption spectroscopy experiment be removed from further consideration in the OTAES program. It should be noted that the successful performance of the OTAES experiments may provide data concerning optics, power monitoring, and far-field spreading losses that will permit the design of a meaningful absorption spectroscopy experiment.

5.4 PHOTON-PHOTON SCATTERING

A proposed experiment to obtain a direct verification of the scattering of light by light has been discarded. The original idea concerned the collision of two intense, highly focused laser beams and the attempt to observe scattered photons at some angle from the direct collision path. An investigation revealed that the probabilities for such a scatter to occur are negligible even under ideal conditions, and therefore the experiment will not be attempted. A brief summary of this investigation is given below.

When two photons with the same frequency ν, the same polarization, and opposite momenta collide, the differential cross section $d\sigma$ for the deflection (of both quanta) by an angle θ is given by[1] (when $h\nu \ll m_o$, the rest mass of the electron)

$$d\sigma = \frac{r_o^2 d\Omega}{2\pi^2 5^2 3^4} \frac{(3+\cos^2\theta)^2}{137^2} \left(\frac{h\nu}{m_o}\right)^6 \qquad (1)$$

r_o is the classical electron radius and is equal to 2.8×10^{-13} cm. The above cross section is extremely small, even for γ-rays; for visible light, the last factor in the expression is smaller than $(10^{-5})^6$, thus it is down by at least 10^{30} from the value for γ-rays. In this analysis, we have used the rest mass of the electron equal to 9×10^{-28} g = 5×10^5 eV; this is in the range of γ-ray energies. Visible light has an energy of a few electron volts.

A number greater than the upper limit for the cross section for 5 eV photons can be obtained by setting $\int d\Omega = 4\pi$ and $\cos\theta = 1$. We then get

$$\sigma_{max} < \frac{(2.8 \times 10^{-13})^2 \times 4\pi}{2\pi^2 \cdot 5^2 \cdot 3^4} \times \frac{16}{137^2} 10^{-30} \text{ cm}^2 = 2 \times 10^{-63} \text{ cm}^2 \qquad (2)$$

Thus, the total number of photons scattered per unit time into all solid angles will be less than σ_{max} times the number of incident photons crossing unit area per unit time times the number of photons from the opposing beam present at the collision site. Let us assume a collision region of length 30 meters. Anything larger seems unfeasible for detection purposes. We shall now demonstrate that this number is many orders of magnitude less than 1.

For convenience, we will consider a laser beam to be focused to 1 cm^2 in area, traveling over a large distance and colliding with an identical laser beam from the opposite direction. If we assume 1000-megawatt lasers operating in a pulsed manner (cw gives even less) over 0.1 μs, emitting 5 eV photons with a repetition rate of 10 pulses per second, then we will have 10^{21} photons interacting with 10^{20} photons during a second, giving a probability of 1 in 5×10^{21} that one photon will be scattered.

---

(1) W. Heitler, The Quantum Theory of Radiation, Third Edition, Oxford Univ. Press, (1954) p. 326.

If, instead, very highly focused beams (down to 10 microns beam diameter) at a separation of a few hundred meters were to be considered, we could do a little better. Expressing $\sigma_{max} < 2 \times 10^{-55}$ micron^2, 10^{20} photons could be interacting with 10^{20} photons per pulse, giving a probability of 1 in 5×10^{16} that one photon will be scattered.

In addition, stray photons and photons in the spatial Gaussian tail of the laser beam will be far more probable in the region of the detector. Also, scattering from particles will be appreciable.

Thus, we believe that with the foreseeable laser technology, even assuming advances towards somewhat greater power and higher frequency, no direct scattering experiment appears promising. An alternative experiment (namely, the scattering of a laser beam in the visible or ultraviolet from a very high energy γ-ray beam) might be conceivable several years from now.

5.5 REMOTE MANUAL OPTICAL ALIGNMENT

5.5.1 Objective

The objective of this experiment was to maintain and/or adjust the alignment of a spaceborne telescope by remote manual observations and commands from an earth station.

5.5.2 Discussion

Telescopes that will be adjusted and aligned and then launched in unmanned spacecraft or telescopes originally adjusted by an astronaut who is in and then has left a manned spacecraft may eventually need realignment. Even small misalignments may seriously comprise the usefulness of the instrument and its data. For example, the allowable tilt error of the secondary in a typical Ritchey-Chretien f/8 system is ± 2 seconds of arc. Beyond this tolerance the tilt error causes the system performance to exceed the theoretical diffraction limit.

Assuming that the candidate optical design will consist of a minimum of a primary mirror and secondary mirror, it will be necessary to employ alignment corrections to the secondary. The number of adjustments for realignment will depend on the various degrees of freedom of misalignment. There is tilt along two axes, axial spacing of component, and decentration.

A problem exists in making a distinction between the various misalignment errors due to the ambiguity of nearly identical image effects arising from decentration and tilt of the secondary mirror. It is possible through judicious use of information obtained by examining Moire fringe patterns to isolate the effects of decentration, angular tilt, and axial shifts that occur with the secondary mirror. Several properties of optical grids and their resulting Moire patterns are described to illustrate their detectable parameters.

a. When light passes through two identical linear grid patterns (separated by a small distance), a rotation of one grid with respect to the other produces a fringe pattern perpendicular to the grid lines.

b. A lateral shift of one of the grid patterns will cause its opaque spaces to coincide with the clear spaces of the other, thereby reducing the light transmitted through the grid.

c. Two superimposed grid patterns with different grating frequencies will cause a predictable curvature in the Moire fringe patterns.

The characteristics of the grids and their respective Moire patterns can be implemented in a misalignment detection system according to the diagram shown in figure 5.5-1. Grid patterns are centered in the X and Y tilt axes of the secondary mirror so that the planes of the grids are perpendicular to their respective axes. The origin of the tilt axes will be just behind

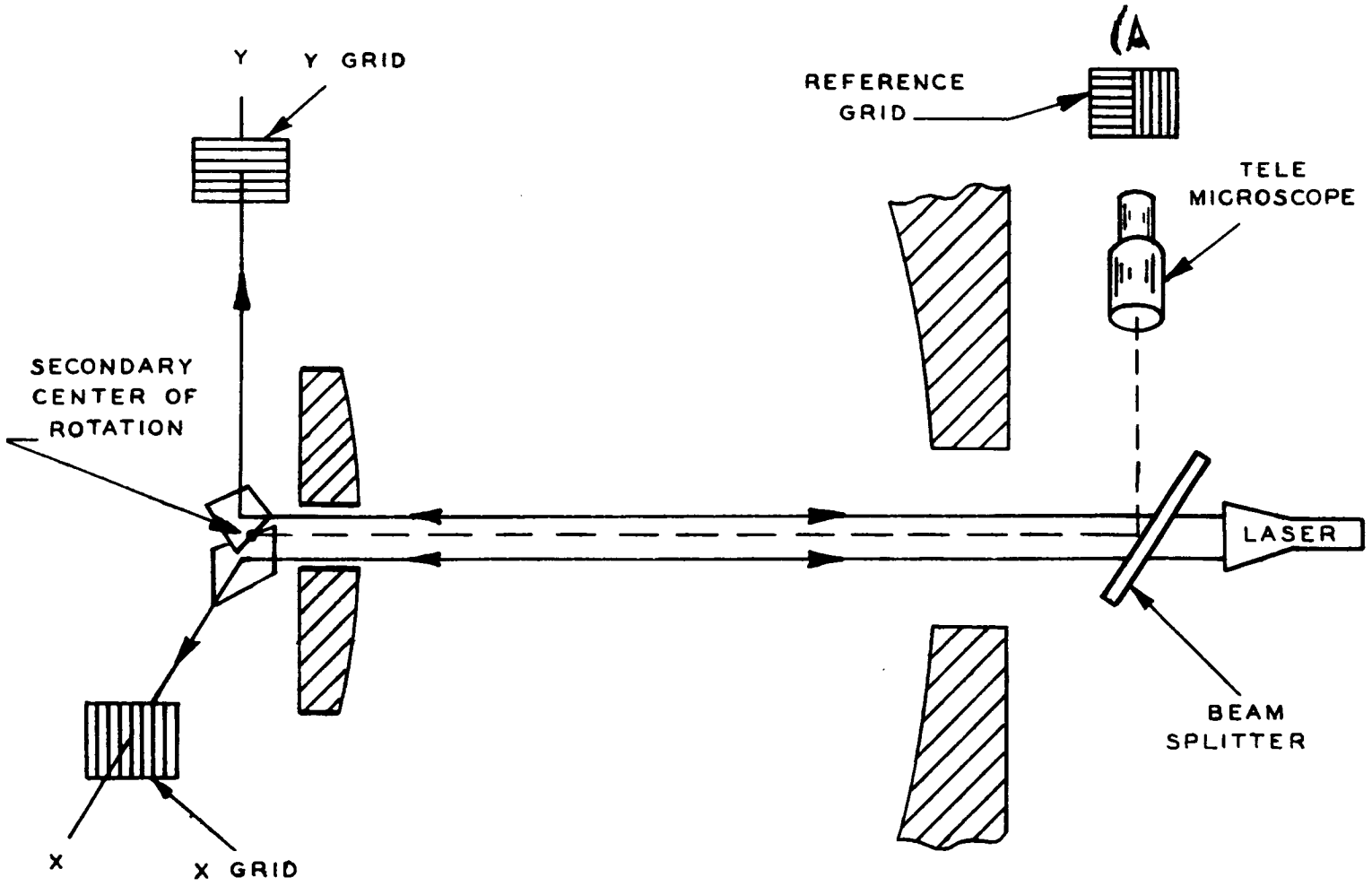


Figure 5.5-1 Remote Manual Optical Alignment

the secondary mirror. A laser beam is directed to a split field mirror by way of the holes in the primary and secondary mirrors. The light is directed along two axes to illuminate the grid patterns. The images of the two grid patterns are picked up by the lens system behind the primary via a beam splitter and are imaged on a reference grid which will appear identical to the axial grids when there is zero misalignment.

When there is pure decentration of the secondary, lines of the imaged grid will be translated across the reference grid, thereby modulating the total amount of light transmitted through the combination. By use of a variable frequency grid, the amount of decentration can be detected by use of an optical autocorrelation technique. At the center position, the total amount of light flux through the system is at a maximum and can be monitored manually or by photometric measurement.

Longitudinal or axial shifts of the secondary mirror will result in a magnification change in the grid pattern as imaged by the lens. The resulting distortions in the Moire fringe patterns, as a result of focal shifts, is identifiable and distinguishable from the other misalignment effects.

Although development is necessary before remote alignment procedures are operational it is difficult to justify the space development of such procedures. Although zero gravity may effect the actuator design the actual operating procedures should not be greatly altered. A characteristic of remote alignment is the time delays between operator actuation (at the control panel), actuator operation (in the spacecraft) and resulting data display (at the control panel). These time delays can be expected to have an effect on the operator efficiency and, in some cases, ability to implement specific tasks. However, these time delays can be simulated on earth based programs and therefore do not require space testing.

5.5.3 Recommendation

It is recommended that the Remote Manual Optical Alignment experiment be deleted as an OTAES candidate. It is felt that all aspects of this experiment can be performed with a ground based test program.

5.6 VISUAL TRACKING RATING

5.6.1 Objective

To obtain information on human acquisition and tracking capabilities under orbital conditions is the objective of the experiment.

5.6.2 Discussion

Ample evidence already exists that, on earth, man's ability in visual tracking cannot compete with that of photoelectric means, especially for protracted periods of time, however our intention is now directed toward space considerations. The general idea of the experiment would be to compare an astronaut's ability to track a star or ground beacon with that of an automatic star tracker or fine guidance system.

The proposed system is shown schematically in figure 5.6.2-1 and operates as follows:

The automatic tracking system is used initially in a closed loop mode that acquires the ground laser beacon and centers it in the telescope. This condition provides a starting point for the manual tracking experiment. A beam splitter near the focal plane provides automatic tracking and manual viewing of the laser beacon. The automatic tracker output is switched from the telescope gimbal controls to a recorder, and the astronaut manually tracks the laser beacon. The automatic tracker must have an offset tracking capability over its entire field of view which must coincide with the usable field of view of the telescope. An image dissector tracker with an electronic servo loop will provide the necessary offset tracking capability. In this mode of operation, the dc error signal obtained by the tracker processing electronics is fed back to the deflection coils and provides an offset null condition. The instantaneous readout from the X and Y deflection coils will be proportional to the manual angular tracking error after conversion to polar coordinates. A continuous record of the tracking conditions is obtained by monitoring the dc level of the deflection coils.

There is no reason to believe that weightlessness would offer any advantages in the areas of visual performance or motor coordination. Experience gained from the Mercury, Vostok, and Gemini flights to data indicates no appreciable degradation in visual or motor abilities during orbit. Neither does the evidence indicate any measurable improvement in these functions as a result of weightlessness.

There is one aspect of human visual performance that is very difficult to rival, and that is the ability to recognize and track a unique target against a complex background (such as a particular terrain feature or the edge of a lunar crater). To design automatic tracking instrumentation for such purposes would involve great efforts in the development of correlation techniques which could not hope to match man's vast neurological complexity.

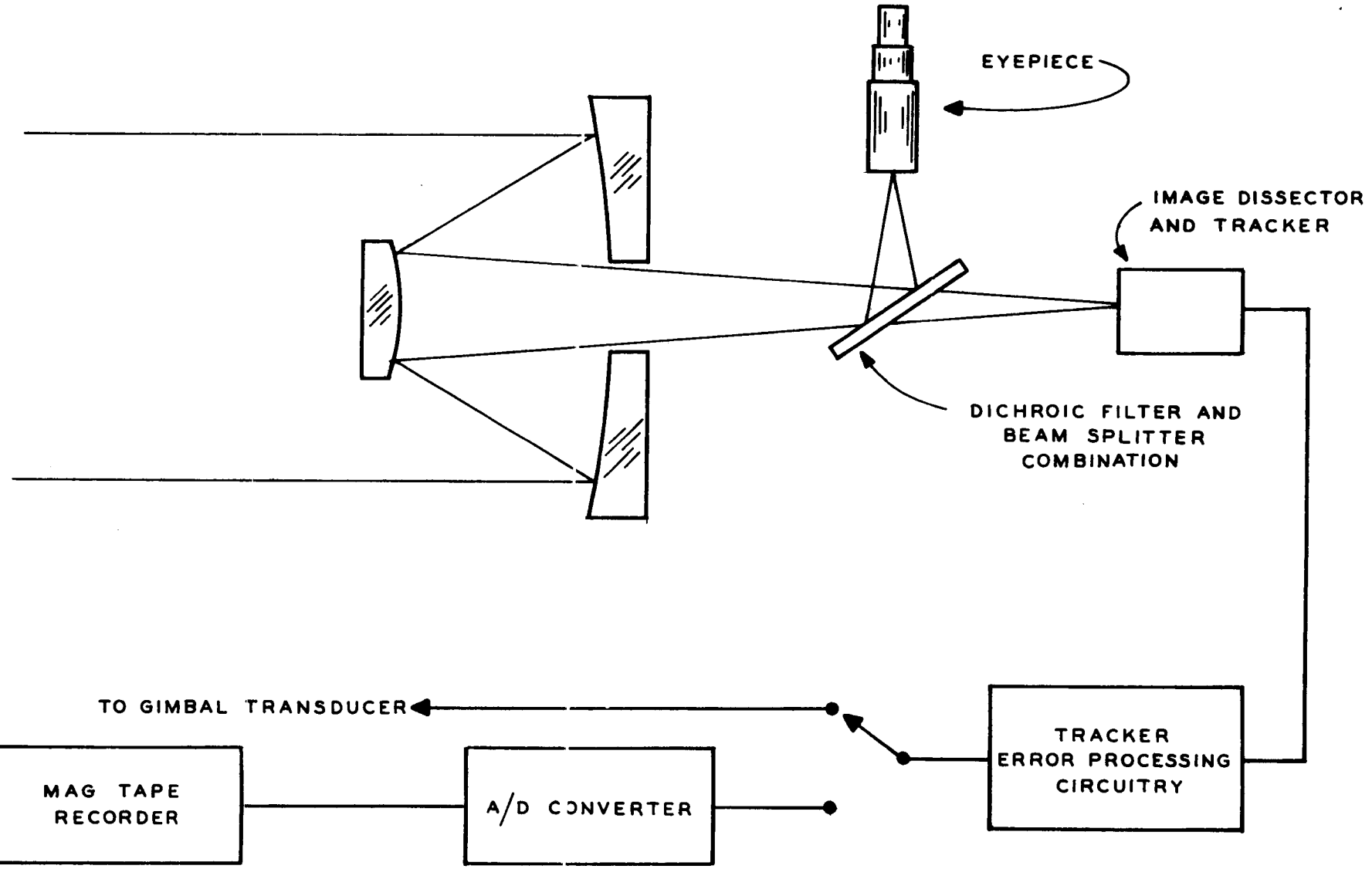


Figure 5.6.2-1. Manual vs Automatic Tracking System

5.6.3 Recommendations

The above considerations, along with analyses of the adverse effects of man's perturbations on the stability of a spacecraft and the fact that ground simulation can be used to predict man's tracking capability quite accurately, led to the recommendation that this experiment be discarded for inclusion in the OTAES program at this time.

5.7 CRYOGENIC COOLING FOR DETECTORS

5.7.1 Objective

The current state-of-the-art will not allow the reliable space operation of a cryogenically cooled detector system over an extended period. For example, at present there are no cryogenic cooling systems which will operate maintenance free for a year or longer. The primary goal is to develop the cryogenic cooling technology so that it will be possible to cool detectors in space to low temperatures (liquid helium) with highly reliable cooling techniques, capable of operation over long durations (2 to 5 years) with a minimum and preferably no attention required from man. The desirable system characteristics of minimum vibration and high efficiency by minimizing the size, weight and power requirements must be stressed.

5.7.2 Discussion

IR detectors can be grouped according to their temperature of operation. Convenient grouping are:

a. Room temperature (295°K)
b. Dry ice temperature (195°K)
c. Liquid Nitrogen temperatures (77°K)
d. Liquid Neon temperatures (27°K)
e. Liquid Hydrogen temperatures (20°K)
f. Liquid Helium temperatures (4°K)

Some examples of detectors that operate in these temperature ranges are given in the following table.

Material	Operating Temperature (°K)	Wavelength of Peak Response (μ)
InAs	295	3.4
PbS	195	2.5
InSb	77	5
Ge:An	60	4.7
Ge:Hg	35	10
Ge:Cd	25	16
Ge:Cu	20	20
Ge:Zn	4.2	36

Note that the doped Germanium detectors which require cryogenic cooling allow detection in the longer wavelengths (8 - 40 μ). These longer wavelength detectors are not only important for earth observation but also as detectors for the newly developed and promising CO_2 (10.4μ) laser.

The Ge:Hg detectors have recently had wide application since they show a high sensitivity in the wavelength region of the infrared window in the

atmosphere, 8μ - 14μ. The temperature region of its most favorable (i.e., background limited) operation is from 30°K down. However, operation of these detectors near this upper limit of 30°K requires absence of even the slightest trace of copper in the germanium. If lower temperatures are available, traces of copper can be tolerated, which should greatly facilitate the production process. Thus the lower temperature makes the use of less pure detectors possible.(1)

It may seem odd that major gains in the detector technology are being paced by advances in the engineering of cryogenic cooling systems which are auxiliary to the detector cell itself but this is indeed the case. As the cryogenic cooling technology advances, the engineering penalties for low temperature cooling will diminish and not only result in longer wavelength operation but will also allow replacement of superior performing low temperature detectors in critical application where operating temperature has been the compromized factor.

The development of detector technology will have direct bearing upon the precise requirements for cryogenic cooling. For instance, photon effects can be observed over a wide range of wavelengths in $H_{g1-x}Cd_x$ Te. Of particular interest is operation in the 8μ to 14μ spectral interval, which was not accessible previously to photon detectors operating at 77°K. Heretofore, the semiconductor having the smallest energy gap, and therefore the longest wavelength intrinsic photo response, has been InSb, whose peak response lay near 7μ at room temperature and 5.2μ at 77°K. Longer wavelength photon effects required employment of extrinsic Ge photoconductors, such as Ge:Cs, Ge:Hg, Ge:Cu, and Ge:Zn, whose operating temperatures lay below 40°K. Response at wavelengths even longer than 14μ is possible with $H_{g1-x}Cd_x$ Te, provided that an operating temperature below 77°K is allowable.(2)(3)

The Woods Hole report has recommended further development of infrared detectors and development of cryogenic apparatus needed to maintain temperatures as low as 0.25°K in a satellite. It is concluded in the report that despite sizable advances in detector technology, the limiting factor in a well-designed infrared spaceborne telescope is detector sensitivity. Unless new breakthroughs occur in photoconductive techniques, the best hope for extending sensitivity beyond 2 microns is to develop thermal detectors cooled below 1°K. The bright sky background in the infrared would reduce the effectiveness of such devices for ground-based observation; however, their significance for space astronomy cannot be overemphasized.

---

(1) Daniels, "Minature Refrigerator Opens New Possibilities for Cryo-Electronics", North American Philips Co., Signal Magazine, Sept. 1965.
(2) "Photon Effects in $H_{g1-x}Cd_x$ Te", Paul W. Kruse, Applied Optics, June 1965, pp. 687-692.
(3) P. W. Kruse, M.D. Blue, J. H. Garfunkel, and W. D. Saur, Infrared Physics, 2, 53 (1962).

The recommended path of technology development will result from an analysis of the most promising approaches to future cryogenic cooling of detectors. Some of the approaches to be evaluated are listed below:

a. Open cycle liquid cooling systems.
b. Open cycle solid cooling systems.
c. Closed cycle Joule Thompson cooling systems.
d. Closed cycle Claude reciprocating engine cooling system.
e. Closed cycle Claude rotary stroking engine cooling system.
f. Closed cycle Sterling engine cooling system.
g. Closed cycle Modified Sterling engine cooling system.
h. Thermoelectric coolers.
i. Thermomagnetic coolers.
j. Passive cooling.

These cooling systems are compared in table 5.7.2-1 and the considerations for selection are enumerated.(4)

The requirement for long duration (2 to 5 years) unattended operation decreases the desirability of the open cycle cooling systems. The closed cycle systems require expansion and compression of the working fluid in order to cool. The P-V diagrams depict this expansion and compressions for the various closed cycle coolers.(5) Except for the turbine type, compressor and expanders, their duration of operation are limited due to the low temperature lubrication and contamination problems. The turbo expanders and turbo compressors are not subject to these operational limitations as the working fluid is used in gas lubrication of the bearing surfaces.

This goal of unattended operation of from two to five years (17,520 to 44,500 hours) will be difficult to attain. Open cycle liquid helium, hydrogen, neon, nitrogen, argon and oxygen systems will have limited operation as they will require continuous supply of cryogenic fluid and can present a major logistics problem. An open cycle solid system will be capable of 14 day maintenance free operation which can be extended to 45 days, and will have a maximum potential life predicted at approximately one year (see figure 5.7.2-1) but will have the limited operation similar to the open cycle liquid systems. Closed cycle J-T systems will operate 500 hours without maintenance and have potential to extend to 1,000 hours. Closed cycle Claude reciprocating engine cooling system will operate 500 hours without maintenance and have predictable state-of-the-art advance to 5,000 hours with an overall potential up to 10,000 hours. The closed cycle Claude and Reverse Brayton utilizing rotary stroking and turbomachinery both will be capable of 10,000 hours of maintenance free operation, and will have an overall potential of the 44,500 hours goal. Closed cycle Sterling cooling systems will operate

(4) Stochl, Current Status and Future Trends of Cryogenic Coolers for Electronic Application. U.S.Army Electronics Laboratory, July, 1964.
(5) Zemansky, Heat and Thermodynamics - 3 rd Edition, pp. 139-151.

Table 5.7.2-1. Several Considerations for Cryo-Cooler Selector

TABLE I: GENERAL CONSIDERATIONS FOR CRYO-COOLER SELECTION		
LIQUID 77°K	30°K	4.2°K
1 - SIMPLE RELIABLE NO NOISE, NO VIBRATION 2 - IMMEDIATE COOL-DOWN 3 - LITTLE OR NO ELECTRICAL POWER REQUIRED 4 - COOLING CAPACITY IS DEPLETED DURING STAND-BY 5 - LIMITED MAINTENANCE-FREE OPERATION 6 - LARGE LOGISTICS BURDEN	1 - SIMPLE RELIABLE, NO NOISE, NO VIBRATION 2 - IMMEDIATE COOL-DOWN 3 - LITTLE OR NO ELECTRICAL POWER REQUIRED 4 - COOLING CAPACITY IS DEPLETED DURING STAND-BY 5 - LIMITED MAINTENANCE-FREE OPERATION 6 - LARGE LOGISTICS BURDEN	1 - NO NOISE, NO VIBRATION 2 - IMMEDIATE COOL-DOWN 3 - LITTLE OR NO ELECTRICAL POWER REQUIRED 4 - REQUIRES HIGHLY SOPHISTICATED HANDLING TECHNIQUES 5 - VERY LIMITED MAINTENANCE-FREE OPERATION 6 - LARGE LOGISTICS BURDEN
SOLID 77°K	30°K	4.2°K
1 - LONGER LIFE THAN EQUIVALENT SIZE LIQUID SYSTEMS 2 - PARTICULARLY SUITED TO LOW HEAT LOAD APPLICATION 3 - REDUCED LOGISTICS BURDEN 4 - REQUIRES SOPHISTICATED FILLING TECHNIQUE 5 - COOLING CAPACITY DEPLETED DURING STAND-BY	1 - LONGER LIFE THAN EQUIVALENT SIZE LIQUID SYSTEMS 2 - PARTICULARLY SUITED TO LOW HEAT LOAD APPLICATIONS 3 - REDUCED LOGISTICS BURDEN 4 - REQUIRES SOPHISTRICATED FILLING TECHNIQUES 5 - COOLING CAPACITY DEPLETED DURING STAND-BY	1 - NOT APPLICABLE
OPEN CYCLE J-T 77°K	30°K	4.2°K
1 - PARTICULARLY SUITED TO REMOTE COOLING APPLICATIONS 2 - LITTLE OR NO ELECTRICAL POWER REQUIRED 3 - NO STAND-BY LOSSES USING HIGH PRESSURE GAS STORAGE 4 - VERY LIMITED OPERATING LIFE-SUBJECT TO PLUGGING 5 - LOGISTICS BURDEN 6 - REQUIRES HIGH PURITY GAS	1 - PARTICULARLY SUITED TO REMOTE COOLING APPLICATIONS 2 - REQUIRES STAGING USING TWO DIFFERENT GASES 3 - NO STAND-BY LOSSES USING HIGH PRESSURE GAS STORAGE 4 - VERY LIMITED OPERATING LIFE-SUBJECT TO PLUGGING 5 - LOGISTICS BURDEN 6 - REQUIRES HIGH PURITY GAS	1 - NOT PRACTICAL IN THIS TEMPERATURE RANGE
CLOSED CYCLE J-T 77°K	30°K	4.2°K
1 - PARTICULARLY SUITED TO REMOTE COOLING APPLICATION 2 - EXTREMELY FAST COOLNESS POSSIBLE 3 - LOW THERMODYNAMIC EFFICIENCY 4 - PARTICULARLY SUBJECT TO PLUGGING 5 - REQUIRES SPECIALIZED RECHARGING EQUIPMENT AND PROCEDURES	1 - PARTICULARLY SUITED TO REMOTE COOLING APPLICATIONS 2 - LOW THERMODYNAMIC EFFICIENCY 3 - RATHER HIGH SPECIFIC POWER REQUIRED 4 - REQUIRES STAGING USING TWO DIFFERENT GASES 5 - BOTH J-T CIRCUITS ARE SUBJECT TO PLUGGING 6 - REQUIRES SPECIALIZED RECHARGING EQUIPMENT AND PROCEDURES	1 - PARTICULARLY SUITED TO REMOTE COOLING APPLICATIONS 2 - REQUIRES STAGING USING THREE DIFFERENT GASES 3 - EACH OF THESE J-T CIRCUITS SUBJECT TO PLUGGING 4 - EXCEPTIONALLY HIGH SPECIFIC POWER REQUIRED 5 - EXCEPTIONALLY HIGH SPECIFIC WEIGHT 6 - REQUIRES SPECIALIZED RECHARGING EQUIPMENT AND PROCEDURES

CLAUDE 77°K	30°K	4.2°K
1 - HIGH THERMODYNAMIC EFFICIENCY 2 - RECIPROCATING OR TURBINE MACHINERY CAN BE USED 3 - SINGLE EXPANDER REQUIRED FOR THIS TEMPERATURE RANGE 4 - REQUIRES COMPLEX TYPE MACHINERY 5 - COMPRESSOR PACKAGE CAN BE REMOTE FROM REFRIGERATOR	1 - HIGH THERMODYNAMIC EFFICIENCY 2 - TWO EXPANDERS REQUIRED FOR THIS TEMPERATURE RANGE 3 - RECIPROCATING OR TURBINE TYPE MACHINERY CAN BE USED 4 - REQUIRES COMPLEX TYPE MACHINERY 5 - COMPRESSOR PACKAGE CAN BE REMOTE FROM REFRIGERATOR	1 - HIGH THERMODYNAMIC EFFICIENCY 2 - EITHER TWO OR THREE EXPANDERS PLUG J-T LOOP REQUIRED FOR THIS TEMPERATURE RANGE 3 - REQUIRES COMPLEX TYPE MACHINERY 4 - RECIPROCATING OR TURBINE TYPE MACHINERY CAN BE USED 5 - COMPRESSOR PACKAGE CAN BE LOCATED REMOTE FROM REFRIGERATOR
STIRLING 77°K	30°K	4.2°K
1 - MOST EFFICIENT THERMODYNAMIC CYCLE 2 - SELF-CLEANING HEAT EXCHANGERS ARE NOT PRONE TO PLUGGING 3 - PARTICULARLY SUITED TO ALL ATTITUDE OPERATION 4 - FOR OPTIMUM PERFORMANCE, ITEM BEING COOLED MUST BE ATTACHED TO COLDHEAD 5 - ITEM BEING COOLED IS SUBJECTED TO VIBRATION OF THE UNIT 6 - AT A SACRIFICE IN PERFORMANCE, AN AUXILIARY LIQUEFACTION LOOP FOR REMOTE COOLING APPLICATIONS CAN BE USED	1 - MOST EFFICIENT THERMODYNAMIC CYCLE 2 - SELF CLEANING HEAT EXCHANGERS ARE NOT PRONE TO PLUGGING 3 - PARTICULARLY SUITED TO ALL ATTITUDE OPERATION 4 - FOR OPTIMUM PERFORMANCE ITEM BEING COOLED MUST BE ATTACHED TO COLDHEAD 5 - ITEM BEING COOLED IS SUBJECTED TO VIBRATION OF THE UNIT 6 - DEPENDING ON HEAT LOAD THIS TEMPERATURE RANGE CAN BE ACHIEVED WITH EITHER SINGLE OR TWO STAGE MACHINE	1 - N/A
MODIFIED STIRLING 77°K	30°K	4.2°K
1 - COMPRESSOR AND REFRIGERATOR PACKAGES CAN BE SEPARATED 2 - SELF-CLEANING HEAT EXCHANGERS ARE NOT PRONE TO PLUGGING 3 - SINGLE STAGE MACHINE REQUIRED FOR THIS TEMPERATURE RANGE 4 - LESS EFFICIENT THAN STIRLING CYCLE MACHINE 5 - SOMEWHAT MORE COMPLEX THAN STIRLING CYCLE MACHINE 6 - ITEM BEING COOLED IS SUBJECTED TO LOW FREQUENCY VIBRATION	1 - COMPRESSOR AND REFRIGERATOR PACKAGES CAN BE SEPARATED 2 - SELF-CLEANING HEAT EXCHANGERS ARE NOT PRONE TO PLUGGING 3 - EITHER SINGLE OR TWO STAGE MACHINE REQUIRED FOR THIS TEMPERATURE RANGE 4 - OVERALL EFFICIENCY IS COMPARABLE TO STIRLING CYCLE MACHINE 5 - SOMEWHAT MORE COMPLEX THAN STIRLING CYCLE MACHINE 6 - ITEM BEING COOLED IS SUBJECTED TO LOW FREQUENCY VIBRATION	1 - COMPRESSOR AND REFRIGERATOR PACKAGES CAN BE SEPARATED 2 - REFRIGERATOR SPEED IS LOW 3 - THREE STAGES PLUS J-T LOOP REQUIRED FOR THIS TEMPERATURE RANGE 4 - ITEM BEING COOLED IS SUBJECTED TO LOW FREQUENCY VIBRATION 5 - REQUIRES RATHER COMPLEX TYPE MACHINERY
SOLID-STATE COOLING DEVICES:		
1 - POTENTIALLY QUIET, VIBRATION-FREE, AND HIGHLY RELIABLE 2 - STAGING OF THERMOELECTRIC WITH THERMOMAGNETIC COOLERS REQUIRED TO ACHIEVE TEMPERATURE OF 100°K AND BELOW FROM AMBIENT 3 - OVERALL EFFICIENCY OF PRESENT DEVICES IS LOW 4 - ACHIEVING TEMPERATURES BELOW 100°K IS BEYOND THE PRESENT STATE-OF-THE-ART 5 - FUTURE ADVANCES ARE HIGHLY DEPENDENT ON MATERIAL BREAK-THROUGHS		

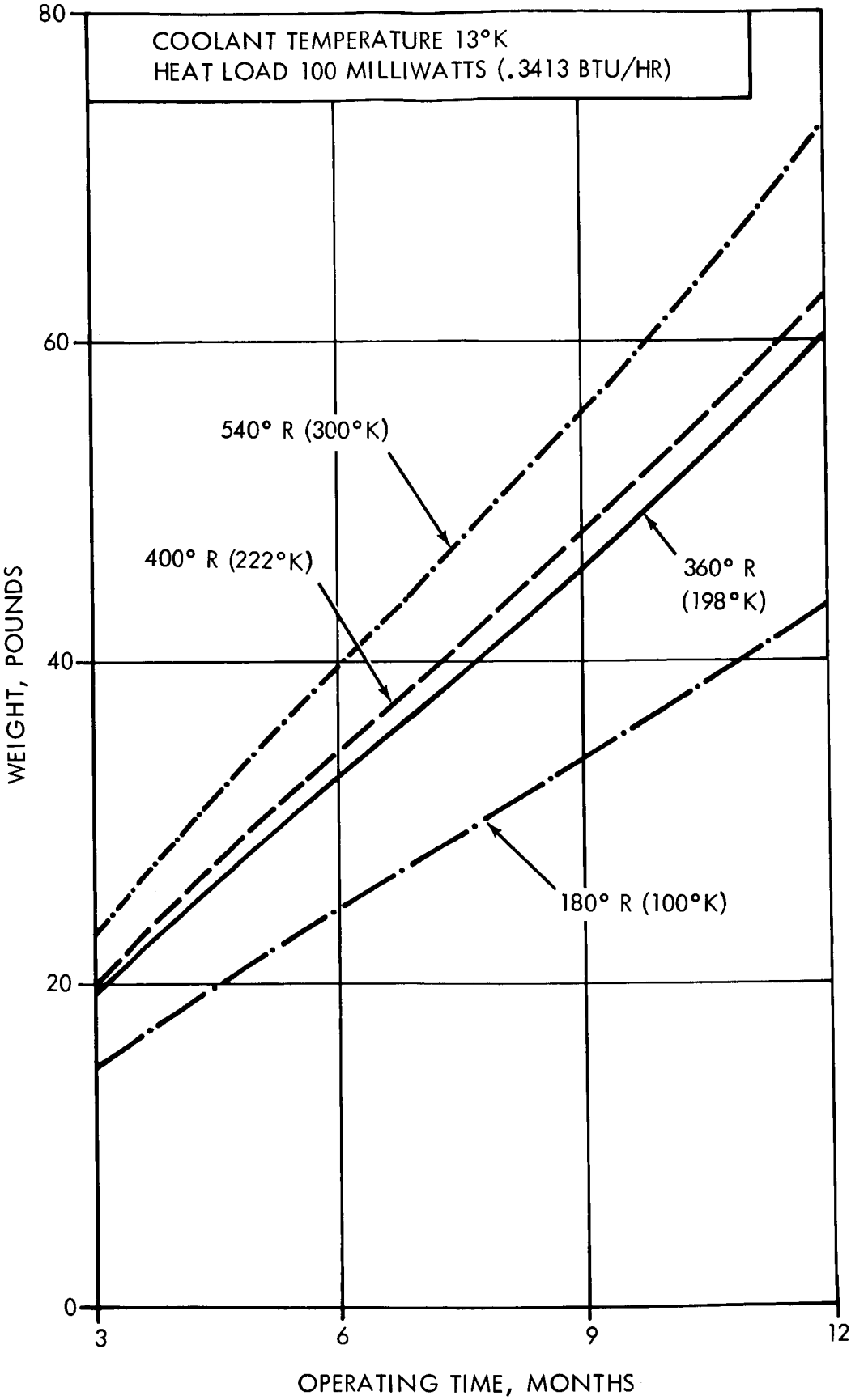


Figure 5.7.2-1. General Considerations for Cryo-Cooler Selection

500 hours without maintenance and have predictable state-of-the-art advance to 2,500 hours with an overall potential up to 3,000 hours. Closed cycle modified Sterling cooling systems will operate 1,500 hours without maintenance and have predictable state-of-the-art advance to 2,500 with an overall potential up to 5,000 hours. The thermoelectric and thermomagnetic solid state cooler both have potential for the 44,500 hour goal of maintenance free operation. Figure 5.7.2-2 compares the maintenance internal for various of the cryogenic cooling systems.(6) Figure 5.7.2-3 compares the operating temperature ranges for these same systems.(6)

The solid state cooling devices are low temperature limited. The Peltier cooler is most efficient between room temperature (295°K) and 200°K whereas the Ettingshausen coolers are most efficient between 200°K and 77°K. Cooling to temperatures below 150°K should be possible with the present state-of-the-art and combination of the Peltier and Ettingshausen coolers. Cooling to 77°K will have to await discovery of materials with larger thermomagnetic figures of merit. The best material available at this time, is the bismuth-antimoney crystal system.

The closed cycles utilizing turbomachinery and or rotating type machinery can be designed so as to use the working fluid as a gas bearing reducing wear between the moving parts until it is practially eliminated. The turbine approach is by no means new in the cryogenic industry since large capacity liquifiers using turbomachinery have been in operation for years. The concept of building a minature cryogenic turbo cooler is very recent. The Claude and Reverse Brayton cycles are ideally suited to the use of the turbo and rotating type of expanders and compressors. The same compressor and expander equipment developed can be used in both cycles. In the Reverse Brayton cycle the working fluid is always single phase whereas this is not the case in the Claude cycle.

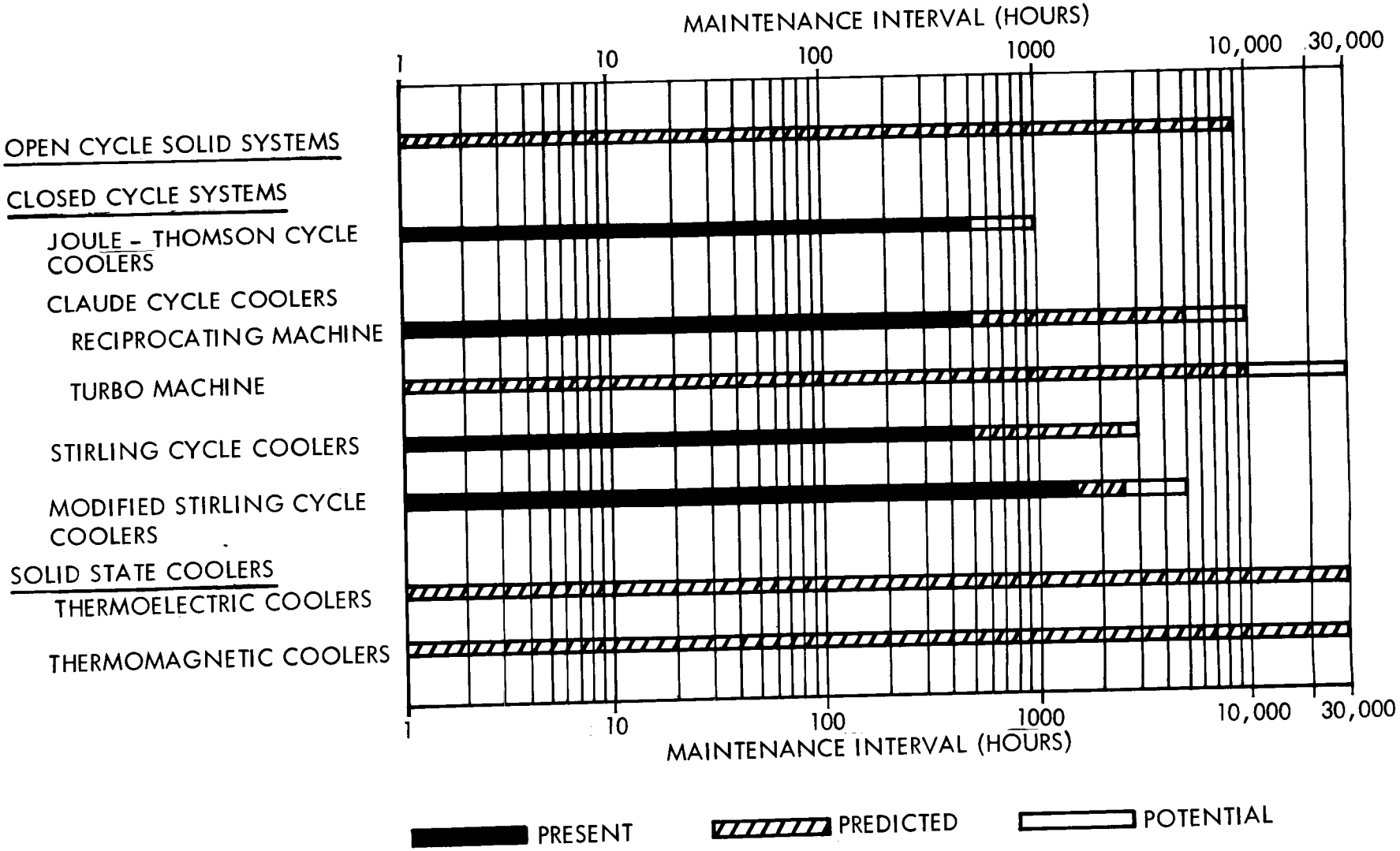
Space testing program does not appear to be a necessary part of the development of the rotary stroking or turbine type of refrigeration equipment. It would, although, be desirable to run a final checkout of the refrigerator in space before placing it in a critical application as a reliability precaution.(7)

One of the elements of the rotary stroking refrigerator in which the absence of gravity field is a consideration is in the gas bearings. This type of bearing is susceptible to a type of dynamic instability known as "half frequency whirl". When bearings operate in this unstable regime (which generally occurs at high RPM's and low loads), the journal orbits in the bearing at approximately half the journal speed, contacts the bearing wall, and usually seizes immediately. There are two common and well known approaches for avoiding this type of instability: a) imposing

---

(6) Stochl, Current Status and Future Trends of Cryogenic Coolers for Electronic Applications, U.S. Army Electronics Lab., July 1964.

(7) Correspondence, meetings and telecons with A.D. Little, AiResearch, and Air Products. Further substantiation by D.B. Mann of the Cryogenic Engineering Laboratory, National Bureau of Standards.



L-682

Figure 5.7.2-2. Maintenance Interval for Various Cryogenic Cooling Systems

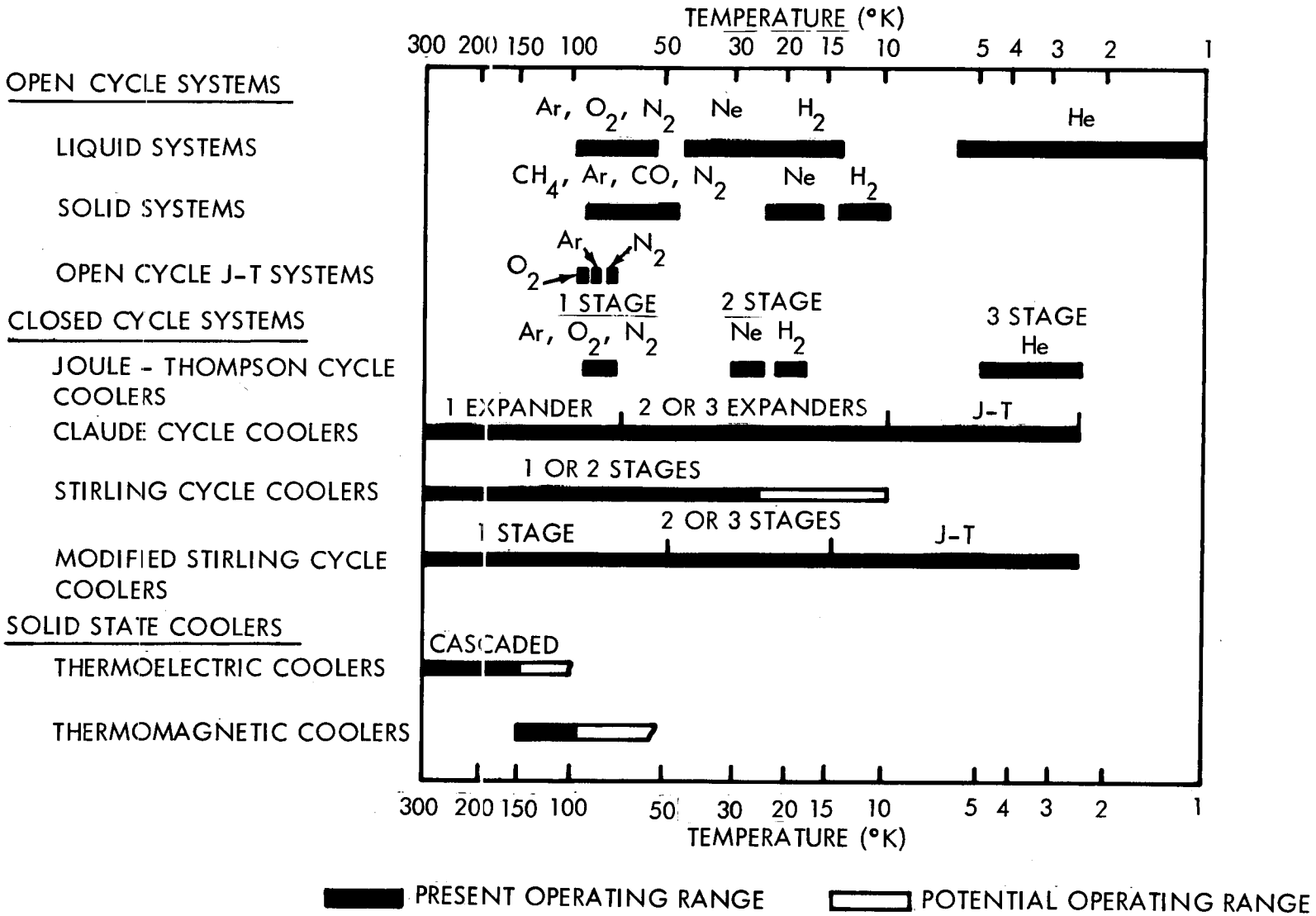


Figure 5.7.2-3. Operating Temperature Ranges For Various Cryo-Cooling Systems

external loads which are not gravity sensitive, and b) altering the geometry of the bearing by interrupting the continuity of the bearing shell to suppress the tendency to whirl. In the rotary stroking refrigerators the rotative speeds are low (1800 RPM), therefore, half frequency whirl is not as much of a problem as in high speed turbomachinery. Further, the major loads on the bearings are not weight loads, but rather are pneumatic loads, electromagnetic loads, and mechanical loads due to misalignment of parts. The weight load is only a small fraction of these other loads; therefore, the performance of the gas bearings is probably independent of the presence or absence of gravity.

Another element which should be considered in the case of an absence of the gravity field is the detector heat exchanger. Heat exchanger processes which rely upon the gravitational effects (that is, free convection and pool boiling) will obviously be effected by a zero gravity environment. On the other hand, processes such as radiation, conduction, and forced convection are unaffected by the gravity field. Heat exchangers may be designed to be of the forced convection type, with flow being maintained by imposed pressure differences rather than by free convection. Therefore, the absence of gravity will not affect the performance of these exchangers. This applies to the all-gas heat exchangers in the cycle, plus the detector heat exchanger just downstream of the J-T valve (which handles a two-phase gas liquid mixture). The flow immediately downstream of the J-T valve is approximately 5 per cent by volume liquid and 95 per cent by volume vapor; therefore, the liquid occurs more as a mist rather than a distinct separate phase. The 5 per cent liquid fraction in this stream provides the refrigeration for cooling the detector, as it boils in the heat exchanger to which the detector is mounted. If this heat exchanger is designed so that the flow is highly turbulent and contains some vortex action, the small liquid droplets will be forced against the walls of the exchanger by non-gravity forces, therefore, the performance of this exchanger will be independent of a gravitational field.

As a final confirmation of the validity of the design for a zero gravity environment, a test of the machine in all attitudes is possible to demonstrate that it is, in fact, insensitive to the direction of the gravity vector. It appears that all this development and testing work can be conducted on the ground, and, therefore, a space testing program is not recommended as part of the development of this specific cryogenic cooling technology.

A turbine type Reverse Brayton cycle 77°K cooler has been produced and is undergoing endurance testing. The equipment used in the Reverse Brayton cycle is identical to that used in the Claude cycle. A turbine type 4.2°K Claude cycle system has been operated in parts and has not yet been operated as a complete system. The development of this system is now under contract.

Another gas bearing type 77°K cooler has been produced which uses the Reverse Brayton cycle in a reciprocator having a novel electromechanical

actuating arrangment in which gas bearings support the stroking pistons. This unit is currently under test and modification. Its ability to operate below 4.2°K is being developed under contract.

The problem of low cycle efficiency and the resulting high power requirement is severe. The theoretical Carnot cycle would require 75 watts of power input to provide 1 watt of refrigeration at liquid helium temperature. Actual refrigeration is reduced by unavoidable inefficiencies in heat transfer, irreversible behavior of expansion and compression equipment, and increased heat leak at low operating temperatures. System efficiencies of five per cent or lower are typical. Thus for 1 watt of refrigeration at 4°K more than 1,500 watts input power is required.(8)

The Sterling Cycle is appealing from an efficiency standpoint as it is the most efficient thermodynamic cycle at 30°K. The P-V and T-S diagram are shown below:

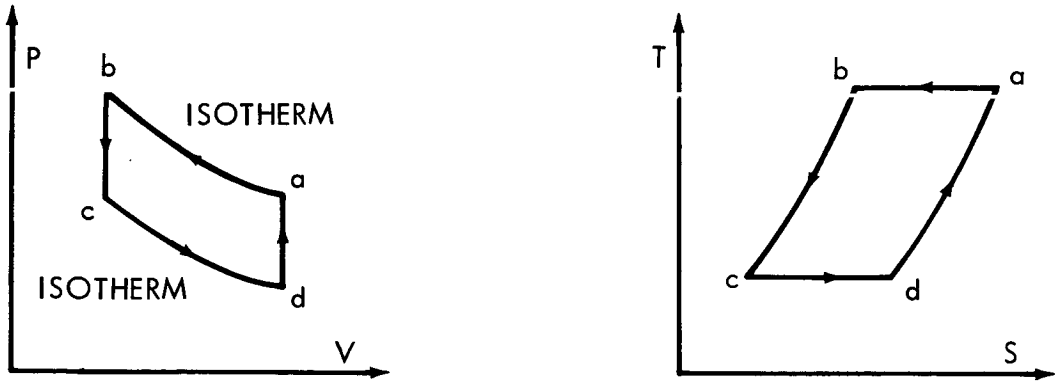


Figure 5.7.2-4.

(8) Cryogenic System for Electronics, Air Products, p. 4.

The Sterling cycle is represented by two isotherms bounded by two constant volume processes. An operating Sterling cycle produces 1.5 watts of cooling at 25°K for 450 watts input. The unit could be further developed to produce 3 watts of cooling at 15°K with 1500 watts input. Lower temperatures would require a modified Sterling cycle. Major problems in the Sterling cycle is the limited length of operating duration of 1,000 hours currently and long range potential to 5,000 hours and the low frequency vibration of the unit.

5.7.3 Recommendations

The promising approaches to cryogenic cooling for detectors of the future appears to be in the following areas:

a. Open cycle solid systems.
b. Solid state cooling systems.
c. Closed cycle gas bearing type cooling system.

Therefore, it is recommended that ground based technological development programs for these approaches be supported. It appears that space technology development will not be necessary and the cooling systems can be developed from ground-based programs directly into space applications. The solid system appears to be limited in operational life and the low temperature it can attain (10°K). The solid state coolers seem also limited as to the low temperature achievable (77°K). Since it is desirable to operate the cooling system of the future over long durations (2 to 5 year goal) and down to below 4.2°K, emphasis should be placed on development of the closed cycle gas bearing type cooling system.

Two basic thermodynamic cycles are well suited to rotary refrigeration equipment, the Claude (liquid helium temperatures) and Reverse Brayton (liquid nitrogen temperatures) cycles which use the gas bearing concept in the compressor and expander. The P-V and T-S diagrams for the Claude cycle are shown below:

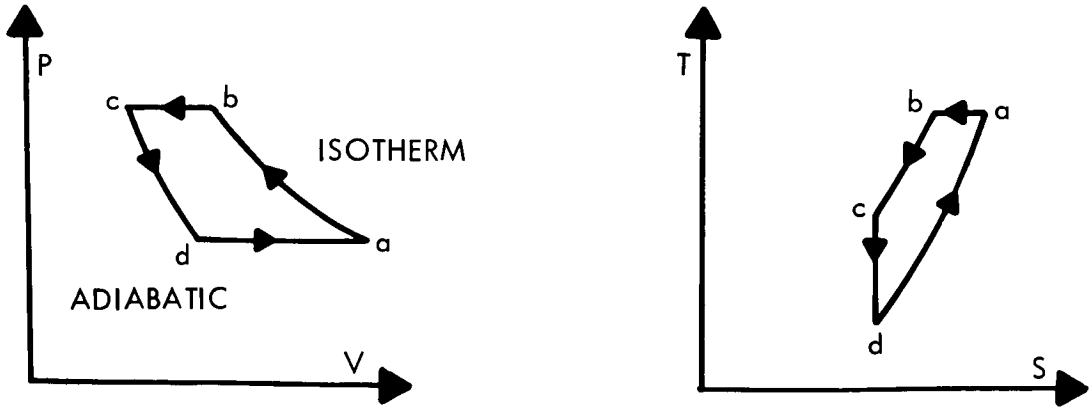


Figure 5.7.3-1.

The Claude cycle is represented by two constant pressure processes bounded by an isotherm, and an isentrope. A block diagram of a 3.6°K Helium Claude Cycle turbomachinery cooling system is shown in figure 5.7.3-2. A block diagram of a 3.6°K Helium Collins Cycle (Variation of the Claude cycle) rotary stroking cooling system is shown in figure 5.7.3-3.

The following design goals for the Collins Cycle rotary stroking cooling system are now being pursued under contract:

Temperature 3.6°K ± .004°K
Refrigeration 1 watt
Power Input 1300 watts
Compressor and Expander Volume 3.7 cu. ft.
Compressor and Expander Weight 100 lbs.

A schematic layout is shown in figures 5.7.3-4 and 5.7.3-5. A photograph of the 77°K unit is shown in figure 5.7.3-6.

The following design goals for the Claude turbomachinery cooling system are now being pursued under contract:

Temperature 3.6°K
Refrigeration 1 watt
Power Input 5 kw (based on actual test)
Compressor and Expander Volume 4 cu. ft.
Compressor and Expander Weight 160 lbs.

A photograph of a helium turbo compressor is shown in figure 5.7.3-7.

The rotary stroking machinery will require development in the expander unit, substitution of gas springs for mechanical springs, and development of power conditioning and control unit. The following schedule of development is proposed:

1966-1967 System Evaluations. Design, build, and test critical components of expander package (expanders, gas springs, motors, power conditioning equipment).

1967-1968 Further development of critical components of expander package for improved performance and reliability. Design, build and test heat exchangers. Assemble and test complete expander package. Design, build and test compressor package and associated electronics.

1968-1969 Further development of all components for improved performance and reliability. Develop operating procedures. Start endurance testing of breadboard machine. Design prototype machine.

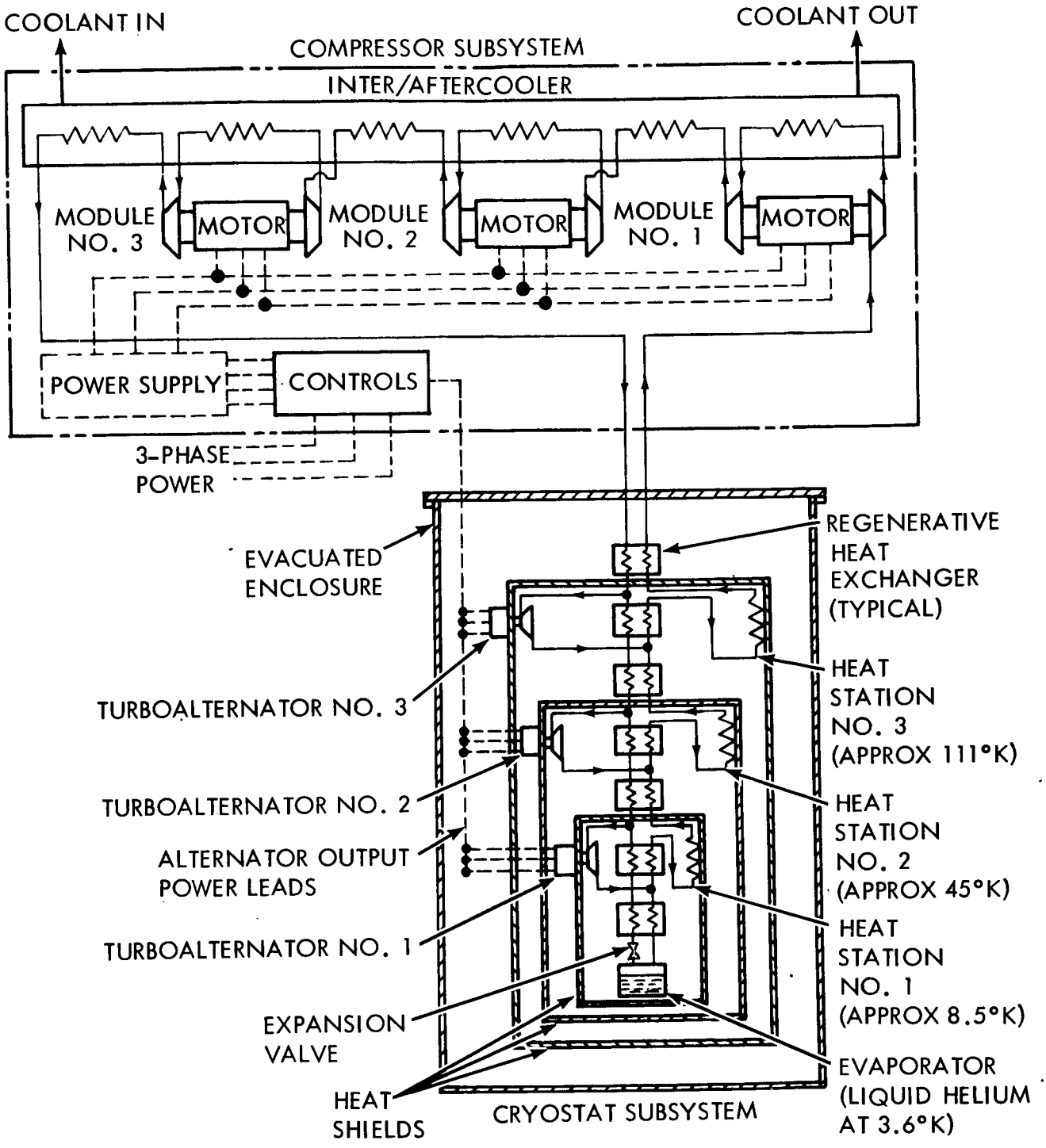


Figure 5.7.3-2. 3.6°K Helium Calude Cycle Refrigeration System

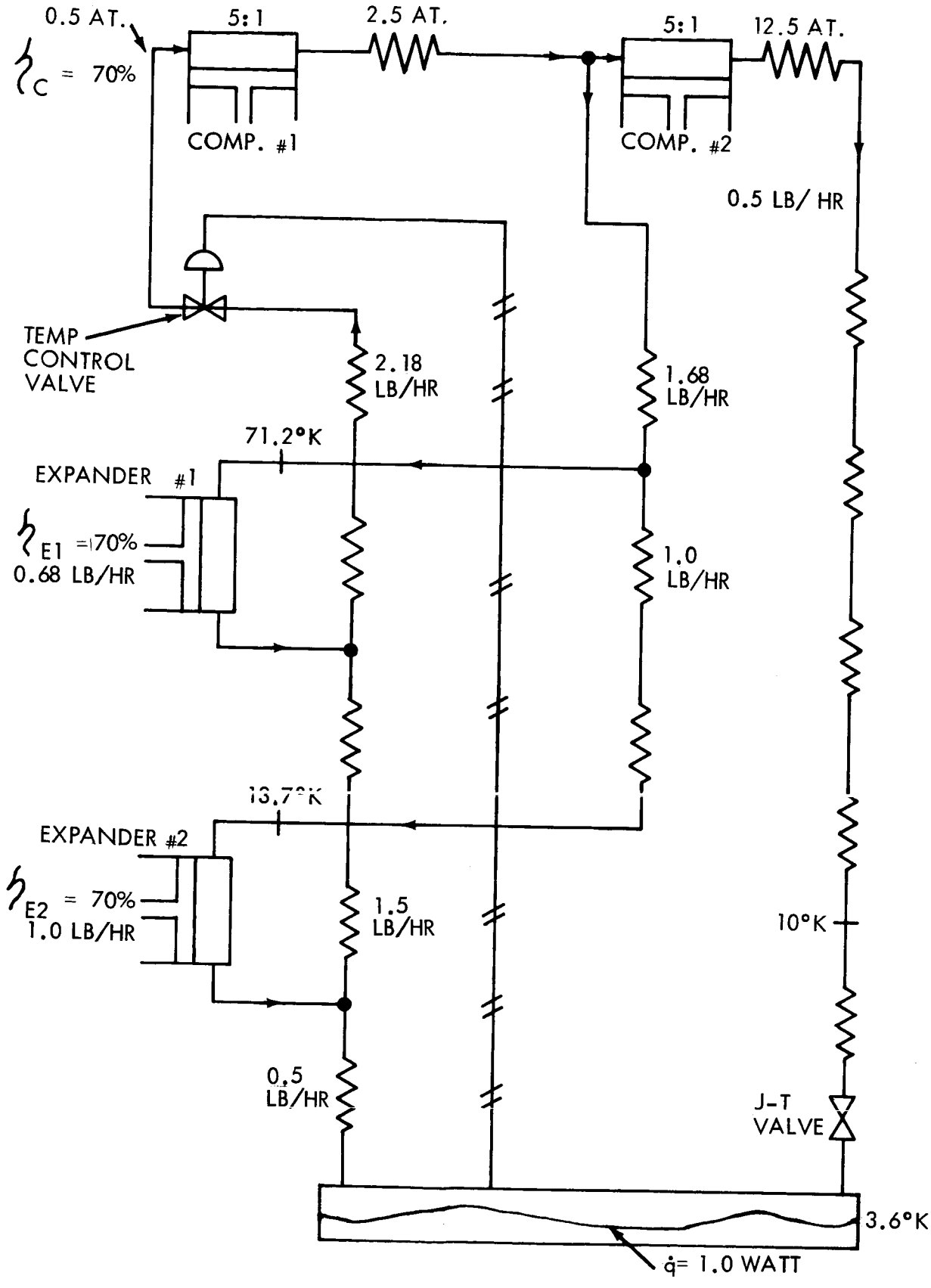


Figure 5.7.3-3. 3.6°K Helium Collins Cycle Refrigeration System

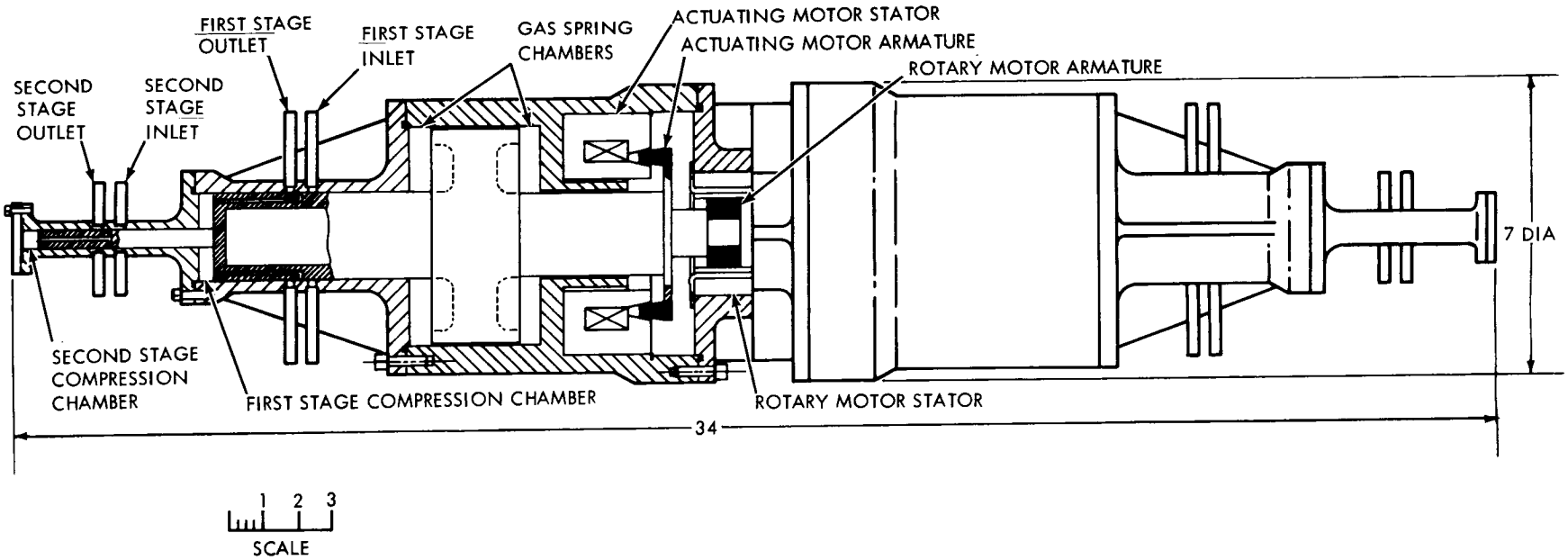


Figure 5.7.3-4. Compressor Package

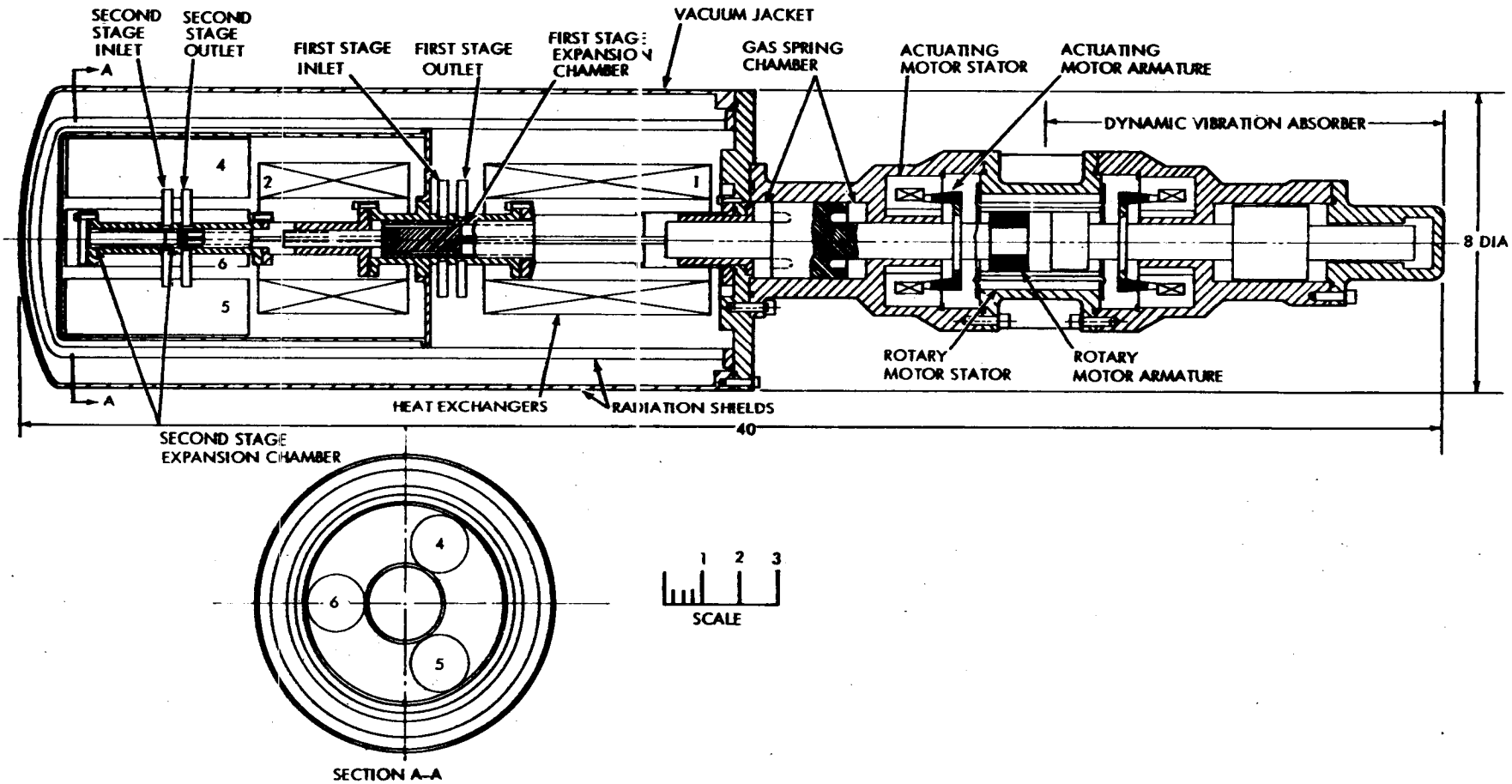


Figure 5.7.3-5. Expander Package

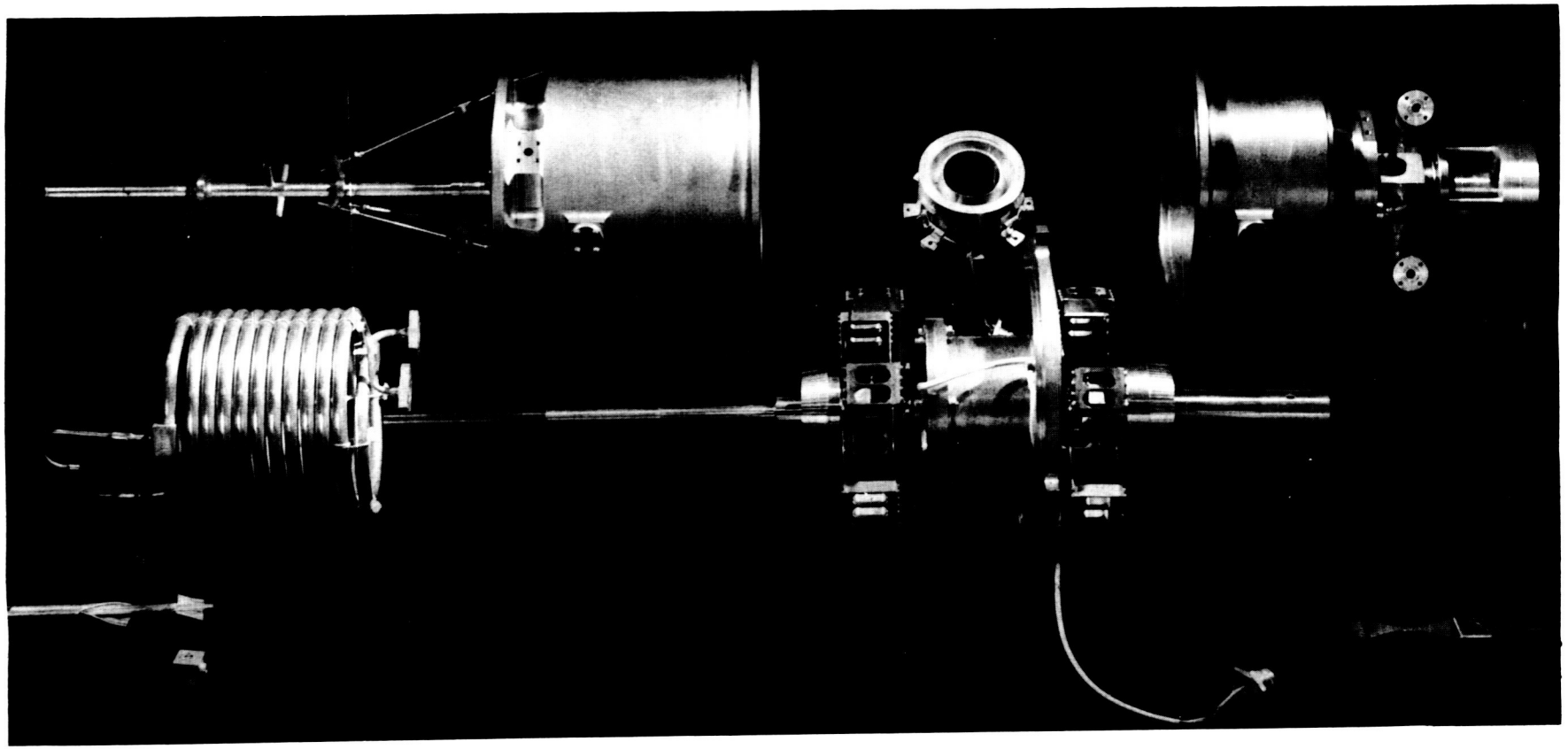
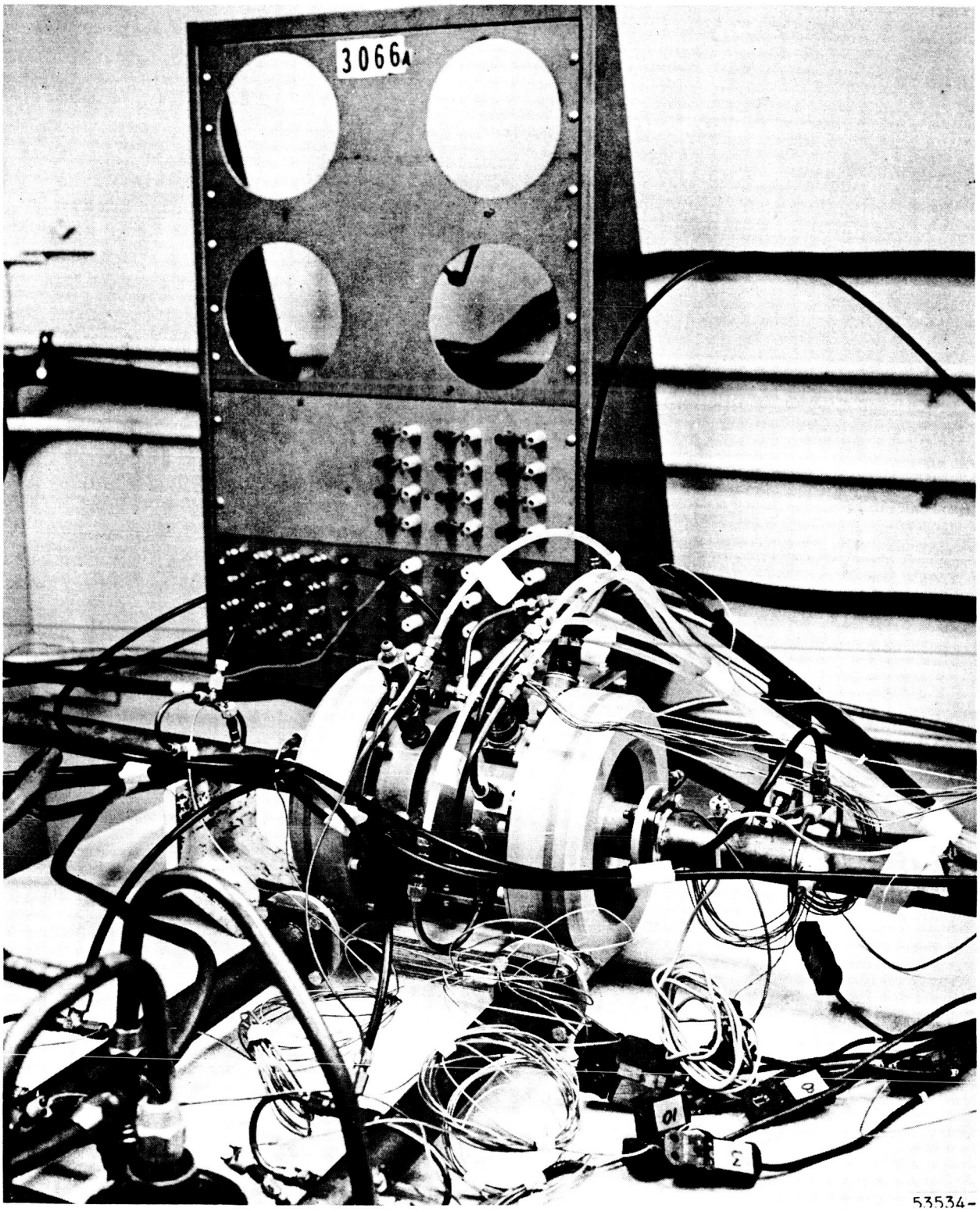


Figure 5.7.3-6. Spaceborne 77°K Refrigerator


3066A
53534-

1969-1970 Build prototype machine. Performance test and endurance test prototype machine.

1970-1971 Build and test flight model. Continue endurance tests on prototype machine.

The turbomachinery will require advances in reduction of bearing losses, some improvements in wheel aerodynamics for the necessarily low specific speeds, high efficiency electric motor drives and improved heat exchanger performance. The turbine machinery could be developed on a schedule approximately $1\frac{1}{2}$ years shorter then the rotary stroking machinery.

The development of the 3.6°K cycle with rotary stroking machinery in accordance to the above schedule will require approximately $250K funding per year. If a crash program is considered with parallel engineering development, then the development could be compressed to three years and a funding level of $500K per year.

The development of the 3.6°K cycle with turbomachinery could be accomplished by 1970 at a funding level of approximately $300K per year.

Essentially, the design of a solid cryogenic cooler is the design of a cryogen storage dewar. The art and technology involved in the development of the dewar have application to the design of the cooler. The need for minimum parasitic heat leak is paramount. The use of multi-foil, radiation-shield types of insulation (so-called superinsulations) are most often called for. Radiation shields cooled by the effluent vapors from the subliming solid can be usefully applied. Use of the sensible heat of these effluent vapors to heat station necessary penetrations for support, fill and vent lines, etc., is good design practice. The use of a secondary solid cryogen in the role of a heat shield for the primary coolant is a worthy recent proposal pursued under a current development. The service demands that a great deal of ingenuity and technical sophistication be applied to the design of low heat leak structural supports and mounting arrangements for the cooled electronic component. Special operational needs involving filling procedures, standby requirements, control and safety are all extremely important to the ultimate design.(9)

The realization of an adequate insulation system for the solid cryogen storage container is a fundamental problem. Data on so-called superinsulations or multi-layer insulations as measured on samples under favorable conditions indicate that their insulation qualities, if retained in application, would make possible reasonably small containers which will hold the solid cryogen for a year or more. In fact, the application has to accomodate complex surfaces and penetrations due to pipes and supports, with the result that the performance of the insulation is seriously degraded in

---

(9) Fowle, Arthur A., "Cooling with Solid Cryogens - A Review", Arthur D. Little, Inc., Cambridge, Massachusetts, Cryogenic Engineering Conference, August 1965.

comparison with that of an ideal blanket. Designs are called for which better methods of application of the insulation. In fact, the performance of subliming refrigerators built to date fall well short of expectations based on theoretical considerations, and better dewar design is needed.

Further investigation is necessary of the methods by which the container is to be filled with solid. One method is to fill the container with the liquid cryogen and, thereafter, produce a solid by reducing its vapor pressure below the triple point by use of a vacuum pump. This method inevitably produces a solid having a somewhat porous structure, because a fraction of the liqud has to be vaporized to provide cooling for the remainder of the solid. The difficulties experienced in producing a solid by vacuum pumping and the porosity of the solid depends on complex interactions involving pumping rate, the thermal conductivities of the various phases of the cryogen, etc. The use of vacuum pumping to produce a solid is relatively simple to apply and its accommodation does not complicate the design of the dewar. However, by the use of this method, it is difficult to see how one can capitalize on the greater density of the pure solid compared with the liquid.

Another method for producing the solid makes use of a separate cooling circuit. The cryogen in its liquid form is introduced into the container. It is frozen by heat exchange with another colder cyrogen circulated in tubes bonded to the inner container or retained in a surrounding vessel. By this method, one can fill the inner container with a dense solid; however, complications in structure, additional heat-leak paths associated with fill and vent lines for the auxiliary cooling circuit and the need for an auxiliary cooling circuit and the need for an auxiliary cryogen supply are introduced.

Temperature control of the item to be cooled may present difficult problems. Control of the equilibrium vapor pressure above the subliming solid is one approach. If close temperature regulation is required, pressure control within fractions of a millimeter of mercury at pressure levels in the neighborhood of 1 torr is necessary.

Control of the temperature of the refrigerated item can also be accomplished by flow control of a portion of the effluent vapors made to effectively exchange heat with this item. A gas or vapor-pressure thermomenter bulb inserted at the item can act as a combined sensing elements and force motor for a flow control valve in the vapor coolant line. This method of control can be used to regulate the temperature of the cooled item about a point set above the temperature of the solid. Other variations and combinations of the outlined approaches to temperature control are possible.

A problem arises when it is desirable to cool a device at temperatures approaching the lower limit of the capability of the solid. In such cases, it is necessary to have close thermal coupling between this device and the solid.

The physical arrangement must allow cooling to take place without generating large temperature gradients. Means for achieving a uniform temperature distribution by employing metal equilibrators (extended surfaces, metal mesh, metal honeycomb, etc.) deserve attention. However, the determination of suitable methods are much handicapped by the complexity of the heat transfer process involved and the lack of data on the thermal properties of solid cryogens.

5.8 PHOTO-ELECTRO-OPTICAL SPACE EXPERIMENT

5.8.1 Objective

The objective of this experiment is to develop fabrication techniques and processes for very high resolution, high quantum efficiency, wide spectral response, and high accuracy (low distortion) photoelectric imaging devices. The devices must be capable of sensing, recording, or preparing for transmission the extremely high density of information available at the focal plane of diffraction limited space telescope systems. With the advent of the space telescope for gathering scientific data on the vast number of celestial objects, it is mandatory that the present state-of-the-art of imaging devices be improved.

5.8.2 Discussion

In presenting this experiment as a discard, a description of the experiment is first given, and then reasons for discarding it as a candidate for OTES.

5.8.2.1 Experiment Description

This experiment is actually a series of experiments which will contribute to the entire family of photoemissive devices. The three important areas to be investigated are cleaning and outgassing, photocathode formation, and final assembly techniques. However, the culmination of these experiments in the realization of a single, very valuable, astronomical device is contemplated -- the electronographic camera.

A brief description of electronography is in order. It has been discovered recently that when electrons, rather than photons, are used to write on photographic emulsions, several very important advantages may be realized. Each electron produces at least one black grain, while at least 100 photons are required to produce a single black grain in the most sensitive emulsions. Electron writing is extremely linear; photon writing is essentially nonlinear and suffers from exposure recirpocity failure. The recordable densities with electrons are greater by factors of 10 to 100 over photon writing which means that the already enormous data capacity of a photograph is increased by a factor of 10 to 100. For electron writing on a photographic emulsion, electrons can be obtained from a photocathode which prcvides further benefits. The quantum efficiency can be as much as 40 per cent (four photoelectrons generated for every 10 incident photons) compared to the one per cent quantum efficiency of photographic materials. The photo-electrons can be amplified or made more energetic by accelerating them through an electric field before striking the emulsion. Thus, the combination of photoelectric and photographic technology results in an extremely valuable tool giving results not possible by either techniques alone -- this is electronography.

Fundamental discoveries have already been made using the electronographic camera on earth-based telescopes. Compromises, however, in the design of the electronograph, when fabricated and operated on earth, must be made because of the confines of the necessary tube envelope and contamination of the photocathode by outgassing from the emulsion. The construction and use of the electronographic camera is an extremely difficult art. The photoemissive surfaces must be processed in a vacuum and, in almost all cases, in the confining space of the envelope where precautions are required to prevent contamination of other vital structures whitin the tube by the photocathode processing. The cathode is usually affected during final seal-off of the tube from a vacuum pump. During operation, electron bombardment of internal structure causes release of photocathode contaminating gases and ions resulting in the ultimate deterioration and destruction of the device. There are numerous other disadvantages of present fabrication techniques which can be overcome by better technology.

There are several advantages of fabricating and operating the electronograph and other photoelectric devices in space which will ease or eliminate many of the problems created by the earth's atmosphere. Some of these are listed below.

a. Elimination of the problems created by the tube envelope, i.e. field emission, optical distortion in face plate, etc.

b. Better outgassing of the substrate because of the large, extremely high, available vacuum of space.

c. Photocathode processing should be easier and superior by the new ion or molecular beam techniques which require a large vacuum; this is difficult to achieve in earth-fabricated devices.

d. Reprocessing the photocathode is possible which extends the lifetime of the device.

e. Repositioning the photocathode for operational use allows configurations which are impossible to achieve in earth-fabricated devices.

f. Large photocathodes are possible because very thin substrates may be used without a supporting faceplate.

g. The state-of-the-art should be advanced. For example, an electronograph with a 7.6 centimeter (3 inch) diameter format with a resolution of 300 to 400 lp/mm at 30 per cent contrast ratio can reasonably be expected in space. In contrast, an earth-manufactured electronograph will give approximately 60 lp/mm in the center of a 2.0 centimeter (0.75 inch) diameter format.

Three proposed configurations of the electronograph are shown in figure 5.8.2.1-1 with the advantages and disadvantages of each listed. A semitransparent cathode is used in the first configuration while an opaque

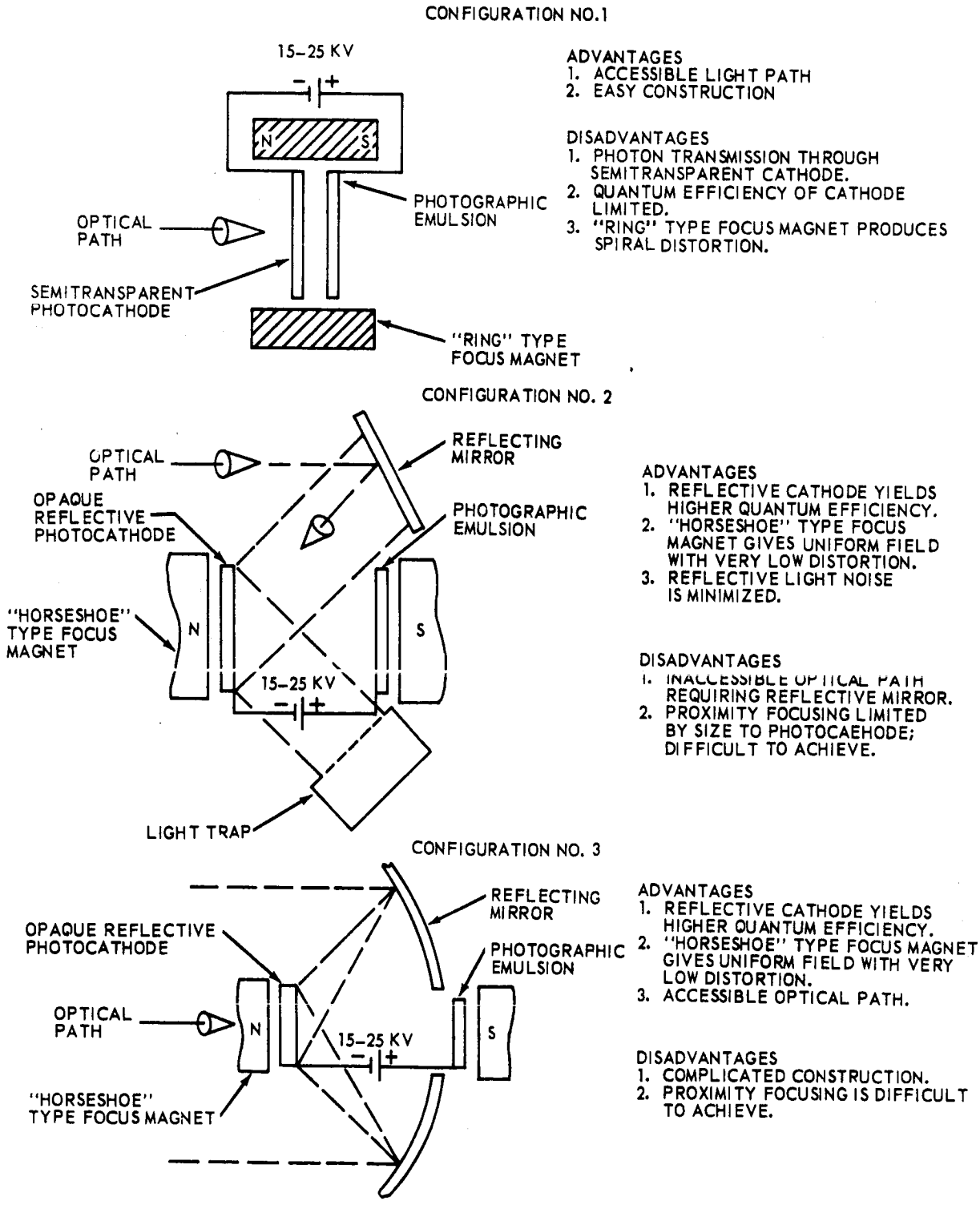


Figure 5.8.2.1-1. Electronographic Camera Configurations

reflective cathode is used in the last two. The semitransparent cathode allows a readily accessible optical path but is limited in quantum efficiency to a theoretical maximum of 50 per cent suffers some reduction in light transmission due to the necessary conducting film (tin oxide or chromium) evaporated on to the substrate and allows some light transmission which may be reflected back to the cathode creating a noise source.(1) The reflective cathode has the advantage of increased quantum efficiency and has practically no reflective light noise, but it has a very inaccessible optical path. Configuration 3 is a possible solution to the awkward delivery of incident light to the photocathode. The performance of each configuration should be experimentally evaluated by measuring resolution sensitivity, grey scale definition, image distortion, and photocathode degradation.

A concept of the equipment required to realize configuration 1 is shown in figure 5.8.2.1-2. The assembly consists of two turret mounts, one containing substrates the other containing photographic emulsions. The turret assemblies can be rotated and translated by means of a servo control system so that the substrate may be in optimum position for photocathode fabrication, and then the photocathode repositioned for operation use. A standard light source, a light transmission detector and an ion or molecular beam gun are required in the fabrication process. It is desirable that the ion beam gun be located distant from the substrate (approximately 15 inches for a 3 inch diameter photocathode) during fabrication so that uniform coating is achieved. Uniformities of better than plus-or-minus one per cent of the mean thickness should be possible using the advantages offered by space processing. On earth, it is extremely difficult to build planar photocathodes two inches in diameter with uniform sensitivity over the surface of better than plus-or-minus three per cent of the mean value. With larger diameters, the problem is even more severe.

During operation the photocathode is positioned co-planar to a fine-grain phosphor screen while critical focusing adjustments are made, and then the screen is replaced by an electron beam recording (EBR) emulsion. Proximity

---

(1) The semitransparent cathode cannot be excessively thick because too much of the incident light is absorbed at such a distance from the vacuum interface that the photoelectrons will not reach the surface with sufficient energy to excape. If the cathode is excessively thin, too much of the incident light is lost by transmission. This transmitted light may be absorbed by the emulsions or reflected back to the photocathode which will reduce the reduction and increase the noise, respectively.

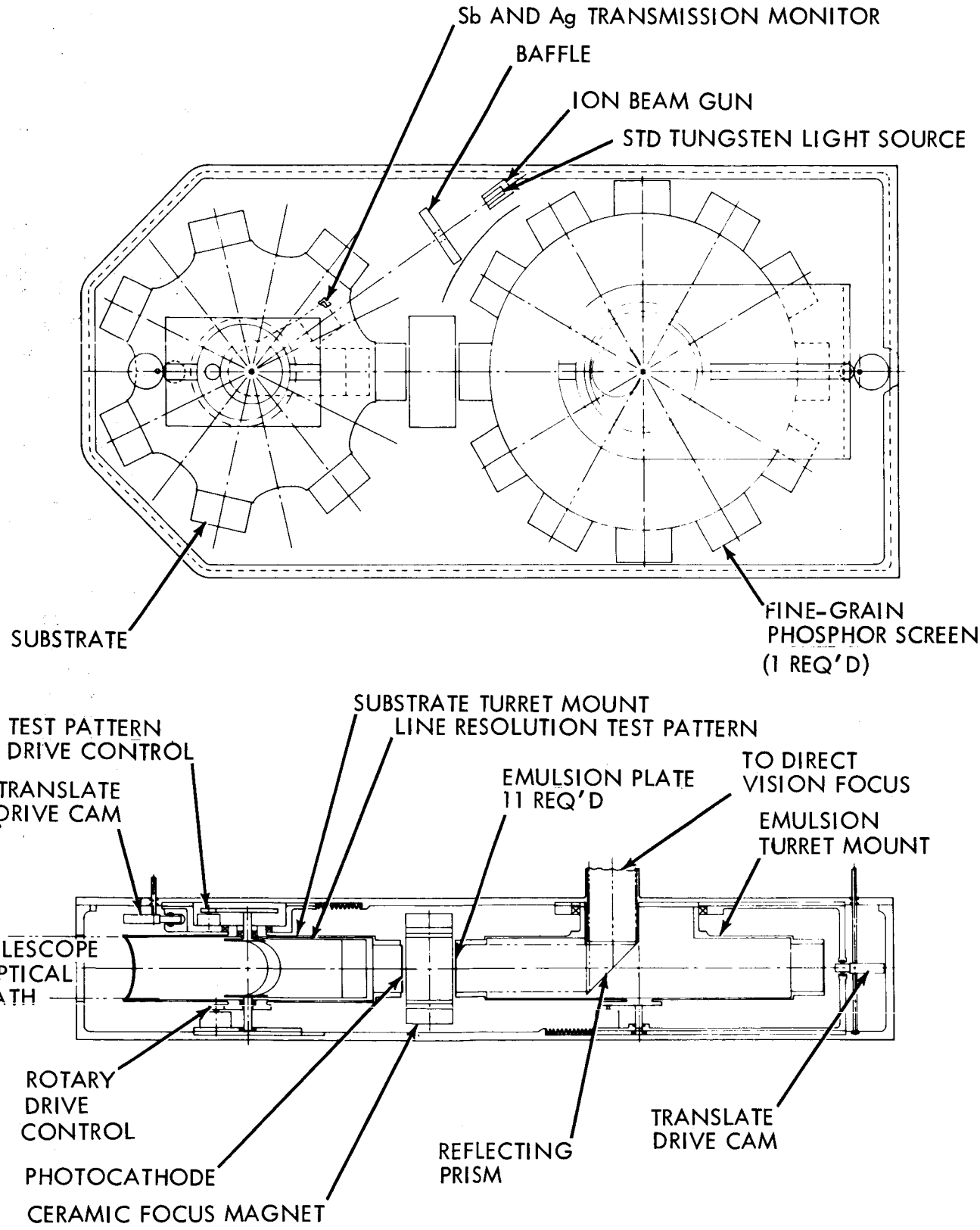


Figure 5.8.2.1-2. Electronographic Camera Equipment

focusing using parallel electric and magnetic fields will give very high resolution. A ceramic "ring" magnet can be used for obtaining the magnetic field; approximately 1300 gauss can be obtained uniformly but not isotropic over 50% of the axial length of the magnet. An appropriate test pattern, such as the USAF 1951 line resolution chart or the recently developed astronomical test pattern designed by Dr. W. A. Baum[2] is needed for performance evaluation. An image magnifier is necessary to view the image on the phosphor screen while focusing.

The experiment begins with baking the substrates at a temperature of approximately 500°C for a period of 10-12 hours. Various types of substrates could be evaluated such as quartz, mica, lithium fluoride (LiF) and aluminum oxide (Al_2O_3). Lithium fluoride is transparent in the ultraviolet to about 1050Å, aluminum oxide to about 1425Å, mica and quartz are not transparent in the ultraviolet. Mica and quartz are relatively inexpensive compared to LiF and Al_2O_3. Aluminum oxide has the highest tensile strength, and therefore may be superior for the large photocathodes. It is desired that the cathodes be as large as possible and as thin as possible. Various sizes from a 3 inch diameter format to a 10 inch diameter format could be used. Two types of support structures would be evaluated, one consisting of edge support only, the other consisting of a mesh support. Aluminum foils 3 inches in diameter and 300 Å thick have already been produced so that large, thin substrates are quite feasible.

After bakeout, the substrates are coated with a conducting material such as tin oxide or chromium. The photoemitters are then produced by the ion or molecular beam techniques. The most valuable photocathodes are those having the best combination of high quantum efficiency and the desired spectral response. The problem area is mostly in the visible and infrared region. The four component tri-alkali ($Na_2KSb(Cs)$) S-20 type surface, the three component (Ag-O-Cs) S-1 type surface, and the two component caesium antimonide (Cs_3Sb) S-9 and S-11 types, sometimes treated with traces of oxygen, are representative of the best types of photocathodes at present. Figure 5.8.2.1-3 shows the spectral response of these cathodes, figure 5.8.2.1-4 shows a comparison of the quantum efficiencies, and table 5.8.2.1-1 gives some properties of these practical photocathodes. The S-9 type would be first fabricated because it is the easiest, and the oxidation procedures would be attempted to convert it into the more sensitive S-11 type. The S-20 would next be experimented with because of its very high quantum efficiency over a wide spectral range. The S-1 type would then be fabricated because it extends farthest into the infrared region (about 1.2 microns).

---

(2) "Laboratory Evaluation of Image Tubes for Astronomical Purposes", Baum, W. A., Advances in Electronics and Electron Physics, Vol. XVI, 1962, Academic Press, New York, New York

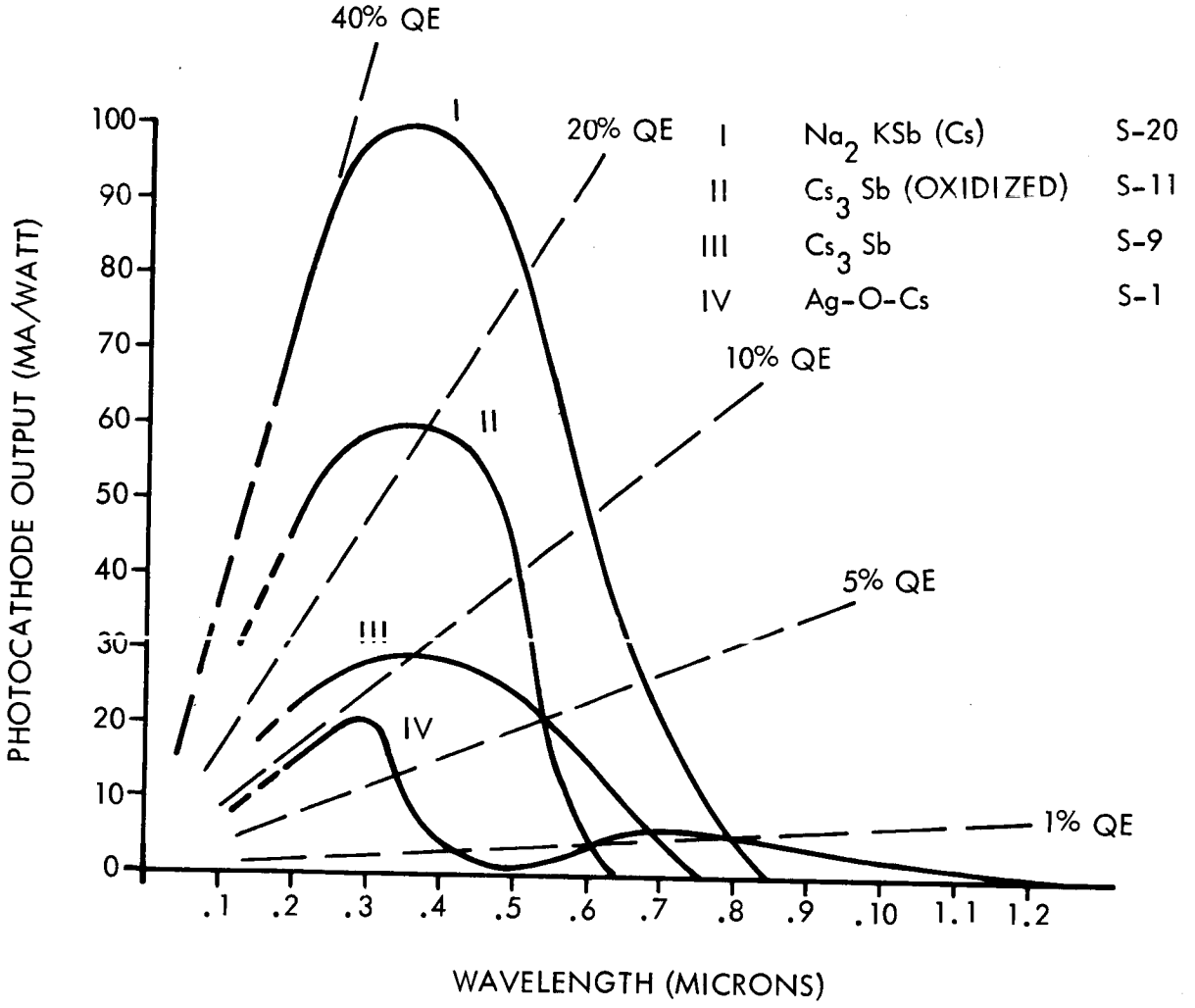


Figure 5.8.2.1-3. Spectral Response of Some Practical Photocathodes

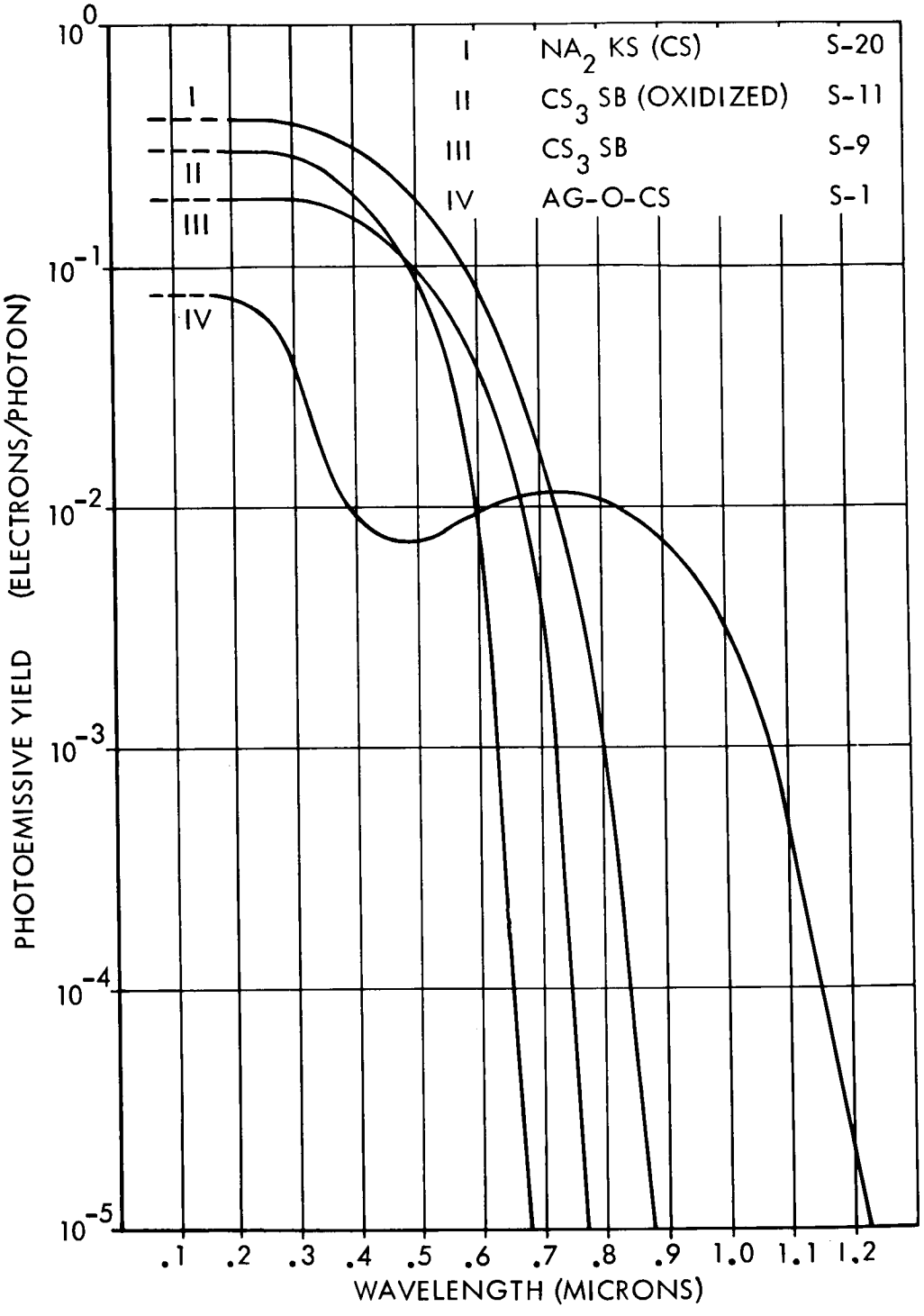


Figure 5.8.2.1-4. Quantum Efficiency of Some Practical Photocathodes

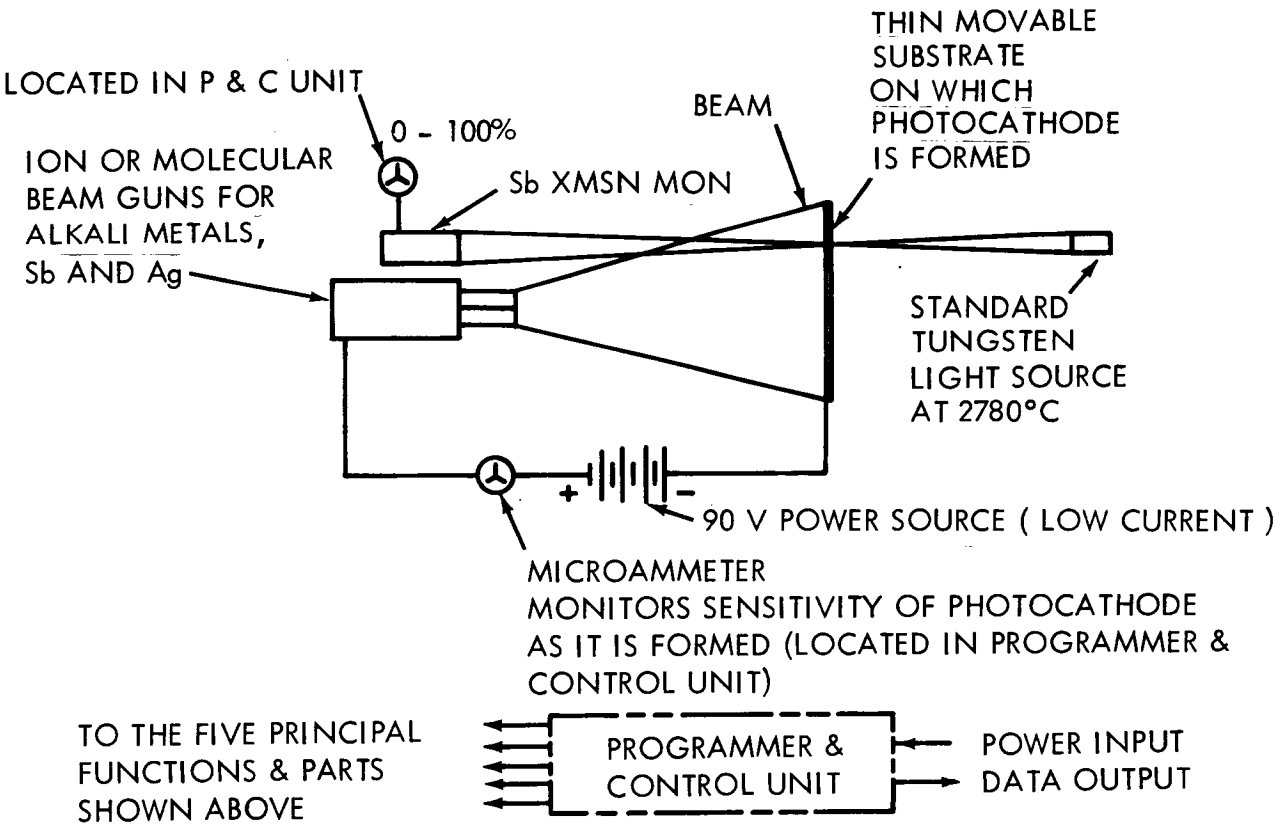
TABLE 5.8.2.1-1

PROPERTIES OF SOME PRACTICAL PHOTOCATHODES

Cathode Type	Peak Å	Maximum Quantum Efficiency at Peak	Maximum Output a/lumen	1% at Peak Å	Thermionic Emission AMPS/cm^2
S-9 Cs_3Sb	4000	20	60	7500	10^{-15}
S-11 Cs_3Sb (oxidized)	4000	30	90	6200	10^{-15}
S-20 $Na_2KSb(Cs)$	4000	40	230	8500	10^{-16}
S-1 $Ag-O-Cs$	8500	1	50	12000	10^{-12}

The conventional techniques of photocathode formation for imaging devices, all of which require the semitransparent type of cathode, start with thermal evaporation of either antimony or silver to a thickness which reduces the substrate's transmission of light from a reference value of 100 per cent to 75 per cent for antimony and 50 per cent for silver. Later the substrate is raised from its initial room temperature to a temperature of 130°C to 220°C depending on which alkali metal vapor is to be reacted with the initial layer. In the case of S-1 surface, the silver base is oxidized by a glow discharge in oxygen or some other oxidation process prior to exposure to caesium vapor at a temperature between 150°C and 200°C. The photoelectric current is monitored to achieve peak sensitivity during alkali metal evaporation. Recycling of the evaporation or yo-yo techniques are frequently used to reach maximum sensitivity. The time required to form these cathodes can be from a few minutes to 4 or 5 hours for a good S-20 surface. The formation time varies considerably depending on the technique and operator; good S-20's have been formed in as little as 20 minutes.

At present, there is apparently more art than science in the formation of good photocathodes. New investigation using molecular beam and ion techniques, however, appears to be putting photocathode technology on a more firm scientific basis. The beam methods technique should be used for space processing because they potentially offer many advantages over the conventional methods requiring a confining envelope. Figure 5.8.2.1-5 shows a schematic of a configuration using the ion beam technique for photocathode formation. Since this technique is in its infancy of development, experiments in earth-based laboratories are necessary prior to using the technique in space.



SCHEMATIC OF PHOTOCATHODE FORMATION EXPERIMENTS
FOR TWO COMPONENT (CS_3Sb), FOUR COMPONENT (Na_2KSb Cs) AND
THREE COMPONENT (Ag-O-Cs) TYPES

Figure 5.8.2.1-5. Schematic for Photocathode Formation

After completing the fabrication process, the photocathode will be transferred to the electronograph. A fine grain phosphor screen will be positioned a few millimenters, co-planar to the photocathode. A line resolution test pattern will be imaged on the photocathode, and the resulting image viewed on the phosphor screen by means of the image magnifier. Critical focusing and adjustments can be made so that resolution is optimized and distortion is minimized. Upon completion of the critical focusing adjustments, the EBR emulsion will be inserted in place of the phosphor screen so that the image is permanently recorded. Various light intensities and exposure times will be used for complete evaluation of the electronograph.

After experimenting with all types of photocathodes a time lapse of 10 to 12 days will be allowed, and then sensitivity measurements will be made to determine cathode deterioration. Various reactivation experiments could be performed to determine the best procedure for obtaining maximum sensitivity when reforming the surface.

5.8.2.2 Development Program

The reason this experiment is not recommended for OTES is that all the required technology must be developed from earth-based experiments prior to attempting the proposed technique in space. The only need for space testing would be for space qualification of a particular photoelectric device developed for a specific application.

There are necessary technology developments which must be accomplished on earth prior to attempting the technique of fabrication and assembly in space. These developments are listed below; some are presently in progress so the current state-of-development is given:

a. Development of the ion beam or molecular beam technique for fabricating photocathodes must be completed. These techniques show promise for fabricating photoemitters by a simple, reproducible procedure yielding consistent results. RCA, under contract by the U.S. Army ERDL, Ft. Belvoir, Virginia, is currently investigating these techniques. At present, the S-9 type has been successfully fabricated by the molecular beam method.(1) No photoemitters have yet been successfully produced by the ion beam technique. Sources for the constituent components are presently being investigated. The advantage of the ion beam method that the ions may be electrostatically and/or electromagnetically focused, and therefore quantitatively controlled to give consistent results. The sources are also more readily available and are easier to handle.

b. Experiments must be performed to determine the vapor pressure of the various types of photoemitters as a function of temperature.

---

(1) "Research studies to Improve the Spectral Response and Efficiency of Photoemitters", Simon R.E., et al., AD 464792L, AD 475673L, April 1965, July, 1965, AD 475674L, October 1965.

It may be that in the very high vacuum of space, disassociation occurs within a short time. The S-9 and S-20 types are believed to have a vapor pressure of approximately 10^{-14} torr at room temperature.(2) At lower temperatures the vapor pressure is lower. Dr. Burns(3) from Dearborne Observatory, Northwestern University, has reported evidence that the vapor pressure of the S-1 type at room temperature is approximately 10^{-7} toor; conclusive experiments are currently being performed.(4) It still remains to determine the disassociation of the S-1 photoemitter when cooled.

c. Reactivation experiments must be performed to determine the best procedure for reforming the photocathode. Recessiation may only be necessary or it may be necessary to refabricate with all the constituent alkali metals.

d. Evaluation must be made on the various EBR photographic emulsions that can be used in the electronographic camera. Some of these emulsions release contaiminating gases if cryogenic cooling is not provided, and the photoemitter is destroyed in a very short time. Some of these emulsions have been evaluated by Technical Operations Inc., under contract by AVRP, Wright-Patterson A.F. Base, Ohio.(5) This report defines the optimum accelerating voltage and compares those films developed for high resolution with those developed for maximum sensitivity. It still remains to evaluate these films in the electronograph to determine the best film for a particular photographic mission.

e. Radiation presents a serious problem in any space photographic mission. Long exposure times are required for photographing faint stars even with the aid of the electronograph, therefore fogging of the emulsion by particulate hard radiation or bremsstrahl secondary radiation may be severe. Therefore, investigation of fabricating and processing

---

(2) Sommer, A.H., David Sarnoff Laboratories, RCA, Princeton, N.Y., Private Communication.

(3) "Fundamental Photosurface Studies", Burns, Jay, AD474 884L, July, 1965.

(4) Dr. Sommer has questioned the validity of Dr. Burns' experimental evidence of the high vapor pressure of the S-1 photoemitter. He feels confident that the vapor pressure of commercial photocathodes such as the S-1, S-11 and S-20 is very low, probably in the 10^{-14} range, simple because of the general shape of the vapor pressure versus temperature curves. He believes that the experimental work on the Cs vapor pressure of cathode materials reported by Kansky and Jeric is most accurate so far. They found a value of 10^{-14} for Cs_3 Sb and 10^{-16} for the S-1 cathode. (LeVide Vol. 15, p. 193 (1960))

(5) "Investigation of Silver Halides for Electron-Beam Recording", Whitney, R. E., Masters, J.I., Nyyssonen, D.; AD 480292, March, 1966.

the emulsion in space should be undertaken to reduce fogging to a minimum. This procedure would also reduce the amount of shielding that would be required.

f. There is a definite need for the development of an infrared photoemitter. The S-1 photoemitter extends farthest into the infrared region, 12,000Å, but has very low quantum efficiency. Considerable effort is being made to understand the limitations of the long wavelength response of the S-1 and S-20 photoemitters. Several methods are currently being investigated to enhance the red response, such as using a reflective substrate, increasing the thickness of the photoemitter, and using a reversed bias p-n junction to generate an electric field to induce photoemission.

5.8.3 Recommendations

It is recommended that the Photo-Electro-Optical Space Experiment be discarded as an OTES experiment. However, it must be emphasized that the concept of fabricating photocathodes in space should definitely not be abandoned but developed in a large vacuum chamber on earth. While investigation of the aforementioned technique for developing photoelectric devices has not culminated in an experiment for OTES, guidelines for earth-based technological developments have evolved that would lead to the application of the fabrication and assembly technique in space.

5.9 OPTICAL TELESCOPE MIRROR COATING IN SPACE

5.9.1 Objectives

Thin films of aluminum constitute one of the best known general-purpose reflective coatings for telescope mirrors. However, it is known that aluminum oxidizes upon exposure to air, and that the Al_2O_3 layer formed on the aluminum coating is detrimental to its reflectance, especially in the ultraviolet part of the spectrum. If the aluminized mirror were never exposed to the atmosphere, this problem would not be encountered. Therefore, there is the possibility that if the aluminization is carried out in space, a significant gain in mirror performance could be achieved.

An associated experiment is that of the mirror-figuring by selective deposition of the aluminum. In general, the figure of a mirror is not perfect and it is conceivable that it could be made more nearly perfect by controlling the local thickness of the aluminum reflective layer.

The purpose of the experiment is to evaluate the improvement to be gained in telescope mirror reflectance and figure by carrying out the coating process in space, possibly with a means of controlling the local thickness of the coating.

5.9.2 Discussion

Mirrors for reflecting astronomical telescopes are normally made of glass or quartz, chosen for their ease of shaping to the correct figure, and their low coefficients of thermal expansion. Since these materials are poor reflectors, a thin coat of some highly reflecting material (usually a metal) is usually placed on them. Originally (until the 1930's) silver was the material commonly used for this purpose. It was chosen for its high reflectance in the visible spectrum (approximately 98 per cent) and for its ease of application (it could be applied by a simple chemical process). However, silver mirror coatings suffer from two inherent disadvantages:

a. Despite the fact that silver is a noble metal, it reacts with certain atmospheric constituents, notably sulphides, and also oxygen, forming a poorly reflecting layer of tarnish on the surface. This necessitates periodic cleaning and re-silvering of the mirror.

b. Silver, even in the elemental state, is a poor reflector in the ultraviolet portion of the spectrum. Figure 5.9.2-1 includes a curve of the reflectance of silver as a function of the wavelength of the incident light. This curve shows that the reflectance of silver drops off sharply below about 4000Å.

As high-vacuum technology was developed in the 1930's, it was learned that highly reflecting metallic films could be formed by vacuum evaporation. In this method of preparation a quantity of the metal is heated to a temperature high enough to cause rapid vaporization and the vapor is allowed to condense on the cooler substrate (the polished mirror), all in high vacuum. Aluminum films formed in this fashion have proved to be particularly useful. Vacuum evaporated aluminum forms a smooth, coherent film which can be highly reflective. As can be seen in figure 5.9.2-1 the reflectance of aluminum approaches that of silver in the infrared and exceeds 90 per cent throughout most of the visible and ultraviolet spectrum down to about 2200Å. Aluminum films, although not unaffected by exposure to the atmosphere, are affected less and more slowly than silver films, thus easing the problem of periodic mirror recoating.

Films of other materials can be formed using a variety of techniques, but none seem to offer the versatility of aluminum with its high reflectance over a wide range of wavelengths. Platinum, for instance, offers a reasonable reflectance in the vacuum ultraviolet (below 1000Å), but is rather poor in the visible and infrared.(1)(2) Also, the formation of platinum films is complicated by the fact that the substrate must be heated to about 200C.

(1) Jacobus, G.F., Madden, R.P., and Canfield, L.R., "Reflecting Films of Platinum for the Vacuum Ultraviolet", Journal of Optical Society of America, 53 (1963), 1084.

(2) Jacobus, G.F., U.S. Army Engineers Research & Development Laboratories, Ft. Belvoir, Va., Private Communication, Feb. 7, 1966.

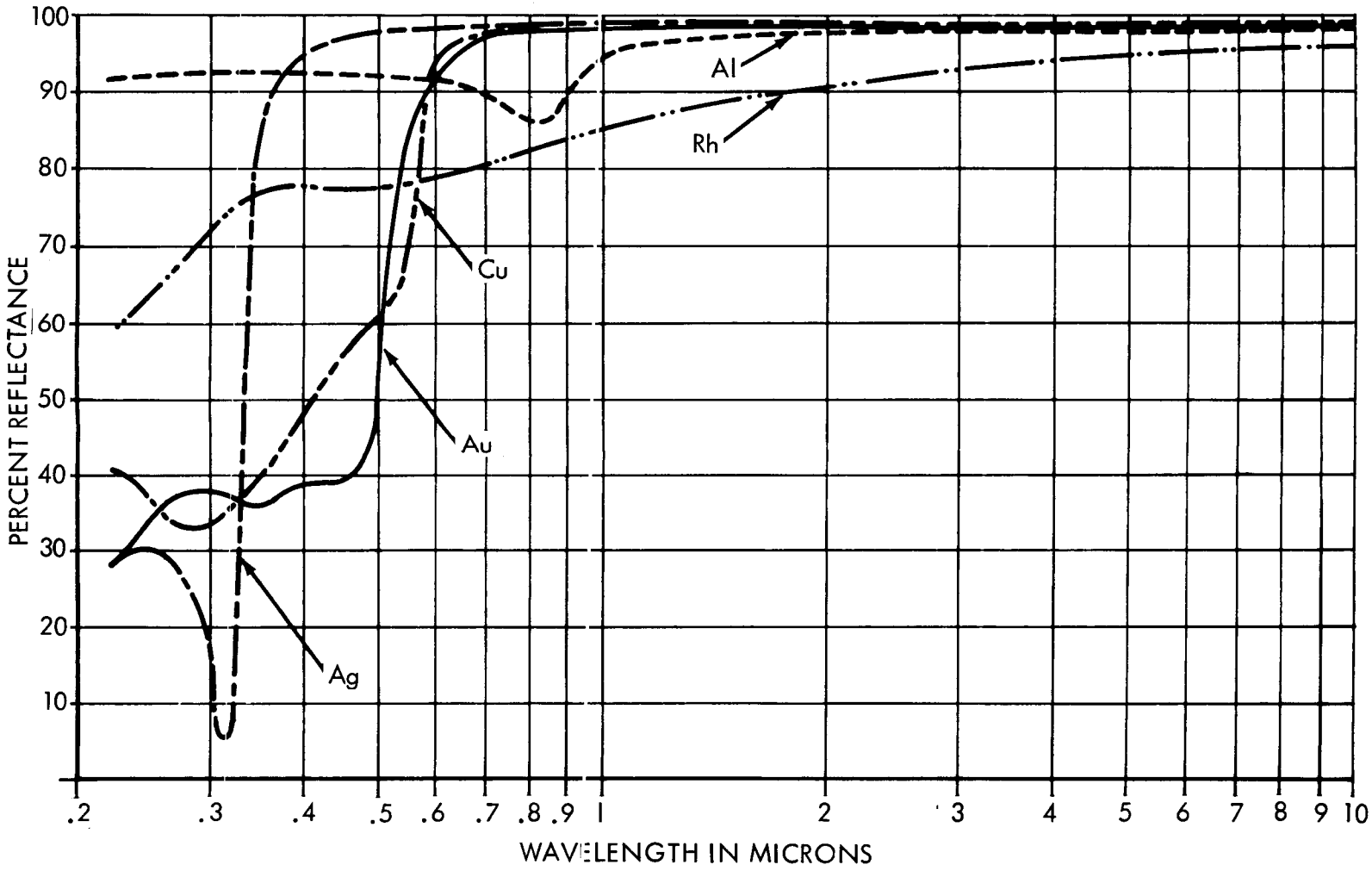


Figure 5.9.2-1. Reflectance of Freshly Deposited Metallic Films as a Function of Wavelength (Reference 3)

For these reasons, aluminum is usually the choice for coating a mirror intended for multipurpose use.

In the study of the reflective properties of thin aluminum films, however, at least two undesirable features have been discovered.

a. In the far-ultraviolet region of the spectrum, the reflectance of aluminum falls to a rather low level (figure 5.9.2-2). The best reflectance which can be obtained from an aluminum film, as seen in the figure, is slightly over 50 per cent at 1026Å (Lyman α).

b. The reflectance of aluminum films is adversely affected by exposure to the atmosphere. The aluminum reacts with atmospheric oxygen to form a surface layer of Al_2O_3. The layer Al_2O_3 is less reflective than the elemental aluminum, especially in the ultraviolet, and is undesirable. The rate of formation of the oxide layer is a variable quantity, depending not only on the amount of oxygen available, but also on such things as the amount of water vapor (figure 5.9.2-3) which apparently catalyzes the reaction in some fashion. Thus, even the aluminum coating mirror requires periodic cleaning and recoating, although it can generally remain in useful service for a longer period than a silvered one.

A considerable amount of research has been devoted to the improvement of the mechanical and optical properties of evaporated aluminum films. It has been discovered that a number of factors influence the quality of the aluminum.(3)(4)(5)(6)(7)(8) Among these factors are: (1) the vacuum at which the evaporation is carried out, (2) the rate at which the evaporation is carried out, (3) the purity of the aluminum used for the evaporation, (4) the substrate temperature during the evaporation, (5) the aging

---

(3) Hass, G., "Filmed Surfaces for Reflecting Optics", Journal of Optical Society of America., 45, (1955), 945.
(4) Holland, L., "The Effect of Gettering on the Reflectivity of Aluminum Films", British Journal of Applied Physics, 9 (1958), 336.
(5) Hass, G., Hunter, W.R., and Tousey, R., "Influence of Purity, Substrate Temperature, and Aging Conditions on the Extreme Ultraviolet Reflectance of Evaporated Aluminum", Journal of Optical Society America, 47 (1957), 1070.
(6) Bennett, H.E., Silver, M. and Ashley, E.,"Infrared Reflectance of Aluminum Evaporated in Ultra-High Vacuum", Journal of Optical Society of America., 53, (1963) 1089.
(7) Hass, G., Hunter, W.R. and Tousey, R., "Reflectance of Evaporated Aluminum in the Vacuum Ultraviolet", Journal of Optical Society of America, 46, (1956), 1009.
(8) Holland, L., Vacuum Deposition of Thin Films, Chapman and Hall, Ltd., London, 1963.

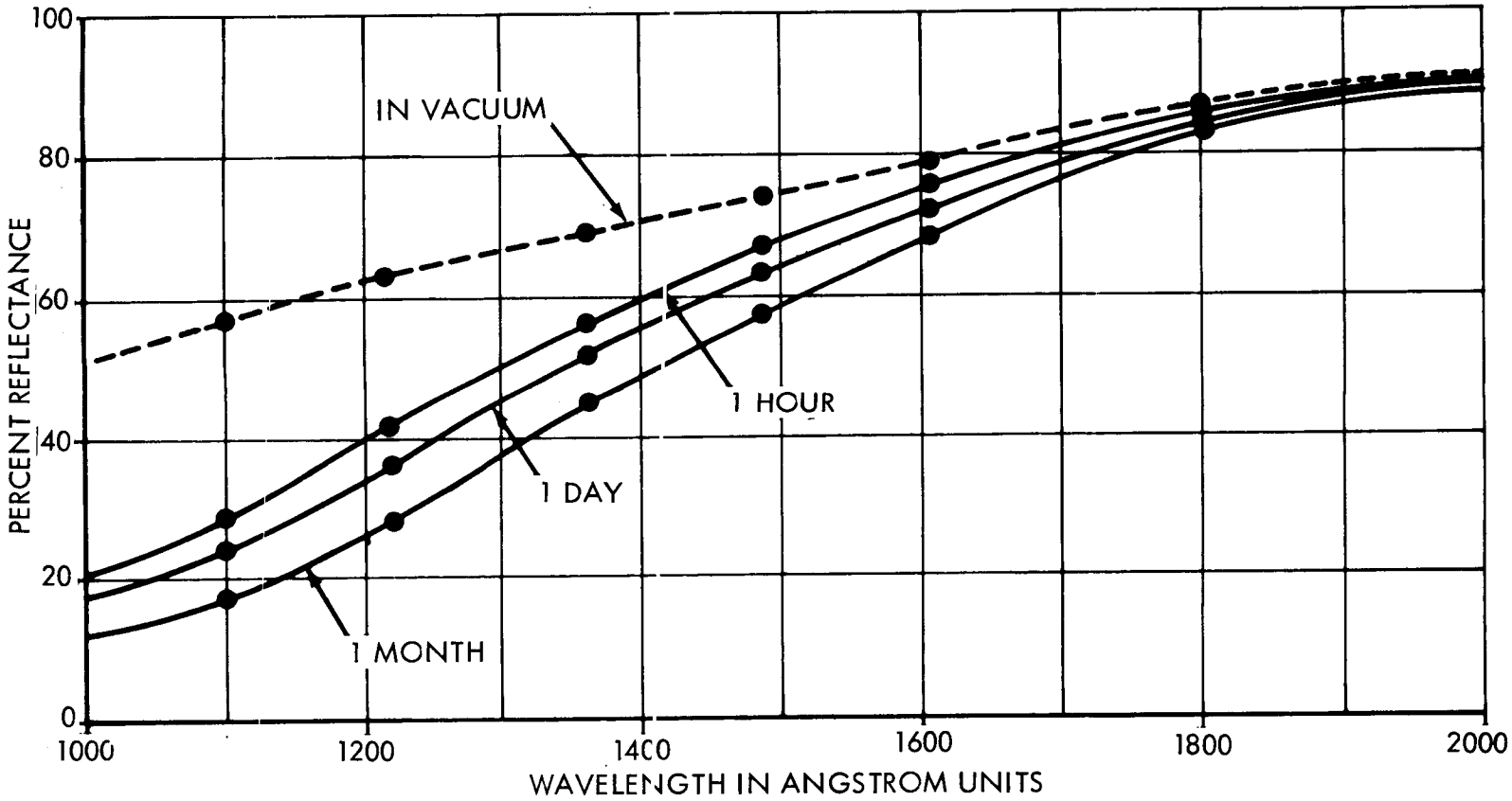


Figure 5.9.2-2. The Reflectance of Best Quality Aluminum Films as a Function of Wavelength for Different Lengths of Time of Exposure to Air (Reference 14)

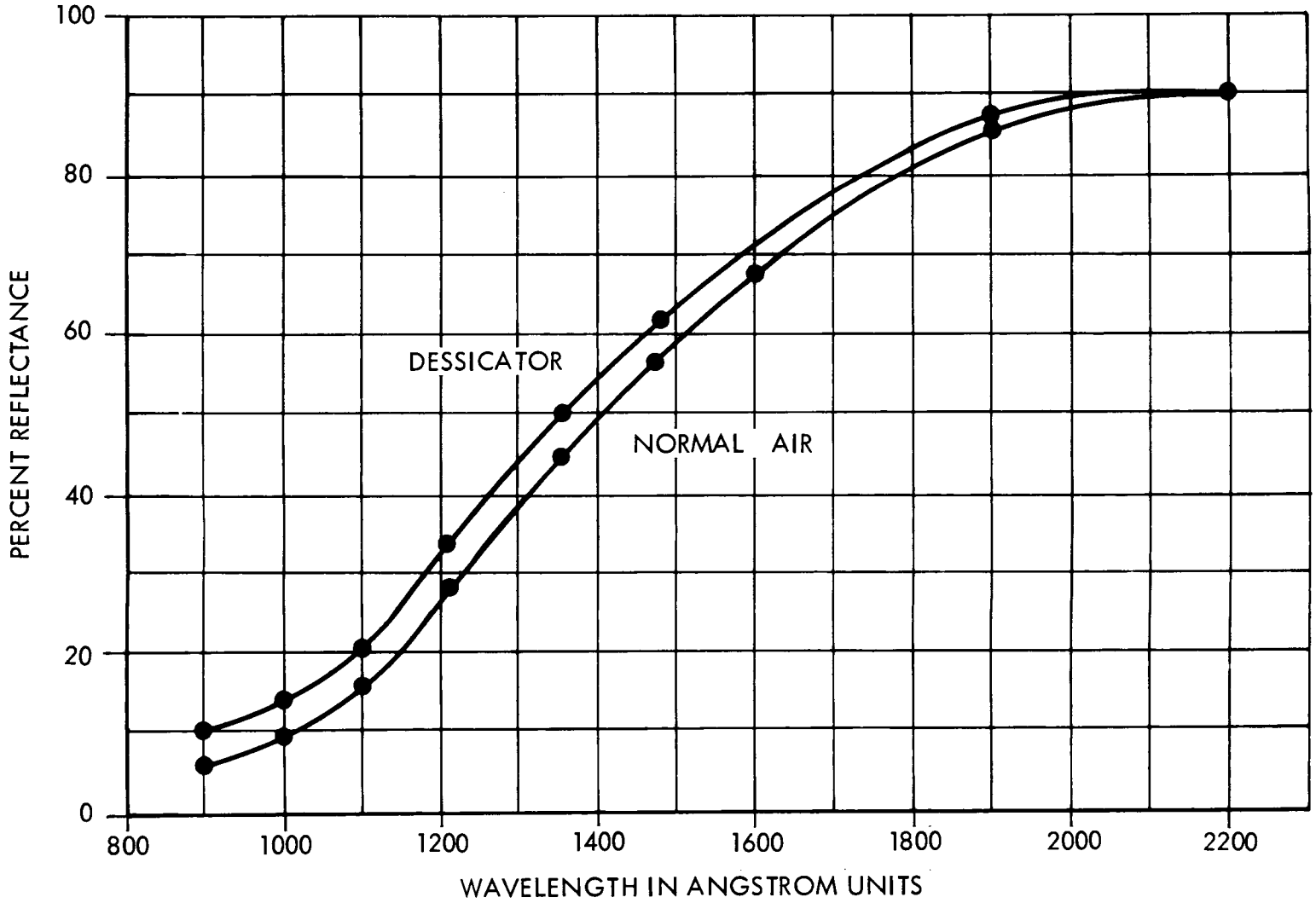


Figure 5.9.2-3. The Effect of Storage in Dry Air (Dessicator) and in Normal Air (30-50% Humidity) on the Reflectance of Pure Aluminum (Age when Measured 2 Months) (Reference 5)

conditions of the coating, (6) the thickness of the film, and (7) the angle at which the evaporated aluminum atoms strike the surface. However, even when all of these parameters are controlled to give the best results possible, the aluminum coating is still less than perfect. The reflectance still decreases in the ultraviolet and is still degraded by oxidation.

Further improvements in aluminum coated mirrors came with the development of dielectric overcoatings. The reflectance of a surface at normal incidence is given in the referenced document.(9)

$$R = \frac{\bar{n}_o - \bar{n}_2}{\bar{n}_o + \bar{n}_2}^2 \qquad (1)$$

where $\bar{n}_o$ is the index of refraction of the first medium and $\bar{n}_2$ is the index of refraction of the second medium. In the case of abosrbing media, for example, aluminum, $\bar{n}$ is a complex number,

$$\bar{n} = n - ik \qquad (2)$$

where k is the aborption coefficient. For reflection at a dielectric metal boudnary, for example, air-aluminum,

$$R = \frac{n_o - n_2 + ik_2}{n_o + n_2 - ik_2}^2 \qquad (3)$$

If a layer of another dielectric material is placed on top of the metal, the reflectance is changed. It becomes wavelength dependent because of interference effects, and a further angular dependence is introduced for the same reason. For a 1/4 wavelength thickness, which gives maximum reflection at that wavelength, and for normal incidence,

$$\left[R = \frac{\bar{n}_o\bar{n}_2 - \bar{n}_1^2}{\bar{n}_o\bar{n}_2 + \bar{n}_1^2} \right]^2 \qquad (4)$$

or

$$\left[R = \frac{n_o (n_2 - ik) - n_1^2}{n_o (n_2 - ik) + n_1^2} \right]^2 \qquad (5)$$

It can be seen from a manipulation of equations (3) and (5) that if a non-absorbing medium with a suitable refractive index (n_1) can be found, the reflectance can be increased by this extra film, called an overcoat. This overcoat can then serve two purposes: increasing the mirror's reflectance in the ultraviolet and protecting the aluminum surface from the atmosphere.

---

(9) Heavens, O.S., Optical Properties of Thin Solid Films, Dover, N.Y., 1965.

A considerable amount of research has also been devoted to the subject of overcoating for mirrors.(10)(11)(12)(13)(14)(15) Silicon monoxide has proved to be a useful material for overcoating purposes. Although the properties of the overcoated mirror depend on the manner in which the overcoat is produced, it is possible to produce a mirror with reflectance of better than 80 percent from 2,200Å to 8,000Å.(10) Unfortunately, the reflectance drops off rapidly below 2,000Å(16) and the material exhibits an absorption peak in the infrared at about 10,000Å. Since it is desirable that a mirror for space applications be usable down to at least 1,026Å (Lyman α) and in the infrared, the silicon monoxide overcoat is not ideal. Other materials which have been studied for this application are magnesium fluoride and lithium fluoride. With these materials it has been possible to produce mirrors which are highly reflective well into the ultraviolet.(15) In fact, it has been possible to produce a mirror, using lithium fluoride overcoating, which has a reflectance of 72 percent at 1,026Å, increasing gradually with increased wavelength until the reflectance in the visible and infrared is essentially the same as a good aluminum surface.(16)

In view of these facts there seems to be no purpose in adding the complexity of mirror coating to a spacecraft. It appears to be possible to construct a mirror in an earth laboratory which is significantly better than an unoxidized aluminum one, and whose properties are unaffected by the earth's atmosphere. This conclusion is supported by Jacobus.(3)

---

(10) Bradford, A.P. and Hass, G., "Increasing the Far Ultra-Violet Reflectance of Silicon Monoxide Protected Aluminum Mirrors by Ultra-Violet Irradiation," Journal of Optical Society of America, 53, (1963), 1096.

(11) York, D.B., "Properties of Evaporated Thin Films of SiO," Journal of Electrochemical Society., 110, (1963), 271.

(12) Bradford, A.P., Hass, G. McFarland, M., and Ritter, E., "Effect of Ultra-Violet Irradiation on the Optical Properties of Silicon Oxide Films", Applied Optics, 4, (1965), 971.

(13) Hass, G. and Scott, N.W., "Silicon Monoxide Protected Front-Surface Mirrors", Journal of Optical Society of America, 39, (1949), 179.

(14) Berning, P.H., Hass, G., and Madden, R.P., "Reflectance-Increasing Coatings for the Vacuum Ultra-Violet and Their Applications", Journal of Optical Society of America, 50, (1960), 586.

(15) Angle, D.W., Hunter, W.R., and Tousey, R., "Extreme Ultra-Violet Reflectance of LiF - Coated Aluminum Mirrors", Journal of Optical Society of America, 51, (1961), 913.

(16) Waylonis, J.F., U.S. Army Engineer Research and Development Laboratories, Ft. Belvoir, Virginia, Private Communication, Feb. 7, 1966.

Another reason advanced for performing the coating operation in space is that aluminum coatings give maximum reflectance when the evaporated atoms strike the surface at normal incidence. In a comparatively small vacuum system this can at best be approximated by using multiple evaporation sources. In space, on the other hand, a single source could theoretically be placed a long distance from the mirror (ideally at the center of curvature of a spherical mirror), thereby achieving the normal incidence condition.

Unfortunately, this would seem to present practical difficulties. In most telescope designs, the secondary mirror is between the primary mirror and its center of curvature. Therefore, in order to coat the primary mirror, either the secondary mirror must be removed, or the source must be placed between the primary and secondary mirrors. In fact, if both were to be coated in one operation, the source would have to be distant from both the secondary and the primary mirrors. It would be difficult to meet these requirements without sacrificing the advantage of having the source far from the mirror surface, or introducing the requirement of assembly after coating.

There is also the associated problem of designing a suitable apparatus so that only the mirror surfaces are coated. This is particularly important since the currently visualized telescope design includes some refracting elements whose performance would be seriously degraded by any aluminum coating. The opinion that these operational difficulties would probably make the idea impractical is confirmed by Rosett.(17)

One further possible problem exists. According to Hass(3) the aluminum evaporation must be carried out quickly (about 5 seconds) in a reasonable vacuum in order to produce a high quality surface. Bennett, et al,(6) find that there is a relationship between vacuum and required evaporation rate to produce a high quality surface -- the poorer the vacuum, the faster the evaporation must be performed. This result seems to be confirmed by Holland(8) who predicts the quality of the surface by calculating the number of impurity atoms and molecules while strike the surface during the evaporation process. Jacobus,(1) a co-worker of Hass, does not agree, but finds that the evaporation must be done quickly regardless of the vacuum.

According to the U.S. Standard Atmosphere,(18) the pressure at an altitude of 100 nautical miles is 1.4 times 10^{-6} torr, the gas particle density is 1.17 times 10^{10} particles/cm^3, and their mean velocity is 9.087 times 10^4 cm/sec. These values indicate that 1.76 times 10^{14} particles would strike unit area in unit time. If a 500Å-thick aluminum film is

---

(17) Rosett, B., (Kollsman Optical Co.,), Private Communication, Feb. 4, 1966.
(18) U.S. Standard Atmosphere, 1962.

deposited in 1 min, about 5 times 10^{15} particles/cm^2/sec would strike the surface. Thus, some 3.5 per cent of the particles striking the surface would be impurities. Furthermore, according to the U.S. Standard Atmosphere, the mean free path for a gas molecule at this 100-mile altitude is about 150 m. If the evaporation source were a large distance from the surface, an appreciable number of aluminum atoms would be scattered before striking the surface, and might strike at an angle, degrading the quality of the coating. Thus, regardless of which workers are correct, it would seem to be difficult to produce a good coating at this altitude, and, according to the results of Bennett, et al, a much shorter evaporation time (less than 1 minute) would be necessary, possibly imposing an operational problem. At high altitudes, the vacuum seems to be no problem, but Hass's results still indicate the necessity of a fast evaporation.

5.9.3 Recommendations

From the above discussion it is concluded that the performance of the mirror coating operation in space would inpose difficult operational requirements and would probably result in a poorer quality mirror than could be fabricated in an earth laboratory. It is, therefore, recommended that the idea be discarded. This does not mean that the ultimate in mirror coating has been achieved, but that further experimentation should be ground-based rather than space-based.

The associated experiment of mirror figure control by controlled deposition of aluminum may have some merit, but not enough information has been gathered to make a definite statement. However, since it seems to be impractical to carry out the evaporation in space, this work would logically be part of a ground-based program, rather than being part of OTES.

Finally, it is recommended that this experiment be reconsidered at a later date in terms of satisfying the objective of refurbishing mirror surfaces degraded by the space environment. This reconsideration should be based on better definition of the actual degradation of optical materials due to the space environment. That is, experiments of the nature described in 4.17 Degradation of Optical Materials should properly proceed the development of refurbishing techniques in space.

6.0 POTENTIAL OTAES EXPERIMENTS

As with any technology program there is a continuing evolution of technological requirements. For that reason new experiments can be expected to evolve during the course of the OTES program. Therefore new experiments will be considered as the possible need becomes apparent. These will then be either rejected or advanced to the recommended status as the investigation indicates. Potential OTES experiments which have not been investigated in sufficient depth to make such a recommendation are presented in this section.

6.1 FAR INFRARED INTERFERENCE SPECTROSCOPY

At wavelengths much shorter than 100Å, the technology involved in sensing and spectroscopy is scarcely different from that used in the visible region, and at wavelengths longer than 7 millimeters the implementation is well within the reach of microwave technology which is already employed in many system concepts. The region from 100Å to 7 millimeters is one in which experiments, both on earth and in space, would be of great value in developing the technology necessary to fill the gap in our observable range of the electromagnetic spectrum. Implementation of this technology holds enormous potential for ultimate measurements in this range and would be of great value for comparison with data obtained using purely visible or purely microwave technology.

Millimeter and submillimeter waves are of particular importance to future scientific measurements which must be made to learn more about planetary atmospheres and the earth's atmosphere, wide-band communications or telemetry, and radio astronomy of the solar system, Milky-Way and extra-galactic sources. A useful supplementation of both optical astronomy and microwave radio astronomy might be achieved by the operation of extra-terrestrial millimeter and submillimeter radio-metric systems. Because water vapor and oxygen absorption are so great in the earth's atmosphere at wavelengths shorter than 3 millimeters, it is difficult to obtain interpretable results from a ground-based observation station. If systems such as interference spectrometers could be perfected for use in space so as to present an opportunity for instrumenting broad frequency coverage in the millimeter and submillimeter range, data could be obtained which would lead to a better understanding of the sources now being observed.

The necessary technology development can be divided into three areas:

a. Optical elements.

b. Detectors.

c. Submillimeter optical systems.

Wavelengths involved range from a few hundred to a few thousand times as long as the visible wavelengths. Therefore for comparable spatial resolution, absolute tolerances in the figure and alignment of reflectors and lenses

are correspondingly greater, as are the required physical dimensions. The reduced accuracy requirements allow new and novel methods of constructing the optical components to be tested and used. Weight being a prime consideration, however, development work is needed to develop lightweight, easily packaged components which will hold their shapes to given tolerances in the severe thermal environment of space.

Development of suitable detectors and detector systems is critical, especially in this part of the spectrum. Two types of detectors have sufficient sensitivity for use in this range, the doped-germanium bolometer and the indium-antimonide photoconductor, both of which have demonstrated in the laboratory sensitivities of 10^{-12}watt/$Hz^{\frac{1}{2}}$. Because the bolometer element must be small and isolated, it is a very fragile device, and it is doubtful that it could survive launch. The element of an indium-antimonide photodetector, however, can be rigidly mounted in a structure having a high probability of survival. A closed-cycle helium cooling system will be necessary for operation of this detector.

It is felt that three types of submillimeter optical systems need continued developmental work:

a. High-Resolution Telescope.

b. Fabry-Perot Interferometer.

c. Submillimeter Interference Spectrometer.

A millimeter telescope with a diameter in excess of 4 meters is a realistic, desirable goal for an orbiting observatory. The development work necessary is in the design of sectioned reflectors of this size and perfection of packaging, deployment, and adjustment techniques commensurate with the needs. These problems can be adequately analyzed and resolved by experimentation on earth.

A Fabry-Perot Interferometer perfected for use in space would have numerous applications:

a. Resonant structure for long-wavelength laser.

b. Extremely narrow-band filter.

c. Spectroscopic chamber.

d. Stabilization cavity.

The instrument would be useful in analyzing atmospheres as part of a planetary probe. Much could be added to optical, infrared, and millimeter technology by conducting experiments on a 4 millimeter Fabry-Perot Interferometer with a stabilized klystron excitation source in a simulated launch and space environment. The investigation which has been directed to this technology area has not been sufficient to justify a recommendation on space experiments.

The interference spectrometer is important as a potential means of remotely sensing the major constituents of planetary atmospheres.

6.2 GROUND RESOLUTION MEASUREMENTS IN EARTH ORBIT

There may be a need for space experiments to be performed to obtain statistical data on the resolution limitations of a telescope system as a function of atmospheric turbidity, spectral band, and orbit altitude. To accomplish this it is necessary to separate the resolution degradation effects due to the atmosphere as opposed to those caused by pointing instability, launch disturbances,mirror figure and intrinsic aberration inherent in the telescope system. The need for such an experiment is exhibited by the numerous applications of the data to serve as guidelines for designing imagery systems for mapping functions, meteorological studies, navigation, and traffic analysis and control. For example, estimates of the required resolution to define cloud characteristics have been given in the range of 20-5000 feet; storm formation studies require a resolution of approximately 500 feet. Mapping functions for defining boundaries and topographic features require resolution in the range of 2-20 feet, whereas traffic identification and control may require extremely high resoltuion in the range of 1-20 feet(1). In designing telescopes for earth sensing as defined above, it is highly desirable to have statistical data of the atmospheric effects on system resolution.

Considerable earth-based studies of the atmospheric disturbance on image quality have been made. Most of the experimental work has been over horizontal paths of limited range, and therefore the results are not applicable to the very long vertical optical path of a telescope in orbit. Some experiments performed by Smith (2) at the University of Florida did establish that photographic resolution is very much dependent upon the location of the disturbance along the optical path. Turbulence located near the camera had a very severe effect on the resolving power of the system, whereas turbulence near the object did not reduce the photographic resolution very much. Even with turbulence midway between the object and the camera the resolving power was only half that obtained in an undisturbed media. Considering these results we could surmise that the resolving power of a telescope system for earth sensing would be considerably better than the same telescope used to observe stellar objects. It would be advantagecus to have statistical data to determine the improvement in resolving power and limitations created by the earth's atmosphere.

Attenuation of photographic contrast by the atmosphere has been studied by Majurowski,(3) and experiments performed using aircraft to make observa-

---

(1) ORL Experiment Progress, Part V, Vol. 1B, IBM Atmospheric and Service Technology, 1966.

(2) "Some Effects of Turbulence on Photographic Resolution", Smith, A.G., Saunders, M. J., Vatsla, M. L; Journal of the Optical Society of America, Vol. 47, No. 8, August 1957.

(3) "Attenuation of Photographic Contrast by the Atmosphere" by Majurowski, M. J., Sink, D. R; Journal of the Optical Society of America, Vol. 55, No. 1, January 1965.

tions at altitudes up to 50,000 feet. The results of these experiments show that at altitudes below 10,000 feet, there is little spectral selection by the atmosphere, and above 10,000 feet the spectral selectivity of the atmosphere approaches that of Rayleigh scattering. Thus, in the red region there is considerably less degradation of contrast than in the blue region. Confirmation of this result at very high altitudes could easily be obtained. It was attempted to make a correlation between types of air masses and contrast degradation. In general, it was found that high contrast transmittance is associated with continental polar air masses, and low contrast transmittance is associated with maritime tropical air masses. There is insufficient experimental data to make a definite statement about the relationship, and verification of the above generalization requires a much larger sample of photographic data under a wider variety of meteorological conditions. This data could very conveniently be obtained from an orbiting telescope for earth-sensing experiments.

Implementing such an experiment to determine the degradation effects of the atmosphere on resolution could be accomplished by making the following measurements:

a. Angular resolution of the optical system from images of point sources of known angular separation, such as star binaries.

b. Ground resolution from known separation of preselected or specially fabricated earth objects.

While making earth observations, meteorological data would be obtained so that a correlation may be made between resolving power and the prevailing weather conditions.

At the time of this writing, it is not possible to make a recommendation on the need for a space experiment.

6.3 SPACE PHOTOGRAPHY EXPERIMENTS

The advent of space photography has created new requirements for photographic emulsions. This has created the need for development programs in this particular area. In some instances space tests may be an important element of this development program. For instance, there is at present a great deal of uncertainty associated with radiation effects on photographic emulsions. A simple evaluation of these effects in earth orbit may contribute substantially to the design of scientific experiments. At any rate, space photography is recognized as a technological area which should be investigated further in terms of OTAES experiments.

6.4 DEGRADATION OF OPTICAL MATERIALS AND COATINGS

In recent years there has been considerable interest in the behavior of optical materials in the space environment. Considerable attention has been devoted to solar cells.(1) Much work has appeared in the literature of solid state physics on the effects of high energy irradiation of optical crystals and glasses. Unfortunately, the irradiation dose is usually much larger than what one would expect to encounter in an earth orbit of one year duration.(2) A continuing effort is required to support the anticipated expansion of space optical activities.(3)

In some cases it is not unreasonable to simulate the effects of space by irradiating with high-energy electrons; but, as mentioned above, the dosages are usually high and actual space testing is desirable. Micrometeoroid densities, particle sizes, and momenta are not predictable and evaluating the effects of these characteristics on optical materials require space testing.

It is expected that an experiment should be designed in which suitably selected samples of optical materials are to be exposed to space for varying time intervals and then returned to earth for physical and optical testing. Conceptually one can consider a simple movable mask device being used in a manner analogous to that used by amateur photographers; i.e., a test strip is made on projection paper to enable the subsequent evaluations to account for the varying exposure times on the various samples. During the experiment auxiliary measurements of the space radiation and micrometeoroid environment are recorded to provide correlation of surface bombardment with optical degradation.

---

(1) F.J. Campbell, "Status of Solar Cell Cover Material Radiation Damage", Proceedings of the Fifth Photovoltaic Specialists Conference, Goddard Space Flight Center, October 19, 1965.

(2) D.F. Heath and P.A. Sacher, "Effects of a Simulated High-Energy Space Environment and the Ultraviolet Transmittance of Optical Materials between 1050 Å and 3000 Å", Applied Optics, June 1966, 5:6, p. 937.

(3) Space Research: Directions for the Future (Part II) Space Science Board, Washington, D.C., January 1966.